Optical Packaging of Microlens over UV-LED-Array

Markus Luetzelschwab

A dissertation submitted for the degree of Doctor of Philosophy

Heriot-Watt University

School of Engineering and Physical Sciences

June 2008

Abstract

This thesis is part of a project entitled "One thousand emitters per square millimetres", an EPSRC project funded under the Basic Technology Programme. The project is jointly run between Heriot-Watt University, The Institute of Photonics at the University of Strathclyde, Imperial College London and the University of Sheffield. The overall aim of the project is to design, manufacture and package a UV-LED array for a variety of bio-medical applications.

The objective of the research work presented here is the support to other partners in the assembly of a microlens array on top of a UV-LED array.

This work focuses on the design, manufacture and characterisation of a packaging structure that places a microlens array on top of a micro-UV-LED array. The required lateral tolerance was defined to be less than 2μm. Two approaches were considered and systematically characterised. In the static approach, the microlens array is to be accurately placed and fixed on the LED array. In the dynamic approach, the microlens array is moveable in the vertical as well as lateral directions. Post processing of the lens and LED arrays has been carried out using a modified UV-LIGA process. The microlens array rests on four posts, to reduce lateral as well as vertical contact area for the static approach, hence reducing the probability of misalignment. Using electroplating of electrodes that are situated on the micro-UV-LED array structure, vertical alignment of the microlens array with sub-micron accuracy has been demonstrated.

The dynamic approach features a vertical electrostatic and a lateral magnetic actuator that can be driven simultaneously. Both actuation methods exert a force on the microlens array without the need of a physical contact, which eases the fabrication and assembly process. As a restoring means, gel bumps are currently employed which exhibit the necessary isotropic elasticity for the lateral and vertical movement. The electrostatic actuator is able to achieve displacements of over 70μm and shows good repeatability with a standard deviation of 0.43μm at a mean value of 24.75μm. The magnetic actuator achieves lateral movement exceeding 50μm. Both actuation methods have been demonstrated to offer sub-micron displacement accuracy. Due to the

viscoelastic properties of the gel bumps and with appropriate equipment, accuracies in the order of tens of nanometres are feasible.

“I have never met a man so ignorant that I couldn’t learn something from him.”

Galileo Galilei (1564-1642)

Acknowledgements

Of all the people I am involved within this research, I am most grateful for the advice, support and motivation from my supervisor, Professor Marc Desmulliez. Many thanks for having given me the chance in the first place of being involved with this immensely interesting project. Merci beaucoup!

I would like to thank Mark Leonard for his advice and support in all cleanroom issues. I also thank all the academic and technical staff as well as the "supersecys" from EM 2.43 for their help and support. Thanks also to many of the colleagues at Heriot-Watt University.

A special thank goes to Dr Dominik Weiland with whom I spent a lot of time in discussions and brainstorming activities especially for manufacturing matters but in particular for the help on software issues.

The entire Scottish adventure would not have been possible without the advice and inspiration of Peter Kaiser who encouraged me to do the MSc and this Ph.D. in the first place.

A huge thank you goes to my parents and my brother with his family, for supporting me throughout my Ph.D., being my backbone in Switzerland and for ensuring a continuous supply of chocolate and fondue cheese. Thanks also to my aunt and my godmother for their support.

Many thanks also to my friends in Switzerland, Britain and Spain or wherever they are.

A very special thanks goes to Paz Gordon, who supported me so much in the last stages of thesis writing and for having coped with me during this time. Thanks also to her family.

ACADEMIC REGISTRY
Research Thesis Submission

Name:	Markus Luetzelschwab		
School/PGI:	EPS / EECE		
Version: *(i.e. First, Resubmission, Final)*	Final	Degree Sought:	Ph.D.

Declaration

In accordance with the appropriate regulations I hereby submit my thesis and I declare that:

1) the thesis embodies the results of my own work and has been composed by myself
2) where appropriate, I have made acknowledgement of the work of others and have made reference to work carried out in collaboration with other persons
3) the thesis is the correct version of the thesis for submission*.
4) my thesis for the award referred to, deposited in the Heriot-Watt University Library, should be made available for loan or photocopying, subject to such conditions as the Librarian may require
5) I understand that as a student of the University I am required to abide by the Regulations of the University and to conform to its discipline.

* *Please note that it is the responsibility of the candidate to ensure that the correct version of the thesis is submitted.*

Signature of Candidate:	M. Luetzelschwab	Date:	6.6.08

Submission

Submitted By *(name in capitals)*:	Markus Luetzelschwab
Signature of Individual Submitting:	M. Luetzelschwab
Date Submitted:	6.6.08

For Completion in Academic Registry

Received in the Academic Registry by *(name in capitals)*:	AMcVittie		
Method of Submission *(Handed in to Academic Registry; posted through internal/external mail)*:	handed in		
Signature:		Date:	6/6/08

Table of Contents

Optical Packaging of Microlens over UV-LED-Array i
Markus Luetzelschwab i
A dissertation submitted for the degree of Doctor of Philosophy i
Heriot-Watt University i
School of Engineering and Physical Sciences i
April 2008 i
Abstract ii
Acknowledgements v
Table of Contents vi
List of Figures viii
List of Tables xvii
Glossary xviii
Publications from the author xxii
Chapter 1 1
Introduction 1
1.1 Motivation and outline of this thesis 1
1.2 Layout and objective of the thesis 2
Chapter 2 5
Literature Review 5
2.1 Introduction 5
2.2 Microactuation methods 5
2.2.1 Definition actuator properties 5
2.2.2 Different actuation methods 9
2.2.3 Comparison of electrostatic and magnetic actuators 33
2.3 Existing static alignment methods 34
2.4 Actuation used for microlenses 37
2.5 Conclusions 38
Chapter 3 40
Design of the Packaging 40
3.1 Original design of the functional layer 50
3.2 Static Approach 51
3.2.1 Reduction of vertical and lateral overdetermination 52
3.2.2 Correction of the alignment 54
3.2.3 Electroplating of the cavities 55
3.2.4 Fixing and sealing 57
3.3 Dynamic approach 58
3.3.1 Electrostatic actuation 59
3.3.2 Viscoelastic behaviour of polymers used as a restoring force 69
3.3.3 Magnetic circuit of the lateral actuator 77
3.3.4 Alternative method to ferromagnetic posts 80
3.3.5 The external driving device and dual actuation 82
Chapter 4 86
Manufacture 86
4.1 Manufacturing of the micro-UV-LED array package structure (μLED) 86
4.2 Manufacture of supporting posts on the substrate of the microlens 91
4.3 Handling of die with small dimensions 95
4.4 Electroplating of accurate electrode thickness for height adjustment 101
4.4.1 Electrical contact with conductive adhesive (first design) 101
4.4.2 Electroplating of current design devices 105
4.4.3 Adhesion problems 108
4.4.4 Conclusions 111
Chapter 5 112
Experimental Characterisation 112
5.1 Noise determination of the measurement setup system 112
5.2 Restoring means and electrostatic actuator 115
5.2.2 Characterisation of the gel bump behaviour 125
5.2.3 Controlling of the vertical alignment using a PID controller in MATLAB® 127
5.3 Magnetic lateral movement 132
5.4 Magnetic lateral movement with the entire floating electrode electroplated 137
5.5 Vertical movement with PDMS restoring means plus UV-curable adhesive 140

Chapter 6 143
Conclusions and Future Work 143
6.1 Conclusions 143
6.2 Future work 145
6.2.1 Magnetic actuator 145
6.2.2 Restoring means 156
6.2.3 Microfabrication of the external driving device 158
6.2.4 μLED-μLens assembly 159
6.2.5 Alternative approach if the μLens and μLED had been delivered as wafers 162
Appendix A 170
Misalignment Correction Calculation 170
Appendix B 175
Electrostatic Force Calculation 175
Appendix C 184
Magnetic Force Calculation 184
Appendix D 190
Processes 190
D.1 Manufacturing of μLED dummy 190
D.2 Manufacturing of the μLens 193
D.3 Different spin height for SU8 195
Appendix E 196
MATLAB® files 196
E.1 MATLAB® file for displacement measurement using optoNCDT2400 via PC 196
References 202

List of Figures

Figure 1-1 Thesis layout. 4
Figure 2-1 Comparison of different actuators by performance indices. The bold line of each actuator stands for its border limits. a) The actuation strain and the actuation stress are brought into context. b) Shows the relation between actuation strain and the resolution [2]. 8
Figure 2-2 Top view of a comb drive actuator. The anchor and stationary electrode with its pad are attached to the substrate. The small levers going from the anchor to the movable structure (and electrodes) work as springs for the restoring force. If a voltage V_1 is applied the movable structure moves to the left until it reaches equilibrium with the restoring force of the spring. The same happens if V_2 is applied, but to the right side. The force F_x in x-direction, as seen on the right hand side is not dependent on x..... 10
Figure 2-3 a) Electrostatic levitation actuator with closed loop feedback controller for positioning. The two electrodes are needed in order to create an electric field between them and the suspended body. b) Lateral force that drives the suspended body back to its initial position [6]..... 12
Figure 2-4 a) Two static comb fingers that have in between the dynamic, grounded comb finger. b) The positioning can be measured by capacitive impedance measurements [8]. 13
Figure 2-5 a) Structure of the distributed electrostatic microactuator with no voltage applied. One single driving unit is emphasised. b) By applying a voltage on the electrodes, the actuator contracts by the distance ΔL [9]. 14
Figure 2-6 a) A permanent magnet is moved in the positive and negative z-directions by running a current through the planar coil. b) Distance versus electromagnetic force. The dot on the curve represents the measurement on the manufactured device [13]..... 16
Figure 2-7 The magnetic material block is attracted by the magnetic field originating from the planar coils beneath. Only an attractive force is possible. The restoring force is created by cantilevers, which are not represented here [15]..... 17
Figure 2-8 Side view of the magnetic actuator and its important dimensions [15]..... 17
Figure 2-9 a) The magnetic force as a function of the number of turns of the coil. b) The magnetic force as a function of the thickness of the magnetic material block [15]..... 18
Figure 2-10 a) Magnetic force as a function of the distance between magnetic material block and the coil. b) Magnetic force as a function of the length of the core [15]..... 18
Figure 2-11 Magnetic microactuator. The magnetic field lines produced by the planar coil are directed via a magnetic path to the air gap where the actuation work is done [16]. 20
Figure 2-12 Bending force as a function of the bending displacement. The straight line represents the linear fit of the measured points [16]..... 21
Figure 2-13 a) Hysteresis curve of a hard magnetic material. b) Hysteresis curve of a soft magnetic material [17]..... 22
Figure 2-14 Magnetic microactuator. The polymer magnet at the end of a cantilever is a permanent magnet and can hence be moved in the positive as well as in the negative vertical direction. This is done by choosing the direction and amount of the current flowing through the planar coil on the back side of the substrate [17]..... 22
Figure 2-15 The horseshoe like magnetic circuits dimensions are 5mm x 5mm x 1mm. To release or attract the permalloy, a current of different directions is passed through the windings. The resulting magnetic field of the windings either supports or counteracts the magnetic field of the permanent magnet [18]..... 23
Figure 2-16 The basic principle of a bimetal actuator. Metal 1 has a higher CTE than metal 2 as shown on the left hand side. If the two metals are now joined together as shown on the right hand side, metal 1 experiences a compressive stress and metal 2 a tensile stress. Because of that stress gradient throughout the structure, the actuator bends downwards. 24
Figure 2-17 A V-structure of cantilevers is attached and fixed to two anchors. If a current I_2 is supplied to the anchors, the current flows through the V-structured cantilevers that thermally expand. Since the structure is fixed on both ends, the elongation L' has to be compensated by moving the tip or the V-structure the distance d..... 26
Figure 2-18 If a current flows through this thermal actuator, the hot beam temperature is higher than the temperature of the cold beam due to the different cross-sectional area [25]..... 27
Figure 2-19 Displacement of the thermal actuator as a function of the input power. If the input power is higher than 14mW, plastic deformation occurs. Graph redrawn from graph found in [26]..... 28
Figure 2-20 Piezoelectric actuator that uses a lever in order to get the appropriate actuation range. In the top picture, no voltage is applied to the piezo element and therefore there is no strain. By applying a voltage to the piezo element the device starts to strain. The cantilever amplifies this movement, which results in a displacement of Δd_2 and exhibiting the angle β on the cantilever with respect to the horizontal plane..... 31

Figure 2-21 a) Side view of the VCSEL- microlens array assembly. The spacer ring determines the vertical distance. b) Top view VCSEL array that features reflective Fresnel zone plates (FZP). Pictures used with courtesy of [35 , 36]..... 35
Figure 2-22 The microlens is aligned with respect to the input signal of the different CCD detectors. The light source is the microscope. The actuation is achieved via different translation and rotation stages and the assembly is fixed in place by using UV-curable adhesive [37]..... 35
Figure 2-23 a) Side view of an assembly of a photodetector on top of an optical device. The lateral alignment is achieved with accurately manufactured alignment pedestals. b) Top view of the assembly. Two alignment pedestals are needed to determine the lateral alignment. [38]. 36
Figure 2-24 Solder self-alignment of a microlens array over a SEED chip. The lateral dimension of the SEED chip measures: 2.8mm x 2.8mm. Picture is a simplified representation taken from [39]. 36
Figure 2-25 The microlens is steered via 4 electrothermal actuators. A four by four array has been fabricated that is flip-chip bonded onto a VCSEL. Drawing is a representation of original [40]. 37
Figure 2-26 The green structure is made of elastic PDMS. If the chambers are pressurised, vertical displacement of the microlens can be achieved. Drawing is a representation of picture from [41]..... 37
Figure 2-27 Both, the frame actuator and lens actuator are electrothermally driven. The angle of the frame with respect to the surface is compensated by the lens actuator and the lens holder. This picture is a representation from drawing of [42]. 38
Figure 3-1 a) Emission spectra of blue and UV LED featuring peaks at 470nm and 370nm ,respectively. b) Current vs optical power output of the aforementioned LED types [46]..... 40
Figure 3-2 a) Picture of a micro-UV-LED array (μLED) produced by Strathclyde University. The active part of the LED of this particular device has a diameter of around 20μm. b) 3D image of the μLED (top) and profile of the LEDs. The height of this sample is around 4.4 μm. 41
Figure 3-3 a) Micrograph of a fraction of a μLens array. The microlens in this particular device has a diameter of around 35μm. b) 3D ZYGO® image of the device from a) reveals a hight of the microlenses of around 3 μm. The thickness of the sapphire substrate measures around 450μm. 42
Figure 3-4 μLens placed over μLED. The microlens is assumed to be a section of a sphere. From a MEMS perspective, the planes M_A and M_B are of importance once the height of the LED (h_L) and microlens (h) are obtained..... 42
Figure 3-5 Packaging of the microlens array (μLens) over the micro-UV-LED array (μLED). The approach has been broken down in two stages. The first part is the static approach where both the lateral and the vertical position are accurately fixed. The second part is the dynamic approach where the lateral position can and the vertical must be variable. 44
Figure 3-6 Exploded view of the post-processed μLED and assembled view of the μLens and μLED. The μLens is presented prior of being flipped and placed onto the μLED. 48
Figure 3-7 a) Top view of the μLED device structure itself. b) μLED chip divided into 4 functional areas. c) Base layer protects area *C* from a shortcut caused by the functional layer..... 49
Figure 3-8 a) The base and functional layers bridge the area where the pads are situated. The covered pads cannot be used. b) The structural layer that follows the layer seen in a) must not cover parts of the pad to keep it free for post processing. 50
Figure 3-9 a) The original design and its electrodes. b) The current design features bigger electrodes, shorter and wider tracks. 51
Figure 3-10 The key features of the static approach consists of, accurate height control with electroplating, 4 posts for the reduction of vertical and lateral contact area and the possibility of correcting a misalignment of the μLED with purposely misalignment of the post towards the μLens. 52
Figure 3-11 The first approach (left side) has the disadvantage that an even, dust free surface over the whole area of the dimple has to be maintained for optimum vertical alignment. In the proposed solution the μLens lies on four posts with minimal contact points. Dust or failure within the structure can be accommodated within reason..... 53
Figure 3-12 F_{actio} is applied and presses only two posts towards the two sidewalls of the cavities..... 54
Figure 3-13 The misalignment of the structural layer towards the LED (1) is measured and accordingly, the posts can be deliberately misaligned towards the lenses (2). Both misalignments compensate each other (3) and the corner lenses and corner LEDs coincide, meaning alignment. 55
Figure 3-14 The thickness $t_{\mu p}$ of the post is measured as well as the thickness of the base layer plus electrode, t_{μ}. Since the intended distance between μLED and μLens, d_{int}, is known, the thickness t_{elect}, that needs to be electroplated can be calculated as shown. On the left hand side is an illustration and micrograph before and after the electroplating process. 56
Figure 3-15 a) If the μLens-posts *A*, *B*, *C* and *D* of the μLens have different heights, the different electroplating thicknesses of the electrodes *A*, *B*, *C* and *D* on the μLED can compensate these variations. Tilting of the array can be corrected. b) Picture of an assembly of the first design with SU8 posts..... 56
Figure 3-16 Gluing and sealing of the μLens over the μLED. The UV-curable adhesive 1 is placed on the borders of the μLED cavity (1). The μLED is placed into the position and a force F_{fix} is exerted to keep the μLens in close contact to its vertical adjustment points (electroplated electrodes) while the

adhesive is curing (2). After curing, a large amount of UV-curable adhesive 2 can be applied around the entire μLens border (3). 57
Figure 3-17 Summary of the key features for the dynamic approach. The approach features an electrostatic vertical actuator as well as a lateral magnetic actuator that can be driven simultaneously.... 59
Figure 3-18 Paschen law curves with different gases. p is the pressure and d the distance [10]..... 60
Figure 3-19 a) Below a separation of 3μm a drastic deviation of the empirically measured graph to the Paschen curve can be observed [52]. b) Field strength as a function of gap distance (by courtesy of [52]). 60
Figure 3-20 a) Ordinary electrostatic actuator with the driving as well as the stationary electrode on a potential. b) The floating electrode reflects the electrostatic field generated by the two stationary electrodes in the proposed concept. 61
Figure 3-21 COMSOL® simulation of the floating electrode placed on top of electrodes. An electric field is generated between each electrode and the floating electrode. Fringing fields are displayed. 62
Figure 3-22 a) Floating electrode situated above fixed electrodes. b) Neglecting fringing fields, the assembly seen in a) can be represented with two capacitors C_1 and C_2 in series. c) The resulting series capacitance can then be calculated..... 62
Figure 3-23 a) Dimensions of one of the electrodes of the μLED. b) Dimensions of the μLens features and floating electrode..... 64
Figure 3-24 a) Display of the charge distribution assuming that the floating electrode is further away at d_2 than at d_1. b) Display of the different electrostatic fields that occur in the setup. 64
Figure 3-25 a) Force as a function of the measured height, h_m, with the SU8 thickness t_s as a parameter. b) Same as in a) but with the relative permittivity, ε_r, as parameter. 65
Figure 3-26 This picture shows the most important parameters that have been varied for the simulations, such as the angle φ, and the distance $t_{(x)}$ at the point $x5$, $t_{(x5)}$ representing the smallest distance of the floating electrode towards the electrodes in z-direction..... 66
Figure 3-27 Tilted floating electrode (green). The colours indicate the potential that is on the electrode and floating electrode. As expected, half of the potential is on the floating electrode..... 66
Figure 3-28 Simulation of a tilted electrode with an angle of 10° and a distance at point $x5$ of $t_{(x5)}$ = 203μm. a) A force , F_{Tot}, of 45μN was obtained with a large dielectric area. b) A total force, F_{Tot}, equals 40μN was obtained by cutting the dielectric covering the electrodes. 67
Figure 3-29 a) Charge density distribution of the electrodes as seen from above. b) Charge distribution of the floating electrode as seen from beneath. In both cases, the floating electrode is tilted with and angle φ of 10° and has a distance $t_{(x5)}$ of 203μm. 67
Figure 3-30 a) Comparison between the simulated results using COMSOL® and the analytical solution. The thickness of the dielectric, t_s, is 60μm and a voltage of 600V is applied with a constant angle of 10°. The graph is the total force, F_{Tot},as a function of $t_{(x5)}$. b) Same as in "a)" but with zero angle. 68
Figure 3-31 a) Qualitative drawing of a positive and negative step response with the different phase labelled in numbers and explained in b and c. b) Dashpot spring system for positive step response. c) Dashpot spring system for negative step response. 70
Figure 3-32 Qualitative consideration of the different nonlinear behaviour for the positive and negative step response of the actuator and polymer as a restoring means. 70
Figure 3-33 Same model as seen in Figure 3-30b but having cut the different connections between elements and replaced it with forces for the derivation of the equation. The setup is rotated 90 degrees. The μLens is on the right hand side, the μLED on the left. 71
Figure 3-34 Dashpot-spring system after the electrostatic force has been switched of and the μLens is moving into the positive z-direction. The additional effects involved are modelled by adding an additional dashpot, b_4 in parallel to the already existing system..... 72
Figure 3-35 SIMULINK® file derived from the equations (3-15) and (3-17). The white, green and blue part represents the dashpot-spring system of the gel. The red part stands for the electrostatic force and the orange part differentiates between a negative or positive movement of m_c in z-direction and adds, in the latter case, a dashpot b_4 to the system. 74
Figure 3-36 Graph generated by SIMULINK® with the model and values shown in Figure 3-34 resembling qualitatively Figure 5-22b from practical measurements in Chapter 5..... 75
Figure 3-37 a) The PDMS bumps are part of the μLED which complicates the fabrication process. b) placement of the PDMS bumps on the μLens..... 76
Figure 3-38 a) Bumps of the μLens are placed in order to fit within the gel cavities that are situated on the μLED. b) Sideview of the μLens and μLED. The diameter of the restoring means is smaller than the diameter of the gel cavity. The thickness of the restoring means, t_{bump}, however needs to be bigger than the thickness of the structure layer, t_{struct}..... 76
Figure 3-39 Magnetic macro actuator. The dummy post that is suspended on the cantilever is attracted with a force, F_{mag}, if a current is passed through the coil..... 77

Figure 3-40 Photograph of a μLED with attached external driving device (EDD). A post is placed within the cavity. This assembly was used for the initial test of the magnetic movement that can be achieved considering the real dimension of the assembly..... 78
Figure 3-41 Due to the magnetic flux, Φ, the two tracks act like a horseshoe magnet and attract the post with the force, F_m , to reduce the distance, d_m. a) Perspective view. b) Top view. c) Side view. 79
Figure 3-42 Magnetic circuit for lateral actuation with its electrically equivalent simplified schematic. On the left bottom corner is a close-up of the air gap between tracks and post. 79
Figure 3-43 a) μLens with floating electrode made of evaporated Ti. b) Instead of just electroplating the post, the entire floating electrode is electroplated with a thickness, t_{fe}. 80
Figure 3-44 The 2 EDDs on each vertical side of the μLens allow to control the yaw of the μLens. a) If EDD 4.2 and 2.2 are active, a anticlockwise momentum θ_2 is generated. b) If EDD 4.1 and 2.1 are active, the momentum θ_1 acts in clockwise direction. 81
Figure 3-45 a) Lateral movement in x direction is possible if both EDDs, 4.1 and 4.2 are active. b) If only EDD 1 is active, only a lateral force F_y is generated. c) The momentum of θ_1 or θ_2 could be increased if each side features 2 EDDs at the expense of increased system complexity. 81
Figure 3-46 With the proposed design the yaw, θ, can be addressed, which allows to manipulate and control all 6 degrees of freedom. 82
Figure 3-47 a) Electrostatic actuator with EDD. b) Magnetic actuator with EDD. c) Both actuation mechanisms constitute the dual actuator. 83
Figure 3-48 a) EDD with coil that generates the magnetic flux. b) EDD prior of winding the coil around the L-shaped Ni wires. c) Top view of the EDD. The isolator is electrically isolating but magnetically conducting. d) Side view of the picture shown in c). 84
Figure 3-49 Experiment where one of the first external driving device is tested for the magnetic attraction of the dummy post that is attached to a polymer cantilever. 84
Figure 4-1 a) Drawing of a μLED with magnetic and electrostatic actuators. b) Photograph of the resulting μLED device. 86
Figure 4-2 Exploded view of the μLED 87
Figure 4-3 Process for base layer. The blue arrow on the left hand side shows the direction at which the cross section on the right hand side is viewed. The dashed line indicates the cut of the cross- section.... 88
Figure 4-4 Process for the functional layer. 89
Figure 4-5 Process for the structural layer. 90
Figure 4-6 a) A pair of electrodes is connected via its pads with the copper wire using conductive paint for the subsequent electroforming process. b) Close-up of a). 90
Figure 4-7 Process for the electroformed layer. 91
Figure 4-8 a) Drawing of a μLens with floating electrodes and ferromagnetic posts for the magnetic actuator. b) Photograph of the μLens. 91
Figure 4-9 Exploded view of the μLens including the restoring means. The right hand side depicts a photograph of step 1 and a SEM picture of a post from step 2. 92
Figure 4-10 Process for floating electrode. 93
Figure 4-11 Process for post (ferromagnetic). 93
Figure 4-12 Process for post (SU8) 94
Figure 4-13 Process for restoring means. 95
Figure 4-14 Photographs taken during the manufacturing process. The respective step is labelled beneath the photograph. 95
Figure 4-15 Geometric consideration of the contact angle, θ_c and the interfacial tensions γ_{SL}, γ_{LG} and γ_{SG}. 96
Figure 4-16 a) solid1 has a bigger interfacial tension between itself and the liquid (photoresist) than solid2. b) The interfacial tension of solid1 is identical with solid2, there is no height disruption caused. 97
Figure 4-17 a) Several layers of tape where stacked on top of each other in order to approximate the thickness of the μLens. b) Non-uniform thickness distribution of the spun SU8 layer due to the different interfacial energies between glass and tape. 97
Figure 4-18 a) μLens and the surrounding coverslides are glued with AZ and baked afterwards. Non uniform AZ distribution can be observed. b) Close-up of a). After having spun SU8 and baking of it, air pockets and non uniformities can be seen on the assembly. 98
Figure 4-19 Distribution slides (right column) are used to pull the edge bead curvature away from the area that will occupy the structure, to make the thickness of the photoresist homogenous for the features. 99
Figure 4-20 a) Assembly for μLens fabrication at fabrication state "a", Figure 4-19 where devices are surrounded by distribution slides. b) Assembly state corresponding to Figure 4-19 "b" prior to exposure. 100
Figure 4-21 μLens of the first design with SU8 posts fabricated using the process explained earlier. The lateral dimensions are 4.5mm x 4.5 mm. a) Photograph of the device, b) height distribution of the μLens posts. 100

Figure 4-22 Comparison of the thickness distribution of the structural layer between the first design and the current design. The first design which was produced without the method of distribution slides exhibits different thicknesses for t_1, t_2 and t_3..... 101
Figure 4-23 a) Top view and corresponding side view of a µLED that has bee glued to a wafer for the evaporation process. The different resistances between particular features are given in both views. b) Same wafer after 3 hours of electroplating with a current of 50mA for an area of around 900µm^2..... 102
Figure 4-24 Side view of a µLED connection pad with its glued wire connection (top). Below is a zoomed-in image, of the interface area between the conductive adhesive and the Ti-layer. A progression of images and pictures shows the electroplating process over time with the resulting improvement of the conductivity of the interface..... 103
Figure 4-25 A possible sealing method: the µLens and µLED is sealed with a conductive adhesive and followed by a layer of electroplated metal that connects the evaporated surrounded areas of the µLens and µLED with each other..... 104
Figure 4-26 a) Micrograph of the electrodes of the µLED prior to electroplating. b) ZYGO® measurement of the same electrodes..... 104
Figure 4-27 a) Micrograph of the electrodes shown in Figure 4-26a after electroplating for 3 hour. b) ZYGO® measurement after electroplating for 3 hours..... 105
Figure 4-28 a) Design of the pads tracks and electrodes of the first design. b) Current design; flaws of the first design have been corrected..... 106
Figure 4-29 The copper wire are attached to the pads using conductive paint..... 106
Figure 4-30 a) Electrode prior to electroplating. b) Electrode after plating with nickel. c) Photograph of the electrode after electroplating..... 107
Figure 4-31 a) Electrode prior to electroplating. b) Electrode after electroplating of around 5µm..... 107
Figure 4-32 a) SU8 layer delaminated during electroplating. The substrate material was glass for this dummy device. b) First design with Si as substrate material. It shows that the SU8 adheres very well to this substrate even after extended electroplating..... 108
Figure 4-33 µLED as supplied by the University of Strathclyde. a) Au LED-connection-pads and tracks of the left upper corner. b) Au connection tracks at the bottom left corner going to the micro-LED array itself..... 109
Figure 4-34 a) Delamination of a sample that has the base and structural layer hard baked with sapphire as a substrate material. b) Delamination also occurred at samples that featured no base layer but just the functional and the structural layer, latter made of hard baked SU8..... 110
Figure 4-35 µLED where THB was used instead if SU8. a) After electroplating, the corner did not show any signs of delamination even after having attempted to lift it with a needle. b) The cavity with the incoming electroplated tracks exhibits no delamination. c) No delamination could be seen looking at the cavity from the opposite side..... 110
Figure 5-1 Setup of the noise measurement that detects the vibrations caused by the building and which is transferred to the setup..... 112
Figure 5-2 Measurement of the noise. Top graph depicts the amplitude as a function of the time and the graph below the normalised power spectra..... 113
Figure 5-3 The gel cushions are placed between the optical-table and the optical-base to dampen the magnitude of the noise generated by the building..... 113
Figure 5-4 The upper graph shows the transient of the noise measurement after having placed gel pads below the optical-table. The graph below shows the normalised power spectra. A prominent peak can be seen at a frequency of 24.38Hz..... 114
Figure 5-5 The noise, caused by the building has been measured during a long term measurement of 24 hours. Step voltages of 200V, 400V and 600V have been applied for a duration of 1 hour. The noise is dependent on the time of the day..... 115
Figure 5-6 Test device with four drops of the liquid adhesive NOA 61 placed over the cavities..... 115
Figure 5-7 The transient signal from the sensor was analysed with the FFT algorithm to extract parameters for an appropriate filter. The graph below shows the power spectrum after the signal was filtered with a Butterworth low-pass filter of 10th order and a cut of frequency of 0.5Hz..... 116
Figure 5-8 Noise and displacement signal as recorded from the micro-epsilon device. The bottom graph shows the signal filtered in MATLAB® using a Butterworth lowpass filter of 10th order and a cut of frequency of 0.5 Hz..... 117
Figure 5-9 A gel bump is placed in the four corners of the µLED within the designated gel cavities. The µLens is then placed on top of it. Gel offers restoring properties and elastic behaviour in all directions. 118
Figure 5-10 a) The µLens is placed on top of the µLED. b) The step voltage from the PC is multiplied by a factor of 100 and the displacement is measured using the optoNCDT 2400. The information is then fed back into the PC via the RS-232 interface..... 118

Figure 5-11 Relative displacement of the μLens array for step responses of 100V, 200V, 400V and 600V without and with the noise filtered out. The graph below is the filtered signal by using a Butterworth filter 5th order with a cut off frequency of 1Hz. 119
Figure 5-12 Step responses for voltages between 0V and 600V with a voltage on and off duration of 1 minute were recorded. Even after 1 minute, the slope of each step response suggests viscoelastic creep behaviour of the gel. 120
Figure 5-13 Height h_0 measured from the top surface of the μLens with respect to the surface of the μLED. 120
Figure 5-14 Height h_{600} measured at the same position as seen in Figure 5-13. This time, a voltage of 600V was applied at the electrodes. 121
Figure 5-15 Long term step response measurements of more than 16 hours with voltages between 0V and 600V and an increment of 50V. 121
Figure 5-16 Zoomed-in graphs from Figure 5-15. 122
Figure 5-17 Zoomed-in graph taken from the shaded area in Figure 5-16. Voltage on and off time is 4 minutes. A slope at the end of each plateau at voltages higher than 200V indicates that creep behaviour is prevalent 122
Figure 5-18 Error bar diagram where 11 measurements of each step voltage are analysed from the measurement seen in Figure 5-15. The confidence interval was chosen to be 95%. 123
Figure 5-19 An arbitrary step response (S6_2) is used for the explanation of the selective filtering method used for the error bar statistics. 124
Figure 5-20 a) Zoomed in sequence (Sx_2) taken from Figure 5-19. b) A defined time slot is taken for which the average value of the displacement is calculated. 124
Figure 5-21 The different averaged step responses are arranged with respect to their voltage from which subsequently an error bar is extracted with a chosen confidence interval of 95%. 125
Figure 5-22 a) Step responses of voltage steps of 1 hour duration were recorded. b) The zoomed in step response taken from a) with a voltage step of 200V and a duration of 1 hour. 126
Figure 5-23 c) Positive 400V and 600V step response show even after one hour a viscoelastic creep behaviour (this graph is a zoomed in image of the shaded area c) of Figure 5-22a. d) Negative step response from 400V and 600V (graph is a zoomed in image of the shaded area d) within Figure 5-22a). 126
Figure 5-24 Step responses recorded for 2 minutes voltage on time and 4 minutes voltage off time and voltages between 200V and 600V with 100V increments. 127
Figure 5-25 a) Step response of a 400V input signal. b) Shows the step response for 200V. While t_u remained approximately the same, t_g changed from 1.1 seconds to 2 seconds. A value in between is taken for calculating the values of the PID controller within MATLAB®. 128
Figure 5-26 For an initial setup, only the P and the I part of the within SIMULINK® was used with a proportional amplification of, $K_p = 0.025$ and an integral value of 1 129
Figure 5-27 a) Step responses were recorded for voltages between 0V and 600V. b) Zoomed in picture of time slot 1 (ts_1) for the 400V step response. c) Time zoom for the time slot, ts_2, where different parameters were obtained 130
Figure 5-28 Left) The setpoint of the closed control loop is changed in discrete set and the response of the system recorded. Right) Zoomed in time slots (ts_1 and ts_2) from the left hand side picture 131
Figure 5-29 Measurement setup for characterising the lateral magnetic actuator. 132
Figure 5-30 Photograph of the distance sensor and a test vehicle for lateral displacement. 133
Figure 5-31 A sequence of pictures taken from a movie that shows the displacement of a post inserted within the cavity of a μLED over a period of 16 seconds. The cavity is filled with a viscous liquid to dampen the movement. A current of 400mA is applied at $t = 0$ second. 134
Figure 5-32 a) Side view of lateral magnetic movement test vehicle. b) Zoomed in picture from a. c) Schematic side view with dimension. 134
Figure 5-33 Step responses for different currents steps were recorded with 10 seconds current on and 20 seconds current off time. a) Step response for 50mA. b) Step response for 100mA 135
Figure 5-34 Step responses for different currents steps were recorded with 20 seconds current on and 40 seconds current off time. a) A series of step responses for 400mA. b) Close-up from a) with a step response from a positive and negative current step 136
Figure 5-35 Comparison between lateral and vertical displacement for the same current steps of 300mA with 10 seconds current on and 20 seconds current off time applied. a) Lateral x-displacement with a difference of around 6μm, b) vertical z-displacement is hardly detectable 136
Figure 5-36 a) The displacement was aimed to be set manually to different integer values to proof that with simple methods, accurate lateral alignment can be achieved. b) Error bar box plot with a whisker range of 1-99% and a box range of 25, 75% of measurements taken for different current steps showing the relative displacement. The average value of the last 25% of the positive and negative step response data were taken and the difference calculated. 137

Figure 5-37 a) μLens with electroplated floating electrodes 1,2 and 4. 3 was subsequently plated as well due to bridging of the Ni. b) Zoom in of corner between floating electrode 1 and 2. c) Zoomed in picture of edge of floating electrode 4. 138
Figure 5-38 a) Electroplated μLens placed onto μLED with external driving device (EDD) attached. b) Close up of EDD and ferromagnetic edge of μLens. c) Side view of μLED, EDD and μLens. 138
Figure 5-39 a) Step currents of 20mA with a current on and off time of 3 minutes and 1 minute respectively yield a displacement of 1μm. b) Same timing but a current of 100mA resulted in displacements that exceeded 14μm. 139
Figure 5-40 By manually passing currents between 0mA and 300mA, different displacements were attempted to estimate the controllability. 139
Figure 5-41 a) μLens is placed onto the μLED with PDMS bumps in between. b) Step voltages of 400V, 500V and 600V where applied. c) A liquid UV-curable adhesive was then placed onto the four corners and the capillary force initially caused a downward movement of the μLens. d) With a superimposed upwards movement of the μLens, the restoring capability of the PDMS bumps are still noticeable..... 142
Figure 6-1 The magnetic circuit might be simulated by using SIMULINK®. 146
Figure 6-2 a) Simplified magnetic circuit schematic as shown in Figure 6-41b. b) Magnetic curve of the material chosen for the magnetic path of the EDD, pads, tracks and the post. 149
Figure 6-3 Discrete values of d_m and F_m can be calculated and presented in a 3-D mapping diagram representing the magnetomotive force, Θ as a function of d_m and F_m. 150
Figure 6-4 The interface between the pad on the μLED and the external driving device (EDD) needs to be electrically conductive as well as having a low magnetic resistance. 150
Figure 6-5 a) Fe particles mixed with 2 component epoxy glue and cured for 1 hour. b) Close-up of a). 151
Figure 6-6 a) A sample of ferromagnetic adhesive was exposed to a magnetic field during curing for 1 hour using Fe wire as a magnetic core material and a current of 700mA. b) The magnetic particles align according to the field lines in order to make the magnetic resistance for the magnetic circuit as low as possible. 151
Figure 6-7 Curing of the ferromagnetic adhesive by passing a magnetic flux, Φ_{cure}, through the magnetic path. The magnetic shortcut is placed between the pads to increase the flux for a given current, I_{cure}. .. 152
Figure 6-8 a) The left Fe wire features an electrical isolation layer. Both Fe wires are immerged into the ferromagnetic adhesive. A high voltage generator was then connected with a DMM in series that measures the electrical current. b) Close-up of two non insulated Fe wires in L-shape that have been immerged in ferromagnetic adhesive. 153
Figure 6-9 Breakdown voltage behaviour of the ferromagnetic adhesive. It is assumed that the voltage can be increased to another step due to properties of the material similar to that of a so called "self healing capacitor". 154
Figure 6-10 After alignment of the ferromagnetic particles during the curing process of the adhesive, a high voltage is applied to burn away possible electrically conductive paths. 154
Figure 6-11 Determination of the magnetic impedance as a function of the displacement of the post, d_m. 155
Figure 6-12 The water drop placed on the μLens evaporates over time, therefore reduces the gravitational force that compresses the gel bumps. From this, a force-displacement graph (right) can be established. 157
Figure 6-13 a) Confocal chromatic measurement system (micro-epsilon, optoNCDT2400). b) High resolution scale with micro gram resolution (Mettler MT5). 157
Figure 6-14 Using a syringe attached to a transition stage, the amount of water that is placed on the μLens can be varied accurately. The end of the tube needs to be close to the μLens so that no drops can be formed. 158
Figure 6-15 a) Manually crafted EDD. b) Microengineered solenoid of 5mm length. c) Zoomed in image of b) with visible ferromagnetive core of high permeability (b) and c) by courtesy of [60]). 159
Figure 6-16 a) EDD could be temporarily attached on the μLED just for the alignment. b)Three detectors are at least necessary to detect the position of the μLens. A hill climbing algorithm could be applied in order that the detector gets the maximal intensity when the lenses are aligned. 159
Figure 6-17 Possible mass fabrication process which makes use of temporary attached External Driving Devices (EDDs). 160
Figure 6-18 Determination of the different tilts by using 3 lasers and a digital camera with either movie mode or long exposure mode. 161
Figure 6-19 a) The maximum separation of the alignment marks (AC1, AC2) produced by the chip manufacturer (IoP) was around 5.7 mm. b) Zoomed in picture of a) exhibiting the alignment mark AC2. 163
Figure 6-20 a) 4 alignment marks fabricated by IoP after intervention by the author. b) Demanded alignment mark dimension. c) Obtained alignment mark. 163

Figure 6-21 a) First design mask where the alignment marks are separated over nearly the entire diameter of the wafer, thereby improving angular alignment accuracy. b) Zoomed-in picture from a) with alignment marks featuring Vernier structures. 164
Figure 6-22 a) µLED-wafer with embedded µLED-chip and alignment marks AW11 and AW12, respectively. b) µLens-wafer with embedded µLens-chips and alignment marks (AW21, AW22). 165
Figure 6-23 a) SU8 or THB structure fabricated on the µLED-wafer by using the alignment marks AW11 and AW12 for accurate alignment. b) Same as a) but for µLens-wafer. 166
Figure 6-24 a) Top view of a µLens which is placed onto the µLED-structure and fixed afterwards with adhesive. b) Top: side view of the situation on the left hand side. Bottom: assembled device. Lateral alignment is achieved trough the µLED-and µLens-structure, vertical alignment through the µLED-structure. 167
Figure 6-25 a) Top view of µLED with µLED-structure and spacer prior of being assembled. b) Top: side view of the situation shown on the left. Bottom: assembled device. Vertical alignment through spacer, lateral alignment through µLens- and µLED-structure. 167
Figure 6-26 Lapping before development in order to protect the fragile structure embedded beneath... 168
Figure 6-27 a) Wafer developed after grinding (lapping). Small structures are preserved. b) Wafer ground after development. The small structures are partly or entirely destroyed. 169
Figure 6-28 The thickness of a ground structure varies from 22.06µm to 23.3µm. This thickness range of 1.26µm. 169
Figure A-1 The structure layer is the only layer on the µLED that needs to be accurately aligned. 170
Figure A-2 Analysis of the misalignment between the different fiducial marks and extraction of the important parameters for the correction process. 170
Figure A-3 The structure layer is not perfectly aligned towards the µLED. 172
Figure A-4 After knowing f and φ, the alignment marks of the post mask (AP1) can be placed exactly f apart and an angle φ misaligned with respect to the alignment marks of the lens array (AL1). 173
Figure A-5 After placing the µLens with the purposefully "misaligned" posts, the initial misalignment of the structural layer with respect to the micro-LED's is compensated and the individual microlenses correspond with the micro-LED's. 173
Figure A-6 For the entire device (µLens and µLED) only one fabrication step is necessary that would utilise external processing. 174
Figure B-1 The difference between t_m and h_m is in x-direction a and in z-direction, b. Given the real dimensions of the device, this difference can be neglected since the angle φ is small. 175
Figure B-2 Geometrical considerations of the movement and tilting of the floating-electrode. h_m is the height measured with the micro-epsilon confocal displacement measurement system. $t_{(x)}$ represents the distance between the electrode and floating electrode at point x. 176
Figure B-3 a) $t(x)$ is assumed to be the same length as the arc, S. Voltage $V_1 = V_2 = V_3$. b) The electrostatic field lines exit the SU8 towards air with an angle of α. This is dependent on β. β is always smaller than φ. 177
Figure B-4 a) The voltage that applies between the floating electrode and the electrode is half of the voltage coming from the voltage source . b) Determination of the capacitance $dC_{(x)}$. 178
Figure B-5 The integration of half of the active area is done by discrete integration of different geometries and then added together which subsequently yields the total force. 181
Figure C-1 The simplification made in Figure 6-41 is only valid if the magnetic resistance of the ferromagnetic material can be linearised. 184
Figure C-2 a) Equivalent electric schematic of the circuit shown in Figure 3-41. The network can only be calculated if the magnetic resistors are assumed to be linear and have NO hysteresis. b) By considering the symmetry network a) can be reduced to the network shown in b). 186
Figure C-3 Two imaginary fluxes, Φ_A and Φ_B are assumed to run in the chosen loops. This methods yields two linear equations for the two unknown variables. This approach ONLY works if the magnetic resistors are assumed to be linear. 186
Figure E-1 SIMULINK® environment for basic step response measurements. Scope 1 depicts the displacement data send by the optoNCDT2400; Scope shows the voltage steps that are applied. Both data are stored within the blue ""to File" block. The green and the red box are S-Functions which are explained in detail within the MATLAB® source code shown below. 196

ALL MISSING PAGES ARE BLANK

IN

ORIGINAL

List of Tables

Table 2-1 Scaling behaviours of different magnetic actuators [11]. 15
Table 3-1 List of challenges (vertical stack) and the area that the problem needs to be connected to. Some problems have a combined cause and therefore more than one point on the concerned challenge.. 45
Table C-1 Nomenclature of the different magnetic resistors that are used within the following equations. 186

Glossary

Symbol	Designation	Units	Comments
Constants, Variables, vectors			
a	linear acceleration	m/s^2	
A	area	m^2	
B_r	Remanent magnetic flux density	T	
$\boldsymbol{B}$	Magnetic flux density	$1T=kg/A/s^2$ (old: Gauss)	Tesla ($1T=10^4G$)
C	capacity	$1F=1A^2s^4/kg/m^2$	Farad
d_1, d_2 d_P, d_{int}, d_P, d_{eff}	distances	m	
m_1, m_2, h_m, a, b, k, t_m, h_0, w_m, s_c	dimensions	m	
U	energy	J=N·m	
$\boldsymbol{E}$	vector of electrostatic field	V/m	
$\boldsymbol{F}$	vector of force	$1N = 1\ kg{\cdot}m/s^2$	Newton
f	frequency	Hz	
g	gravitational acceleration constant	m/s^2	$g = 9.81m/s^2$
H	Magnetic field strength	A/m	$1A/m=4*\pi/1000$ Oe (Oested)
H_c	Coercive field strength	A/m	
I, i	Electrical current	A	Ampere
K_s	Proportional gain		
K_p	Proportional amplification	-	
L	Scaling variable		
L	Induction	1H = 1V*s/A	Henry
l	length	m	
m	mass	kg	
M	momentum of torque	$1m^2*kg/s^2=1N*m$	
M_z	Constant magnetisation	$m^2*kg/s^2=N*m$	
N	Number of turns in electric coil		
n	Index of refraction		
P	Power	W	Watt
p	Pressure	$1\ Pa = 1\ N/m^2$	Pascal
p	Pressure	1Torr = 1/760*atm	1atm = 101.325 Pa
Q	charge	1C = 1 A*s	Coulomb
r	radius	m	
$\mathcal{R}$	Magnetic resistance /reluctance	At/Wb	
R	Electric resistance	Ω	
S_{air}	Magnetic cross section area	M^2	
$t_{\mu p}$, t_μ, t_{elect}	thicknesses	m	
t	time	s	Second
t_g	Compensation time	s	
t_u	Dwell time	s	
T	Temperature	°C or K (Kelvin)	$T = t_{celsius}+273.15K$

T_{Tr}	Transition temperature	°C or K (Kelvin)	
V	Voltage	V	Volt
X_L	Inductive impedance	Ω	(imaginary number)
X_C	Capacitive impedance	Ω	(imaginary number)
z_a, z_b, z_c	Relative displacements (z-direction)	m	
$\alpha, \beta, \varphi,$	angle	rad or degrees	
ε_0	permittivity free space	$8.854188 \cdot 10^{-12}$F/m	
ε_r	relative permittivity	-	Air=1; Glass=5; glue = 4.04 (NOA61)
μ_0	Permeability of vacuum (air)	$4 \cdot \pi \cdot 10^{-7}$H/m	
μ_r	relative permeability	-	
μ	Micro 10^{-6}		
η	viscosity	1poise =100cps =0.1N*s/m^2	water=1cps glue = 450cps (NOA61) glycerine=1486cps
Θ	Magnetomotive force	A	Ampere
Φ	Magnetic flux	1Wb=1V*s	
ρ	Charge density	C/m^2	
γ	Interfacial tension	N/m	
π	Pi	-	3.1416
ω	Angular frequency	rad /s	ω =2πf

Mathematical operators

a, b.....	Scalars	
A, B, ...	Scalars, Constants	
A, B,...	Vectors	
$A \cdot B$, AB	Multiplication	Within the text the multiplication sign for dimensions, the x is used (e.g. 4.5mm x 4.5mm).
x, y, z	Cartesian coordinates	
x, y, z	Cartesian direction vectors of unity length	**z** is in general defined as vertical direction
•	Dot product	
×	Vector product	
Δ	Difference	
dl	Infinite decimal segment of l	
$\frac{d}{dx}$	Derivation with respect to x	
$\frac{\partial}{\partial x}$	Partial derivation with respect to x	
∇	del or nabla operator	$\nabla \equiv \mathbf{x}\frac{\partial}{\partial x} + \mathbf{y}\frac{\partial}{\partial y} + \mathbf{z}\frac{\partial}{\partial z}$

Labelling of different parts of the project

EDD	**E**xternal **d**riving **d**evice: provides electrostatic and magnetic energy for the actuators featured on the μLED
EDDI	**E**xternal **d**riving **d**evice **I**nterface: magnetic interface within EDD that must yield maximal magnetic conductivity by maximal electric resistivity
μLED	micro-UV-**LED** array chip with structure as well as the dummy device of it

µLens	microlens array chip with structure as well as the dummy devices of it
P-EDDI	Pad-external driving device interface: the magnetic and electric interface between the pad of the µLED and the EDD

Processes

LIGA	lithography, electroplating, injection-moulding
PVD	Physical Vapour Deposition
SMA	Shape Memory Alloy

Equipment

A/D output card	Analog output card PCI 6208V, Adlink	
DMM	Digital Multi Meter (Fluke® 77III)	
IGBT	Insulated-gate bipolar transistor	
Scale	Mettler Toledo MT5 scale	
optoNCDT2400	optoNCDT 2400, confocal chromatic displacement sensor from micro-epsilon (IFD 2400-3)	Resolution: 0.04µm Max. measuring rate: 1000Hz
TAMARACK®	Tamarack® exposure and alignment tool	
ZYGO®	Viewmeter ZYGO® white light phase shifting interferometer	

Materials, chemical elements

Al	Aluminium
Al_2O_3	Aluminium oxide
Au	Gold
AZ	Positive photoresist AZ 9260 ®
Be	Berylium
Fe	Iron
Ga	Gallium
In	Indium
Mg	Magnesium
Nitinol™	Ni-Ti shape memory alloy
Ni	Nickel
N	Nitrogen
Si	Silicon
SU8	Negative photo resist SU 8 from Microchem
Terfenol®	Magnetostrictive material
Ti	Titanium
PDMS	Polydimethylsiloxane
THB	THB 151N Negative photo resist from JSR

Expressions

CCD	Charge-coupled device
CTE	Coefficient of thermal expansion
dB	decibel
FZP	Fresnel zone plates
MOCVD	Metal organic chemical vapour deposition
PZT	Piezo transformer

RMS	Root mean square
SEED	Self-electro-optic effect device
TTL	Transistor transistor logic
VCSEL	Vertical cavity surface emitting laser

Publications from the author

Peer reviewed journal articles

- M. Luetzelschwab, D.Weiland, E. Abraham and M. P. Y. Desmulliez " MEMS-based packaging of a UV-LED array ," Micro & Nano Letters, vol 2, Issue 4, pp. 99-102, December 2007

Conference Papers

- M. Luetzelschwab, M. P. Y. Desmulliez, D. Weiland "Microlens / UV-LED array packaging solution for dynamic and static alignment", Accepted to IEEE/CMPT International Electronic Systems and Technology Conference (ESTC), 1-4 September 2008, Greenwich, UK.

- M. Luetzelschwab, D. Weiland, and M. P. Y. Desmulliez, "Adaptive optical packaging of microlens over UV-LED-Array," Smart Systems Integration, Paris, France, pp. 215-222, 2007.

- M. Luetzelschwab, D. Weiland, M. P. Y. Desmulliez, "Adaptive Packaging Solution for a Microlens Array Placed over a Micro-UV-LED Array," EPTC, Singapore, pp. 338-342, 2007.

- M. Luetzelschwab, D. Weiland, and M. P. Y. Desmulliez, "Smart Packaging of Microlenses over a UV-LED Array," EMPC 2007, Oulu, Finland, pp. 161-166, 2007.

- M. Luetzelschwab, D. Weiland, and M. P. Y. Desmulliez, "Adaptive Packaging for a Microlens array placed over a Micro-UV-LED array", IPAS, Chamonix, France, pp. 129-138, 2008.

Chapter 1

Introduction

1.1 Motivation and outline of this thesis

This work aims to find active and passive alignment and packaging solutions, which bring a microlens array and a micro-UV-LED array together according to the requirements of the end-user. In order to achieve the demanded accuracy, several methods have been studied and some approaches have been experimentally tested. A further objective of the thesis is to manufacture monolithically such solutions at low temperature and directly on top of the micro-UV-LED and microlens arrays. The chosen approaches offer interesting possibilities for mass fabrication without the need for expensive external manipulation equipment, necessitating thereby only external sensors for the dynamic alignment. They are not restricted to this particular device/objective and might find use in environments where the aforementioned manipulation equipment is not available but reasonable manufacturing accuracy achievable.

In the static approach the microlens array is fixed on top of the micro-UV-LED array with high accuracy in the lateral as well as the vertical directions. No further movement of the microlens array is permitted once the assembly has been sealed. In the dynamic approach the microlens array is able to move in the vertical direction to adjust the focal point of the system and in the lateral directions if scanning is required for example. The lateral accuracy, however, must not be affected by that vertical movement. This is expected to be a challenging part due the friction and stiction effects that are expected to be predominant at such a scale. Different actuation methods have been considered depending on the force or displacement required for the proposed system. A novel lateral magnetic actuation method, which can be activated independently and alongside the vertical actuation, has been designed and tested.

1.2 Layout and objective of the thesis

The objective of this thesis is to present and explain the work conducted by the author during his Ph.D. study at the Microsystems Engineering Centre (MISEC) at Heriot-Watt University in Edinburgh, United Kingdom. A visual layout of the thesis is provided at the end of this chapter.

Chapter 2: Literature review. This chapter assesses different kinds of actuators that are being used within the MEMS community and, in the context of packaging, comments on their advantages and disadvantages concerning manufacturing issues as well as forces and displacements that are feasible. Furthermore, actuators that have been used for microlens movement are mentioned.

Chapter 3: Concept. In this chapter are explained the different challenges that had to be addressed during this research, especially the limitations imposed on the micro-UV-LED array and microlens array chip. Different approaches that tackle these challenges are presented. This chapter also features the closed-form expression of movement of the device subject to the electrostatic force and restoring means.

Chapter 4: Manufacture. This chapter describes the manufacturing steps used for the packaging structure of the micro-UV-LED and microlens arrays. A modified UV-LIGA process is utilised, in which the photoresist does not only act as a mould for the electroforming but also serves as a structural material. The processes have to be kept within certain parameters, so that the performance of the delivered devices is not compromised. The chapter also explains on how to tackle the post-processing of singulated die for packaging as opposed to the more convenient wafer-level packaging process.

Chapter 5: Analysis and experimental characterisation. The setup of experiments and the analysis of the obtained results are presented and discussed in this chapter. Experimental results are compared to the theoretical derivations obtained in Chapter 3. A closed-loop feedback system is also explained, which allows highly accurate vertical displacements.

Chapter 6: Conclusions and future work. The final chapter summarises the completed work and provides ideas and possible approaches to solve persisting problems which could not be addressed in the duration of this Ph.D. project. Some approaches have already been partially tested but need further development.

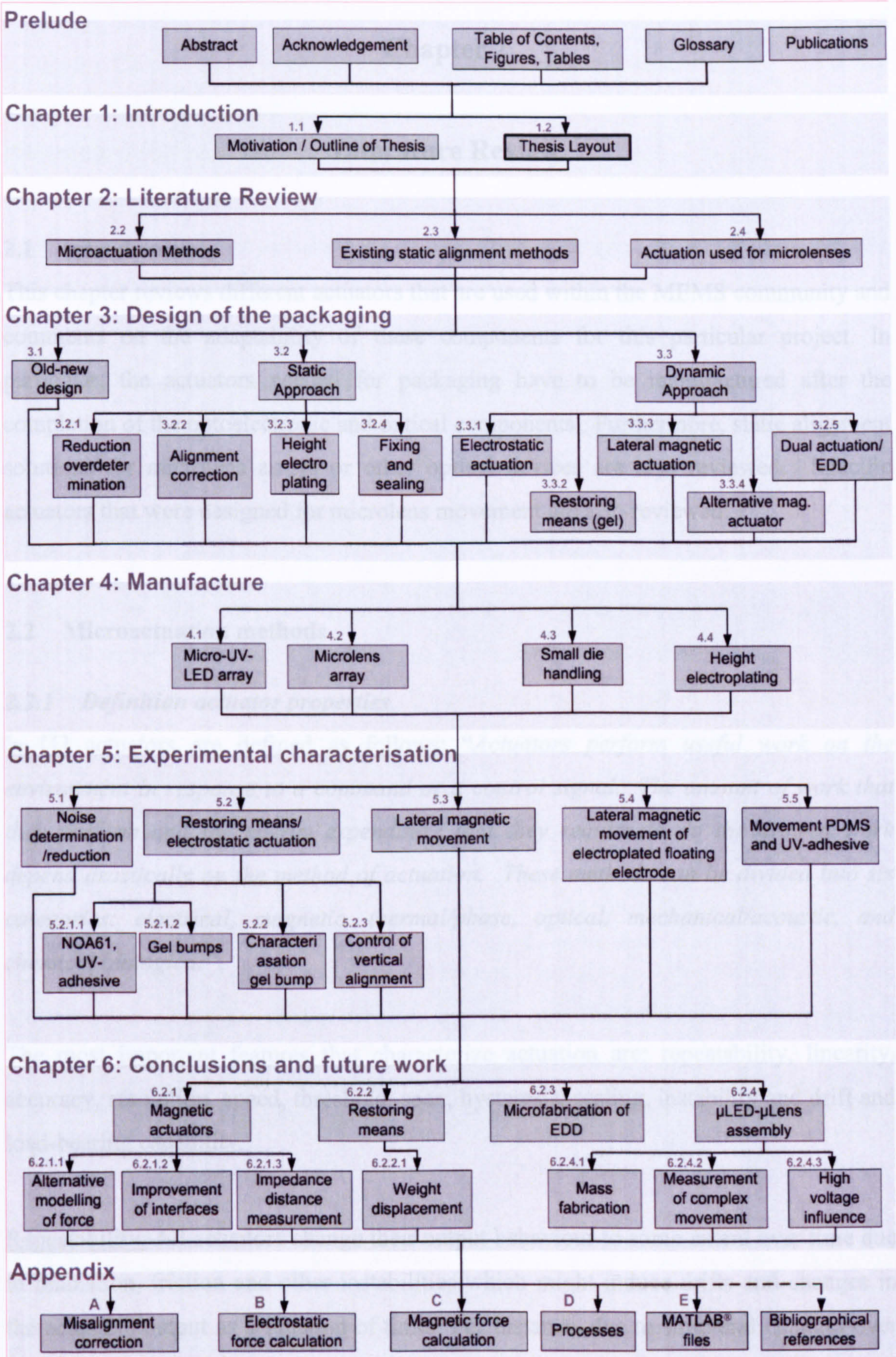

Figure 1-1 Thesis layout.

Chapter 2

Literature Review

2.1 Introduction

This chapter reviews different actuators that are used within the MEMS community and comments on the adaptability of these components for this particular project. In particular, the actuators needed for packaging have to be manufactured after the completion of the optoelectronic and optical components. Furthermore, static alignment solutions for microlens arrays or other optical devices are also reviewed. Specific actuators that were designed for microlens movement are also reviewed.

2.2 Microactuation methods

2.2.1 Definition actuator properties

In [1] actuators are defined as follows: "*Actuators perform useful work on the environment in response to a command or a control signal. The amount of work that they perform and the energy expenditure that they require to do the desired work depend drastically on the method of actuation. These methods can be divided into six categories: electrical, magnetic, thermal/phase, optical, mechanical/acoustic, and chemical biological*".

The most important features that characterize actuation are: repeatability, linearity, accuracy, resolution, speed, threshold, span, hysteresis, scaling, instability and drift and load-bearing capability.

Repeatability: All actuators change their output behaviour to some extent over time due to relaxation, friction and other instabilities which might induce drifts and changes in the actuators output as a function of time. For instance, due to structural changes over time, the restoring behaviour of an actuator might change. Therefore, the actuator might not return to its initial position. This problem can be alleviated by applying a closed-loop feedback system.

Linearity: The linearity of an actuator refers to the linearity of its output as a function of its input. This is normally expressed as a percent of its full-scale output. Due to the actuation methods that are considered and the way the restoring force will act, the movement of the microlens will be nonlinear by nature.

Accuracy: Accuracy is a measure of how near the output of an actuator approximates a desired calibrated scale.

Resolution: The resolution is defined by the input value to the actuator that yields the smallest increment at its output. For an electrostatic actuator, the resolution translates into the minimum change in the voltage applied to the electrodes for a detectable movement of the microlens array.

Velocity: In what time can an actuator perform a difference of output value? In practical terms: how many micrometers per second is an actuator able to move? Depending on its application, this might be of importance since it can be a boundary condition for deriving the maximum operating frequency of the actuator.

Threshold: Threshold is defined as the input value above which the output performs the smallest initial increment.

Hysteresis: This phenomenon is very common in magnetism. The path that the output moves by increasing the input is different form the one where the input is decreased. If a magnetic actuation method is used a marked hysteresis behaviour will result especially if hard magnetic materials are used. This is a major problem for many control mechanisms.

Noise: Noise is an undesired disturbance within the frequency band where the system is operating. It can originate from the actuator itself even in the absence of noise in the input and of disturbances from the environment. The noise on the input is magnified and is so able to disturb even mechanical actions.

Instabilities and drift: All influences from the environment that change the output value of an actuator.

Load-bearing capability: An actuator changes its output value when a force is exerted even if the input value is kept constant. As a consequence, it is important that the mechanical characteristics of a load are investigated.

A method has been reported, where different types of actuators are compared based on matching performance characteristics [2]. The mechanical requirements can be force, displacement, stiffness, size, mass, response time, power, efficiency and resolution. The mechanical contribution to mass from power supplies and other peripheral devices are neglected. The actuators considered were: high strain piezoelectric, magnetostriction, shape memory alloy, hydraulic, thermal expansion and moving coil actuation. Unfortunately, the electrostatic actuation method is not mentioned in this article. It is stated that not all actuators are suited for a cyclic operation. Particularly the resetting force of shape memory alloys is reported to be restrictive. At high frequencies there are two limits regarding the cyclic operation: the maximum power per unit volume, p_{max}, and the maximum frequency of operation, f_{max}. Taking piezoelectric and magnetostrictive actuators as examples, the maximum power is determined in order to prevent overheating. The maximum frequency is defined as the frequency of the first mechanical resonance. Above that frequency, an actuator is not able to operate its load properly. For devices that depend on temperature change, such as thermal expansion actuators or shape memory actuators, the maximum frequency is dependent on the time for the heat transfer. It is reasonable to assume that, in the later case, the heat transfer is the determining factor since the mechanical resonance frequency can be expected to be far higher.

The article compares the different actuation methods by displaying them on so-called property charts. For the purpose of this research thesis the comparison of the graphs of actuation stain vs actuation stress and actuation stain vs. resolution is sufficient. As shown in Figure 2-1a and Figure 2-1b. An estimated line for electrostatic actuation has been drawn in the same figures. The thick lines stand for the loci of the values of maximum actuation stress versus actuation strain for a given class of actuator.

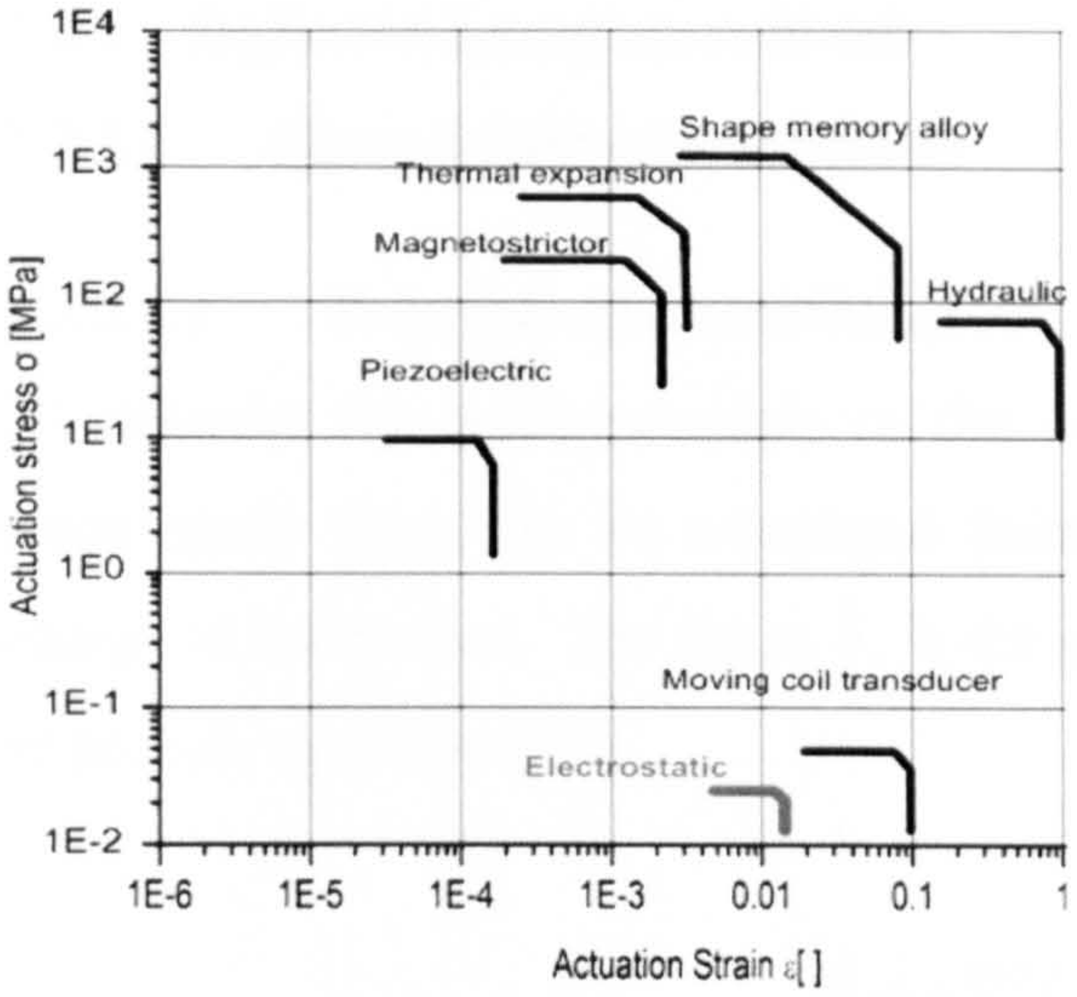

a)

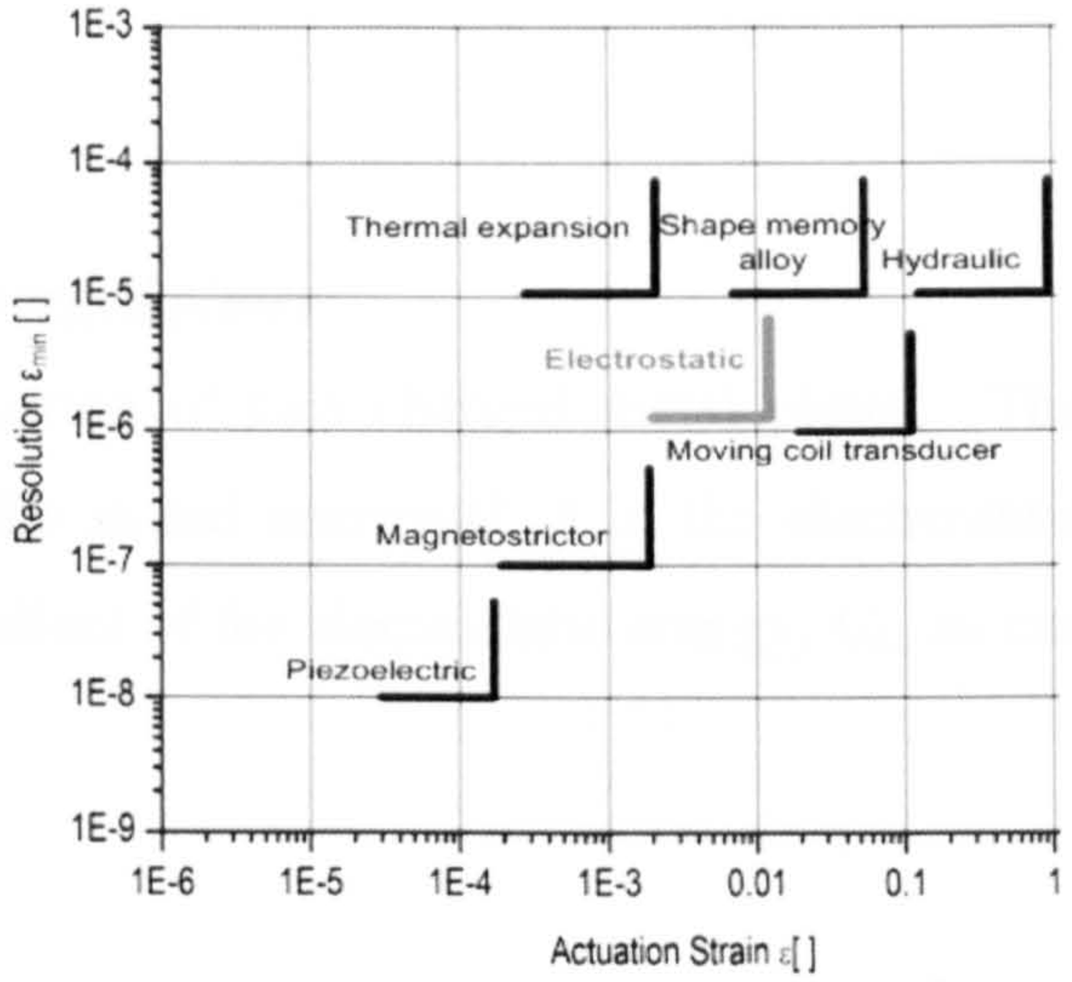

b)

Figure 2-1 Comparison of different actuators by performance indices. The bold line of each actuator stands for its border limits. a) The actuation strain and the actuation stress are brought into context. b) Shows the relation between actuation strain and the resolution [2].

The actuation stress should not be interpreted as being a function of the actuation strain. On the right hand side of the diagram lie the actuators that are able to perform high stroke because the strain is large. On the top of the diagram are actuators, which exhibits high stress. Hence, these actuators would be suitable for tasks where large forces are required. For instance, the shape memory alloy and the hydraulic actuator show large stroke and large stress capabilities, whereas a piezoelectric actuator exhibit lower stroke capability but reasonable stress values. The location of the electrostatic actuator has been determined by comparison with the other actuators. The electrostatic device creates more strain than the thermal expansion, the magnetostrictor or the piezoelectric actuators. It has however less strain than the moving coil actuator and the hydraulic actuator. Using that diagram the electrostatic actuator exhibits reasonable strain but not much stress and hence force. Figure 2-1b compares the different actuation methods with regard to actuation strain and resolution. The boundaries are now restricted downwards for each actuator since the smaller the resolution, the better. The resolution of an electrostatic device is better than the resolution of a shape memory alloy but worse than that of a magnetostrictor. Whether the resolution of an electrostatic actuator is better than that of a moving coil transducer cannot be assessed at this stage.

2.2.2 Different actuation methods

2.2.2.1 Electrostatic microactuator

2.2.2.1.1 Principle of actuation of two charged plates

[3] describe the basic principle of the actuation of two charged metal plates. The electrostatic force can be calculated from the stored energy (U_E) in the electrostatic energy of the device. The force, F, is the gradient of the electrostatic energy, U_E, as can be seen in equation (2-1).

$$\mathbf{F} = -\nabla U_E \tag{2-1}$$

In terms of potential energy, the gradient shows the direction of increase in potential energy. [3] state that it is important to keep in mind, by having a system of say a capacitor (with movable electrodes) and an energy source as a battery, that one has to consider the system as a whole concerning the energy and not just solely the capacitor. By increasing the capacitance (the plates move closer), the electrochemical energy stored in the battery as well as the total free energy are reduced. In other words, the battery performs the necessary work to bring the plates of the capacitor closer together and therefore the electrochemical energy stored in the batteries becomes smaller. The displacement current flowing from the battery to the capacitor causes an energy reduction of the whole system owing to radiation and resistive losses. In most cases though, these losses can be regarded as small compared with the energy in the capacitor and battery.

2.2.2.2 Comb drive microactuator

The comb drive microactuator uses electrostatic forces to achieve displacement. The device consists of two interdigitated finger structures that have a different potential. Figure 2-2 displays the top view of a comb drive microactuator. The anchors, which are attached to the substrate, are electrically grounded. The beams going from the anchors to the movable structure act not only as cantilevers for the restoring force but also maintain the electrical connection to the moveable electrodes. The substrate and moveable structures are normally connected to a potential in order to prevent an electrostatic force in the vertical direction that could cause stiction. If V_2 is applied to the right static electrode, the movable structure is pulled to the right and moves until the electrostatic force is equal the restoring force exerted by the beams. If the gap between

the fingers is decreased or/and the number of fingers increased, a higher force is obtained.

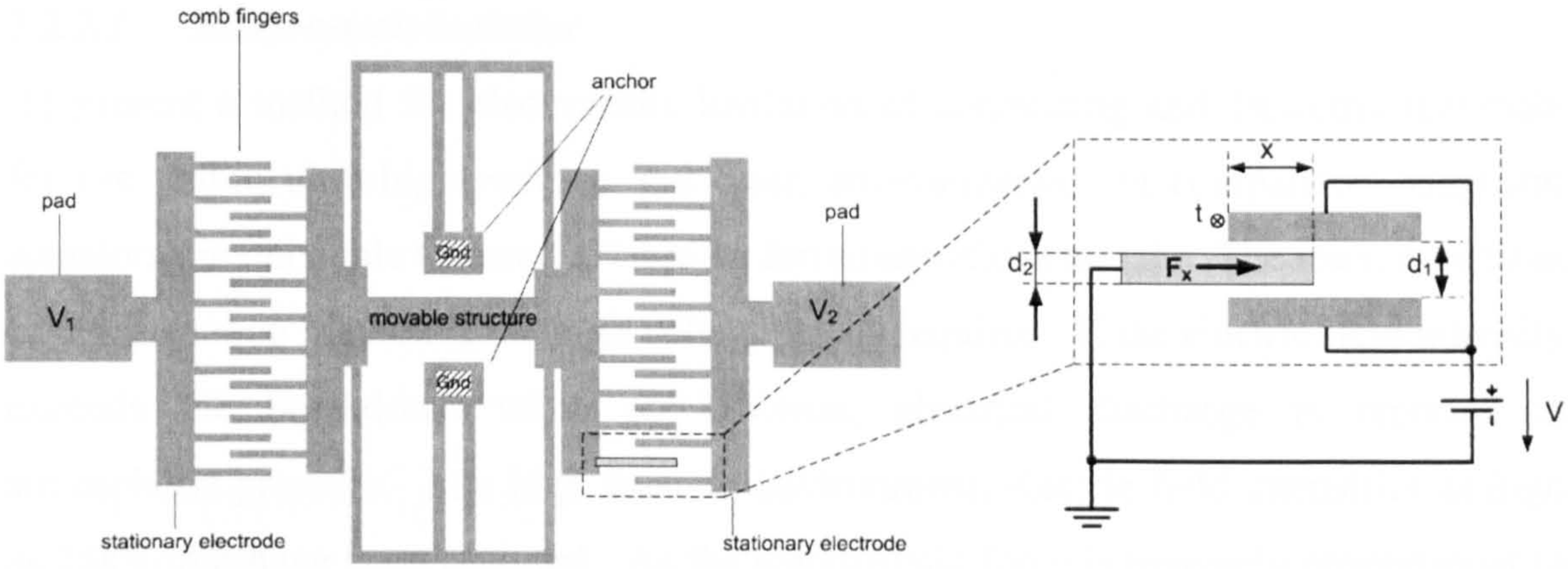

Figure 2-2 Top view of a comb drive actuator. The anchor and stationary electrode with its pad are attached to the substrate. The small levers going from the anchor to the movable structure (and electrodes) work as springs for the restoring force. If a voltage V_1 is applied the movable structure moves to the left until it reaches equilibrium with the restoring force of the spring. The same happens if V_2 is applied, but to the right side. The force F_x in x-direction, as seen on the right hand side is not dependent on x.

The force exerted on one finger of the electrode that is attached to the movable structure can be calculated by using equation (2-2).

$$\mathbf{F}_x = \frac{1}{2} \cdot \frac{\varepsilon_0 \cdot t \cdot d_2}{d_1 \cdot (d_1 - d_2)} \cdot V^2 \tag{2-2}$$

$\boldsymbol{F}_x$ is the electrostatic force towards the x-direction, ε_0 is the permittivity of vacuum (and air), d_1 is the separation of the fingers of the static electrode. d_2 is the height of the movable electrode finger. t is the thickness of the fingers and V stands for the voltage. The force is not dependent on the penetration depth of the electrode finger into the static electrode. This makes the system easy to control since no pull in effect is recognisable. Furthermore, this method is suited for large movements due to the lack of the $1/d^2$-dependency (where d is the distance between two electrodes) encountered in ordinary electrostatic actuators.

A large displacement can only be achieved, if the microactuator element moves parallel to the capacitor plate [4]. In this case, the force is constant during the movement if the fringing field can be neglected. Forces of up to 0.2mN and displacement of up to 10μm for a voltage of 50V have been reported [3]. [5] have built a comb drive actuator, by

using polysilicon surface micromachining, which achieved displacements of around 30μm at an applied voltage of 20V.

2.2.2.3 Electrostatic levitator

[6] present a method for electrostatic levitation of conducting and dielectric materials for use within ultra-high-vacuum and clean environments. In comparison, magnetic actuators are only able to assert a force on ferromagnetic materials. The main drawback of this actuation method is the high voltage levels required. If the electric field intensity exceeds the breakdown value of 3kV/mm, electrical discharge is reported at atmospheric pressure. In a high vacuum environment, electric field intensities as high as 15kV/mm have been reported. As the electrostatic force is inversely proportional to the square of the distance between the electrodes and the suspended object, it is necessary to actively control the voltage on the electrode in order to achieve a stable positioning of the object as shown in Figure 2-3a. The position is measured and compared with the reference. A PD controller compares the two signals and leads the output to a voltage amplifier, which applies the driving voltage directly to the electrodes. If a metal (conductor) is used as the suspended body, the free charges within the metal body accumulate very fast and uniformly on the surface towards the electrodes, yielding thereby a fast response time. In a dielectric used as a suspended body, the charges are not able to move fast due to the high resistivity. In addition, the polarisation of the dipoles within the dielectric material takes a certain amount of time. The suspension force exerted on the dielectric material increases gradually until it can levitate the body. The response time is therefore slow and introduces delay in setting up the body in the requested position. The slow response time has a further aggravating influence on the positioning of the body. As can be seen in Figure 2-3b, a restoring force is also generated when the suspending dielectric body is laterally shifted. This restoring force is caused since the charges on the slightly conductive dielectric are not able to relax fast enough to the new situation. Hence, an electric field is generated that is not only in the vertical position but also has a lateral component. All these effects makes the handling of a dielectric material slower and hence more inert as opposed to a conductive metal body [7].

Air humidity plays an important role for levitation of glass bodies. The increase of air humidity increases the conductivity of the surface and therefore the charges can move much faster, reducing the suspension time [6].

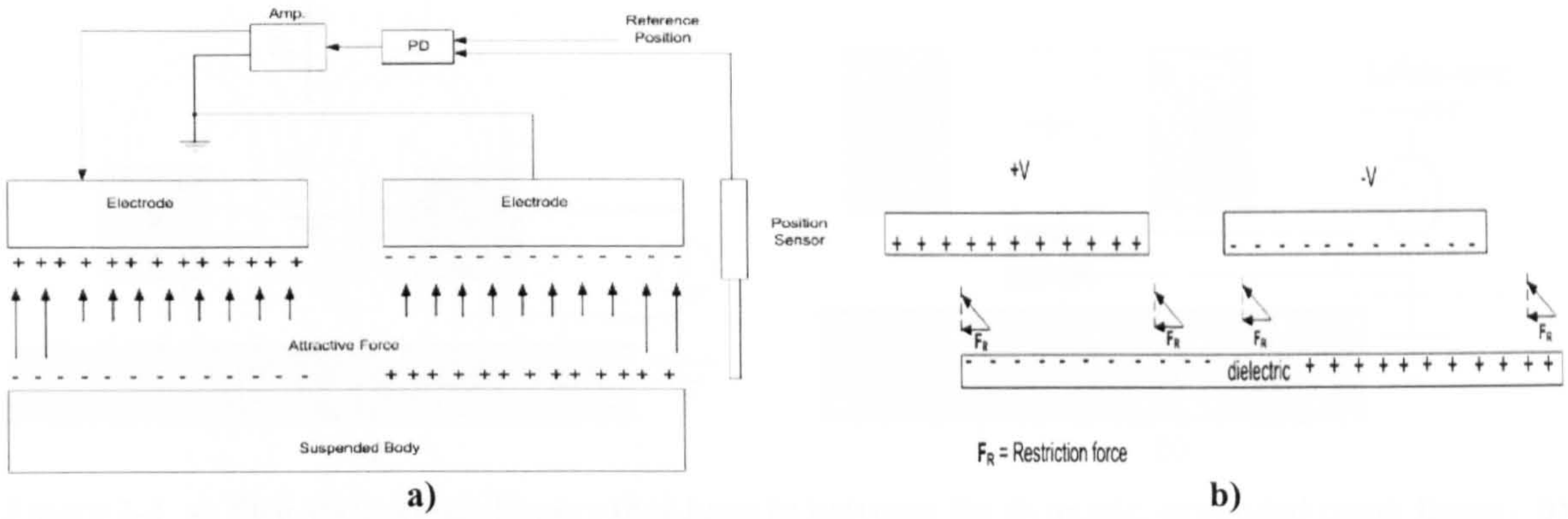

Figure 2-3 a) Electrostatic levitation actuator with closed loop feedback controller for positioning. The two electrodes are needed in order to create an electric field between them and the suspended body. b) Lateral force that drives the suspended body back to its initial position [6].

2.2.2.4 Vertically-actuated electrostatic comb drive with in situ capacitive position detection

[8] report a vertical driven electrostatic actuator. The principle of the actuation method is illustrated in Figure 2-4a. The two shaded squares represent the static comb fingers, where the voltage V is applied. A moving comb finger is situated 2μm from each static comb finger. The former is set to ground potential like the substrate of the entire system. The distribution of the electrostatic field is asymmetric around the moving comb finger, generating thereby an electric field energy density gradient and therefore a force $\boldsymbol{F}_z$. This force lifts the moving comb finger away from the ground. The moving comb is anchored to the substrate with a spring (not represented in Figure 2-4a). The movement stops when the electrostatic force, $\boldsymbol{F}_z$, is equal to the sum of the gravitational force of the moving comb itself and the restoring spring force. Figure 2-4b illustrates in a simple way the detection mechanism. Attached to the moving comb is the upper plate of a capacitor. The lower plate is placed on top of the substrate. By using a capacitive sensing circuit, the distance of the plate can be inferred from the capacitive impedance. Using that method, a micro-mirror, used for phase shifting diffraction interferometry, can be vertically moved between 1μm to 2μm with an applied voltage of 30V [8]. Furthermore, a position control accuracy better than 5nm was achieved with the use of a feedback system.

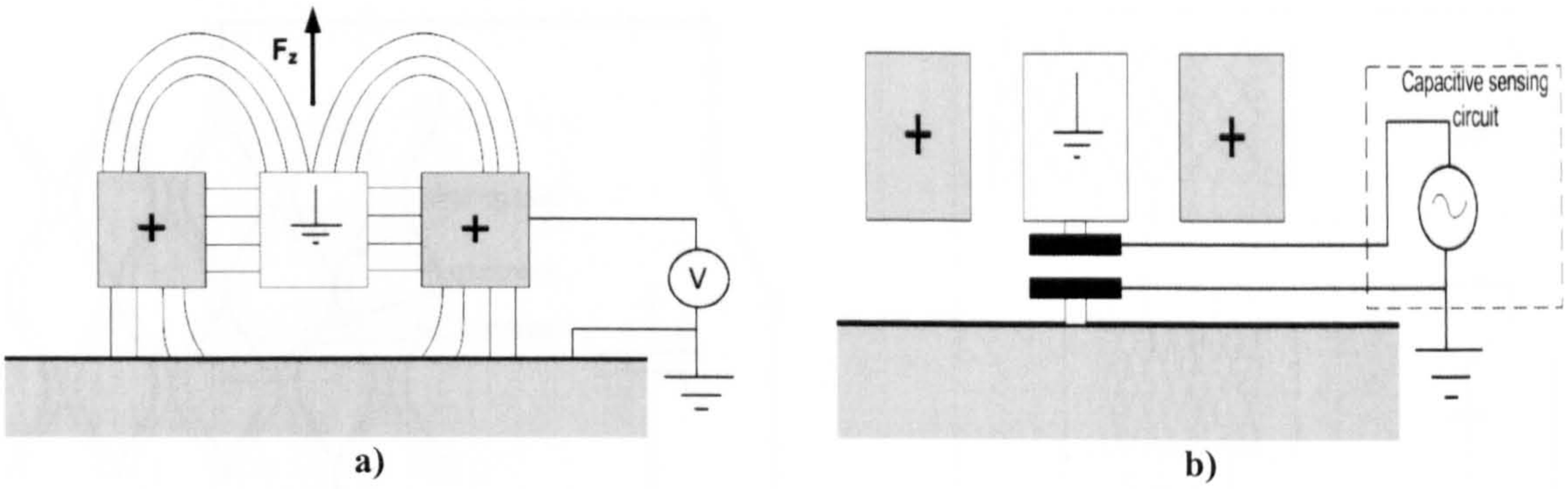

a) b)

Figure 2-4 a) Two static comb fingers that have in between the dynamic, grounded comb finger. b) The positioning can be measured by capacitive impedance measurements [8].

2.2.2.5 Distributed Electrostatic Micro Actuator (DEMA)

[9] reports an actuator that makes use of small driving units consisting of two wave-like electrodes as seen in Figure 2-5a. The actuator consists of several driving units, which contract by applying a voltage on their electrodes as seen in Figure 2-5b. The force is considerable for each unit, since the gap distance is small, due to the tiny dimensions of the unit itself. If many driving units are placed in parallel, a large force can be achieved at the expense of a small displacement. If the driving units are positioned in series, a large displacement can be achieved at the expense of a small developed force. However, by placing many units in parallel as well as in series, a large displacement and large force can be obtained simultaneously. This actuation method is similar to the one used by the muscle, where a driving unit represents a muscle cell. In order to get an easy deformation of the driving structure, the insulators as well as the electrodes have to be very thin. Since the DEMA is driven by many distributed units, dust does not affect as much this type of actuator. The displacement can be sensed by capacitance measurement. A maximum displacement of 28μm was measured when a voltage of 160V was applied to the microfabricated actuator of dimensions 5mm x 4mm x 5μm. Through FEM simulation, a force of 6.3μN, was obtained by applying 200V to an actuator of the same dimensions.

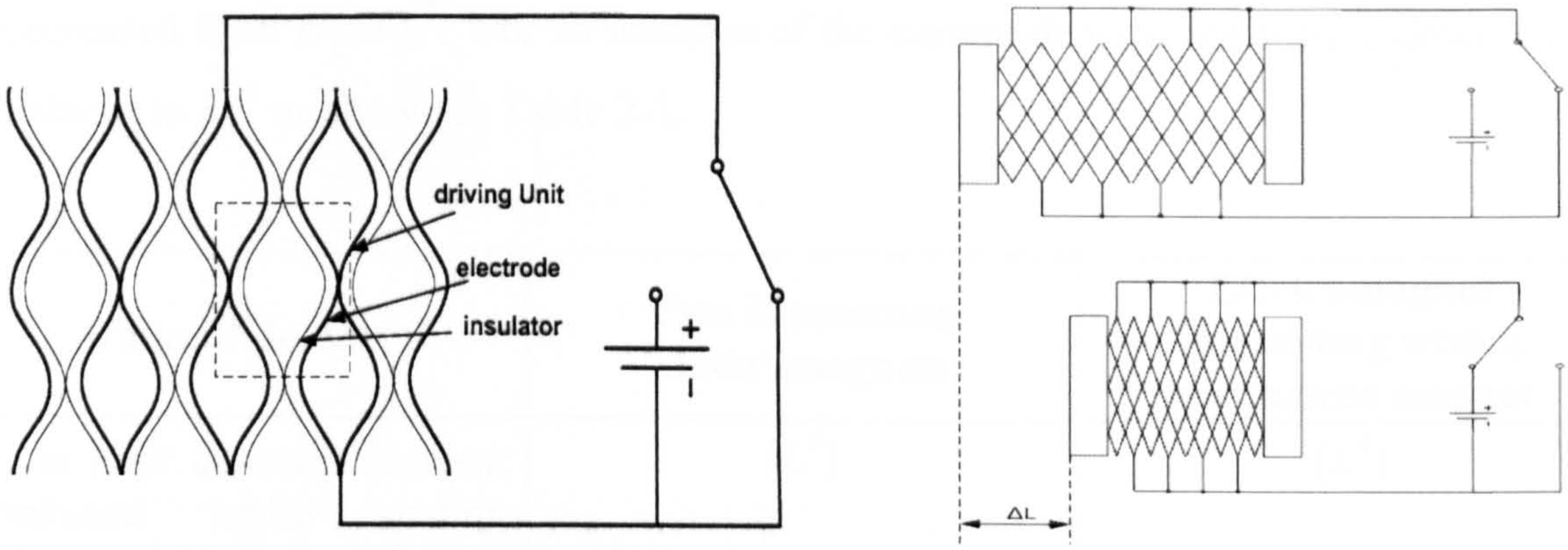

a) b)

Figure 2-5 a) Structure of the distributed electrostatic microactuator with no voltage applied. One single driving unit is emphasised. b) By applying a voltage on the electrodes, the actuator contracts by the distance ΔL [9].

2.2.2.6 Magnetic Actuators

In the macro-world, electromagnetic motors dominate the field of actuators [10]. Equation (2-3) describes the infinitesimal force $d\boldsymbol{F}$ generated per wire segment $d\boldsymbol{l}$ with a current of I, subject to a magnetic field of flux density $\boldsymbol{B}$. The larger the wire cross-section area, the more charges per time can be transported. The multiplication between the current, I, and the wire segment $d\boldsymbol{l}$ implies the dependency of force due to the volume. This formula takes into account an external magnetic field already existing in form of a permanent magnet, for instance.

$$d\mathbf{F} = I \cdot d\mathbf{l} \times \mathbf{B} \tag{2-3}$$

By scaling down the dimension, L, of a magnetic actuator, the force decreases by L^3. Without permanent magnets or an external magnetic field, the scaling down can increase up to L^4. [11] present three particular cases. In the first scenario of two interacting electromagnets, the force decreases by the L^4 if the current density is kept constant in order to avoid electromigration effects. In the second scenario, it would be possible to run an electromagnetic actuator at higher current densities at the expense of much less efficiency since heat can be more easily removed from a small volume. This results in a more favourable scaling down of L^3. In the last scenario one is able to drive the current density as high as the wire gets to its limit concerning the maximum temperature. This requires a constant temperature difference between the wires and the surroundings. A scaling down of $L^{2.5}$ can then be achieved. The use of permanent magnets instead of electromagnets provides better scaling properties, since the former maintain their strength. For a constant current density, the power of the scaling factor is

decreased from L^4 to L^3. For an increase of the current density, the scaling down factor reduces to $L^{2.5}$ as shown in Table 2-1.

Current density *J*	**Two interacting electromagnets**	**Electromagnet interacting with a permanent magnet**
J is kept constant (current reduced while scaling down)	$[L^4]$	$[L^3]$
J is increased (current constant while scaling down)	$[L^3]$	$[L^{2.5}]$
J driven to maximal value that can be dealt by the coil	$[L^2]$	$[L^2]$

Table 2-1 Scaling behaviours of different magnetic actuators [11].

The manufacturing process of such magnetic devices at the micro-scale is inhibited by the planar processes used in the microelectronic industry [10]. Electroplating and screen printing have also been used to deposit ferromagnetic films [12]. Although, the magnetic properties of thin films are claimed to be different from their bulk counterparts, the thickness of the magnetic materials deposited for this research work is in excess of 5μm and the materials can be considered as bulk.

A levitation method designed by [13] uses a permanent magnet as the levitated object as shown in Figure 2-6a. The permanent magnet is suspended by beams in the middle of a planar coil represented by circular cross sections. The coil is planar on top of the silicon surface and ensures a good heat flow within the device. Figure 2-6b shows the electromagnetic force generated as a function of the distance *z*. The height of the permanent magnet is of the order of 2mm. If the permanent magnet had been initially positioned vertically in the middle of the coil, no actuation force could occur by symmetry of the flux density.

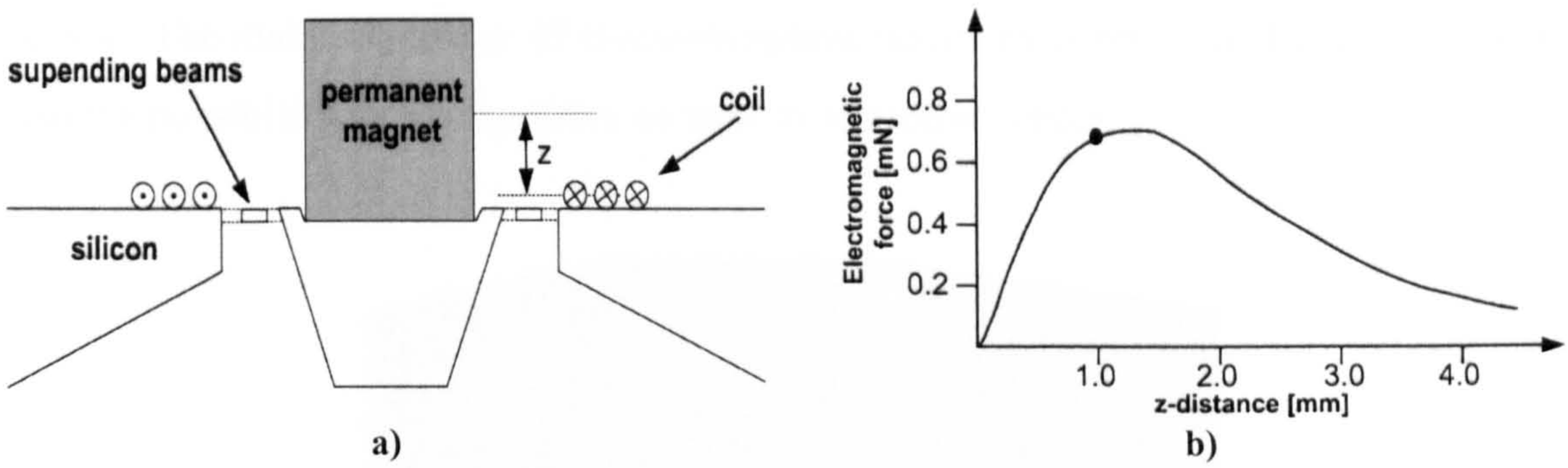

Figure 2-6 a) A permanent magnet is moved in the positive and negative z-directions by running a current through the planar coil. b) Distance versus electromagnetic force. The dot on the curve represents the measurement on the manufactured device [13].

Equation (2-4) shows the force generated in the z-direction due to the magnetic field generated by the planar coil:

$$\mathbf{F}_z = \mu_z \cdot \mathbf{z} \cdot \int \frac{\partial B_z}{\partial z} \cdot dV \,, \tag{2-4}$$

where $\boldsymbol{F}_z$ is the force in the z direction, μ_z is the magnetisation of the permanent magnet, $\boldsymbol{z}$ is the unity vector in the z-direction, and $\partial B_z/\partial z$ is the gradient of the magnetic flux density in the z-direction. dV is an infinite small volume element. As the force is proportional to the volume of the magnet, thin magnetic layers can therefore not generate large forces.

The ability to shrink permanent magnets such as rare-earth magnets is restricted to a thickness of around 20μm due to the occurrence of a magnetically reversed layer at that thickness [10]. Smallest commercial magnets are available only at the size of approximately 0.3mm, which might be a limiting factor for many MEMS devices. Their accurate positioning in hybrid assembly might also create difficulties. However, with a driving current of 300mA, an elevation of the permanent magnet by 143μm was achieved, with a mean slope of 24μm per 100mA [10]. [14] use this method to levitate the rotor of a micro motor. Magnets with a typical thickness of 1 mm achieve forces up to 150μN using planar gold coils of 30μm in width, 26μm in height and with a 20μm spacing. A current of 650mA produces a vertical magnetic field of 407A/m at the centre between the coils.

Another method is proposed by [15]. A planar coil as well as a ferromagnetic core are utilised to apply a force to a magnetic material block (not illustrated) suspended by four

beams. The main advantage of electromagnetic actuators is not only the large force but also the possibility to get repulsive as well as attractive forces.

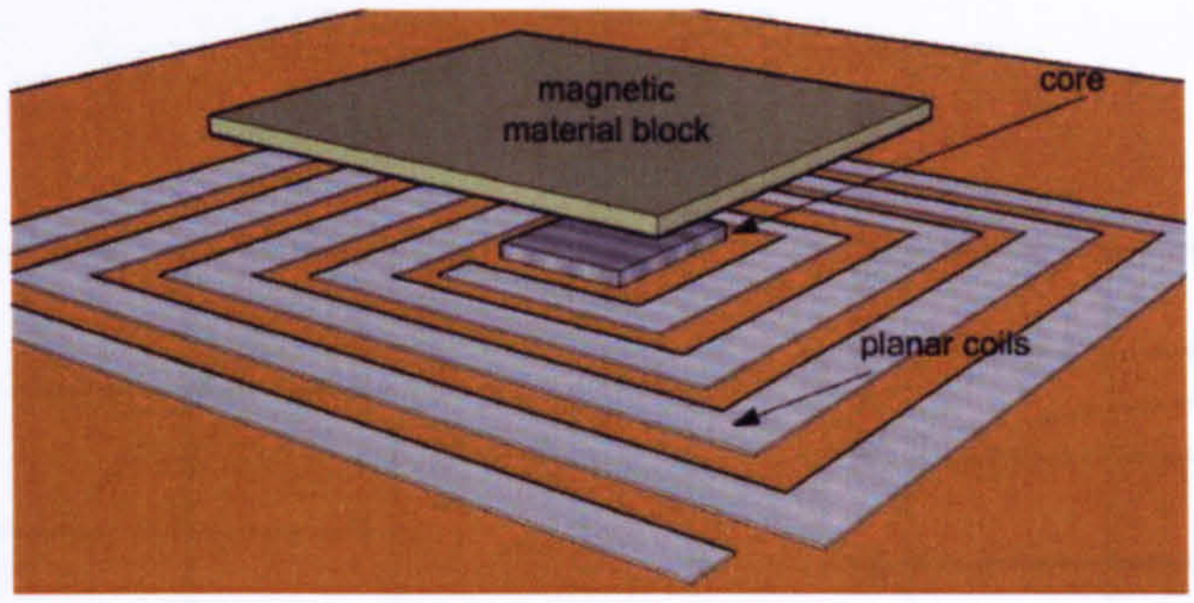

Figure 2-7 The magnetic material block is attracted by the magnetic field originating from the planar coils beneath. Only an attractive force is possible. The restoring force is created by cantilevers, which are not represented here [15].

Figure 2-8 shows a side view of Figure 2-7 and the different dimensional parameters that were changed in order to investigate the behaviour of the force [15]. w_m is the width and t_m the thickness of the magnetic material block. The thickness of the planar coil is t_c and the separation from one conductor to the other is labelled s_c whereas the width of a coil conductor is w_c. w_{core} is the width of the core and d is the distance between the magnetic material block and the planar coil. Numerical values have been chosen for illustration purposes.

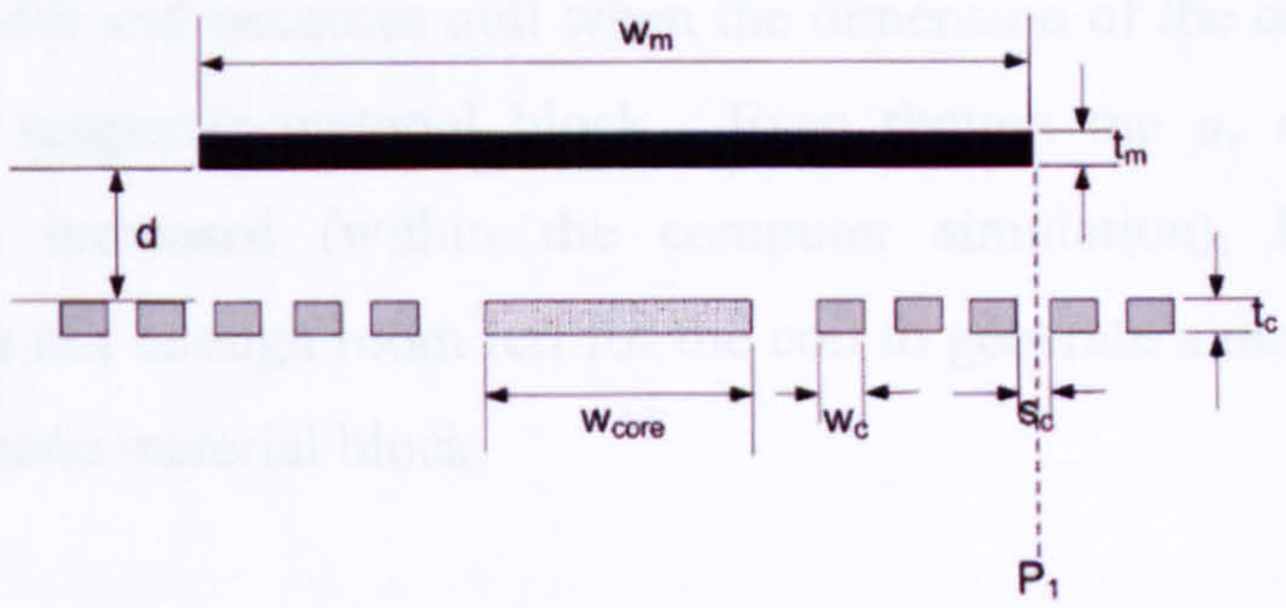

Figure 2-8 Side view of the magnetic actuator and its important dimensions [15].

Figure 2-9a presents the force as a function of the number of turns on the planar coil. The force is zero if there is no turn, hence no coil. The force increases steadily up to a number of 10 turns, above which no significant increase of the force occurs. After this limit, indicated by the point P_1 in Figure 2-8, each additional turn of the coil is further away from the magnetic material block. According to the law of Biot-Savart, the magnetic field intensity originating from an element of current, decreases with the square of its distance to the magnetic material block. Figure 2-9b gives the force as a

function of the thickness of the magnetic material block, t_m. By increasing the thickness, the force increases linearly at the expense of increased volume and weight of the suspended magnetic material block. This weight limits the maximal frequency of operation.

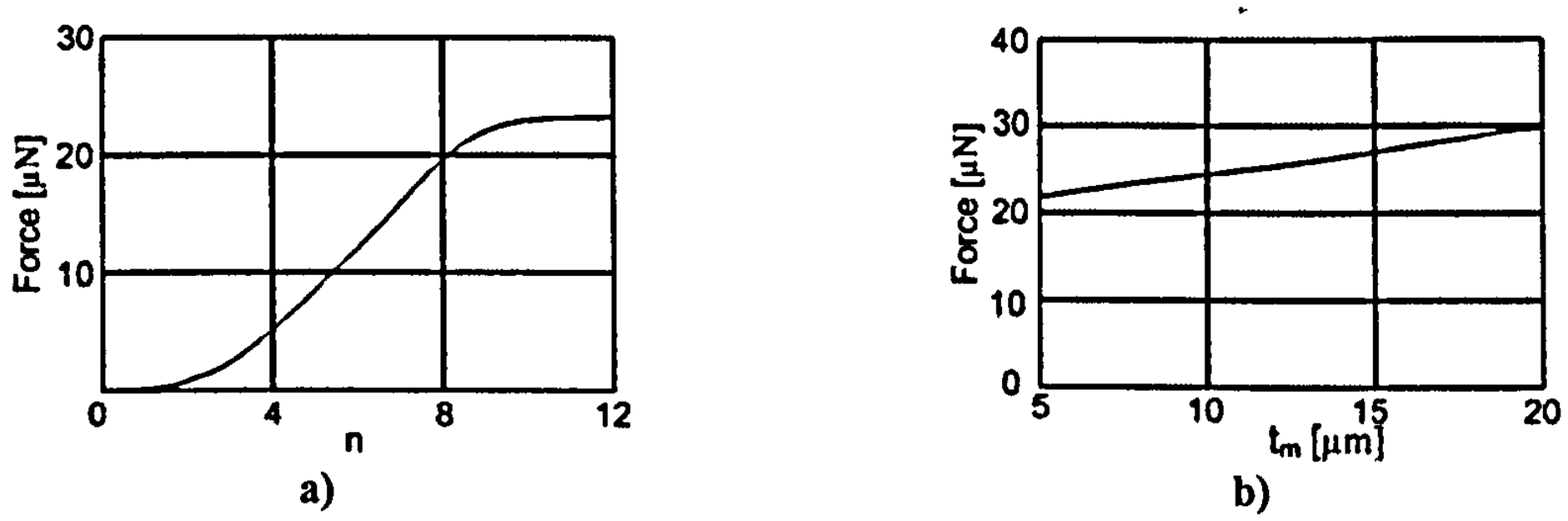

Figure 2-9 a) The magnetic force as a function of the number of turns of the coil. b) The magnetic force as a function of the thickness of the magnetic material block [15].

As expected, the smaller d, the higher the force on the magnetic material according to the law of Biot-Savart as shown in Figure 2-10a. Figure 2-10b shows the relationship between the force and the width of the core. In this example, the width of the magnetic material block w_m is equal to 800µm. Without a core ($w_{core} = 0$) there is already an attractive force of around 17µN. By adding a core material of increased width in the middle of the planar coil, the magnetic flux is increased, which creates an attractive force up to an optimum value. After that point, the force starts decreasing with increasing core width and becomes null when the dimension of the core is to equal the dimension of the magnetic material block. Even though the μ_r component in the magnetic path is increased (within the computer simulation), beyond a certain dimension, there is not enough room left for the coil to generate a magnetic field in the region of the magnetic material block.

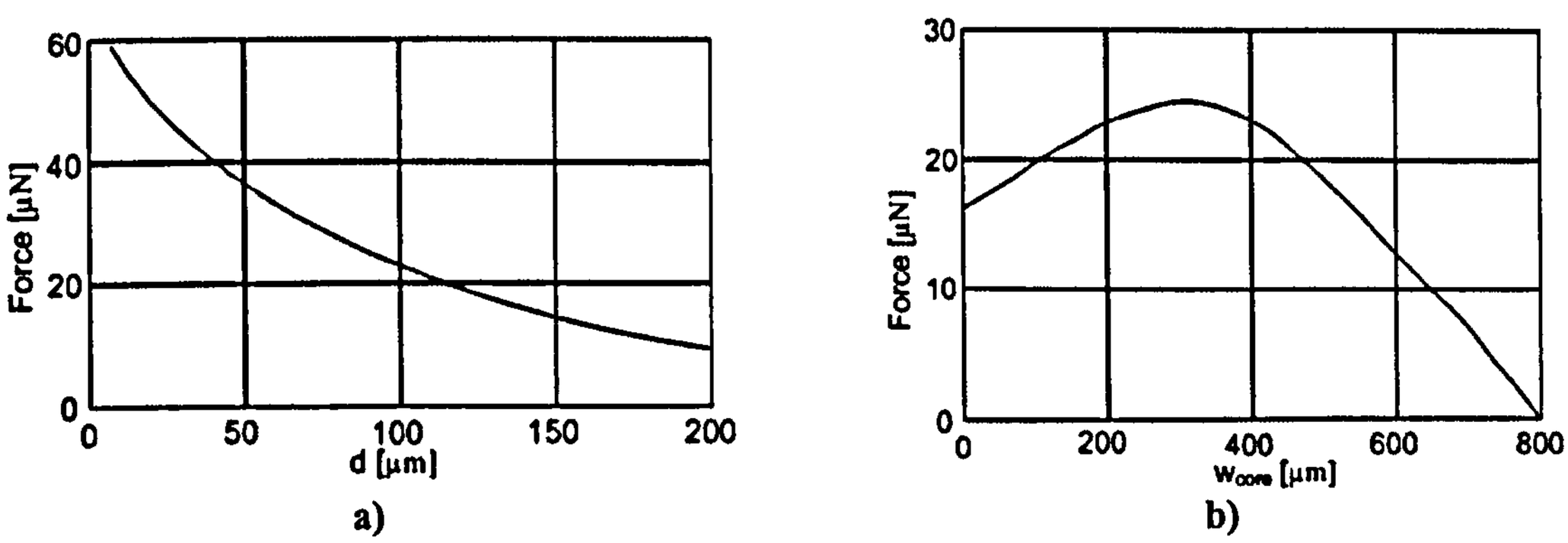

Figure 2-10 a) Magnetic force as a function of the distance between magnetic material block and the coil. b) Magnetic force as a function of the length of the core [15].

[15] also considers the increase of the cross-section of the coil in order to obtain a stronger magnetic field. If w_c is increased, the cross-section of the conducting coil also increases at the expense of the spacing between the coil conductors, s_c. This reduces the amount of windings possible and therefore goes against the requirement for stronger fields. Hence, the only permissible parameter for change is the height of the coil, t_c. The production of the coils and core involves the use of AZ photoresist and the electroplating of Cu or NiFe. For the deformable structure, a polyamide layer is created, by spinning it on top of a silicon wafer. The magnetic material block is then electroplated. The polyimide structure is subsequently released by etching Si with KOH. Finally, the structure is cut out by an excimer laser. The length and width of one of the supporting beams are 1000μm and 20μm respectively. Deflections of about 100μm have been stated. The entire beam structure is mounted about 100μm above the planar coil. With a current of 0.5A, the deflection of the structure was 4μm. The authors did not mention the amount of turns on the planar coil but about 8 turns are assumed to have been used for that experiment.

[16] present an electromagnetic actuator for micro-relay applications. The actuator consists of a cantilever beam and a planar electromagnetic coil within a low-reluctance magnetic circuit. If a current of 80mA is fed into the coil, an actuation force of 200μN is generated. Theoretically, a driving current of 800mA is feasible for a resulting force in the mN range. Variable reluctance actuators require the optimisation of magnetic permeability, air gap reluctance, magnetic core reluctance and beam spring constant. Permalloy is used for the cantilever material and copper for the coil. The design also features next to the air gap a permalloy magnetic flux return path. Equation (2-5) gives the magnitude of the magnetic force F_{mag}, which is the gradient of the magnetic energy field, U_{mag}, which exists within the air gap.

$$\left|\mathbf{F}_{mag}\right| = \left|\nabla U_{mag}\right| = \frac{1}{2}\left(\frac{N \cdot I}{\Re}\right)^2 \frac{\partial \Re}{\partial l} \tag{2-5}$$

N is the number of turns of the field generating coil, I is the current flowing through the coil and $\mathscr{R}$ is the magnetic reluctance given by equation (2-6),

$$\Re = \frac{l_{core}}{\mu_{core} \cdot A_{core}} + \frac{l_{gap}}{\mu_{gap} \cdot A_{gap}}, \tag{2-6}$$

where l_{core} is the magnetic path length within the permalloy core material (Figure 2-11), A_{core} is the cross section of the core and μ_{core} is the permeability of the core ($\mu_{r\_core} \cdot \mu_0$). l_{gap} is the magnetic path length within the air gap, A_{gap} its cross section and μ_{gap} is the permeability of air (μ_0).

Figure 2-11 shows a simplified drawing of the actuator. The permalloy cantilever beam works not only as a restoring element but also as a magnetic flux conductor. The return path for the magnetic flux Φ is attached to the substrate. Therefore, the magnetic core of the coil is only interrupted by the air gap, which is of course necessary for the actuation. In [16], a lot of optimisation was necessary in order to achieve a magnetic path with the least reluctance possible. One of the most important features of the core material is the relative permeability, which can vary largely with different materials. By neglecting this important parameter, the reluctance of the magnetic circuit is not dominated by the air gap and hence less actuation force is achievable.

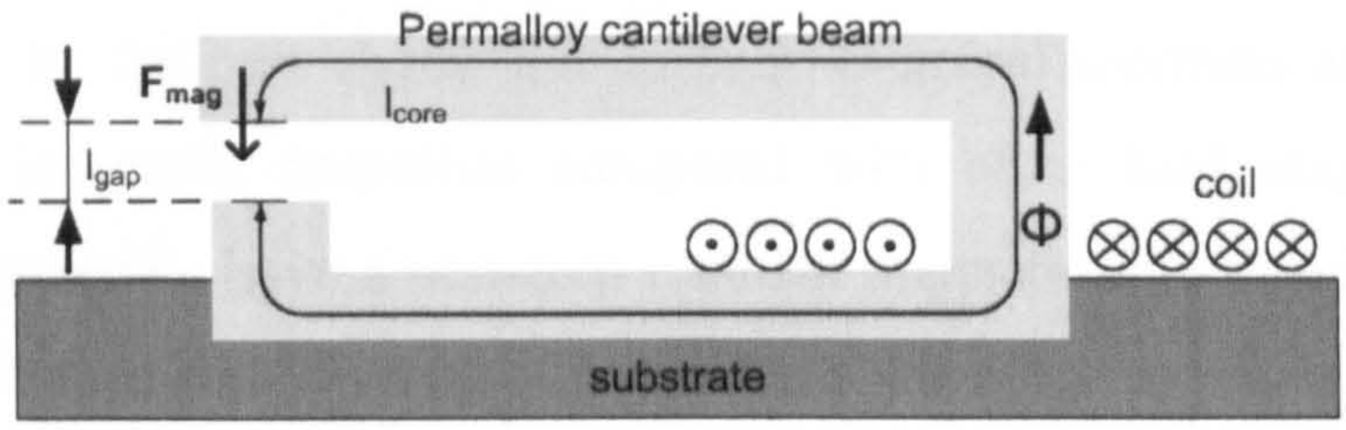

Figure 2-11 Magnetic microactuator. The magnetic field lines produced by the planar coil are directed via a magnetic path to the air gap where the actuation work is done [16].

For the highest efficiency, the reluctance of the air gap must be much bigger than the reluctance of the core. A large height of the core structure, necessary for a low magnetic reluctance, is difficult due to the planar process used. Additionally, the magnetic reluctance of the small air gap is also limited by the microstructure of the actuator. In order to achieve the maximum power output, the magnetic reluctance of the air gap should be equal the magnetic reluctance of the core in analogy with the highest power delivery in the electrical domain. The relation between the bending force and the resulting displacement is shown in Figure 2-12. The dimensions of the beam are 650μm in length, 200μm in width and 10μm in height. The force was not applied by the actual actuator since this force is, as already reported, limited to approximately 200μN. The

graph shows a very linear curve which goes up to a displacement of 50μm with a force of around 950μN. A Young's modulus of 95.6GPa is reported.

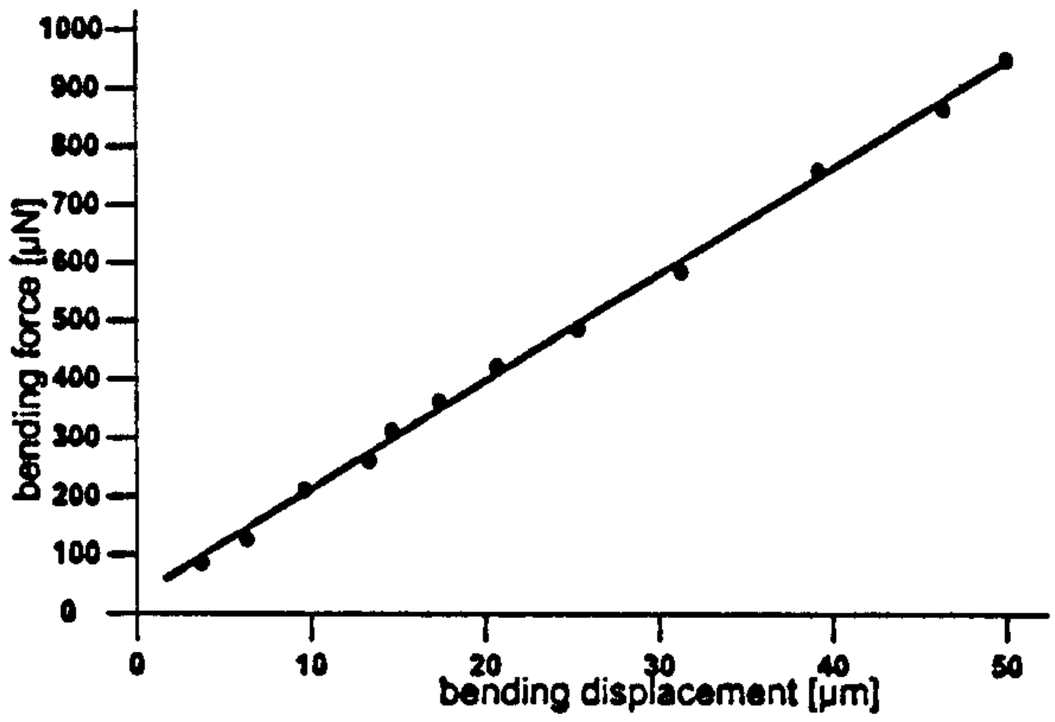

Figure 2-12 Bending force as a function of the bending displacement. The straight line represents the linear fit of the measured points [16].

[17] report a magnetic microactuator that uses a composite material, which is a mixture of a polymer with a powder of ceramic ferrites. This material is compatible with standard micromachining processes. The deposition of hard magnetic material is difficult to achieve by electroplating, sputtering or evaporation processes. For example, the preparation of samarium-cobalt and neodymium-iron-boron magnets requires high temperature, pressing and sintering that is destructive to most MEMS devices. Ceramic ferrites prove to be the best choice due to their chemical inertness at the expense of relatively small magnetic properties compared with other hard magnetic materials. Hard magnetic materials have a non-zero remnant magnetic flux density, B_r, when the external field becomes zero (Figure 2-13a) and can therefore be regarded as permanent magnets. In order to reduce this remnant magnetic flux density B_r within the material, an external coercive field intensity, H_c, has to be applied. B_r and H_c are strongly material dependent. For better understanding a curve of an idealised magnetic curve of a soft magnetic material is shown in Figure 2-13b which does not exhibit any hysteresis.

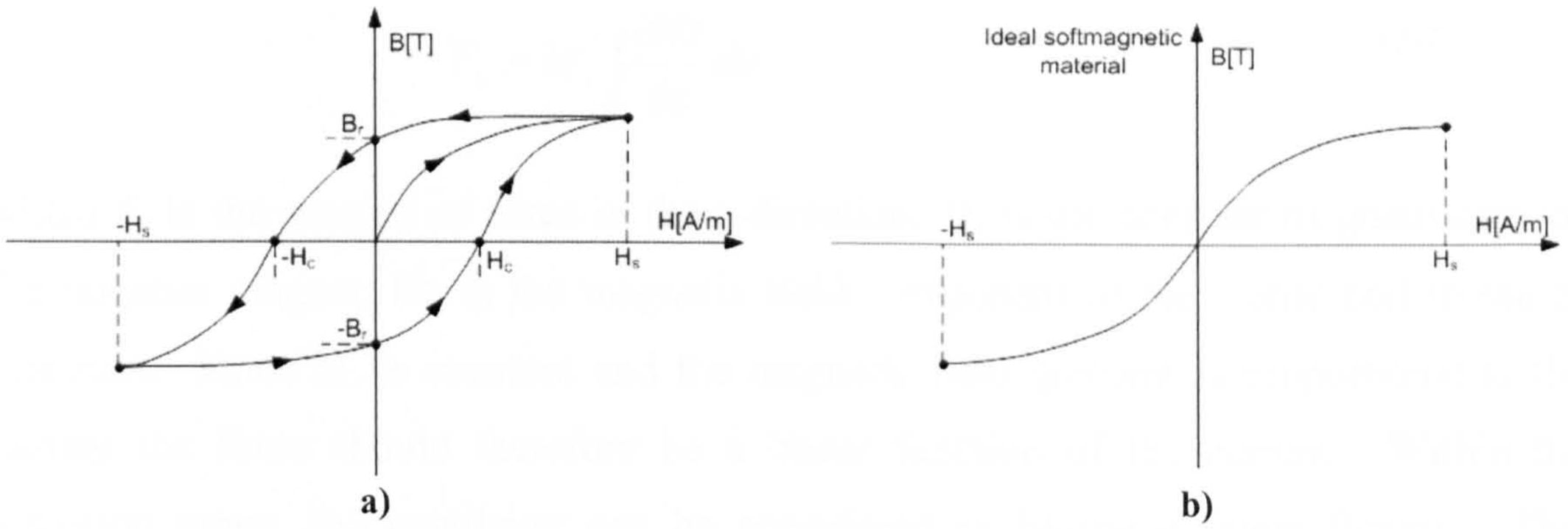

Figure 2-13 a) Hysteresis curve of a hard magnetic material. b) Hysteresis curve of a soft magnetic material [17].

Hard magnetic materials are favoured for magnetic actuation due to their good scaling and the large forces that can be generated. Furthermore, it is possible to obtain an attractive force instead of a repulsive force, by reversing the current within the coil. The polymer magnetic material is placed on top of the free end of the cantilever beam. A planar coil is manufactured on the opposite side of the substrate as shown in Figure 2-14.

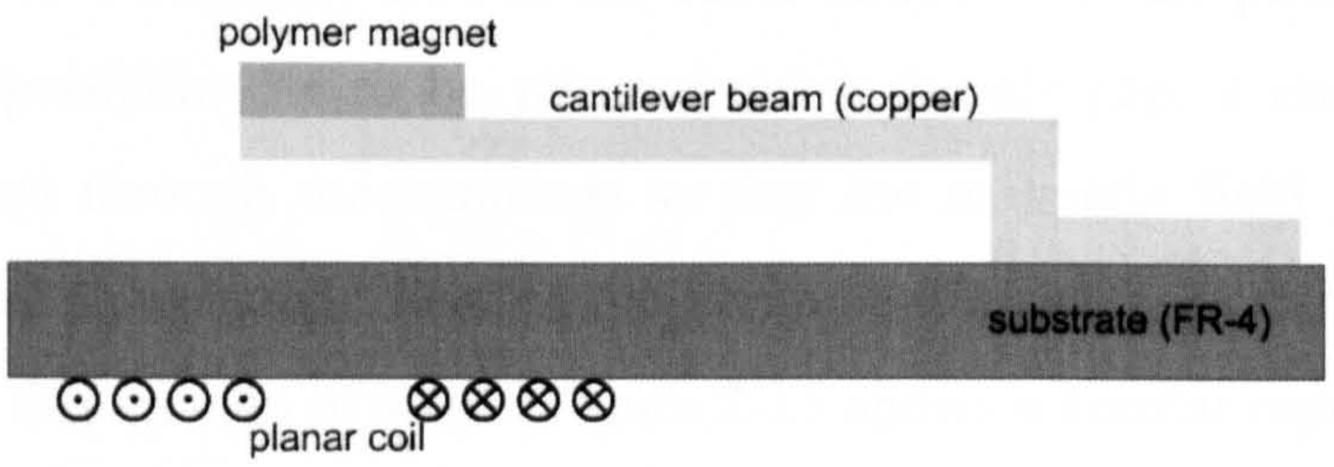

Figure 2-14 Magnetic microactuator. The polymer magnet at the end of a cantilever is a permanent magnet and can hence be moved in the positive as well as in the negative vertical direction. This is done by choosing the direction and amount of the current flowing through the planar coil on the back side of the substrate [17].

Strontium ferrite powder, of particle size of around 1.5μm, was mixed with DuPont PI-2555 polyimide with addition of some chemical substances that improved the particle dispersion. The material was mixed for 72 hours at 5rpm within a ball mill. The composite material was then spun on a wafer and patterned. Subsequently the material was cured for 1 hour at 300°C. Upon the final cure, the magnetic polymer was exposed to an external magnetic field. The samples where then measured by making use of a vibrating sample magnetometer. For a concentration of 95% polymer material coercive field strength of 4000Oe and a remnant flux density of 3000 Gauss have been reported. The force generated by this actuator is given by equation (2-7),

$$\mathbf{F_z} = M_z \int_V \frac{\partial Hz}{\partial z} dv \qquad (2\text{-}7)$$

where $\boldsymbol{F_z}$ is the amount of force in the z-direction, M_z is the constant magnetisation of the polymer magnet, Hz is the magnetic field component of the planar coil in the z-direction. Since M_z is constant and the magnetic field gradient is proportional to the current the force should therefore be a linear function of the current. Within the actuation range, the cantilever can be considered as having a linear flexure. This implies that the deflection is a linear function of the current flowing through the planar coil. With this method a hard magnetic actuator can be realised by making use of a low temperature batch-fabrication-compatible process. With a current of just 20mA a deflection of over 0.3mm is achieved.

[18] use a magnetic actuator for bringing a vertical mirror into bistable positions. The cantilever beam provides the restoring force. A current is passed through the windings, only if the state needs to be changed. If the permalloy is away from the air gap, a current that creates a magnetic flux in the same direction as the permanent magnet is applied. If the permalloy is to be released from the air gap, a current in opposite direction is passed through the windings so that the magnetic field generated by the windings opposes the magnetic field of the permanent magnet. A current of 1A needs to be applied for this change of state. Figure 2-15 shows a similar representation of the setup described in [18]. The driving circuit's magnetic dimensions are 5mm x5mm x 1mm and the permalloy attached to the beam measures 1mm x 1mm x 100µm.

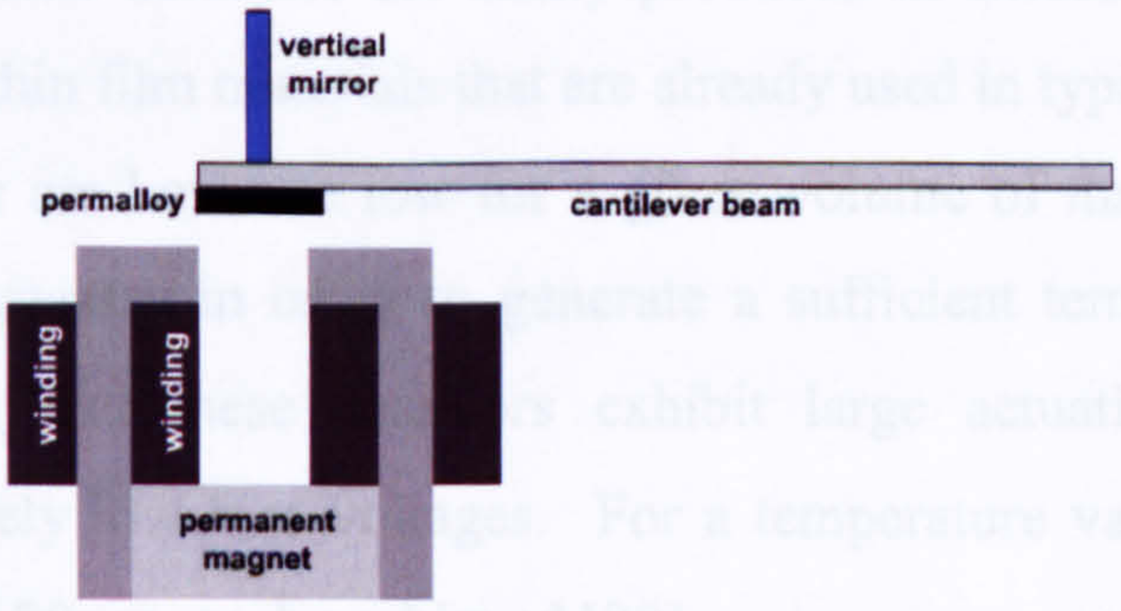

Figure 2-15 The horseshoe like magnetic circuits dimensions are 5mm x 5mm x 1mm. To release or attract the permalloy, a current of different directions is passed through the windings. The resulting magnetic field of the windings either supports or counteracts the magnetic field of the permanent magnet [18].

2.2.2.7 Bimorph actuator/bimetallic thermal actuator

The bimetallic actuator consists of two metals of different coefficients of thermal expansion (CTE) that are joined together. If the actuator is heated, the different expansions between the metals cause internal stress and bending of the structure. For the largest deflection per unit of temperature, materials should have the largest CTE difference. Figure 2-16 illustrates the basic principle of a bimetal actuator. Metal 1 has a higher CTE than metal 2, hence it expands more with temperature as seen on the left hand side of the figure. The two metals are now joined together, by soldering, gluing or as depicted symbolically by using a nut and bolt. Metal 1 experiences a compressive stress, since metal 2 restricts its full expansion. On the other hand, metal 2 experiences a tensile stress since metal 1 forces it to expand more. The bimetal bends and a deflection is noticeable on the tip of the actuator.

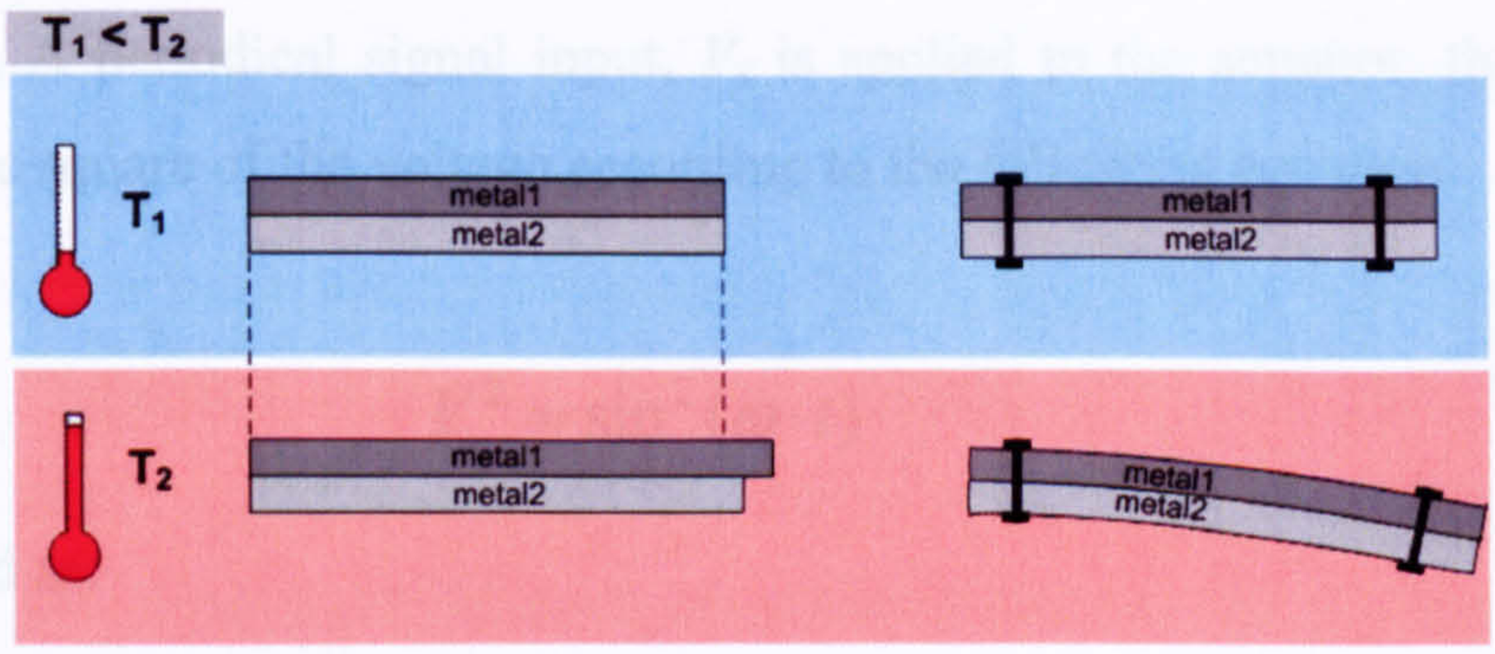

Figure 2-16 The basic principle of a bimetal actuator. Metal 1 has a higher CTE than metal 2 as shown on the left hand side. If the two metals are now joined together as shown on the right hand side, metal 1 experiences a compressive stress and metal 2 a tensile stress. Because of that stress gradient throughout the structure, the actuator bends downwards.

[12] state that bimetallic actuators are easily produced in silicon-based microsystems due to the variety of thin film materials that are already used in typical silicon processes. The generated forces are however low for a given volume of material. Furthermore, high currents are necessary in order to generate a sufficient temperature change. In contrast, [19] argue that these actuators exhibit large actuation forces and high deflections at relatively low bias voltages. For a temperature variation of 60 Kelvin, deflections of around 20μm can be achieved [20].

2.2.2.8 Thermal actuators

Compared with electrostatic microactuators of similar size, thermal actuators have the ability to provide larger deflections and greater force [21]. A chevron microactuator is shown in Figure 2-17. Two cantilevers are connected together in a V-shape at each end

and connected to the substrate via a rigid anchor at the other end. A current passing through both anchors heats up the cantilevers that expand by *L'*. The cantilever on the right side of the figure cannot be moved from the anchor side, the left cantilever is moving by the distance h in order to compensate for the elongation *d*.

If several of these actuators are placed behind each other and the tips of the V-cantilevers are connected with each other, the force can be easily increased. A chevron RF switch made of polysilicon, sputtered gold and low stress silicon nitride as a structural material is presented in [22]. The V-shape generates forces, which range from hundreds of μN to up to mN. An output force of 8mN with an input power of 180mW is reported. The displacement of these actuators is usually not large. Displacement amplifiers are needed to transform the strong force into a large displacement. Information about the frequency response of the chevron microactuator has been reported [23]. A periodical signal input, *V*, is applied to the actuator; the temperature varies with the square of the voltage according to the following equation

$$V^2 = \sin^2(\omega \cdot t) \tag{2-8}$$

also expressed as:

$$V^2 = \frac{1}{2} \cdot (1 - \cos(2 \cdot \omega \cdot t)) \tag{2-9}$$

The term with the cosine shows the doubling of the frequency. The power is independent of the voltage polarity. Therefore, one electrical cycle generates two mechanical cycles. For a frequency of 500Hz, the actuator temperature varies from around 40°C to 370°C. The actuator has enough time to cool down. No steady temperature increase, superimposed over the oscillation, is reported. However, above a certain frequency, the actuator is not able to cool down to its initial temperature. By increasing the frequency to 5kHz the oscillation continues at a higher temperature and a lower amplitude. There it cycles between 147°C and 233°C, with an offset value of around 190°C. At even higher frequencies, it is reported, that the oscillation finally stops and the temperature reaches a value according to the RMS value of the signal. The 3dB frequency where the amplitude of the signal has half of its original value is in

the order of 1 to 2.6kHz. The measured thermal time constants are between 60 and 160μs.

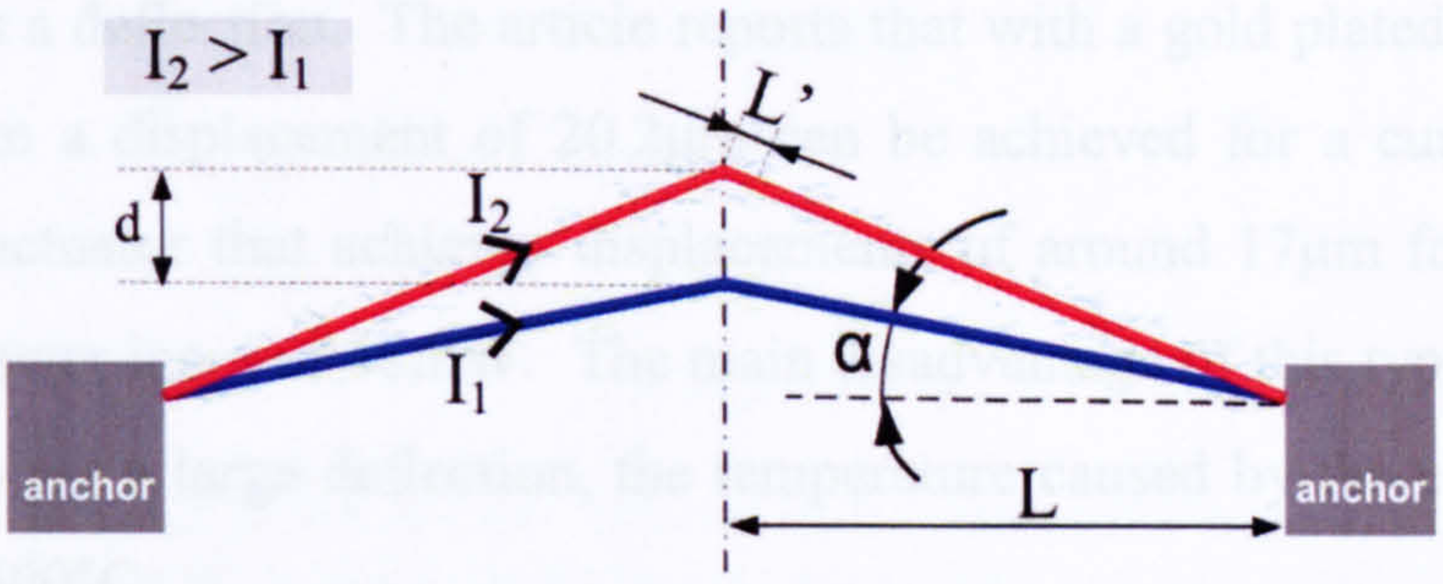

Figure 2-17 A V-structure of cantilevers is attached and fixed to two anchors. If a current I_2 is supplied to the anchors, the current flows through the V-structured cantilevers that thermally expand. Since the structure is fixed on both ends, the elongation L' has to be compensated by moving the tip or the V-structure the distance d.

A chevron actuator does not have to be produced by using special materials as with magnetic actuators [24]. Another advantage compared to the electrostatic actuator is the low drive in voltage and real estate needed by this actuator. Furthermore, the chevron actuator produces a larger force than its electrostatic counterpart. An electrostatic comb drive actuator is capable of producing a force density of around 20μN/mm^2. On the other hand, the chevron actuator of [24] has a value of about 3700μN/mm^2. The displacement and dimensions of such an actuator are shown in Figure 2-17. The equation governing the displacement is:

$$d = \left[L^2 + 2 \cdot L \cdot L' - L \cdot \cos(\alpha)^2\right]^{\frac{1}{2}} - L \cdot \sin(\alpha), \tag{2-10}$$

where L is the projection of one beam, L' is the displacement due to the temperature and α is the pre-bent angle of the beam. The actuator works by exhibiting a high surface temperature of around 800°C, which is unfavourable for many purposes. For instance, the photoresist SU8 would not be able to endure this high temperature if the actuator was in near proximity. Furthermore, if the actuator were directly subjected to a biological or physical sample, it would damage irredeemably the specimen.

[25] report an electrothermally driven microactuator, which applies the so-called hot-cold-beam conductor technique, as seen in Figure 2-18. A current, I, is supplied via the anchor into the actuator. The cross-section area within the hot beam is smaller than the cross-section area of the cold beam. Due to the smaller cross-sectional area the

resistivity of the hot beam is higher than that of the cold beam. Since the current is the same in both beams, the temperature within the hot beam is higher than the temperature within the cold beam. This causes the hot beam to expand more than the cold beam, which generates a deflection. The article reports that with a gold plated actuator with a length of 250μm a displacement of 20.2μm can be achieved for a current of 6.2mA. [21] report an actuator that achieves displacements of around 17μm for a length L of 230μm and a power input of 18mW. The main disadvantage of this type of actuators is that, in order to get a large deflection, the temperature caused by the electrical current easily exceeds 500°C.

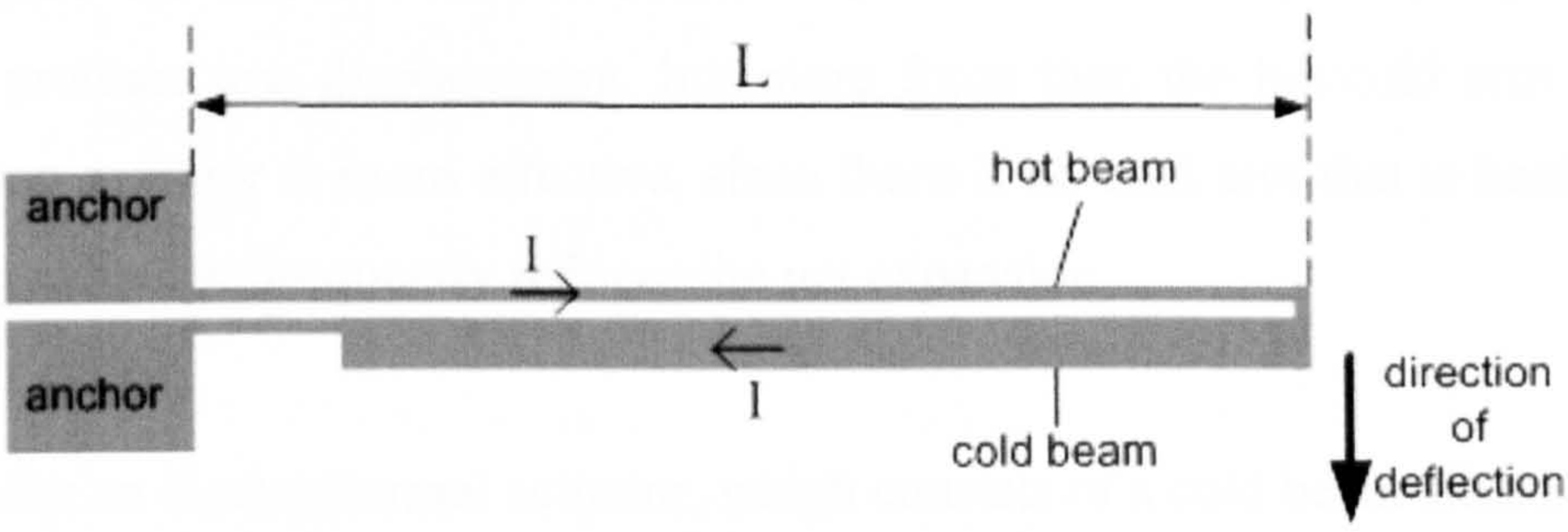

Figure 2-18 If a current flows through this thermal actuator, the hot beam temperature is higher than the temperature of the cold beam due to the different cross-sectional area [25].

[26] report also such high temperatures (660°C) with a length of the hot-beam of 240μm. Reliability tests have been conducted where the actuator survived more than 100 million cycles for a tip displacement of 12μm and a driving power of 8mW. The deflection curve as a function of the input power is shown in Figure 2-19. The deflection is relatively linear with respect to the input power. However, at a deflection of around 17μm the hot-beam exhibits plastic deformation. The failure rate depends on the total time the actuator is elevated at higher temperatures rather than on the number of cycles.

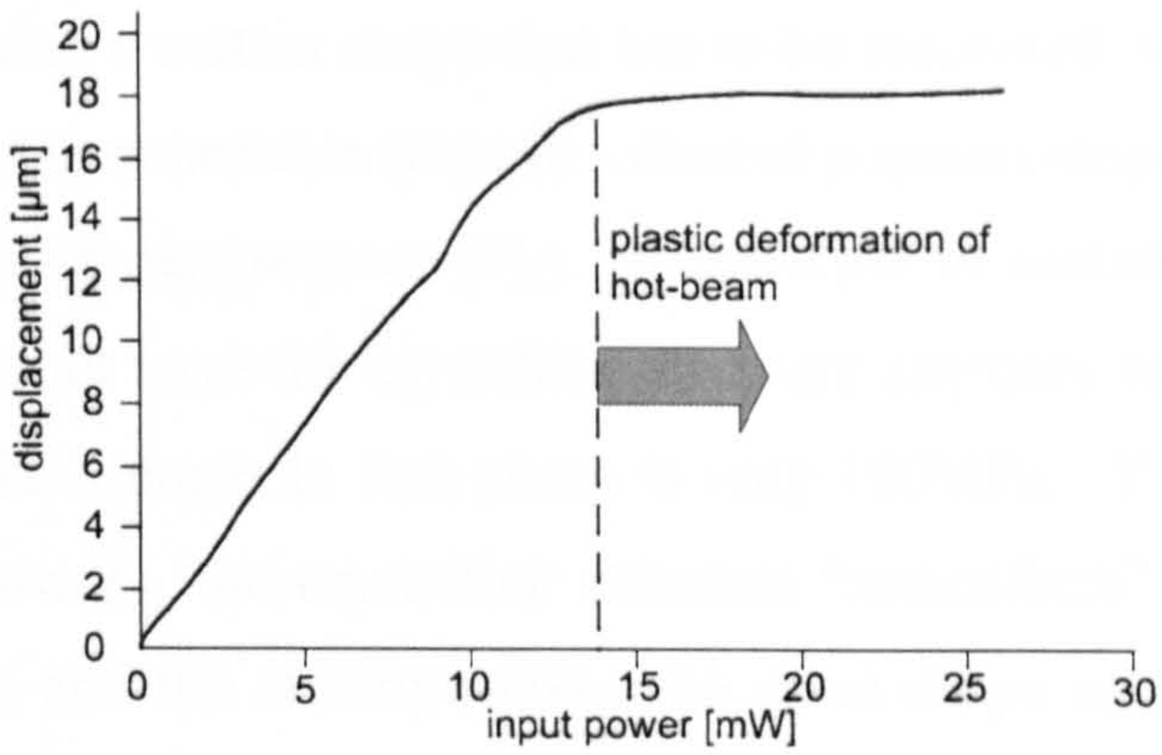

Figure 2-19 Displacement of the thermal actuator as a function of the input power. If the input power is higher than 14mW, plastic deformation occurs. Graph redrawn from graph found in [26].

[23] compare the hot/cold arm actuators with the chevron actuators. The chevron actuators produce less displacement, but more force than the hot/cold arm actuators. The chevron actuator is more effective, since there is no cold arm that is heated up and expanding, which subsequently reduces the net expansion.

[27] describe an electrothermal actuator, which consists of a cold beam situated between two hot beams. The angle of the cold beam is bigger than the one of the hot beams (angle with respect to a horizontal line between anchor and shutter). At one side, all the beams are connected to a respective anchor and on the other side they are all connected to a shutter. Four of these shutters constitute an artificial iris. A current is only passed from one hot beam to the other. The hot beams are thermally isolated by undercutting the underlying substrate. This further increases the temperature difference between the cold and the hot beams. For the actuation of the iris, a power of 240mW is necessary to achieve maximal optical attenuation. [27] expect that, compared with a chevron actuator that uses 4 hot beams, the proposed actuator delivers twice the thermal efficiency.

2.2.2.9 Shape Memory Alloy (SMA)

During heating, the SMA undergoes martensitic transformation, which leads to shape recovery [10]. The shape recovery takes place at the so-called transition temperature also called austenite temperature. SMAs are formed above the austenite temperature where the crystalline structure is highly ordered. During cooling down the austenite phase changes into the martensite phase. In this phase the crystal structure is usually plagued with twin planes that makes possible the deformation of the crystalline structure throughout the alloy [1].

The process for forming a certain shape that has to be recovered is as follows. During training of the SMA, the material is fixed in a desired position/shape and then heated up well above the transition temperature (T_{tr}). If the alloy is cooled into the martensite phase, the alloy does not have the crystalline structure anymore and is easy to deform plastically. The yield strength in that phase is only 100MPa. If the material is now heated up again above T_{tr}, the crystalline structure "remembers" its form during the training of the SMA and the structure takes the same shape as the desired position. During this phase transition from martensite to austenite, a pressure is generated that is as high as 100MN/m^2 and hence results in a substantial force. The austenite phase has a much higher yield and is able to endure stresses of up to 560MPa. The temperature interval over which the change takes place is 10°C to 20°C. Nitinol™ is a TiNi alloy that is commercially available and has a 1:1 Ti:Ni-ratio. By increasing the Ni content, the transition temperature decreases at a slope of 25°C per 0.2% Ni. The material can be deposited as thick as 50µm and exhibits similar behaviour as the bulk material. At room temperature the deposited material is amorphous and needs to be crystallised at around 500°C. In general for TiNi-alloys the operating temperature is limited to 70°C for a bandwidth of 5Hz. In [28], an SMA micropump has a maximal frequency of 1.2Hz. The SMA also displays a hysteresis behaviour due to the relatively long cooling times, which makes the actuation more difficult to control. The voltage level is TTL compatible and the biocompatibility is also good. From an energy-density point of view, the SMA outperforms electrostatic and magnetic actuation by a factor of around 26 and 10, respectively. An actuation range from 10µm to mm can be performed with a SMA [10]. The SMA can be driven either externally by a heat source or directly by supplying a current through the structure itself.

2.2.2.10 Magnetostriction (Terfenol D®) actuation

[1] present precision displacement achieved by a magnetostrictive actuator. Displacement of 10-100µm with accuracy of positioning of up to 0.1µm is reported. Terfenol™ is a magnetostrictive material that exhibits expansion when immersed in a magnetic field. Terfenol™ is mechanically stronger than piezoelectric materials and can handle higher temperatures. Additionally Terfenol™ changes its shape faster than a piezoelectric material. However Terfenol™ does not operate at high frequencies and is more expensive than piezomaterials. Since the magnetostrictive material conserves the volume, the width of a beam gets smaller when its length increases more than 0.1% of the original length. From a construction point of view, the actuator beam can be

manufactured in a manner similar to piezoelectric material. The lever amplification does not need to be as high as for the piezoelectric material. On the other hand, a coil must be manufactured in the vicinity to the Terfenol™ block. Terfenol™ can exert pressures up to 55MPa and is fairly brittle when a tensile stress is applied. On the other hand, it can cope well with a compressive stress (tensile strength 28MPa, compressive strength 700MPa). Terfenol™ is chemically not inert and should not be exposed to an oxidizing environment due to its iron content. Furthermore, Terfenol™ has the largest amount of strain compared to other materials classified as magnetostrictive.

2.2.2.11 Piezoelectric material

Piezoelectric material presents a small elongation in the order of 0.09% of the total length of the material. A lever with an amplification ratio of one to ten is required to achieve a displacement of 10μm, when using a rather unrealistic 1mm long piezoelement. A further problem is the deposition of the piezoelectric material. The usage of sol-gel dictates a processing temperature of up to 900°C, which is far too high for the micro-LEDs of the device to be packaged and exceeds the temperature range of the negative photoresist SU8. [29] give a short explanation of the sol-gel process itself.

The sintering of a modified PZT structure requires temperatures between 700°C and 1000°C [30]. After sintering, the structure needs to be attached with electrodes and polarised by applying an electric field of 20kV/cm while immerged within a 120°C silicon-oil bath for one hour. In [31] the integration of PZT films with existing semiconductor technology places several limitations on the deposition and processing parameters associated with the ferroelectric film. Furthermore, a strict thermal budget needs to be observed in order to preserve the underlying semiconductor structures.

A slight reduction of the temperature is stated by [32]. By applying the hydrothermal method, the wafer encounters the highest temperature of 300°C where it is pre-baked for 10 minutes. The only possibility is to incorporate a bulk piezo-element into the microfabricated structure. This process creates difficulties since the piezoelement has to be placed very accurately between the electrodes, or even integrated within the entire fabrication process.

As mentioned before, piezoelectric actuators can develop a huge stress and hence force. The devices exhibit however a small strain, which limits their range of actuation. The microlens array is to be actuated in a range of +/- 5µm. A total actuation of 10µm is therefore required, which is not feasible with a piezoelectric device unless a 10mm long piezoelement is manufactured. A design has to be found which amplifies this distance by a certain factor in order to achieve the appropriate range of movement for the µLens. Figure 2-20 shows a possible solution. The µLens is attached to a lever at a distance l_2 to the pivot. The piezoelement is asserting its force to the lever at a distance l_1 from the pivot. Due to the geometrical restrictions of the device, the total length of the cantilever can be estimated to be around 800µm; hence l_2 is chosen to be 800 µm. Assuming the intended actuation range (Δd_2) to be 10µm, the angle of the cantilever towards the horizontal direction can be calculated. Since the angle is very small it can be assumed that angle φ equals $tan(\varphi)$.

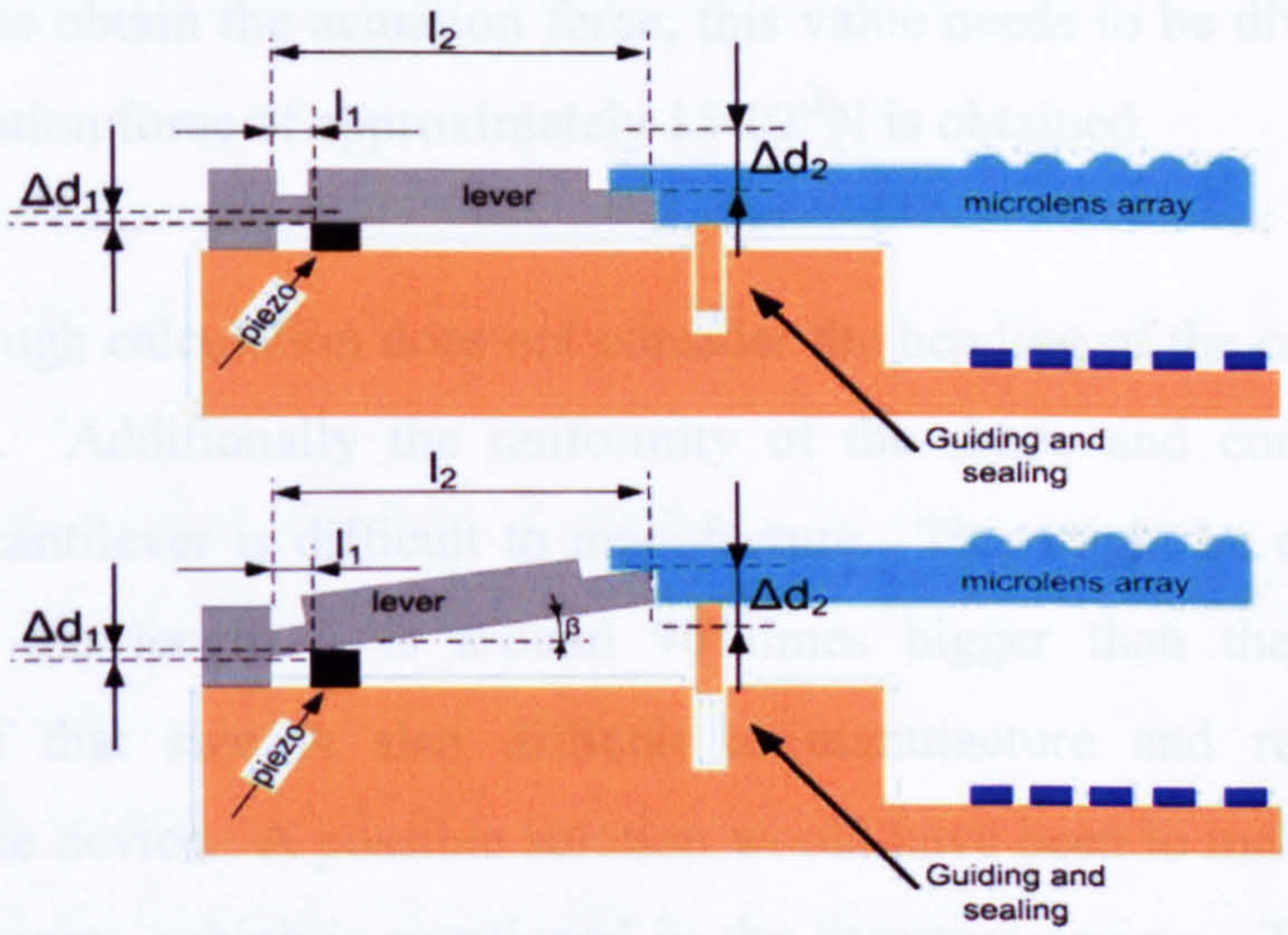

Figure 2-20 Piezoelectric actuator that uses a lever in order to get the appropriate actuation range. In the top picture, no voltage is applied to the piezo element and therefore there is no strain. By applying a voltage to the piezo element the device starts to strain. The cantilever amplifies this movement, which results in a displacement of Δd_2 and exhibiting the angle β on the cantilever with respect to the horizontal plane.

As a consequence, a direct ratio between Δd_2, Δd_1, l_2 and l_1 can be calculated according to equation (2-11).

$$\frac{\Delta d_2}{\Delta d_1} = \frac{l_2}{l_1} \tag{2-11}$$

The dimensions Δd_2, Δd_1 and l_2 are known and l_1 can be calculated by using equation (2-11). Due to this leverage, the force which can be exerted on the microlens array is proportional to the two different lateral lengths l_1 and l_2 and can be calculated from the equilibrium of moments:

$$|\mathbf{F}_1| \cdot l_1 = |\mathbf{F}_2| \cdot l_2 \tag{2-12}$$

where F_1 is the force applied by the piezoelement at the distance l_1 and F_2 is the force actuating the microlens array at distance l_2 from the pivot. From equation (2-12), the amount of force acting on the microlens array is around 90 times smaller than the force exerted by the piezoelement. The stress originating from a piezoelement is of the order of $35 \cdot 10^6 N/m^2$ [33]. A width of 400µm and a depth of 100µm seem realistic for the given device. Multiplying the area of the piezoelement with the stress yields a force F_1 of around 1.4N. This is a huge force for such a small device. As stated in equation (2-12), in order to obtain the actuation force, this value needs to be divided by 90. In that way an actuation force of approximately $15 \cdot 10^{-3} N$ is obtained.

However, this rough calculation does not consider the bending of the cantilever subject to such a force. Additionally the uniformity of the shape and consistency of the material of the cantilever is difficult to manufacture. This might be considered to be important since the length l_2 is around 90 times bigger than the length l_1. A piezoelement of that size is also difficult to manufacture and requires accurate positioning on the device. A possible solution would have been to make use of the so-called sol-gel process, which is mentioned in the literature review. This method was abandoned, since the manufacturing temperatures involved within this process exceeds the temperature limitation of the micro-UV-LED array. Moreover, the task of placing the electrodes on top and at the bottom of the piezoelement was considered extremely difficult. For all these reasons, piezoelectric actuation has been discarded as a mechanism to actuate the microlens array.

2.2.3 Comparison of electrostatic and magnetic actuators

One of the main advantages of electrostatic actuation is the simpler manufacturing process than for all other actuators, since, in most of the cases, a thin film of two metal plates is sufficient to build a simple electrostatic actuator. [34] argue against the widespread belief within the MEMS community, that electrostatic microactuators are more favourable that the magnetic approaches. For 1μm air gaps, magnetically generated forces can be made much larger than by using the electrostatic approach. Even on microscale, magnetic field energy densities can be two orders of magnitude greater than electric field densities. For instance in conventional motors, which make use of iron, the magnetic flux density is limited to 1.5 Tesla (T) due to saturation effects. Nevertheless, an energy density of two times the value of the electrostatic field can be achieved in that way. Thin ferromagnetic films can achieve flux densities of 2T. With the use of superconducting magnets, the flux density could be up to 2500T, whereas 100T are regarded to be destructive for the device generating the field. [34] also take up the issue of efficiency. The magnetic actuator cannot be as efficient as an electrostatic actuator since, in order to produce an electromagnetic field, a current has to flow, whereas for an electrostatic field just a potential difference is necessary. This is not only true for the DC state of an actuator but also for the higher frequency ranges. Even though the charges move from one side of the electrostatic plate to the other and hence a charge and discharge current is observed, the electrostatic actuator is still more efficient because the losses within the magnetic actuator due to eddy currents and hysteresis losses are more dominant. Then again, this comparison assumes that the majority of loss is caused by electrical rather than mechanical losses. These mechanical losses are due to stiction and friction, which are predominant within a microdevice. These mechanical losses render in fact all types of magnetic actuators nearly equal in efficiency. The electronics, which powers the actuator, has also a power consumption, which is probably much higher than the acting device itself. System efficiency should hence be regarded as a whole.

In the context of this project, the actuator to be chosen must develop maximal force within a confined space to move the microlens array provided that heat dissipation is kept within reasonable limits. Since the system has dimensions in the mm range compared to the micrometer range of the actuator, heat dissipation can be neglected. The main advantages of the magnetic microactuator lie in its diversity of uses for different applications, especially in the macroscale and the limited interferences with

electronic circuits. This applies if the magnetic flux is well confined and the induction can be neglected if no fast changes of the magnetic field appear. Electrostatic systems tend to wear because of damage caused by electrical breakdowns in the gap. This is especially important since some actuators are meant to work in a harsh environment with aggressive chemicals and biologic samples. Hence, these materials are not only able to attack the structure of the device but also alter the dielectric constant within the driving electrostatic field. Magnetic actuators in contrast are not susceptible to such influence since few chemical and biological samples exhibit magnetic properties that would influence the driving force. One of the restrictions that apply to magnetic microactuators, that use a permanent magnet, is the maximal temperature. Above 200°C, degradation in magnetic performance has been reported. In conclusion, to achieve tasks with μm precision, the actuator itself does not require to be of micron size [34]. For many applications, which require high-speed positioning with micrometer accuracy, magnetic actuators are in many respects to be favoured.

2.3 Existing static alignment methods

[35 , 36] describe an alignment method of the microlens array with reflective Fresnel zone plates (FZP) that are manufactured onto the VCSEL edges and alignment marks on the corresponding edges of the microlens array. The device is shown in Figure 2-21a. A wide planar alignment beam with uniform irradiance distribution is then shone onto the assembly. If the microlens is in its ideal position, the reflected spot of the FZP focus on the alignment marks of the microlens array. Four lateral alignment marks are used. The vertical alignment is achieved by using a spacer ring which is only described to be "precisely machined". Figure 2-21b shows a picture of VCSEL from the top. A test device achieved alignment accuracy of 9μm. The authors however claim that a theoretical accuracy below 2μm is feasible. After alignment, the assembly is fixed with UV-curable adhesive.

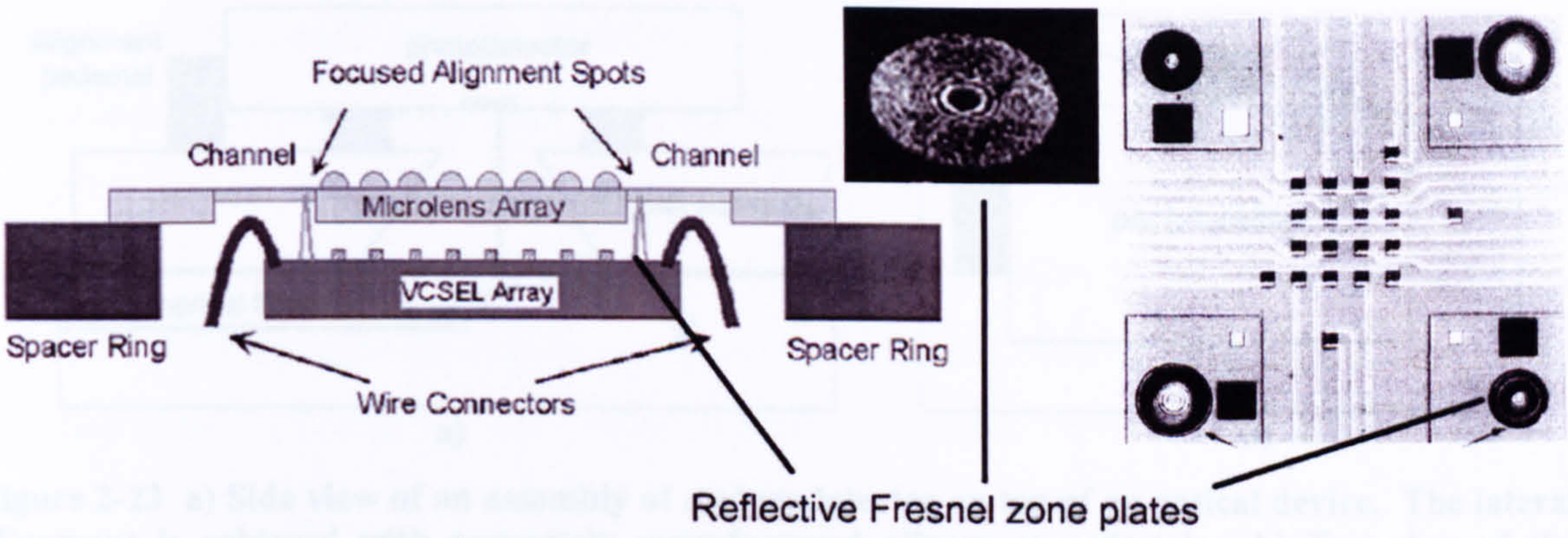

Figure 2-21 a) Side view of the VCSEL- microlens array assembly. The spacer ring determines the vertical distance. b) Top view VCSEL array that features reflective Fresnel zone plates (FZP). Pictures used with courtesy of [35 , 36].

[37] align with submicron accuracy a microlens array on top of a CCD array using transitional stages. The assembly is fixed by using UV-curable adhesive. Figure 2-22 shows a simplified representation of the drawing found in [37]. The microscope is used to enlighten selectively specific areas of the microlens array. The alignment itself is detected via the CCD device, which gives a feedback to the different translation stages and rotation stage to bring it to its optimal position.

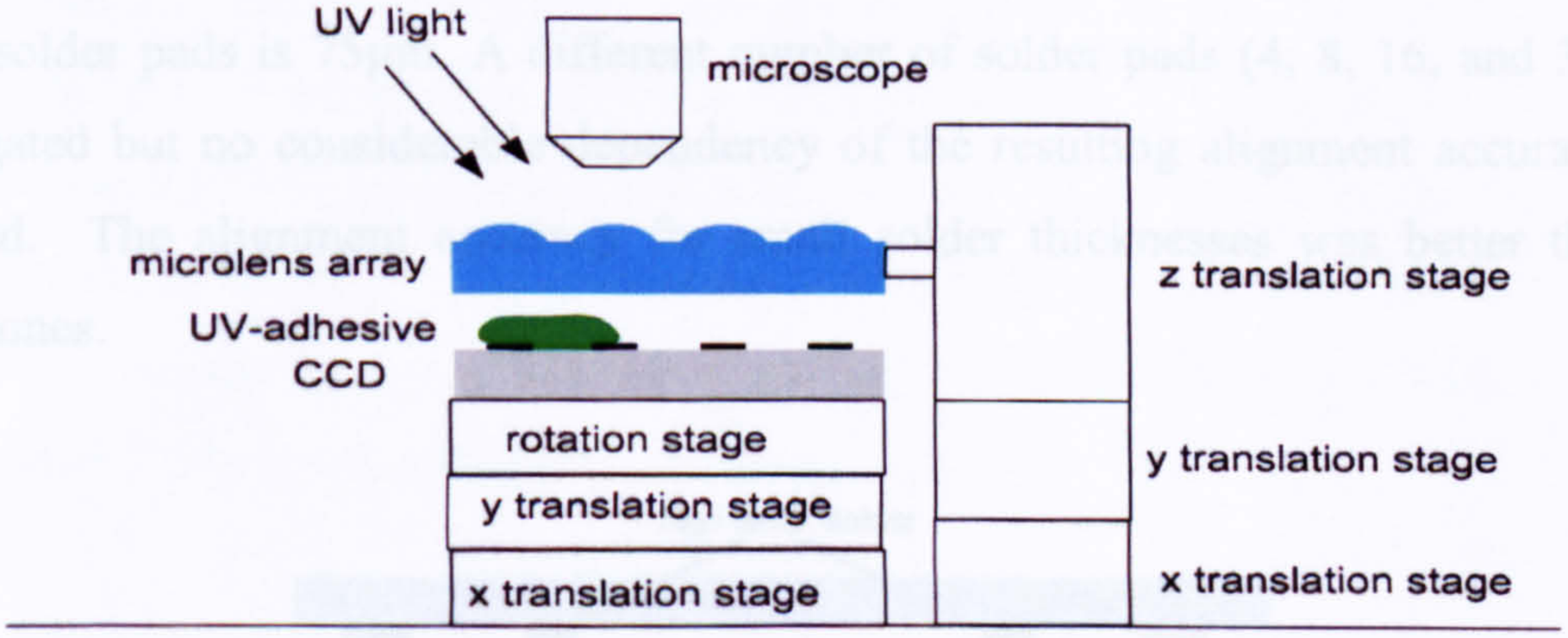

Figure 2-22 The microlens is aligned with respect to the input signal of the different CCD detectors. The light source is the microscope. The actuation is achieved via different translation and rotation stages and the assembly is fixed in place by using UV-curable adhesive [37].

[38] use alignment pedestals to achieve accurate lateral alignment for a photodetector placed over an optical device as shown in Figure 2-23. The alignment pedestals are formed through electroplating of NiFe with a mould previously patterned with photoresist. It is mentioned that an estimated lateral alignment accuracy of ± 5μm is achievable.

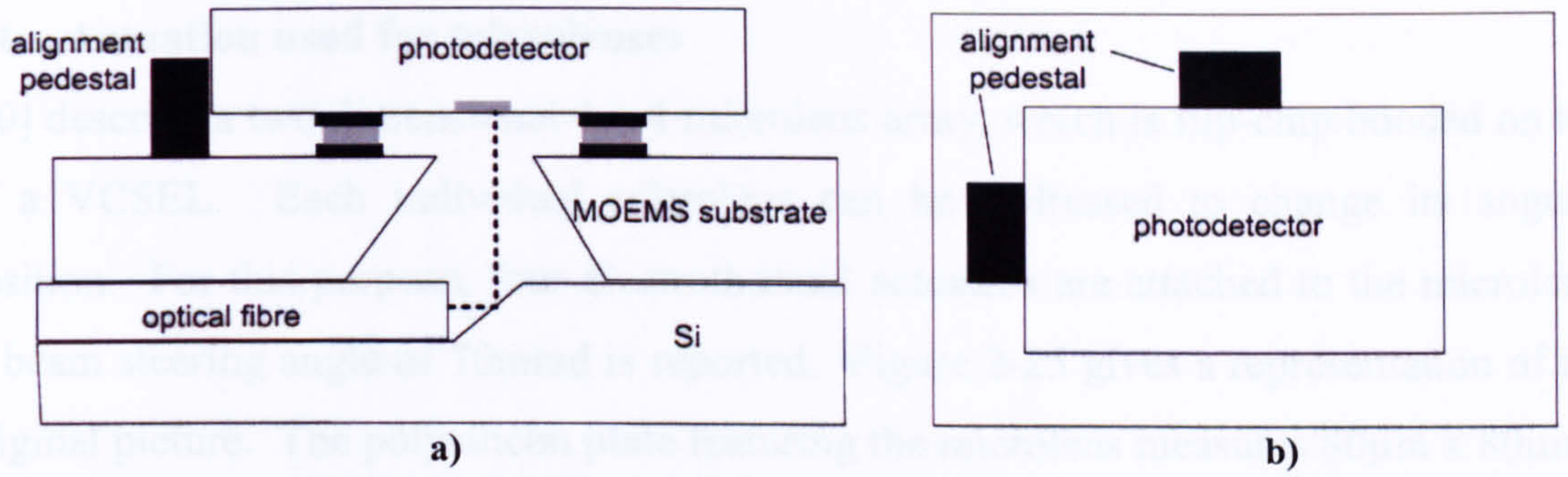

Figure 2-23 a) Side view of an assembly of a photodetector on top of an optical device. The lateral alignment is achieved with accurately manufactured alignment pedestals. b) Top view of the assembly. Two alignment pedestals are needed to determine the lateral alignment. [38].

[39] report an alignment accuracy of less than 0.3µm by using solder self-alignment. No solder-flux is used since the native oxide film of the solder pad is removed with an active atmosphere prior to the assembly. Figure 2-24 shows a simplified representation of the original picture. The microlens array is placed onto the substrate with low temperature solder and connected with the self-electro-optic effect device (SEED) using a high temperature solder. The connection between substrate and SEED is obtained with low temperature solder. Since the high temperature solder solidifies earlier during the cool down process, the crucial alignment between microlens and SEED is firstly obtained. The lateral dimension of the (SEED) is 2.8mm x 2.8mm. The width of the square solder pads is 75µm. A different number of solder pads (4, 8, 16, and 32) was investigated but no considerable dependency of the resulting alignment accuracy was observed. The alignment accuracy for small solder thicknesses was better than for thicker ones.

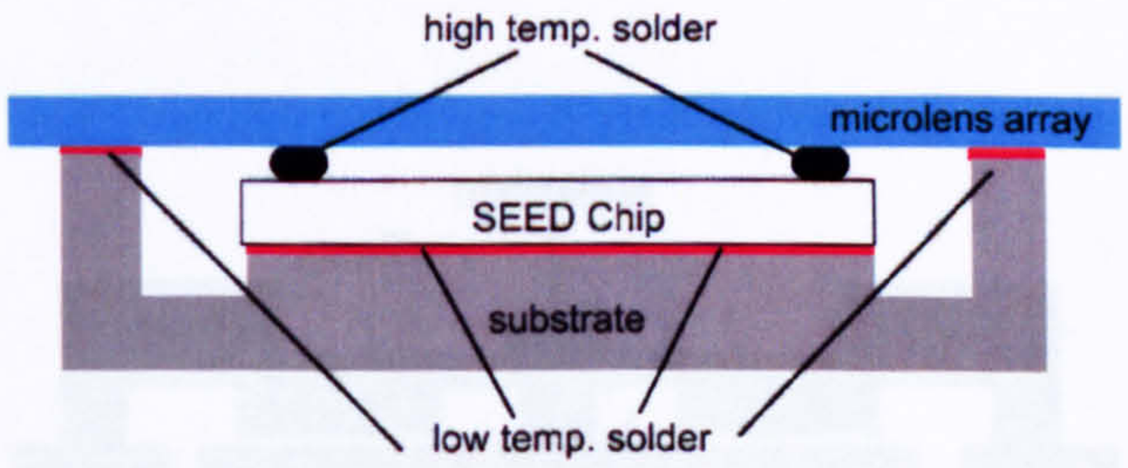

Figure 2-24 Solder self-alignment of a microlens array over a SEED chip. The lateral dimension of the SEED chip measures: 2.8mm x 2.8mm. Picture is a simplified representation taken from [39].

2.4 Actuation used for microlenses

[40] describe a two dimensional 4 x 4 microlens array, which is flip-chip bonded on top of a VCSEL. Each individual microlens can be addressed to change its angular position. For this purpose, four electrothermal actuators are attached to the microlens. A beam steering angle of 70mrad is reported. Figure 2-25 gives a representation of the original picture. The polysilicon plate featuring the microlens measures 80µm x 80µm.

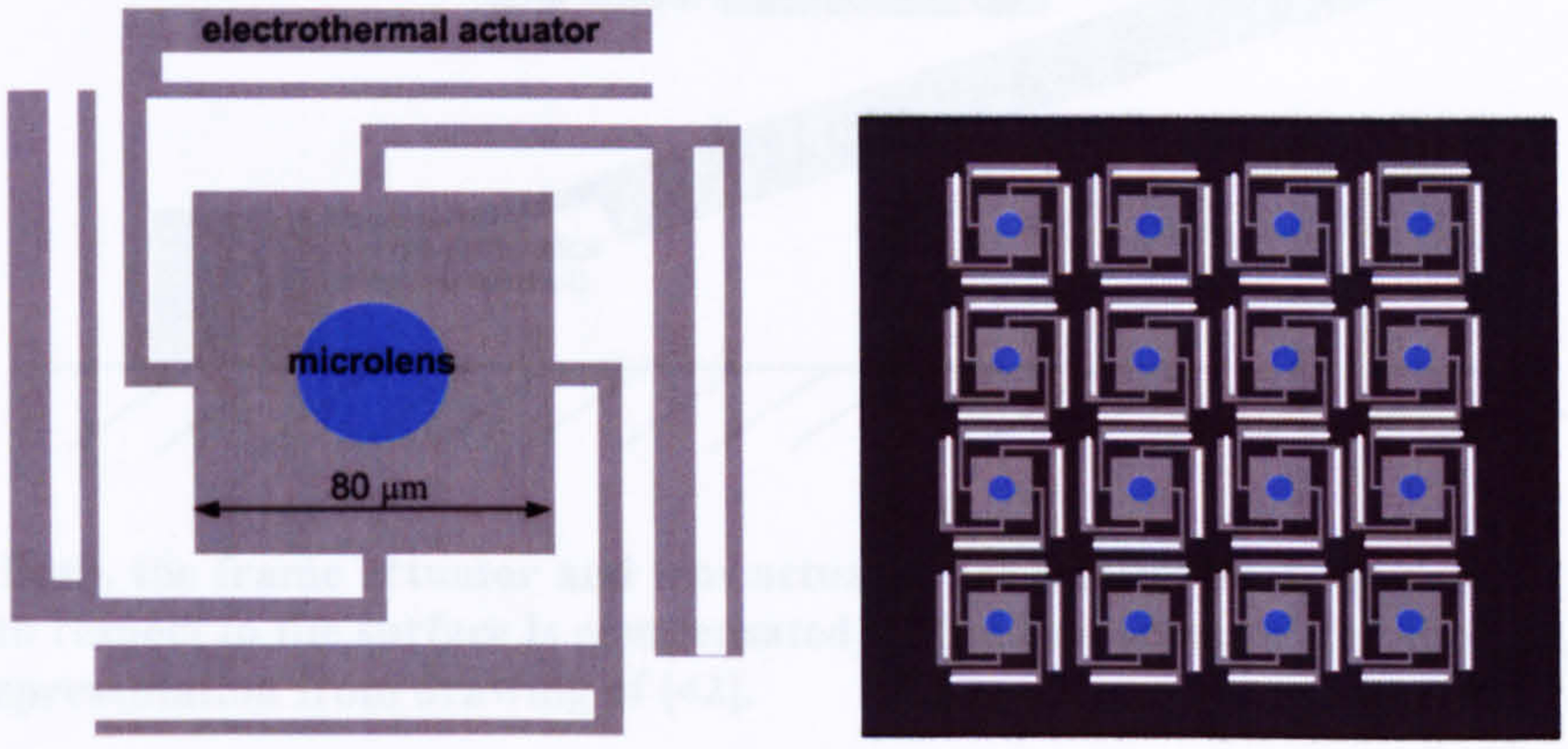

Figure 2-25 The microlens is steered via 4 electrothermal actuators. A four by four array has been fabricated that is flip-chip bonded onto a VCSEL. Drawing is a representation of original [40].

[41] propose a system in which the microlens array is driven by a pneumatic actuator. Figure 2-26 gives a representation of the original drawing. The green, moving part is made of elastic PDMS (polydimethylsiloxane) as well as the microlens itself. Via the air supply, the chambers can be pressurised or depressurised to move the structure and hence the microlens in vertical direction. By applying a pressure of 54KPa, a vertical deflection of 10.4µm was achieved.

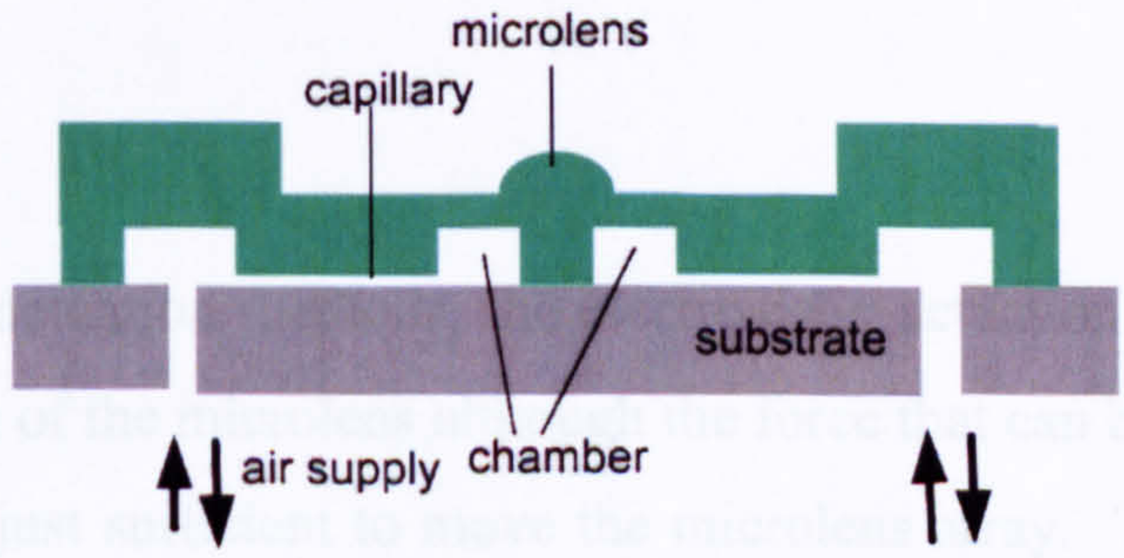

Figure 2-26 The green structure is made of elastic PDMS. If the chambers are pressurised, vertical displacement of the microlens can be achieved. Drawing is a representation of picture from [41].

[42] report a microlens scanner that is driven with electrothermal actuators as shown in Figure 2-27. The frame actuator lifts up the frame where the lens actuator and lens holder are attached. The lens actuator lifts at the same time the lens holder with respect

to the frame, therefore compensating the angular mismatch towards the substrate. The lateral dimension of the actuator is 700µm x 320µm. An overall vertical displacement of 280µm is achieved with an applied voltage of 10V and a resulting current of 12mA. The electrothermal actuator consists of Si that is surrounded by SiO_2 and toped with an Al layer. The Si serves as heating resistor for the actuation.

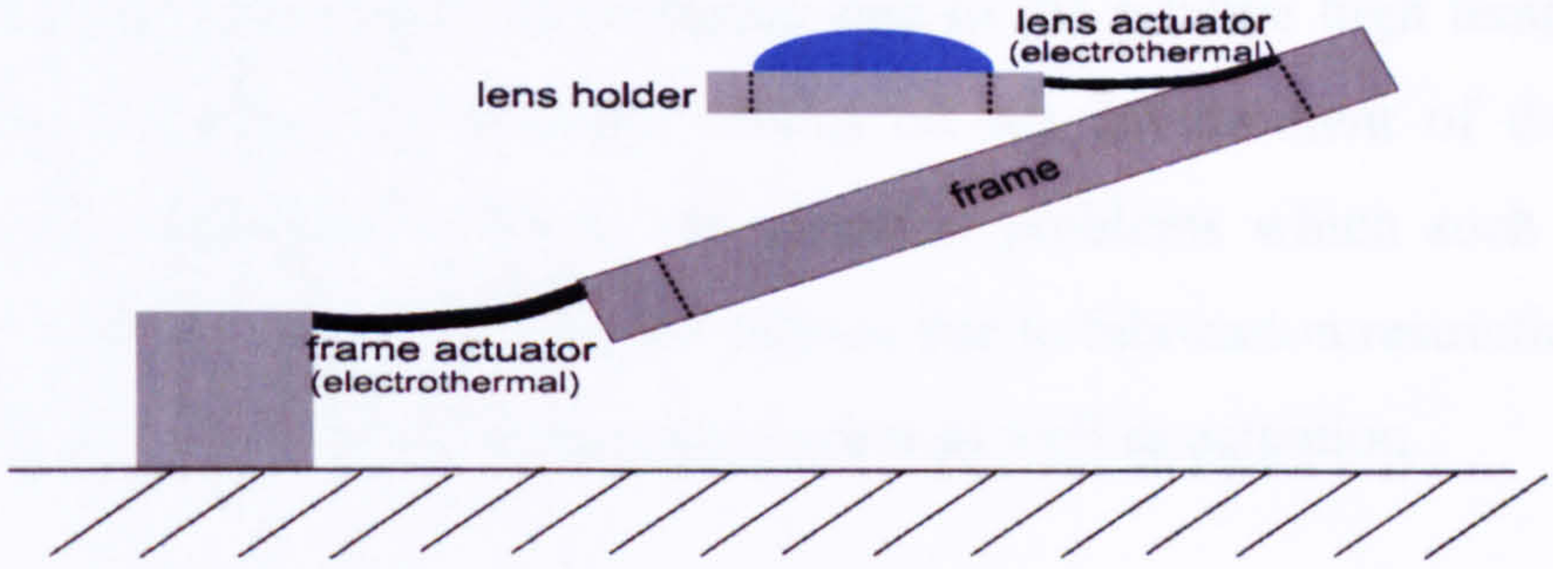

Figure 2-27 Both, the frame actuator and lens actuator are electrothermally driven. The angle of the frame with respect to the surface is compensated by the lens actuator and the lens holder. This picture is a representation from drawing of [42].

[43] assemble a single lens over a VCSEL in order to control the angle of the beam. This is achieved by laterally shifting the microlens in x- and y-direction using an electrostatically driven 2-dimensional comb actuator. This enables 2-D scans. The applied voltage is in the order of 70V to achieve a deflection of 10µm.

[44] report a PDMS microlens that is placed on a ferromagnetic platform suspended by springs. An external magnetic field is applied to move the platform and hence the microlens. The lateral dimension of the platform measures 3mm x 2mm. The assembly has a resonance frequency of 215.2Hz with an angle of 23°.

2.5 Conclusions

From the described actuation methods, the electrostatic actuation has been chosen for the vertical actuation of the microlens although the force that can be generated with this actuation method is just sufficient to move the microlens array. The devices provided are singulated and rather fragile; this narrows down the manufacturing processes that can be employed, and indirectly the actuation method that can be added to the die. Furthermore, the laboratory where this project is conducted, has its own limitations. The use of piezoelectric or magnetostrictive actuators was discarded due to the processing temperature, which would have destroyed the LEDs but also due to the lack

of achievable stroke. The SMA was discarded for temperature reasons as well since the required shape of the SMA needs to be obtained at a temperature of around 500°C. This had to be done prior to the assembly and the shape as well as the dimension would have been difficult to predict. The accurate placement of these actuators onto the provided micro-UV-LED array considering the adhesion and electrical contacts, would have been challenging as well due to the limited accuracy of the mask aligner. The electrothermal actuator was considered not to be adequate due to the relative high temperatures that appear during actuation, for possible effects on the environment of the subsequent device but most importantly due to the adhesion problems which such temperatures cause. Bimetallic actuators were not considered due to fabrication restrictions as well as predicted adhesion problems during manufacture as well as actuation.

By using a special kind of electrostatic actuator, the microlens array only features a floating electrode which does not need to be connected to any potential and therefore wire which eases the manufacture and assembly process considerably. Combined with a simple restoring means, such as gel bumps, this vehicle enabled early measurements and a means of changing fast the properties of the entire actuation system by changing the amount of gel. One of the disadvantages of this actuation method is the usage of high voltages of up to 600V. This voltage is brought into perspective by considering the dimensions of the sapphire microlens array (6mm x 6mm x 0.45mm) and its subsequent weight that needs to be actuated.

Later within the project, it was decided that lateral movement of the microlens would be required as well. For this reason, a magnetic actuator was chosen. Compared to the other described actuation methods, this type of actuator is the most feasible from a fabrication point of view as long as the magnetic flux can be generated externally. A major reason however, was the fact, that the microlens could be actuated by a "remote" field without a physical contact towards the micro-UV-LED array, provided that the microlens features ferromagnetic structures. The magnetic field responsible for the lateral movement can coexist with the electrostatic field, thereby allowing simultaneous lateral and vertical movement of the microlens. This dual actuation requires an external device, that supplies the assembly with electrical as well as magnetic energy. Such a device is explained within this thesis and working prototypes have already been constructed.

Chapter 3

Design of the Packaging

The objective of this work is to find a packaging solution that allows the static and/or dynamic alignment of a microlens array (there onwards defined as μLens) on top of a micro-UV-LED array (μLED) as illustrated in Figure 3-5. Both parts have been manufactured by the Institute of Photonics (IoP) at Strathclyde University. The μLED die measures 8.2mm x 8.2mm and hosts on an area approximately 2mm x 2mm (3mm x 3mm), 4096 micro-LEDs. The sapphire μLens has lateral dimensions of 6mm x 6mm and a thickness of up to 450μm. A variety of different sizes and dimensions of both, arrays and their components (microlens and LED), were produced by IoP. Figure 3-2a shows a particular μLED array and its connection tracks. Own measurements were conducted by using a ZYGO® white light interferometer as shown in Figure 3-2b top and bottom. The height of the grown micro-LED (LED) with respect to the sapphire substrate measures approximately 4.4μm. The LEDs have a diameter of around 20μm, a pitch of approximately 42μm and are produced on MOCVD-grown InGaN/GaN LED wafers using a sapphire substrate and multiquantum wells which are designed for light emission at 470nm [45]. Wavelengths of down to 370nm have also been reported as shown in the emission spectra in Figure 3-1a [46]. Figure 3-1b shows the current vs optical power output. The blue LED drains 30mA by achieving a optical power output of nearly 700μW[46].

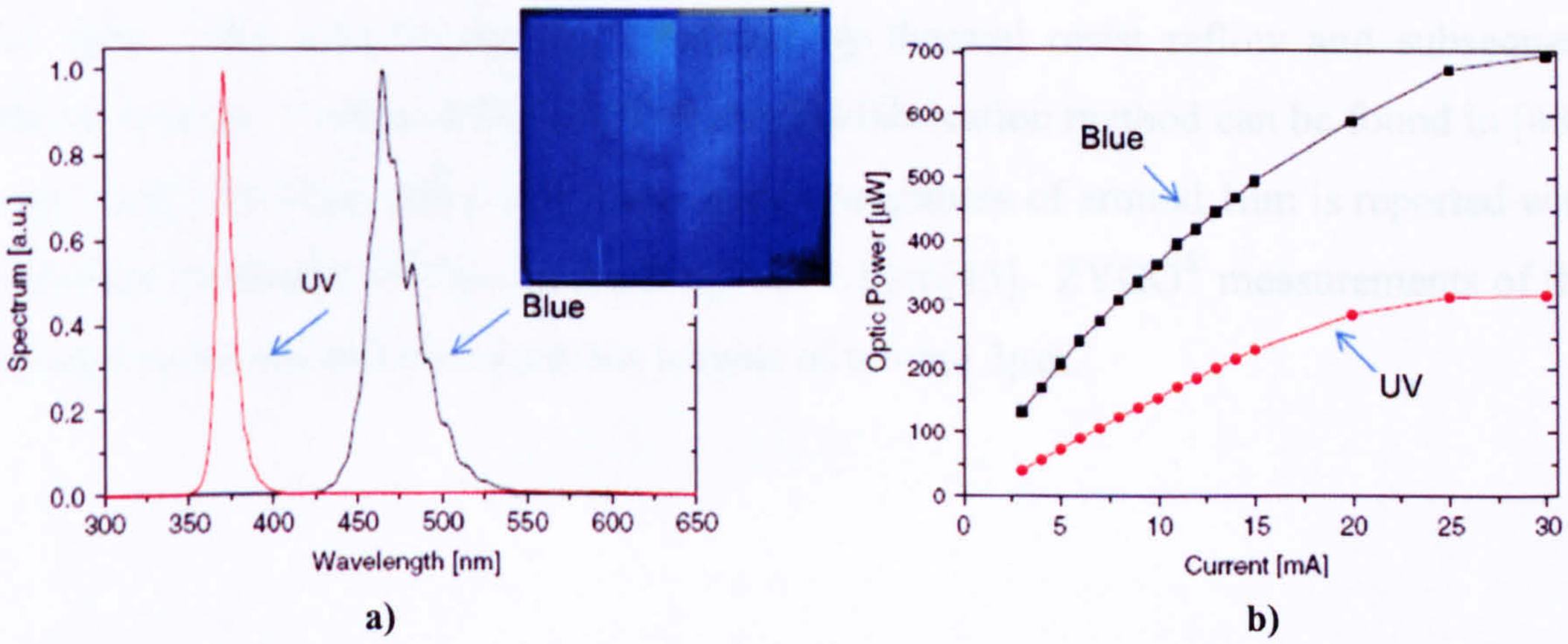

a) b)

Figure 3-1 a) Emission spectra of blue and UV LED that features peaks at 470nm and 370nm , respectively. b) Current vs optical power output of the aforementioned LED types [46].

The micro-LED consists of 2.3μm of undoped GaN and 1.4μm of n-doped GaN, over which a 200nm cladding layer capped with 100nm of Mg-doped AlGaN, was used. 20nm of Mg-doped GaN is utilised as a contact layer and the quantum wells consist of seven periods of 2nm InGaN and 10nm of AlGaN, acting as barriers. A Lambertian emission profile was used to simulate and compare the emission pattern obtained by using confocal microscopy. A second moment beam divergence (full angle) of 70°±5° was measured at a wavelength of 468nm using an objective numerical aperture (NA) of 0.75. For UV light (370nm) using the same NA, a divergence of 75°±3° is reported. The simulated value is 71° [47].

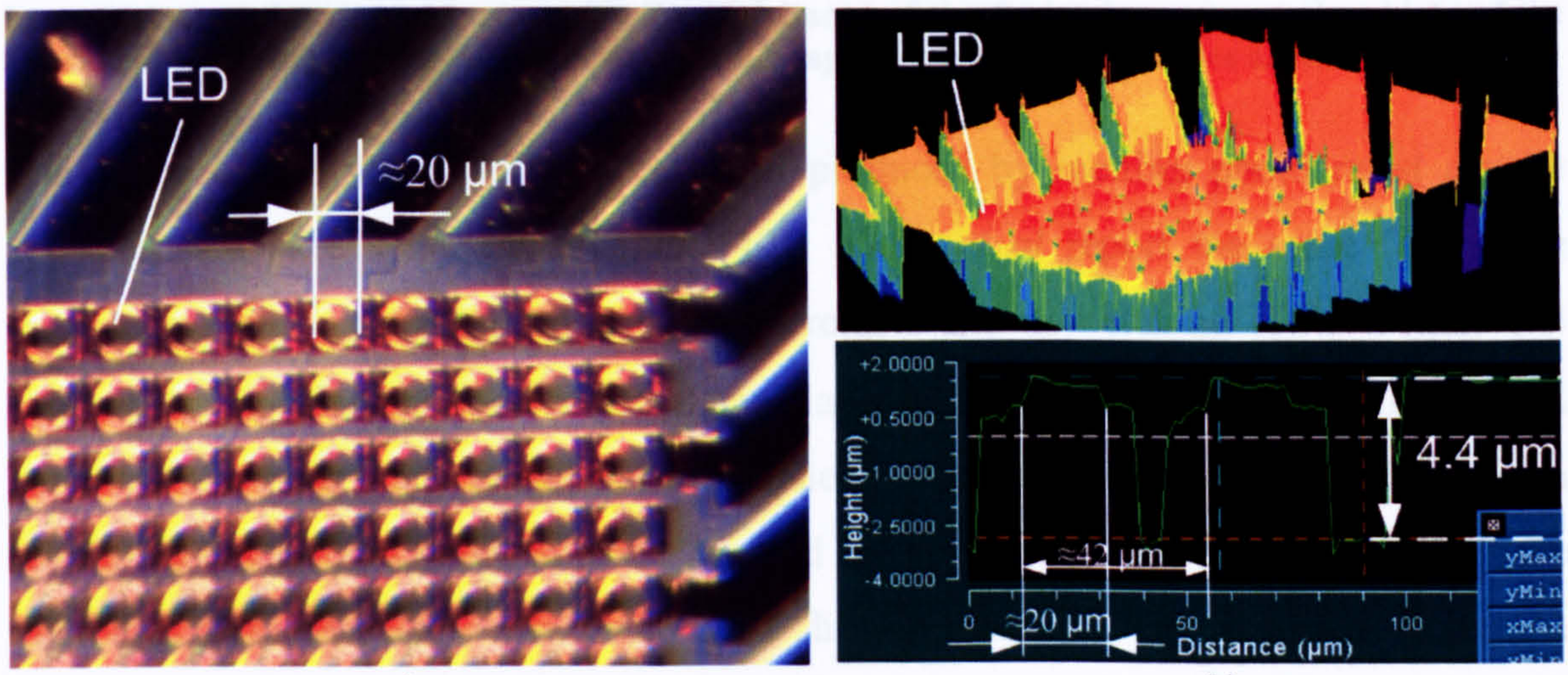

Figure 3-2 a) Picture of a micro-UV-LED array (μLED) produced by Strathclyde University. The active part of the LED of this particular device has a diameter of around 20μm. b) 3D image of the μLED (top) and profile of the LEDs. The height of this sample is around 4.4 μm.

Figure 3-3a shows the micrograph of a fraction taken from the μLens array. The substrate material is sapphire, which is not only transparent for visible light but also for UV light. The microlenses are fabricated by thermal resist reflow and subsequent plasma etching. Further information about this fabrication method can be found in [48]. Focal length of 44μm and a root mean square roughness of around 1nm is reported with microlens diameters of 20μm and a height of 1.5μm[45]. ZYGO® measurements of the pictured specimen exhibit microlens heights of around 3μm.

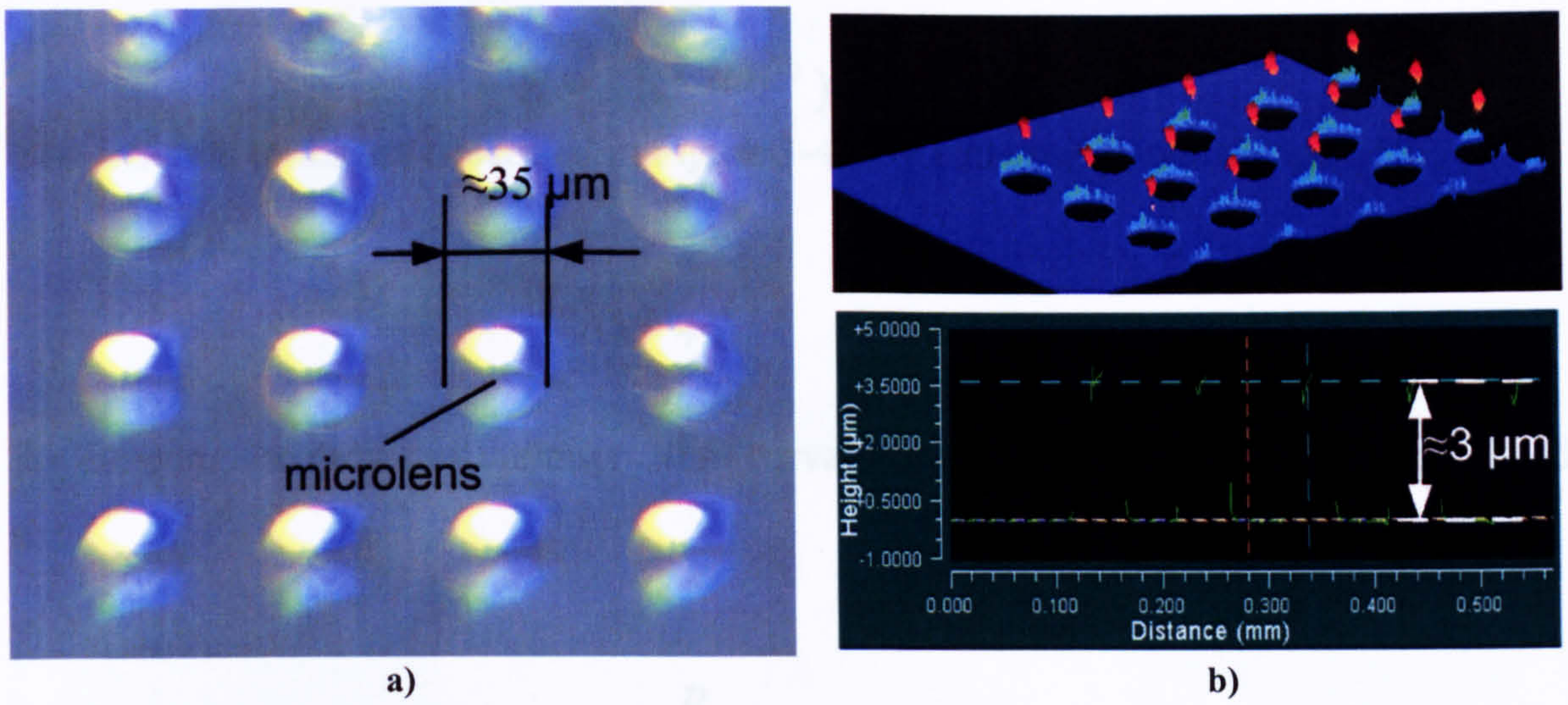

a) b)

Figure 3-3 a) Micrograph of a fraction of a µLens array. The microlens in this particular device has a diameter of around 35µm. b) 3D ZYGO® image of the device from a) reveals a hight of the microlenses of around 3 µm. The thickness of the sapphire substrate measures around 450µm.

The shape of the microlens that has been produced by melting photo resist can be approximated as a spherical segment [49]. Oder *et al* report the same for nitride microlenses that are fabricated with resist reflow and dry etching [50]. Figure 3-4 shows the simplified situation of the µLens placed on top of the µLED with dimensional parameters. *R* represents the radius of the sphere. *r* is the radius of the intersection area (circle) that is formed between plane M_A and the sphere. *h* stands for the height of the microlens with respect to the plane M_A. In this situation, the microlens acts as a collimator for the outgoing beam of the LED. Given the parameters of the microlens array shown in Figure 3-3 and the thickness of the substrate, this appears to be the only reasonable configuration for the assembly.

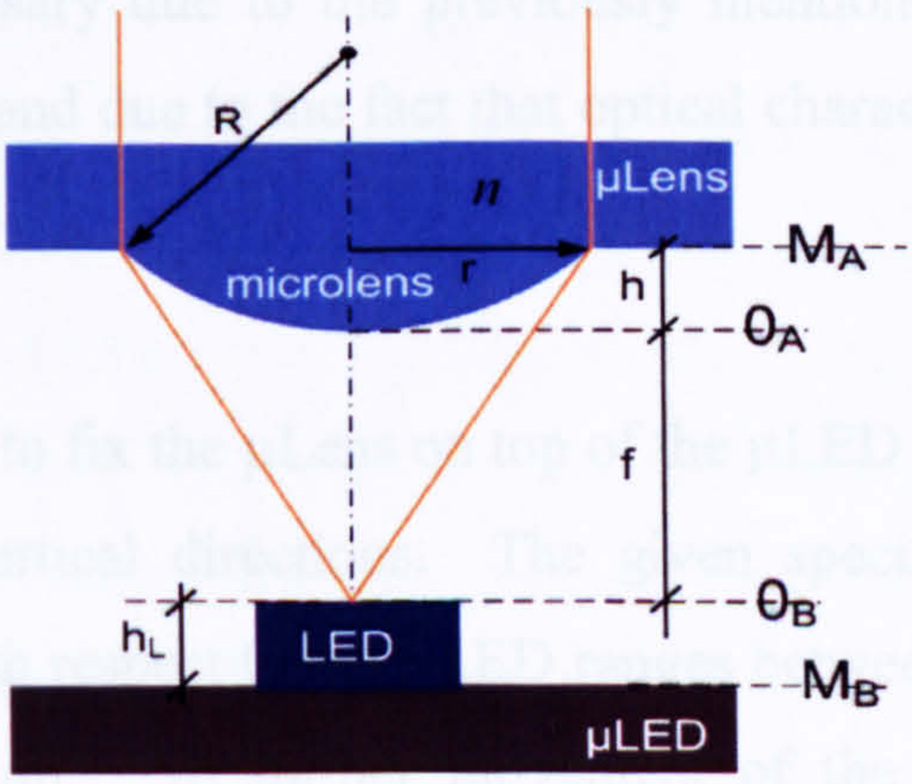

Figure 3-4 µLens placed over µLED. The microlens is assumed to be a section of a sphere. From a MEMS perspective, the planes M_A and M_B are of importance once the height of the LED (h_L) and microlens (h) are obtained.

The height, h, can be obtained by the following equation of a sphere segment [49]:

$$h = R - (R^2 - r^2)^{\frac{1}{2}}. \tag{3-1}$$

The different terms are described in Figure 3-4. By isolating R, one obtains [50]:

$$R = \frac{r^2 + h^2}{2 \cdot h}. \tag{3-2}$$

By knowing the radius of the microlens' curvature, the focal length, f, can be calculated to:

$$f = \frac{R}{n-1}, \tag{3-3}$$

where n is the refractive index of the microlens material [50]. Wavelength dependencies (dispersion [51]) of the lens material are neglected and a refractive index of 1.8 (470nm [45]) is assumed for sapphire within the different light spectra of the LED.

By using parameters shown in Figure 3-3 and the above mentioned parameters, the focal length, f, is calculated to be around 65µm. Hence from an optical perspective, the distance between the optical planes O_A and O_B, representing the distance between the top surface of the LED and the lowest point of the surface of the microlens, are of importance as shown in Figure 3-4. However, from a packaging perspective, the distance between the flat substrate surface of the µLens-chip (M_A) and the substrate of the µLED-chip (M_B), and its accurate alignment are of predominant interest. This differentiation was necessary due to the previously mentioned variety of the optical devices delivered by IoP and due to the fact that optical characterisation was not part of this thesis.

The static approach aims to fix the µLens on top of the µLED with high accuracy in the lateral as well as the vertical directions. The given specifications for the vertical distance of the µLens with respect to the µLED ranges between 30µm and 100µm with a lateral tolerance of 2µm. No further movement of the µLens is expected after assembly. Several challenges need to be considered in order to achieve a highly accurate alignment. The predominant goal for the dynamic approach is to construct a mechanism, which is able to move the µLens in the vertical direction with high accuracy in order to adjust the focal point. The magnitude of movement is required to

be around +/-5μm. Different approaches have been considered as possible actuation methods depending on the force or displacement required for the proposed system. Another requested actuation method is the magnetic actuation that allows lateral movement.

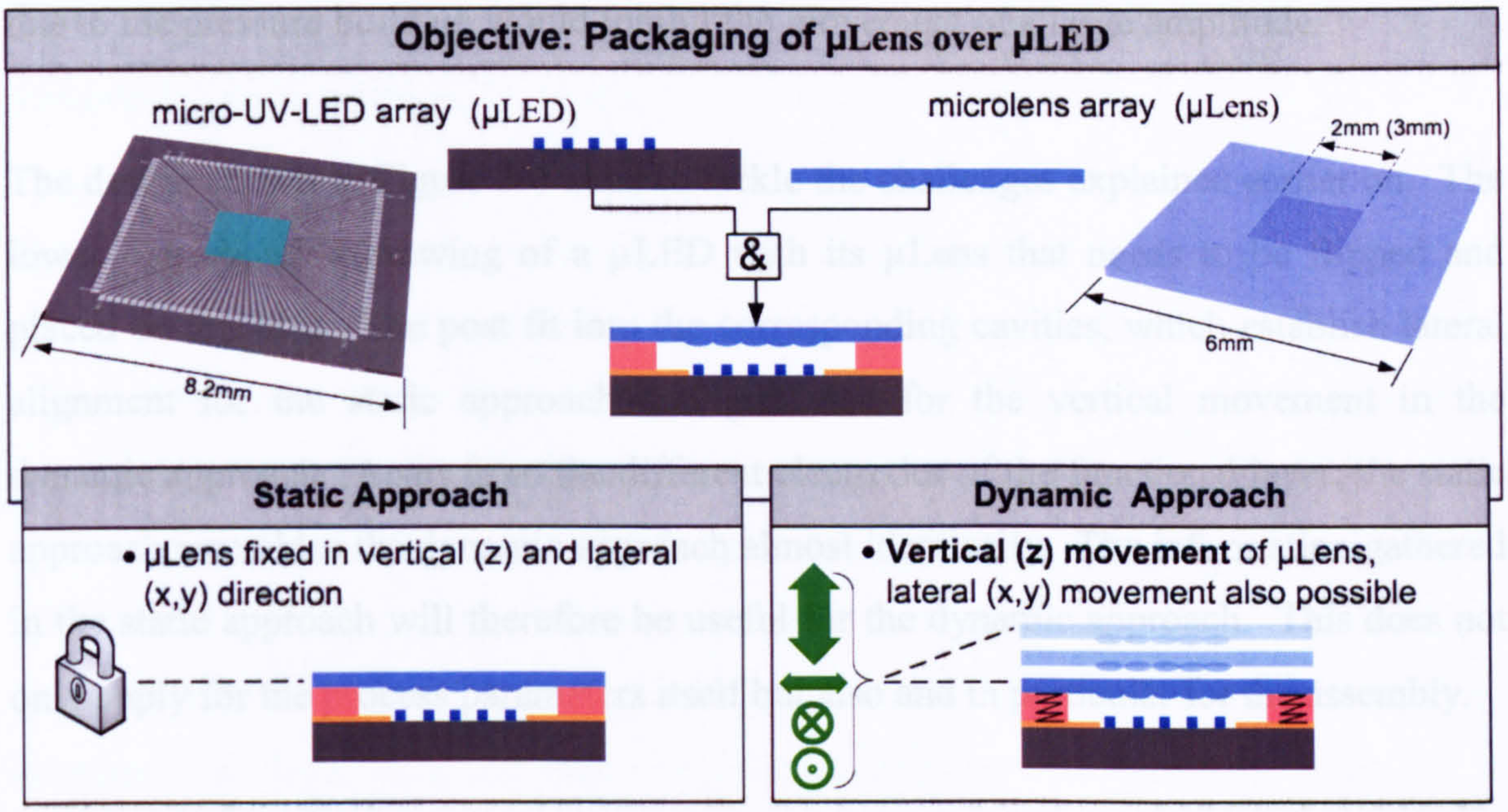

Figure 3-5 Packaging of the microlens array (μLens) over the micro-UV-LED array (μLED). The approach has been broken down in two stages. The first part is the static approach where both the lateral and the vertical position are accurately fixed. The second part is the dynamic approach where the lateral position can and the vertical must be variable.

Table 3-1 presents a list of the major identified challenges numbered on the left hand side of the spreadsheet. The causes of these challenges are: "Device features", "Small lateral chip dimension", "Target specification", "Processes and equipment" and "Physical restrictions" (Table 3-1, top right corner). In "Device features" the fragile nature of the LED structure, the connection paths situated on the μLED, the alignment marks and the features of the μLED may cause problems. The relevant features are in the order of 20μm and the relatively rough and bulky packaging processes need to be handled with care. In "Small lateral chip dimension" challenges are due to the size of the delivered die that is not in a wafer form. These need to be processed with considerable effort. "Target specification" are restrictions that come with the packaging requirements. Such properties include the maximal required displacement or the initial distance between μLED and μLens. "Processes and equipment" describes the limitations due to processes and equipment. Any process cannot be used for the fabrication of the package; for example, too high a temperature would jeopardize the functionality of the μLED. The equipment used also restricts the possibilities to achieve

certain goals. Our clean room is mainly equipped for handling wafers. Certain alignment procedures cannot be used since it would either scratch the mask or the device that is to be exposed. The "Physical Restrictions" category includes effects from the "outside world" or basic physical principles that cannot be overcome. For example, if the μLens and μLED formed a sealed compound, the force created within the cavity due to the pressure build up would inhibit the movement of a large amplitude.

The design shown in Figure 3-6 aims to tackle the challenges explained earlier on. The lower part shows a drawing of a μLED with its μLens that needs to be flipped and placed on top of it. The post fit into the corresponding cavities, which establish lateral alignment for the static approach and guidance for the vertical movement in the dynamic approach. Apart from the different electrodes of the functional layer, the static approach resembles the dynamic approach almost identically. The information gathered in the static approach will therefore be useful for the dynamic approach. This does not only apply for the process parameters itself but also and in particular for the assembly.

C	Identified challenge	Problem category				
		Device features	Small lateral chip dimension	Target specification	Processes and equipment	Physical restrictions
1	Packaging process **NOT** at the end of the device fabrication			X		
2	Surface tension problem for photoresist		X		X	
3	Equipment designed to process wafer				X	
4	Only UV-LIGA process available at MISEC				X	
5	Tedious gluing of chips on wafer induces stress and reduces yield **TREMENDOUSLY**		X			
6	Alignment on exposure tool due to uneven and small surface of glued μLED / μLens chips		X		X	
7	Process temperature as small as possible to protect micro-LEDs	X			X	
8	LED-bond-pads to be kept free for wirebonding after packaging	X		X		
9	Relative large displacement and force necessary (weight of μLens)			X		X
10	Only indirect alignment marks on μLEDs useable	X		X		
11	If dynamic approach to be sealed→ physical restrictions to changes of the environment			X		X
12	Alignment of a "6 degrees of freedom system"			X		
13	Accurate spinning of intended thickness of photoresist restricted (5-10% of absolute thickness)				X	
14	Alignment marks on μLens initially not present, new μLens however features some wide ones	X				
15	Alignment marks on μLED very close together (problem of angular misalignment)	X				
16	Height restrictions for restoring means due to pre-specified μLens - μLED -distance range			X		
17	Lateral guidance with post cavity might cause difficulties due to friction and tolerance				X	
18	Tilt measurement (3 points necessary)				X	
19	LED-bond-pads completely surround the micro-LED array → "bridge" necessary	X		X		
20	Alignment marks of μLED need to be kept untouched until structural layer	X			X	
21	Micro-LEDs gold pads and tracks to be protected during processing	X			X	

Table 3-1 List of challenges (vertical stack) and the area that the problem needs to be connected to. Some problems have a combined cause and therefore more than one point on the concerned challenge.

The device shows features necessary for vertical electrostatic movement as well as lateral magnetic movement. As restoring means, gel bumps are inserted in the cavities.

The pads are used for the manufacturing process but also for the subsequent operation of the device. In the former, they provide the electrical current to grow the electroformed layer. In the latter, they serve as interface for the voltage and the magnetic flux used for the actuators. The entire structure has to be designed in a way that leaves the LED-bond-pads free, since they need to be wire bonded after the packaging has taken place. The exploded view of the build up of the structure is presented in the top part of the picture.

Base layer. The base layer provides the protection and isolation, at the evaporation stage, for the connection tracks that lie between the bond pads of the LEDs and the LEDs themselves. While the connection tracks must be completely covered to prevent a short-circuit between the tracks during operation, the LED-bond-pads must not be covered since they will be used after the packaging process. This layer also provides a material with a high dielectric constant which is necessary since during the actuation, voltages of up to 600V are to be applied between the electrodes. This layer is typically between 4 to 7μm thick and made of SU8. Alternative materials are sought for, in particular materials that exhibit higher dielectric constants and better adhesion properties to sapphire/gold. The accuracy for this layer is not crucial as long as the pads are not covered after this process step.

Functional layer. The functional layer serves for the static approach solely as a seed layer for electroplating the part of the electrode that lies within the cavity. The electrode used differs slightly from the one used in the dynamic approach. In this approach, the cavity is not electroplated, which otherwise would prevent the insertion of the post. The electroplating process therefore adds only material to the pads and tracks used subsequently for the magnetic actuator. Each of the 4 pairs of electrodes, together with the corresponding floating electrode (explained in the next chapter), constitutes a vertical electrostatic actuator. The alignment accuracy of this layer with respect to the previous one is not of high importance provided that the electrodes are evaporated onto the insulating base layer.

Structural layer. The structural layer makes up the main bulk of the entire package. In the static approach the cavities are used to align laterally the posts of the μLens. In the dynamic approach, the cavities are meant to serve as a lateral guidance during the actuation. The layer serves also as a mould for the subsequent electroformed layer. The

structural layer also hosts gel cavities, which are used for placing gel bumps. This is the only layer that needs to be very accurately aligned to the alignment marks based on the μLED chip itself.

Electroformed layer. The electroformed layer uses the functional layer as a seed layer. For the static approach this layer is used to electroplate a certain thickness to the electrodes that are situated within the cavity. In the dynamic approach, the electroformed tracks and pads, together with the ferromagnetic post situated on the μLens, make up the lateral magnetic actuator.

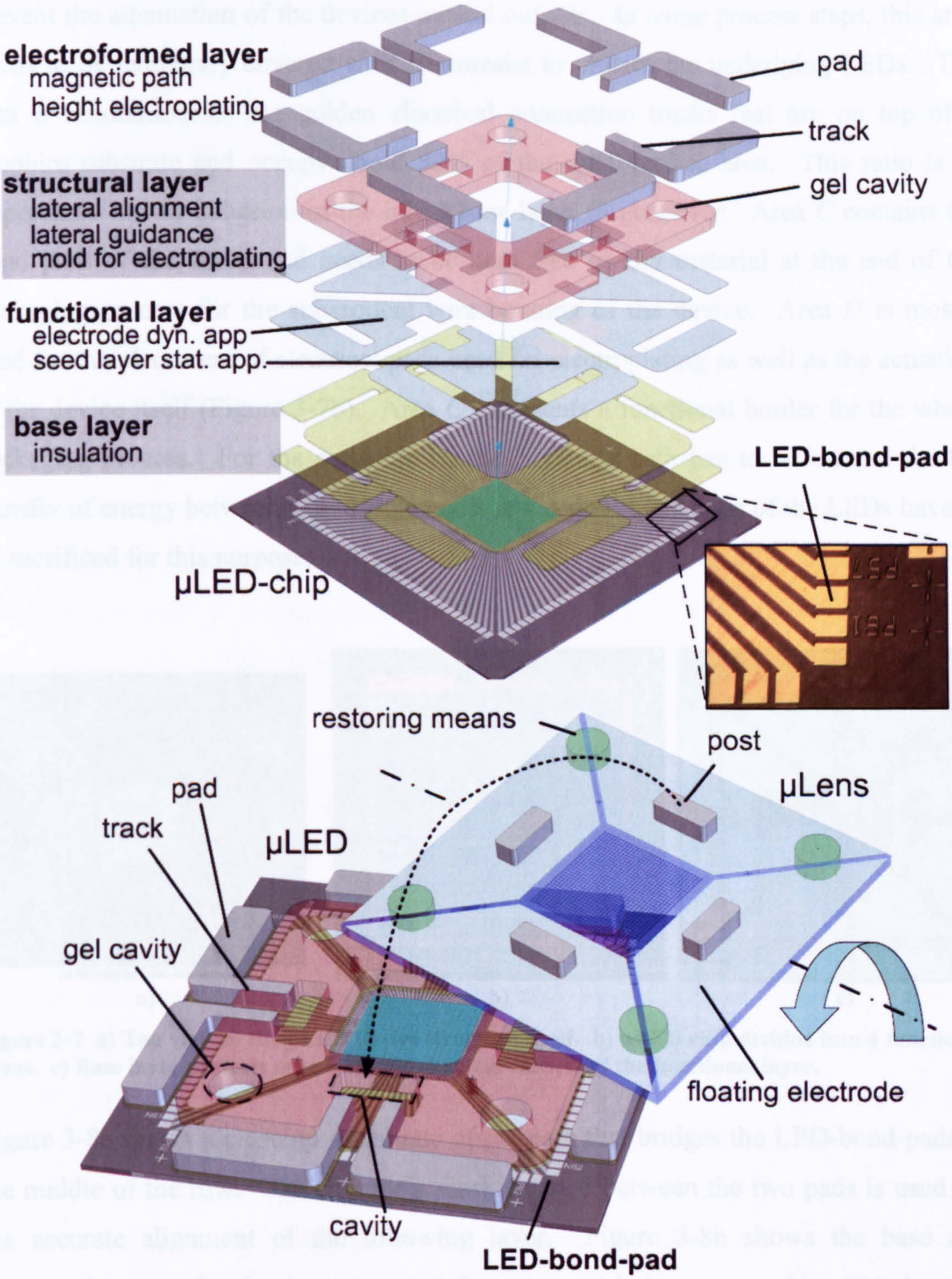

Figure 3-6 Exploded view of the post-processed µLED and assembled view of the µLens and µLED. The µLens is presented prior of being flipped and placed onto the µLED.

The µLED chip features different areas that need to be considered for the structure of the package (Figure 3-7a). The device itself was not designed for packaging; hence different compromises had to be made in order to achieve the given goals. Figure 3-7b shows the diverse areas *A*, *B*, *C*, and *D*, each of which serve different purposes and are therefore needed to be treated individually during fabrication and assembly. Area *A*, where the LEDs are situated, needs to be ultimately free of any deposited material to

prevent the attenuation of the devices optical outputs. In some process steps, this area needs to be temporary covered with photoresist to protect the underlying LEDs. The area *B* accommodates the golden electrical connection tracks that are on top of a sapphire substrate and occupy about 50% of the total surface area. This ratio is of importance for the adhesion of the initial base layer (Figure 3-6). Area *C* contains the bond pads of the LEDs and needs to be kept free of any material at the end of the packaging process for the subsequent wire bonding of the device. Area *D* is mostly used for the placement of electrical pads used for electroplating as well as the actuation of the device itself (Figure 3-7b). Area *C* represents a functional border for the whole packaging process. For the actuation of the device, a path has to be created for the transfer of energy between *D* and *B*; hence a few central bond pads of the LEDs have to be sacrificed for this purpose.

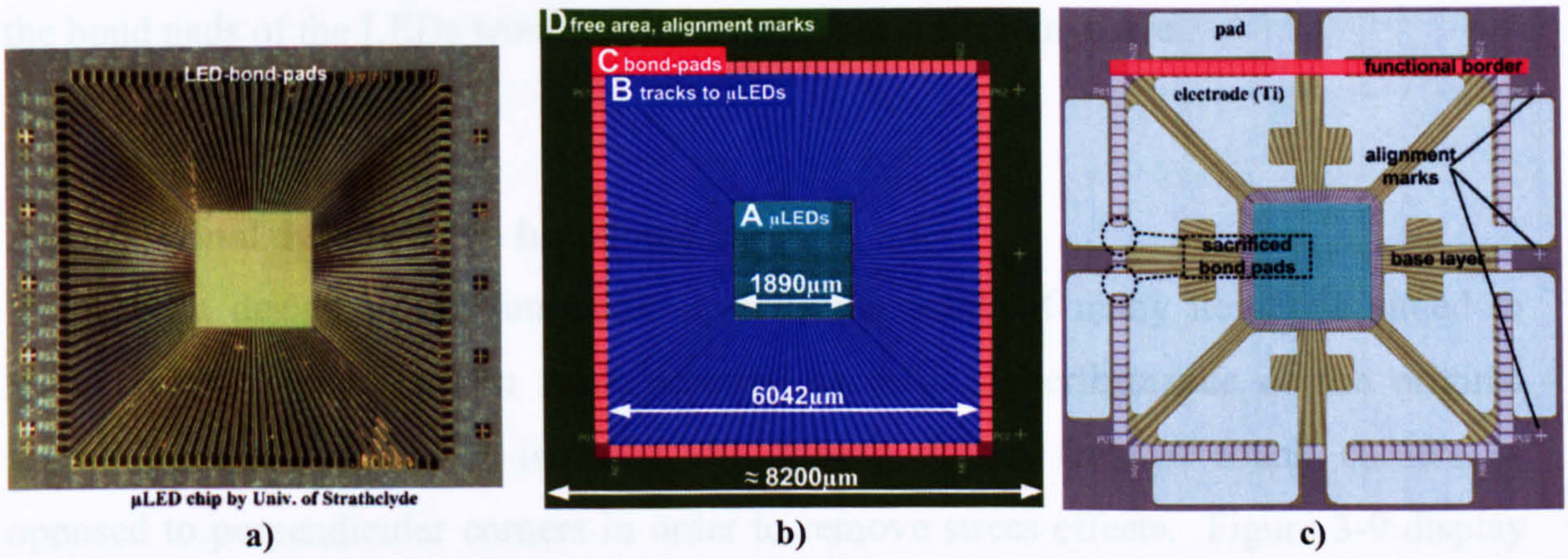

Figure 3-7 a) Top view of the µLED device structure itself. b) µLED chip divided into 4 functional areas. c) Base layer protects area *C* from a shortcut caused by the functional layer.

Figure 3-8a shows a close up schematic of the path that bridges the LED-bond-pads in the middle of the row. The alignment mark situated between the two pads is used for the accurate alignment of the following layer. Figure 3-8b shows the base and functional layers after having processed the structural layer on top of it. This layer is also designed to restrict the accessibility to the bond pads of the LED.

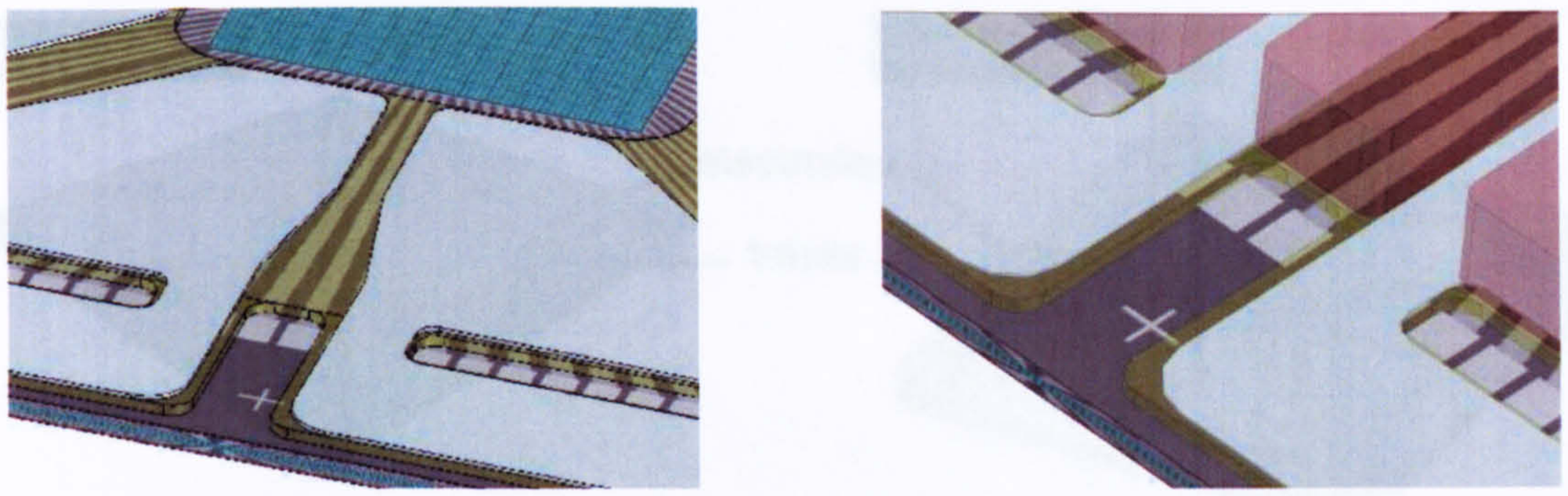

a) b)

Figure 3-8 a) The base and functional layers bridge the area where the pads are situated. The covered pads cannot be used. b) The structural layer that follows the layer seen in a) must not cover parts of the pad to keep it free for post processing.

The LEDs in the four corners have not been sacrificed as they are more useful for the characterization of the alignment and tilt of the μLens. B is the area where the sealing takes place for the static approach and where the actuation of the μLens occurs in the dynamic approach. It was not practical to have the sealing already on the area D, since the bond pads of the LEDs would not have been accessible anymore.

3.1 Original design of the functional layer

The current design of the functional layer is the result of many iterations aimed to eliminate the weaknesses in manufacturing as well as performance of the original assembled prototype. For instance, the current design features round corners as opposed to perpendicular corners in order to remove stress effects. Figure 3-9 display the original and current functional layers. The current design (Figure 3-9b) features electrodes with a much bigger area, thereby creating higher electrostatic forces. The tracks connecting the pads to the electrodes have been broadened and shortened for more robustness during manufacture and increased current performance for magnetic actuation. The current design is also expected to improve the electroplating performance with respect to the current density distribution and the stress effects of the caused such as the current crowding effect.

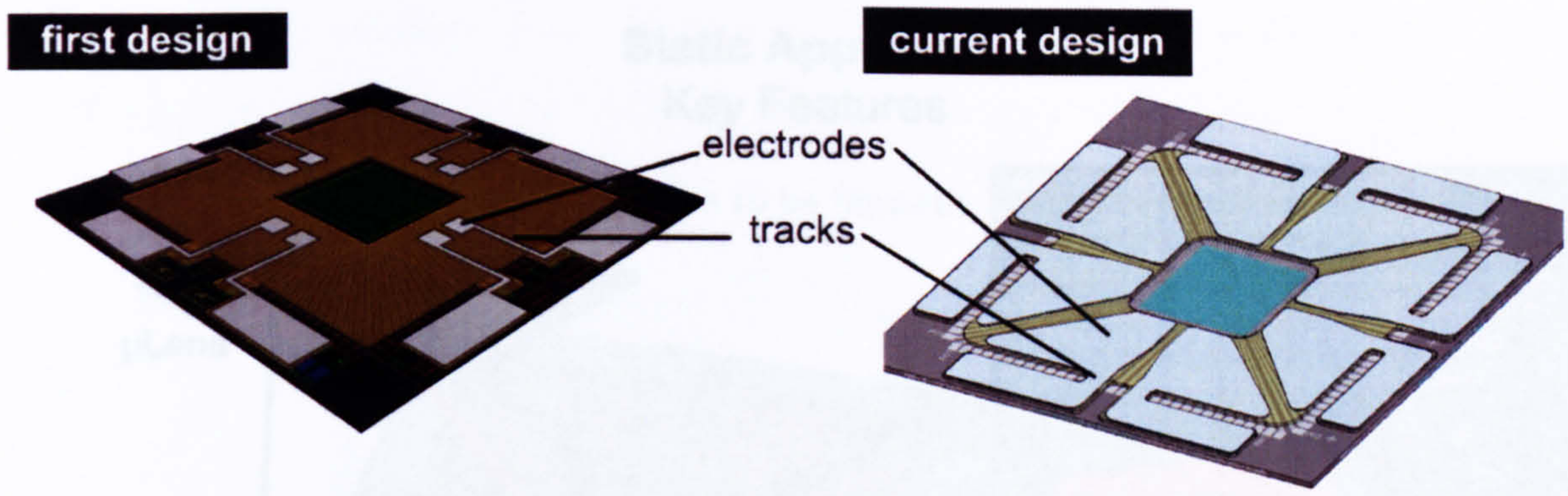

Figure 3-9 a) The original design and its electrodes. b) The current design features bigger electrodes, shorter and wider tracks.

3.2 Static Approach

The objective of the static approach is to place the μLens on top of the μLED, aligning it, fixing it in place and finally sealing it as explained in Figure 3-10. The μLens can either feature SU8 or Ni posts. The latter can be electroplated by using the floating electrodes as a seed layer. The material of the floating electrodes is also used for the SU8 posts as adhesion promoter. A limited accuracy on the thicknesses of the posts or of the structural layer is obtained by spin coating the viscous photoresist material. For this reason, each of the cavities on the structural layer has electrodes that can be electroplated within sub-micron accuracy (Figure 3-10, green box). Four posts are used that fit into the cavities of the structural layer of the μLED in order to keep the contact area between the μLED and μLENS arrays as small as possible (Figure 3-10, red box). Theoretically, sixteen lateral contact areas are possible between all the posts and cavities, but only two contacts are used such as to reduce overdetermination (Figure 3-10, blue box). If the structural layer is misaligned with the μLED-chip during exposure, the misalignment can be measured and a corrective misalignment of the posts can be done with respect to the μLens in order to compensate for that fault (Figure 3-10, grey box).

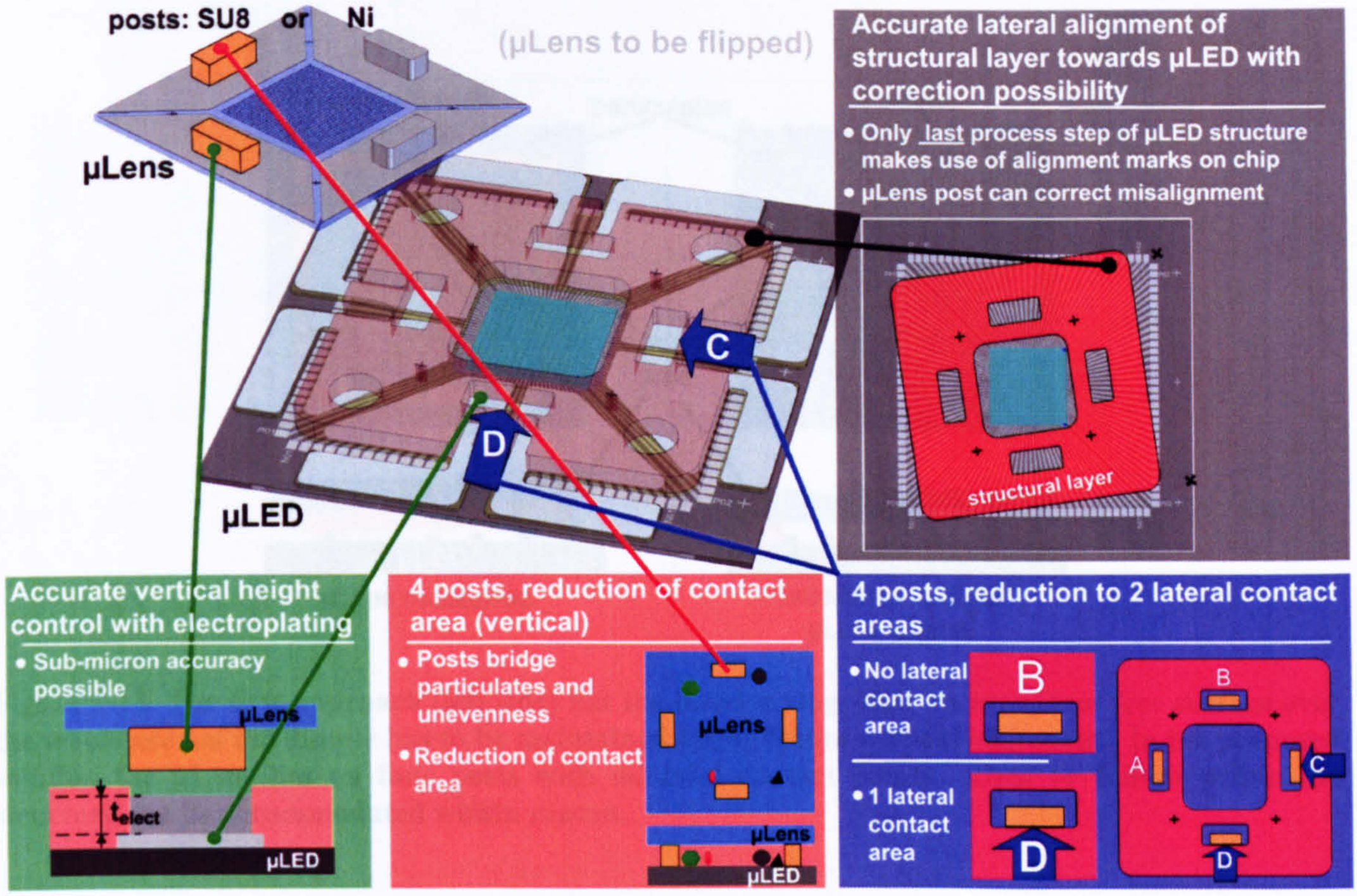

Figure 3-10 The key features of the static approach consists of, accurate height control with electroplating, 4 posts for the reduction of vertical and lateral contact area and the possibility of correcting a misalignment of the µLED with purposely misalignment of the post towards the µLens.

3.2.1 Reduction of vertical and lateral overdetermination

The term "overdetermination" defines here the number of alignment points/areas, which are necessary to determine the position of a 3 dimensional body, which has 3 Cartesian and 3 angular degrees of freedom. By attaching 3 posts of arbitrary length to one side of the µLED, one already restricts it in its vertical direction as well as in two angular directions (roll and yaw). If two of these posts are fixed onto the surface, the µLED is completely restricted within its 3 dimensional space, since the lateral movement and angular pitch are also prevented.

3.2.1.1 The use of posts to reduce contact area

The left hand side of Figure 3-11 illustrates the first approach taken: a dimple structured on the µLens and a trench on the µLED. Both trench and dimple surround the centre of the device in order to have a mechanical sealing. This approach has severe disadvantages. In Figure 3-11 (left side top view), the orange area depicts the surface where the µLens dimple lies on the bottom of the trench of the µLED. This area is relatively large and just one dust particle on either the dimple or trench surface suffices

to cause vertical misalignment. Additionally the uneven thickness of the spun SU8 layer is a concern and is difficult to avoid especially at the die level.

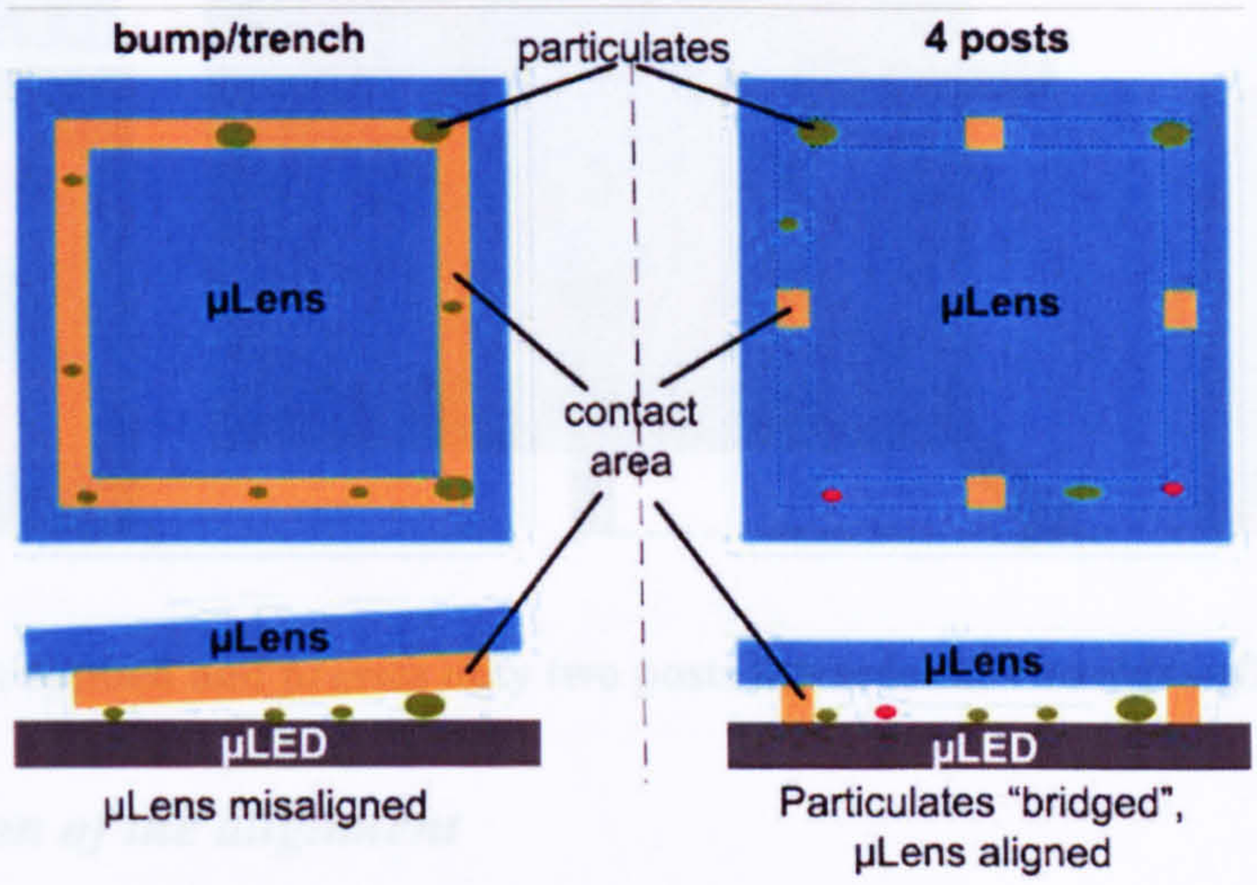

Figure 3-11 The first approach (left side) has the disadvantage that an even, dust free surface over the whole area of the dimple has to be maintained for optimum vertical alignment. In the proposed solution the µLens lies on four posts with minimal contact points. Dust or failure within the structure can be accommodated within reason.

On the right hand side of Figure 3-11 the µLens rests on four posts which have a small contact surface. The four posts are able to bridge the unevenness and contamination that lies between them. In addition, dust particles, as long as they are smaller than the posts, do not affect the alignment. The contact area of the posts itself needs to be free of dust and even. The probability of misalignment in vertical direction depends only on the contact area between µLens and µLED.

3.2.1.2 Reduction of contact area between posts and cavity in lateral direction

The concept of using small contact areas between µLens and µLED was also pursued concerning the lateral direction as shown in Figure 3-12. The left part of the figure shows the µLens and µLED prior to assembly (1). The dimensions of the posts on the µLens are smaller than those of the cavities on the µLED, making it easier to align roughly the two devices. A force, $\boldsymbol{F}_{actio}$, applied diagonally to the µLens, moves the µLens until it touches the sidewalls of *A* and *D*. The reaction forces, $\boldsymbol{F}_{reactio\_x}$ and $\boldsymbol{F}_{reactio\_y}$, establish equilibrium and alignment. With the proposed method, only 2 sidewalls as opposed to 16, need to be highly accurate, hence reducing the possibility of misalignment. This method allows the precise alignment without the need for a high precision alignment tool.

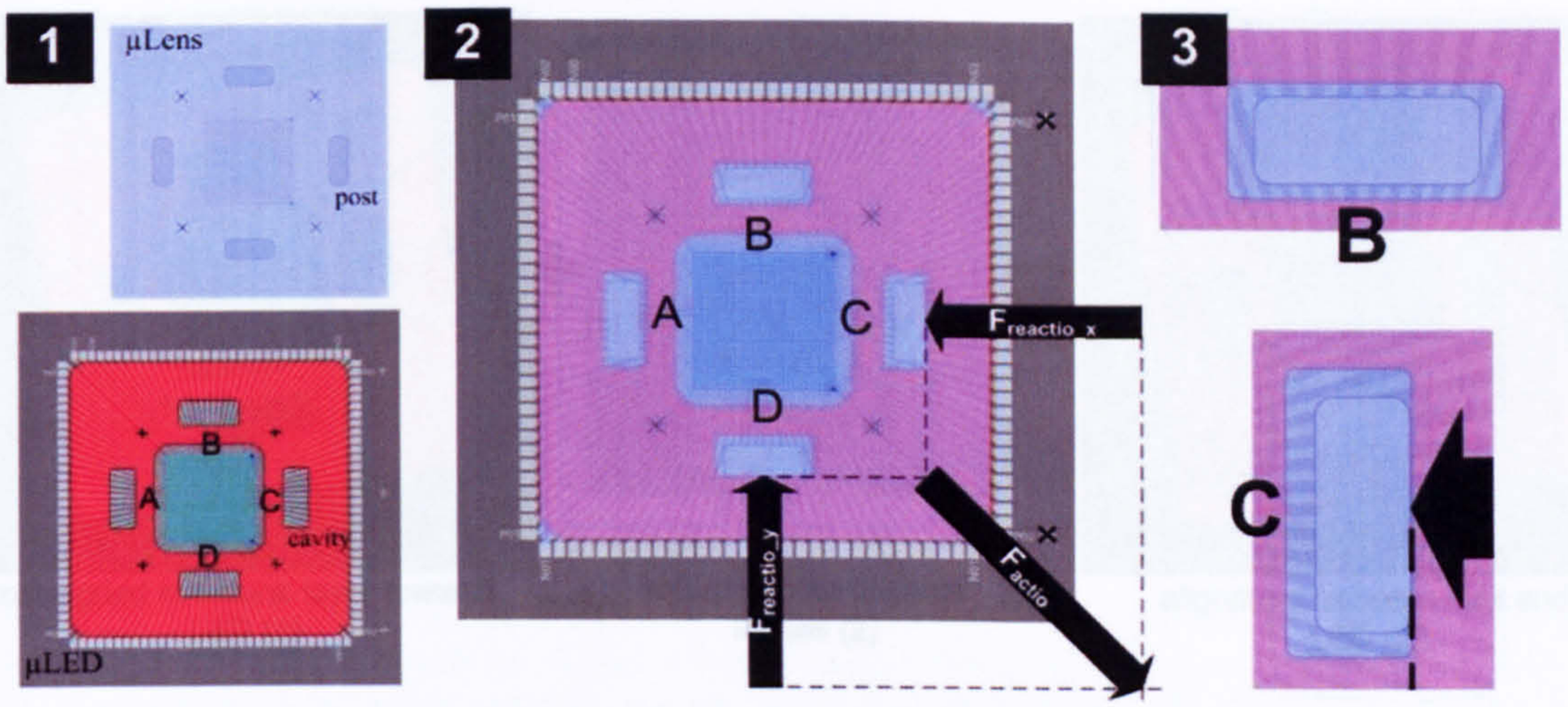

Figure 3-12 F_{actio} is applied and presses only two posts towards the two sidewalls of the cavities.

3.2.2 Correction of the alignment

The structural layer of the µLED is solely responsible for the lateral alignment, and, as such, needs to be aligned accurately with respect to the µLED. The base and functional layers are not crucial for the alignment and therefore do not contain alignment marks. If several subsequent alignments were to be performed during manufacturing, a cascading effect of the amount of misalignment would likely appear. The superposition of several alignment marks would also create optical difficulties. For these reasons, a process employing only one crucial alignment step for the µLED was designed, where the initial alignment marks on the µLED-chip are used.

This design allows also the compensation of a possible misalignment of the structural layer with respect to the LEDs as shown in Figure 3-13. The yellow dots represent each of the four corners of the LED-array and the black dots represent the corner lenses on the µLens. After having investigated the misalignment of the structural layer with respect to the LEDs (1), the posts on the µLens could be placed in a way that compensates this prior measured misalignment (2). If the µLens is then placed on top of the µLED, the two misalignments compensate each other and the lenses coincide with the LED (yellow and black dots fit) (3). For the mathematical description of this misalignment compensation mechanism, the reader is referred to Appendix A.

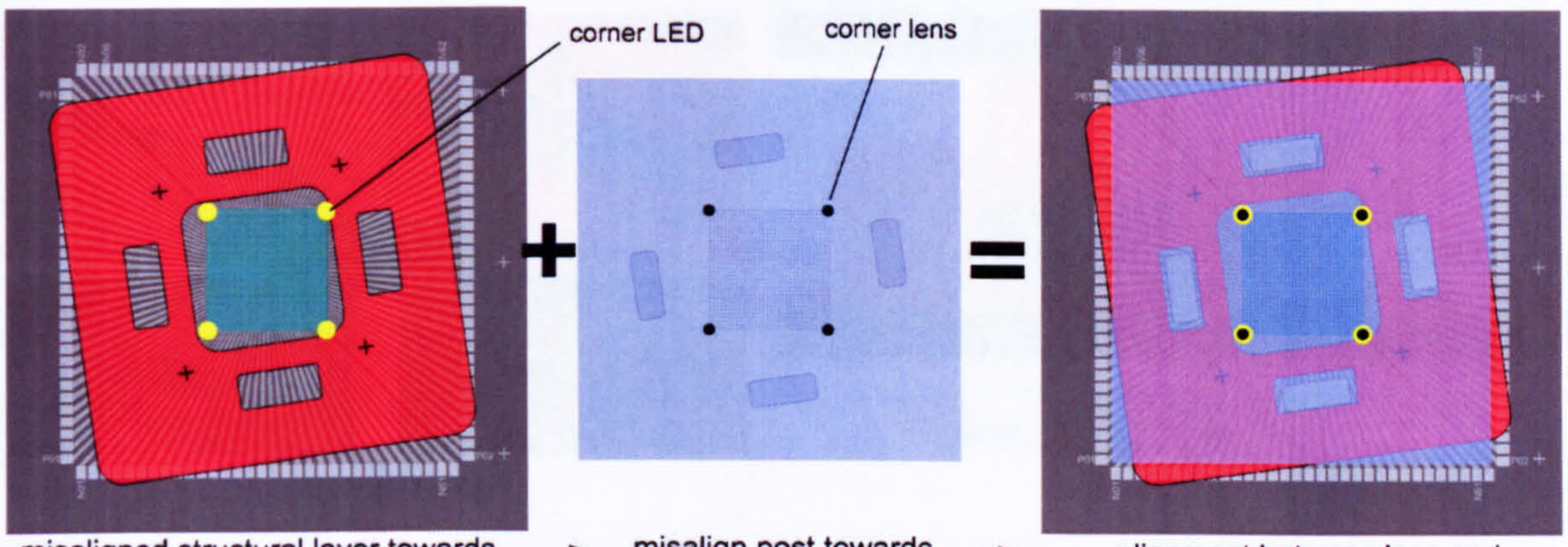

Figure 3-13 The misalignment of the structural layer towards the LED (1) is measured and accordingly, the posts can be deliberately misaligned towards the lenses (2). Both misalignments compensate each other (3) and the corner lenses and corner LEDs coincide, meaning alignment.

3.2.3 Electroplating of the cavities

As shown in Figure 3-10, each cavity in the structural layer has a pair of electrodes that can be electroplated independently in order to change the thickness of the electrodes. This feature is responsible for the highly accurately vertical alignment since the electroplating growth rate can be monitored accurately. Deposition rates for Ni from 12μm/h (1A/dm^2) to 120μm/h (10A/dm^2) have been reported [10], thereby allowing sub-micron accuracy in the vertical direction. Figure 3-14 illustrates the principle of the height adjustment process for a single μLens post. Firstly, the thickness (or height), $t_{\mu p}$, of the μLens post is measured using the Viewmeter ZYGO® white light phase shifting interferometer. The total thickness of the base layer and electrodes, t_{μ}, is then measured with respect to the substrate of the μLED. Since the intended distance, d_{int}, between the μLED and μLens is known, the electroplating thickness, t_{elect}, that needs to be grown is:

$$t_{elect} = d_{\text{int}} - t_{\mu p} - t_{\mu} \tag{3-4}$$

The plating of the electrodes is only meant to be for the fine adjustment of the height, although an electroplating thickness of more than 20μm can be achieved. The vertical height can be determined either by measuring the thickness of the base-layer or the thickness of the μLens post. The thickness accuracy of the spun SU8, however, is restricted to approximately 10% of the thickness. Additionally the height distribution is not even, which could cause a tilting of the μLens if no adjustment means were available.

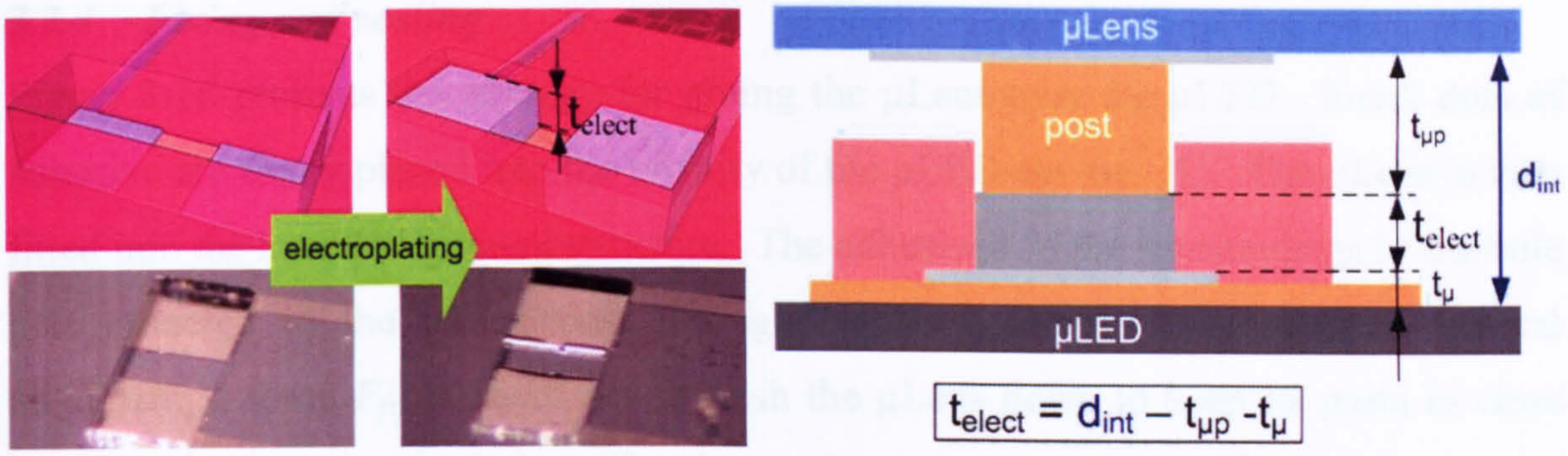

Figure 3-14 The thickness $t_{\mu p}$ of the post is measured as well as the thickness of the base layer plus electrode, t_μ. Since the intended distance between µLED and µLens, d_{int}, is known, the thickness t_{elect}, that needs to be electroplated can be calculated as shown. On the left hand side is an illustration and micrograph before and after the electroplating process.

Figure 3-15 shows an exaggerated rendering of a µLens that possesses a huge variation in the individual thickness of each µLens-post (*A*, *B*, *C*, and *D*). For clarity, the structural layer, which is responsible for the lateral alignment, is not displayed. The thickness of the base layer is assumed to be uniform. In order to achieve a constant d_{int} across the entire µLens array, different thicknesses of metal are electroplated on each pair of electrodes. For example, the µLens post *A* has a large thickness. Therefore, the electrode pair *A* does not need to have a thick layer of electroplated metal. On the other hand, µLens-post *C* is very thin. A thick layer of metal needs then to be grown on top of the electrode pair *C*. In that way the sum of the thicknesses of the µLens-post A and the corresponding electrode pair A is the same as of the sum of the thickness of µLens-post *C* and the electrode pair *C*. The same applies for *B* and *D*. If the µLens is now placed on top of these electrodes, it should not exhibit any tilting at the desired height.

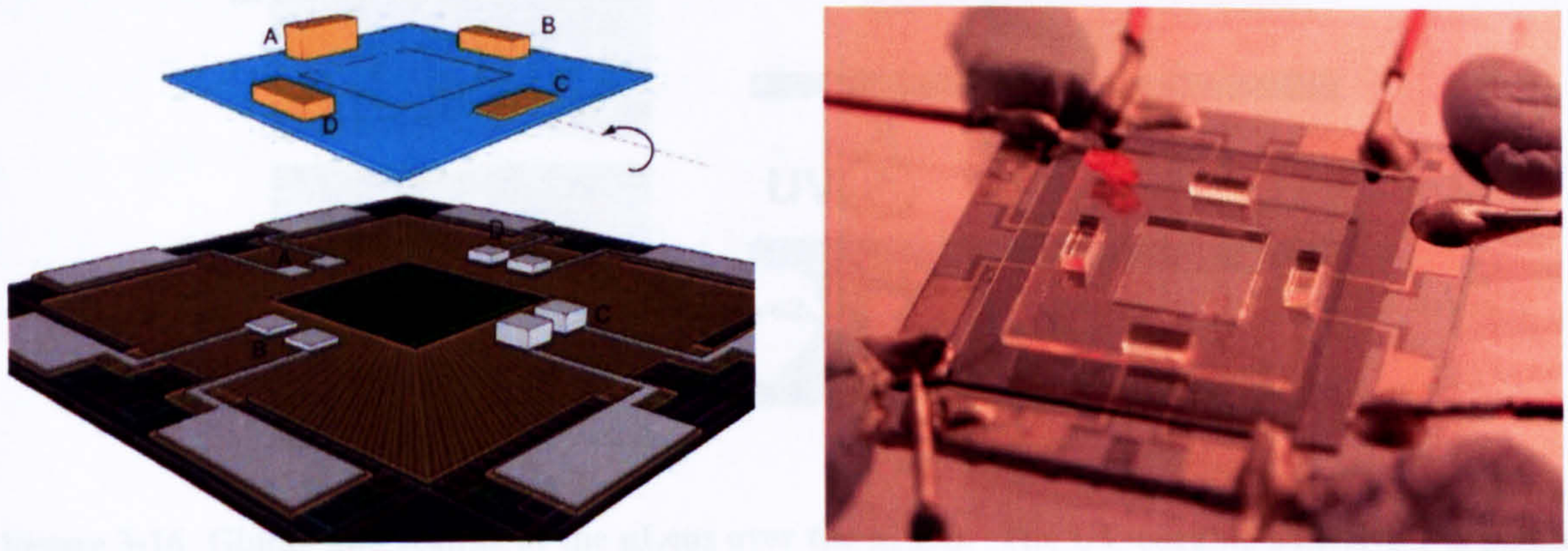

a) b)

Figure 3-15 a) If the µLens-posts *A*, *B*, *C* and *D* of the µLens have different heights, the different electroplating thicknesses of the electrodes *A*, *B*, *C* and *D* on the µLED can compensate these variations. Tilting of the array can be corrected. b) Picture of an assembly of the first design with SU8 posts.

3.2.4 Fixing and sealing

Figure 3-16 presents the strategy for gluing the μLens over the μLED. Small dots of adhesive are firstly placed into the vicinity of the μLED cavities (1). The μLens is then fitted into the lateral alignment structure. The adhesive1 in the surroundings of the hole gets attracted to the μLens post through capillary forces. For accurate vertical alignment, a force F_{fix} is necessary to push the μLens down to keep its posts in close contact to the electroplated electrodes during the curing process (2). During the vertical positioning, the air or outgassing of adhesive that is in between the μLED and the μLens can escape. After the adhesive on each post has been cured, the device is ready for the subsequent sealing process, as shown in the third step (3). The adhesive is applied around the entire perimeter of the μLens and μLED. Since the μLens is already fixed to the μLED, there is no possible misalignment due to buoyancy or capillary effects caused by the considerable amount of adhesive 2. Due to capillary effects the adhesive will be pulled into the cavity until it reaches an equilibrium position. Stress that is caused during the curing process of the UV-adhesive and its effect on the μLens as well as μLED structures, would be a matter of future investigations.

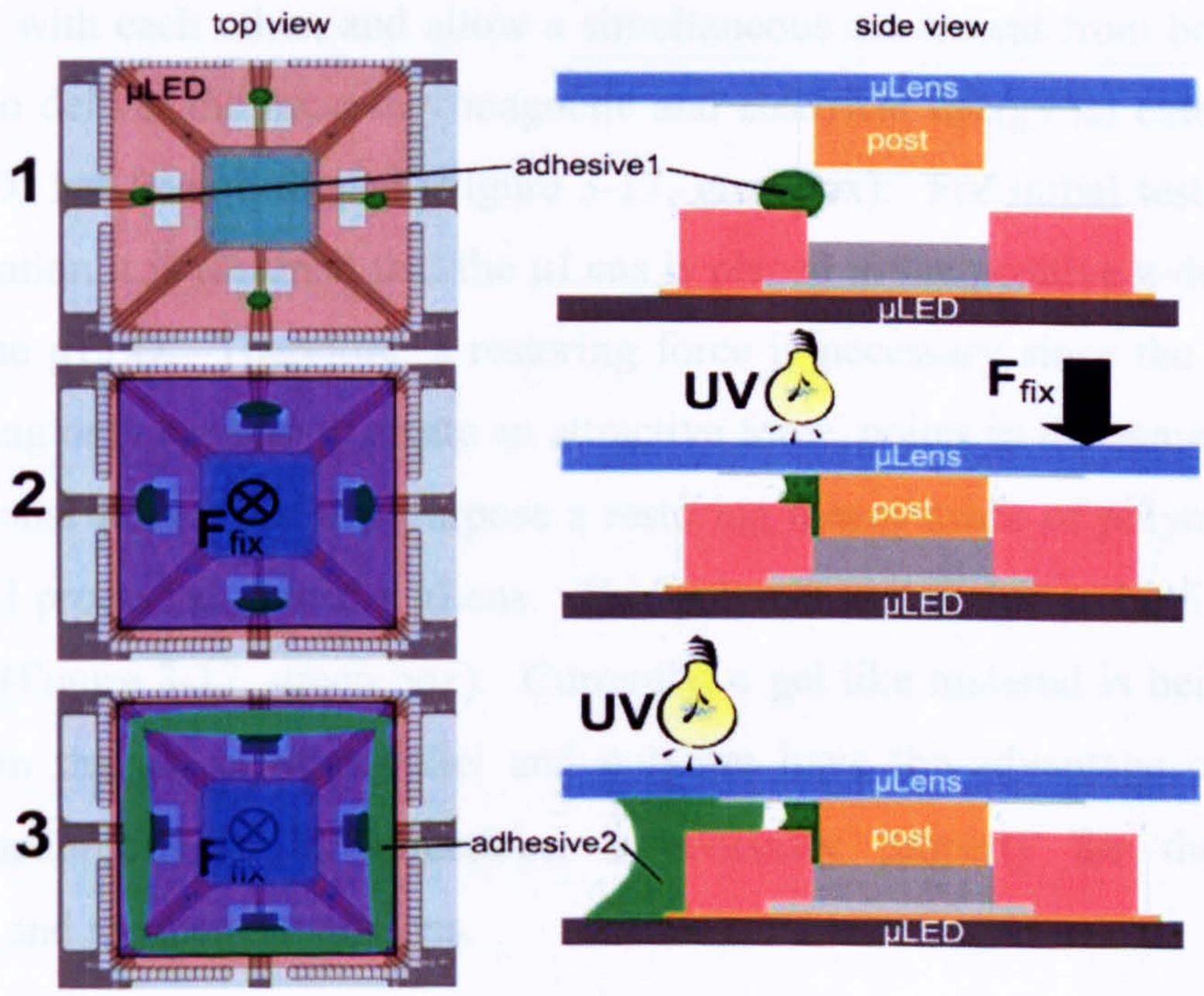

Figure 3-16 Gluing and sealing of the μLens over the μLED. The UV-curable adhesive 1 is placed on the borders of the μLED cavity (1). The μLED is placed into the position and a force F_{fix} is exerted to keep the μLens in close contact to its vertical adjustment points (electroplated electrodes) while the adhesive is curing (2). After curing, a large amount of UV-curable adhesive 2 can be applied around the entire μLens border (3).

3.3 Dynamic approach

In the dynamic approach the μLens can be moved in the vertical direction in order to change the focal point. Figure 3-17 provides an overview of the most important features necessary for this approach. The electrostatic actuator consists of a pair of electrodes that lie on the base layer of the μLED and the floating electrode that lies above both electrodes. This floating electrode does not need to be attached to any electrical potential, therefore no wire is required that would potentially disturb the alignment and movement of the μLens. Each side of the square sized μLED has a pair of electrodes thereby allowing tilting of the μLens into every direction (Figure 3-17, blue box). The design also features lateral magnetic actuators where the pads and tracks of the μLED serve as conductor for the magnetic flux, Φ, and attract the post that is made of a ferromagnetic material which is attached to the μLens. One actuator is on each side of the μLED, permitting the alignment in the positive and negative x- and y-directions (Figure 3-17, red box). As for the electrostatic actuator, no physical connection is necessary for the μLens to achieve this movement. This is not only an important feature for the operation of the μLens itself but it also eases the manufacturing and assembly of the devices. The electrostatic and magnetic fields do not interfere with each other, and allow a simultaneous movement from both actuation methods. To deliver the necessary magnetic and electrical energy an external driving device (EDD) has been designed (Figure 3-17, grey box). For initial tests and for its normal operation it is assumed that the μLens is placed in the positive z-direction with respect to the μLED. Therefore, a restoring force is necessary since the electrostatic actuator, being only capable to create an attractive force, points in the same direction as the gravitational force. For this purpose a restoring means made of polymer has been designed and processed onto the μLens. This polymer material is to be fitted into the gel cavities (Figure 3-17, green box). Currently, a gel like material is being used and placed within the gel cavities. Gel and polymer have the advantage of exhibiting restoring capabilities in all directions, a necessary property for the combined electrostatic and magnetic actuations.

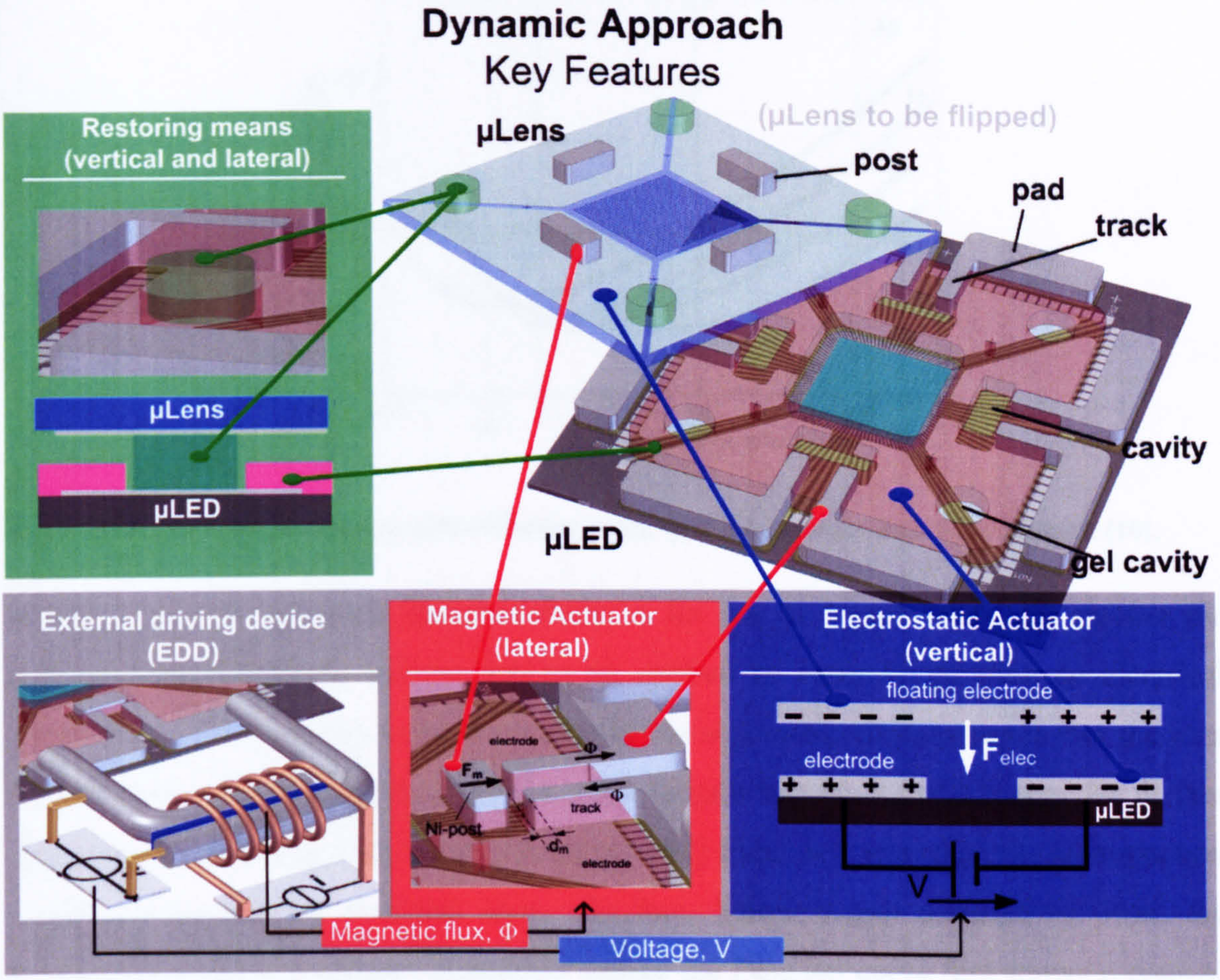

Figure 3-17 Summary of the key features for the dynamic approach. The approach features an electrostatic vertical actuator as well as a lateral magnetic actuator that can be driven simultaneously.

3.3.1 Electrostatic actuation

3.3.1.1 Electrical breakdown considerations

The magnitude of the electric field must be traded off against the electrical breakdown behaviour according to Paschen's law [10] as shown in Figure 3-18. p is the pressure of the gas and d the distance. The electrodes on the µLED are 460µm away from each other. However, this distance is not the limiting condition, since the floating electrode is meant to be around 20 to 200µm above the two driving electrodes on the µLED. Hence, the minimal distance, *d*, between the two driving electrodes needs to be multiplied by a factor of 2. This yields a minimal plate separation distance, *d*, of 40µm. According to Paschen's law, the electrical breakdown voltage depends on the electrodes spacing as well as the pressure and nature of the gas immersing the electrodes. This law does not describe any non-gaseous dielectric, which could be used as an insulator.

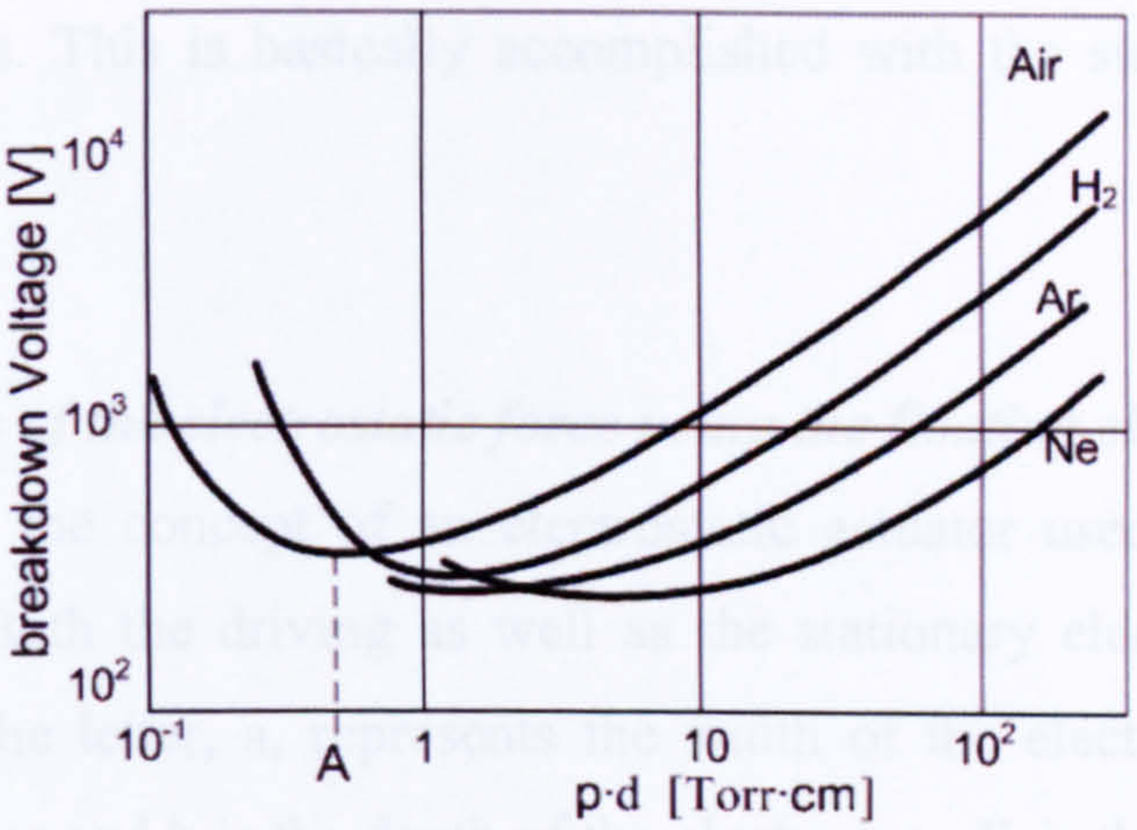

Figure 3-18 Paschen law curves with different gases. p is the pressure and d the distance [10].

Below a certain separation distance (Point A for Air in Figure 3-18), the smaller the distance gets, the more voltage has to be applied in order to provoke an electrical breakdown. This appears to be contradictive but a possible explanation is that the ions do not have enough mean free path in order to gain enough kinetic energy for further ionisation by colliding with other molecules. [52] found however that this phenomenon could not be seen in practical tests. In fact, below a gap distance of 3μm, the breakdown voltage decreases drastically unlike the Paschen curve that shows a gradual increase in the breakdown voltage as shown in Figure 3-19.

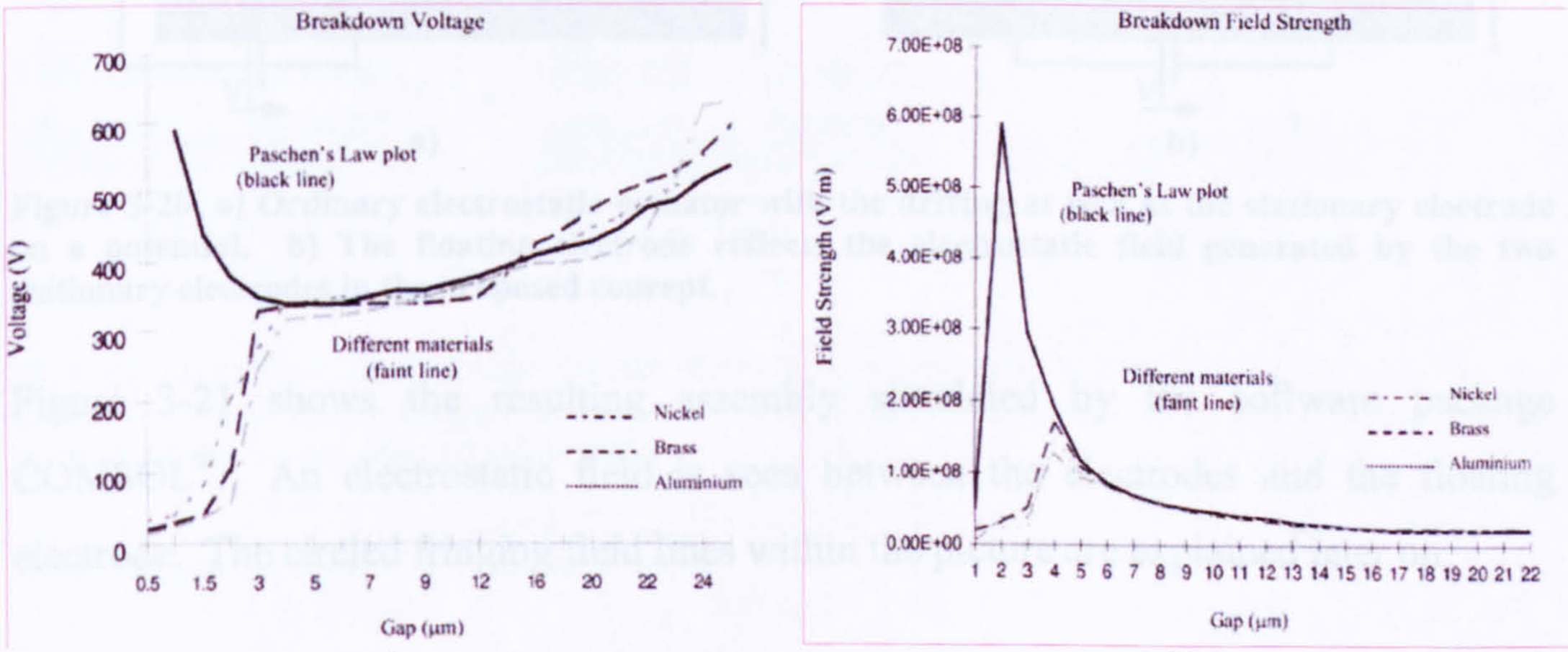

Figure 3-19 a) Below a separation of 3μm a drastic deviation of the empirically measured graph to the Paschen curve can be observed [52]. b) Field strength as a function of gap distance (by courtesy of [52]).

The electric field strength required for a breakdown in air is around 3MV/m. The maximum voltage that can be applied between the driving electrodes, before electrical breakdown occurs, is therefore around 120V if the floating electrode lies 20μm above the electrodes. This value can be increased if a layer of dielectric material is placed on

top of the electrodes. This is basically accomplished with the structural layer of the μLED.

3.3.1.2 Reduction of the electrostatic force using the floating electrode

Figure 3-20a shows the concept of an electrostatic actuator used in the majority of MEMS actuators. Both the driving as well as the stationary electrodes is connected with a potential. The letter, a, represents the width of the electrode, d the distance between the electrodes and b is the depth of the electrodes. F_z is the force generated by such an assembly. Figure 3-20b shows the concept of the proposed electrostatic actuator. Each of the two stationary electrodes that sit on the substrate has a potential. The floating electrode is not connected to any potential and reflects the electrostatic field from one electrode to the other. The floating electrode has no wire attached which could potentially disturb the movement. This is in particular important since the floating electrode is situated on the μLens.

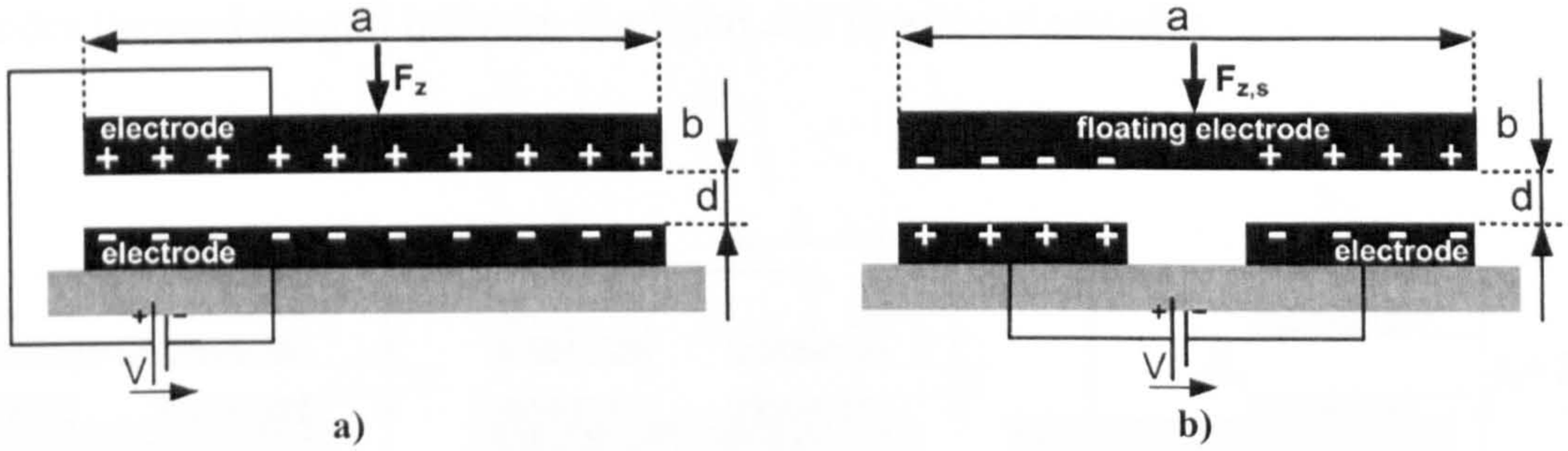

Figure 3-20 a) Ordinary electrostatic actuator with the driving as well as the stationary electrode on a potential. b) The floating electrode reflects the electrostatic field generated by the two stationary electrodes in the proposed concept.

Figure 3-21 shows the resulting assembly simulated by the software package COMSOL®. An electrostatic field is seen between the electrodes and the floating electrode. The circled fringing field lines within the picture are explained later on.

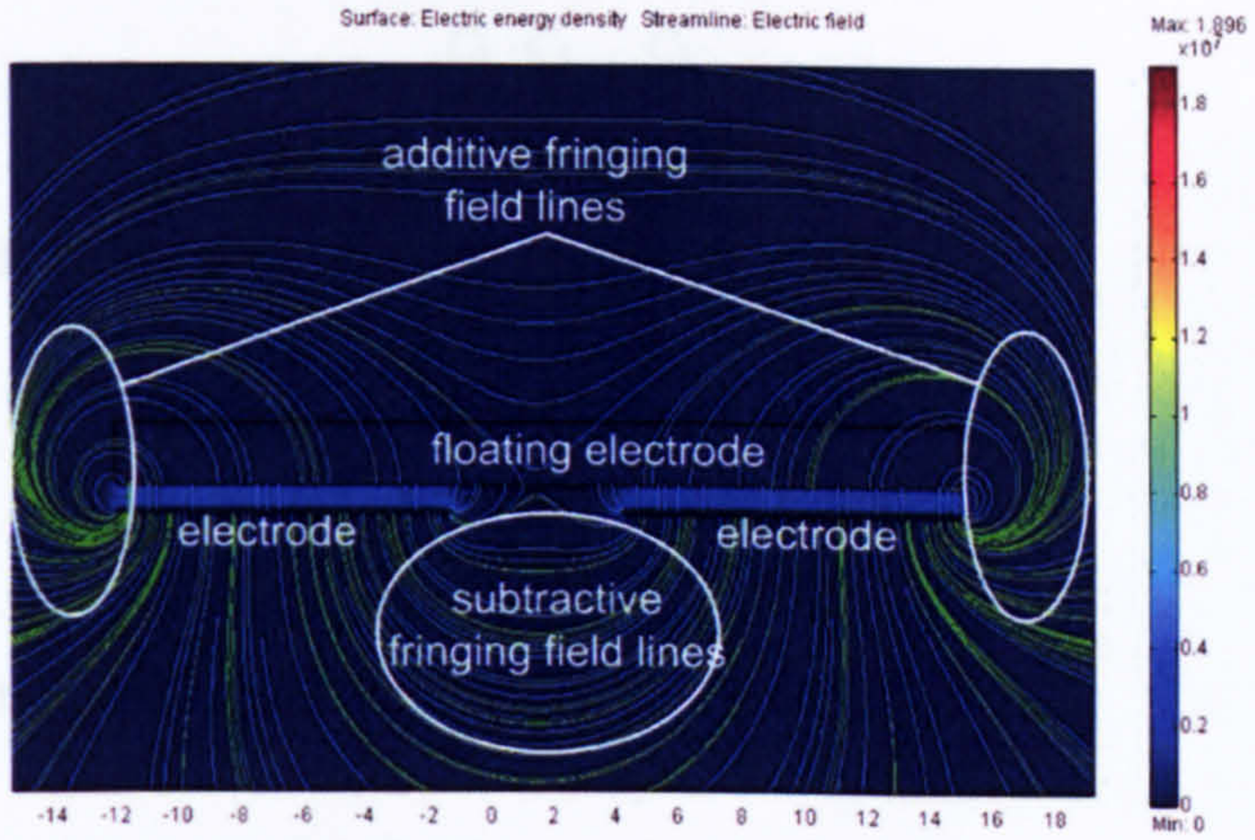

Figure 3-21 COMSOL® simulation of the floating electrode placed on top of electrodes. An electric field is generated between each electrode and the floating electrode. Fringing fields are displayed.

Figure 3-22 shows how the floating electrode can be modelled as a series capacitance, C_s. The width of the floating electrode is a, k is the width of the electrode, b is the depth of the floating electrode as well as the fixed electrode and d represents the distance between floating electrode and fixed electrodes. V is the voltage applied between the electrodes. Possible fringing fields have been neglected between the fixed electrodes themselves and between the fixed and floating electrodes.

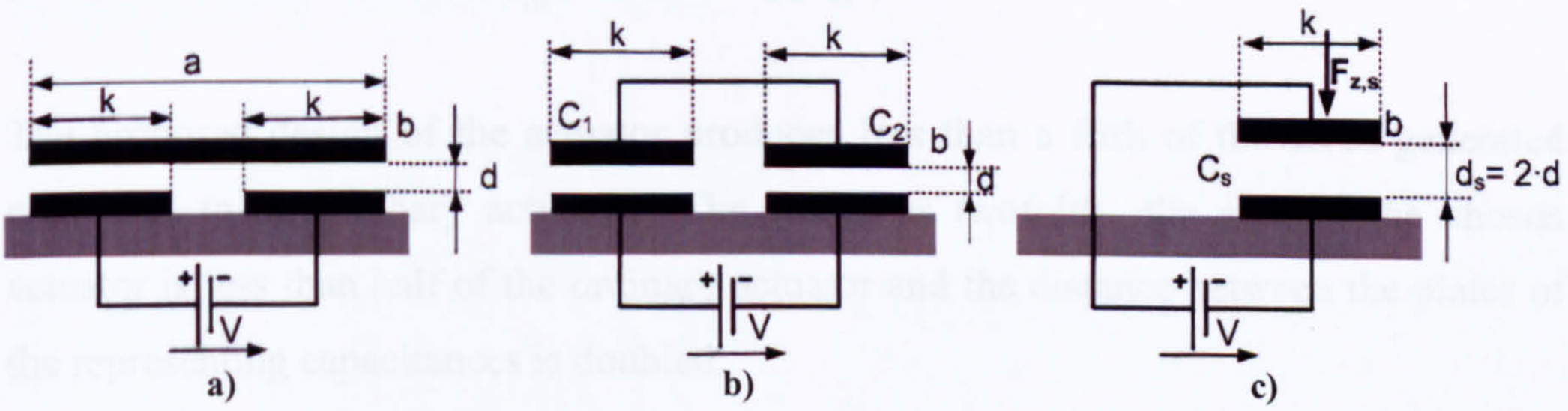

Figure 3-22 a) Floating electrode situated above fixed electrodes. b) Neglecting fringing fields, the assembly seen in a) can be represented with two capacitors C_1 and C_2 in series. c) The resulting series capacitance can then be calculated.

Each capacitance can be calculated as

$$C_1 = C_2 = \frac{\varepsilon_0 \cdot \varepsilon_r \cdot k \cdot b}{d} \tag{3-5}$$

The area between the two capacitors on the floating electrode can be regarded as an ideal conductor. This assembly then represents C_1 and C_2 connected in series, and the total series capacitance C_s is:

$$C_s = \frac{C_1 \cdot C_1}{C_1 + C_1} = \frac{C_1}{2} \tag{3-6}$$

The energy stored within the capacitor C_s is:

$$U_s = \frac{C_s \cdot V^2}{2} = \frac{C_1 \cdot V^2}{4} = \frac{\varepsilon_0 \cdot \varepsilon_R \cdot k \cdot b \cdot V^2}{4 \cdot d} \tag{3-7}$$

The force, $F_{z,s}$ obtained is then:

$$\mathbf{F}_{Z,S} = \nabla U_S = -\hat{\mathbf{z}} \frac{\varepsilon_0 \cdot \varepsilon_R \cdot k \cdot b \cdot V^2}{4 \cdot d^2} \tag{3-8}$$

Equation (3-9) is a modification of equation (3-8) by replacing the width of the electrode, k, with a multiple of the width of the floating electrode. Furthermore, a correcting factor, P_1, is added to take the field lines of the fringing field between the electrodes into account.

$$\mathbf{F}_{Z,S}\Big|_{k=\frac{4}{10}a} = -\hat{\mathbf{z}} \frac{\varepsilon_0 \cdot \varepsilon_R \cdot a \cdot b \cdot V^2}{10 \cdot d^2} \cdot P_1 \tag{3-9}$$

The proposed design of the actuator produces less than a fifth of the force generated compared to an ordinary actuator. The reason is twofold: the area of the chosen actuator is less than half of the ordinary actuator and the distance between the plates of the representing capacitances is doubled.

3.3.1.3 Calculation of the force

The calculation of the electrostatic force requires to know the dimensions of the electrode sitting on the μLED as shown in Figure 3-23a and Figure 3-23b. These dimensions as well as the geometries are of importance for both the analytical description and the simulation of the force.

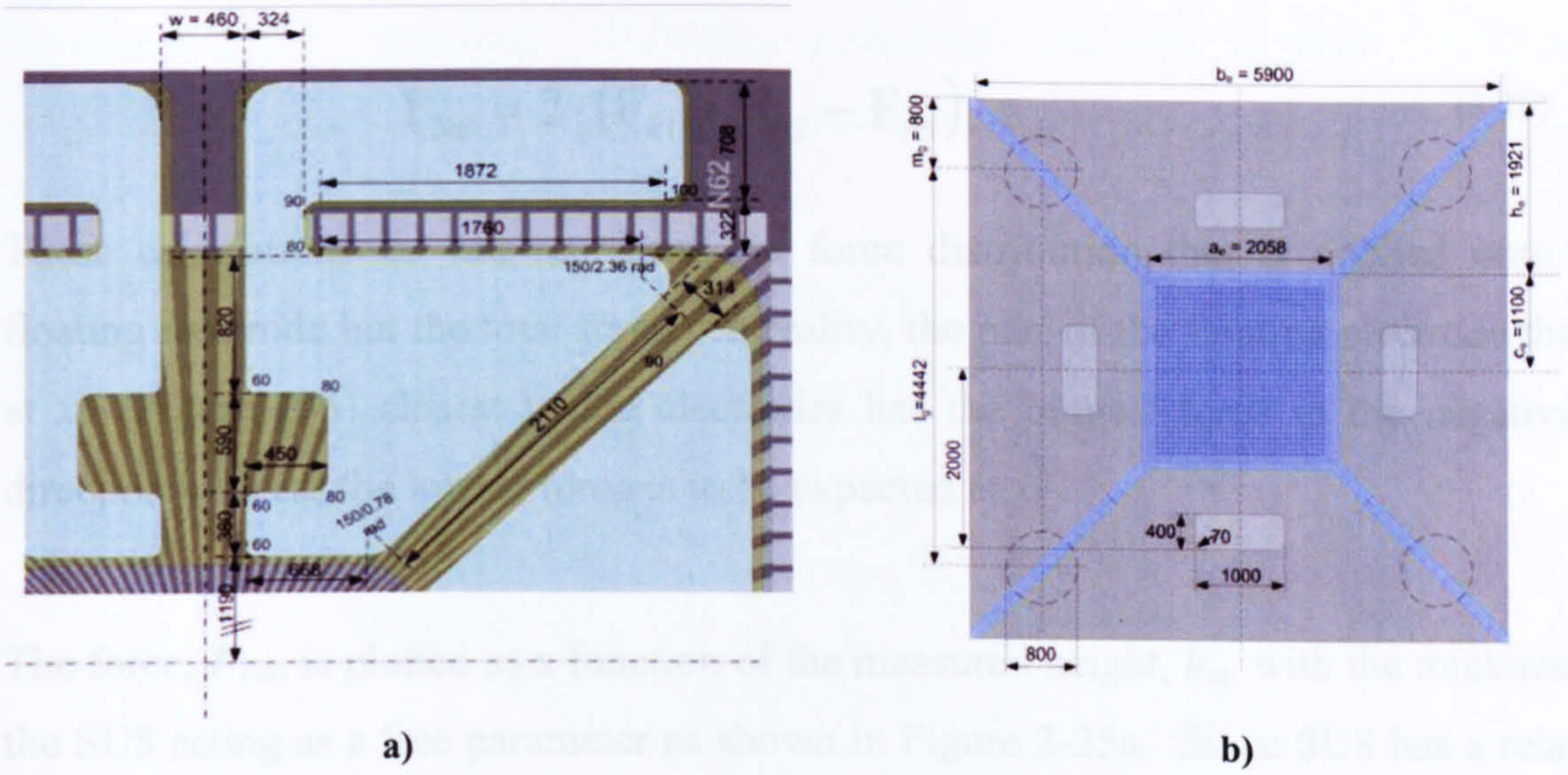

a) b)

Figure 3-23 a) Dimensions of one of the electrodes of the μLED. b) Dimensions of the μLens features and floating electrode.

Figure 3-24a illustrates the charge distribution in the case where the floating electrode (not represented in the figure) is closer at d_1 than at d_2. At d_2 the charge density, ρ_{s1}, is bigger since the floating electrode, being in closer proximity to the fixed electrodes, causes a stronger electrostatic field. Figure 3-24b shows the situation from a perspective with the floating electrode represented in transparent green. The introduction of the tilt for the expression of the electrostatic force is important to obtain as much a general expression as possible.

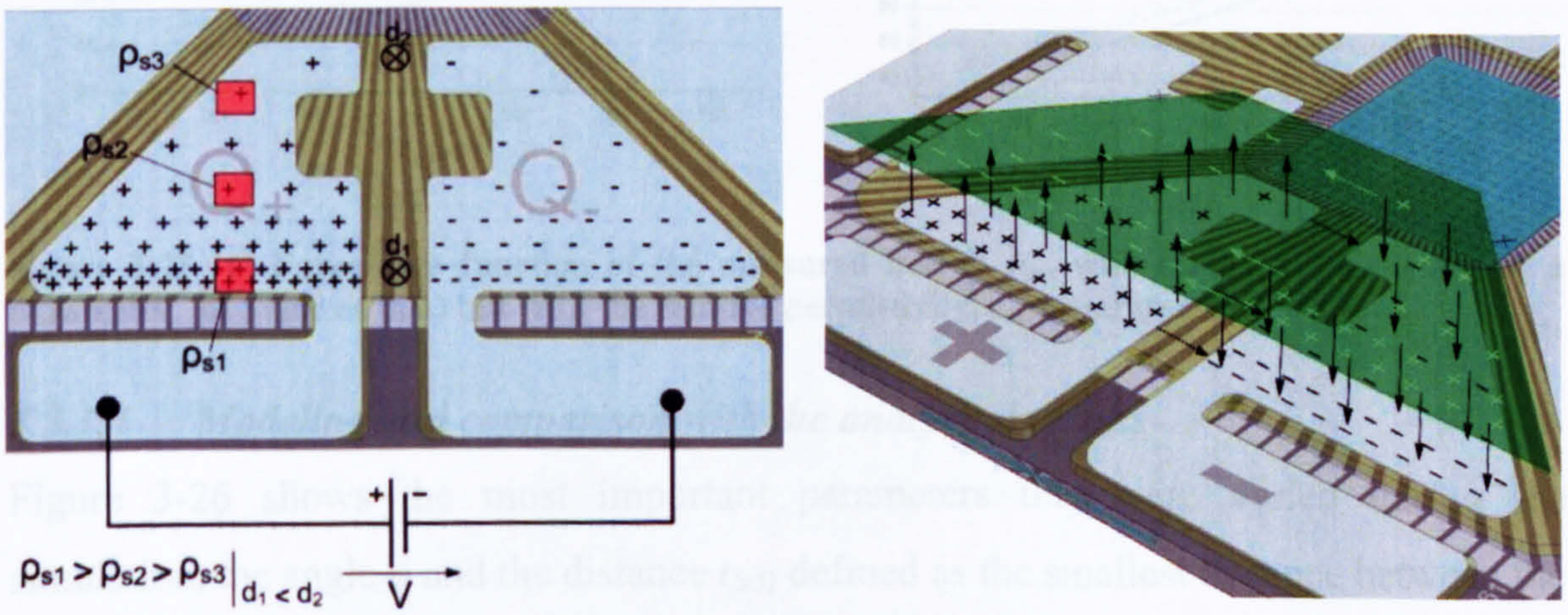

a) b)

Figure 3-24 a) Display of the charge distribution assuming that the floating electrode is further away at d_2 than at d_1. b) Display of the different electrostatic fields that occur in the setup.

The interested reader is referred to Appendix B where the calculations of the different terms found in equation (3-10) $\boldsymbol{F}_{R1}$, $\boldsymbol{F}_{R2}$ and $\boldsymbol{F}_{R3}$ are carried out in greater details.

$$\mathbf{F}_{Tot} = 2 \cdot \left(\mathbf{F}_{R1} + \mathbf{F}_{R2} - \mathbf{F}_{R3} \right). \tag{3-10}$$

These calculations do not represent the force distribution that is applied onto the floating electrode but the total force. In reality, the part of the floating electrode that is at *x5* (Figure B-5) closest to the electrodes has the biggest force in the negative z-direction whereas the lowest force is to be expected at *x1*.

The force, $\boldsymbol{F}_{Tot}$, is plotted as a function of the measured height, h_m, with the thickness of the SU8 acting as a free parameter as shown in Figure 3-25a. Since SU8 has a relative permittivity of 3, the higher the part of t_s of the total distance t_x, the higher the force $\boldsymbol{F}_{Tot}$. In Figure 3-25b, the permittivity is taken this time as a varying parameter. The higher the relative permittivity, ε_r, the higher the capacitance and the resulting force $\boldsymbol{F}_{Tot}$.

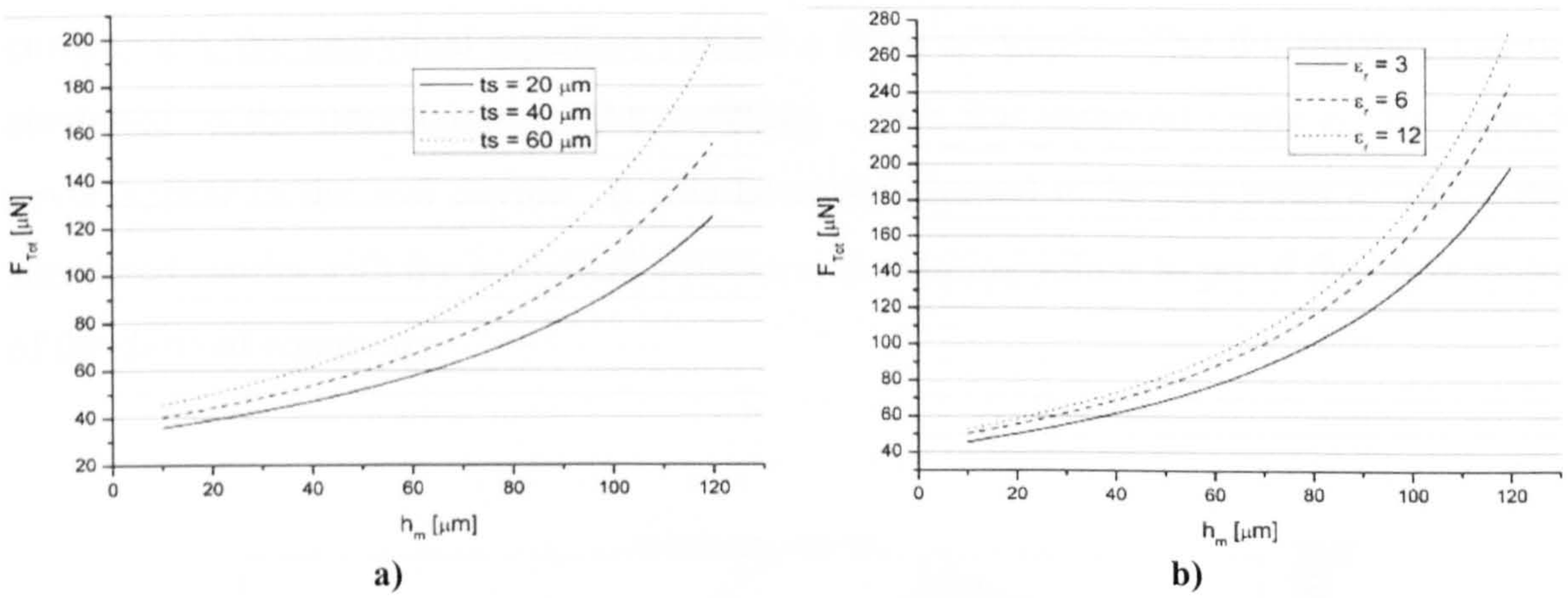

a) b)

Figure 3-25 a) Force as a function of the measured height, h_m, with the SU8 thickness t_s as a parameter. b) Same as in a) but with the relative permittivity, ε_r, as parameter.

3.3.1.4 Modeling and comparison with the analytical results

Figure 3-26 shows the most important parameters that were varied during the simulation, the angle φ and the distance $t_{(x5)}$ defined as the smallest distance between the floating and the fixed electrodes. Using COMSOL® the electrostatic actuator was modeled and results were compared to analytical results. Figure 3-27 shows the potential of the electrodes with the colour coding on the right hand side. One electrode has a potential of 0V (blue colour) and on the other, 600V are applied. The floating electrode has exactly half the applied voltage, namely 300V. The floating electrode, from a potential point of view, can be regarded as the conductor which connects the two capacitors that are in series and hence features half of the voltage that is applied

between the two capacitors. The floating electrode lies with an angle of 10° with respect to the electrodes, perfectly aligned above the electrodes.

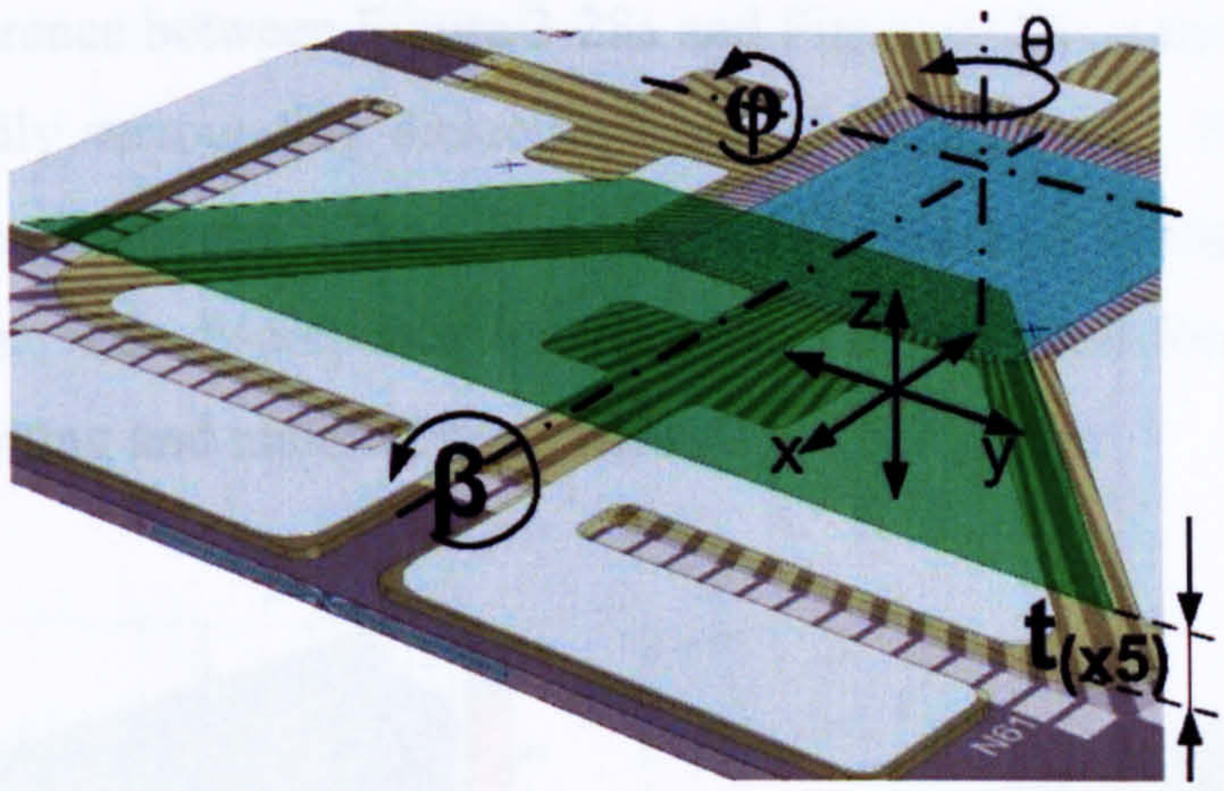

Figure 3-26 This picture shows the most important parameters that have been varied for the simulations, such as the angle φ, and the distance $t_{(x)}$ at the point $x5$, $t_{(x5)}$ representing the smallest distance of the floating electrode towards the electrodes in z-direction.

The distance $t_{(x)}$ at the point x5 is 503µm which yields a total force, $\boldsymbol{F}_{Tot}$ of 7.3µN. In comparison, the analytical equation yielded a force of 5.6µN. The discrepancy can be attributed to the uncertainty of the meshing. Also the assumed angle of 10° would never appear in the real device. It was however deemed to be important to check the simulated results with the analytical equations at extreme values to proof the correctness of the derived equations.

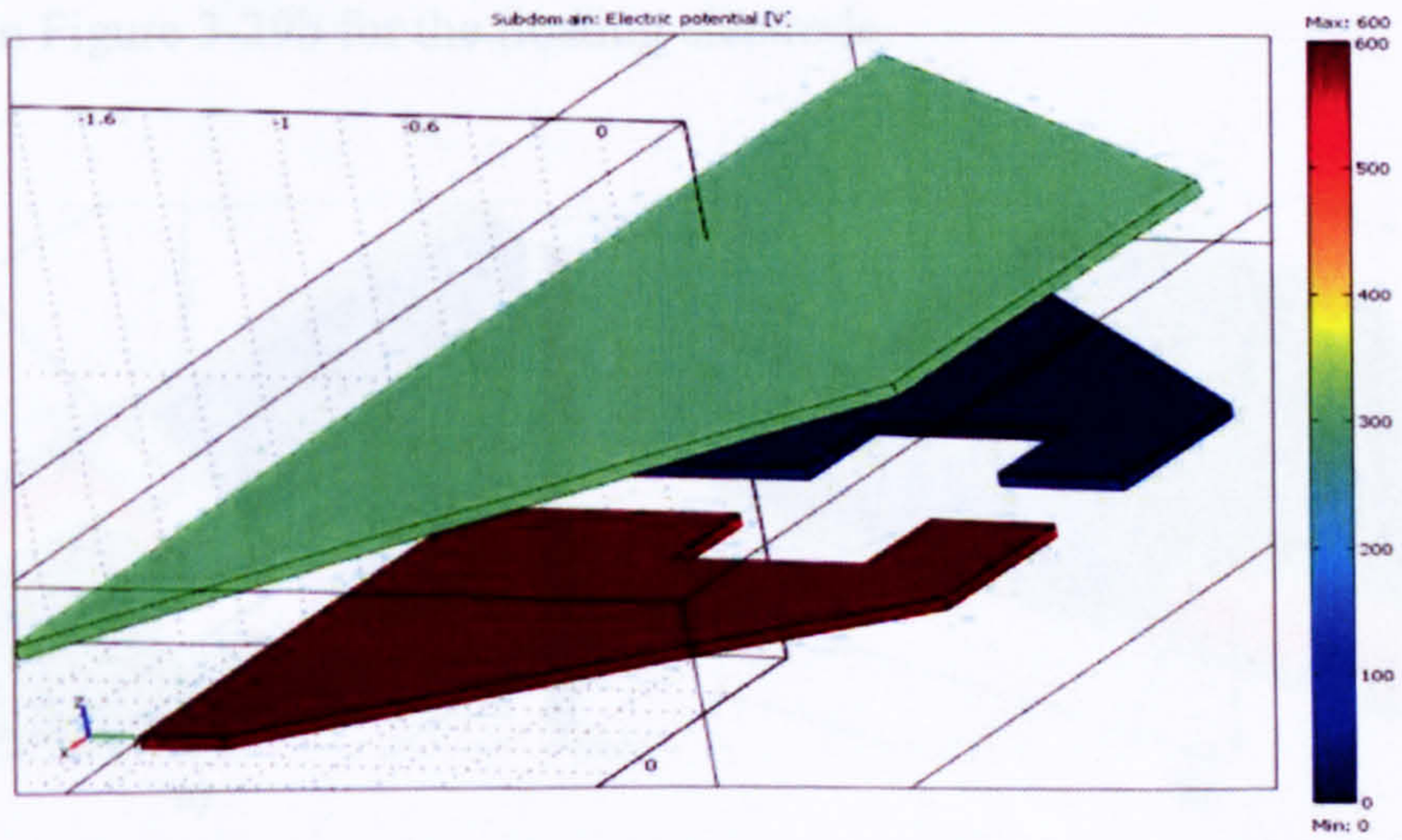

Figure 3-27 Tilted floating electrode (green). The colours indicate the potential that is on the electrode and floating electrode. As expected, half of the potential is on the floating electrode.

Figure 3-28 shows the assembly where the floating electrode is again tilted with an angle of 10° and a voltage of 600V is applied between the electrodes. The smallest vertical distance between the floating electrode and the electrodes at point $t_{(x5)}$ is 203µm. The difference between Figure 3-28a and Figure 3-28b is that, in Figure 3-28b, parts of the laterally surrounding dielectric material is cut away. This results in 5µN less force than seen in Figure 3-28a. The value of Figure 3-28b would be closer to the analytical solution. The discrepancy between the values of the force stems from the settings of the meshing and material properties.

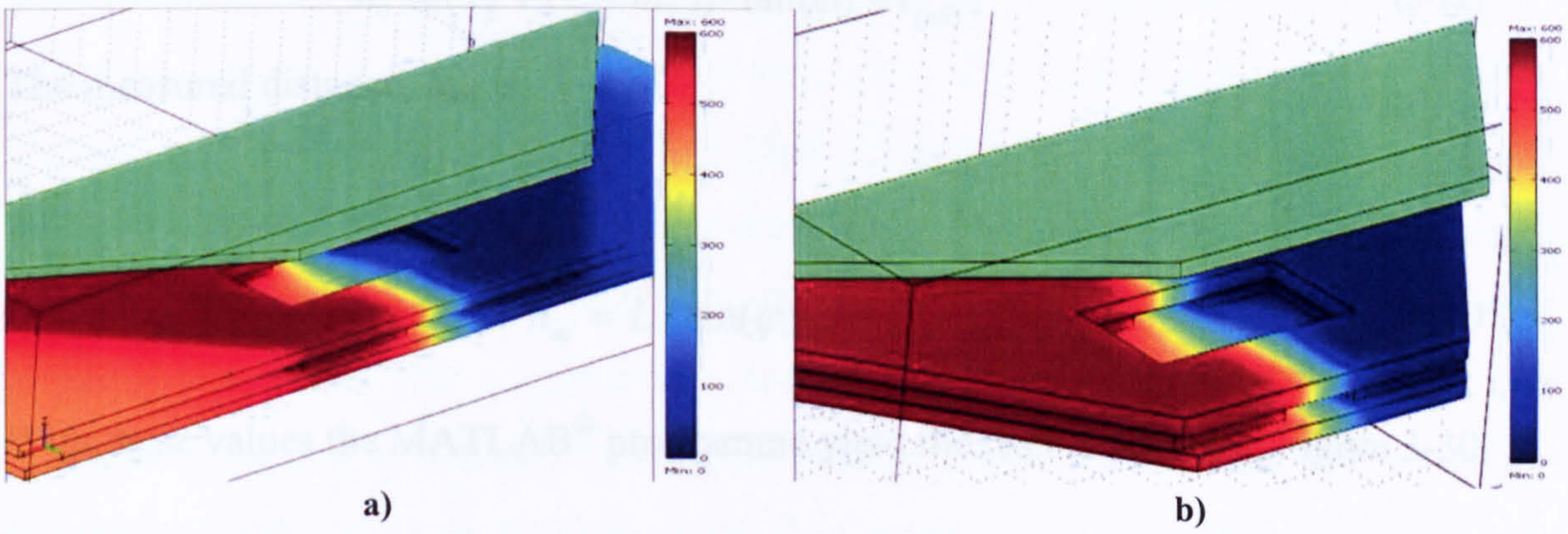

Figure 3-28 Simulation of a tilted electrode with an angle of 10° and a distance at point *x5* of $t_{(x5)}$ = 203µm. a) A force , F_{Tot}, of 45µN was obtained with a large dielectric area. b) A total force, F_{Tot}, equals 40µN was obtained by cutting the dielectric covering the electrodes.

Figure 3-29 shows the charge distribution of the fixed electrodes (Figure 3-29a) and the floating electrode (Figure 3-29b). The highest charge density is found at the lateral place where the floating electrode comes closest to the electrodes $t_{(x5)}$ at x_5. The same can be seen in Figure 3-29b for the floating electrode.

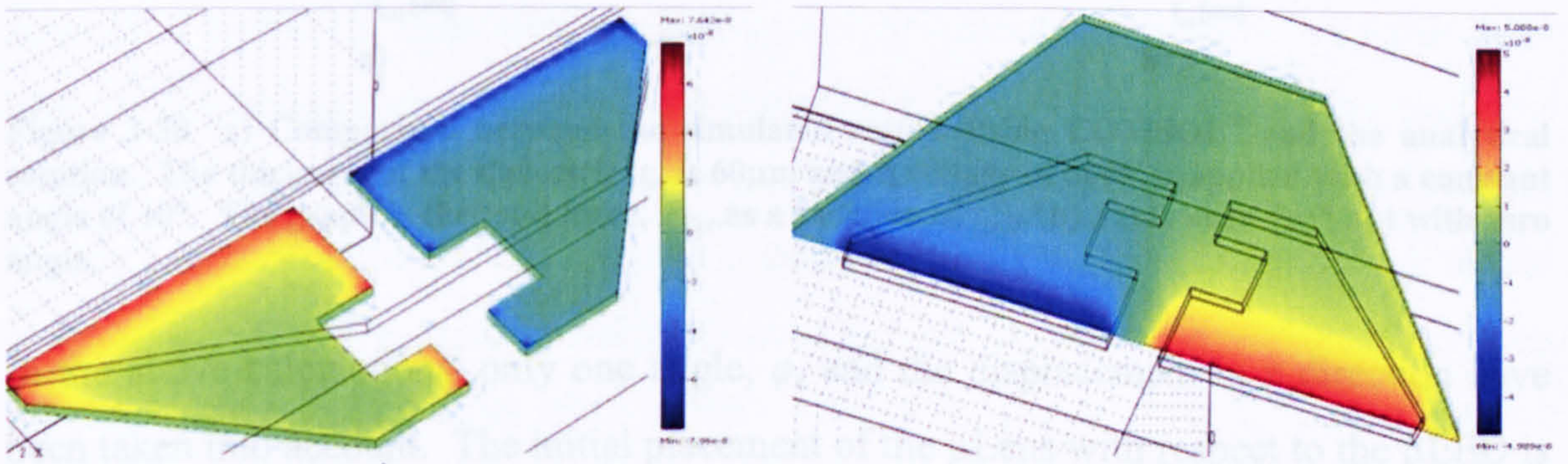

Figure 3-29 a) Charge density distribution of the electrodes as seen from above. b) Charge distribution of the floating electrode as seen from beneath. In both cases, the floating electrode is tilted with and angle φ of 10° and has a distance $t_{(x5)}$ of 203µm.

Equation (3-11) shows the relation between the angle φ and other distances

$$\frac{L}{h_m} = \frac{1}{\tan(\varphi)} = \frac{x + (L - m_2)}{h_0 - t_{(x)}}, \tag{3-11}$$

where all other terms are shown in Figure .

By knowing the angle φ and the distance $t_{(x5)}$ at x_5, the absolute distance between electrode and floating electrode can be calculated:

$$h_0 = (x_5 + (L - m_2)) \cdot \tan(\varphi) + t_{(x5)}. \tag{3-12}$$

The measured distance, h_m, is:

$$h_m = L \cdot \tan(\varphi) \tag{3-13}$$

With these values the MATLAB® programme yield the results shown in Figure 3-30.

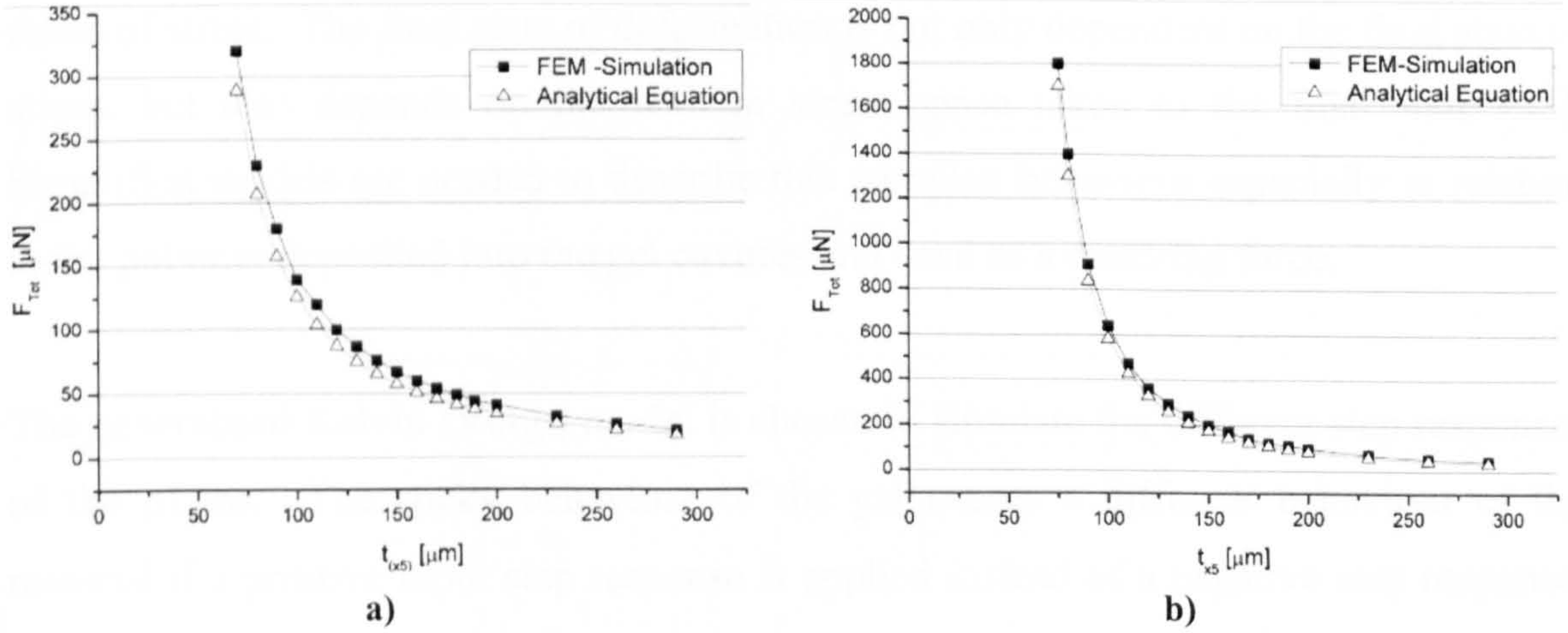

Figure 3-30 a) Comparison between the simulated results using COMSOL® and the analytical solution. The thickness of the dielectric, t_s, is 60µm and a voltage of 600V is applied with a constant angle of 10°. The graph is the total force, F_{Tot}, as a function of $t_{(x5)}$. b) Same as in "a)" but with zero angle.

In the above calculations, only one angle, φ, and the displacement in z direction have been taken into account. The initial placement of the µLens with respect to the µLED is horizontal (Figure 3-26). The angles β and θ as well as the Cartesian displacement in x- and y-direction have been neglected (Figure 3-26). The maximal error between the FEM simulation and the closed form expression is less than 17% for an applied voltage of 600V, a tilt of 10° and a dielectric thickness of 60µm as shown in Figure 3-30a. The

more the electrodes and floating electrodes are separated the bigger the error is. With no tilt, the maximum error is less than 10% as shown in Figure 3-30b.

3.3.2 Viscoelastic behaviour of polymers used as a restoring force

An elastic material, when subjected to a sudden stress, exhibits an instant deformation. Such a material can be modelled as a perfect mechanical spring. The energy is not dissipated but stored instead. A Newtonian viscous fluid, on the other hand, responds with a steady flow process if a constant stress is applied. Energy is dissipated and not stored and the behaviour of the fluid can be modelled as a dashpot. Some materials, called viscoelastic materials show both behaviours, if a sudden stress is applied [53]. Examples of viscoelastic materials are rubber and silicones as well as a large class of biomaterials [54]. Viscoelastic materials have also a "memory effect" or "elastic after-effect" as first described by Boltzmann (1874). If a viscoelastic material is subjected to an initial stress, and, after a short time interval, a second stress is applied, the material response is not only predefined by the current state of stress, but is also determined by all previous states of stress: in other words, the material has a memory for the entire past states of stress. The final state of deformation is not only dependent on the final state of stress, but also depends on the path in stress space taken to the final state [53]. Simplified models are needed to describe this complex behaviour especially in relation to the polymer deposited into the gel cavities and used as a restoring force.

The generalised Kelvin (Voigt) model is chosen to simulate the different step responses of the μLens. The sticky behaviour of the gel causes a different behaviour of the material if a positive input step response is applied instead of a negative step response. The different phases are numbered and shown in Figure 3-31a as a time displacement diagram and the corresponding elements are numbered accordingly in Figure 3-31b and Figure 3-31c. For the phase 4 (green), a dashpot d_3 in parallel with the spring k_3 has been added in series to the already existing spring-dashpot system. This addition contributes to the continuous creep of the viscoelastic material. Since the slope of this creep is far less than during the phases 1 to 3, it is assumed that the viscosity of d_3 must be considerably higher than that of b_2 and b_1, respectively (Figure 3-31b). The dashpots b_1 and b_2, and springs k_1 and k_2 are identical as they represent just different locations within the same material. Likewise, the masses m_A and m_B are expected to have the same value and are negligible compared to m_C, the mass of the μLens. Figure 3-31c

shows the system of the negative step response with a dashpot b_4 added to the system due to the stickiness of the gel bump. The force that causes the displacement is highly nonlinear and changes strongly as a function of the displacement itself.

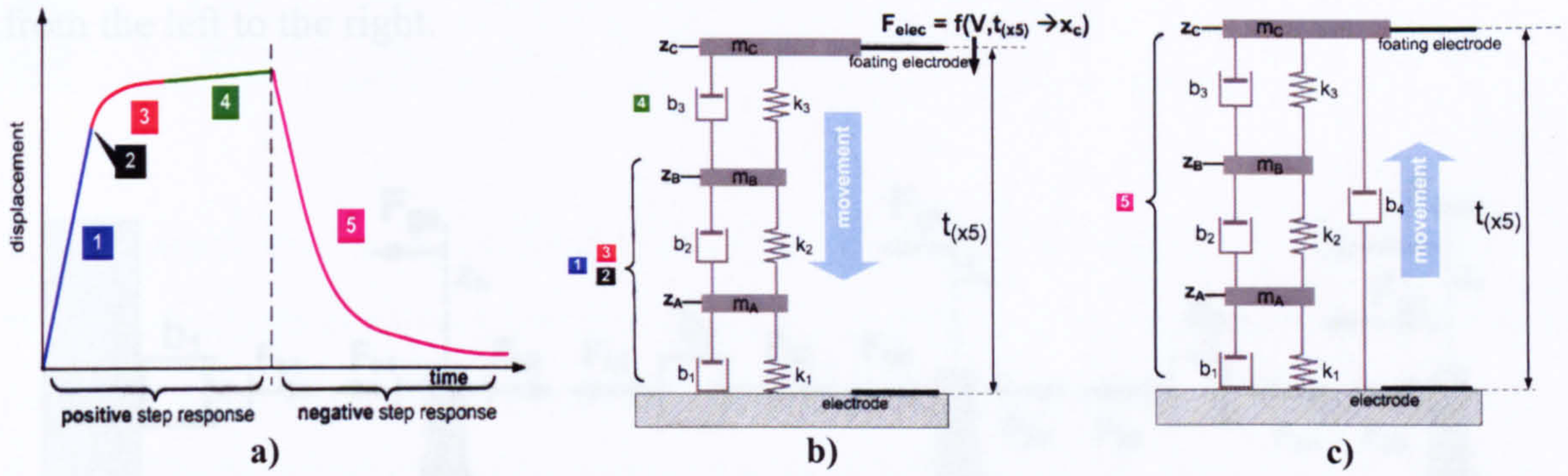

Figure 3-31 a) Qualitative drawing of a positive and negative step response with the different phase labelled in numbers and explained in b and c. b) Dashpot spring system for positive step response. c) Dashpot spring system for negative step response.

The springs k_1 and k_2 in the model are nonlinear. Being a "non compressive" gel, the material keeps its volume constant as illustrated in Figure 3-32 (steps 1-3). The increase in the opposing force is provided by an additional parallel spring/dashpot system. Figure 3-32 (step 4 to 6) is an attempt to explain the different behaviours of the negative step response, once the electrostatic force is not applied. The effect that comes into play is the stickiness of the used gel polymer towards the µLens and µLED while the contact area is reduced when the polymer gets back to its initial shape.

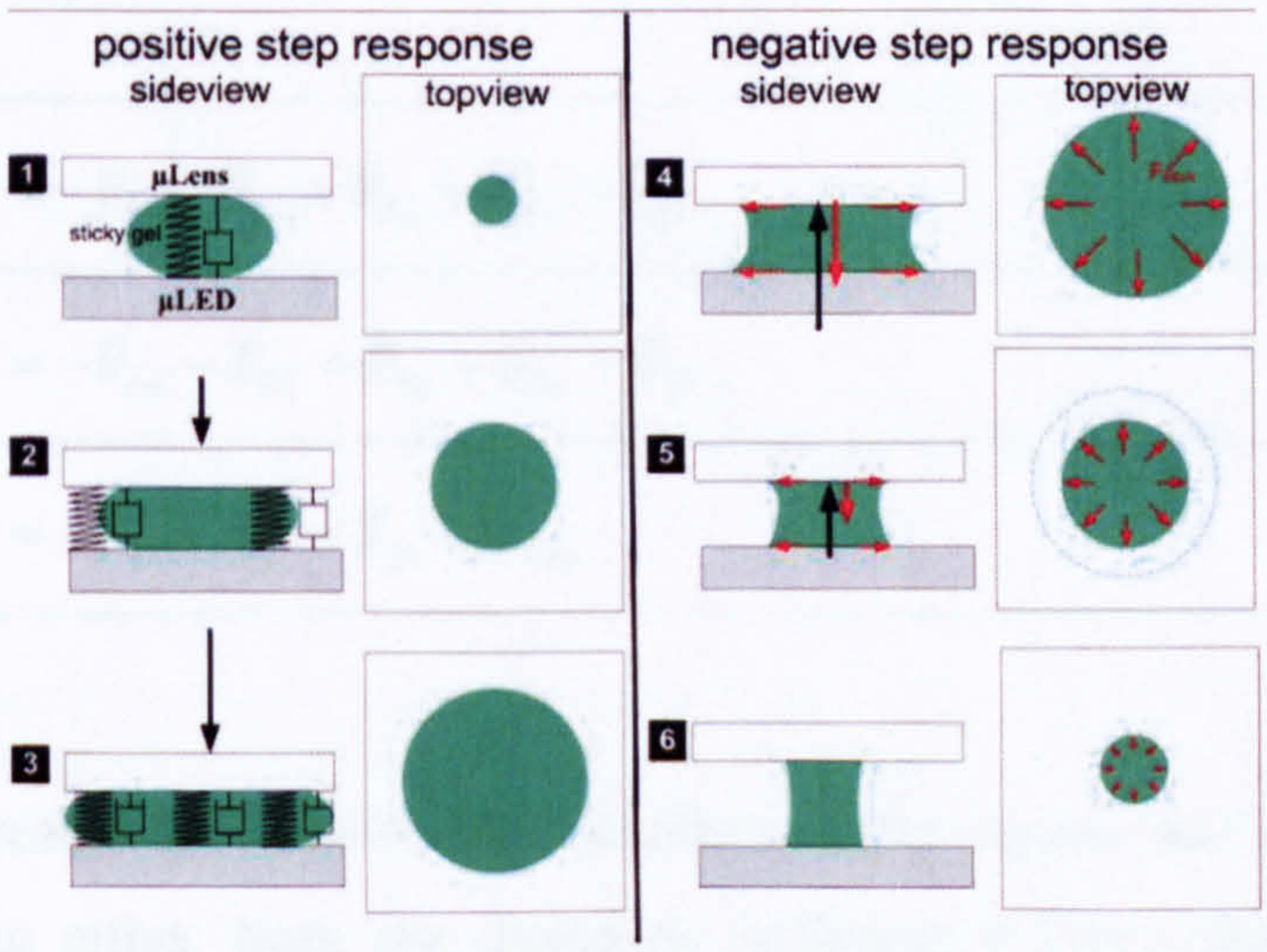

Figure 3-32 Qualitative consideration of the different nonlinear behaviour for the positive and negative step response of the actuator and polymer as a restoring means.

This adhesion effect might be alleviated if a different material, such as the photo-patternable PDMS is used.

Figure 3-33 depicts a 90 degrees rotated (for clarity) model from the positive step response, taken from Figure 3-31b. The connections between the elements are separated and replaced by individual forces to obtain terms for the modal analysis, necessary for the matrix of the movement equations [55]. The positive z-direction is from the left to the right.

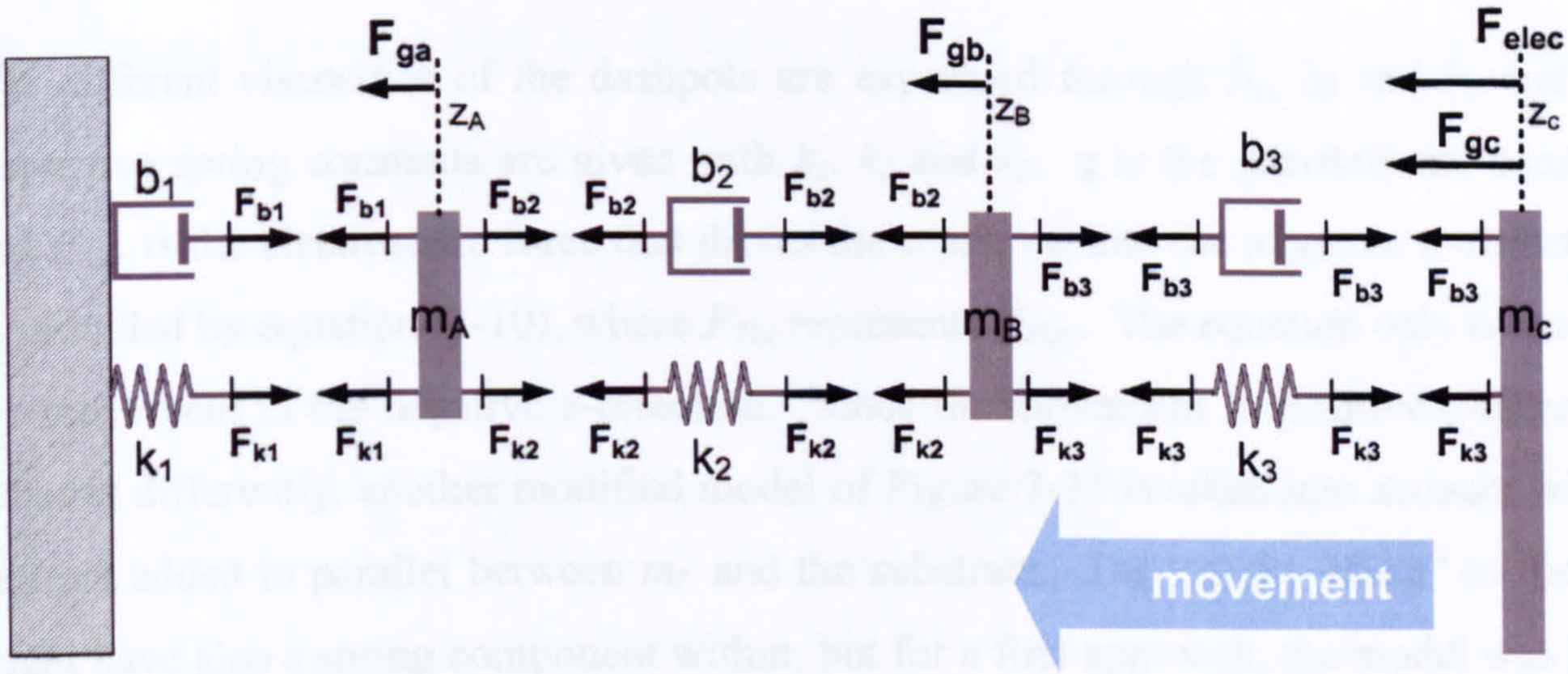

Figure 3-33 Same model as seen in Figure 3-31b but having cut the different connections between elements and replaced it with forces for the derivation of the equation. The setup is rotated 90 degrees. The μLens is on the right hand side, the μLED on the left.

Three objects are moved by an external force, necessitating three equations to obtain a solution. Equations (3-14) show the differential equations describing the movement of I the mass, m_A, II the mass m_B and III the mass m_C.

I	$m_A \cdot \frac{d^2 z_A}{dt^2} = -\mathbf{F}_{b1} - \mathbf{F}_{k1} + \mathbf{F}_{b2} + \mathbf{F}_{k2} - \mathbf{F}_{gA}$
II	$m_B \cdot \frac{d^2 z_B}{dt^2} = -\mathbf{F}_{b2} - \mathbf{F}_{k2} + \mathbf{F}_{b3} + \mathbf{F}_{k3} - \mathbf{F}_{gB}$
III	$m_C \cdot \frac{d^2 z_C}{dt^2} = -\mathbf{F}_{b3} - \mathbf{F}_{k3} - \mathbf{F}_{gC} - \mathbf{F}_{elec}$

(3-14)

z_A, z_B and z_C represent the relative displacements of the masses and $\boldsymbol{F}$ are the individual forces originating either from the dashpots, indicated by the subscript b or from a spring, indicated by the subscript k and gravity, indicated by the subscript g. $\boldsymbol{F}_{elec}$ stands for the electrostatic force. By replacing the individual forces as shown in Figure 3-33 with the corresponding terms for the springs and dashpots, the system of differential equations I to III becomes (equations(3-15)).

I	$m_A \cdot \frac{d^2 z_A}{dt^2} = -\frac{dz_A}{dt} \cdot b_1 - z_A \cdot k_1 + \left(\frac{dz_B}{dt} - \frac{dz_A}{dt} \right) \cdot b_2 + (z_B - z_A) \cdot k_2 - m_A \cdot g$
II	$m_B \cdot \frac{d^2 z_B}{dt^2} = -\left(\frac{dz_B}{dt} - \frac{dz_A}{dt} \right) \cdot b_2 - (z_B - z_A) \cdot k_2 + \left(\frac{dz_C}{dt} - \frac{dz_B}{dt} \right) \cdot b_3 + (z_C - z_B) \cdot k_3 - m_B \cdot g$
III	$m_C \cdot \frac{d^2 z_C}{dt^2} = -\left(\frac{dz_C}{dt} - \frac{dz_B}{dt} \right) \cdot b_3 - (z_C - z_B) \cdot k_3 - m_C \cdot g - \mathbf{F}_{elec}$

(3-15)

The different viscosities of the dashpots are expressed through b_1, b_2 and b_3 and the respective spring constants are given with k_1, k_2 and k_3. g is the gravitational constant and $\boldsymbol{F}_{elec}$ is the electrostatic force that drives the mass, m_c into the negative z -direction, as provided by equation (3-10), where $\boldsymbol{F}_{Tot}$ represents $\boldsymbol{F}_{elec}$. The equation only considers the movement in the negative z-direction. Since the movement in positive z-direction behaves differently, another modified model of Figure 3-33 is taken into account with a dashpot added in parallel between m_C and the substrate. The "sticky effect" of the gel might have also a spring component within, but for a first approach, the model was kept as simple as possible.

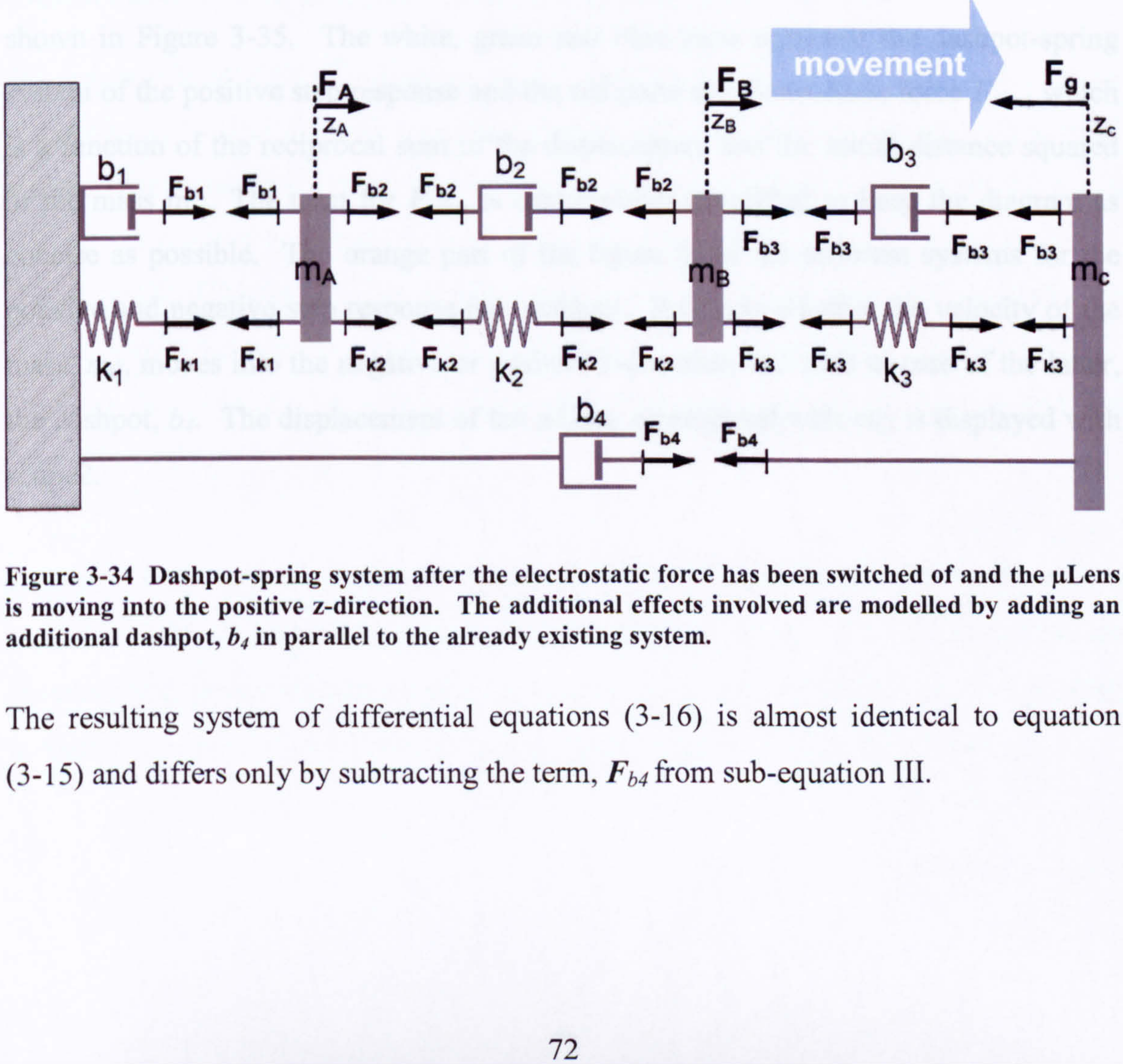

Figure 3-34 Dashpot-spring system after the electrostatic force has been switched of and the µLens is moving into the positive z-direction. The additional effects involved are modelled by adding an additional dashpot, b_4 in parallel to the already existing system.

The resulting system of differential equations (3-16) is almost identical to equation (3-15) and differs only by subtracting the term, $\boldsymbol{F}_{b4}$ from sub-equation III.

I	$m_A \cdot \frac{d^2 z_A}{dt^2} = -\mathbf{F}_{b1} - \mathbf{F}_{k1} + \mathbf{F}_{b2} + \mathbf{F}_{k2} - \mathbf{F}_{gA}$
II	$m_B \cdot \frac{d^2 z_B}{dt^2} = -\mathbf{F}_{b2} - \mathbf{F}_{k2} + \mathbf{F}_{b3} + \mathbf{F}_{k3} - \mathbf{F}_{gB}$
III	$m_C \cdot \frac{d^2 z_C}{dt^2} = -\mathbf{F}_{b3} - \mathbf{F}_{k3} - \mathbf{F}_{gc} - \mathbf{F}_{b4}$

(3-16)

By replacing the forces with the different properties of the dashpots and spring one yields:

I	$m_A \cdot \frac{d^2 z_A}{dt^2} = -\frac{dz_A}{dt} \cdot b_1 - z_A \cdot k_1 + \left(\frac{dz_B}{dt} - \frac{dz_A}{dt}\right) \cdot b_2 + \left(z_B - z_A\right) \cdot k_2 - m_A \cdot g$
II	$m_B \cdot \frac{d^2 z_B}{dt^2} = -\left(\frac{dz_B}{dt} - \frac{dz_A}{dt}\right) \cdot b_2 - \left(z_B - z_A\right) \cdot k_2 + \left(\frac{dz_C}{dt} - \frac{dz_B}{dt}\right) \cdot b_3 + \left(z_C - z_B\right) \cdot k_3 - m_B \cdot g$
III	$m_C \cdot \frac{d^2 z_C}{dt^2} = -\left(\frac{dz_C}{dt} - \frac{dz_B}{dt}\right) \cdot b_3 - \left(z_C - z_B\right) \cdot k_3 - m_C \cdot g - z_C \cdot b_4 .$

(3-17)

Equation (3-15) and (3-17) were then placed into the software package SIMULINK® as shown in Figure 3-35. The white, green and blue parts represent the dashpot-spring system of the positive step response and the red parts the electrostatic force $\boldsymbol{F}_{elec}$, which is a function of the reciprocal sum of the displacement and the initial distance squared of the mass m_c. The term for $\boldsymbol{F}_{elec}$, is considerably simplified to keep the diagram as concise as possible. The orange part of the figure takes the different systems for the positive and negative step response into account. It detects whether the velocity of the mass, m_C, moves into the negative or positive z-direction and adds in case of the latter, the dashpot, b_4. The displacement of the µLens, represented with m_C, is displayed with scope2.

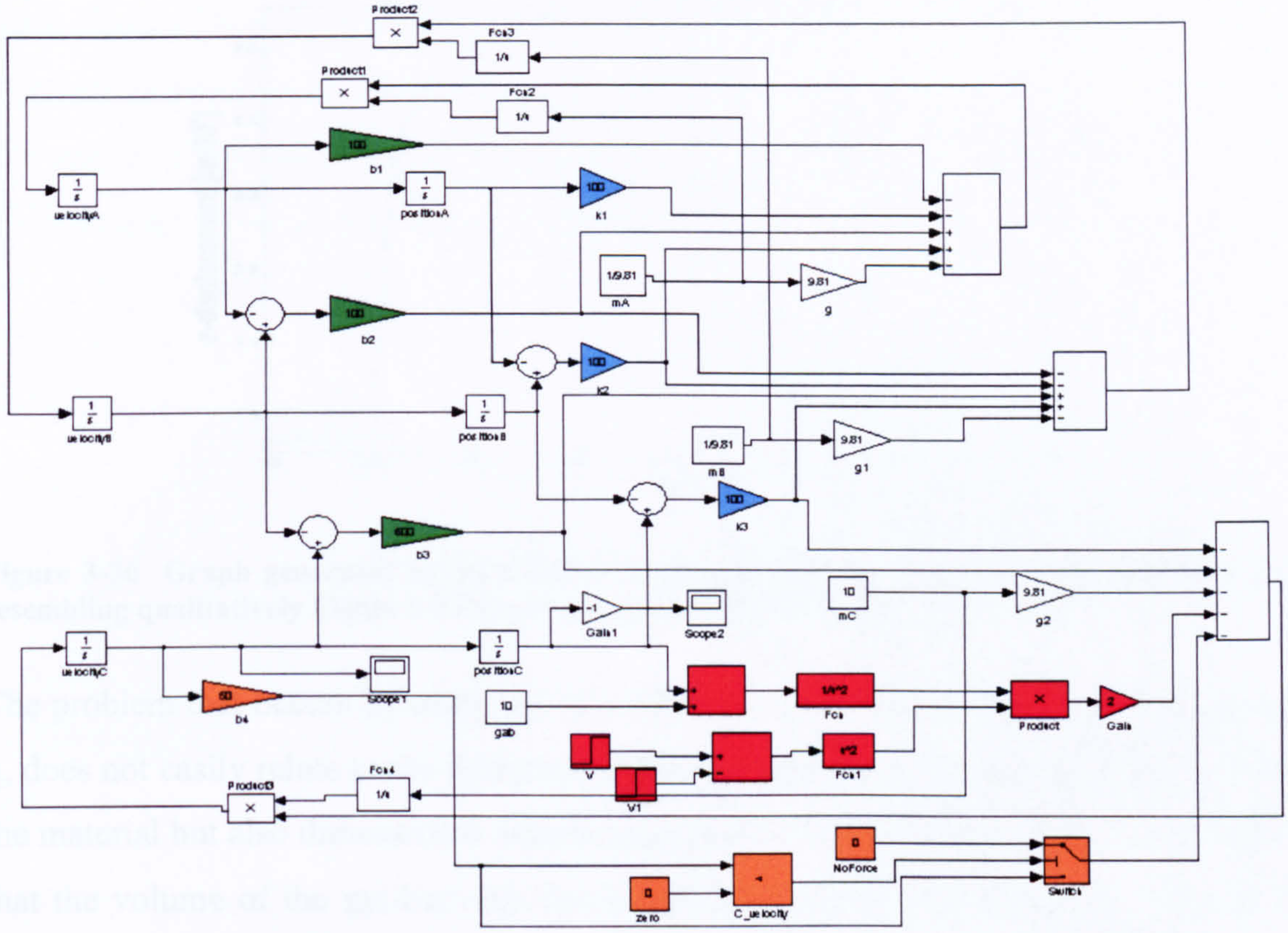

Figure 3-35 SIMULINK® file derived from the equations (3-15) and (3-17). The white, green and blue part represents the dashpot-spring system of the gel. The red part stands for the electrostatic force and the orange part differentiates between a negative or positive movement of m_c in z-direction and adds, in the latter case, a dashpot b_4 to the system.

The usage of SIMULINK® leaves open the possibility to replace the gains for the spring constants (k_1, k_2 and k_3) with nonlinear lookup tables or function blocks with several inputs. The same property applies for the viscosity constants of the dashpots b_1, b_2, b_3 and b_4. A qualitative approach is attempted to get a similar waveform as shown in Figure 5-22b, Chapter 5. The absolute values (i.e. of the dashpots and springs) are chosen somewhat arbitrary, but the values relative to each other are on the basis of studying the physical behaviour of the step responses as well as the gel and the assembly itself.

Figure 3-36 displays the graph that was generated with the SIMULINK® model shown in Figure 3-35. It resembles qualitatively the graph from the step responses that are obtained with practical measurements as shown in Figure 5-22b, Chapter 5. A positive voltage step is applied at 40 seconds and a negative step voltage at 70 seconds.

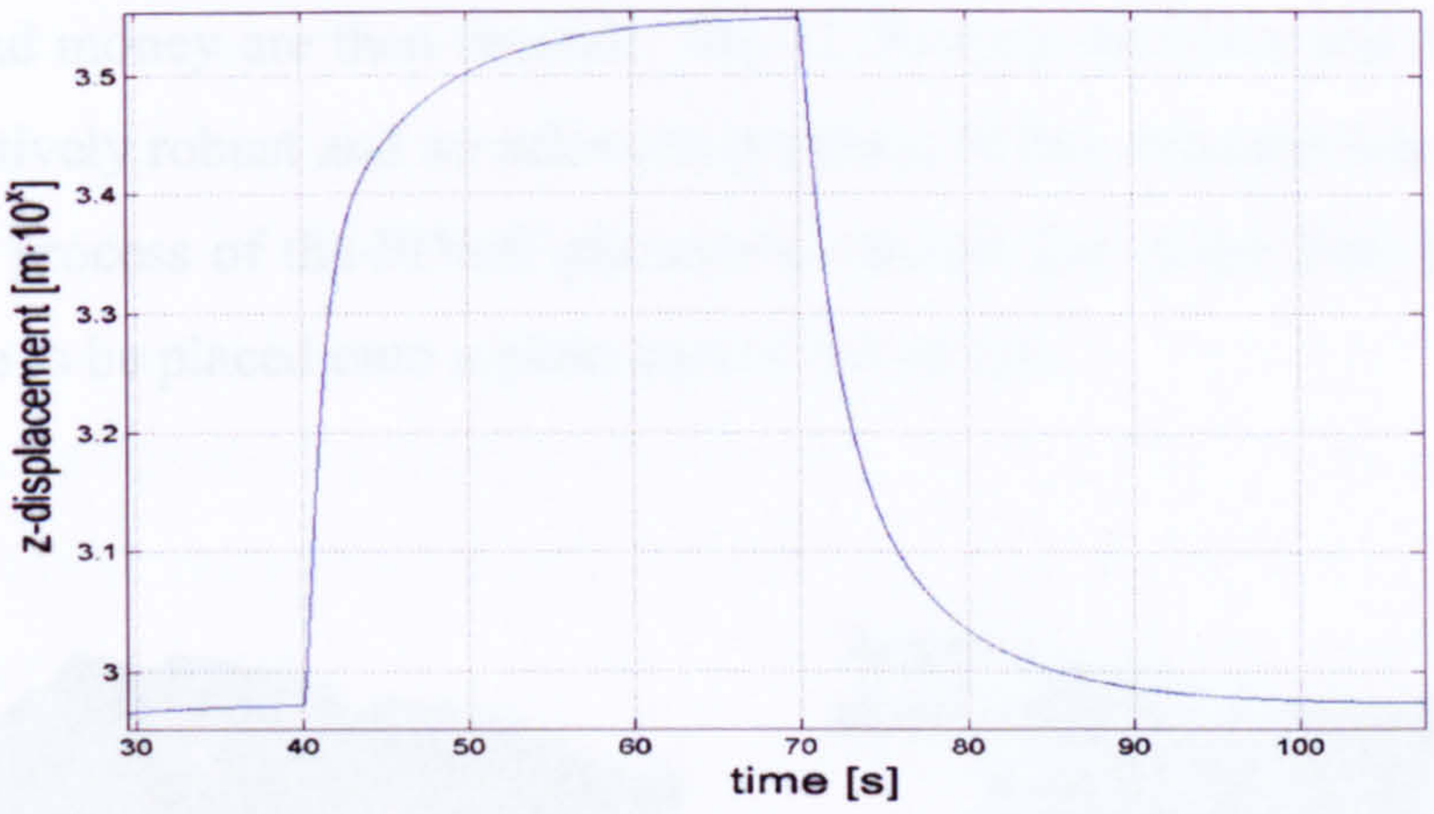

Figure 3-36 Graph generated by SIMULINK® with the model and values shown in Figure 3-35 resembling qualitatively Figure 5-22b from practical measurements in Chapter 5.

The problem that occurs by using viscosity-data from the literature is that the viscosity, η, does not easily relate to the dashpot coefficient used within the model, since not only the material but also dimensional aspects play a role. One approach might be to assume that the volume of the gel between two plates stays constant in form of a cylinder of radius, $r_{(t)}$, and height, $h_{(t)}$. If the gel is compressed between the plates (µLens and µLED), the gel-plates contact area changes over time that suggests a radial as well as a circular flow of the gel with respect to the plates. This creates a frictional force which is at least a function of the radius, $r_{(t)}$ and its derivative $dr_{(t)}/dt$, the height, $h_{(t)}$ and the viscosity, η, as parameter.

3.3.2.1 Positioning of photo-patternable "gel" bumps

The crude gel bumps are to be replaced by a photo-patternable PDMS bumps to allow a more reliable control and better analysis of the restoring structure. Figure 3-37a displays a possible solution by placing the restoring means into the gel cavities, which are situated on the µLED. There are however several reasons not to choose this option. Firstly, by adding another process, the developer of the PDMS might attack the structure layer. Secondly, the UV-LED array chip itself is considered to be more fragile to chemical as well as physical exposure than the lens array, therefore reducing the amount of process steps is preferable. Thirdly, the gel cavities, having a diameter of around 400µm, might trap air within the holes, therefore preventing the PDMS structure to be deposited within the hole. Figure 3-37b proposes to place the restoring means onto the µLens itself. The µLens array itself, consisting of sapphire, is physically as well as chemically more robust. The µLens array is also not the subject of many process steps and is not as expensive as the µLED. In case of process failure, not as

much time and money are then wasted. The Ti floating electrode and the posts (Ni or SU8) are relatively robust and no adhesion problem of this structure has been observed. The spinning process of the PDMS photoresist should also cause little problems, since the bumps are to be placed onto a plain area of the μLens.

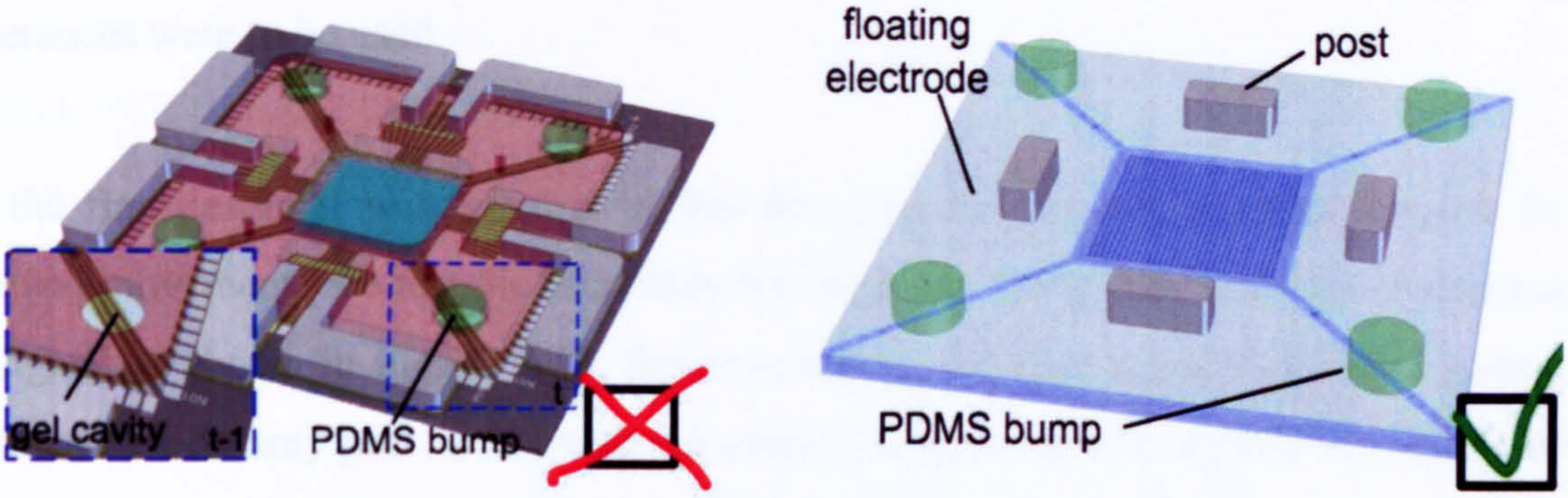

a) b)

Figure 3-37 a) The PDMS bumps are part of the μLED which complicates the fabrication process. b) placement of the PDMS bumps on the μLens.

Figure 3-38a shows the μLED with its gel cavities and the μLens with its restoring means on each corner. The μLens is flipped by 180° and placed in a way that the restoring means fit into the gel cavity as indicated in Figure 3-38b.

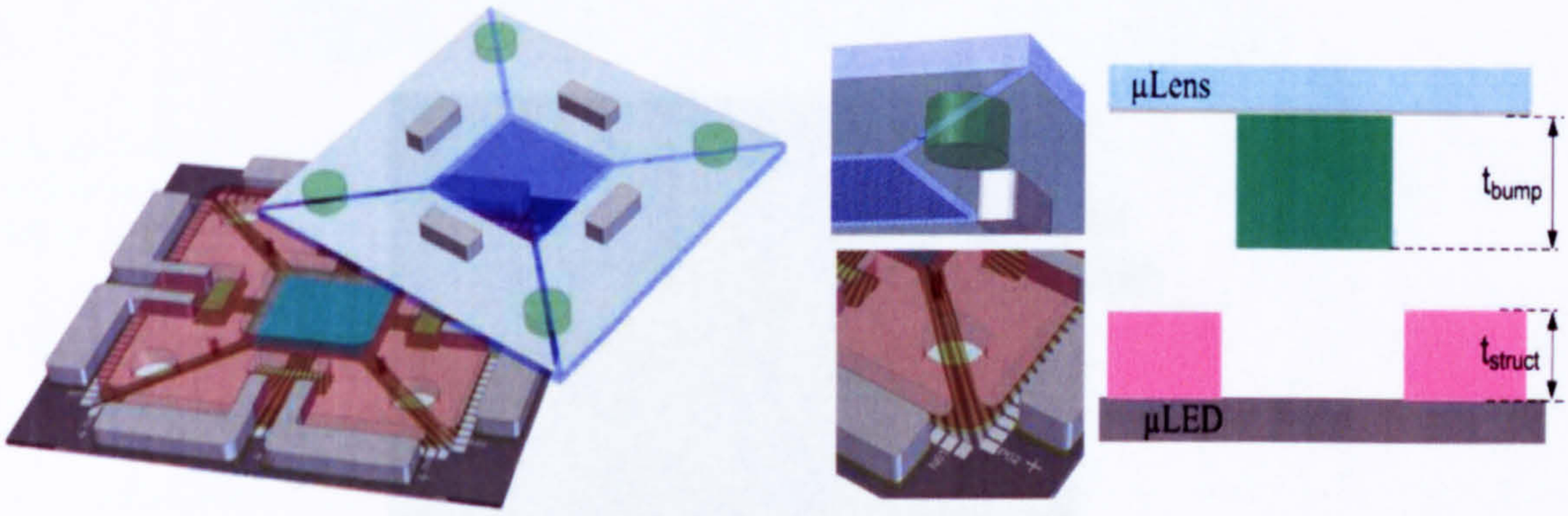

a) b)

Figure 3-38 a) Bumps of the μLens are placed in order to fit within the gel cavities that are situated on the μLED. b) Sideview of the μLens and μLED. The diameter of the restoring means is smaller than the diameter of the gel cavity. The thickness of the restoring means, t_{bump}, however needs to be bigger than the thickness of the structure layer, t_{struct}.

3.3.3 Magnetic circuit of the lateral actuator

A magnetic actuator has been designed to achieve lateral movement in both x- and y-directions. The passive alignment provided by the post-cavity system is unlikely to achieve the necessary lateral accuracy while the μLens is moved in the vertical direction. Furthermore, the friction and possible debris within the post cavity system might have caused the entire vertical movement to be impossible if too tight lateral tolerances were to be used.

In the first design it was anticipated that the magnetic actuation would be used for vertical movement. To test the feasibility for magnetic movement, a macro device was designed as shown in Figure 3-39. Superpermalloy has been chosen for the magnetic path and the dummy post as this material exhibits a large relative permeability of 20000 and a rather low hysteresis behaviour. This material is UV-LIGA compatible and can be electroformed onto the functional layer. The thickness of the magnetic path, 50μm, is relatively small. When a current is passed through the coil, the dummy post gets attracted to the magnetic path. The cantilever made of a polymer provides the restoring force. The device proves that with an appropriate restoring means, controllable and stable vertical displacements are feasible. Although the use of magnetic actuation for vertical displacement was discarded, the experiment demonstrated the practicality of this actuation mechanism.

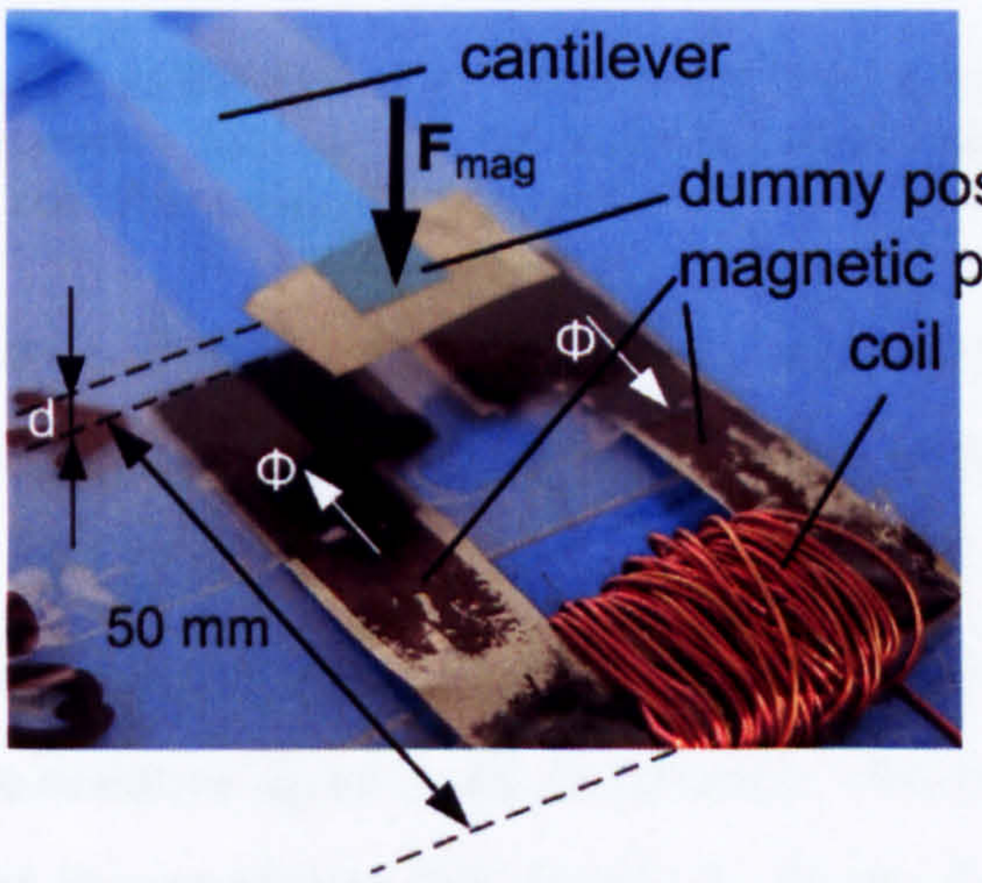

Figure 3-39 Magnetic macro actuator. The dummy post that is suspended on the cantilever is attracted with a force, F_{mag}, if a current is passed through the coil.

Figure 3-40 presents the μLED with an External Driving Device (EDD) already assembled. In this set-up lateral actuation is performed. The wires of the EDD are made of purified Ni. This material has a fair relative permeability value of 600. The Ni post of a μLens was taken and placed within the cavity that was filled with a viscous fluid. A current of around 400mA was passed through the coils and a displacement of over 50μm could be observed by using a microscope. In future devices, it is anticipated that the EDD, pads, tracks and posts are to be made of superpermalloy which has considerable more relative permeability and less hysteresis behaviour than Ni. The initial distance between post and the tracks (d_m) will be around 10μm, which is far less than the present 50μm. The driving current is therefore expected to be drastically reduced.

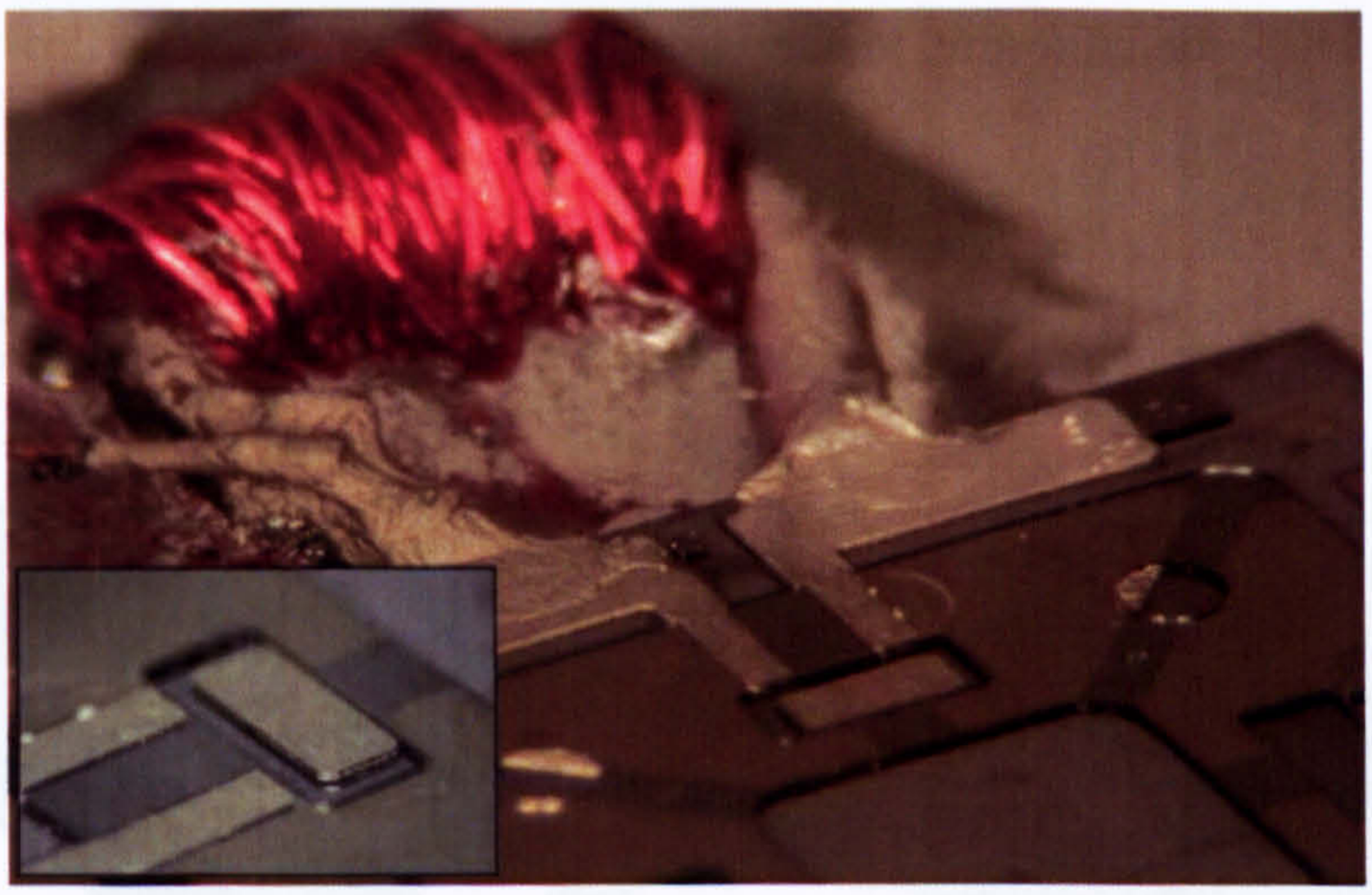

Figure 3-40 Photograph of a μLED with attached external driving device (EDD). A post is placed within the cavity. This assembly was used for the initial test of the magnetic movement that can be achieved considering the real dimension of the assembly.

The magnetic actuation responsible for the lateral displacement can be described as follows. The magnetic flux, Φ, passes along the magnetic path and reaches the cavity of the μLED where the post of the μLens is situated as shown in Figure 3-41. Here the two tracks act as a controlled horseshoe magnet and attract the ferromagnetic post with a force $\boldsymbol{F}_m$ to make the distance d_m as small as possible. Since the post is attached to the μLens the entire μLens is moved into this direction. Each of these actuators is attached to the side of the μLED, thereby moving the μLens in both x- and y-directions. The aforementioned gel or PDMS bump, having elastic properties also in lateral directions, plays an important role in this movement.

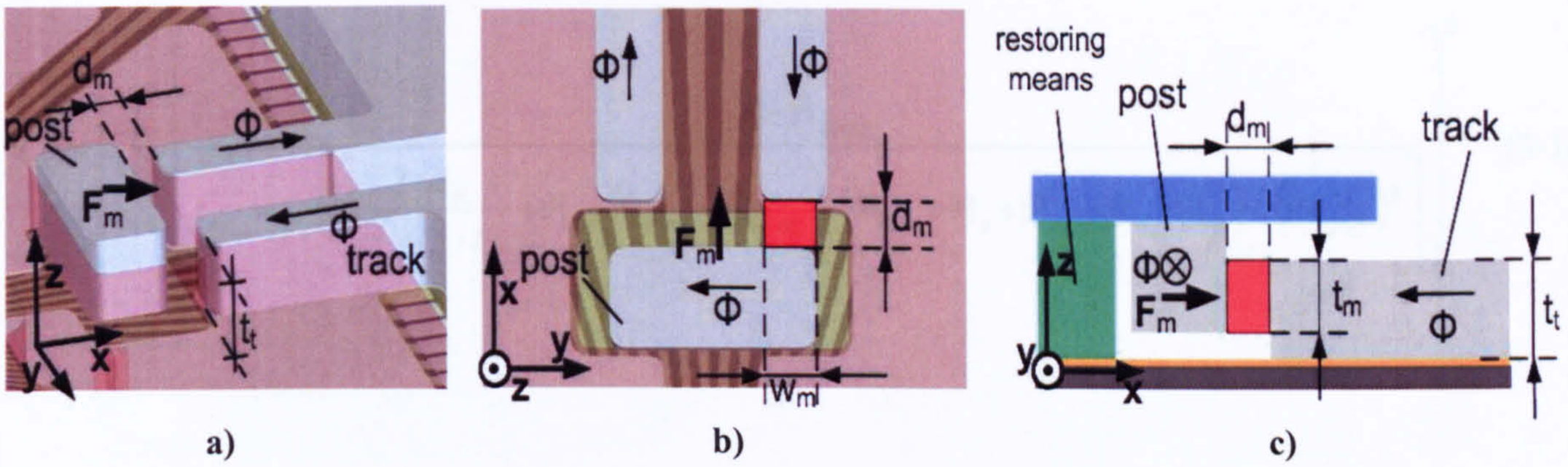

Figure 3-41 Due to the magnetic flux, Φ, the two tracks act like a horseshoe magnet and attract the post with the force, F_m , to reduce the distance, d_m. a) Perspective view. b) Top view. c) Side view.

Figure 3-42 shows the electrically equivalent simplified schematic of the magnetic circuit responsible for the lateral movement of the μLens. The white coloured nonlinear magnetic resistors represent either Fe or Ni. These materials exhibit a magnetisation curve with a hysteresis. The introduction of hysteresis behaviour makes the whole calculation as well as the control of the displacement complicated.

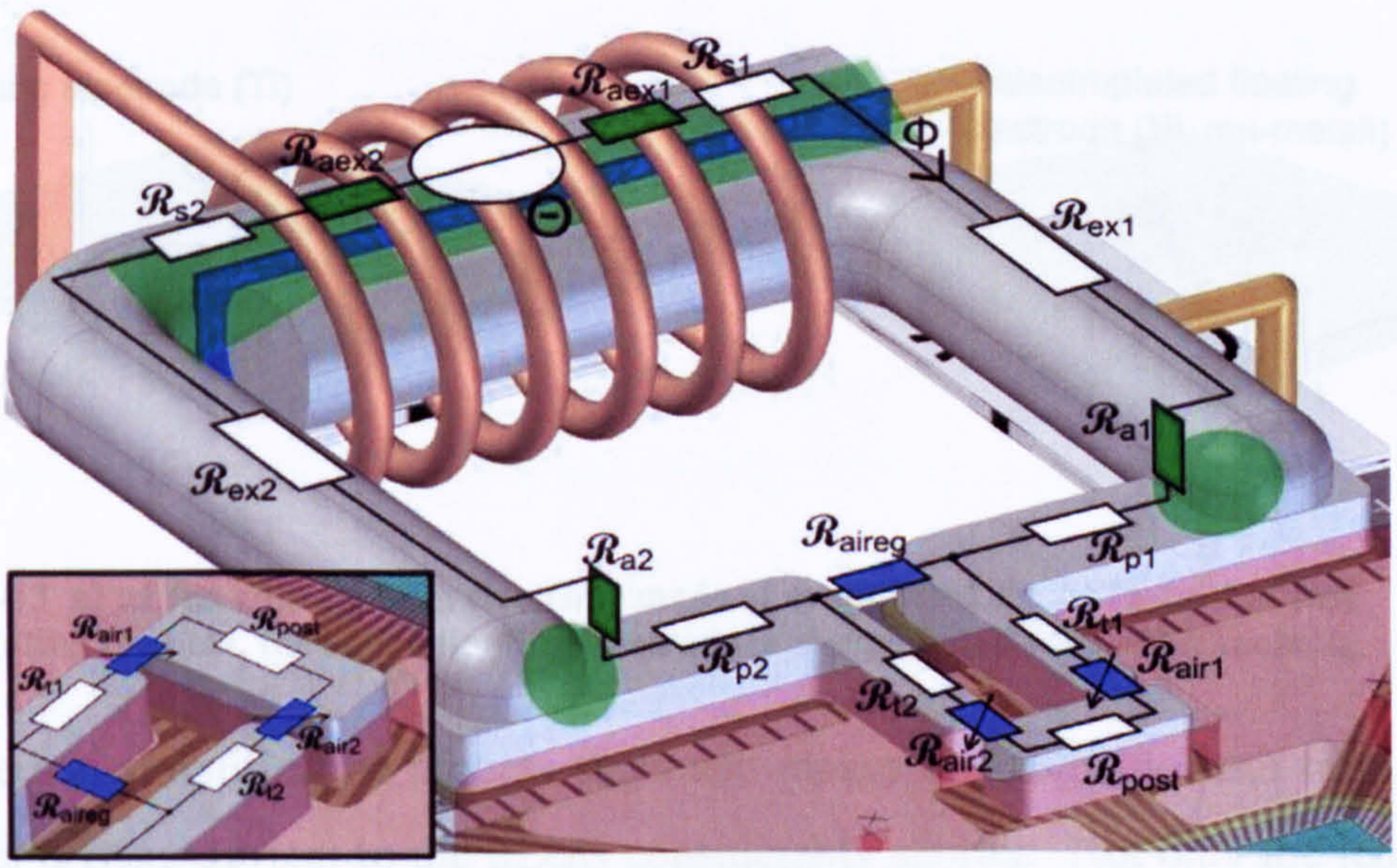

Figure 3-42 Magnetic circuit for lateral actuation with its electrically equivalent simplified schematic. On the left bottom corner is a close-up of the air gap between tracks and post.

For a magnetic material exhibiting a low magnetic hysteresis behaviour and driven within a range in which the nonlinearity of the device can be neglected, an analytical solution for the magnetic force can be obtained. The final expression of this force is given by equation (3-18). The definitions of the different parameters and the derivation of this equation is provided in Appendix C.

$$\mathbf{F}_m = \mathbf{x}\frac{1}{\mu}\cdot\left(\frac{\Theta\cdot\Re_{aireg}}{t_m\cdot w_m\cdot\left[\left(\frac{2\cdot d_m}{\mu\cdot w_m\cdot t_m}+\Re_t+\Re_{post}+\Re_{aireg}\right)\cdot\left(\Re_{aex}+\Re_s+\Re_{ex}+\Re_a+\Re_p\right)-\left(\Re_{aireg}\right)^2\right]}\right)^2 \quad (3\text{-}18)$$

3.3.4 Alternative method to ferromagnetic posts

Instead of electroplating a post onto the floating electrode as shown in Figure 3-17, the entire floating electrode can be electroplated with ferromagnetic material of thickness t_{fe}, as illustrated in Figure 3-43b. Currently, only Ni has been electroplated, but it is anticipated to electroplate material with much higher magnetic permeability such as mu-metal.

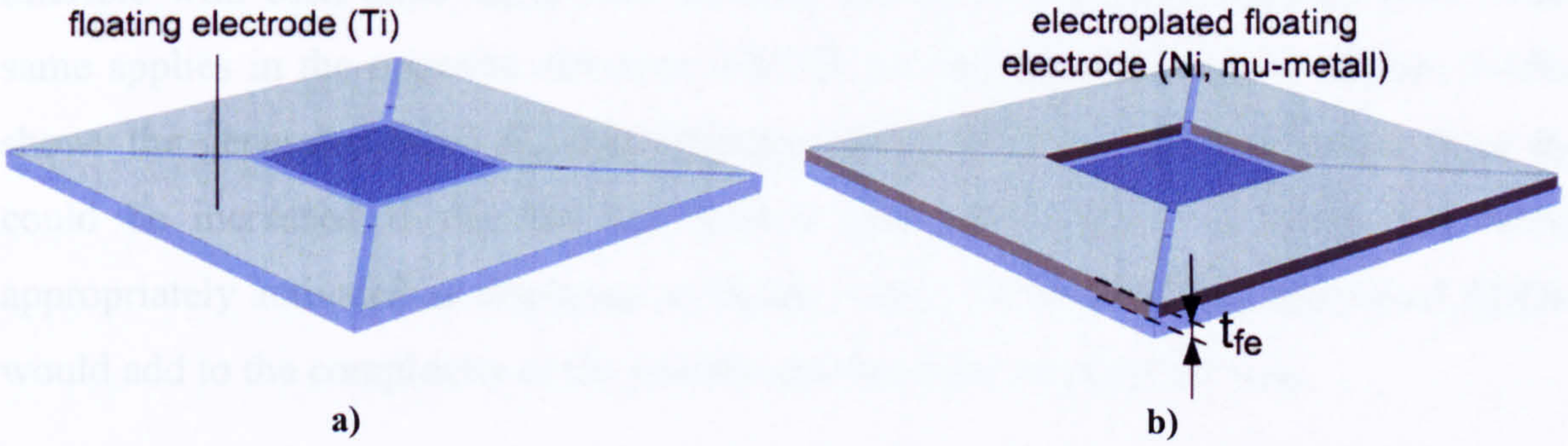

Figure 3-43 a) μLens with floating electrode made of evaporated Ti. b) Instead of just electroplating the post, the entire floating electrode is electroplated with a thickness, t_{fe}.

This method simplifies the process steps and makes the magnetic path from the EDD (external driving device) to the μLens considerably shorter. Not only the length of the magnetic path is of importance but also the reduction of the different interfaces which cause significant losses. The μLens has longer magnetically accessible sides. Figure 3-44 shows a μLens with electroplated floating electrodes surrounded by 6 EDDs. EDD 1 and 3 are placed as for the initial device, but, on the vertical sides, 2 additional EDDs are placed on each side, namely 2.1, 2.2, 4.1 and 4.2. As shown in Figure 3-44a, currents are passed through EDD 2.2 and 4.2 which cause the magnetic forces $\boldsymbol{F}_{2.2}$ and $\boldsymbol{F}_{4.2}$, which in turn generate a momentum $\boldsymbol{\theta_2}$. On the other hand, if only EDD 4.1 and 2.1 are active, the opposite momentum, $\boldsymbol{\theta_1}$, is applied to the μLens as Figure 3-44b suggests. This allows the control of the angle θ (yaw) of the μLens which is a degree of freedom that was still missing from the earlier device.

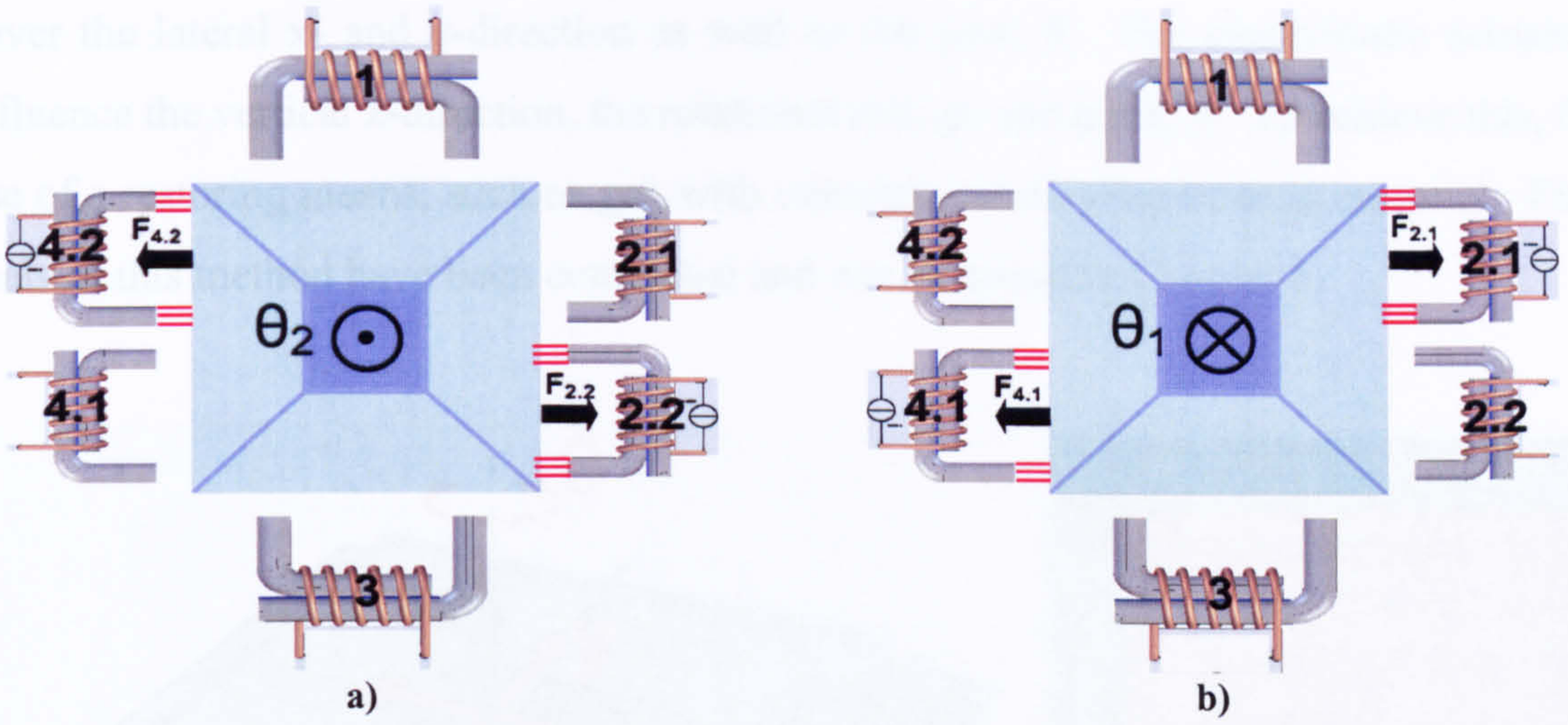

Figure 3-44 The 2 EDDs on each vertical side of the µLens allow to control the yaw of the µLens. a) If EDD 4.2 and 2.2 are active, a anticlockwise momentum θ_2 is generated. b) If EDD 4.1 and 2.1 are active, the momentum θ_1 acts in clockwise direction.

In case EDD 4.1 and 4.2 are active at the same time as shown in Figure 3-45a, a lateral movement in x-direction is possible caused by, F_x the sum of the forces $F_{4.1}$ and $F_{4.2}$. The two generated magnetic paths within the addressed floating electrode do not interfere with each other since each actuator has its own closed magnetic path. The same applies in the opposite direction if EDD 2.1 and 2.2 were active. Figure 3-45b shows the generated force F_y, that originates from EDD 1. The momentum θ_1 or θ_2 could be increased if the top and bottom side also featured 2 EDDs and were appropriately activated as displayed in Figure 3-45c. However, these additional EDDs would add to the complexity of the system and therefore increase the cost.

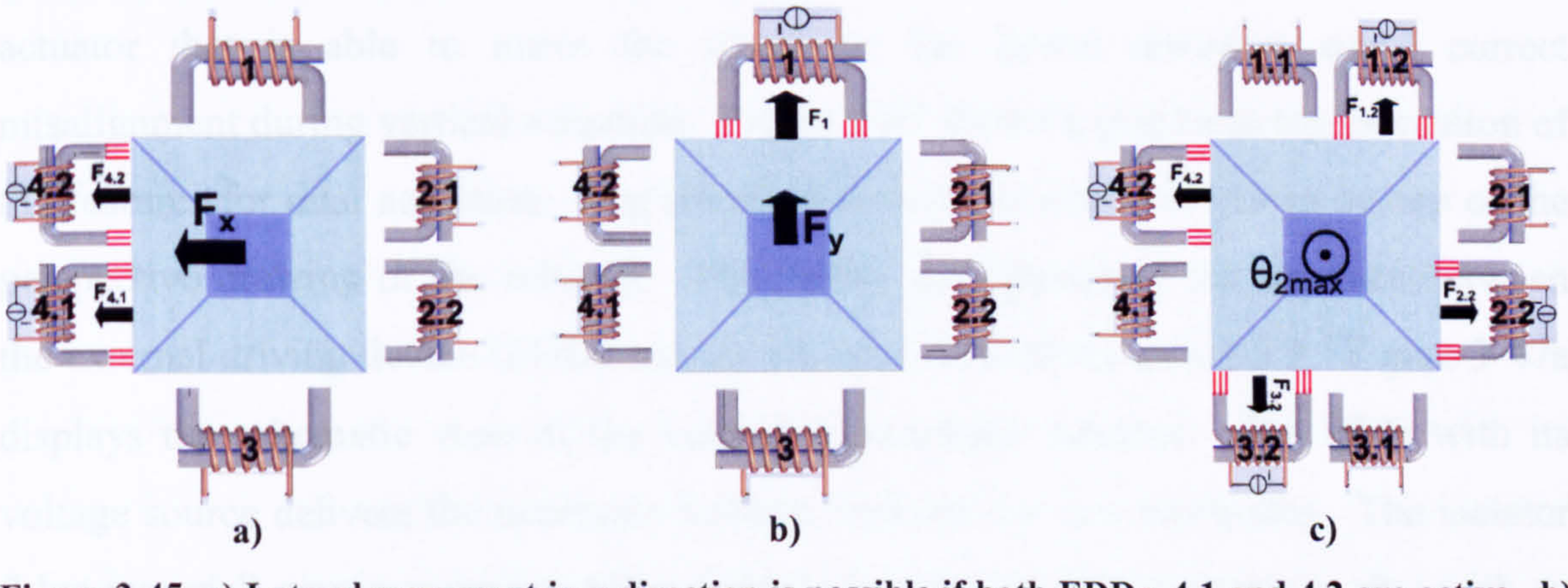

Figure 3-45 a) Lateral movement in x direction is possible if both EDDs, 4.1 and 4.2 are active. b) If only EDD 1 is active, only a lateral force F_y is generated. c) The momentum of θ_1 or θ_2 could be increased if each side features 2 EDDs at the expense of increased system complexity.

The aforementioned modification allows, within limitations concerning the amount of angle and displacement, to address all 6 degrees of freedom that exist for the µLens. Figure 3-46 gives an overview of these translational and rotational degrees that are addressed with the corresponding actuator and restoring force. The magnetic actuators

cover the lateral x- and y-direction as well as the yaw, θ. The electrostatic actuators influence the vertical z-direction, the rotational roll, φ, and pitch, β. To achieve this, the use of a restoring means, such as gel, with isotropic elastic properties is essential. First trials of this method have been conducted and can be found in Chapter 5.

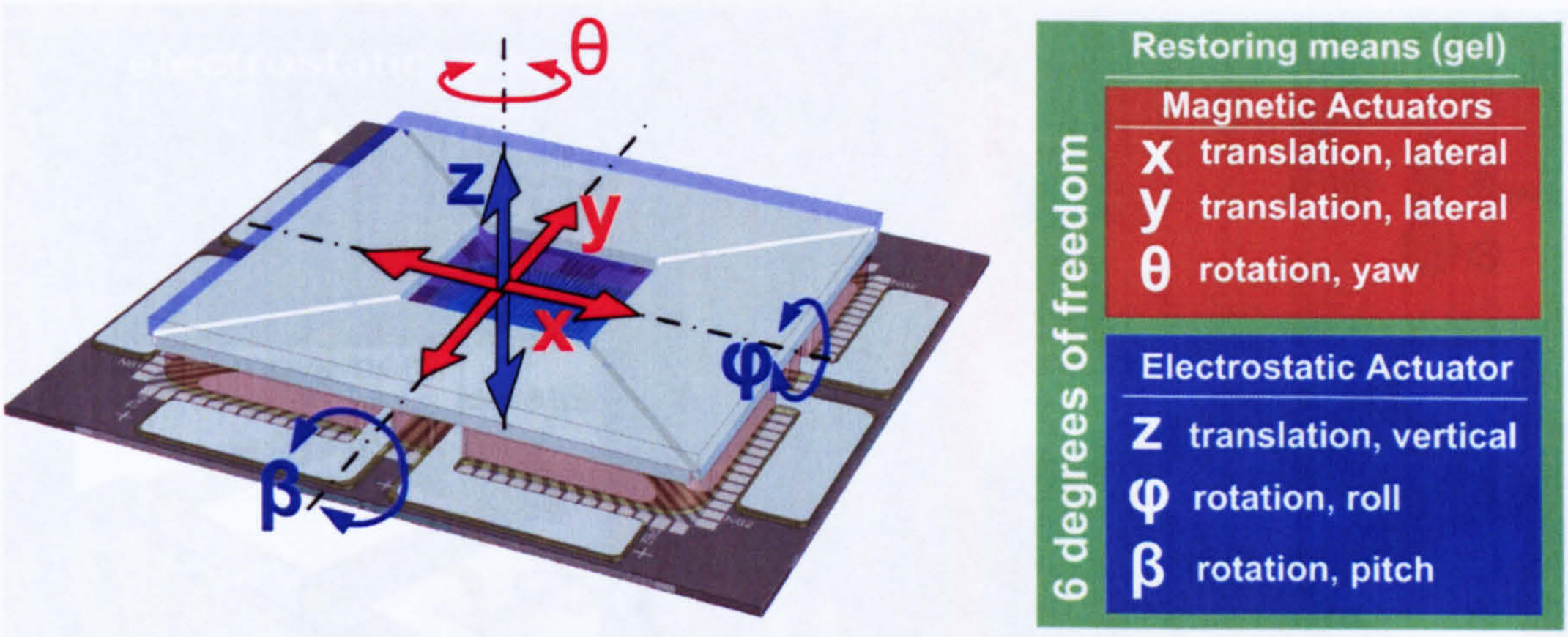

Figure 3-46 With the proposed design the yaw, θ, can be addressed, which allows to manipulate and control all 6 degrees of freedom.

3.3.5 The external driving device and dual actuation

Both electrostatic and magnetic actuators can be operated simultaneously. This is an important feature, as the guidance of the post cavity system might not be accurate enough due to fabrication inaccuracies. If the clearance is too large between the post and the cavity, the vertical movement will cause lateral shift of the µLens. Hence an actuator that is able to move the µLens in the lateral direction could correct misalignment during vertical actuation. Figure 3-47 shows a graphical representation of the features for dual actuation. The electrical equivalent circuit is drawn on top of the perspective drawing of the actuator. The yellow dots represent the interface between the external driving device (EDD) and the actuator situated on the µLED. Figure 3-47a displays the schematic view of the vertical electrostatic actuator. The EDD with its voltage source delivers the necessary voltage between the two electrodes. The isolator (blue material) serves as an electrical isolator depicted in the schematic as R_{iso} with an ideal infinite resistance. In practice, the resistor has to withstand voltages of up to 600V without causing a shortcut. Figure 3-47b depicts the magnetic circuit for the lateral movement. The blue isolator material is now represented by a magnetic resistance $\mathcal{R}_{aex}$, which should be minimum to achieve the largest magnetic resistance to achieve the most magnetic flux, Φ, for a given magneto motive force, Θ. The different magnetic

resistances of the EDD and the actuator are represented by one magnetic resistor each. Figure 3-47c shows the combination of both actuators. The magnetic and electric circuit are depicted within the schematic. The two fields coexist without influencing each other.

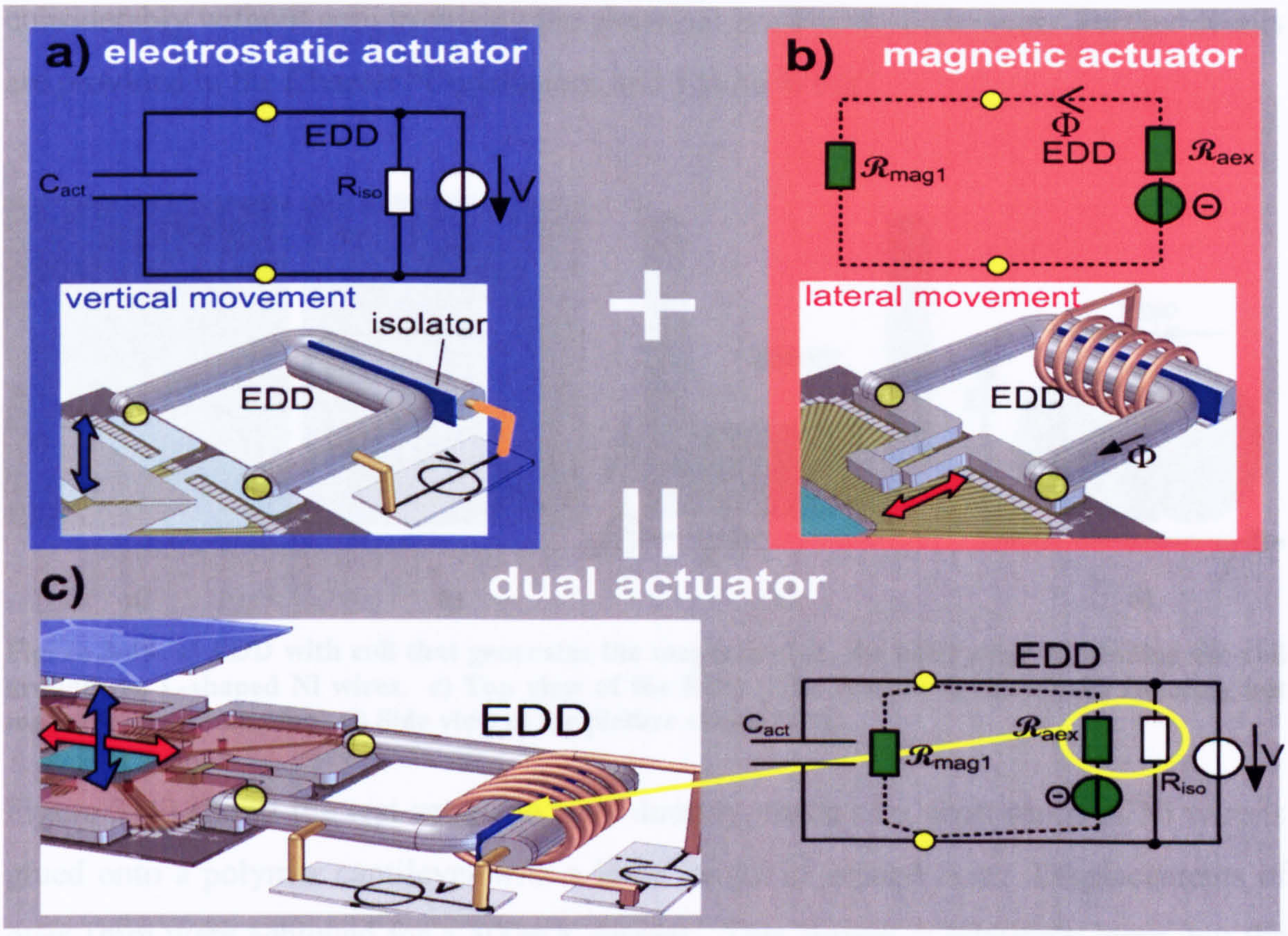

Figure 3-47 a) Electrostatic actuator with EDD. b) Magnetic actuator with EDD. c) Both actuation mechanisms constitute the dual actuator.

For the EDD isolator, a compromise had to be found between the electrical isolation and magnetic conductivity. The electrical isolator has to withstand voltages of up to 600V without causing electrical breakdown which would suggest that the thickness of the isolator should be as large as possible. This however would result in a bigger air gap for the magnetic system. Figure 3-48 shows a prototype of a working EDD. In Figure 3-48a, the two big L-shaped metal wires are made of Ni and the small ones consists of superpermalloy with diameters of 1mm and 0.5mm, respectively. Superpermalloy exhibits a large magnetic permeability with a relative small hysteresis. The combination between these different shapes replicates the real situation of the magnetic path found in the subsequent device (Figure 3-48b). Figure 3-48c shows a drawing of the device from the top view. The L-shape is used to have maximal contact area for the magnetic flux to pass from one magnetic wire to the other. Figure 3-48d shows a side

view where the surface of the ferromagnetic wire is flattened. d_{gap} is a key dimension of the assembly. If it is too small, electrical breakdown will occur, and therefore hinder the electrostatic actuation. If it is too large, the resistance of the magnetic path will be too high thereby demanding a large amount of current to pass a flux that is able to cause any movement. If an appropriate dielectric is used, the gap distance can be decreased considerably without compromising the electrical breakdown behaviour. Further details are provided in the Chapter "Conclusions and Future Work".

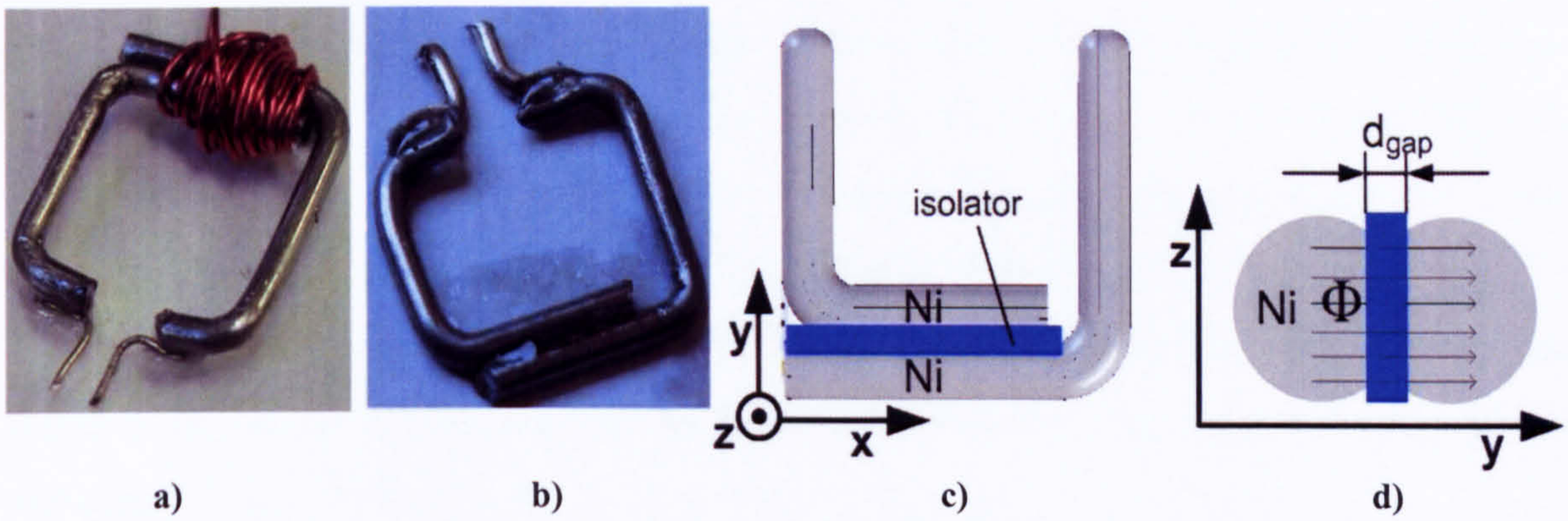

a) b) c) d)

Figure 3-48 a) EDD with coil that generates the magnetic flux. b) EDD prior of winding the coil around the L-shaped Ni wires. c) Top view of the EDD. The isolator is electrically isolating but magnetically conducting. d) Side view of the picture shown in c).

Figure 3-49 shows the test setup. A post dummy, made of a short piece of Ni wire is glued onto a polymer cantilever with a lever length of around 5cm. Displacements of over 1mm were achieved for a 300mA current. This current is relatively large, but the initial distance between the ends of the tracks with respect to the post is far more than in the real device.

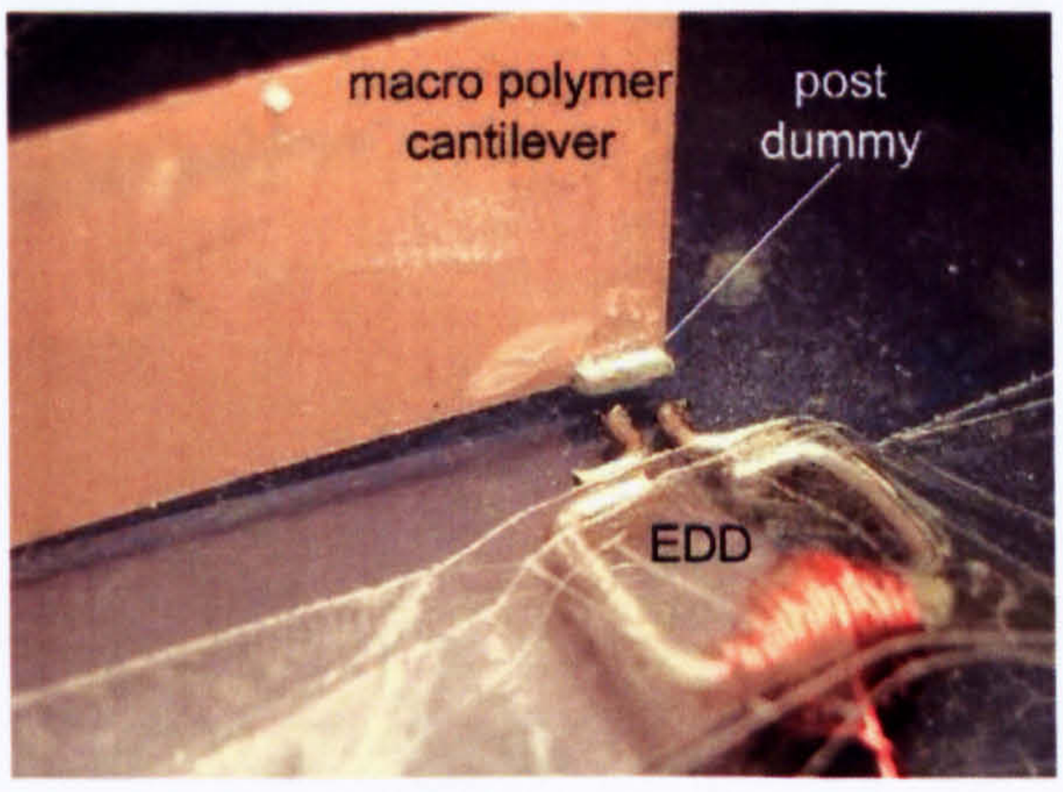

Figure 3-49 Experiment where one of the first external driving device is tested for the magnetic attraction of the dummy post that is attached to a polymer cantilever.

After the magnetic movement had been successfully tested, the EDD was then taken and connected to a high voltage source. It was able to withstand voltages of over 600V without causing any breakdown.

Chapter 4

Manufacture

4.1 Manufacturing of the micro-UV-LED array package structure (µLED)

The fabrication process of the structure on top of the µLED is performed with a modified UV-LIGA process. "LIGA" stands for the German words "**Li**thography, **G**alvanoformung, **A**bformung" which can be translated as "lithography, electroplating, injection-moulding". LIGA is usually performed using a very expensive synchrotron apparatus which creates highly collimated X-rays that are used for exposing X-ray sensitive polymers. In our case, Ultra Violet light is used which is not as accurate as X-rays but is a far cheaper alternative. The attribute "modified" means that not only the electroplated metal is used, but also the UV-sensitive photo resist for the build up of the structure.

This chapter focuses on the processes as well as the materials involved in the manufacture of the structures such as those shown in Figure 4-1a and Figure 4-1b. This structure, one of the many possible variations that have been created for magnetic and electrostatic actuation, has been chosen as it encompasses the largest number of the manufacturing steps used. The function of a particular layer is only briefly mentioned as detailed design information has been provided in Chapter 3. The exact process parameters at each process step are reported in details in Appendix E where a "cleanroom ready" process checklist is presented.

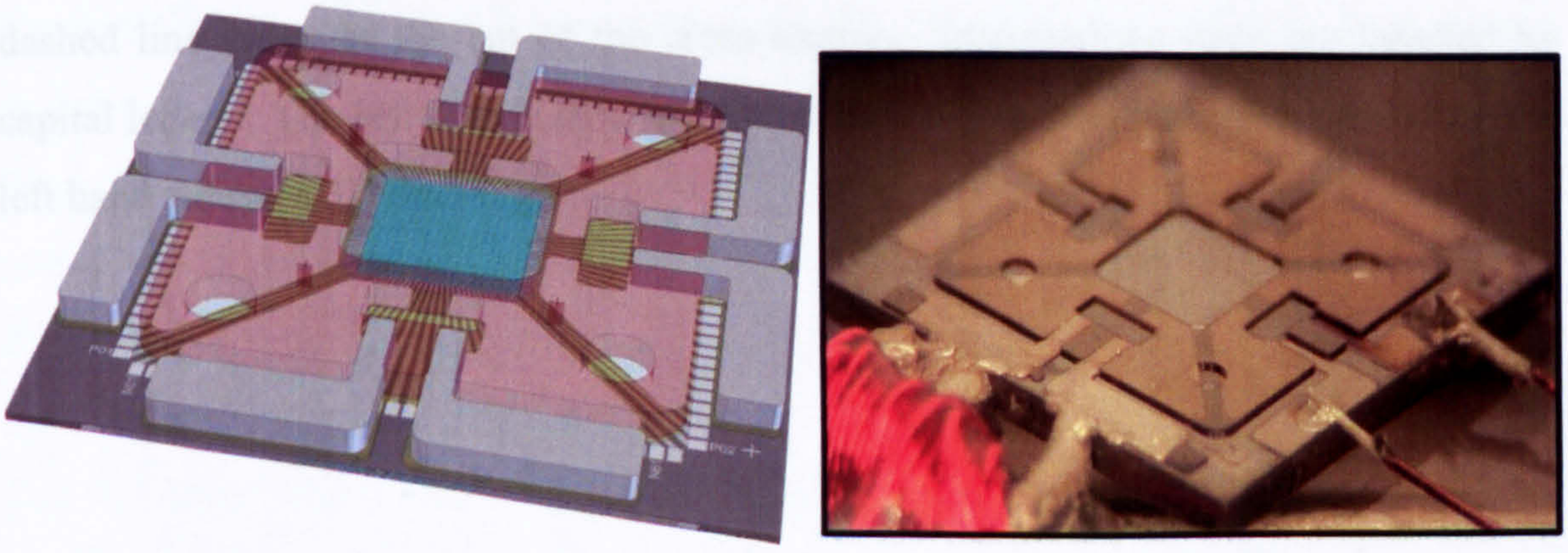

a) b)

Figure 4-1 a) Drawing of a µLED with magnetic and electrostatic actuators. b) Photograph of the resulting µLED device.

Figure 4-2 presents an exploded view of all existing layers with some photographs of the actual device after deposition of specific layers.

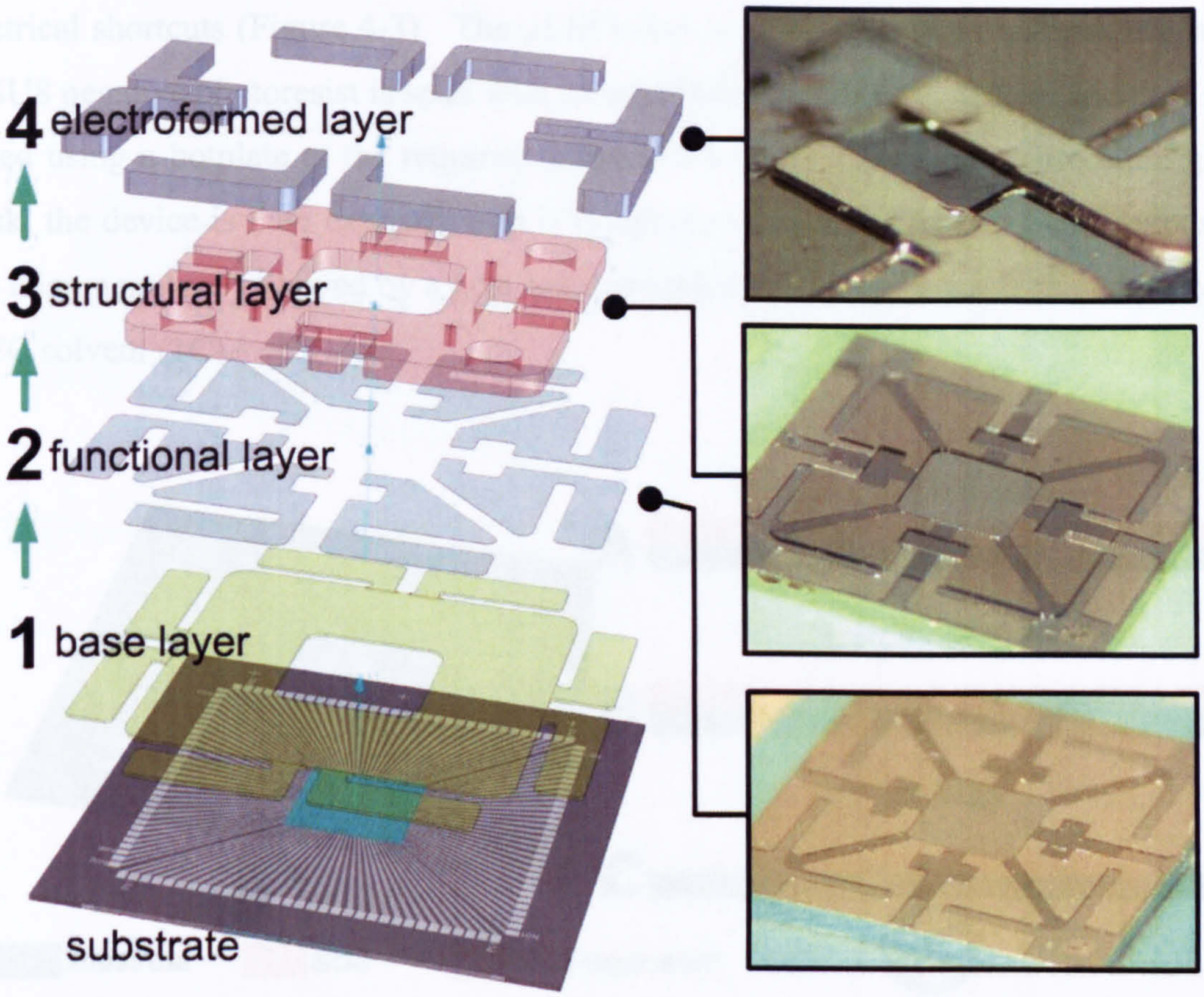

Figure 4-2 Exploded view of the μLED.

The individual process steps are presented from Figure 4-3 to Figure 4-7. On the left-hand side of each picture is featured the number of the corresponding steps shown in Figure 4-2. The layer by layer build up seen on the right hand side of the picture is explained at the bottom of each picture. The blue arrow on the left hand side in Figure 4-3 shows the direction of the cross-section presented on the right hand side. The dashed line indicates the cut of the cross-section. Intermediate steps are labelled by capital letters. The last step is labelled with a bold capital letter and represented on the left hand side as a 3D drawing.

Step 1: base layer

In the first step, the base layer protects the underlying electrical connection pads from electrical shortcuts (Figure 4-3). The μLED-chip is glued on a glass wafer and a layer of SU8 negative photoresist is spun with an approximate thickness of 5μm and then soft baked using a hotplate at the required temperatures (**1**A). Through a chromium glass mask, the device is then exposed with UV-light by using the TAMARACK® exposure and alignment tool followed by a post bake process (**1**B). The device is then developed in EC solvent (**1C**).

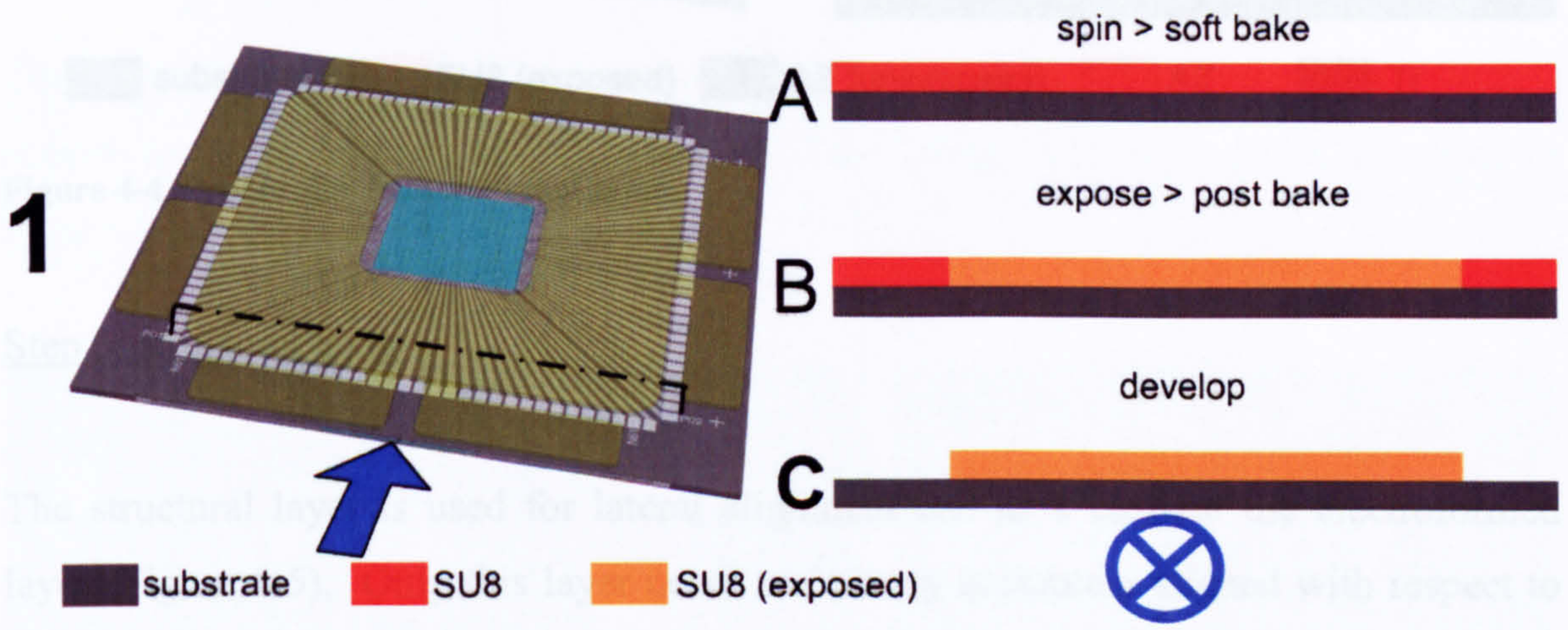

Figure 4-3 Process for base layer. The blue arrow on the left hand side shows the direction at which the cross section on the right hand side is viewed. The dashed line indicates the cut of the cross- section.

Step 2: functional layer

The second step builds the functional layer, which is used as electrodes for the electrostatic actuator as well as a seed layer for the electroformed layer (Figure 4-4). A layer of AZ 9260® positive photo resist (AZ) is spun at a thickness of approximately 8μm, followed by a bake on the hotplate. The device is then removed from the hotplate and left for re-hydration for more than 1 hour. The device is then exposed (**2**A). After developing the exposed structures with AZ-developer the device is placed into the e-beam evaporator, where a thin layer of around 200nm of titanium (Ti) is deposited (**2**B). The AZ layer which has, during the evaporation process, served as a mask, is now removed by immersing the device in acetone followed by rinsing with IPA. A more

gentle method is to immerse either in EC-solvent or IPA, but more time is necessary for the process (**2C**).

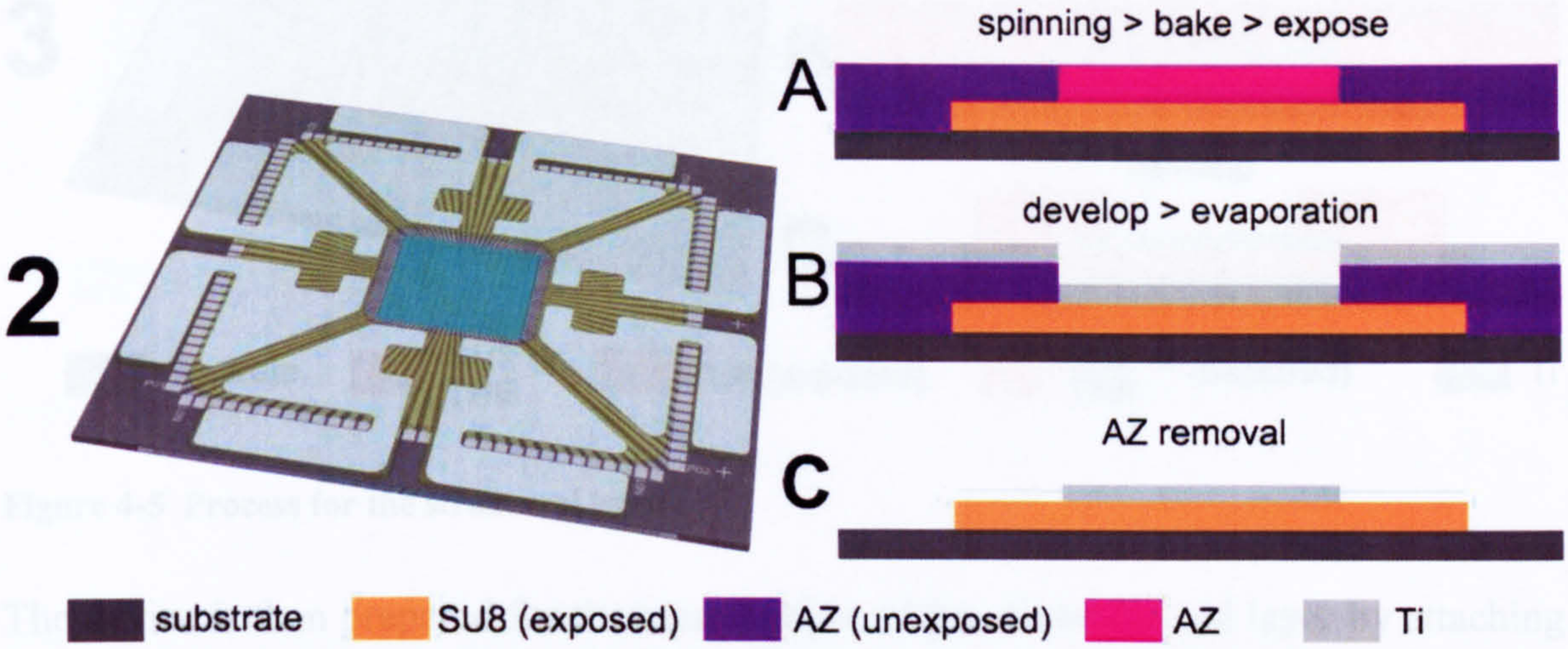

Figure 4-4 Process for the functional layer.

Step 3: structural layer

The structural layer is used for lateral alignment and as a cast for the electroformed layer (Figure 4-5). Only this layer needs to be very accurately aligned with respect to the alignment marks of the μLED-chip. Initially SU8 was solely used for this structure. However, delamination occurred frequently in particular during the subsequent electroplating process. The negative photoresist THB 151N from JSR was chosen instead which exhibits better adhesion. The process steps are similar with the exception that no post bake is required for THB in **3**B. A layer of negative photo resist (SU8 or THB) is spun onto the device and soft baked afterwards using a hotplate (**3**A). The device was then exposed and in case SU8 is used, post baked (**3**B). Thereafter, the photo resist is developed (**3C**).

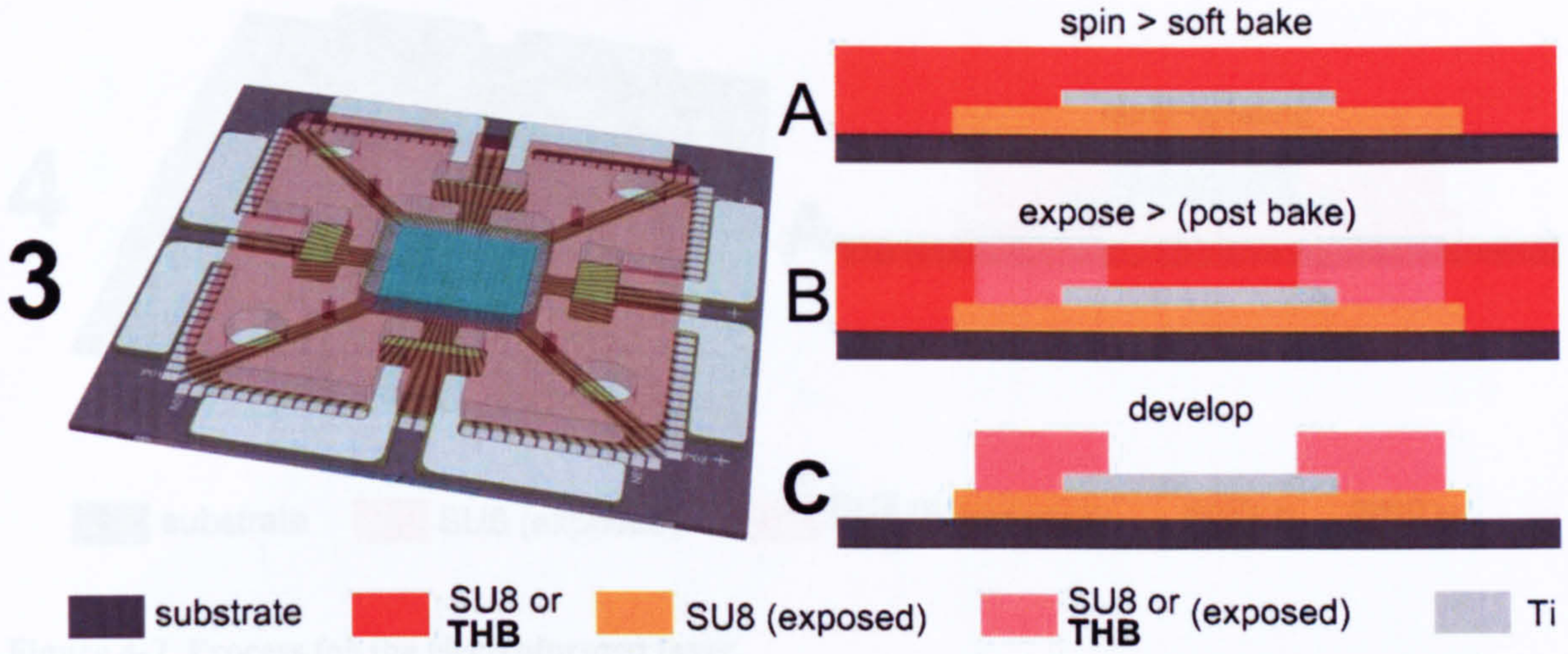

Figure 4-5 Process for the structural layer.

The device is then prepared for the manufacture of the electroformed layer by attaching copper wires to the pads of the functional layer using conductive paint as shown in Figure 4-6.

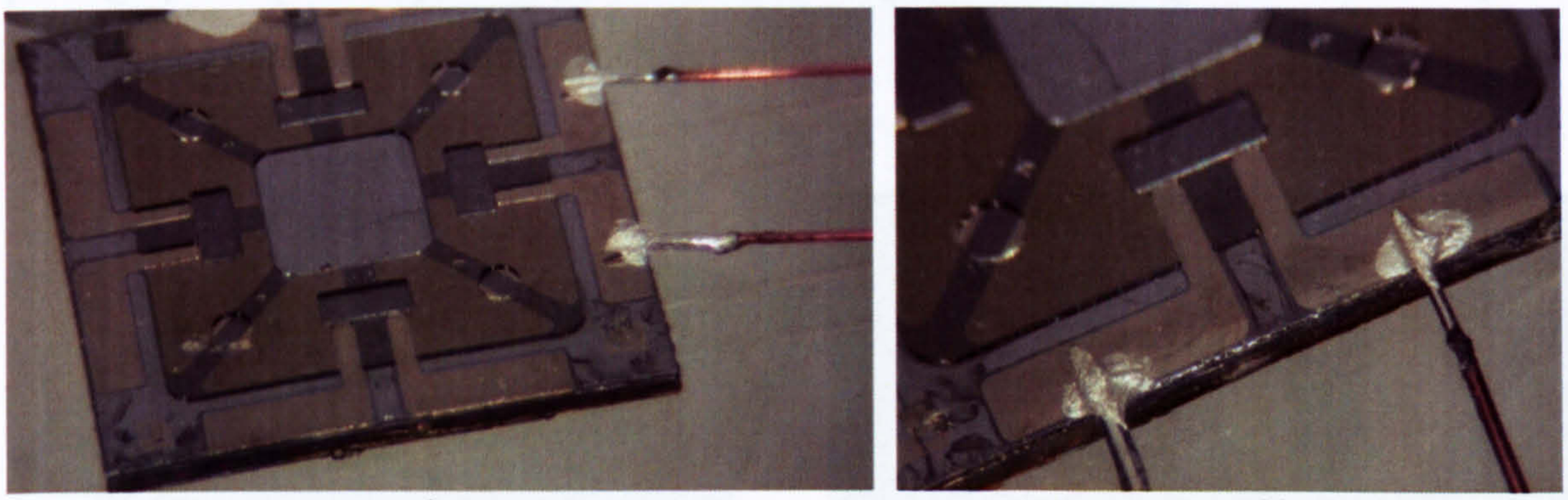

a) **b)**

Figure 4-6 a) A pair of electrodes is connected via its pads with the copper wire using conductive paint for the subsequent electroforming process. b) Close-up of a).

Step 4: electroformed layer

The electroformed layer serves for accurate vertical height adjustment or as part of the magnetic path for the magnetic actuator (Figure 4-7). After having connected the copper wires that provide the current for the electroplating process, the device is immersed into an electroplating bath. An auxiliary electrode which has a much bigger area is also plated and keeps the current density as constant as possible (**4A**).

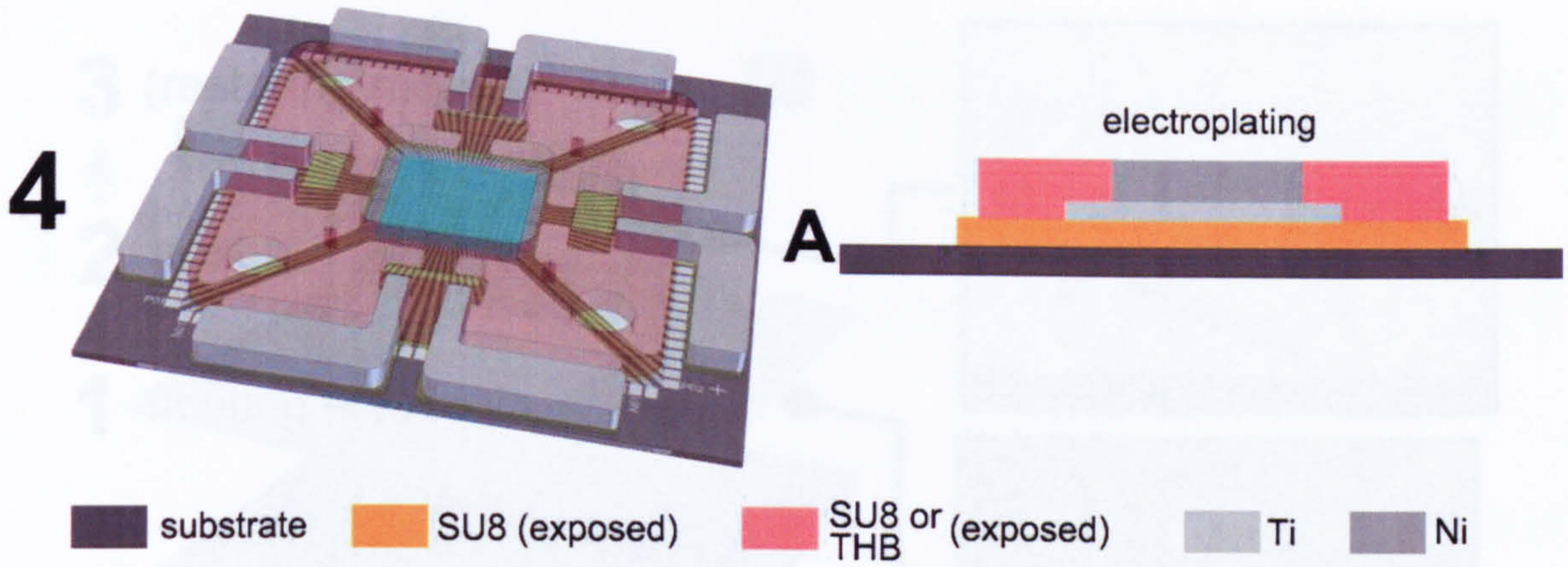

Figure 4-7 Process for the electroformed layer.

4.2 Manufacture of supporting posts on the substrate of the microlens

For the manufacture of the μLens, the same modified UV-LIGA process is applied as for manufacturing the μLED. Figure 4-8a and Figure 4-8b show the drawing and photograph respectively, of a μLens with its trapezoidal floating electrodes and posts made of ferromagnetic material such as nickel.

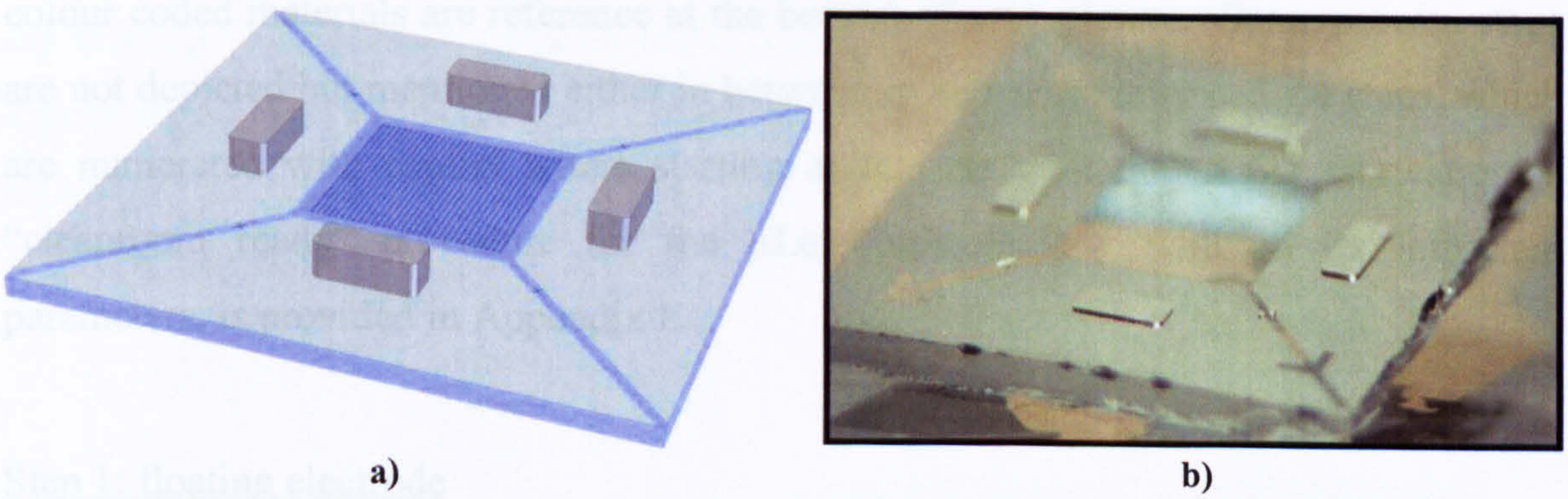

a) b)

Figure 4-8 a) Drawing of a μLens with floating electrodes and ferromagnetic posts for the magnetic actuator. b) Photograph of the μLens.

Figure 4-9 shows the exploded view of a μLens with each production step involved. The production starts at step 1 with the floating electrode and ends at step 3 with the restoring means. On the right hand side is a picture that represents step 2 and above is a SEM picture that presents a part of a single post.

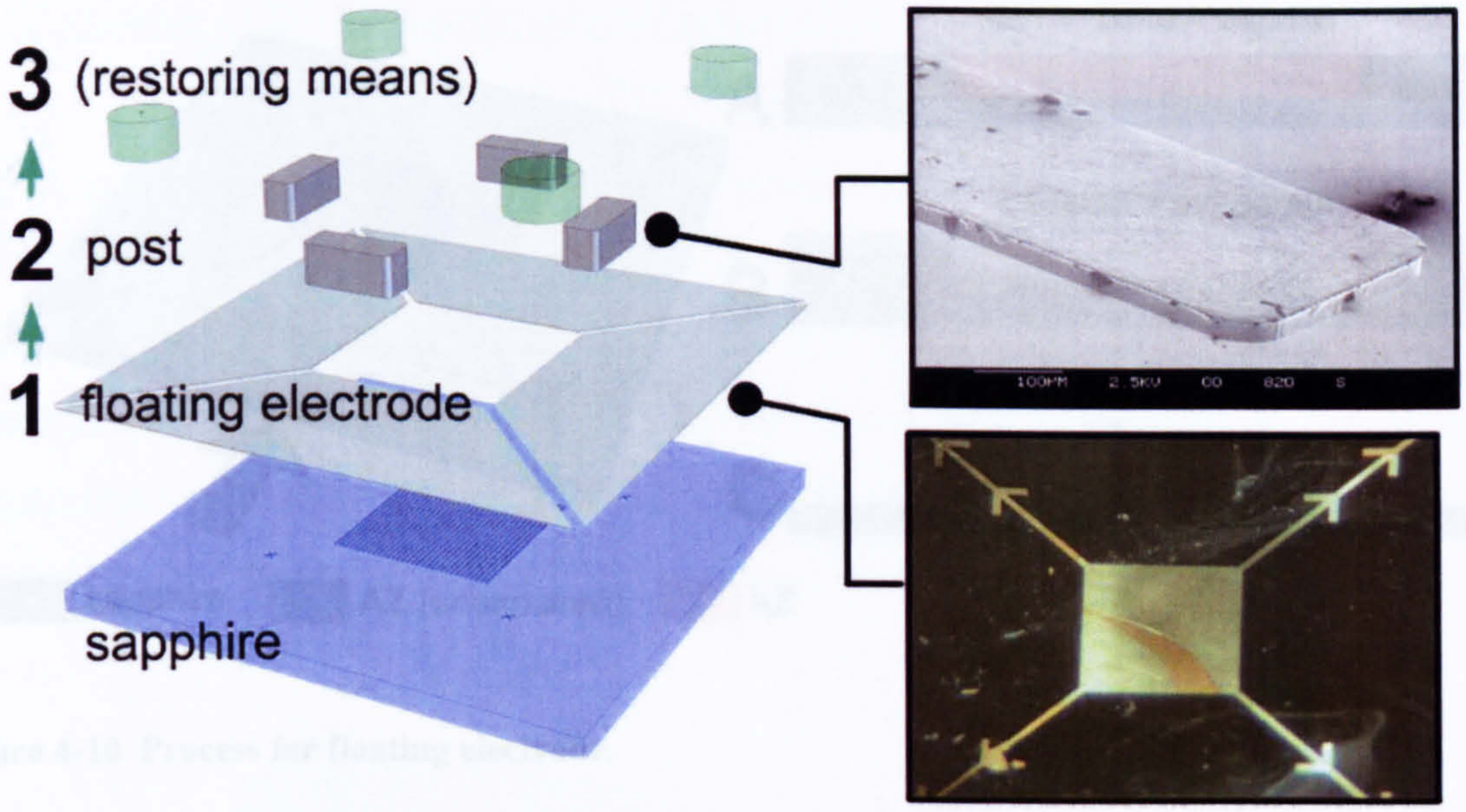

Figure 4-9 Exploded view of the µLens including the restoring means. The right hand side depicts a photograph of step 1 and a SEM picture of a post from step 2.

Figure 4-10 to Figure 4-13 show the three different steps that are needed to manufacture the device seen in Figure 4-9. Two components can be manufactured in step 2: the ferromagnetic posts or the SU8 posts. Each of the pictures contains on the left hand side a 3-D representation of the last intermediate step shown on the right hand side. The colour coded materials are reference at the bottom of each picture. Some process steps are not depicted but mentioned either in between or above the intermediate steps, which are numerated with capital letters starting at A. As with the µLED fabrication, a "cleanroom ready" procedure for the µLens manufacture, with all its important parameters, is provided in Appendix E.

Step 1: floating electrode

The floating electrodes are the counterparts of the electrodes that lie on the µLED. Together they make up the electrostatic actuator. These layers are also used as a seed layer and adhesion promoter for either the metal or SU8 posts (Figure 4-10). A layer of AZ 9260® (AZ) is spun with a thickness of around 7µm, which is then baked at 110°C. After resting for more than one hour (re-hydration of the polymer) the device is then exposed (**1**A), developed using AZ-developer, dried and placed within the e-beam evaporator (PVD) to deposit a thin layer of Titanium (Ti) (**1**B). Thereafter, the device is immersed into acetone to remove the AZ that served as an evaporation mask before (**1C**).

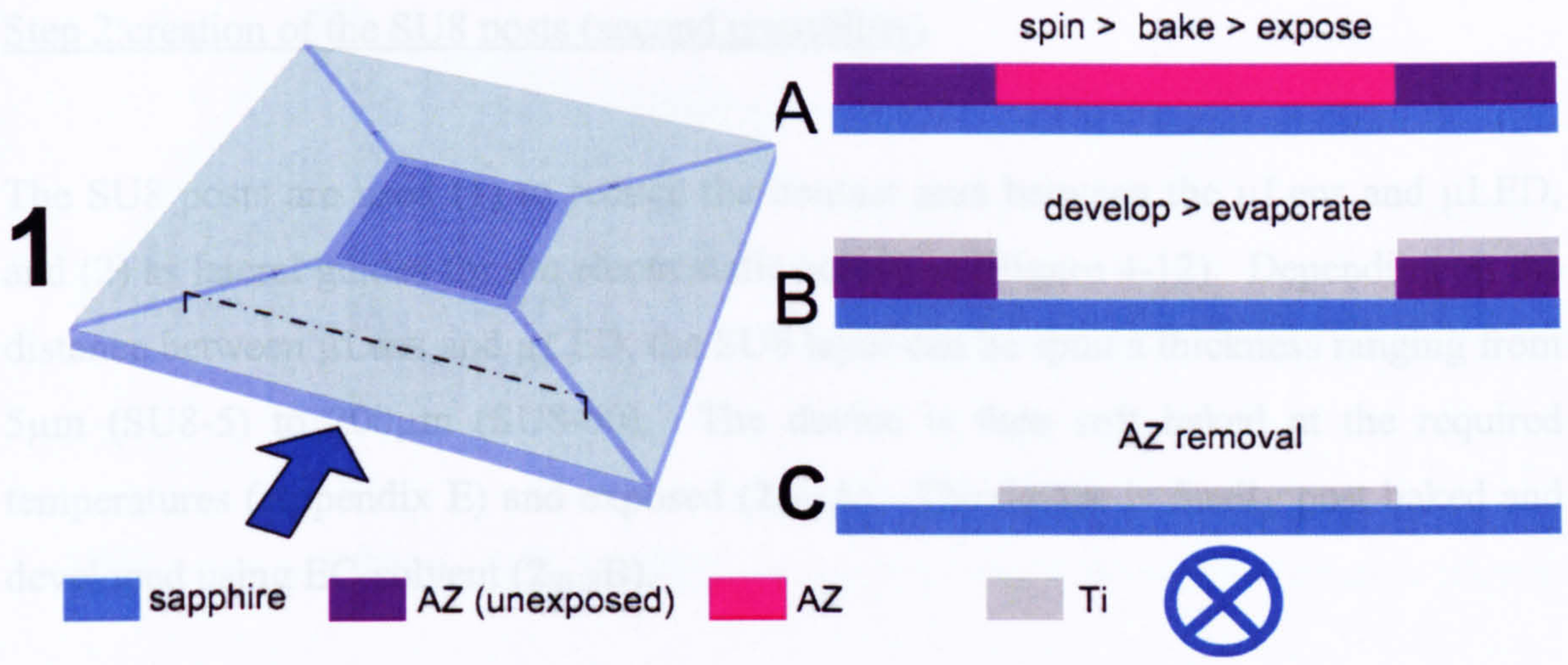

Figure 4-10 Process for floating electrode.

Step 2: creation of the ferromagnetic posts (first possibility)

The ferromagnetic post together with the magnetic tracks on the electroformed layer of the μLED, form the lateral magnetic actuator (Figure 4-11). A layer of around 30μm of AZ is spun onto the device. The device is then baked at 110°C and subsequently exposed (**2**A). The assembly is then developed in AZ developer. Wires are attached to the floating electrodes for preparation to the electroplating process. The device is then immersed into the nickel (Ni) electroplating bath and electroplated (**2**B). The device is finally immersed in acetone to remove the AZ which has served as a mould for the electroplating (**2C**).

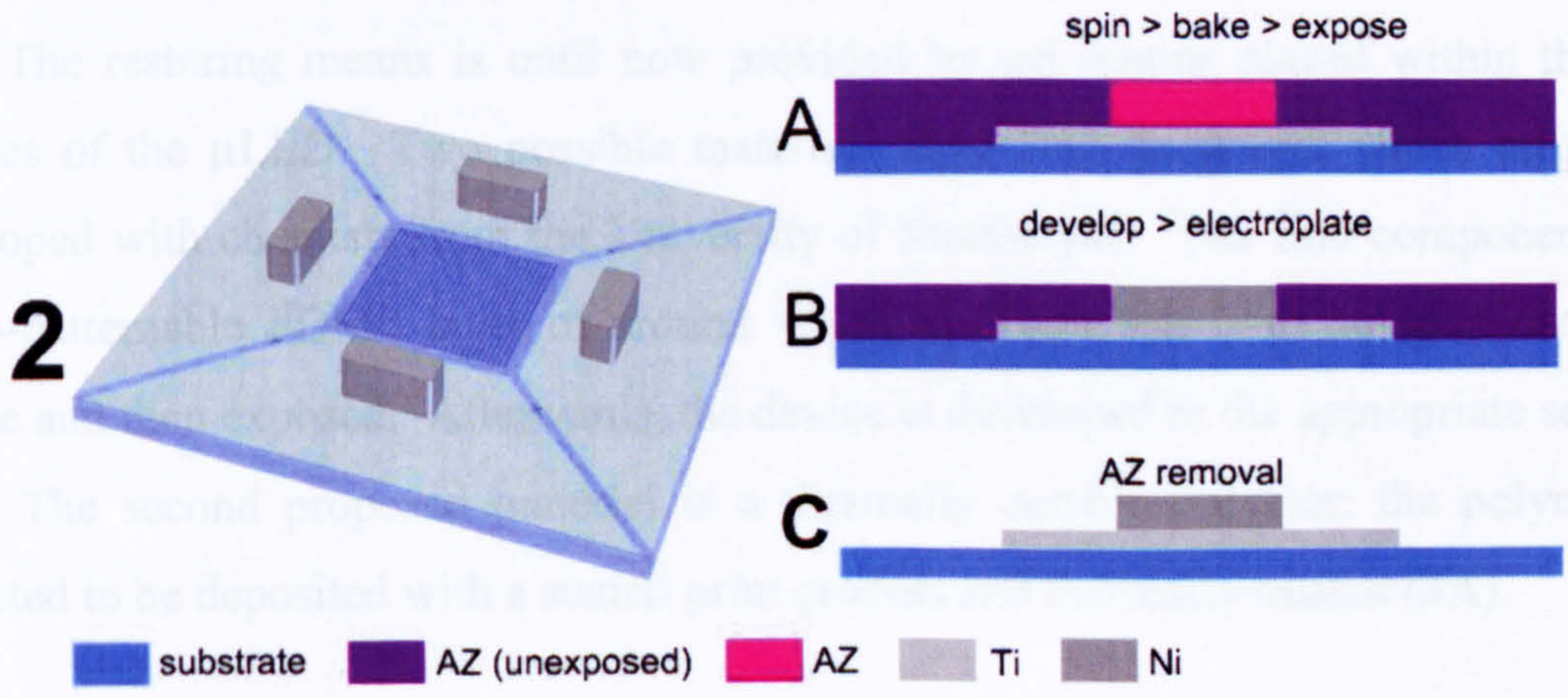

Figure 4-11 Process for post (ferromagnetic).

Step 2:creation of the SU8 posts (second possibility)

The SU8 posts are used (1) to reduce the contact area between the μLens and μLED, and (2) as lateral guides for the electrostatic actuation (Figure 4-12). Depending on the distance between μLens and μLED, the SU8 layer can be spun a thickness ranging from 5μm (SU8-5) to 200μm (SU8-50). The device is then soft baked at the required temperatures (Appendix E) and exposed ($\mathbf{2}_{SU8}$A). The device is finally post baked and developed using EC-solvent ($\mathbf{2}_{SU8}\mathbf{B}$).

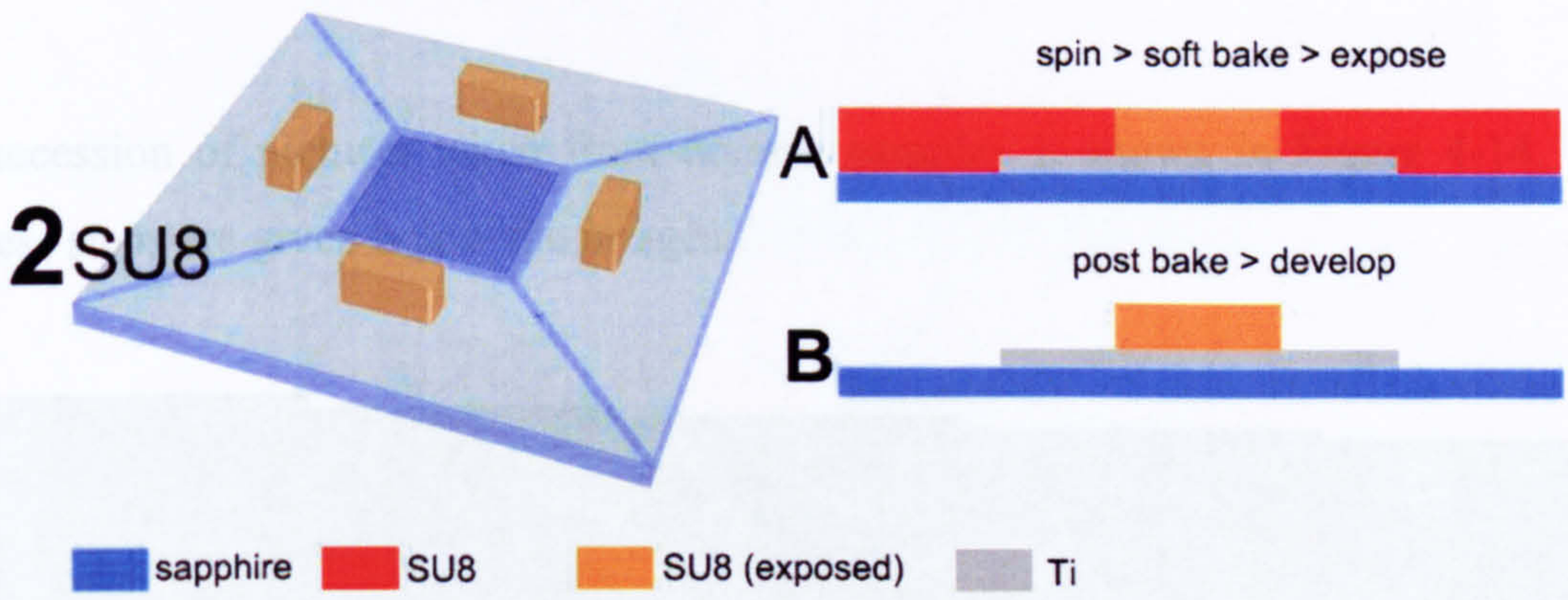

Figure 4-12 Process for post (SU8).

Step 3: (restoring means)

The restoring means is supposed to provide restoring capabilities in the vertical and lateral directions. This step is mentioned in brackets since it has not yet been carried out. The restoring means is until now provided by gel bumps placed within the gel cavities of the μLED. Two possible materials have been proposed, which might be developed with chemists from the University of Strathclyde. The first component is a photo-patternable PDMS layer of around 40μm to 60μm that is to be spun onto the device and then exposed. Afterwards, the device is developed in the appropriate solvent (**3A**). The second proposed material is a thermally curable polymer: the polymer is expected to be deposited with a stencil print process and thermally treated (**3A**).

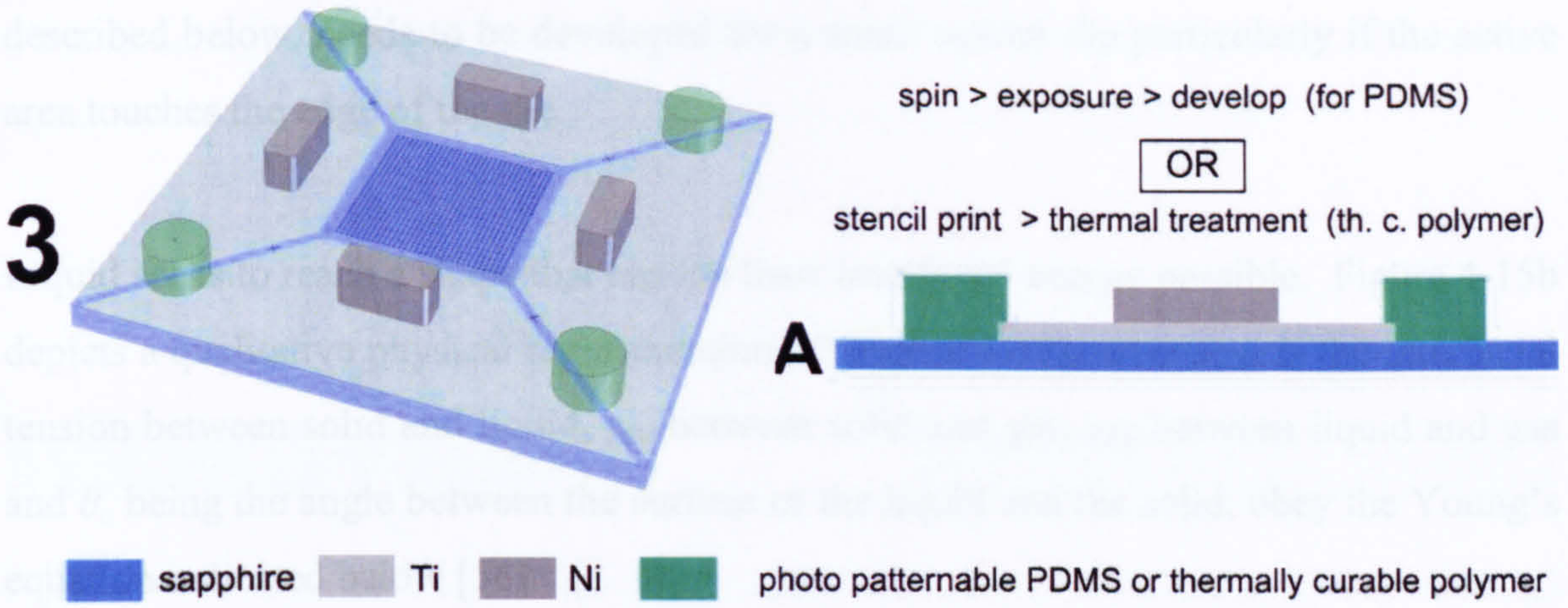

Figure 4-13 Process for restoring means.

A succession of pictures taken from diverse samples is shown in Figure 4-14. The process steps are given below the images.

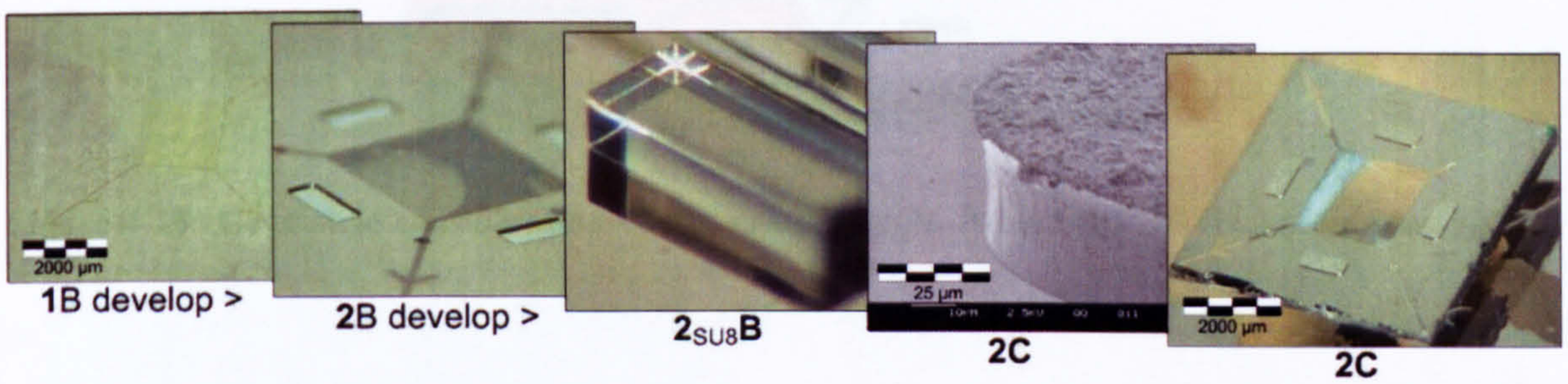

Figure 4-14 Photographs taken during the manufacturing process. The respective step is labelled beneath the photograph.

4.3 Handling of die with small dimensions

Both µLED and µLens arrays have been sent to MISEC, singulated, with no post-processing carried out prior to packaging. In addition, the active area of each device is close to the physical dimension of the die. The whole fabrication process of the packaging, i.e. the manufacturing of functional, structural layers, posts, etc., is thus rendered more complicated by the small dimensions of the die. Solutions to overcome these packaging issues are described in this section.

One of the most important manufacturing difficulties is to obtain a uniform thickness of the resist across a small die once the resist has been spun. The different material surface energies involved create the well known bead effect at the edge of the die. Whilst the situation can be remedied on a wafer scale through various methods, a new solution,

described below, needs to be developed for a small square die particularly if the active area touches the edge of the die.

Liquid seeks to reach a shape that has the least interfacial energy possible. Figure 4-15b depicts a qualitative physical representation of Figure 4-15a, where γ_{SL} is the interfacial tension between solid and liquid, γ_{SG} between solid and gas, γ_{LG} between liquid and gas and θ_c being the angle between the surface of the liquid and the solid, obey the Young's equation indicated below [56].

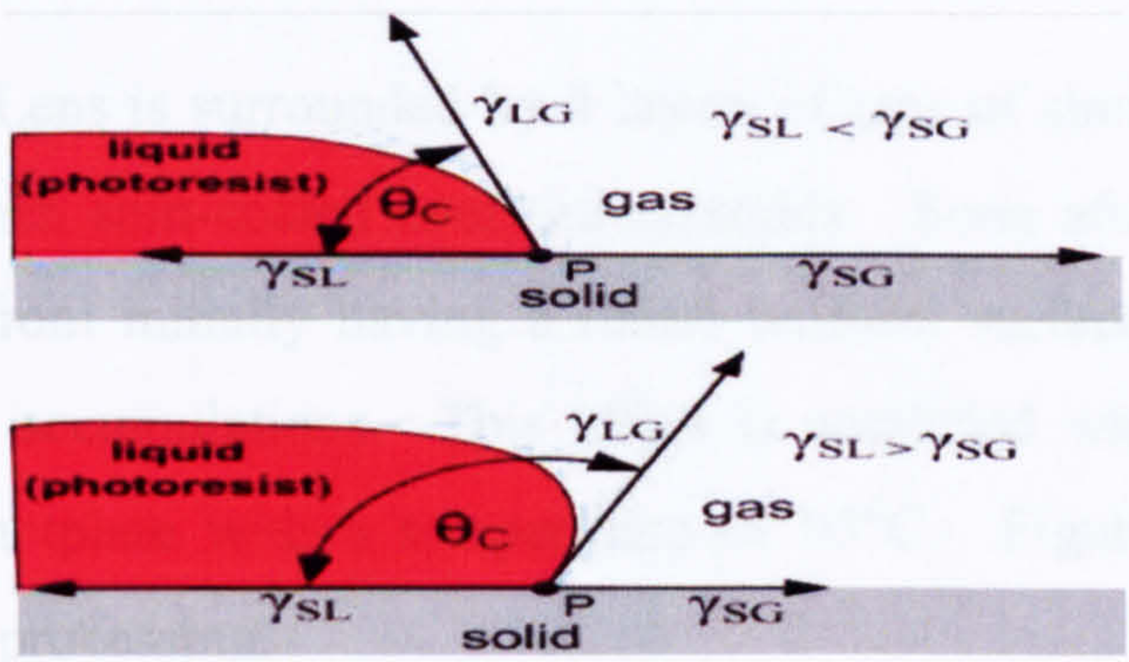

Figure 4-15 Geometric consideration of the contact angle, θ_c and the interfacial tensions γ_{SL}, γ_{LG} and γ_{SG}.

$$\cos(\theta_c) = \frac{\gamma_{SG} - \gamma_{SL}}{\gamma_{LG}} \tag{4-1}$$

If the interfacial tension between solid and liquid (γ_{SL}) is smaller than the interfacial tension between solid and gas, as shown in Figure 4-15b top, equation (4-1) yields a contact angle (θ_c) which is smaller than 90°; the liquid is wetting the solid. If γ_{SL} is bigger than γ_{SG}, the angle becomes bigger than 90°, therefore the liquid has as little surface in common with the solid as possible. The different interfacial tensions must comply with the thermodynamic equilibrium, therefore γ_{SG} - γ_{SL} - γ_{LG} can never become negative. Furthermore, the term on the right-hand side of equation (4-1), cannot be less than 1 [56].

Let us consider two geometrically similar solids, placed side by side, covered by a liquid of volume, V_L, as shown in Figure 4-16a and Figure 4-16b. If $\gamma_{SL1} > \gamma_{SL2}$ (Figure 4-16) more photoresist accumulates above solid2 than above solid1, resulting in a thicker layer of resist over solid 2. In Figure 4-16b no relocation of the liquid takes

place since both solids have the same interfacial surface tension. Since the volumes are equal, the height t_{mean} in Figure 4-16a is equal to t_L seen in Figure 4-16b.

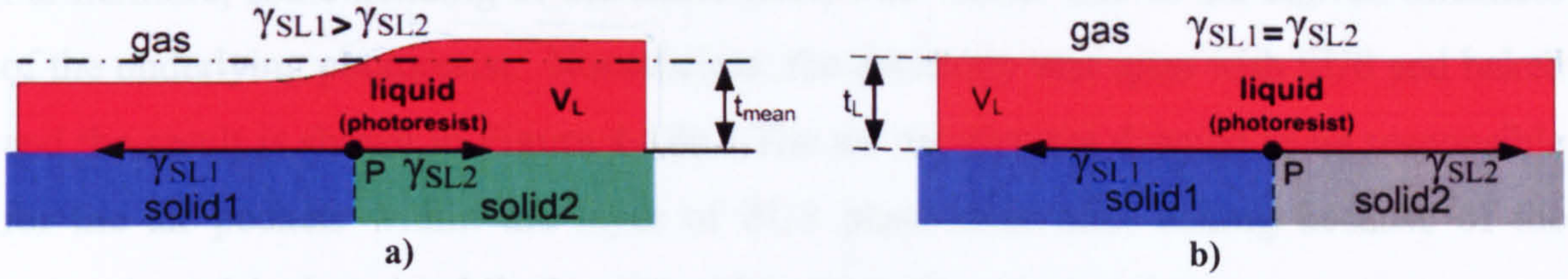

Figure 4-16 a) solid1 has a bigger interfacial tension between itself and the liquid (photoresist) than solid2. b) The interfacial tension of solid1 is identical with solid2, there is no height disruption caused.

In Figure 4-17a the μLens is surrounded by 4 layers of tape of similar thickness as for the μLens. SU8 is then spin-coated over the assembly. Soon after the spinning, the photoresist changed from initially having a rather uniform surface towards a surface with depressions and accumulations. This effect is amplified when the assembly is placed on top of a hotplate with a temperature of 95°C. Figure 4-17b shows the resulting system after processing.

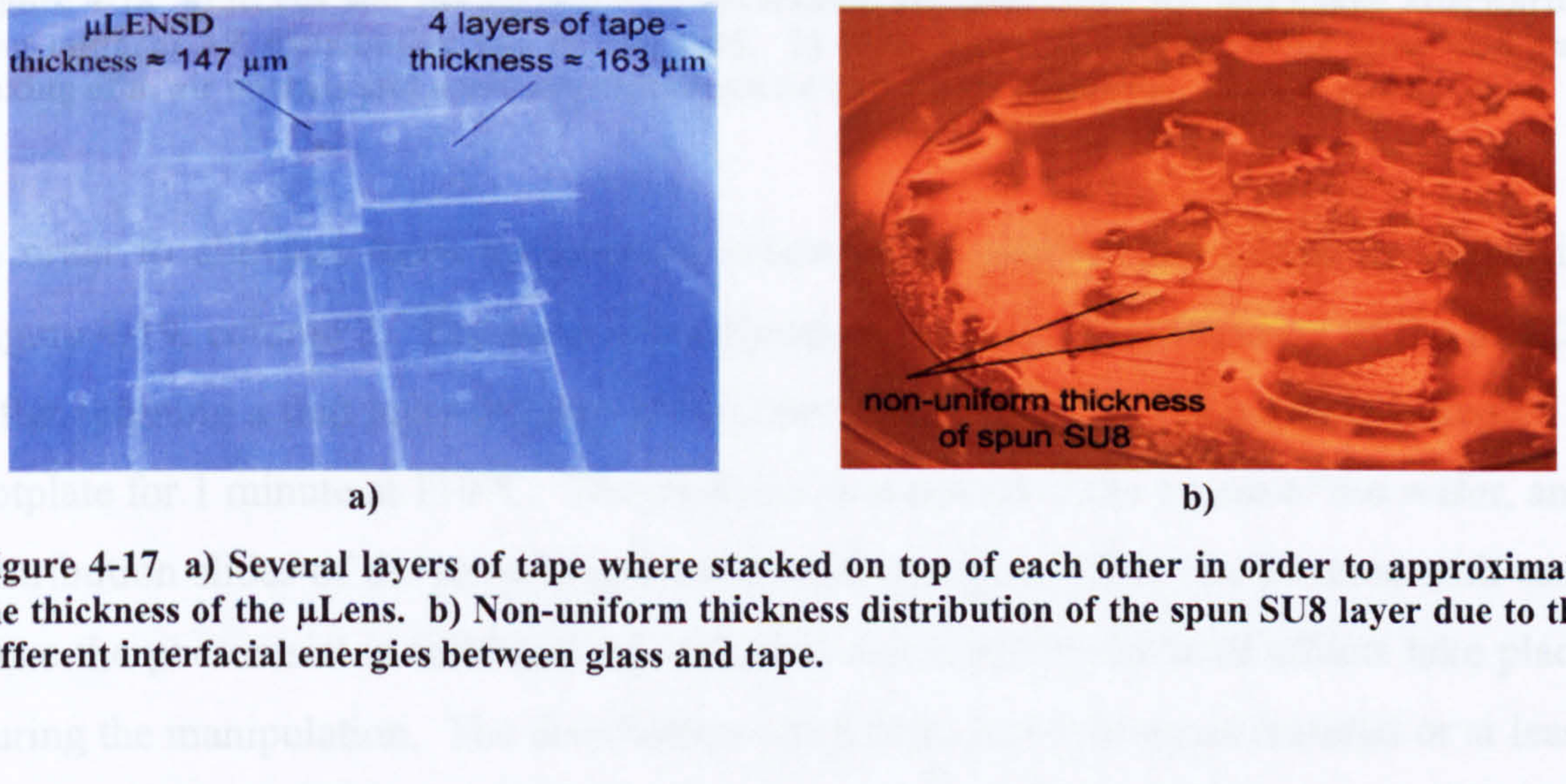

Figure 4-17 a) Several layers of tape where stacked on top of each other in order to approximate the thickness of the μLens. b) Non-uniform thickness distribution of the spun SU8 layer due to the different interfacial energies between glass and tape.

For the purpose of achieving a uniform resist height after spinning, the same material should be used to surround the microlens. In that respect, a glass wafer was used and covered with a thin layer of AZ photoresist. The μLens was then placed at the centre and larger slides of the same material and thickness were placed around the μLens as shown in Figure 4-18a. This process proved to be rather tedious since the AZ viscous resist showed strong capillary action and the slides could only be moved with difficulties. This movement caused an accumulation of the photoresist at the edges in

the direction of motion. Beneath the slides, the capillary force caused a redistribution of the AZ, which was amplified and subsequently maintained during and after baking. Air cavities were created between the slides and the wafer, in particular close to the edges. Furthermore, some bending of the slides itself was visible due to the uneven thickness of the underlying photoresist. Nonetheless, the assembly was spun with SU8 and baked and the result is shown in Figure 4-18b. The air cavities are deemed to be responsible for the air pockets within the layer of SU8 photoresist after baking because of the expansion of the hot air while the assembly is placed on the hotplate.

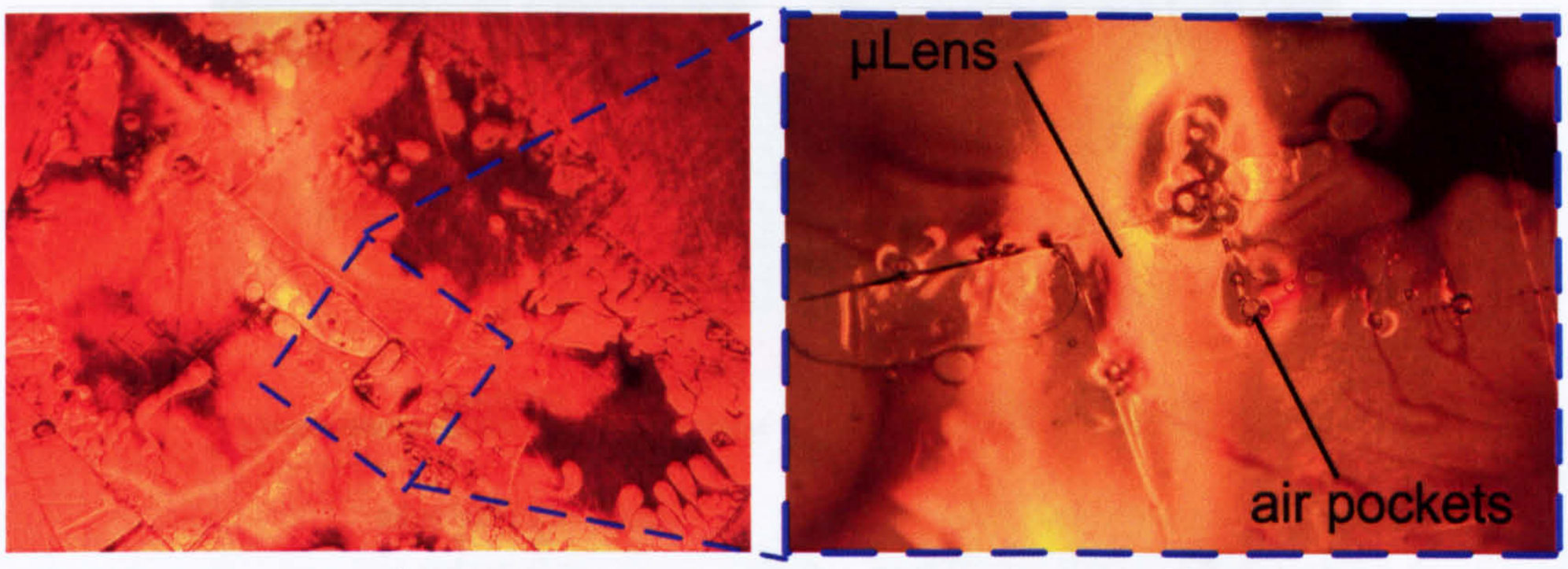

Figure 4-18 a) µLens and the surrounding coverslides are glued with AZ and baked afterwards. Non uniform AZ distribution can be observed. b) Close-up of a). After having spun SU8 and baking of it, air pockets and non uniformities can be seen on the assembly.

In order to alleviate these problems, a process was used for the µLens as shown in Figure 4-19, column 2. The same principle applies also to the production of the µLED. After spinning a thin layer (≈3µm) of AZ onto the glass wafer, the wafer is baked on a hotplate for 1 minute at 110°C. The µLens is then placed at the centre of the wafer, and distribution slides of the same height are placed around it. This can be done with ease since the photoresist is solid and no viscosity- and capillary-induced effects take place during the manipulation. The distribution slides must be of the same material or at least possess a similar surface tension with regards to the considered liquid ($\gamma_{SLd} = \gamma_{SL\mu}$). The assembly is then placed shortly on a hotplate to temporarily fix the pieces (a). In the following step, SU8 is spun onto the structure. Due to the presence of distribution slides, the edge bead curvature is shifted away from the µLens, leaving a uniform height distribution over the important areas of the µLens (b). The assembly is then exposed to UV-light in a photolithographic step (c). It is important to protect the distribution slides from exposure for better removal of the structure. EC-solvent is then used for the development of the SU8, which also dissolves the AZ, which is not covered by the

μLens or distribution slides (d). Due to the area of the distribution slides and μLens, a solvent would need a very long time to penetrate the gap containing AZ due to the diffusion-limited nature of the dissolution process. Hence, to release gently the μLens, the assembly is placed on a hotplate for approximately 10 seconds with a temperature of 90°C (e). This process permits the deposition of photoresist at a constant height across the entire structure to be packaged by removing the edge bead curvature away from the centre.

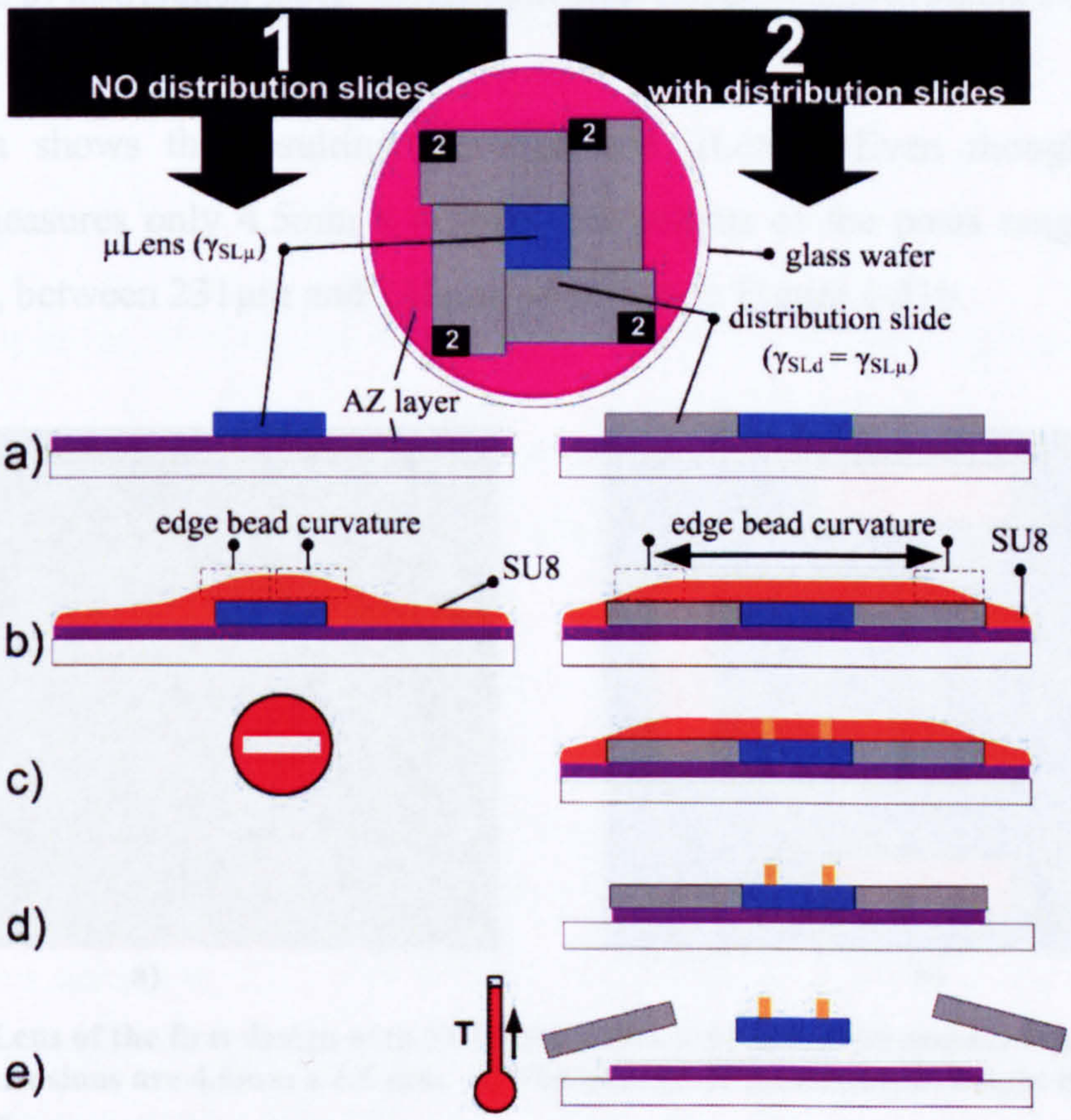

Figure 4-19 Distribution slides (right column) are used to pull the edge bead curvature away from the area that will occupy the structure, to make the thickness of the photoresist homogenous for the features.

Figure 4-20a shows 4 microlens arrays (μLens), which have been surrounded by distribution slides as shown in Figure 4-19. Figure 4-20b shows the assembly for the production of 6 μLED. The material initially chosen was silicon since SU8 adheres very well to it. To reduce costs, leftovers from the cutting of the μLED were used as distribution slides.

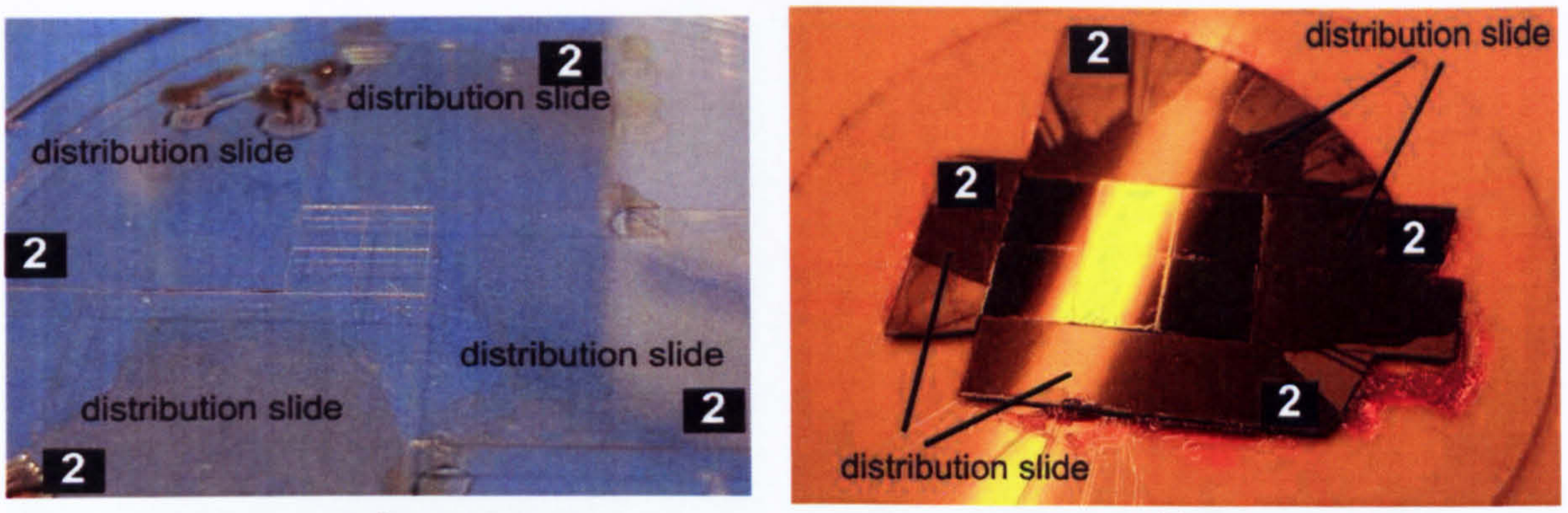

a) b)

Figure 4-20 a) Assembly for μLens fabrication at fabrication state "a", Figure 4-19 where devices are surrounded by distribution slides. b) Assembly state corresponding to Figure 4-19 "b" prior to exposure.

Figure 4-21a shows the resulting manufactured μLens. Even though the lateral dimension measures only 4.5mm x 4.5mm, the heights of the posts range, across the entire device, between 231μm and 235μm, as shown in Figure 4-21b.

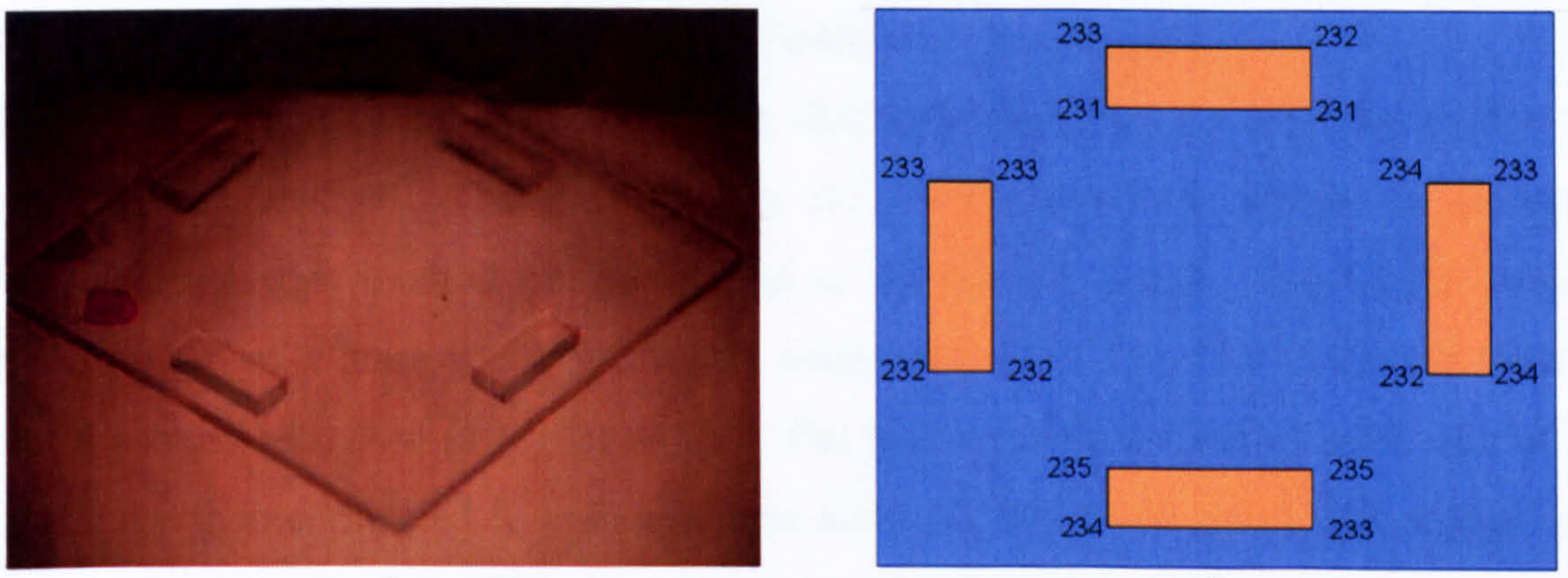

a) b)

Figure 4-21 μLens of the first design with SU8 posts fabricated using the process explained earlier. The lateral dimensions are 4.5mm x 4.5 mm. a) Photograph of the device, b) height distribution of the μLens posts.

This method has several advantages, as shown in Figure 4-22. In the production of the first design, the distribution slide method was not used, resulting in different thicknesses between the corners with $t_1 \approx 35\mu m$, $t_2 \approx 70\mu m$ and $t_3 \approx 30\mu m$. On the other hand, the height distribution of the current design seems to be homogenous throughout the edge with $t_1 \approx 43\mu m$, $t_2 \approx 45\mu m$ and $t_3 \approx 44\mu m$.

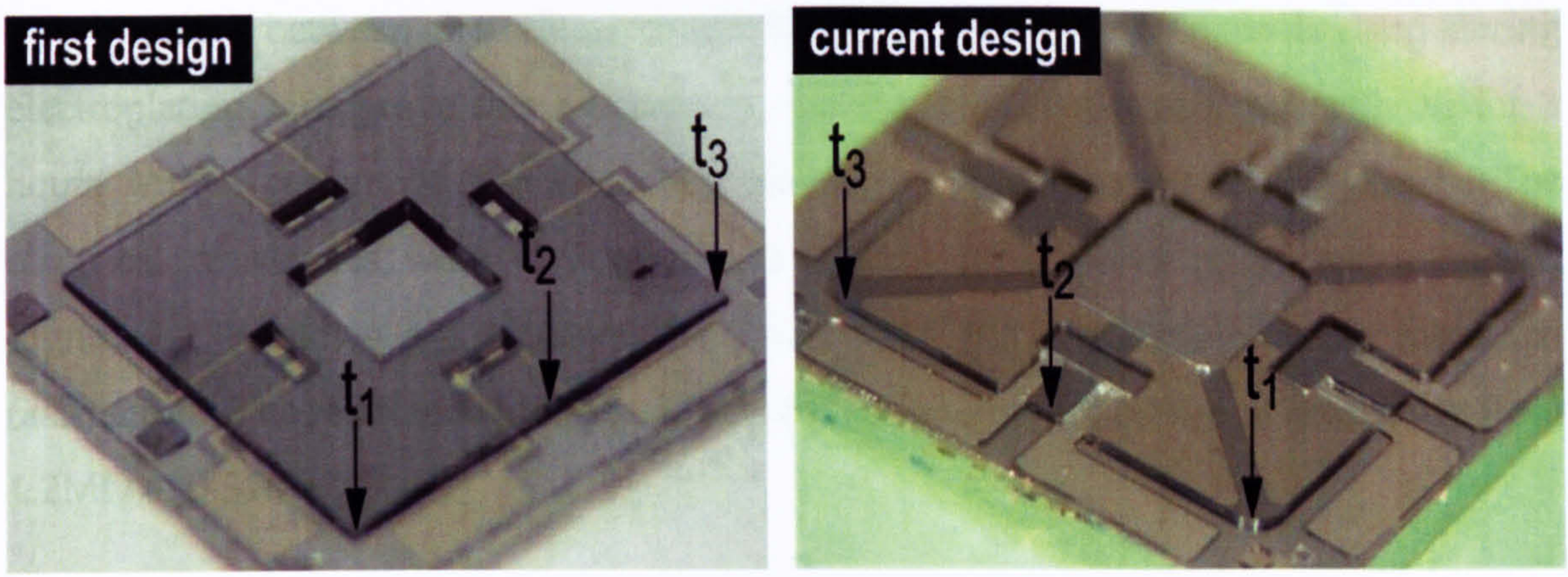

Figure 4-22 Comparison of the thickness distribution of the structural layer between the first design and the current design. The first design which was produced without the method of distribution slides exhibits different thicknesses for t_1, t_2 and t_3.

4.4 Electroplating of accurate electrode thickness for height adjustment

4.4.1 Electrical contact with conductive adhesive (first design)

The determination of the thickness of the electroplated layers was initially carried out with the first design. The methodology for the measurement process is presented nonetheless as this method can be applied to the current design. The μLED array is glued on top of a glass wafer previously evaporated with Ti. The Ti layer is divided into 4 sectors as shown in Figure 4-23a. The two connection pads on each side of the μLED are then connected to the respective sector on the wafer using thin copper wire and conductive adhesive. This was done on each of the four sides of the device. With this assembly, selective electroplating can be achieved by addressing a single pair of electrodes, to equalise possible different heights of the μLens posts. As Figure 4-23a illustrates, the different resistances that were measured to determine the initial conditions for the electroplating process. The conductivity of the adhesive was as expected. Furthermore, the resistance between the copper wire and the conductive adhesive was measured and within the expected range. However, the resistance between the adhesive and the underlying Ti layer was far higher than anticipated with a value of around 1.2MΩ. This led to the conclusion that a huge interface resistance exists which is probably caused by chemical effects between the conductive adhesive and the Ti. This effect would prevent high currents to flow through the material as required during electroplating.

The interface between the adhesive and the Ti is thin but could be bridged during electroplating. To prove this assumption, one sector was electroplated with Ni for 3 hours with a current of 50mA and an electroplating area of around 900μm^2. The electrical resistances were then measured and compared with prior measurements. Figure 4-23b shows a picture of the wafer after electroplating and the measured resistances. The resistance between Ti and the conductive adhesive fell drastically from 1.2MΩ to 3.3Ω.

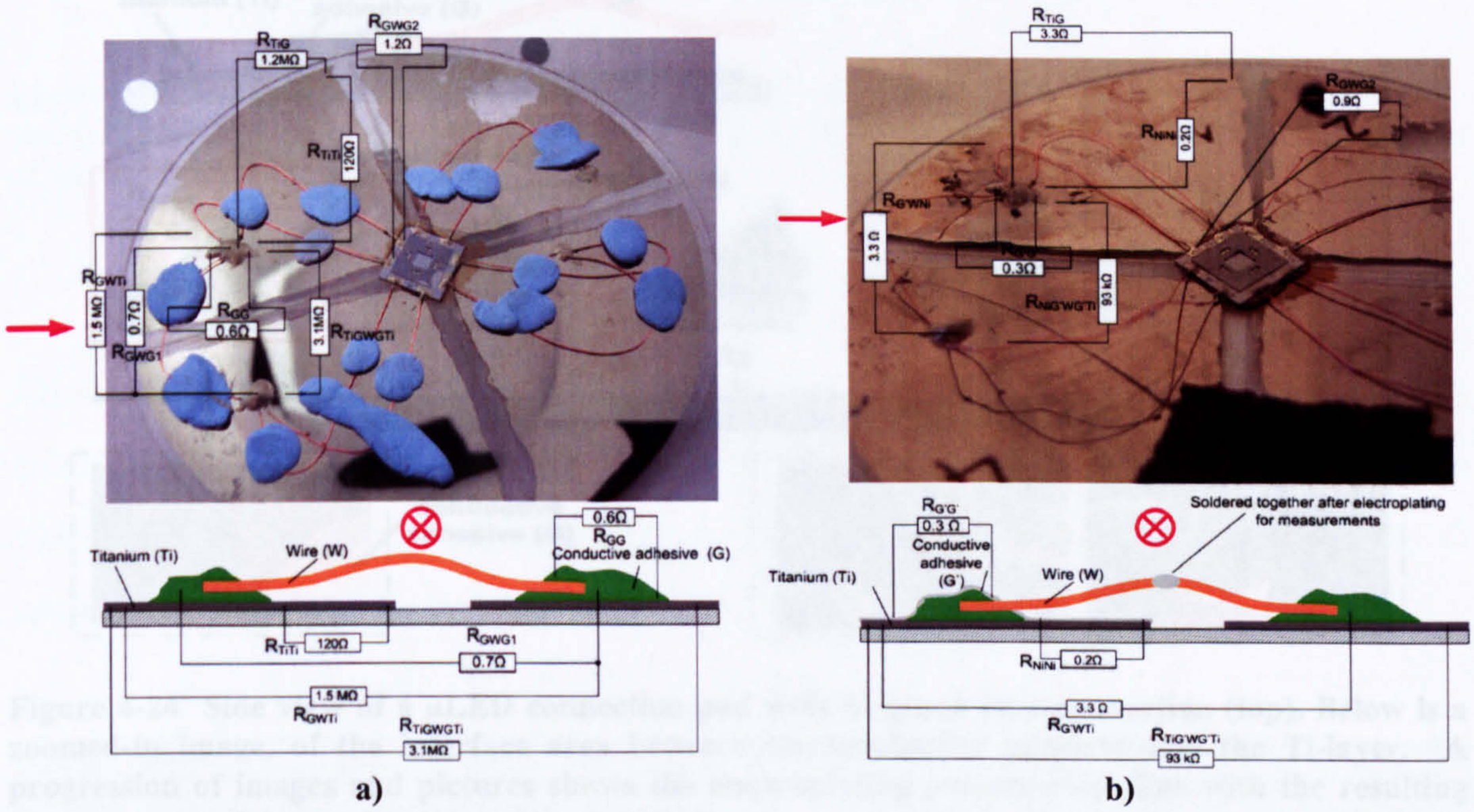

Figure 4-23 a) Top view and corresponding side view of a μLED that has bee glued to a wafer for the evaporation process. The different resistances between particular features are given in both views. b) Same wafer after 3 hours of electroplating with a current of 50mA for an area of around 900μm^2.

Figure 4-24 provides a side view of the μLED connection pad and a possible explanation about the cause of the bridging. In this side view, the copper wire, which provides the electroplating current, is attached to the conductive adhesive. The zoomed-in image shows the different layers: the conductive adhesive and Ti-layer, and a transition-layer responsible for the high resistance. At time t_1, the assembly has not yet been electroplated; therefore, the conductive material of the glue as well as the Ti-layer are separated by the transition layer. At t_2 the assembly has already been electroplated for a certain time. The Ni-layer is only growing on the surface of the conductive adhesive and of the wire connected to it. No electroplating occurs on the Ti-layer. At t_3 the thickness of the Ni-layer on top of the adhesive has grown thicker but still does not touch the Ti-layer. The Ni-layer touches the Ti-layer at the time t_4. This causes an electrical conductive contact and allows a current to flow to the Ti-layer where the

electroplating process starts. Because electroplating takes place on the Ti-layer and the surface of the adhesive, the two layers grow together, t_5. The contact between the connection pads and the conductive adhesive is not only done by physical contact but also by a metallic connection. This explains the low resistance of 3.3Ω compared with the initial value of 1.2MΩ. For the subsequent devices, conductive paint was used which exhibited instantly low electric resistance.

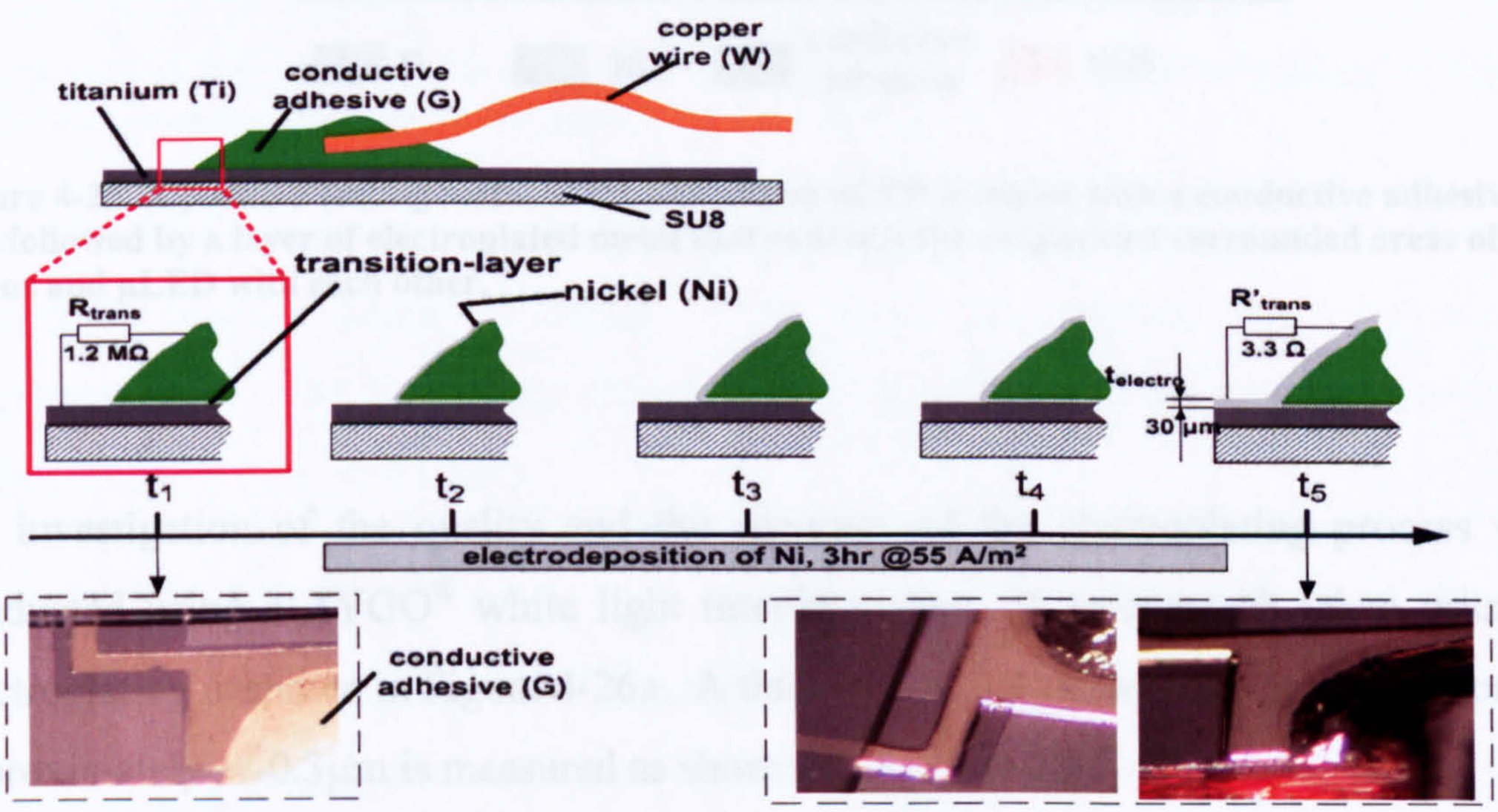

Figure 4-24 Side view of a µLED connection pad with its glued wire connection (top). Below is a zoomed-in image, of the interface area between the conductive adhesive and the Ti-layer. A progression of images and pictures shows the electroplating process over time with the resulting improvement of the conductivity of the interface.

This bridging effect might be used for sealing applications as described in Figure 4-25. Surrounding edge areas of the µLens as well as the µLED are evaporated with Ti (1). Conductive adhesive is placed on the edge of the µLens in order that the Ti-layer of the µLens and µLED are covered (2). The assembly is then electroplated by connecting one or both of the Ti layers to a current source (3). During electroplating, the cavity is protected from incoming humidity by the adhesive itself and later by the hermetic metal sealing.

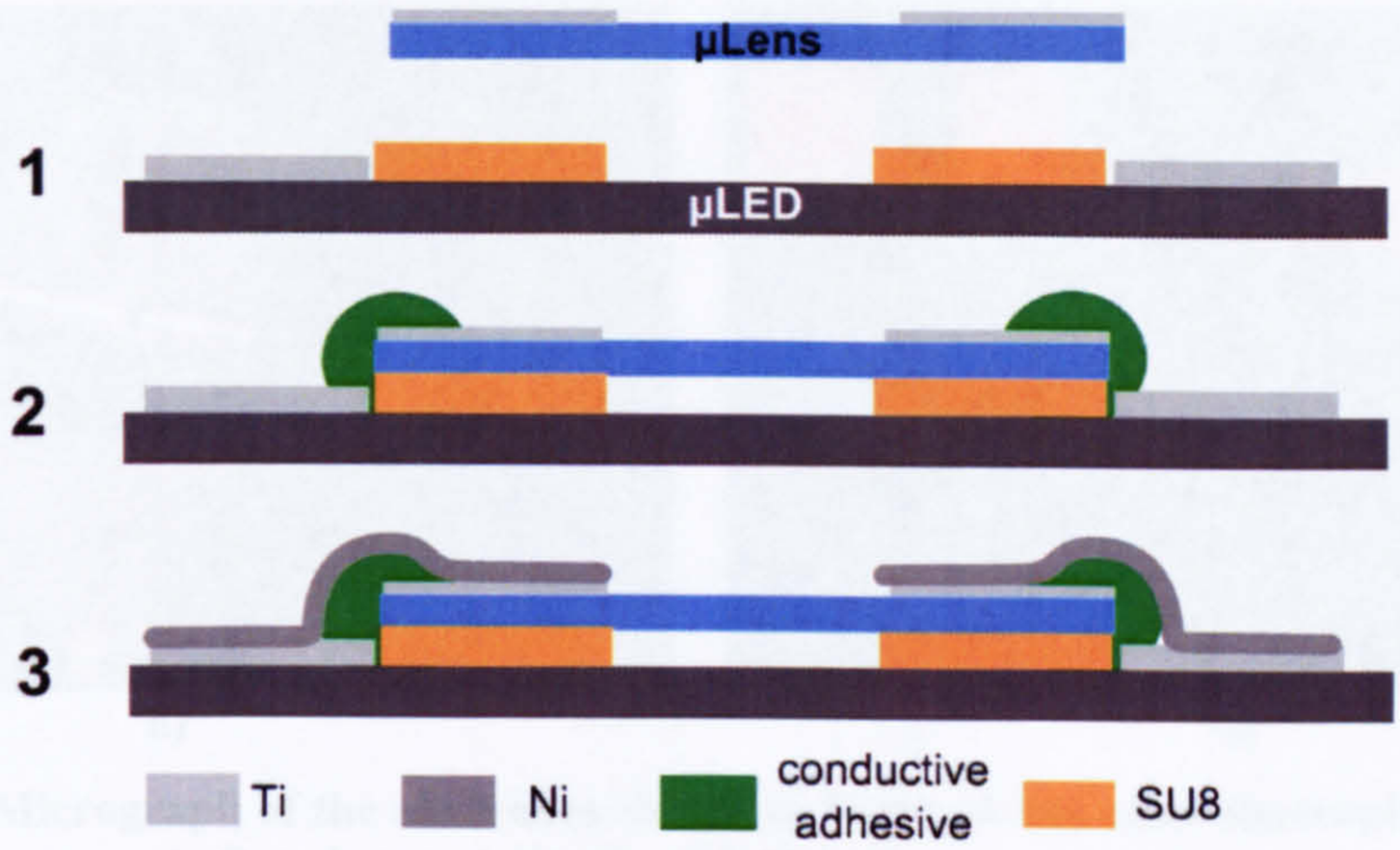

Figure 4-25 A possible sealing method: the µLens and µLED is sealed with a conductive adhesive and followed by a layer of electroplated metal that connects the evaporated surrounded areas of the µLens and µLED with each other.

An investigation of the quality and the accuracy of the electroplating process was conducted using a ZYGO® white light interferometer. A micrograph taken prior to electroplating is shown in Figure 4-26a. A thickness of 6.4µm with a height variation of approximately +/-0.3µm is measured as shown in Figure 4-26b.

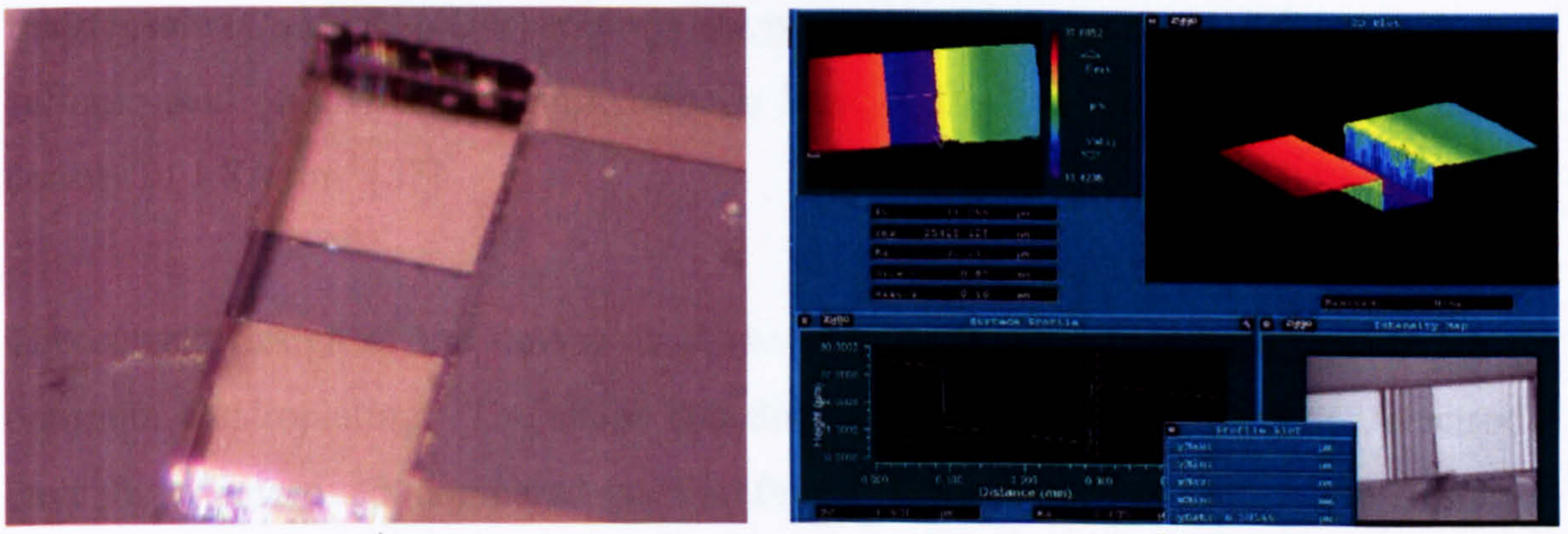

a) b)

Figure 4-26 a) Micrograph of the electrodes of the µLED prior to electroplating. b) ZYGO® measurement of the same electrodes.

In total the sample was electroplated for 3 hours at a current of 50mA (Figure 4-27a). The electroplating area was assumed to be roughly a bit less than a quarter of the wafer area at around 900µm^2. This resulted in a total height of around 36µm. The height variation was of the order of +/- 1µm (Figure 4-27b).

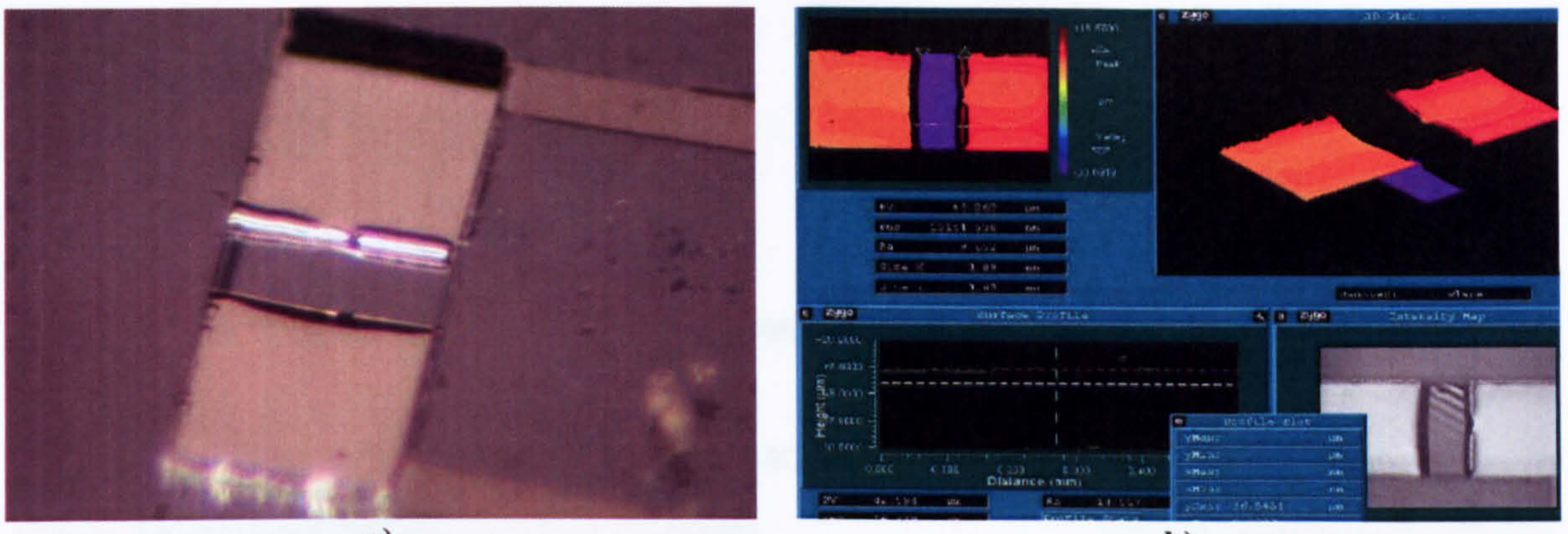

Figure 4-27 a) Micrograph of the electrodes shown in Figure 4-26a after electroplating for 3 hour. b) ZYGO® measurement after electroplating for 3 hours.

Thereafter, the same section was electroplated for another 24 minutes at 50mA as an attempt to reach a height of 40µm. This value was derived using the rule of proportionality. The following measurements showed that the height distribution ranged from 38.5µm to 40.7µm.

4.4.2 Electroplating of current design devices

A new electroplating bath, based on a formulation from FH Zweibruecken (Germany), was set up. It consists of 76g/l of $Ni(NH_2SO_3)_2$, 30g/l of boric acid and 1g/l of fluortenside ($C_{16}H_{20}F_{17}NO_3S$) whereas the pH level of 3.5 to 4 was regulated with amid sulfonic acid (40g/l). The temperature is kept at 54°C with a recommended current density of 1.8A/dm^2 [57].

The current design of the device as shown in Figure 4-28b has been carried out for optimum electroplating. The shape and dimension of the pads, tracks and electrodes have been improved compared to the first design (Figure 4-28a). For instance, unnecessary corners have been removed and the remaining corners have been rounded in order to reduce stress during the electroplating process. In the first design, delamination of the Ti-Ni layer was observed in particular on the thin and sharp-cornered tracks. As a consequence, the tracks were considerably broadened for better adhesion but also for more electrical conductivity towards the electrode. The part of the electrode that lies within the cavity is on three sides surrounded by a big conductive area. Since the old design already provided submicron accuracy as far as electroplated layers are concerned, few experiments were planned for the current design in that respect.

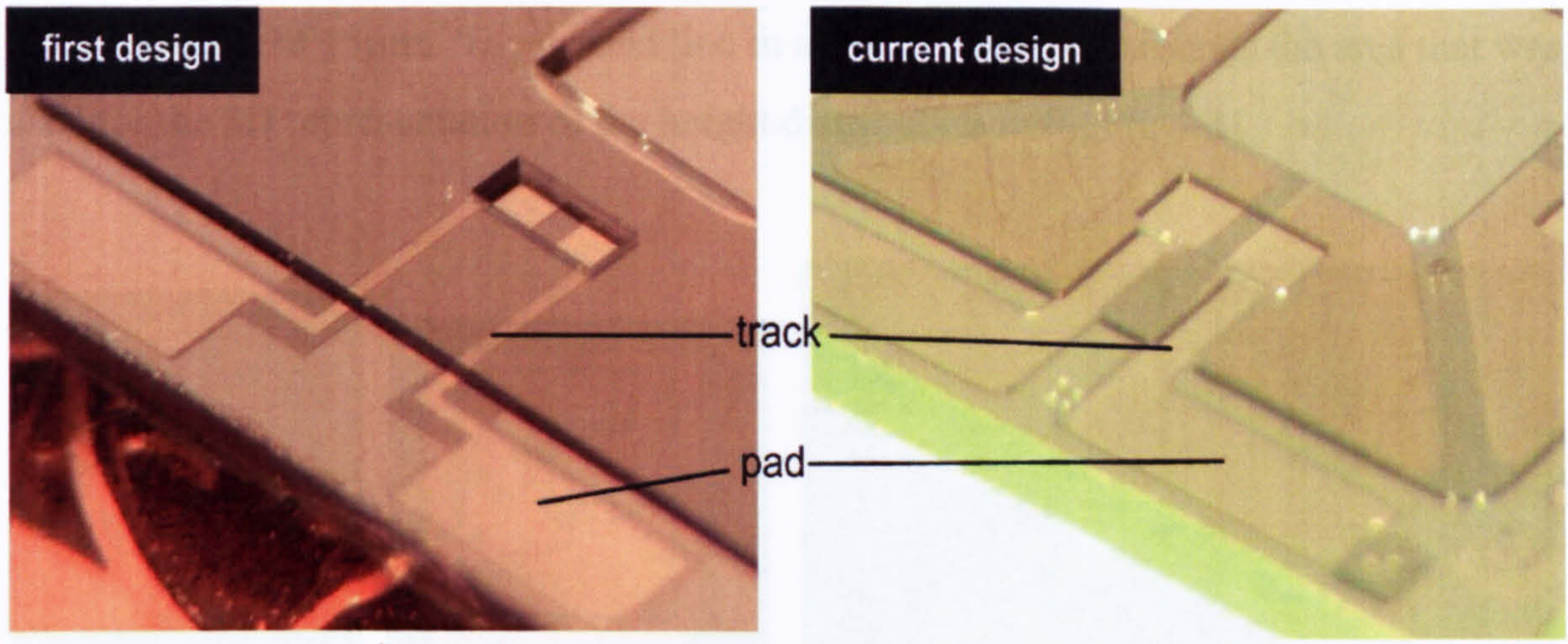

Figure 4-28 a) Design of the pads tracks and electrodes of the first design. b) Current design; flaws of the first design have been corrected.

A further improvement was the use of conductive paint as opposed to conductive adhesive, which establishes very good conductivity instantly. The slight disadvantage is the poor mechanical stability compared to the adhesive. Figure 4-29 shows an assembly ready for the electroplating process used for the magnetic actuation. The copper wires are attached to the pads using conductive paint.

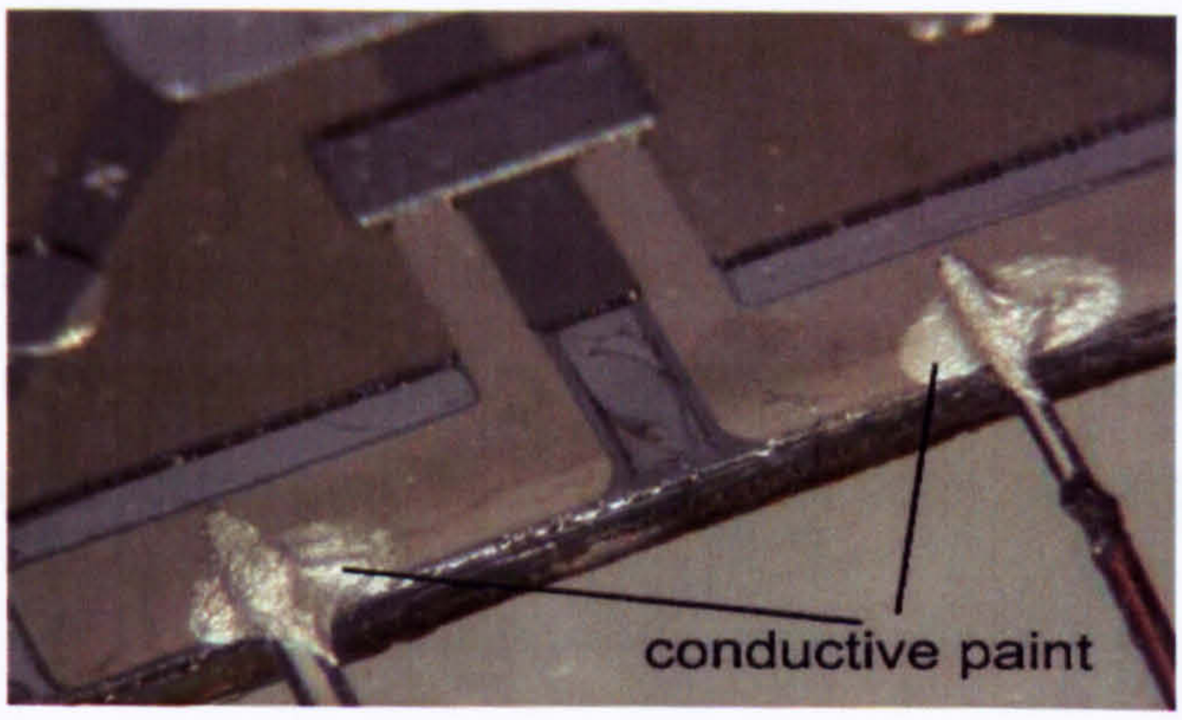

Figure 4-29 The copper wire are attached to the pads using conductive paint.

Figure 4-30a and Figure 4-30b show the distribution of the surface height of an electrode prior and after electroplating, respectively. A photograph of the electroplated electrode is shown in Figure 4-30c. After having measured the height and the surface distribution of the Ti electrode, the device was electroplated for a certain time. Since the electrode is so small, an auxiliary electrode was employed to make the electroplating process and the final layer thickness more tolerant to variations of the current and connection resistance between the different plating sessions. The height of the electrode was then measured and the time needed to reach the desired height for the electrode calculated. A measured thickness between 15.1μm and 15.6μm was obtained for an

intended value of 15µm. The dashed line in all three images surrounds the area that was used for the 3D representation of the height distribution in Figure 4-31.

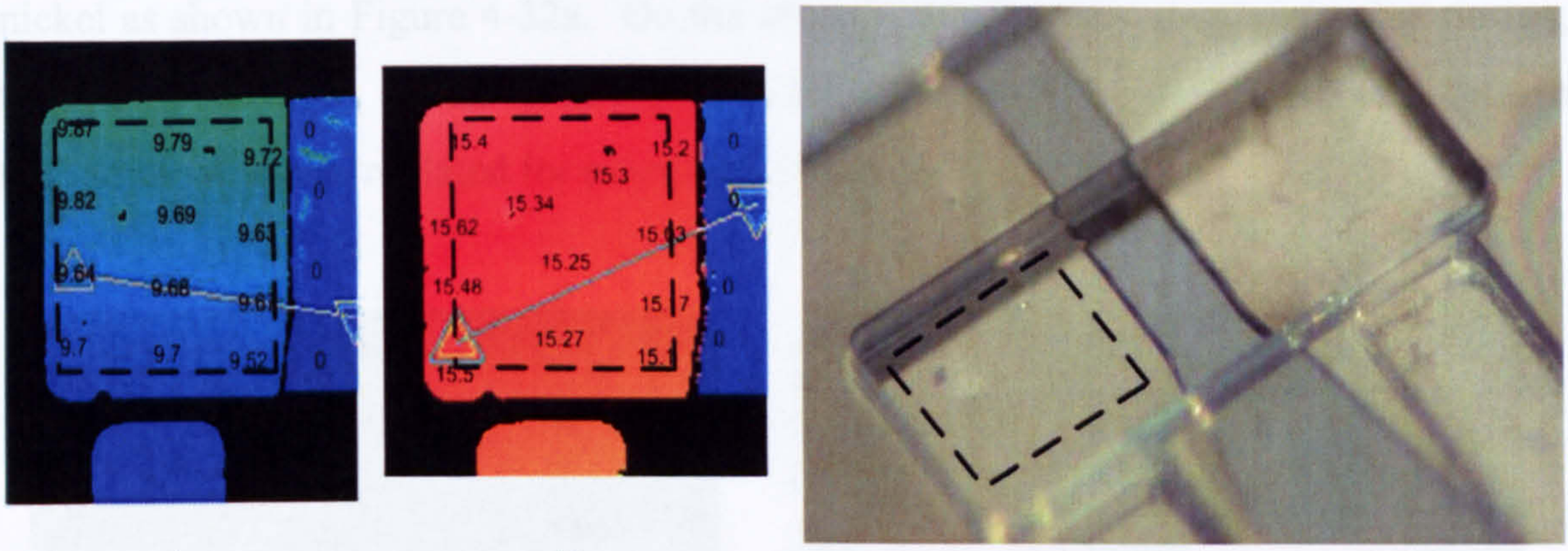

a) b) c)

Figure 4-30 a) Electrode prior to electroplating. b) Electrode after plating with nickel. c) Photograph of the electrode after electroplating.

To create the image shown in Figure 4-31, a MATLAB® program was developed that imports the data from ZYGO® into MATLAB®. The program allows to choose an area (as shown with a dashed rectangle in Figure 4-30a and Figure 4-30b) and equalises the tilt which is caused by the uneven placement of the µLED beneath the sensor.

The lateral dimensions of the measured field is 400µm x 400µm and the vertical direction has a range of only 2µm, therefore non-uniformities appear exaggerated which is useful for this investigation. The two peaks are artefacts from previous production steps and have been discarded for the determination of the accuracy of the electroplating process itself.

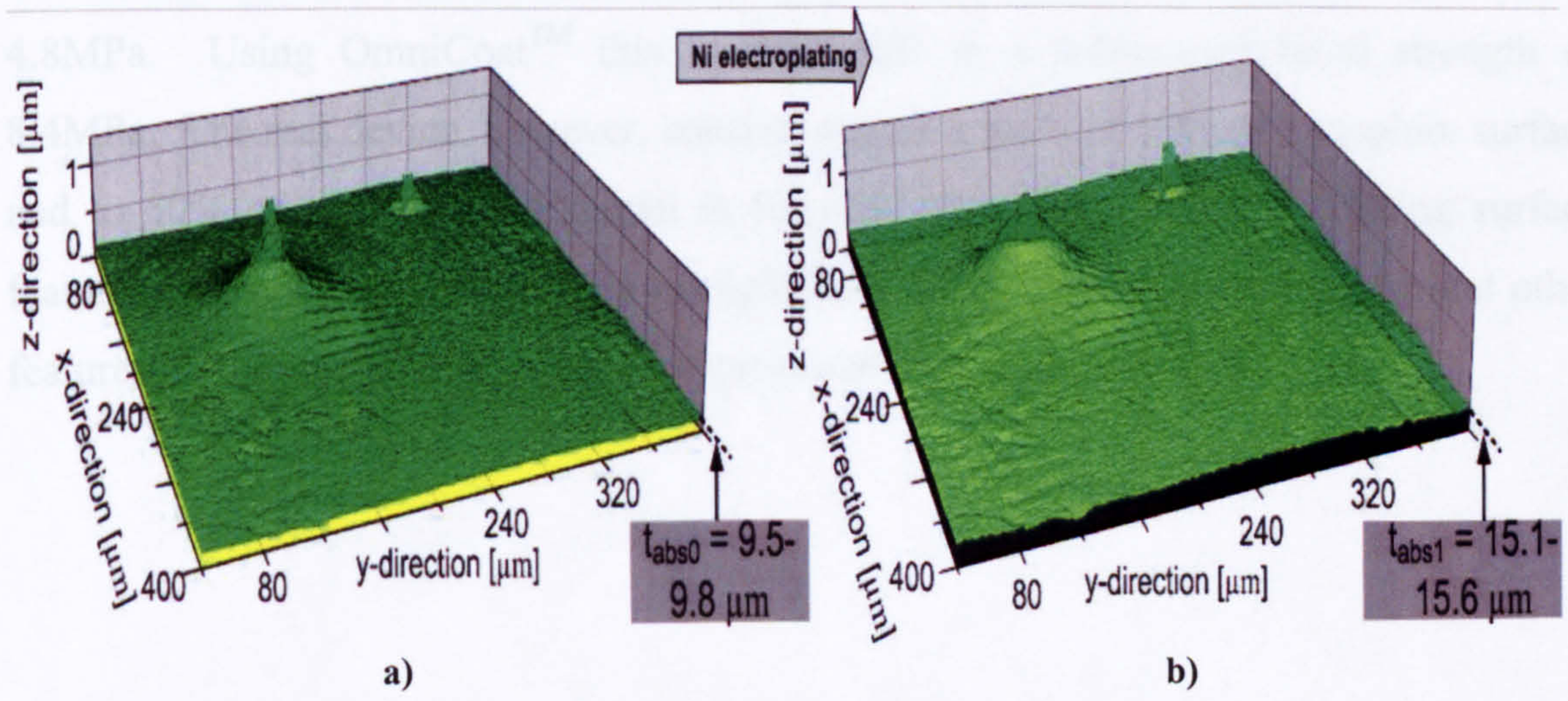

a) b)

Figure 4-31 a) Electrode prior to electroplating. b) Electrode after electroplating of around 5µm.

4.4.3 Adhesion problems

The adhesion of SU8 onto the glass substrate of the dummy devices is not satisfactory. Delamination of the SU8 layer took place when the sample was electroplated with nickel as shown in Figure 4-32a. On the other hand, when examining the first design, using a Si substrate, as shown in Figure 4-32b, no delaminating occurred even though the sample was electroplated for more than 3 hours.

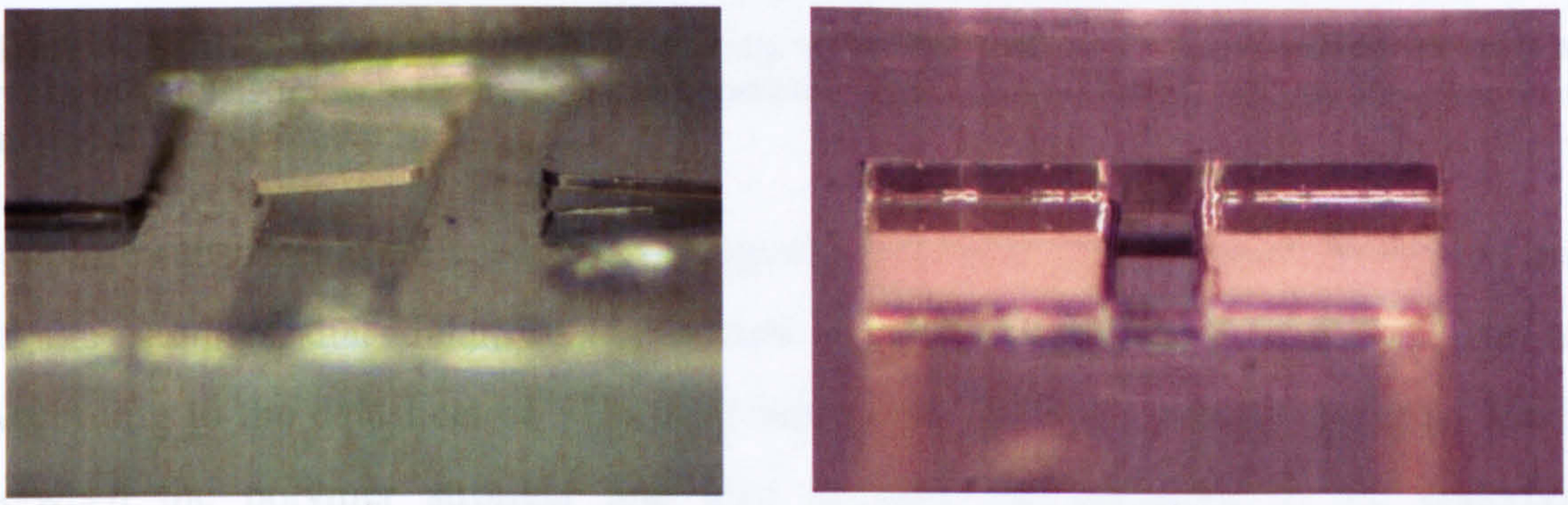

a) b)

Figure 4-32 a) SU8 layer delaminated during electroplating. The substrate material was glass for this dummy device. b) First design with Si as substrate material. It shows that the SU8 adheres very well to this substrate even after extended electroplating.

To improve the adhesion of SU8 to glass, the adhesion promoter OmniCoat™ (Microchem) has been purchased. The subsequent device, however, will be made of sapphire which has different surface properties. Up to this point it is not clear whether the SU8 will stick better to that substrate than ordinary glass. Nonetheless, a considerable area of the device is covered with gold tracks, which work as connection tracks for the μLED. [58] investigated the adhesion behaviour of SU8 spun on gold. It was concluded that by using OmniCoat™, the adhesion could be increased by 75%. It is also stated that Si has a bond strength of 20.7MPa to SU8 whereas gold yields just 4.8MPa. Using OmniCoat™ this would result in a subsequent bond strength of 8.4MPa. The real device, however, consists approximately to 50% of a sapphire surface and to 50% of gold (Au) as shown in Figure 4-33. The etching of locking surface features was not considered, since it might have compromised the Au tracks and other features on the μLED-chip, if not an appropriate etch-mask was used.

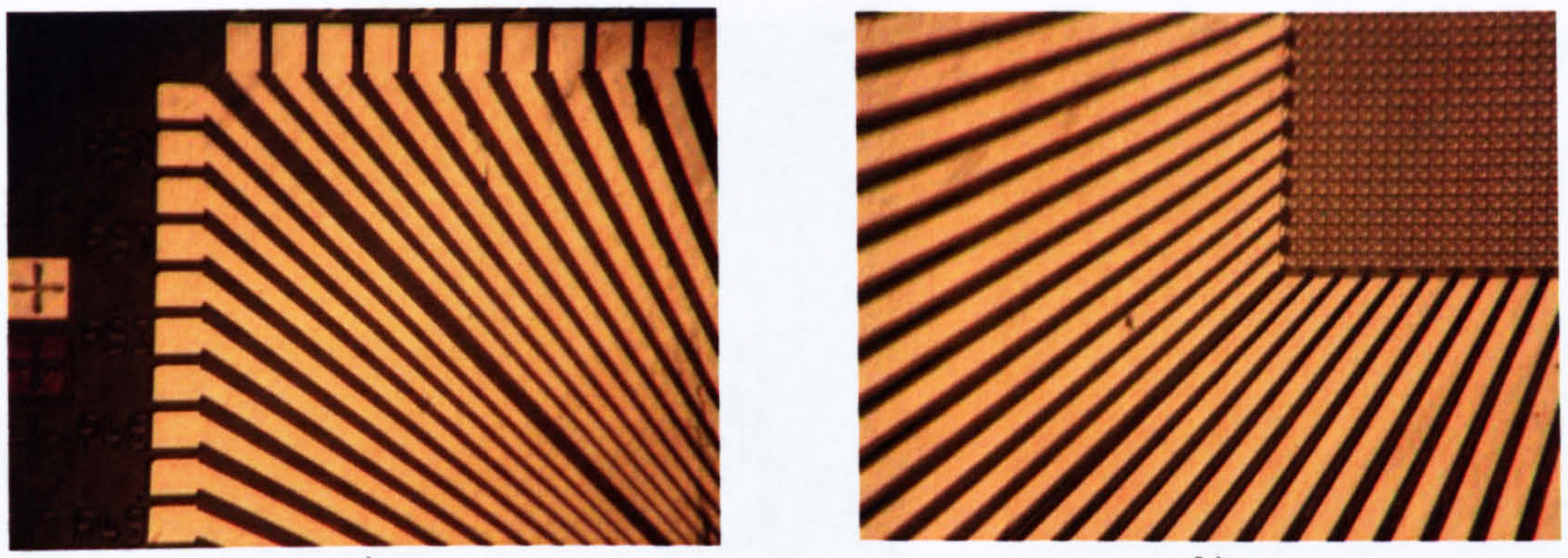

a) b)

Figure 4-33 μLED as supplied by the University of Strathclyde. a) Au LED-connection-pads and tracks of the left upper corner. b) Au connection tracks at the bottom left corner going to the micro-LED array itself.

Sapphire substrates were used for investigating this issue. It was found throughout most of the samples that delaminating occurs whether OmniCoat™ was used or not. According to the datasheet of SU8 hard baking of SU8 should make the cross linking between the polymer stronger and also improve the adhesion to the underlying substrate. Owing to that, a sapphire substrate was used and after the base layer had been developed, the sample was placed within an oven that was initially at room temperature and then within 30 minutes ramped up to 200°C where it remained for 30 minutes at this temperature. Thereafter it was cooled down by simply switching of the oven waiting for 3 hours. The wafer was then processed accordingly and the same procedure was conducted with the structural layer. Investigation under the microscope unveiled, that nevertheless, delamination took place. It was suspected that a possible mismatch between the base layer and structural layer, both being SU8 but having a different "processing history", might cause a stress that causes the delamination. Therefore, the same process was conducted with the difference that the base layer was not fabricated. The Ti was directly evaporated onto the sapphire substrate followed by the hard baked structural layer. As Figure 4-34a and Figure 4-34b illustrate, both methods yielded negative results since delamination occurred nonetheless. The delamination got worse, when the samples were put into the electroplating bath. This was the reason, why the first samples featuring the means for magnetic actuation are seen to have a Si substrate as opposed to a sapphire, since SU8 adheres very well to Si.

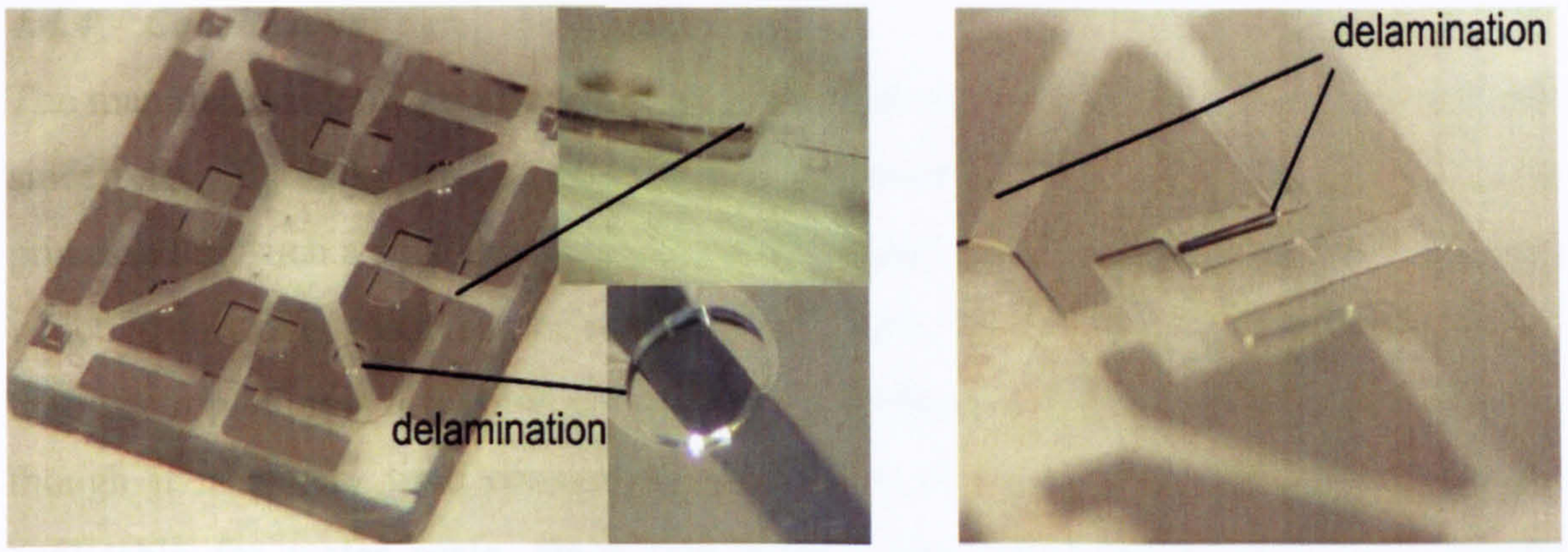

a) b)

Figure 4-34 a) Delamination of a sample that has the base and structural layer hard baked with sapphire as a substrate material. b) Delamination also occurred at samples that featured no base layer but just the functional and the structural layer, latter made of hard baked SU8.

However, a substitute for SU8 was sought and found with the negative photoresist THB. First it was attempted to build the base as well as the structural layer with this material, but this proved not to be feasible, since the base layer was always destroyed when the AZ layer needed to be removed after the evaporation process. THB is susceptible to acetone or even EC-solvent, which is necessary for the removal of the AZ mask. Hence, the base layer remained SU8 (without hard baking) and only the structural layer was replaced by THB. Rough investigations under the microscope showed, that no delamination is visible after development. A sample was then taken and electroplated for 2 hours with a current density of $0.25A/dm^2$. Repeated trials revealed that no delamination occurred. Figure 4-35 shows different samples that were investigated after having emerged it for a long period (>2h) within the electroplating solution. Figure 4-35a show even the scratches that were caused by a very thin needle in an attempt to lift off the corner of the structural layer. As shown, no delamination occurred even after this treatment. Figure 4-35b and Figure 4-35c do not show any signs of delamination either.

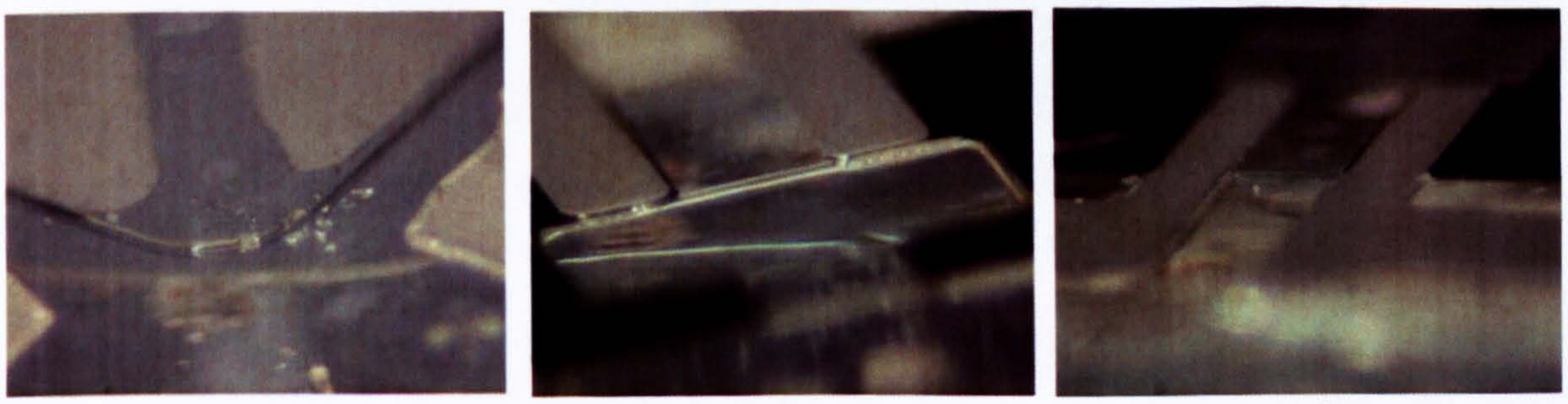

a) b) c)

Figure 4-35 µLED where THB was used instead if SU8. a) After electroplating, the corner did not show any signs of delamination even after having attempted to lift it with a needle. b) The cavity with the incoming electroplated tracks exhibits no delamination. c) No delamination could be seen looking at the cavity from the opposite side.

4.4.4 Conclusions

The manufacturing of the μLens and μLED on the die level, proved to be very difficult since relatively bulky structures, involving photoresist of high viscosity, needed to be processed on such a small area. The cleanroom used is not equipped for die fabrication which is only one reason for the resulting low yield. It has however been demonstrated, that electroplating is a feasible solution for obtaining accurate vertical alignment, even though it is a very time consuming task. The solutions found are not necessarily applicable for wafer scale, since this project was concerned with a very specific packaging problem.

Chapter 5

Experimental Characterisation

5.1 Noise determination of the measurement setup system

To determine the noise of the optical measurement setup system, a glass wafer was placed on the sample table and the time transient was recorded with the confocal chromatic displacement sensor from micro-epsilon®(optoNCDT2400). Its proprietary software was chosen for the initial measurements since it allows a high sample frequency of 1000Hz. In later measurements, the sensor output data is processed and analysed by MATLAB® which only allows a sample frequency of 30Hz. Figure 5-1 describes the setup. Both sample table and sensor are attached to the optical table. Due to the vibrations within the building caused by people, machines and airflow, these vibrations are transferred to the optical table which is not vibration controlled. Since the sensor is attached via a x-, y-, z-stage on a cantilever like structure, it is expected that the amplitude of the vibration would be amplified. The recorded vibration is predominantly due to the movement of the sensor itself with respect to the sample table and not by the μLens itself.

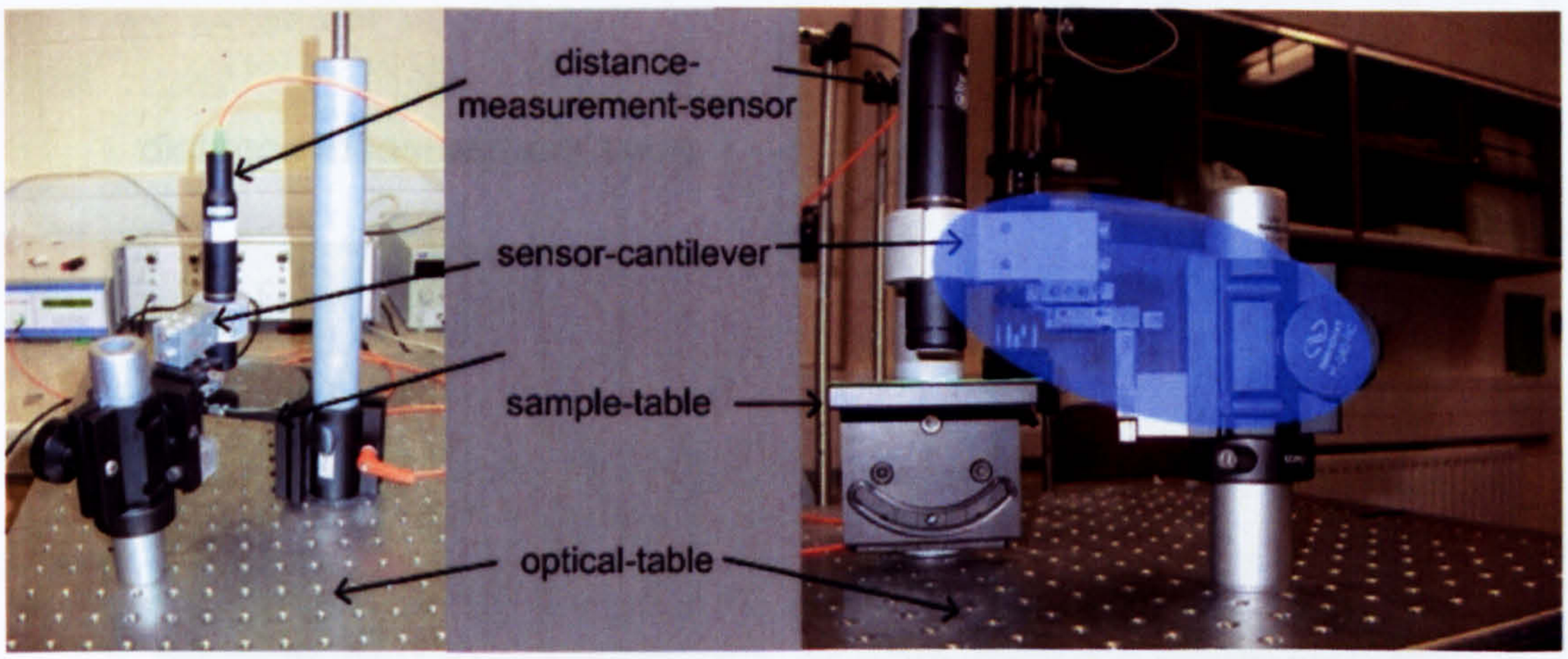

Figure 5-1 Setup of the noise measurement that detects the vibrations caused by the building and which is transferred to the setup.

Figure 5-2 shows the measurement taken to estimate the noise. The top graph depicts the amplitude of the vibration as a function of time. The amplitude exceeds a value of 1μm. To further investigate the vibration behaviour, a normalised power spectrum has

been calculated and shown in Figure 5-2 (bottom). The highest peak is at a frequency of around 16Hz.

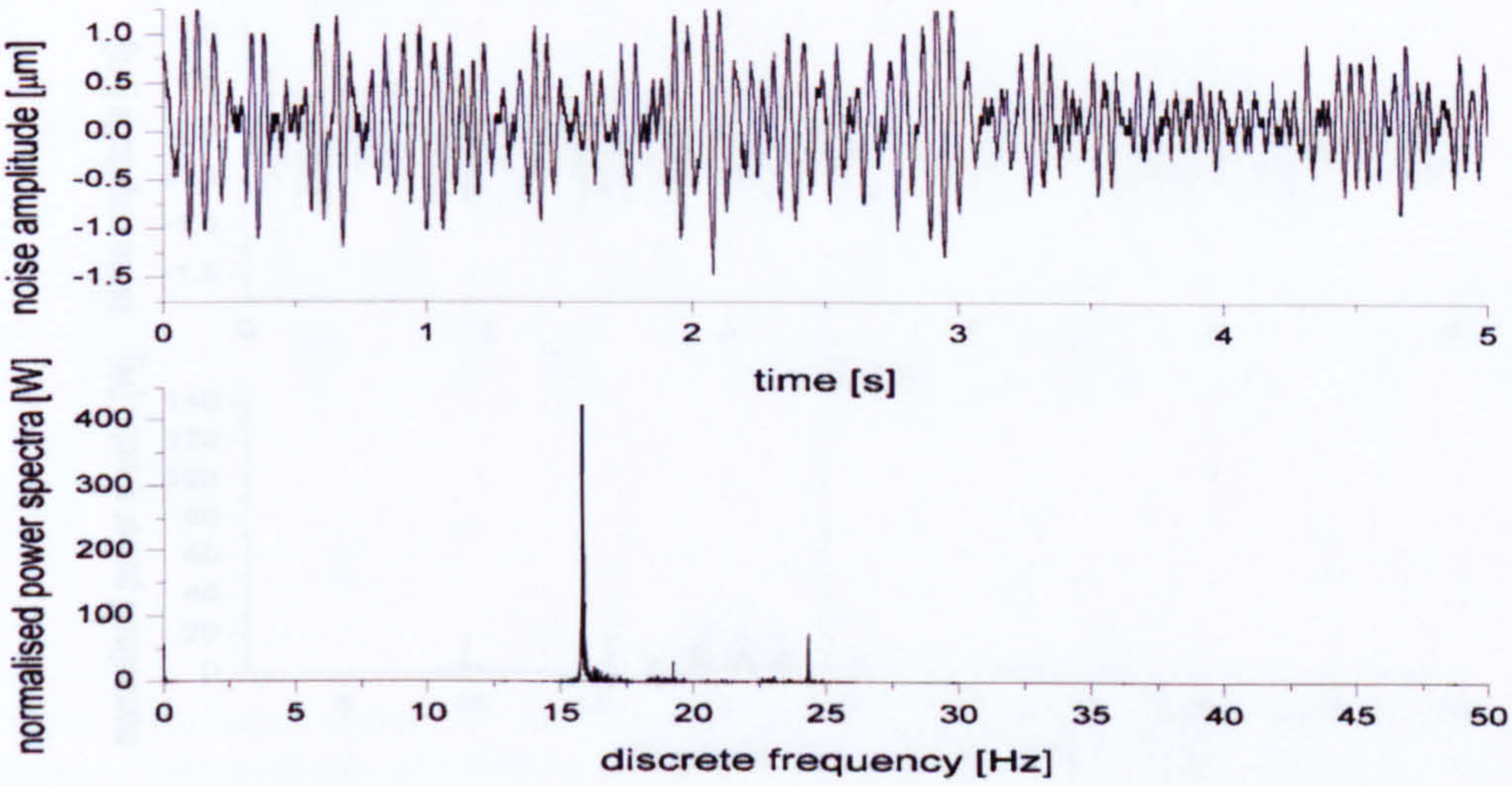

Figure 5-2 Measurement of the noise. Top graph depicts the amplitude as a function of the time and the graph below the normalised power spectra.

As no vibration isolated optical table was available for this project, another means of reducing the vibration was considered as shown in Figure 5-3. The optical table was placed on top of four gel cushions situated on the optical base. Due to the viscoselastic properties of the gel cushion, it was expected that the magnitude of the vibration could be reduced.

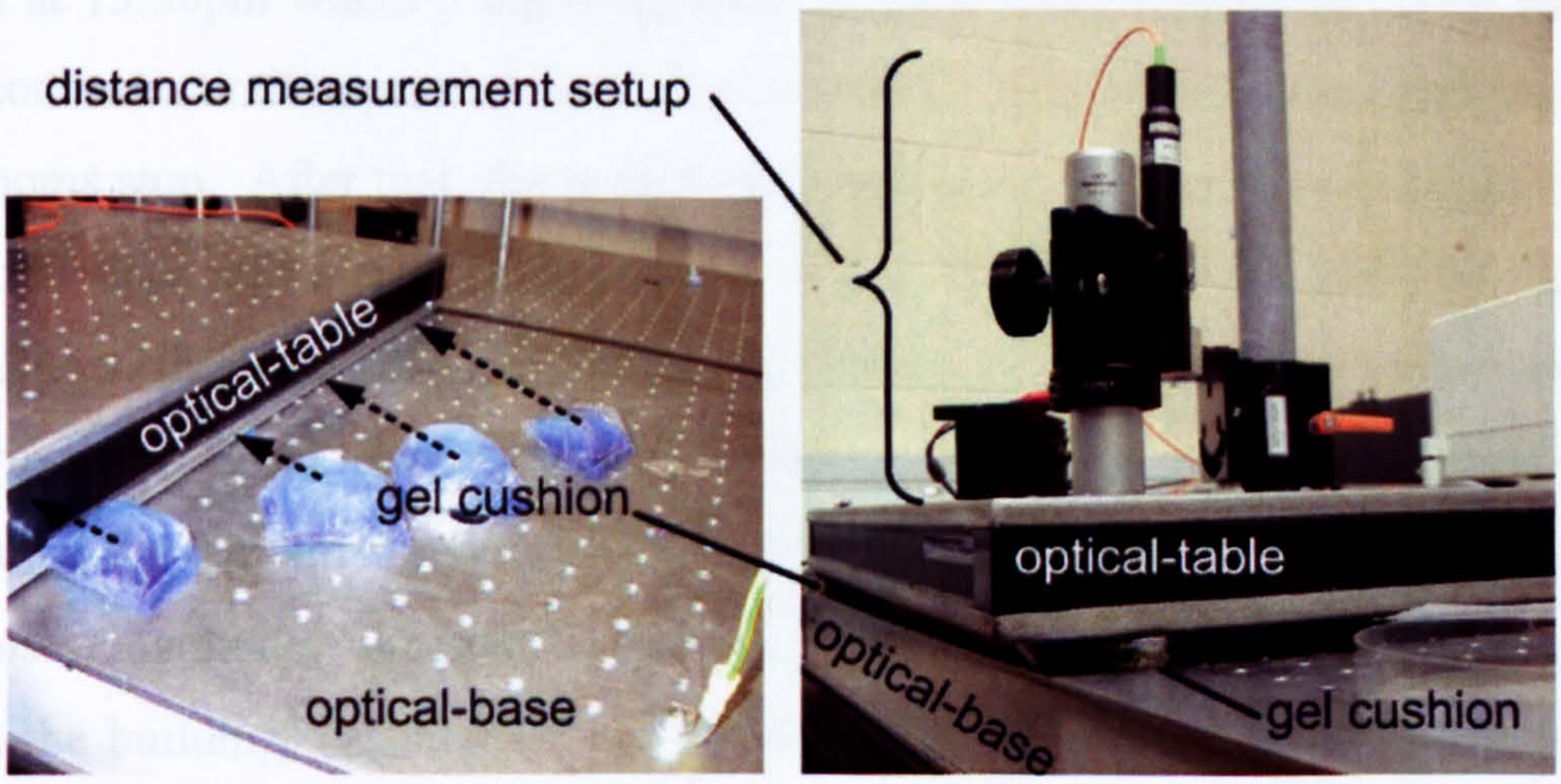

Figure 5-3 The gel cushions are placed between the optical-table and the optical-base to dampen the magnitude of the noise generated by the building.

Figure 5-4 shows the resulting measurements. The magnitude as a function of time has been reduced by a factor of around 2. The normalised power spectrum indicates that a

frequency shift to around 24Hz as well as an attenuation of the magnitude of the peak has taken place.

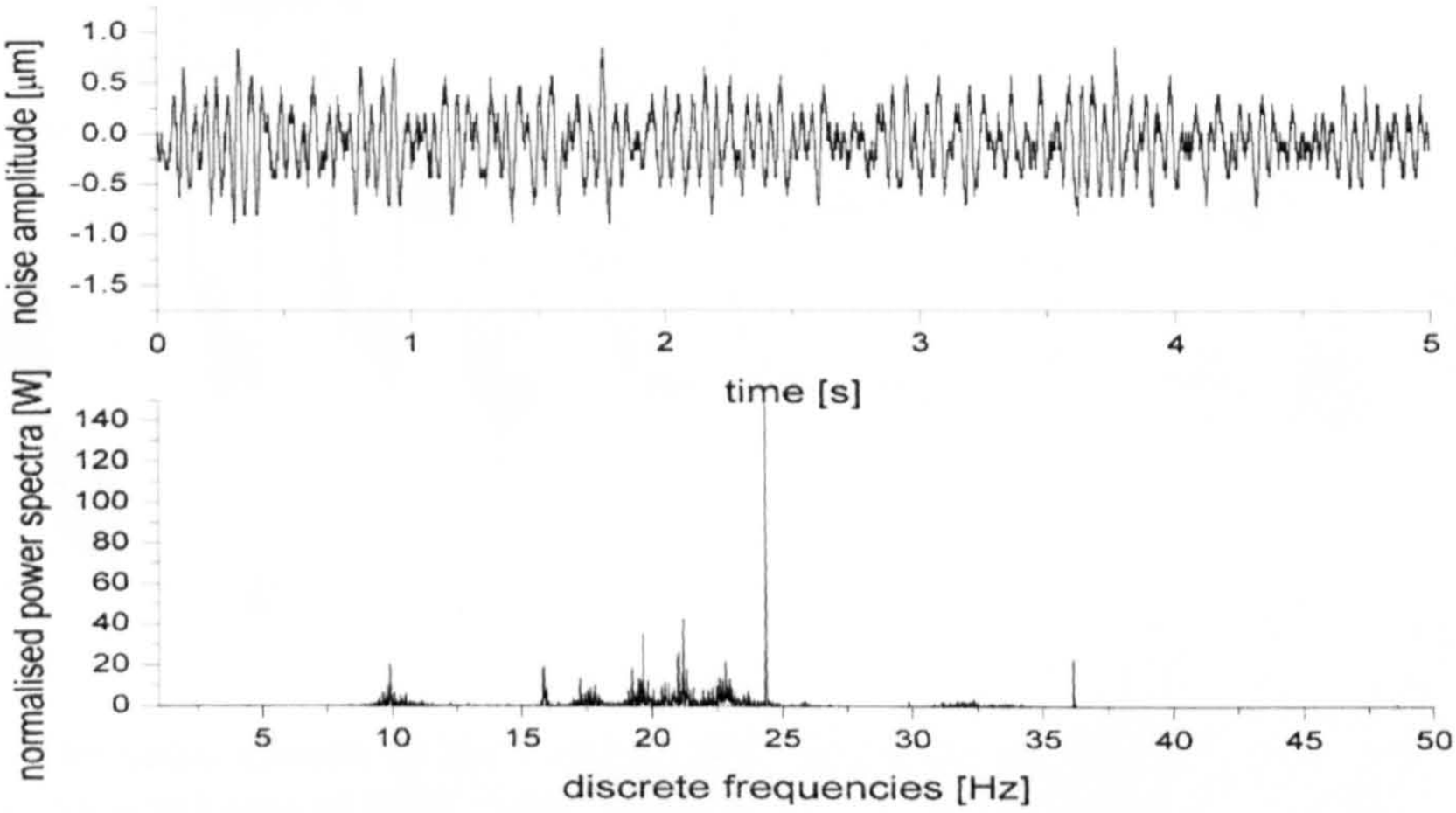

Figure 5-4 The upper graph shows the transient of the noise measurement after having placed gel pads below the optical-table. The graph below shows the normalised power spectra. A prominent peak can be seen at a frequency of 24.38Hz.

To verify that the vibration originates from the building, a long term measurement was carried out. Figure 5-5 displays the 25 hours step-response of the overall system for several voltage steps of the electrostatic actuator. The time of day is shown at the top. The measurement was taken during term time, when many students are around during the day, which results in more vibration of the building itself. The measurement was started at 13:30pm where a big magnitude of noise can be observed. This magnitude level continues until approximately 16:30pm where most of the classes and transition to classrooms stop. After that, the noise level remains constant at a lower magnitude until 21:30pm, since still a reasonable amount of people are within the building. Despite a few outliers, the level of noise remains at a relative low magnitude until 07:00am the following day. From that time onwards, cleaners start their work and machines such as generators for the climate system run in a higher mode, which result in an increase of the noise magnitude. At around 09:00am, classes start and hence many students are within the building, causing the magnitude of noise to be riding to the same level as seen on 13:30pm the day before.

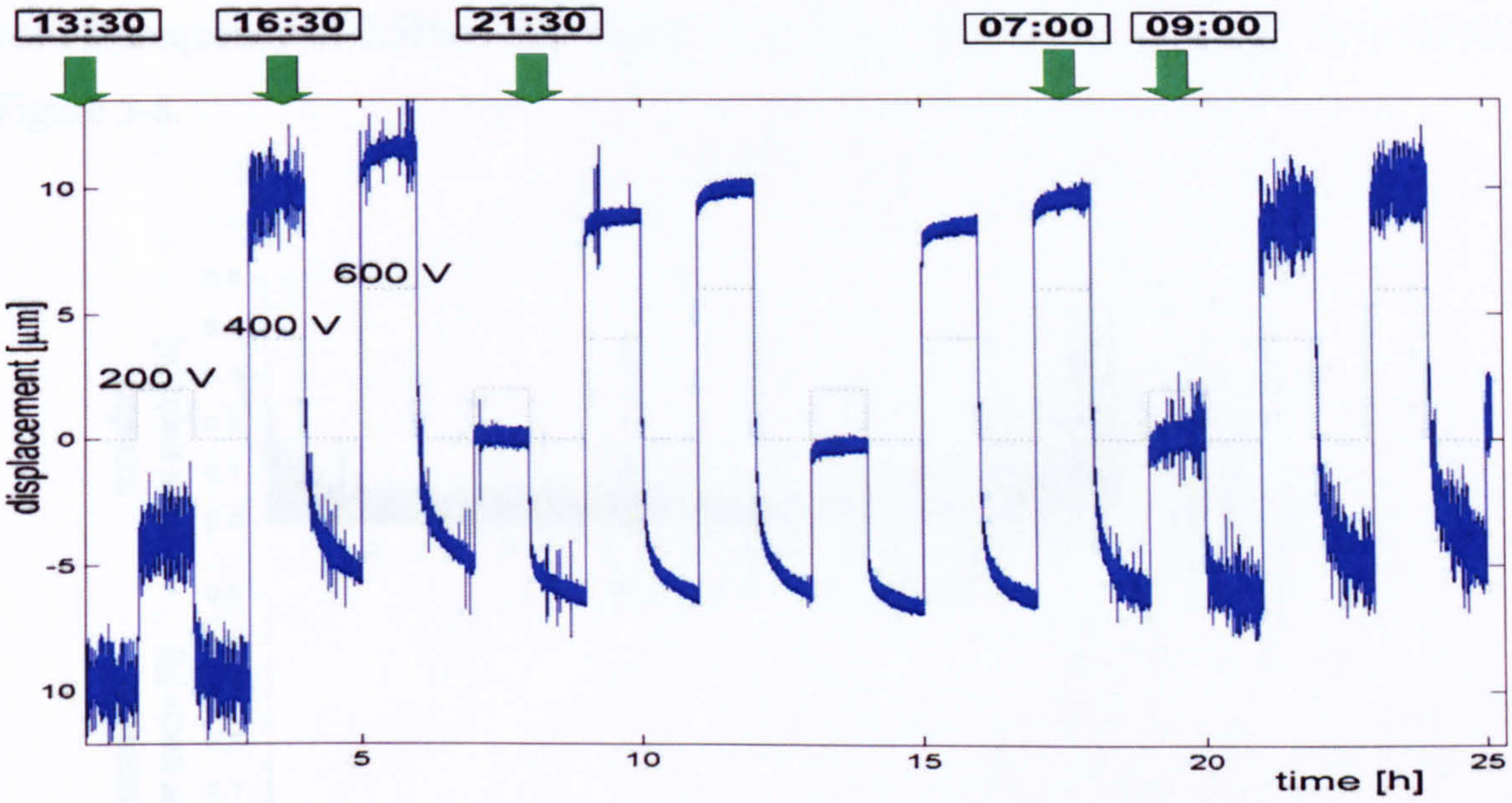

Figure 5-5 The noise, caused by the building has been measured during a long term measurement of 24 hours. Step voltages of 200V, 400V and 600V have been applied for a duration of 1 hour. The noise is dependent on the time of the day.

5.2 Restoring means and electrostatic actuator

5.2.1.1 NOA61 glue distributed over the entire lens area as restoring means

In an initial experiment, four relatively large drops of the liquid adhesive NOA61 were placed on top of the µLED structure (Figure 5-6) and the µLens was placed on top. Due to the gravitational and capillary force, the µLens moved towards the negative z-axis.

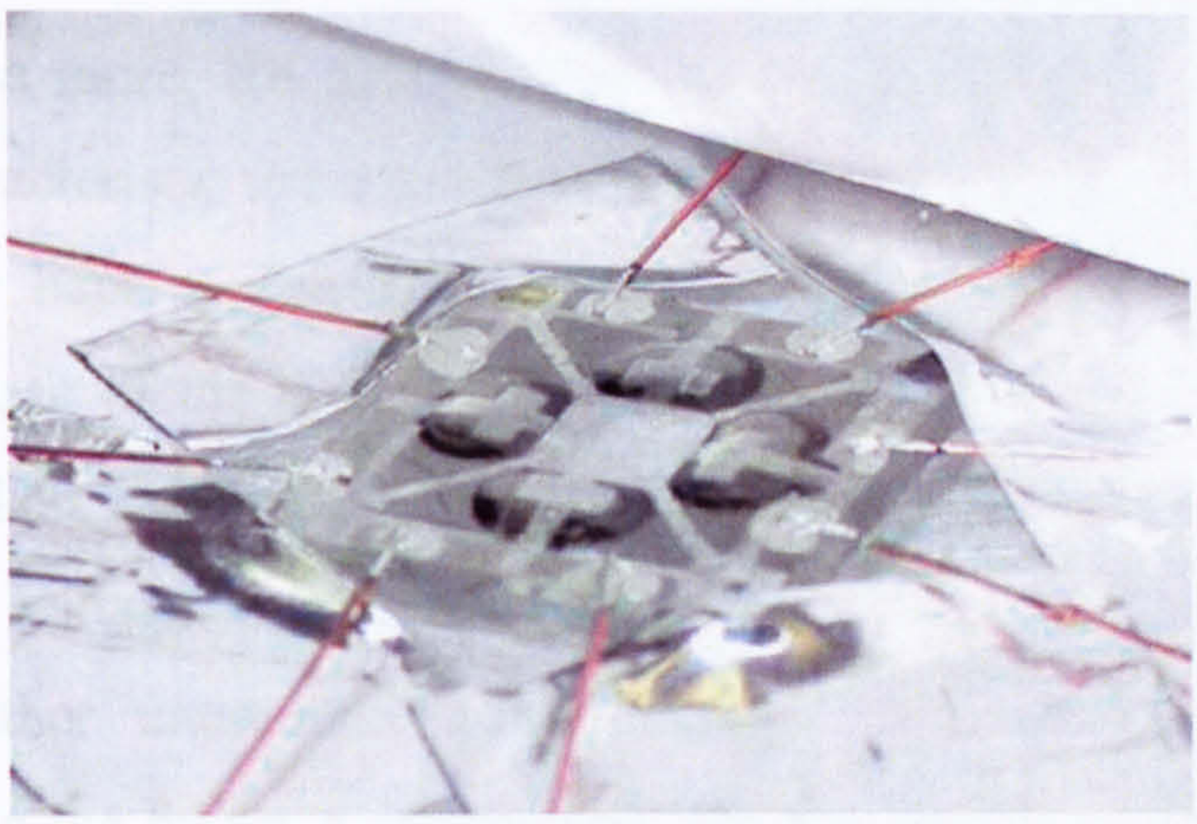

Figure 5-6 Test device with four drops of the liquid adhesive NOA 61 placed over the cavities.

Superimposed over the actual movement is the previously discussed noise. The transient signal from the distance measurement device was analysed in MATLAB® and the normalised power spectrum was calculated as shown in Figure 5-7. From these measurements, the system was characterised and a low-pass filter with the appropriate parameters were chosen. A Butterworth low-pass filter of 10^{th} order was used with a

cut-off frequency of 0.5Hz. The results of the filtering in the time domain are shown in Figure 5-8.

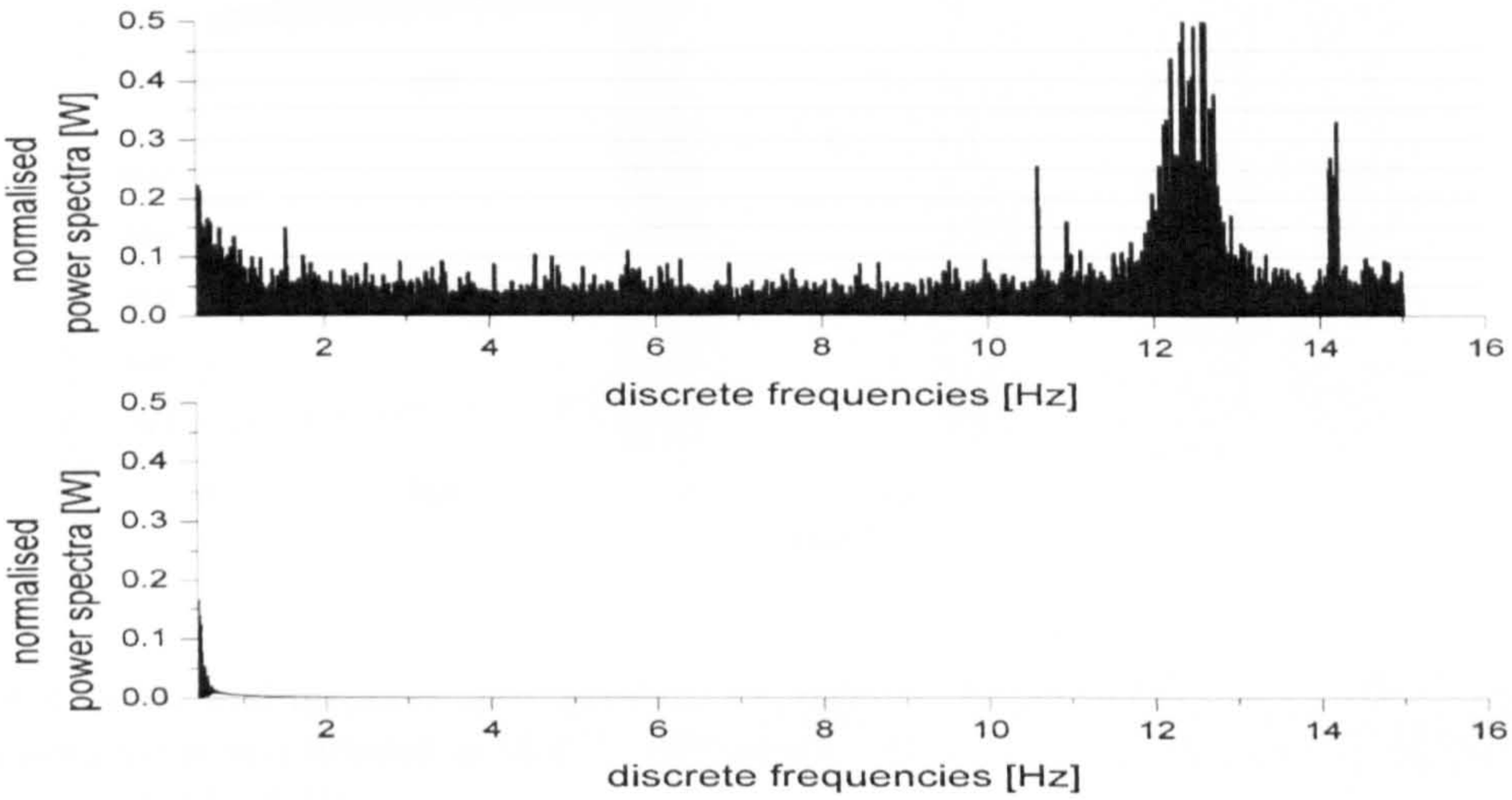

Figure 5-7 The transient signal from the sensor was analysed with the FFT algorithm to extract parameters for an appropriate filter. The graph below shows the power spectrum after the signal was filtered with a Butterworth low-pass filter of 10^{th} order and a cut of frequency of 0.5Hz.

After 30 minutes, the μLens is assumed to have reached an equilibrium position at around 394.5μm as shown in Figure 5-8. A voltage of 300V was applied to one pair of electrodes via the connections wires attached to the pads. The distance between the μLens and the sensor increased exponentially. After switching off the voltage, the μLens shortly went back to an initial position of 398.7μm after 200 seconds. After applying 300V once more, the distance from the sensor to the μLens was increased again with the characteristic exponential curve and after switching off the voltage the μLens went nearly back to the value of the previous cycle. A steady but rather unpredictable increase of the distance towards the negative z-direction occurs in the following cycles. This experiment revealed that (1) an electrostatic force is developed by application of a voltage at the electrodes, but (2) the use of a liquid as a restoring means exhibits rather unpredictable behaviour. This measurement is of value nevertheless since in the future, a viscoelastic polymer will be used between the μLens and μLED as restoring means to counteract the attractive capillary force originating from the liquid UV-curable adhesive. No electrolytic effect was observed on the liquid due to the high voltages. Static alignment via the dynamic approach is explained in Chapter 6.

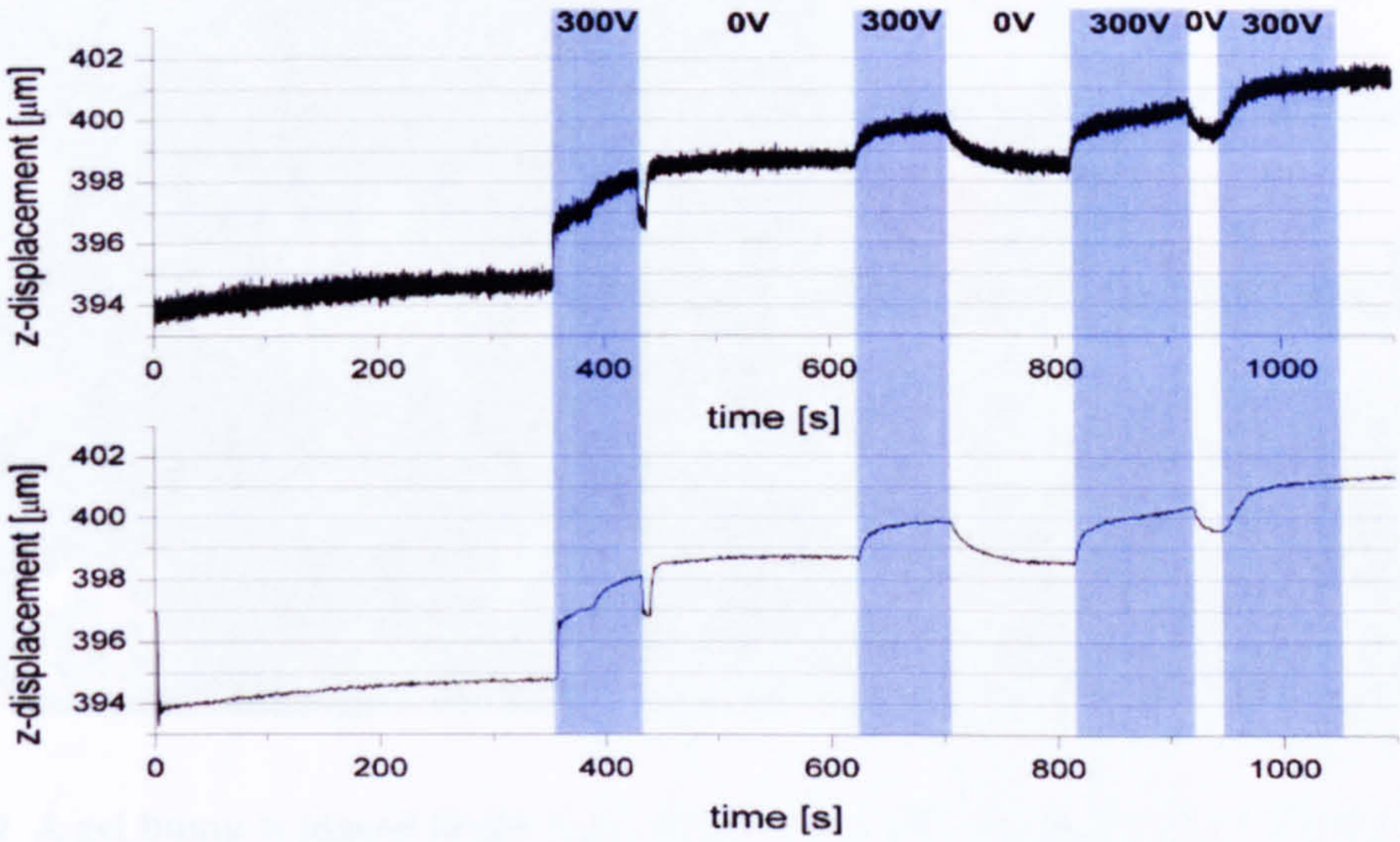

Figure 5-8 Noise and displacement signal as recorded from the micro-epsilon device. The bottom graph shows the signal filtered in MATLAB® using a Butterworth lowpass filter of 10th order and a cut of frequency of 0.5 Hz.

5.2.1.2 Gel pads as a means of restoring force

Due to the capillary effect of the liquid adhesive, another restoring force material was investigated. A silicone gel similar to the one found in IT hand-wrist support cushions was considered. Gel exhibits densities similar to liquid but have the structural coherence of a solid therefore no capillary effect is to be expected. One of the main advantages is the ease of fabrication of these restoring means compared to cantilever beams. Another advantage of gel is its isotropic elastic properties, which are of importance for the lateral magnetic movement. For the initial experiments, each of the four small pieces of gel was cut out and placed into the gel cavities situated on the µLED as shown in Figure 5-9. The gel bump establishes equilibrium with the restoring force, $\boldsymbol{F}_{res}$, being equal to the sum of the electrostatic force, $\boldsymbol{F}_{elec}$, and the gravitational force, $\boldsymbol{F}_{g}$. The gel bumps used differ for each experiment in volume and shape and also lateral placement, which makes them difficult to characterise. The author of this thesis is in contact with chemists from the University of Strathclyde to find a material, which has similar elastic behaviour, but is either photo-curable or thermo-curable. By having control over the shape of the restoring means, and conducting different experiments with changing parameters, one could derive important property information about the material used which is necessary for the analytic and numerical modelling of the system. However, while the adhesion of the gel towards the µLens and µLED is a disadvantage for the control and modelling, it offers benefits for the assembly of the two devices. Once placed, the µLens does not fall off even if the device is tilted 90 degrees.

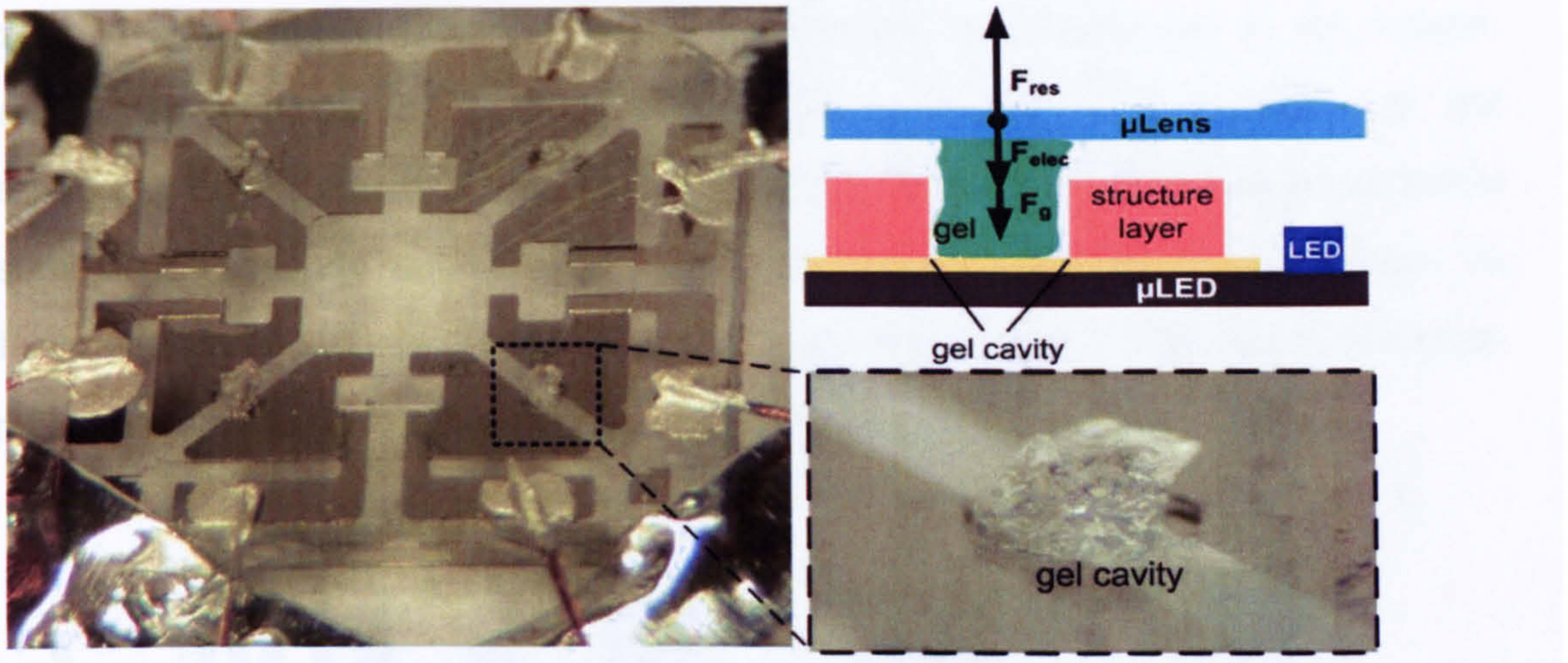

Figure 5-9 A gel bump is placed in the four corners of the µLED within the designated gel cavities. The µLens is then placed on top of it. Gel offers restoring properties and elastic behaviour in all directions.

Figure 5-10a shows a photograph of the system with the µLens posed over the µLED with gel bumps placed in between. The wires establish the voltage supply for the electrostatic actuator. Figure 5-10b gives an impression of the experimental setup. The PC provides via the A/D output card the time variant voltages between 0V and 10V which is fed into the voltage controlled high voltage generator. This device is necessary to achieve the high electrostatic field strengths for the actual movement. The displacement is measured by using the optoNCDT2400. The z-displacement signal is then fed back into the computer via a RS-232 interface (serial port). The MATLAB® SIMULINK® software package analyses the data and generates the time variant voltages on the PC output. The data filtering is again carried out within MATLAB® by using a 5th order Butterworth filter with a cut off frequency of 1Hz.

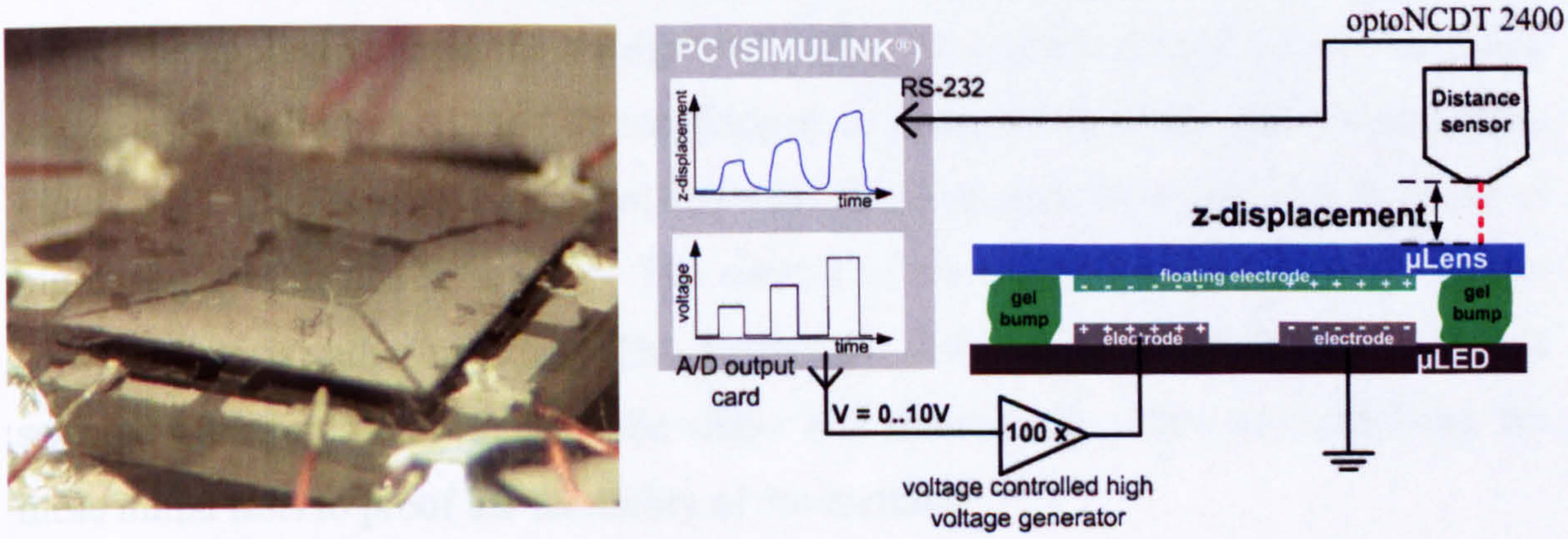

a) b)

Figure 5-10 a) The µLens is placed on top of the µLED. b) The step voltage from the PC is multiplied by a factor of 100 and the displacement is measured using the optoNCDT 2400. The information is then fed back into the PC via the RS-232 interface.

Figure 5-11 shows the unfiltered signal at the top and the filtered one at the bottom. Different step voltages of 100V, 200V, 400V and 600V are applied and the corresponding displacement is recorded. Only the relative value of the displacement is measured as the absolute value depends on the initial distance of the distance sensor. A displacement can be already observed for a voltage step of 100V. The largest variation, 10μm, is observed for an applied voltage of 600V.

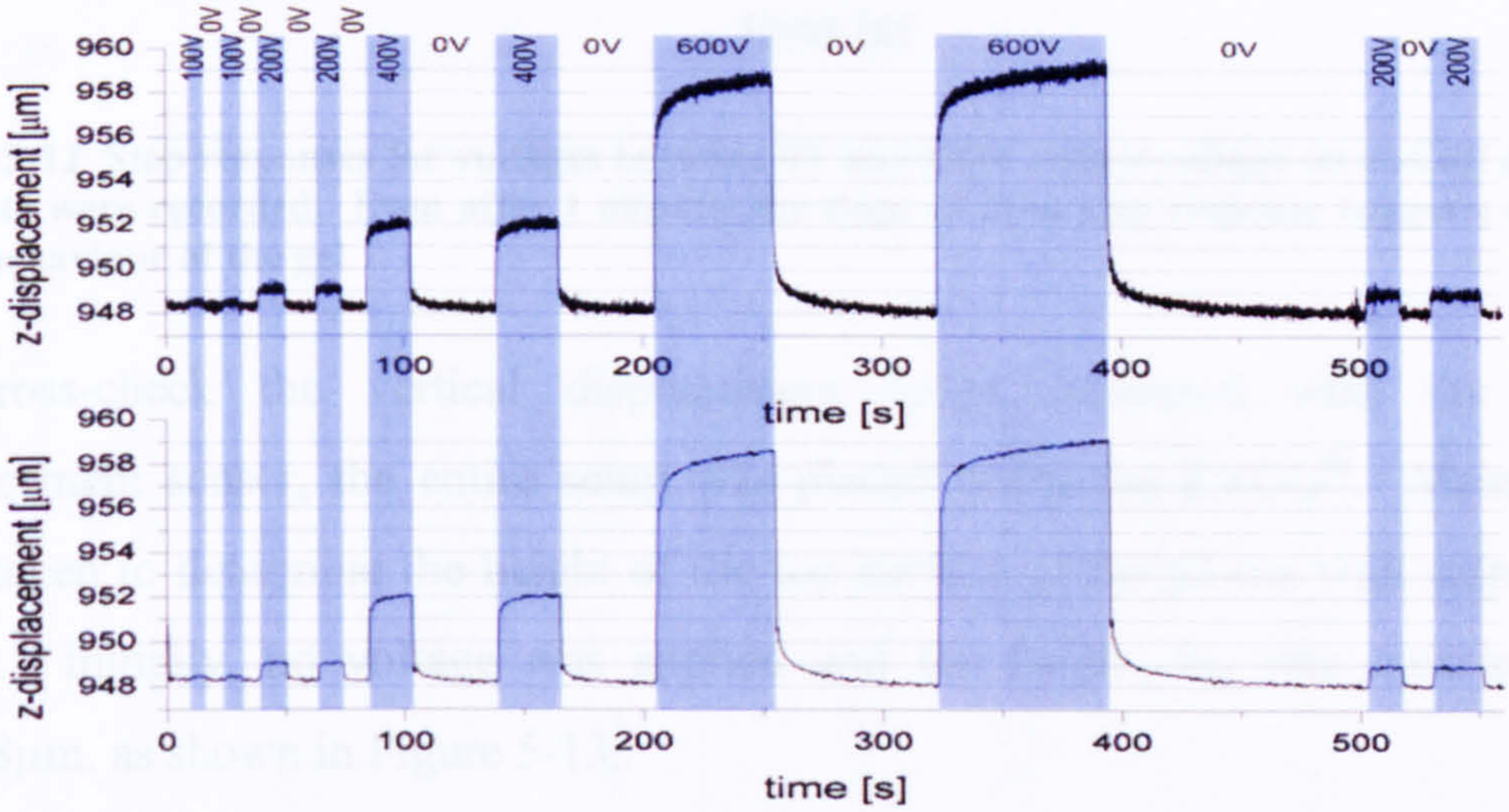

Figure 5-11 Relative displacement of the μLens array for step responses of 100V, 200V, 400V and 600V without and with the noise filtered out. The graph below is the filtered signal by using a Butterworth filter 5th order with a cut off frequency of 1Hz.

By using gel bumps of different (unintended) arbitrary shapes, the displacement of the μLens shown in Figure 5-12 was recorded. The voltage ranges from 0V to 600V by 50V increments, a voltage duty cycle of 50% and a period of 2 minutes. Below 50V the displacement is not detectable due to the noise of the signal. Above this value, the creep behaviour of the viscoelastic gel bumps becomes visible since, even after one minute of voltage on-time, the gel bump does not establish static equilibrium. The higher the applied voltage, the stronger the effect. The magnitude of the step response obeys a parabolic behaviour. The difference in shape as well as magnitude between Figure 5-11 and Figure 5-12 suggest that even slight changes in the gel bumps result in big changes in device behaviour. The control of the shape including height within a certain range is rather random. The gel bumps were cut out from the gel bulk and selected afterwards according to the shape and dimensions. This was satisfying for these initial tests to proof the feasibility of the method.

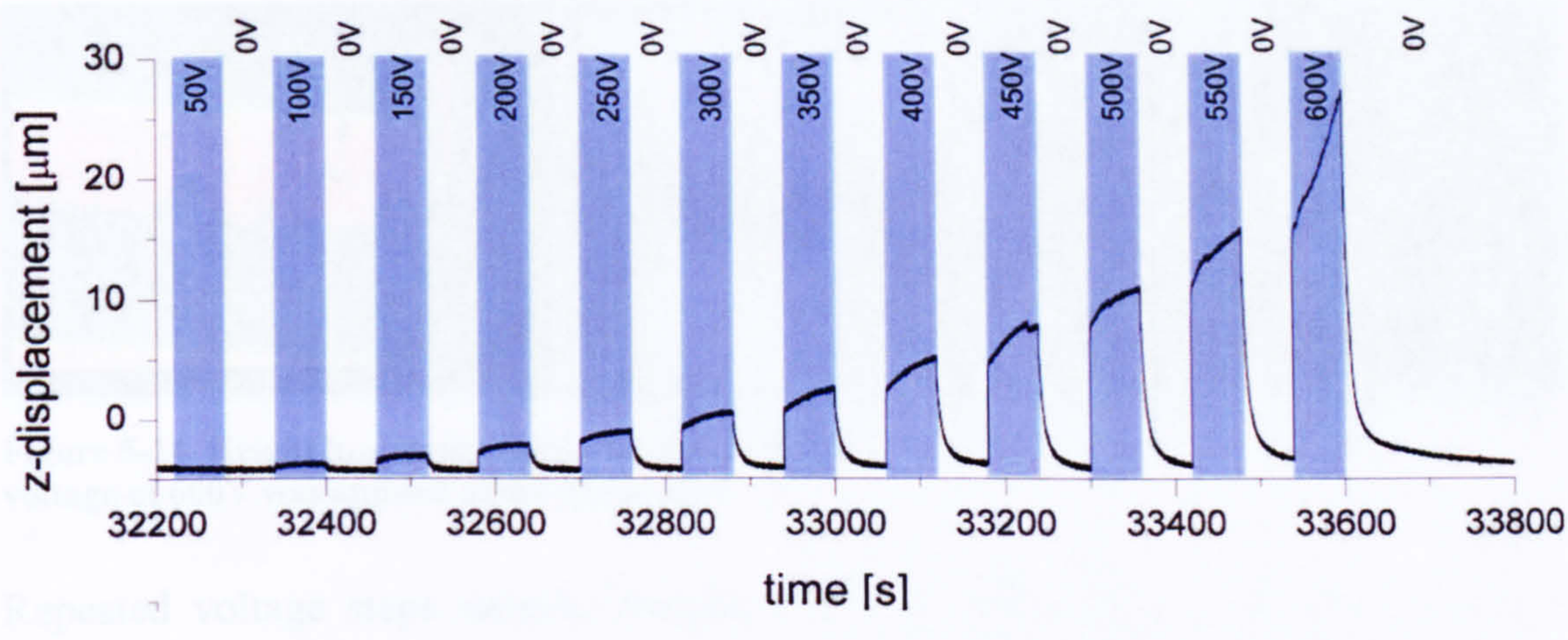

Figure 5-12 Step responses for voltages between 0V and 600V with a voltage on and off duration of 1 minute were recorded. Even after 1 minute, the slope of each step response suggests viscoelastic creep behaviour of the gel.

To cross-check the vertical displacement range measured with the confocal displacement sensor, the entire setup was placed under the ZYGO®. Measurements were taken to determine the height of the top surface of the µLens with respect to the tracks. Initially, no voltage was applied and the height, h_0, was measured to be 264.68µm, as shown in Figure 5-13.

Figure 5-13 Height h_0 measured from the top surface of the µLens with respect to the surface of the µLED.

A voltage of 600V was then applied between the electrodes which yielded a height, h_{600}, of 188.34µm (Figure 5-14). In other words, the edge of the µLens, has moved over 75µm. In a second measurement, the height of the SU8 structure layer was determined to be between 30 and 40µm.

Figure 5-14 Height h_{600} measured at the same position as seen in Figure 5-13. This time, a voltage of 600V was applied at the electrodes.

Repeated voltage steps ranging between 0V and 600V with a 50V increment were performed over a duration of more than 16 hours as shown in Figure 5-15.

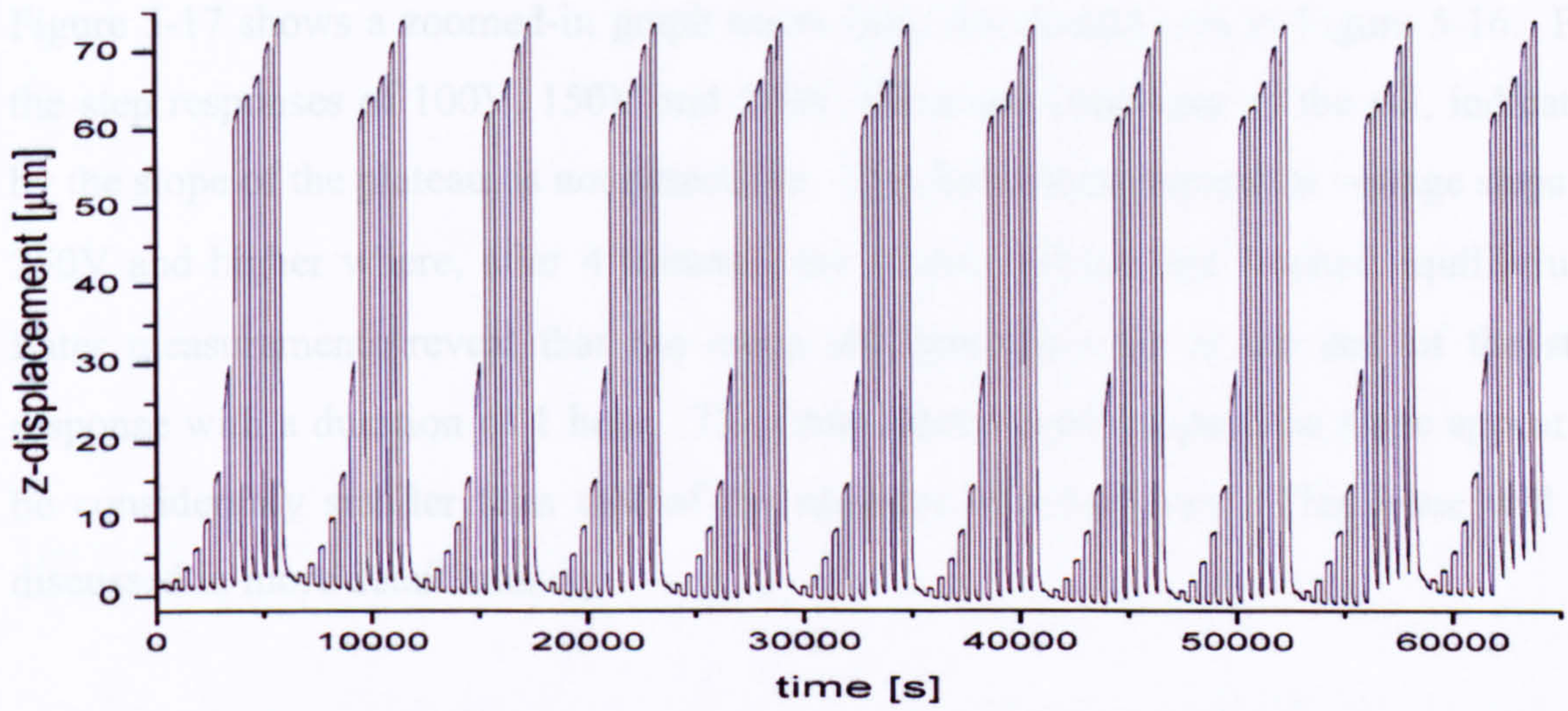

Figure 5-15 Long term step response measurements of more than 16 hours with voltages between 0V and 600V and an increment of 50V.

With this assembly, a displacement of around 1µm (Figure 5-16 and Figure 5-17) can already be observed at a voltage step of 100V. Figure 5-16 shows that, up to a voltage of 350V, the height as well as the slope of the plateau follows a parabolic curve. At 400V however, the behaviour of the slope changes. Flatter slopes are measured for voltages between 450V and 600V. After a certain compression of the gel bump, the restoring force is believed to have increased more than the electrostatic force.

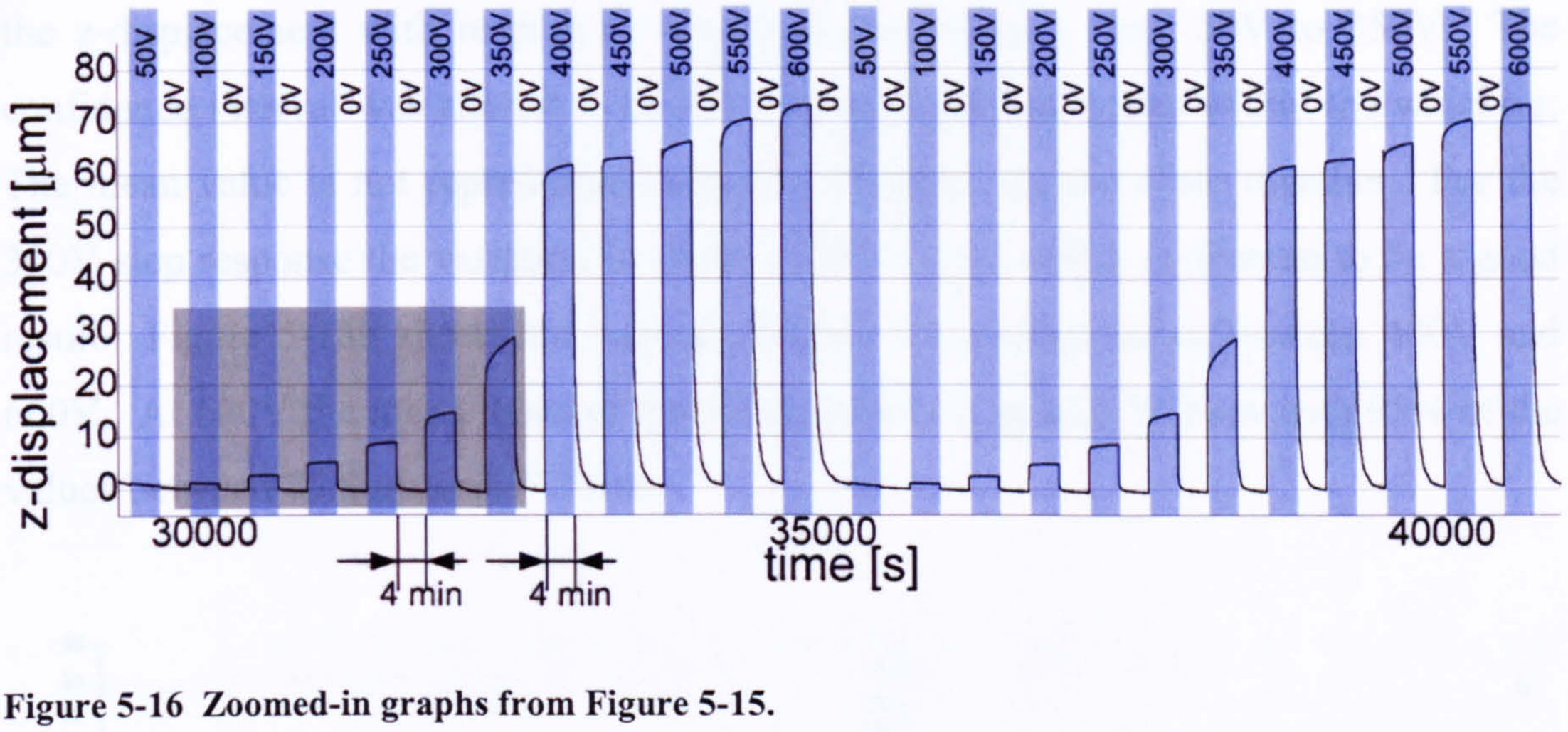

Figure 5-16 Zoomed-in graphs from Figure 5-15.

Figure 5-17 shows a zoomed-in graph taken from the shaded area in Figure 5-16. For the step responses of 100V, 150V and 200V, the creep behaviour of the gel, indicated by the slope of the plateau, is not detectable. This behaviour changes at voltage steps of 250V and higher where, after 4 minutes, the µLens still has not reached equilibrium. Later measurements reveal that the creep still remains even at the end of the step response with a duration of 1 hour. The time constants of the positive slope appear to be considerably smaller than that of the negative step response. This issue will be discussed in more detail later on.

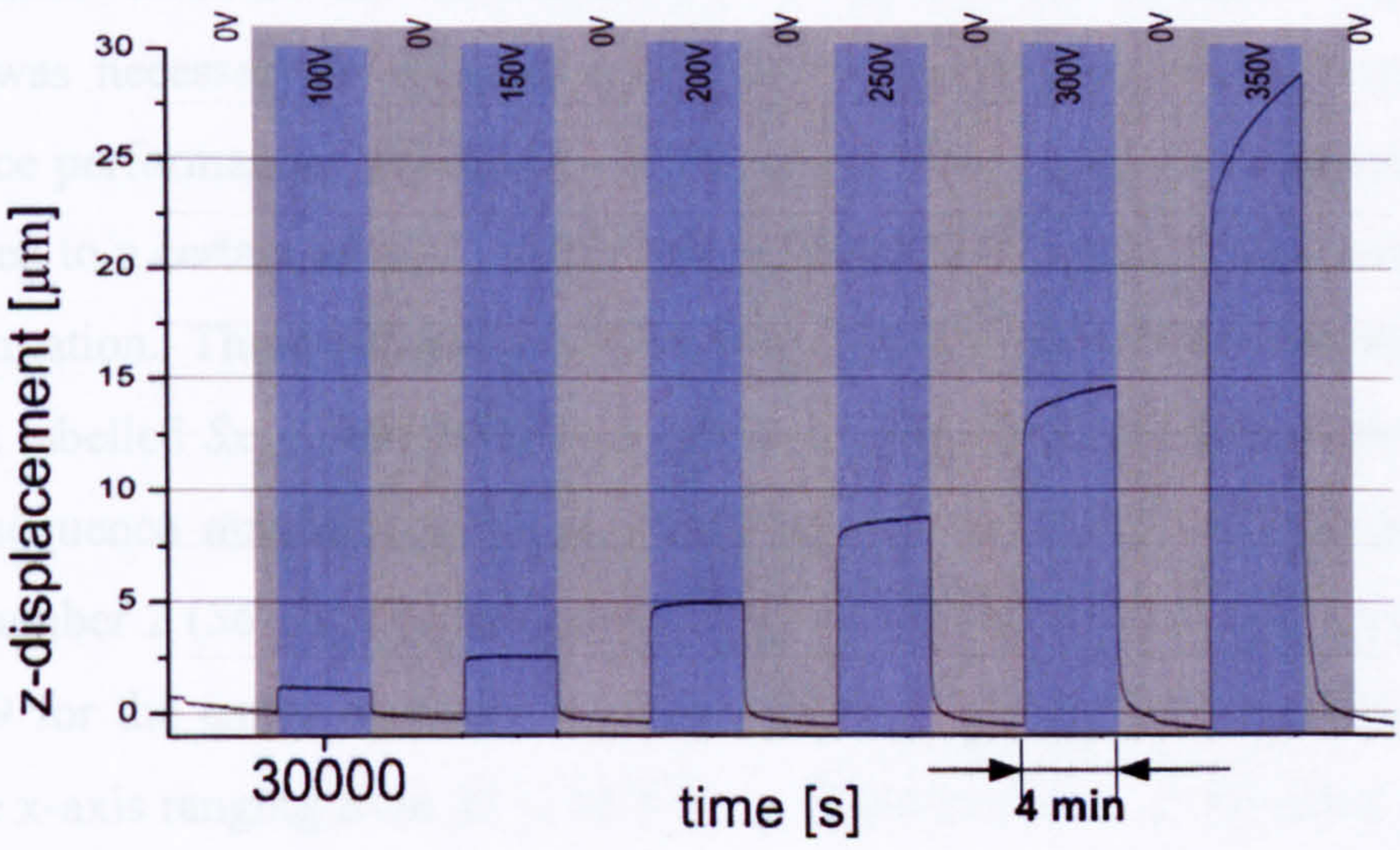

Figure 5-17 Zoomed-in graph taken from the shaded area in Figure 5-16. Voltage on and off time is 4 minutes. A slope at the end of each plateau at voltages higher than 200V indicates that creep behaviour is prevalent.

Step responses for each voltage have been compared over the measured time interval. For each step response, 11 values of the displacement were obtained from the filtered signal (Figure 5-15). Figure 5-18a shows the statistical variation (mean and range) of

the z-displacement with respect to a voltage step ranging from 50V to 350V. The confidence interval was chosen to be 95% representing the values within the whiskers. The mean value is not represented since the whiskers are too close together. For the 300V step response the variation is of the order of 1μm which is deemed to be a good result. Figure 5-18b shows the values obtained for voltage steps between 400V and 600V. At 600V the mean value of the displacement is around 76.5μm with 95% of the values between 75.8μm and 77.2μm.

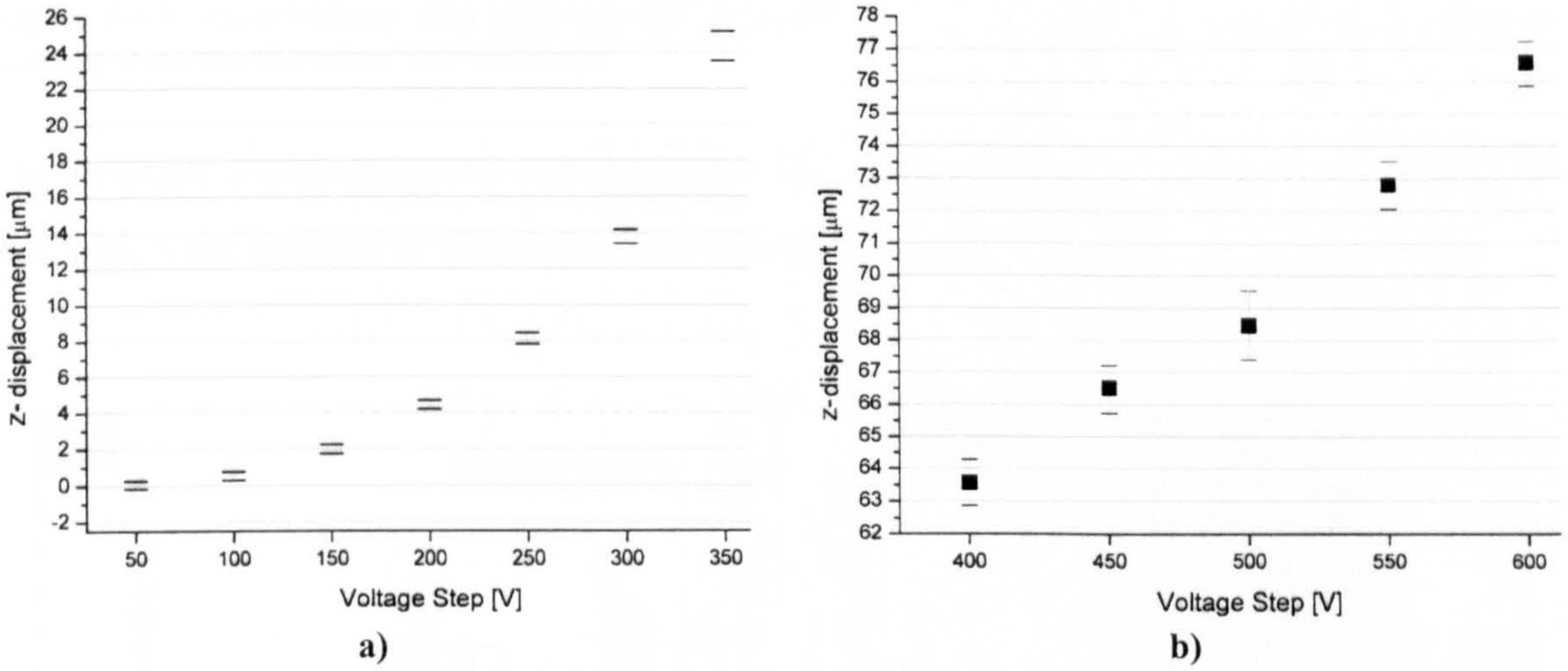

Figure 5-18 Error bar diagram where 11 measurements of each step voltage are analysed from the measurement seen in Figure 5-15. The confidence interval was chosen to be 95%.

Due to external vibrations and the non trivial behaviour of the viscoelastic gel bump, a procedure was necessary to eliminate possible outliers that would not represent the actual device performance. By using a Butterworth filter, these disturbances can only be eliminated to a certain extent. Additional filtering for the entire signal would distort useful information. Three sequences of increasing voltage steps were undertaken. Each sequence is labelled *Sx_y*, with *x* being a certain voltage step within a sequence, and y being the sequence number itself. In the following, the voltage step response 6 in sequence number 2 (*S6_2*) is investigated. Figure 5-20a shows the zoomed in graph of Figure 5-19 for the entire sequence 2. The different voltage step response labels are beneath the x-axis ranging from *S1_2* to *S12_2*. From this, *S6_2* is extracted and scaled up as shown in Figure 5-20b.

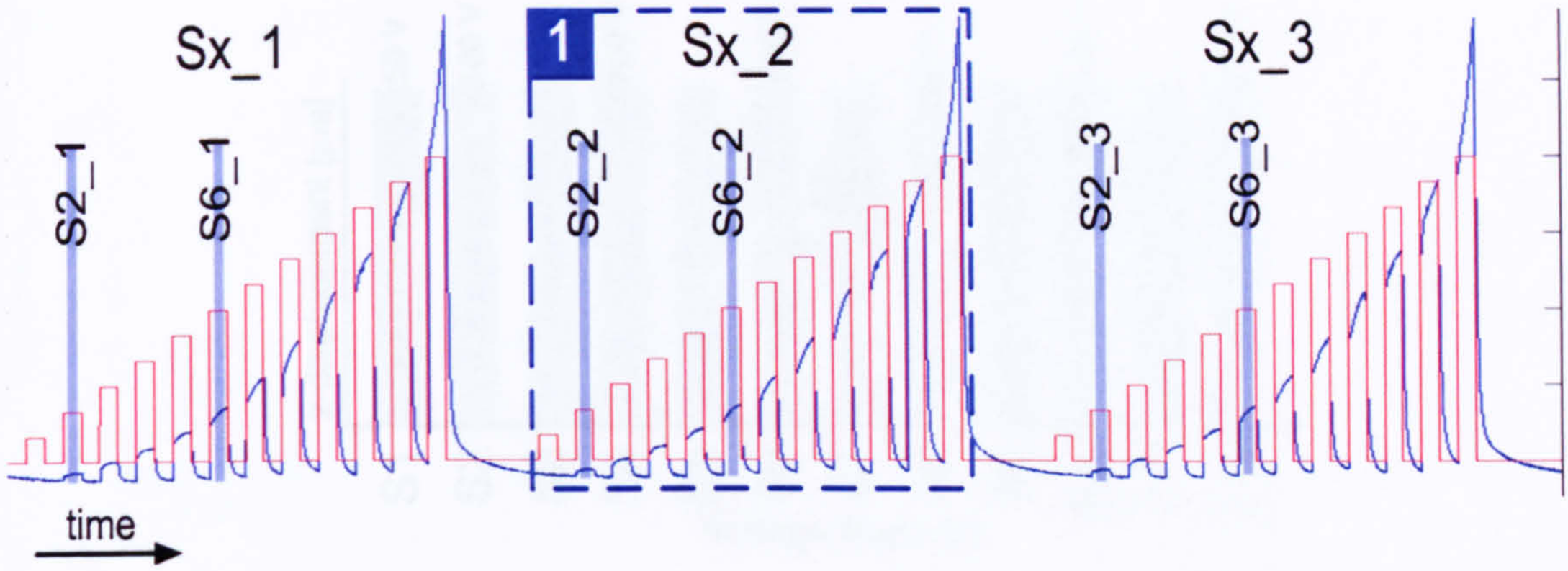

Figure 5-19 An arbitrary step response (S6_2) is used for the explanation of the selective filtering method used for the error bar statistics.

The average displacement is calculated for the values that lie within a defined time slot and which are situated at a defined time from the positive slope of the voltage step.

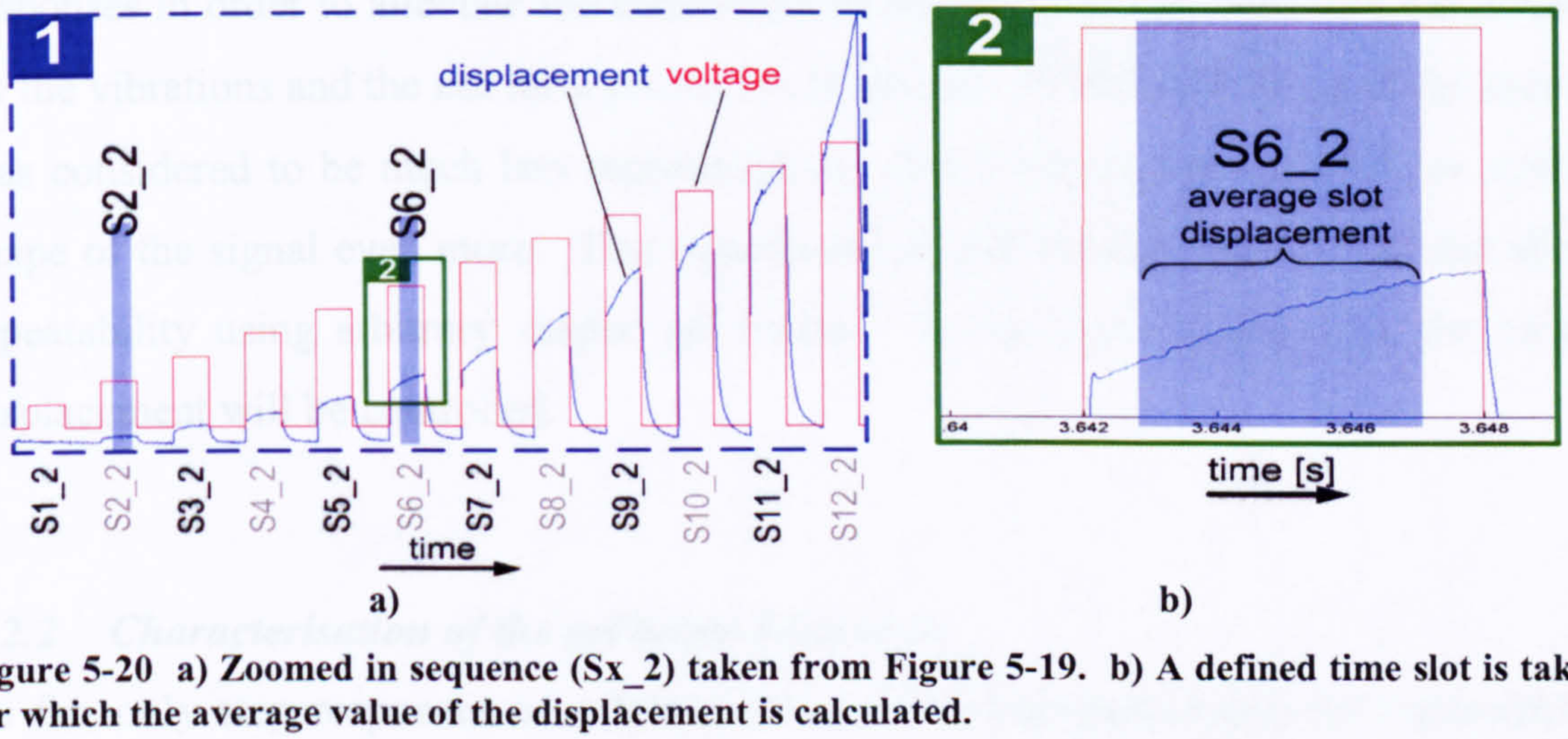

Figure 5-20 a) Zoomed in sequence (Sx_2) taken from Figure 5-19. b) A defined time slot is taken for which the average value of the displacement is calculated.

This measurement is carried out for all step responses and the different values for each step response, originating from the 11 different sequences, are compared and analysed as shown in Figure 5-21. For instance, the value of *S6_2* as seen in Figure 5-20b is placed within the column of all *S6* step responses which represent 300V.

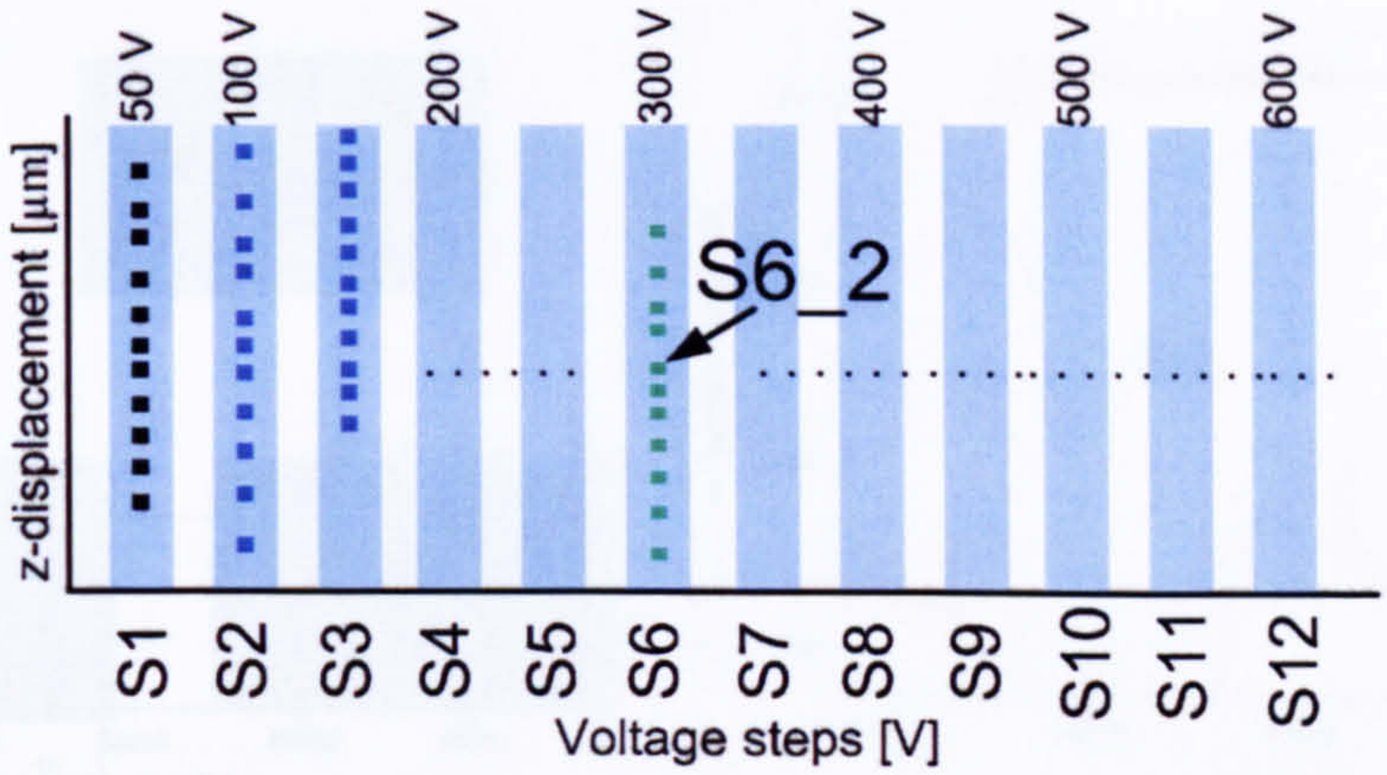

Figure 5-21 The different averaged step responses are arranged with respect to their voltage from which subsequently an error bar is extracted with a chosen confidence interval of 95%.

From these values, the mean and the confidence interval for 95% can be calculated that leads to graphs such as shown in Figure 5-18. It was regarded as appropriate to use the averaging over a well defined time interval in order to compare the different step responses in order to alleviate the differences of the shape of the step responses caused by the vibrations and the not ideal properties of the gel. A further filtering of the system was considered to be much less representative, since it would have altered the overall shape of the signal even more. This experiment should be seen as an initial test about repeatability using arbitrary shaped gel bumps. In the future application, the height displacement will be controlled.

5.2.2 Characterisation of the gel bump behaviour

So far, only step responses of a few minutes were investigated and the repeatability estimated. It is however interesting to see, how the gel bumps perform if a step voltage of 1 hour is applied. Figure 5-22a shows the step responses of 200V, 400V and 600V for a voltage on and off-time duration of 1 hour. Figure 5-22b is the zoomed in graph seen in Figure 5-22a. At the positive step response, the displacement starts with a steep slope and settles at around 250µm from which it continues to creep for another 30 minutes. Thereafter it reaches equilibrium. The negative step response appears to be slower than the positive one and the creep behaviour is much more accentuated as is indicated with the slope β.

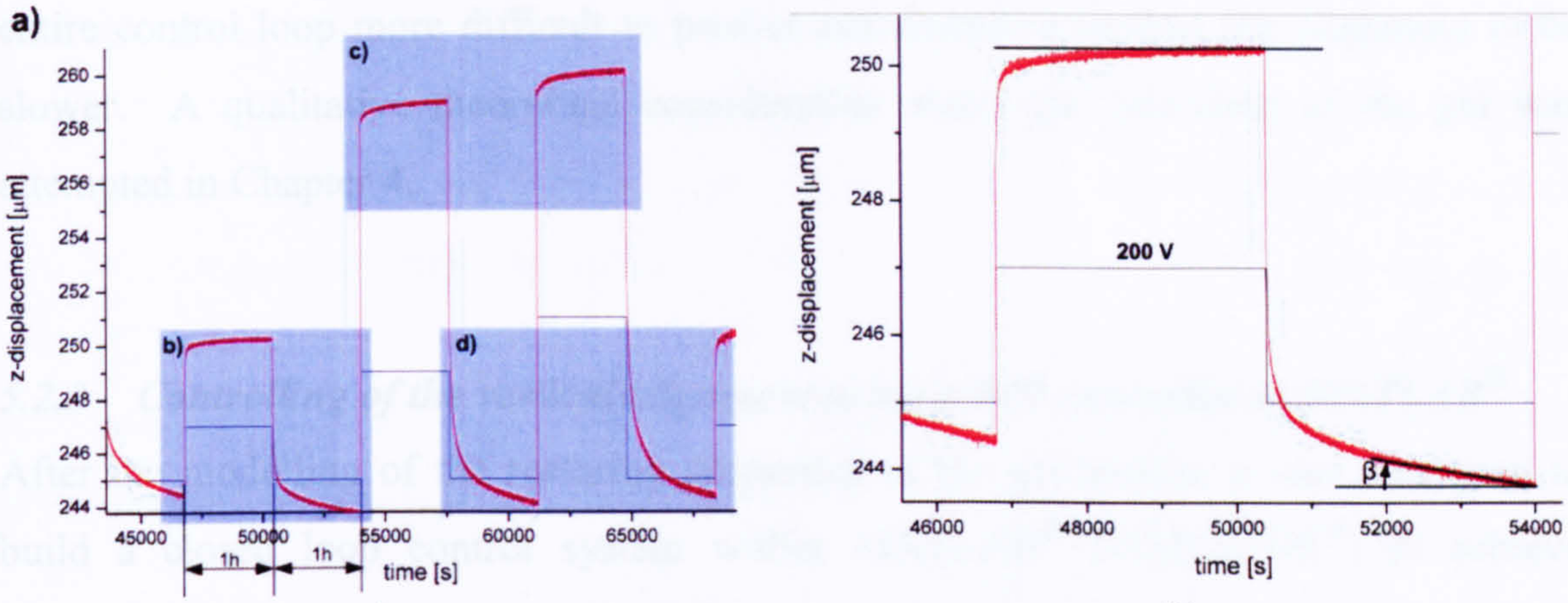

a) b)

Figure 5-22 a) Step responses of voltage steps of 1 hour duration were recorded. b) The zoomed in step response taken from a) with a voltage step of 200V and a duration of 1 hour.

Figure 5-23c represents the zoomed in graph within area c) shown in Figure 5-22a. Whereas at a voltage step of 200V, an equilibrium was established which caused the creep to a halt, the 400V step response continues to creep with a slope, β_4, even after a duration of 1 hour. At a voltage step of 600V this effect becomes even more apparent, and indicated by the slope β_6. Further long term step responses (>2 hours) would be necessary to investigate, whether or when the creep stops before the µLens touches the µLED. Certainly, the break down voltage, would also be a limiting factor. The negative step responses are similar to the positive ones with the difference that the negative step responses are slower. This effect is attributed to the adhesive properties of the gel which come in effect when the µLens is released (Figure 5-23d).

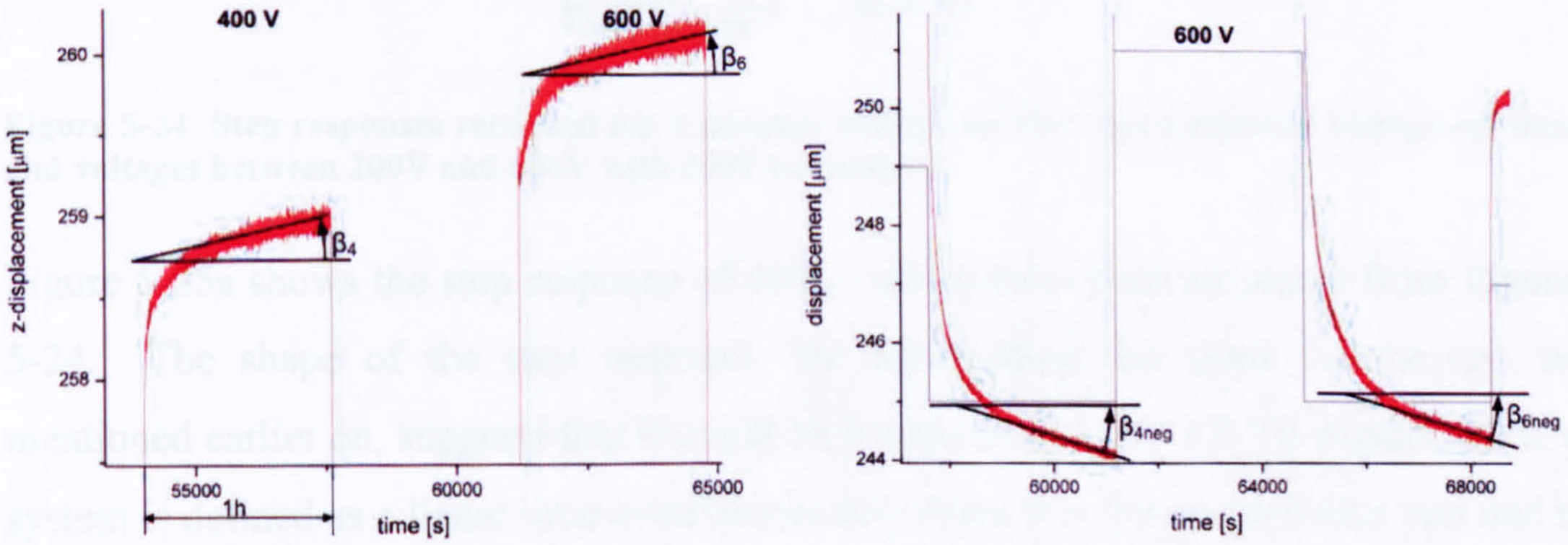

c) d)

Figure 5-23 c) Positive 400V and 600V step response show even after one hour a viscoelastic creep behaviour (this graph is a zoomed in image of the shaded area c) of Figure 5-22a. d) Negative step response from 400V and 600V (graph is a zoomed in image of the shaded area d) within Figure 5-22a).

The difference between the positive and negative step response can be considered to be a hysteresis which is an unwanted property of the used material. In particular the analytical calculation will be challenging if not impossible to obtain. It also makes the

entire control loop more difficult to predict and therefore renders the alignment to be slower. A qualitative theoretical consideration about the behaviour of the gel was attempted in Chapter 4.

5.2.3 Controlling of the vertical alignment using a PID controller in MATLAB®

After the modelling of the restoring properties of the gel bumps, it was attempted to build a closed loop control system within MATLAB® (SIMULINK®) to achieve different displacements very accurately. For that purpose, the step response was recorded as shown in Figure 5-24. The voltage step started from a value of 200V with 100V increments and a voltage on time of 2 minutes and a voltage off time of 4 minutes. These step responses were measured repeatedly. The slope, due to the viscous behaviour as shown in Figure 5-23, is neglected.

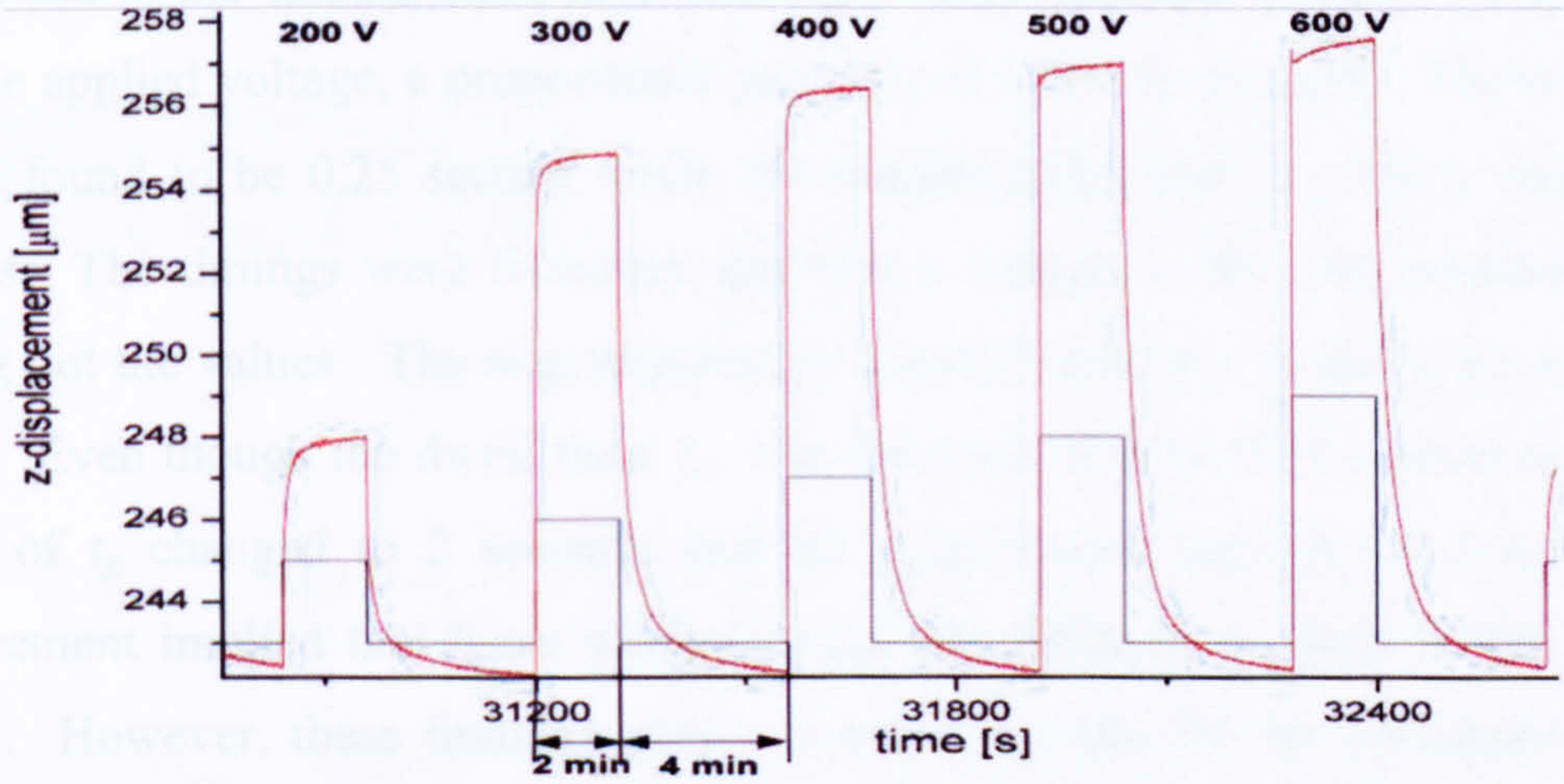

Figure 5-24 Step responses recorded for 2 minutes voltage on time and 4 minutes voltage off time and voltages between 200V and 600V with 100V increments.

Figure 5-25a shows the step response of 400V, which have been extracted from Figure 5-24. The shape of the step response, by disregarding the slope on the top, as mentioned earlier on, suggests that it might be treated as if it was a P-Tn system. Such a system is defined as a linear time invariant model where P is the proportional part and n determines how many energy storing elements, such as a mass or spring, are within the system path.

The assembly was treated as a mere P-T2 system, even though the nonlinear behaviours of the electrostatic actuator and gel render this assumption somehow simplistic. A further simplification was made by just regarding the positive step responses in order to

find the values necessary to feed the PID controller. Even if the system is assumed to be a P-T2, it is impossible to find the properties of the energy elements within by just obtaining the values found from the step response. As an example, one can consider two RC low-passes connected in series. The obtained values of the step response, the gain (K_s), dwell time (t_u) and compensation time (t_g) do not give enough information to derive the values of R_1, R_2, C_1 and C_2 that are used as an electrical example within the governing differential equation shown in equation (4-1).

$$V_{in}(t) = R_1 \cdot C_1 \cdot R_2 \cdot C_2 \cdot \frac{d^2 V_{out}(t)}{dt^2} + \left(R_1 \cdot C_1 + R_2 \cdot C_2\right) \cdot \frac{dV_{out}(t)}{dt} + V_{out}(t) \qquad (5\text{-}1)$$

The initial displacement is 242.3µm and reaches a "quasi-static" value of 256.3µm. "Quasi-static" because the displacement continues after the step voltage has been applied due to the viscous behaviour of the gel. By dividing the relative displacement with the applied voltage, a proportional gain, K_s, of 0.034 is obtained. The dwell time, t_u, was found to be 0.25 second while the compensation time, t_g, has a value of 1.1 seconds. The timings were found by applying a tangent to the step response and by reading out the values. The step response in Figure 5-25b was found to have different values. Even though the dwell time, t_u, was determined to be 0.25 second as well, the values of t_g changed to 2 seconds and the proportional gain, K_s to 0.028. Other measurement implied that these values change for different voltages within a certain margin. However, these findings give a rough estimation for the parameters that are used to program the PI controller for optimal performance.

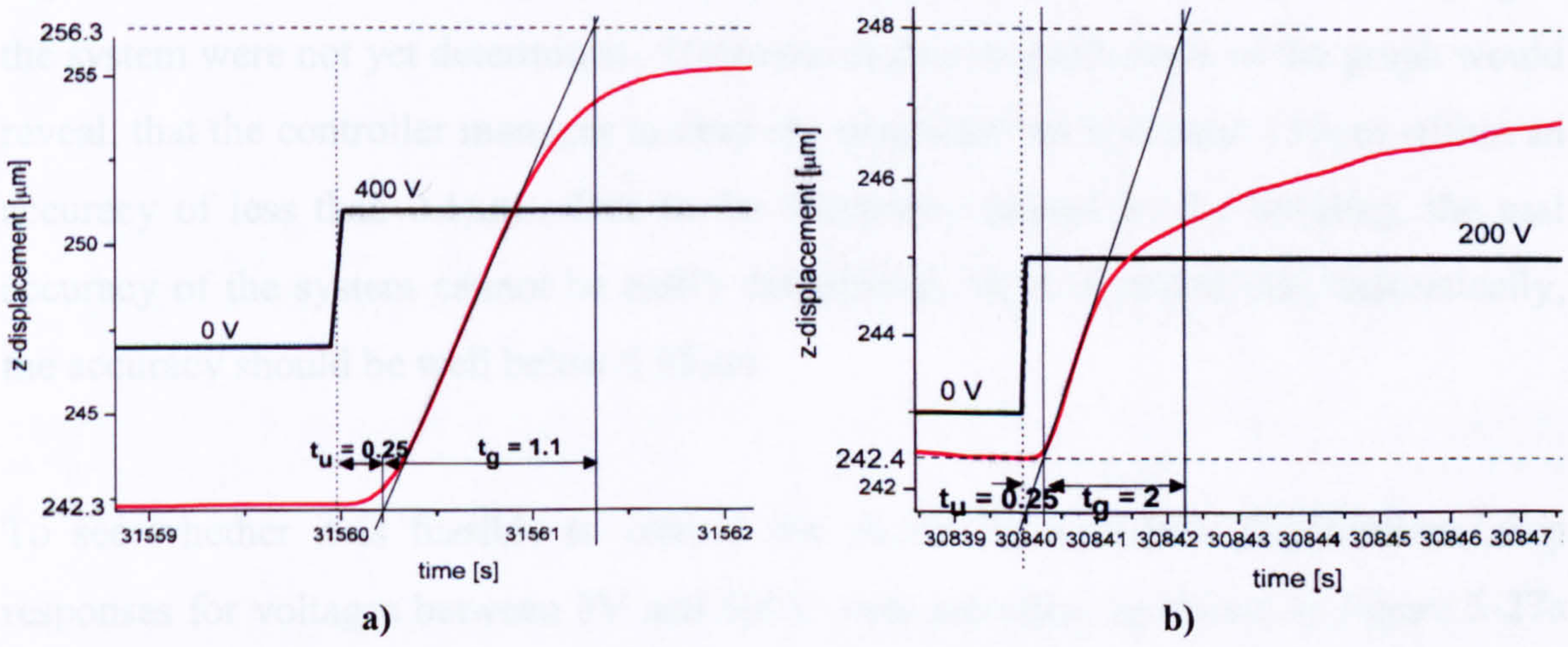

Figure 5-25 a) Step response of a 400V input signal. b) Shows the step response for 200V. While t_u remained approximately the same, t_g changed from 1.1 seconds to 2 seconds. A value in between is taken for calculating the values of the PID controller within MATLAB®.

An initial test was conducted by setting up a controlled loop by using SIMULINK® as a PID controller. The displacement was, as with the previous measurements, determined by using the optoNCDT2400 as shown in Figure 5-26. This set up determines, how accurate the alignment can be conducted. External sensors are essential, since in the near future, no in-situ sensors within the μLED itseft are projected. The values of the static amplification was obtained by considering the graph in Figure 5-24 even though the gel bumps for the controlled loop were different as seen in Figure 5-26b. Nevertheless, as an approximate initial value, the findings of Figure 5-25 were used and a proportional amplification of 0.025 was chosen. The differential part of the controller was not used and, as a value for the integral part, the default value 1 was used.

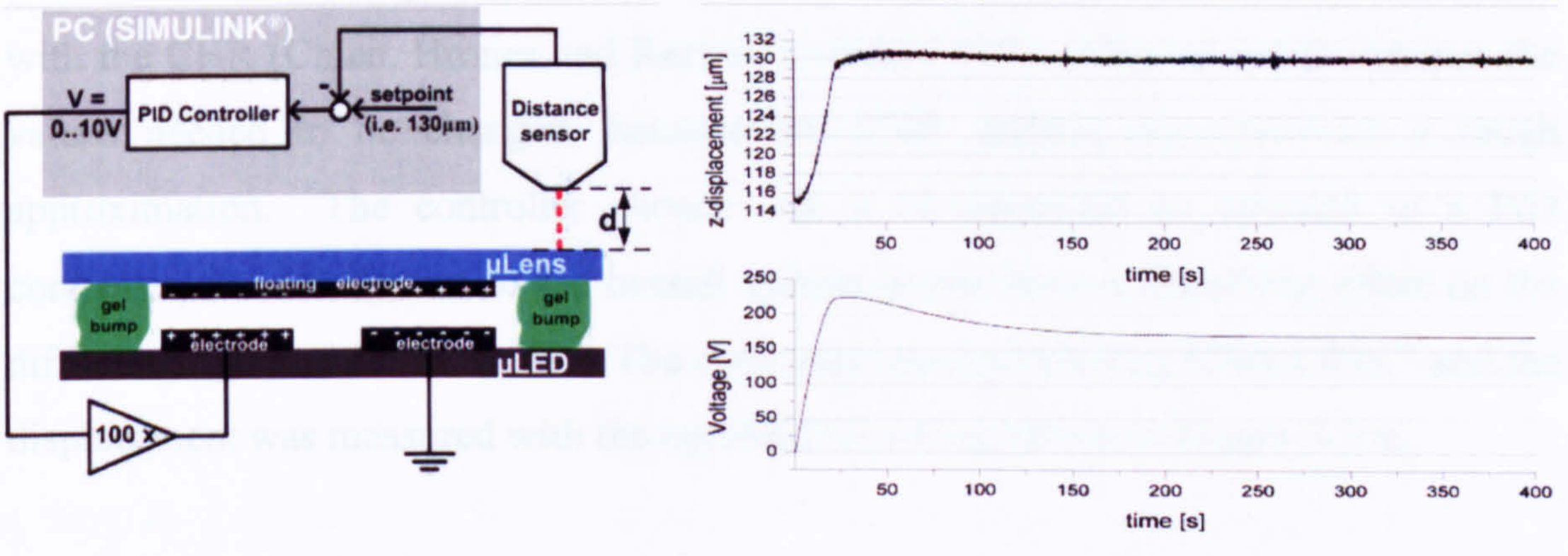

a) b)

Figure 5-26 For an initial setup, only the P and the I part of the within SIMULINK® was used with a proportional amplification of, $K_p = 0.025$ and an integral value of 1.

Starting at a displacement of around 116μm the PID-controller manages to settle to the setpoint value of 130μm within 50 seconds. This is still a long time, but it should be kept in mind that only the PI part of the controller was used and the values belonging to the system were not yet determined. However, higher magnification of the graph would reveal, that the controller manages to keep the displacement at around 130μm within an accuracy of less than 0.1μm. Due to the vibrations caused by the building, the real accuracy of the system cannot be easily determined. It is expected that, theoretically, the accuracy should be well below 0.05μm.

To see whether it is feasible to control the μLens for a certain displacement, step responses for voltages between 0V and 600V were recorded, as shown in Figure 5-27a with a voltage on time and off time of 2 and 6 minutes, respectively. The step responses shown in Figure 5-27b at time slot 1 (ts_1) are not flat but have an angle β. This indicates

that the restoring force does not reach equilibrium but instead slowly continues to increase. Moreover, the response to the rising edge of the step is much faster compared to the falling edge. It is assumed that the adhesive properties of the gel and its memory properties with regard to stress and strain are the main causes of this behaviour. The mathematical description is not trivial as well as the physical effects within the system. In a first approach, the step response of the system at 400V was treated as if it was a P-T2 controlled path again. For this treatment, the slope with the angle β was neglected. By drawing a tangent to the positive slope, the dwell time, t_u, and compensation time, t_g, could be determined to be 0.25 second and 0.65 second, respectively (Figure 5-27c). The proportional gain (K_s) extracted to be around 0.03. The dwell time, t_u, however, seemed to be quite consistent for the different voltage steps with a value in the order of 0.25 second. Knowing this information, the corresponding parameters were calculated with the CHR (Chien, Hrones and Reswick) method [59]. After an initial test run, the values needed to be changed, because the CHR method only provides a rough approximation. The controller chosen was a PI controller as opposed to a PID controller, since the noise of the overall system would have a disturbing effect on the differential part of the controller. The controller was set up using SIMULINK® and the displacement was measured with the optoNCDT2400 as shown in Figure 5-26a.

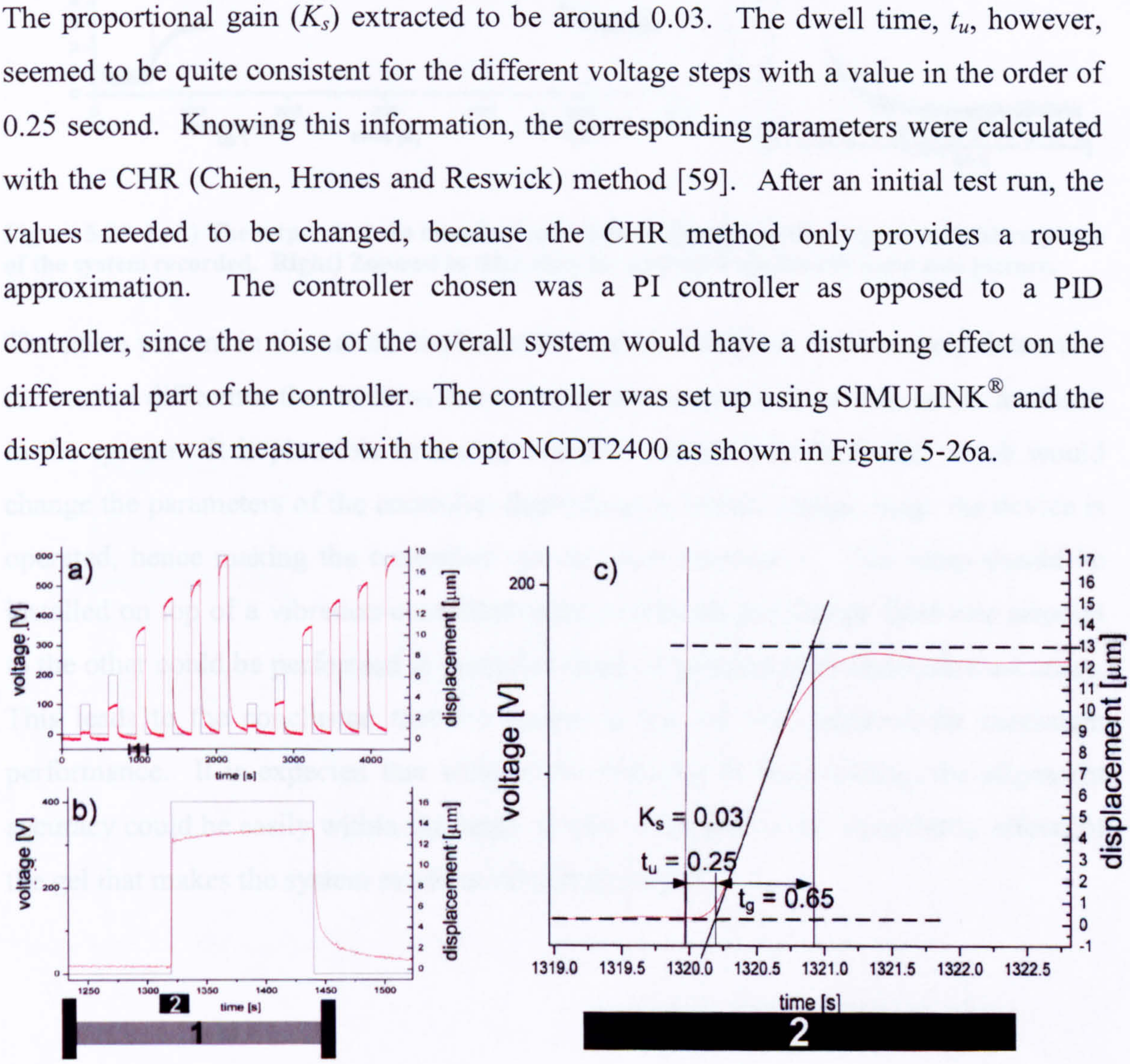

Figure 5-27 a) Step responses were recorded for voltages between 0V and 600V. b) Zoomed in picture of time slot 1 (ts_1) for the 400V step response. c) Time zoom for the time slot, ts_2, where different parameters were obtained.

Figure 5-28 (left) shows the result of a closed loop feedback test run. The grey solid line stands for the intended displacement which was set prior to the run. The black line is the actual displacement. The respective setpoint is achieved after approximately 25

seconds for the positive step response and around 30 seconds to 35 seconds for the negative step response. The right hand side of Figure 5-28 shows the zoomed in time slots for ts_1 at the top and for ts_2 at the bottom.

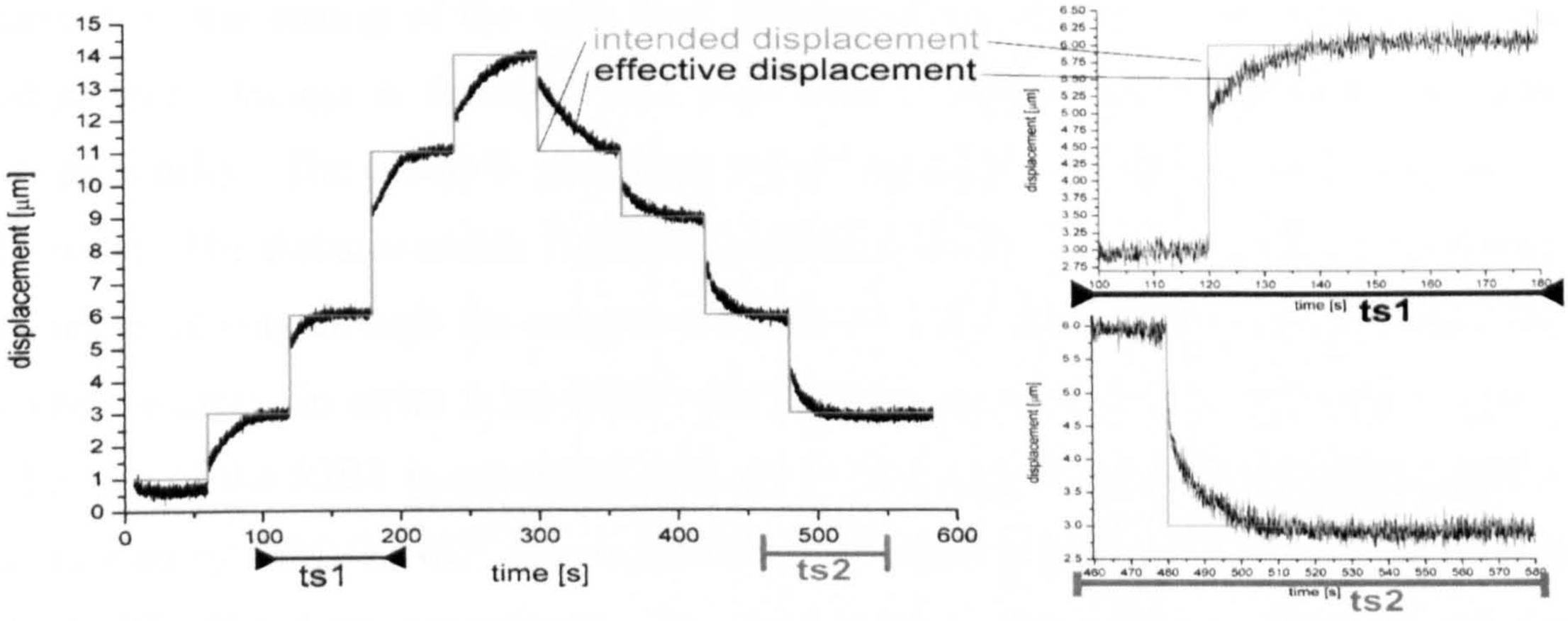

Figure 5-28 Left) The setpoint of the closed control loop is changed in discrete set and the response of the system recorded. Right) Zoomed in time slots (ts_1 and ts_2) from the left hand side picture.

The noise present in the actual displacement makes it difficult to accurately determine the control difference that remains due to the measurement itself as well as the feedback to the system. It is plausible to use an adaptive control loop feedback, which would change the parameters of the controller depending on which voltage range the device is operated, hence making the controlled system more responsive. The setup should be installed on top of a vibration-controlled table. By hand, the change from one setpoint to the other could be performed in much less than 25 seconds with reasonable accuracy. This leads to the conclusion that the system is not yet well adjusted for maximum performance. It is expected that without the vibration of the building, the alignment accuracy could be easily within the range of tens of nm due to the viscoelastic effects of the gel that makes the system mechanically more inert.

5.3 Magnetic lateral movement

The performance of the magnetic actuator was also investigated by focussing the optoNCDT2400 on the vertical edge of the μLens. The measurement of the lateral displacement was difficult since the surface of the vertical edge is rather rough. This is caused by the cutting of the very hard sapphire glass, which causes chipping on the edges even though a diamond saw was used. Figure 5-29 illustrates the setup schematically. The μLens is placed on top of the μLed with small amounts of gel in between. The distance sensor is placed in order to detect lateral movement. A current, which is flowing through the actuator coil of the EDD, is provided by an adjustable DC current source. In series is an IGBT which serves as a switch for the current supply. The gate of the IGBT is connected with the A/D output card of the PC which itself is controlled by SIMULINK®. It provides the gate with voltages of 0V and 4V to switch the IGBT off and on, respectively. The data of the distance sensor is received via the serial port of the PC. With this assembly, it is possible to have the displacement information synchronised with the voltage output and hence current that flows through the actuator coil.

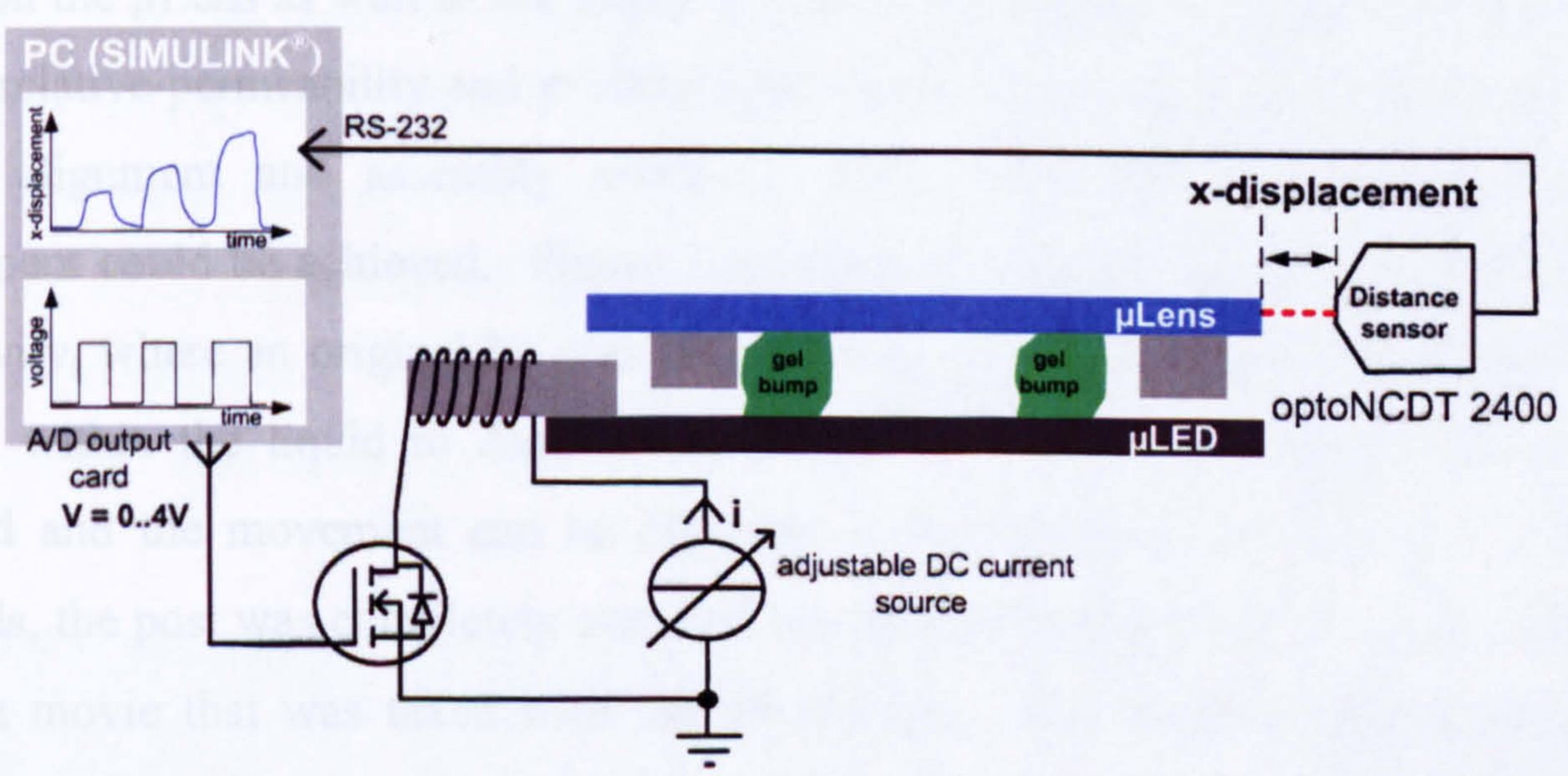

Figure 5-29 Measurement setup for characterising the lateral magnetic actuator.

Figure 5-30 shows a photograph of the assembly described in Figure 5-29. The height of the μLens, 140μm, is considerably smaller than the diameter of the lens of the distance sensor.

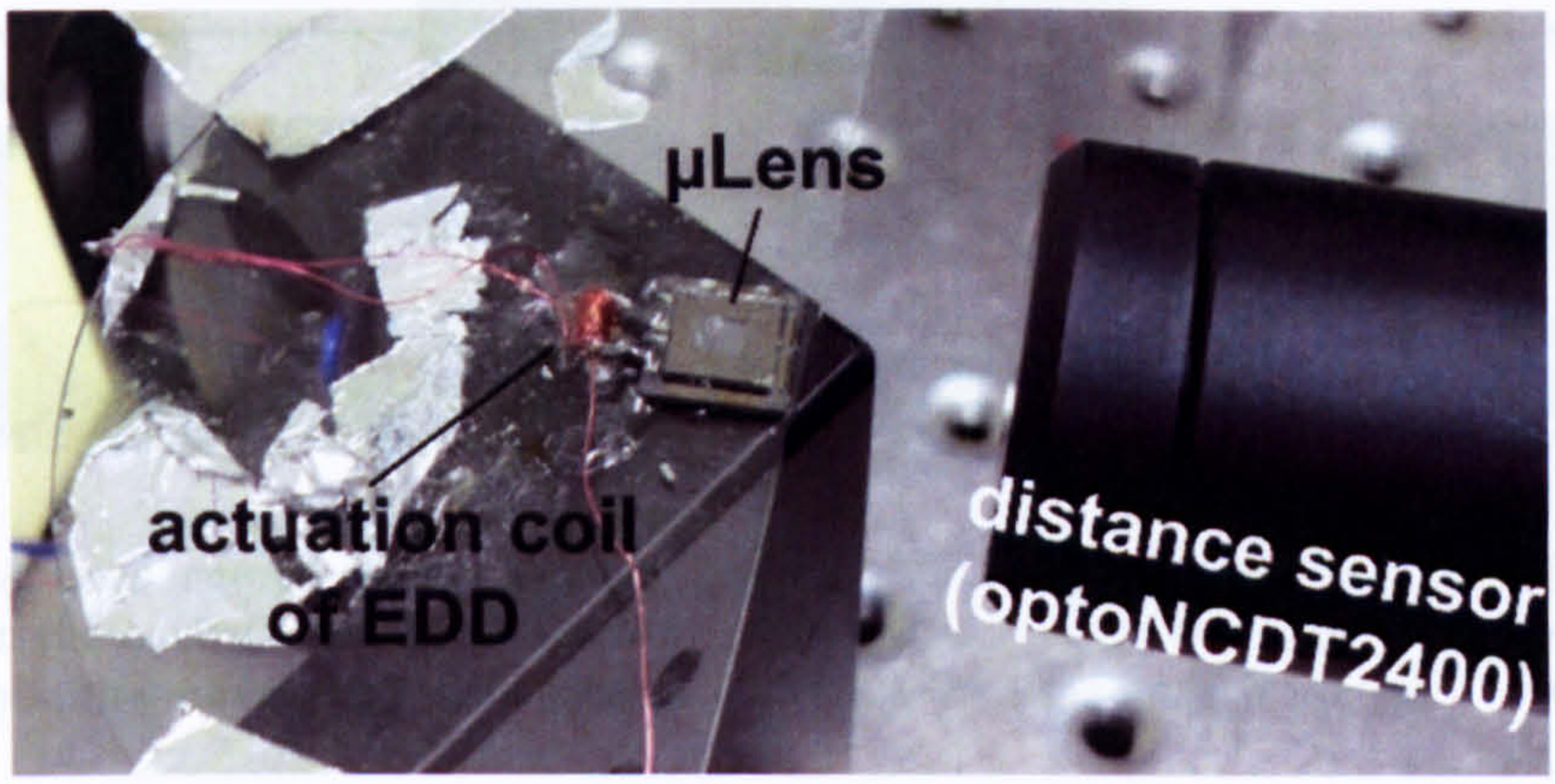

Figure 5-30 Photograph of the distance sensor and a test vehicle for lateral displacement.

The original device, where the magnetic post are used for the attractive force, caused difficulties, since the placement of the μLens was not easy to achieve the best lateral force, due to the rather random gel bumps used as restoring means. Furthermore, the posts on the μLens as well as the tracks and pads of the μLED consist of Ni, which has a low relative permeability and exhibits a hysteresis behaviour that is complicating the entire alignment and assembly process. Even with these drawbacks, magnetic movement could be achieved. Figure 5-31 shows the device (top) and the close up of the cavity, where an original Ni post was inserted. A viscous liquid (silicone oil) was placed within the liquid to dampen the movement. A step current of 400mA was applied and the movement can be observed in the sequence of pictures. After 16 seconds, the post was completely attracted towards the tracks. The sequence originates from a movie that was taken with the microscope. The lateral displacement sensor could not be used since the angle and the sidewalls of the post would have been too narrow.

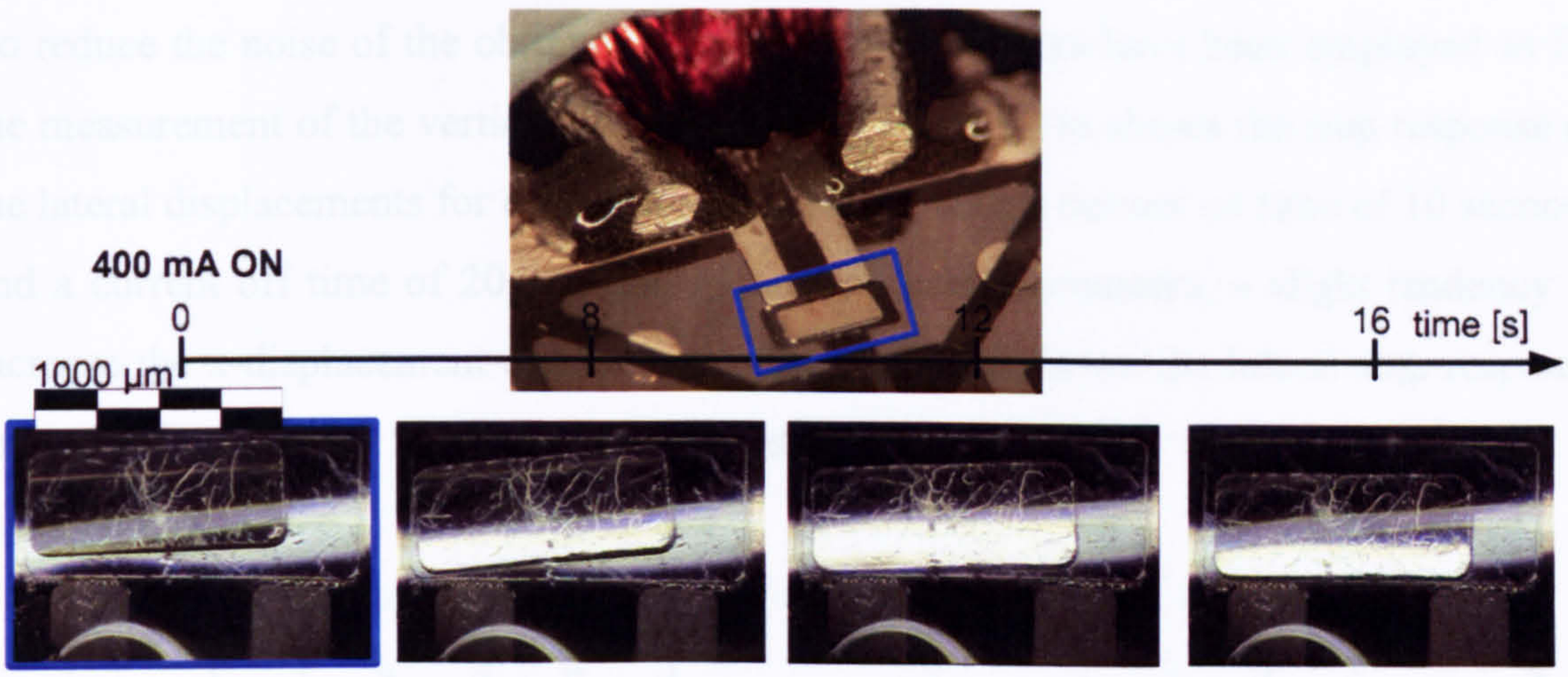

Figure 5-31 A sequence of pictures taken from a movie that shows the displacement of a post inserted within the cavity of a µLED over a period of 16 seconds. The cavity is filled with a viscous liquid to dampen the movement. A current of 400mA is applied at $t = 0$ second.

A good magnetic path and relatively high driving currents are needed to counteract the weight of the µLens. To remedy that situation a ferromagnetic rod was glued to one of the edges of the µLens as shown in Figure 5-32b and Figure 5-32c. This rod reduces the length of the magnetic path tremendously. However, as Figure 5-32b shows, the distance between the ferromagnetic rod towards the EDD, around 500µm, is still relatively high for these measurements. Future devices will be placed much closer (50µm to 100µm) to the EDD which will greatly reduce the magnitude of the driving currents. Ideally, the height of the magnetic part of the EDD, t_{EDD}, is to be bigger than the height of the top surface of the µLens, t_L, if the electrostatic actuator is not exerting a force. This reduces, for further devices, the effect of the lateral movement at the expense of vertical displacement.

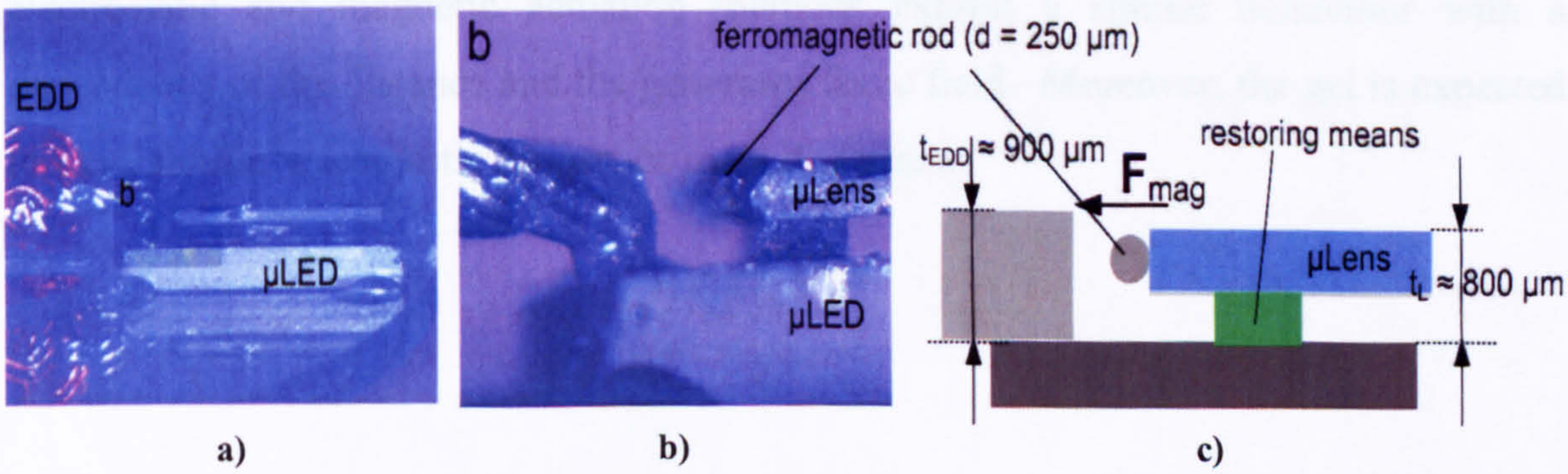

a) b) c)

Figure 5-32 a) Side view of lateral magnetic movement test vehicle. b) Zoomed in picture from a. c) Schematic side view with dimension.

To reduce the noise of the obtained graphs, the same filters have been employed as for the measurement of the vertical displacement. Figure 5-33a shows the step response of the lateral displacements for current steps of 50mA with a current on time of 10 seconds and a current off time of 20 seconds. During the measurements, a slight tendency to increase the x-displacement can be seen. Figure 5-33b shows the lateral step response for currents of 100mA and the same timings as in Figure 5-33a.

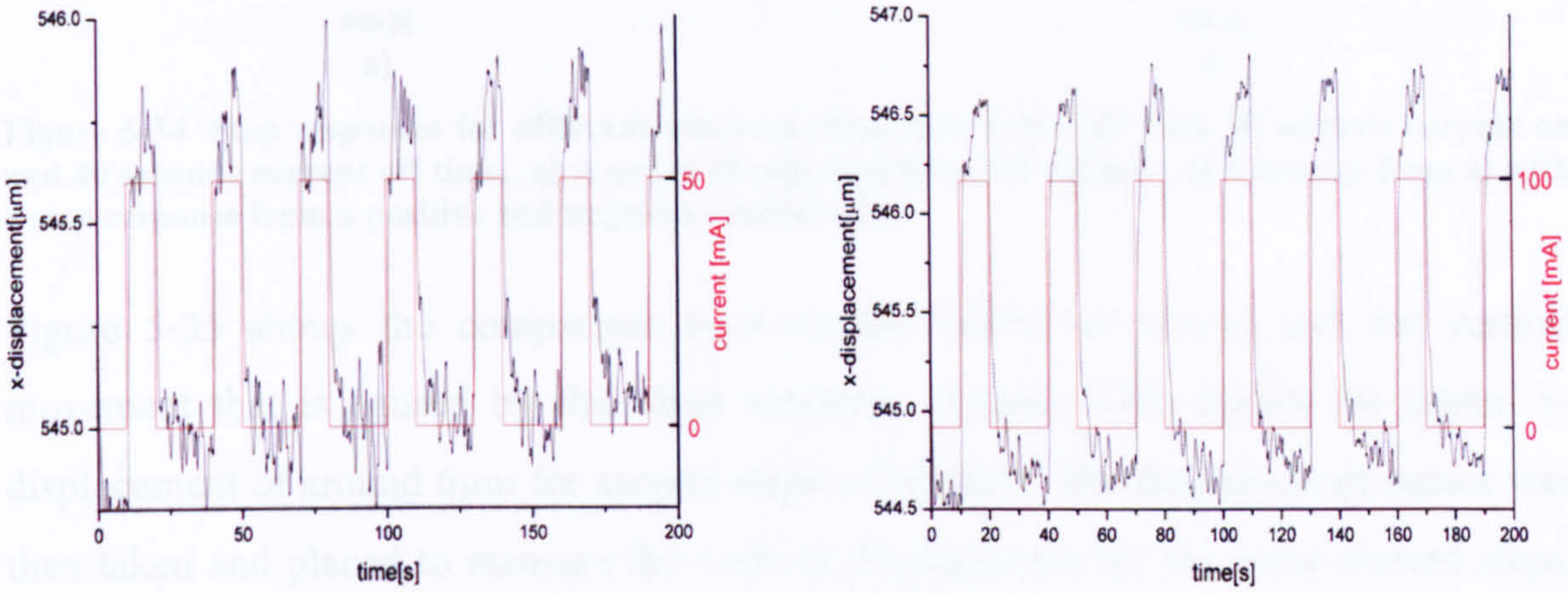

Figure 5-33 Step responses for different currents steps were recorded with 10 seconds current on and 20 seconds current off time. a) Step response for 50mA. b) Step response for 100mA.

Lateral displacements of more than 6µm were achieved with current steps of 400mA with 20 seconds current on and 40 seconds current off times as shown in Figure 5-34. The absolute displacement for the current on and off times is relatively constant. Figure 5-34b shows a zoomed out time slot taken from Figure 5-34a. The curve of the positive as well as the negative step response show strong similarities with the graphs shown for the electrostatic vertical displacements. This is attributed to the fact that both electrostatic and magnetic actuation methods exhibit a similar behaviour with a dependency of the distance and the generated force field. Moreover, the gel is expected to have similar viscoelastic properties in all directions.

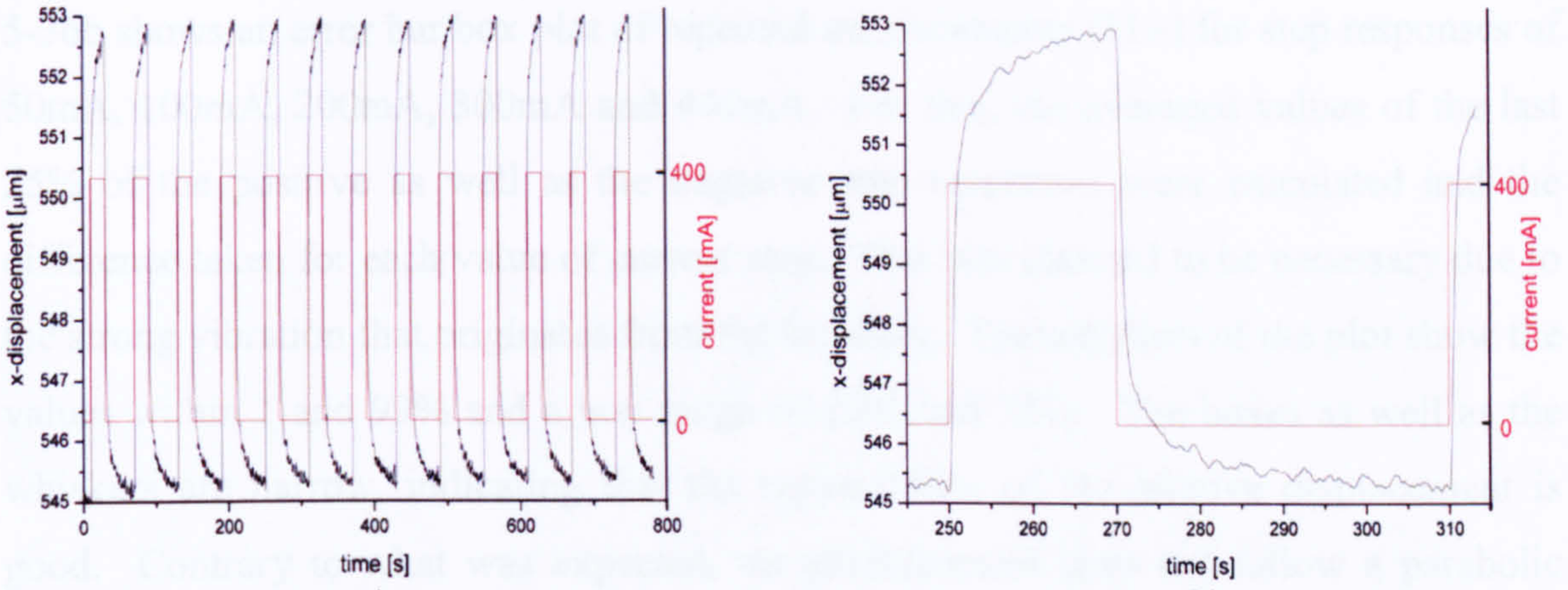

Figure 5-34 Step responses for different currents steps were recorded with 20 seconds current on and 40 seconds current off time. a) A series of step responses for 400mA. b) Close-up from a) with a step response from a positive and negative current step.

Figure 5-35 shows the comparison between the lateral movement and the vertical movement that is caused by the same actuator. Figure 5-35a shows the lateral x-displacement of around 6µm for current steps of 300mA. The displacement sensor was then taken and placed to measure the vertical displacement for the same current steps. Figure 5-35b shows the resulting graph. An insignificant vertical displacement can be observed. It can be concluded that the vertical displacement of the µLens is not much influenced by the lateral actuation, which is an important property of the assembly.

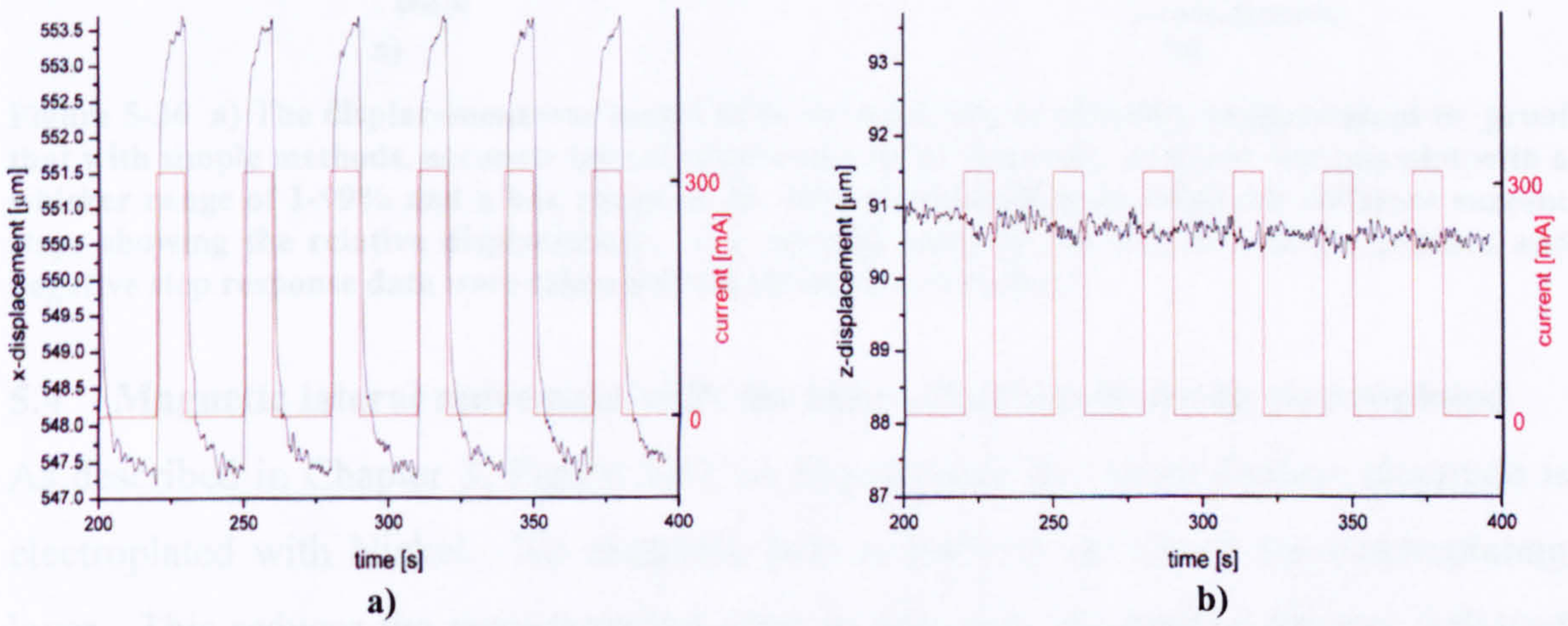

Figure 5-35 Comparison between lateral and vertical displacement for the same current steps of 300mA with 10 seconds current on and 20 seconds current off time applied. a) Lateral x-displacement with a difference of around 6µm, b) vertical z-displacement is hardly detectable.

The vertical displacement was further investigated by trying to set manually the displacement to certain integer values between 546µm and 555µm as shown in Figure 5-36a. Within a certain margin, the values could be achieved relatively quickly. A controlled loop feedback system for the vertical electrostatic displacement was not set up, since a voltage controlled current source had either to be purchased or built. Figure

5-36b shows an error bar box plot of repeated measurements (11+) for step responses of 50mA, 100mA, 200mA, 300mA and 400mA. For this, the averaged values of the last 25% of the positive as well as the negative step responses were calculated and the difference taken for each value of current step. This was deemed to be necessary due to the strong vibration that originates from the building. The whiskers of the plot show the values within 1 and 99% and a box range of 25% and 75%. The boxes as well as the whiskers are narrow, indicating that the repeatability of the relative displacement is good. Contrary to what was expected, the displacement does not follow a parabolic curve. However, these initial measurements need further investigation and more experiments have to be conducted for characterisation, which would be part of future work.

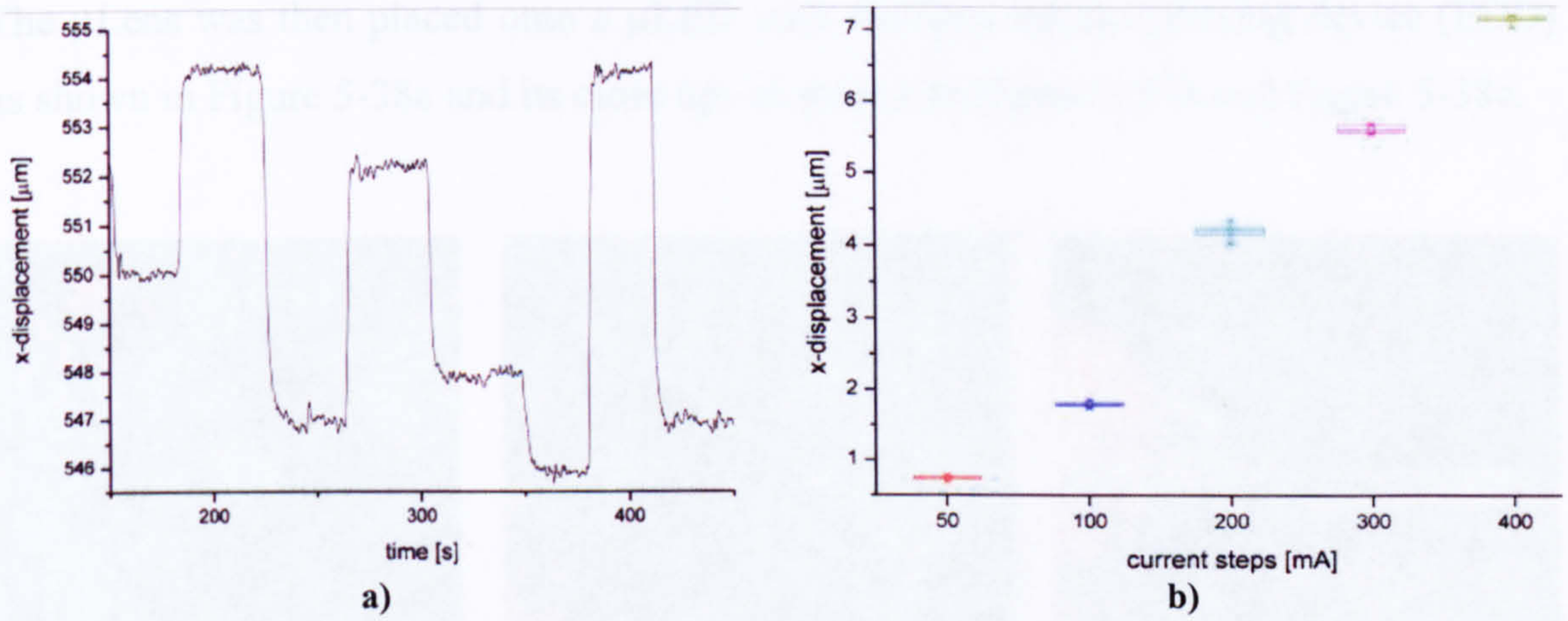

Figure 5-36 a) The displacement was aimed to be set manually to different integer values to proof that with simple methods, accurate lateral alignment can be achieved. b) Error bar box plot with a whisker range of 1-99% and a box range of 25, 75% of measurements taken for different current steps showing the relative displacement. The average value of the last 25% of the positive and negative step response data were taken and the difference calculated.

5.4 Magnetic lateral movement with the entire floating electrode electroplated

As described in Chapter 3, Figure 3-43, in this version, the entire floating electrode is electroplated with Nickel. No magnetic post is built up on top of the electroplating layer. This reduces the manufacturing steps to only one evaporation process followed by electroplating. Figure 5-37a shows a µLens that was connected with electroplating wires to allow the floating electrodes 1, 2 and 4 to be plated. A thickness of approximately 170µm was electroplated with a current density of 1.8A/dm^2. Floating electrode 3 was not connected, but was subsequently plated with a reduced height since after a certain time, the electroplating of 4 and 2 caused conductive bridges. In a future device, this effect can be eradicated by either designing a mask, thereby covering the gap between the floating electrodes, or by just increasing the gap distance between

them. It is important that the floating electrodes are insulated from each other to exclude electrical interferences between electrodes.

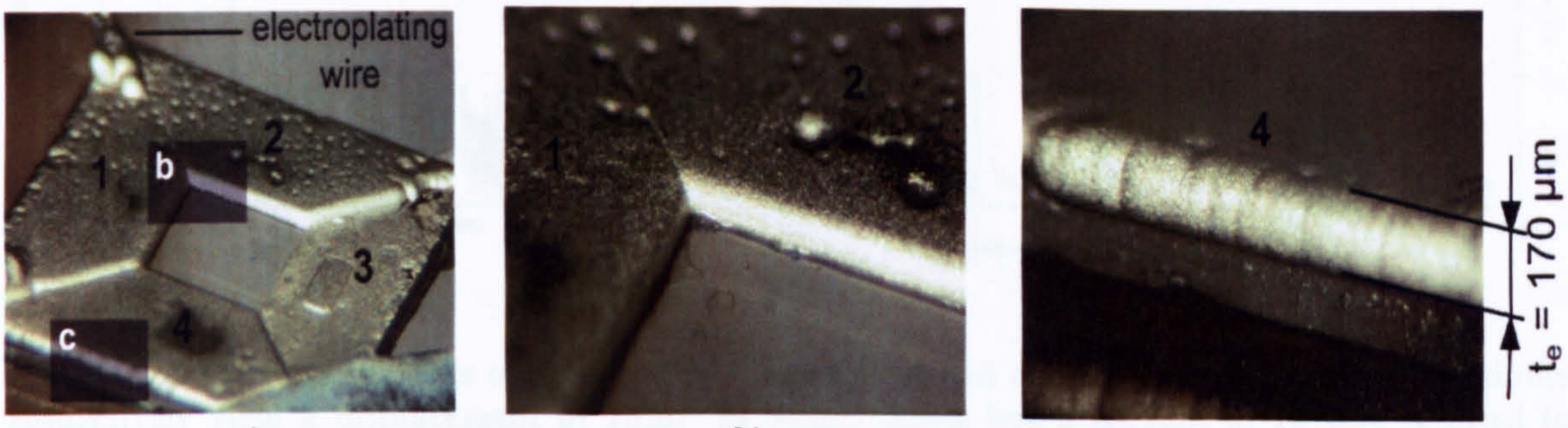

a) b) c)

Figure 5-37 a) µLens with electroplated floating electrodes 1,2 and 4. 3 was subsequently plated as well due to bridging of the Ni. b) Zoom in of corner between floating electrode 1 and 2. c) Zoomed in picture of edge of floating electrode 4.

The µLens was then placed onto a µLED with attached external driving device (EDD) as shown in Figure 5-38a and its close ups as shown in Figure 5-38b and Figure 5-38c.

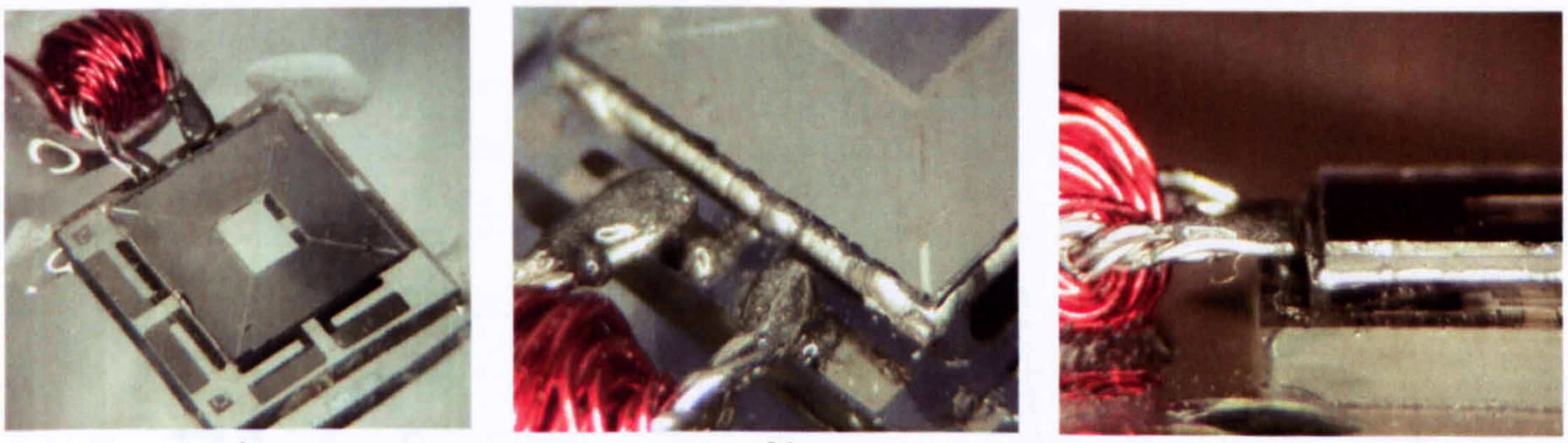

a) b) c)

Figure 5-38 a) Electroplated µLens placed onto µLED with external driving device (EDD) attached. b) Close up of EDD and ferromagnetic edge of µLens. c) Side view of µLED, EDD and µLens.

The measurement setup used is shown in Figure 5-29. Step currents of 20mA were used with a current on and off time of 3 minutes and 1 minute respectively which resulted in displacements of approximately 1µm as shown in Figure 5-39a. Using the same time parameters but a current of 100mA, repetitive displacements of over 14µm were achieved.

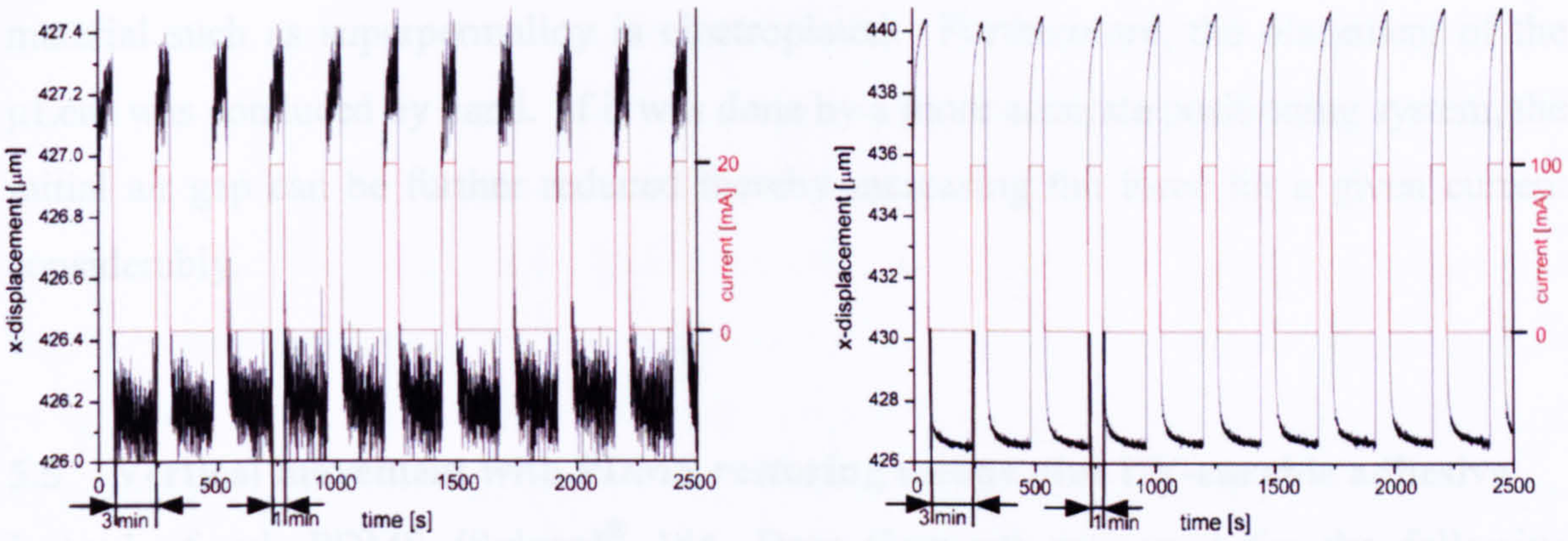

Figure 5-39 a) Step currents of 20mA with a current on and off time of 3 minutes and 1 minute respectively yield a displacement of 1µm. b) Same timing but a current of 100mA resulted in displacements that exceeded 14µm.

Another experiment was conducted by changing the current by hand in order to estimate how controllable the adjustment of a certain lateral x-displacement is. Figure 5-40 shows the attempts to achieve displacements between 435µm and 490µm that are multiples of 5µm or 10µm. These displacements required currents between 0mA and 300mA. The maximal relative displacement was 50µm.

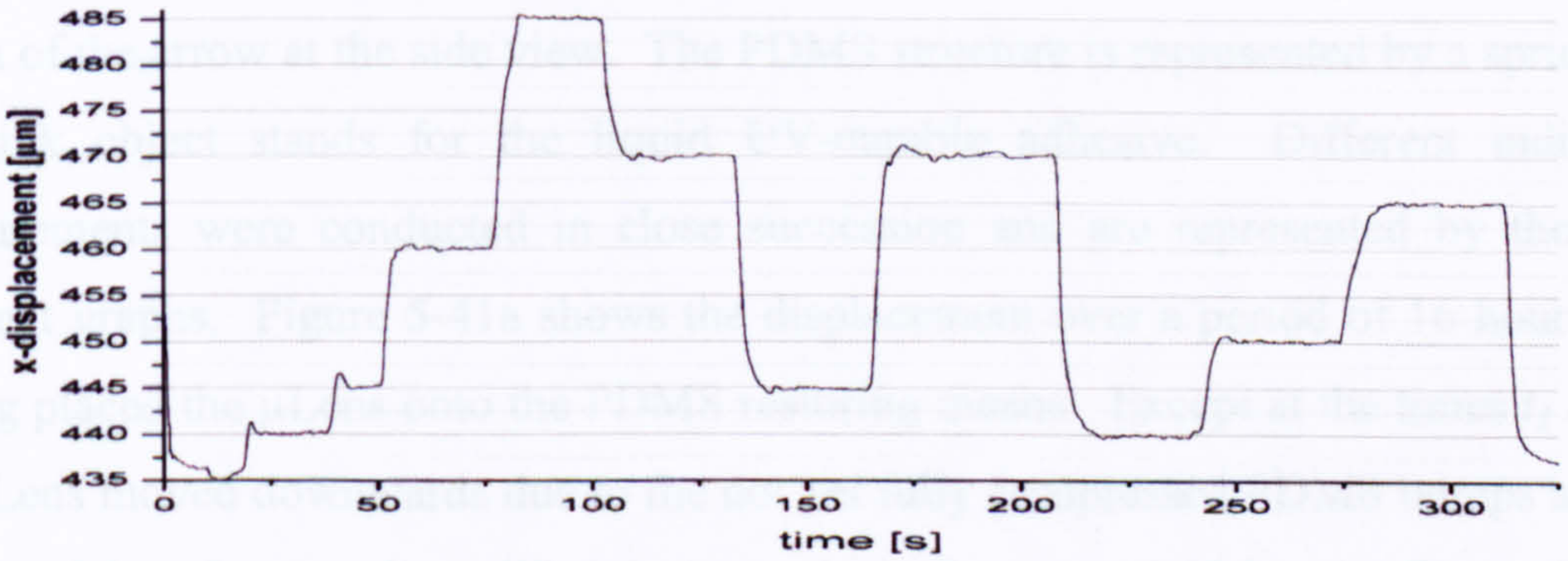

Figure 5-40 By manually passing currents between 0mA and 300mA, different displacements were attempted to estimate the controllability.

Compared with the finding in Chapter 5.3 these results might suggest that the bulk of electroplated Ni performs better than a superpermalloy rod. Even though the mass of the ferromagnetic material plays a role for the attractive force, the much higher permeability of superpermalloy should easily outperform the mass difference. The author expects, that the discrepancy is caused by the closer placement of the µLens with respect to the EDD. The controllability in all ranges of the displacement was good. Even though the EDD was relatively close to the ferromagnetic edge of the µLens, no pull-in effect was witnessed. This is attributed to the damping properties of the used gel. It is assumed that the currents can be still drastically reduced if instead of Ni

material such as superpermalloy is electroplated. Furthermore, the placement of the μLens was conduced by hand. If it was done by a more accurate positioning system, the initial air gap can be further reduced thereby increasing the force for a given current considerably.

5.5 Vertical movement with PDMS restoring means plus UV-curable adhesive

Instead of gel, PDMS (Sylgard® 184, Dow Corning) was used for the following experiment as a restoring means. A drop was placed onto a glass wafer and cured for over 48 hours. The estimated thickness of the drop was in the order of 100μm. Using a scalpel, small rectangular pieces were cut out with estimated lateral dimension of 150μm x 150μm. One piece of PDMS was then placed into each of the gel cavities. The measurement setup is the same as shown in Figure 5-10b. Figure 5-41 shows the different phases that were investigated. The red arrow, seen on the side view of the μLED-μLens assembly and on the graph itself symbolises the downward movement of the μLens. The green arrow stands for the upward movement. The dashed arrow connotes the long term tendency of the movement which is also indicated with the length of the arrow at the side view. The PDMS structure is represented by a spring and the pink object stands for the liquid UV-curable adhesive. Different individual measurements were conducted in close succession and are represented by the three different graphs. Figure 5-41a shows the displacement over a period of 16 hours after having placed the μLens onto the PDMS restoring means. Except at the times t_1 and t_2, the μLens moved downwards due to the not yet fully compressed PDMS bumps and the weight of the μLens until equilibrium is reached after around 15 hours. The end value of the displacement is labelled as z_1. The upwards movements, indicated by the green arrows appeared after around 1 hour and 10 hours, respectively, for a duration of approximately 25 minutes. Whereas different slopes of the downwards movement, due to structural changes and alignments, might be expected, the author has no explanation for this sudden upwards movement. In particular the relative long duration of these upward movements, if external influence can be dismissed, raises questions. Continuing at the displacement z_1, step voltages of 400V, 500V and 600V with a duty cycle of 6 minutes and a voltage on time of 2 minutes for a duration of 1 hour, were applied as shown in Figure 5-41b. As expected and indicated (red arrow), the μLens moved downwards at each voltage step and fully relaxed during the zero voltage period (green arrow). Displacement z_2 at the end of the measurement was found to be close to

z_1. Starting at displacement z_2 four drops of liquid UV-curable adhesive (NOA 63) were placed at each corner and until t_3 (≈20min) the µLens was pulled downwards presumably due to the capillary action of the liquid. The ripple seen superimposed on the envelope curve is caused by the electrostatic actuation of the µLens using the same actuation parameters as described in Figure 5-41b. This actuation was used as a source of agitation, assuming that it would have an accelerating effect on the flow of the liquid to establish equilibrium earlier. After t_3 however, the µLens was moving upwards even after 1.5 hours when the measurement was stopped. So far, no reasonable explanation has been found for this behaviour. Figure 5-41d shows a zoomed in area taken from Figure 5-41c. The tendency for the upward movement is clearly visible and indicated with the dashed green arrow. However, later investigations revealed that this "upward movement" was most certainly caused by the stage of the displacement sensor. For a limited time an absolute displacement in the range of almost 1µm can be achieved. The restoring properties of the PDMS bumps are clearly visible even though the step responses are dampened and minimised compared with Figure 5-41b. In comparison with Figure 5-8, where only a liquid but no restoring means was used, this behaviour exhibits clearly deterministic components.

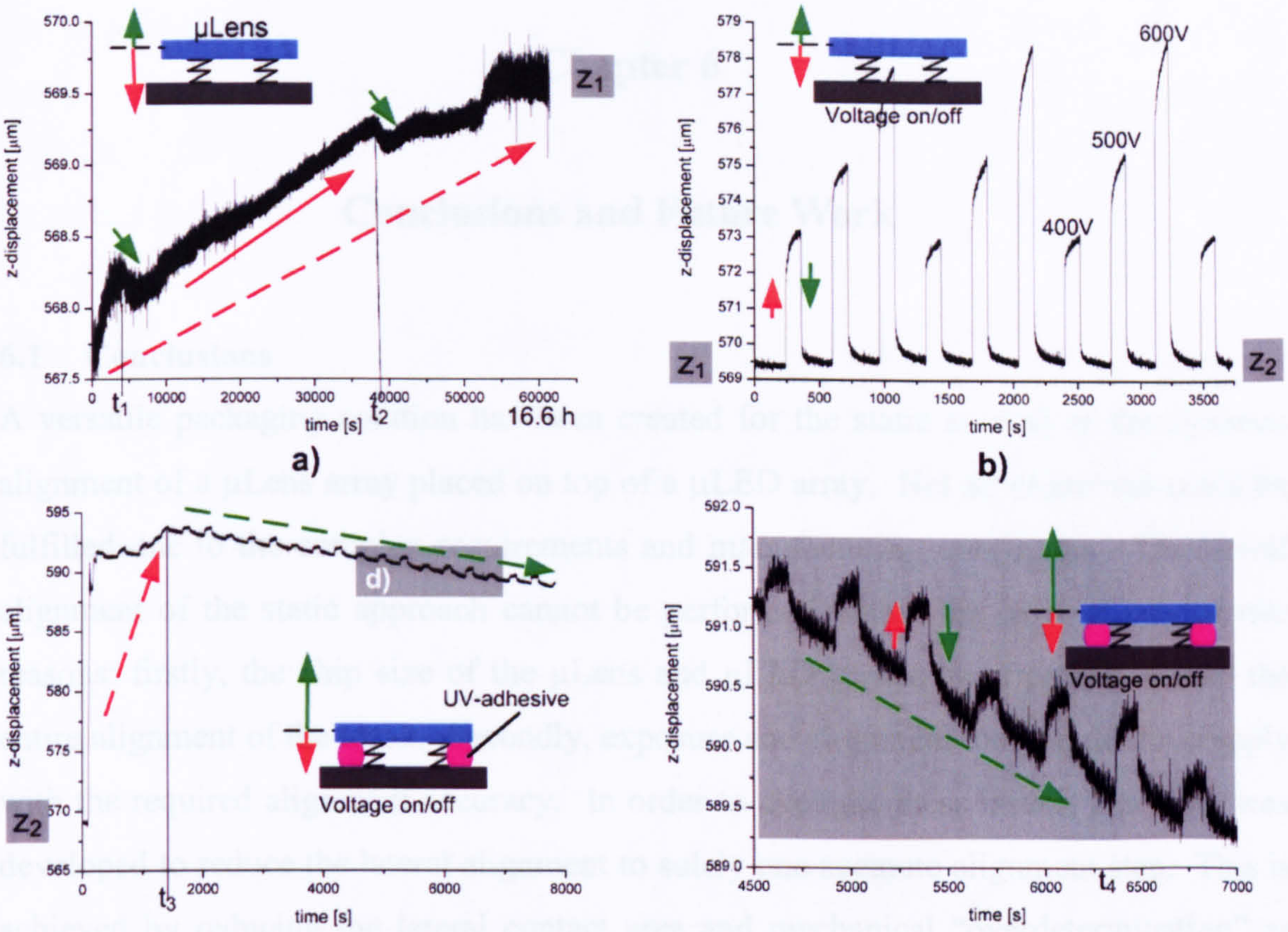

Figure 5-41 a) µLens is placed onto the µLED with PDMS bumps in between. b) Step voltages of 400V, 500V and 600V where applied. c) A liquid UV-curable adhesive was then placed onto the four corners and the capillary force initially caused a downward movement of the µLens. d) With a superimposed upwards movement of the µLens, the restoring capability of the PDMS bumps are still noticeable.

The experiment was aimed to find indications of the feasibility to counteract the capillary force of a liquid, such as UV-curable adhesive, with the restoring means of a polymer for achieving repeatable displacements. The promising findings justify further experiments and investigations.

Chapter 6

Conclusions and Future Work

6.1 Conclusions

A versatile packaging solution has been created for the static as well as the dynamic alignment of a µLens array placed on top of a µLED array. Not all objectives could be fulfilled due to the complex requirements and manufacturing constraints. The lateral alignment of the static approach cannot be performed within the MISEC lab for two reasons: firstly, the chip size of the µLens and µLED causes huge problems with the entire alignment of the mask. Secondly, exposure and alignment tool would not comply with the required alignment accuracy. In order to alleviate these issues, a process was developed to reduce the lateral alignment to solely one accurate alignment step. This is achieved by reducing the lateral contact area and mechanical "overdetermination" as much as possible by using the post-cavity structure. Even though the vertical alignment was initially thought to be the most challenging part, it turned out that the post-cavity structure eased that problem tremendously and that the fine adjustment of the vertical alignment could be done, at sub-micron accuracy, by electroplating the electrodes situated within the cavities.

For the dynamic approach, an electrostatic actuator was used which allows to keep the µLens physically undisturbed from any wire. It features a floating electrode, which reflects the electrostatic field generated by the underlying electrodes situated on the µLED. This not only eases the manufacturing process but also the subsequent assembly.

Instead of cantilevers, gel bumps were initially used for providing the restoring force in the vertical direction. The gel bumps are placed within the gel cavities situated on the µLED. Together with the electrostatic actuator, displacements of more than 75µm could be achieved with a voltage of 600V. The repeatability of the displacement is good with a standard deviation of 0.43µm and a mean value of 24.75µm. This test was conducted for a duration of more than 16 hours. Using a closed loop feedback system, alignment accuracy of less than 500nm could be observed with a projected accuracy of

less than 100nm if a vibration insulated table were to be used. The drawback of the gel bump is the unpredictable and uncontrollable shape that makes an accurate analysis difficult. Therefore, photo-patternable or thermocurable polymers with very soft properties are envisaged to be used in the near future.

Lateral movement of the μLens was not only considered to be useful but rather essential. The posts have been designed to be considerably smaller than the cavities and an actuator for lateral movement was devised that exploits a magnetic field. Measurements showed that lateral displacements of the order of 6μm for currents of 400mA are possible. A modified magnetic actuator, where the entire floating electrode was electroplated with Ni, achieved lateral displacements of 50μm with currents of maximal 300mA. Smaller currents are possible if better magnetic materials are used.

An external driving device (EDD) was developed, which provides the magnetic actuator with the required magnetic flux as well as a voltage for the electrostatic actuator. This allows simultaneous vertical electrostatic and lateral magnetic movements. Together, the EDD, the magnetic plus the electrostatic actuator and the restoring gel provide a novel actuation possibility where 5 degrees of freedom can be controlled. In Chapter 3, a small modification of the process is suggested to control all possible 6 degrees of freedom. Having this capability, the static approach can be achieved via the dynamic approach by using for instance UV-curable adhesive and fixing the μLens in place, once the alignment has been established. For this, the EDD could only be temporarily attached to the μLED.

Many of the findings and solutions are not restricted to this particular system and might be successfully employed for other devices. The Ph.D. project has been a success even though the actual packaging solution could not be processed in its entirety, because of the multitude of challenges that had first to be overcome.

6.2 Future work

A multitude of future work has been identified during this research project which could only be partly or not addressed. Time, expertise, the complexity of some problems and appropriate equipment were the major limiting factors. The future work can be classified as follows:

- Magnetic actuator, where possible approaches are presented for the modelling of magnetic forces, improvements of the magnetic path and the measurement of the displacement.

- Restoring means, where a setup is presented to find properties of the restoring means by using the available equipment.

- Microfabrication of the external driving device.

- µLens-µLED assembly, which highlights possible mass fabrication for static approach devices using dynamic alignment. This section also provides a possibility to determine the tilt of the µLens over all three axes.

6.2.1 Magnetic actuator

This chapter proposes alternative methods of how to model the magnetic force and its intrinsic non-linearity. Furthermore, the improvement of the magnetic path to increase the achievable force for a given current without jeopardizing the electrostatic properties is discussed and partially tested.

6.2.1.1 Alternative modelling of force

The magnetic actuator with its non-linearity with respect to the post distance and resulting force as well as the non-linearity and hysteresis of the *H-B diagram* of the ferromagnetic material, poses a considerable challenge for its modelling. The following two paragraphs suggest different approaches to that problem.

6.2.1.1.1 Lookup tables in SIMULINK® for modelling magnetic nonlinearity

For a magnetic material with little hysteresis, the magnetic circuit can be simulated by using SIMULINK®. The magnetic resistors need then to be replaced by different lookup tables obtained either empirically or through manufacturer datasheets, as shown in Figure 6-1. Since most of the magnetic curves are *H-B* diagrams, these diagrams needed to be converted to *H-Φ* diagrams since it is Φ, Φ_1 and Φ_2 that flow through the magnetic resistors. The assembly of the resistors and other elements cannot be simply replaced as Figure 6-1 might imply, but an appropriate equation has to be derived which complies with the simulation needs. Other elements such as gain, for constant magnetic resistors for air, and summation elements need also to be used.

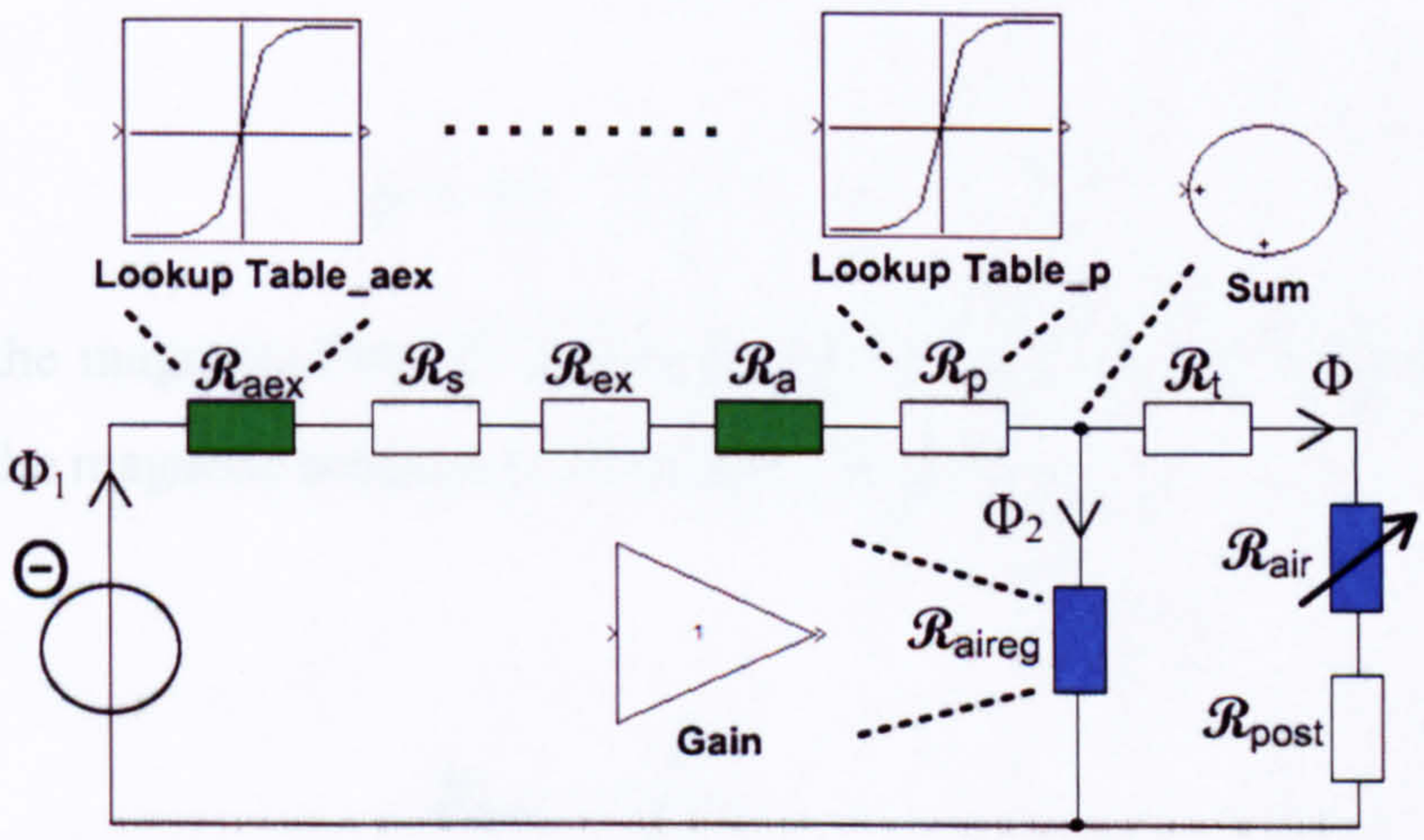

Figure 6-1 The magnetic circuit might be simulated by using SIMULINK®.

6.2.1.1.2 Calculation of the magnetomotive force for a given air gap and force

Let us suppose that the ferromagnetic core with an air gap and all dimensions as well as the magnetisation curve are known. If the magnetomotive force is given and the magnetic flux density needs to be calculated, one faces the problem that the magnetic field strength over the ferromagnetic material and the air gap is not known. This yields two unknown quantities with just one equation. However, if the magnetic flux density is known, the electromotive force can be calculated. This approach is explained by using the considered magnetic circuit shown in Figure 6-2. For clarity, only one magnetic material is used with its magnetisation curve shown in Figure 6-2b. The hysteresis is neglected. The magnetic force with which the post is attracted is $\boldsymbol{F}_m$, the distance of the air gap, d_m, is assumed. The distance d_m is related to the length of the air gap, l_{air}:

$$l_{air} = 2 \cdot d_m . \tag{6-1}$$

By assuming the absolute value of the magnetic force, F_m, the magnetic flux density, B_{air} is:

$$B_{air} = \frac{F_m \cdot \mu_0}{w_m \cdot t_m} \tag{6-2}$$

with w_m being the width of the air gap where the magnetic field is situated, t_m is the height of the magnetic field (Figure 3-41) and μ_0 is the magnetic permeability of air. After having obtained B_{air}, the magnetic flux within that branch (Figure 6-2a) is:

$$\phi = B_{air} \cdot w_m \cdot t_m . \tag{6-3}$$

By knowing the magnetic flux, Φ, and the cross section, A_{post}, the flux density which exists within the magnetic resistance of the post, $\mathcal{R}_{post}$, is:

$$B_{post} = \frac{\phi}{A_{post}} . \tag{6-4}$$

Knowing B_{air}, the magnetic field strength, H_{post}, can be obtained by using the magnetisation curve shown in Figure 6-2b. The magnetic field strength of the air gap is:

$$H_{air} = \frac{B_{air}}{\mu_0} . \tag{6-5}$$

The product of the magnetic field strength, H, and the length, l, of the magnetic resistor is sometimes referred to as magnetic voltage. As in the electrical domain, the sum of the magnetic voltages within the branch where Φ flows is equal to the magnetic voltage of the branch where Φ_2 flows:

$$H_{aireg} \cdot l_{aireg} = H_{post} \cdot l_{post} + H_{air} \cdot l_{air}, \tag{6-6}$$

where H_{aireg} is the magnetic field strength which lingers within $\mathcal{R}_{aireg}$ and l_{aireg} is the known distance between the two tracks. By solving equation (6-6) towards H_{aireg} and placing it into equation (6-7)

$$B_{aireg} = \mu_0 \cdot H_{aireg}, \tag{6-7}$$

one obtains the magnetic flux density between the tracks, B_{aireg}. Knowing the cross section of the magnetic field within air between the tracks, A_{aireg}, the magnetic flux, Φ_2, is:

$$\phi_2 = B_{aireg} \cdot A_{aireg}. \tag{6-8}$$

Both Φ and Φ_2 are known and with the magnetic "Kirchhoff 1" one yields for the magnetic flux, Φ_1:

$$\phi_1 = \phi + \phi_2. \tag{6-9}$$

The magnetic flux density, B_{edd2}, is:

$$B_{edd2} = \frac{\phi_1}{A_{edd2}}. \tag{6-10}$$

where A_{edd2} is the cross section of the magnetic path represented by $\mathcal{R}_{edd2}$. The magnetic field strength, H_{edd2} within $\mathcal{R}_{edd2}$ can be obtained through the magnetic curve in Figure 6-2b. The same is done with the magnetic resistance $\mathcal{R}_{edd1}$ by calculating the magnetic flux density B_{edd1}:

$$B_{edd1} = \frac{\phi_1}{A_{edd1}}, \tag{6-11}$$

with A_{edd1} being the cross section of the magnetic path represented by $\mathcal{R}_{edd1}$. Using the magnetic curve in Figure 6-2b, the magnetic field strength, H_{edd1}, within $\mathcal{R}_{edd1}$ is obtained. By applying the "magnetic Kirchhoff 2" the magnetomotive force, Θ, is obtained by summing up the different magnetic field strengths, H and magnetic length l on one loop as shown in equation (6-12).

$$\Theta = H_{edd1} \cdot l_{edd1} + H_{edd2} \cdot l_{edd2} + H_{aireg} \cdot l_{aireg} \,. \tag{6-12}$$

The magnetomotive force, Θ, is:

$$\Theta = I \cdot N \,. \tag{6-13}$$

with, I being the current that flows through the coil of the EDD and N being the number of windings. With the derivation in this section, the current, I, that is needed for exerting a force, F_m on the post, which is situated the distance, d_m away from the tracks, can be obtained.

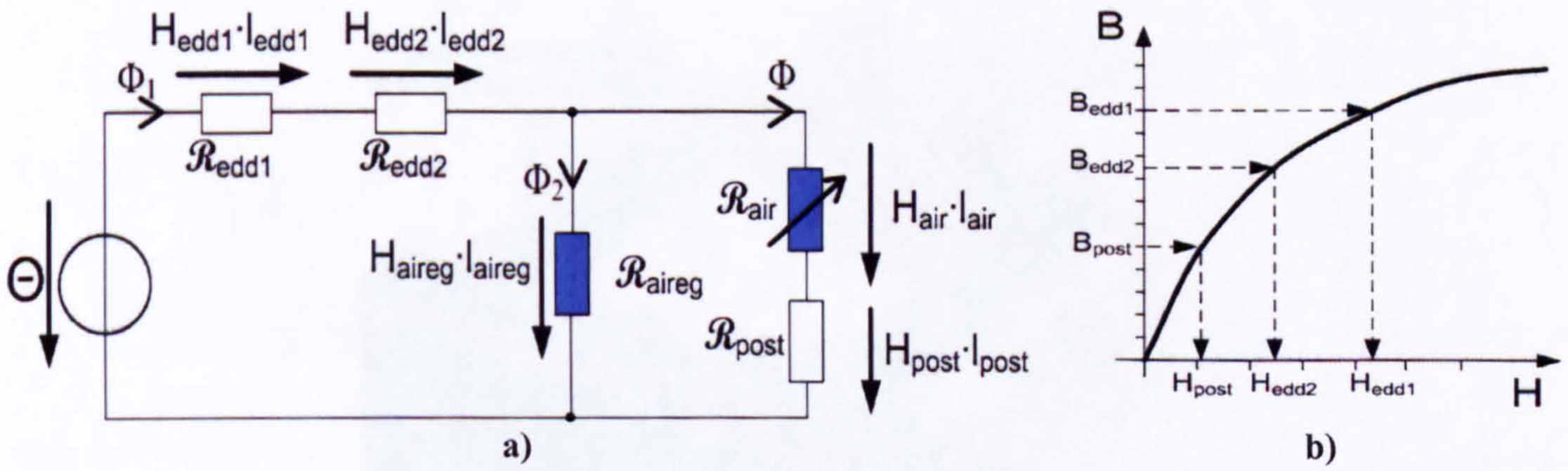

Figure 6-2 a) Simplified magnetic circuit schematic as shown in Figure b. b) Magnetic curve of the material chosen for the magnetic path of the EDD, pads, tracks and the post.

Figure 6-3 shows a possible mapping of the magnetomotive force, Θ, as a function of F_m and d_m. This would necessitate a considerable amount of calculations for each F_m-d_m pair. The magnetic curve of a material could be fed into a lookup table of SIMULINK® to calculate the magnetomotive force. From that, a 3D surface diagram could be obtained which might then later be use as a lookup table itself for the control circuit of the lateral magnetic movement.

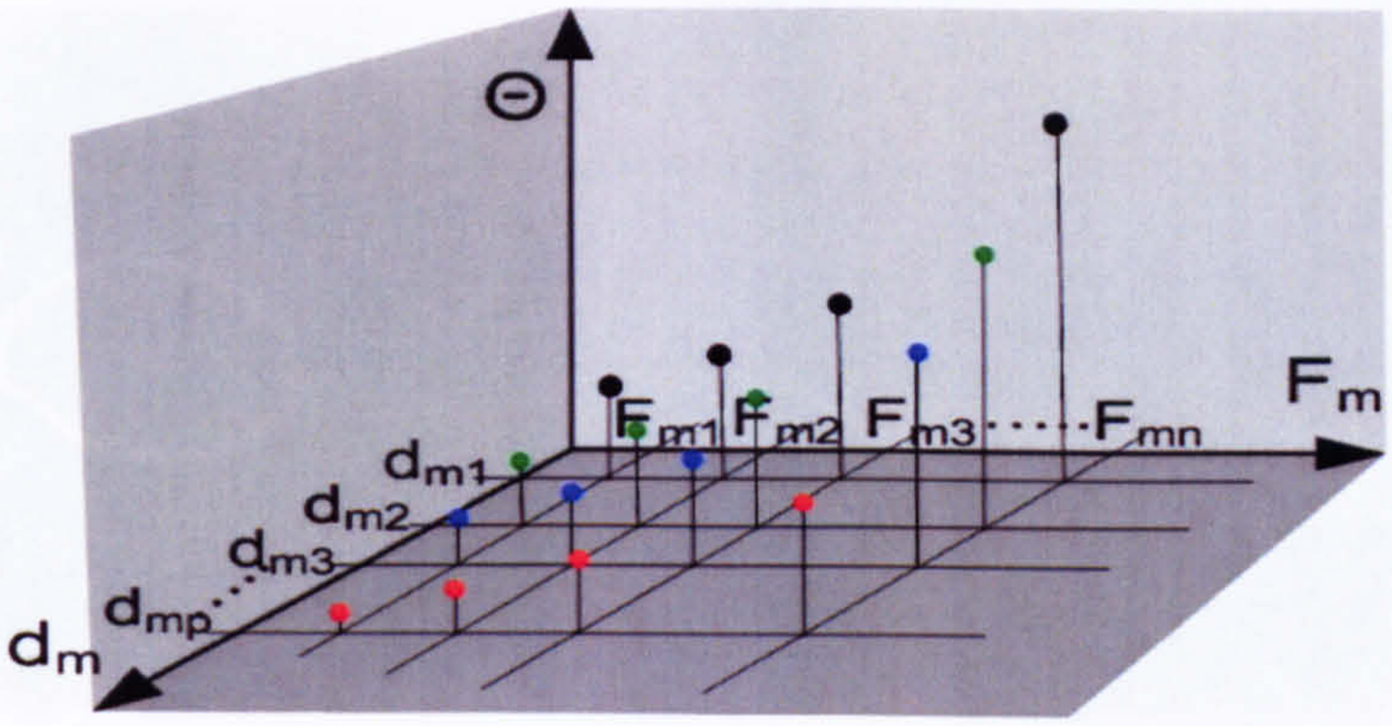

Figure 6-3 Discrete values of d_m and F_m can be calculated and presented in a 3-D mapping diagram representing the magnetomotive force, Θ as a function of d_m and F_m.

6.2.1.2 Manufacturing of improved magnetic interfaces

The interface between the external driving device and the pad, which is situated on the μLED, needs to be electrically conductive for delivering the high voltage to the electrodes but must also exhibit a low magnetic resistance for the lateral magnetic actuation.

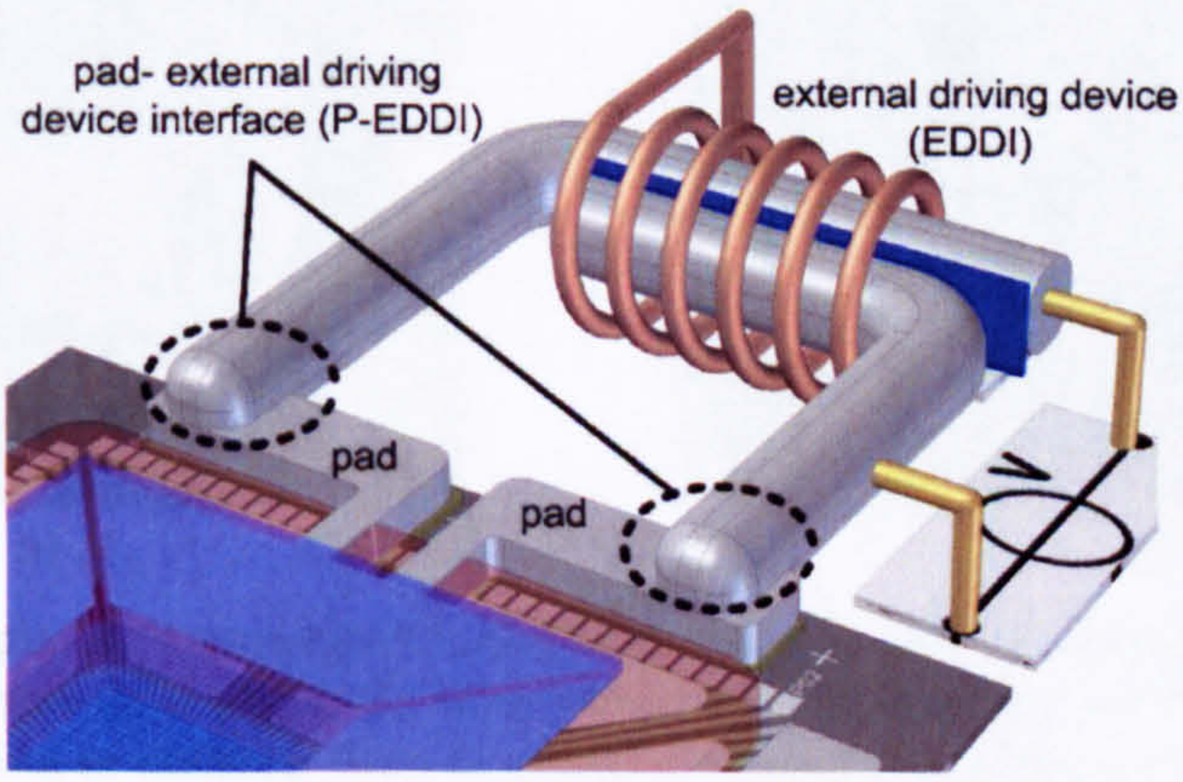

Figure 6-4 The interface between the pad on the μLED and the external driving device (EDD) needs to be electrically conductive as well as having a low magnetic resistance.

To achieve this, a 2 component epoxy adhesive with suspended ferromagnetic particles could be deposited over the interface (P-EDDI). To investigate the magnetic behaviour of this mix, a Fe wire (99.5%) was grinded into powder and mixed with epoxy adhesive (UHU®). One half of the mixture was then placed on a glass wafer without any external field and left to cure for 1 hour as shown in Figure 6-5. The Fe particles seem to distribute relatively homogenous over the entire volume of the drop.

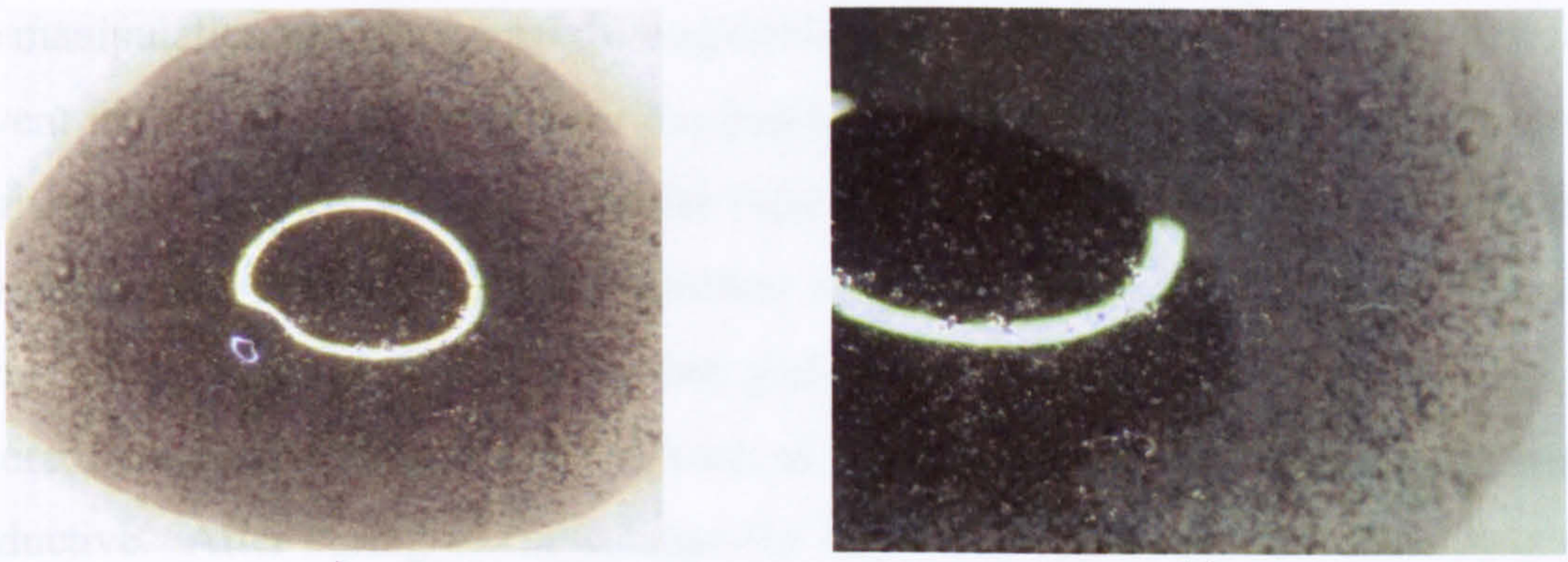

a) b)

Figure 6-5 a) Fe particles mixed with 2 component epoxy glue and cured for 1 hour. b) Close-up of a).

The other half of the sample was placed within a magnetic field, during the curing process. The magnetic field was generated by a coil made of 40 windings and a Fe wire with 1mm of diameter as a magnetic core material. A current of 700mA was passed through the coil. The ferromagnetic particles arranged themselves along the magnetic field lines to minimise the magnetic resistance of the entire magnetic circuit (Figure 6-6).

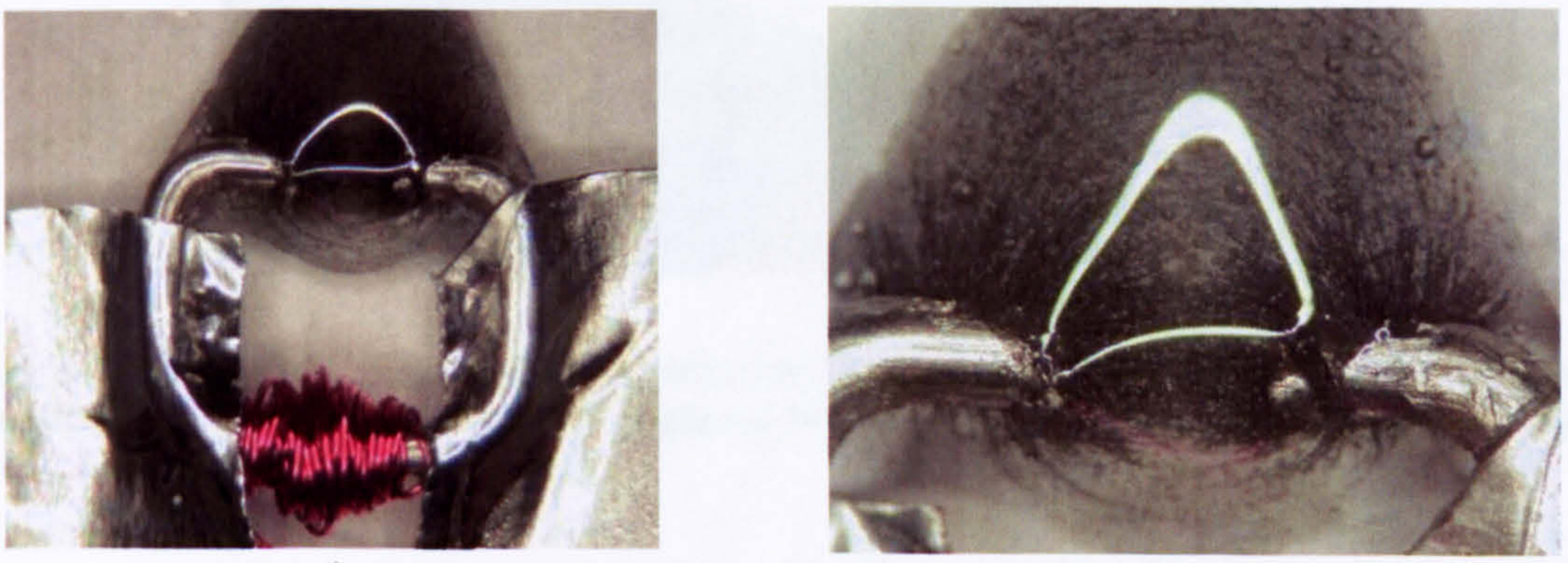

a) b)

Figure 6-6 a) A sample of ferromagnetic adhesive was exposed to a magnetic field during curing for 1 hour using Fe wire as a magnetic core material and a current of 700mA. b) The magnetic particles align according to the field lines in order to make the magnetic resistance for the magnetic circuit as low as possible.

Figure 6-7 shows a picture of the curing of the ferromagnetic adhesive. After having placed the ferromagnetic adhesive over the interface, a magnetic short-circuit (piece of ferromagnetic material) is placed between the two paths to make the magnetic flux, Φ_{cure}, as big as possible for a given current I_{cure}. This current is chosen to be as high as possible and limited only by the thermal behaviour of the coil. The flux created exerts a strong force on the ferromagnetic particles to overcome the viscous drag force. The particles place themselves to make the overall magnetic circuit as less resistant as possible. After 1 hour of curing the particles remain in their ideal places; the current can be switched off and the magnetic short-cirquit removed.

The manipulation of the external driving device should be kept at a minimum in order to prevent the lift up of the pads from the fragile μLED structure. Firstly the μLED is to be glued onto a glass wafer (or similar rigid surface). Then the already (completely) assembled EDD is then placed into position so that the ends of the EDD come as close to the pads as possible. The EDD is then glued onto the glass wafer. Once the adhesive is cured, conductive lacquer will be used to make the interface (P-EDDI) electrically conductive. After curing of the lacquer the ferromagnetic adhesive is placed onto the interface and cured while a magnetic flux is passed through the magnetic circuit. This can be achieved simultaneously with all four external driving devices.

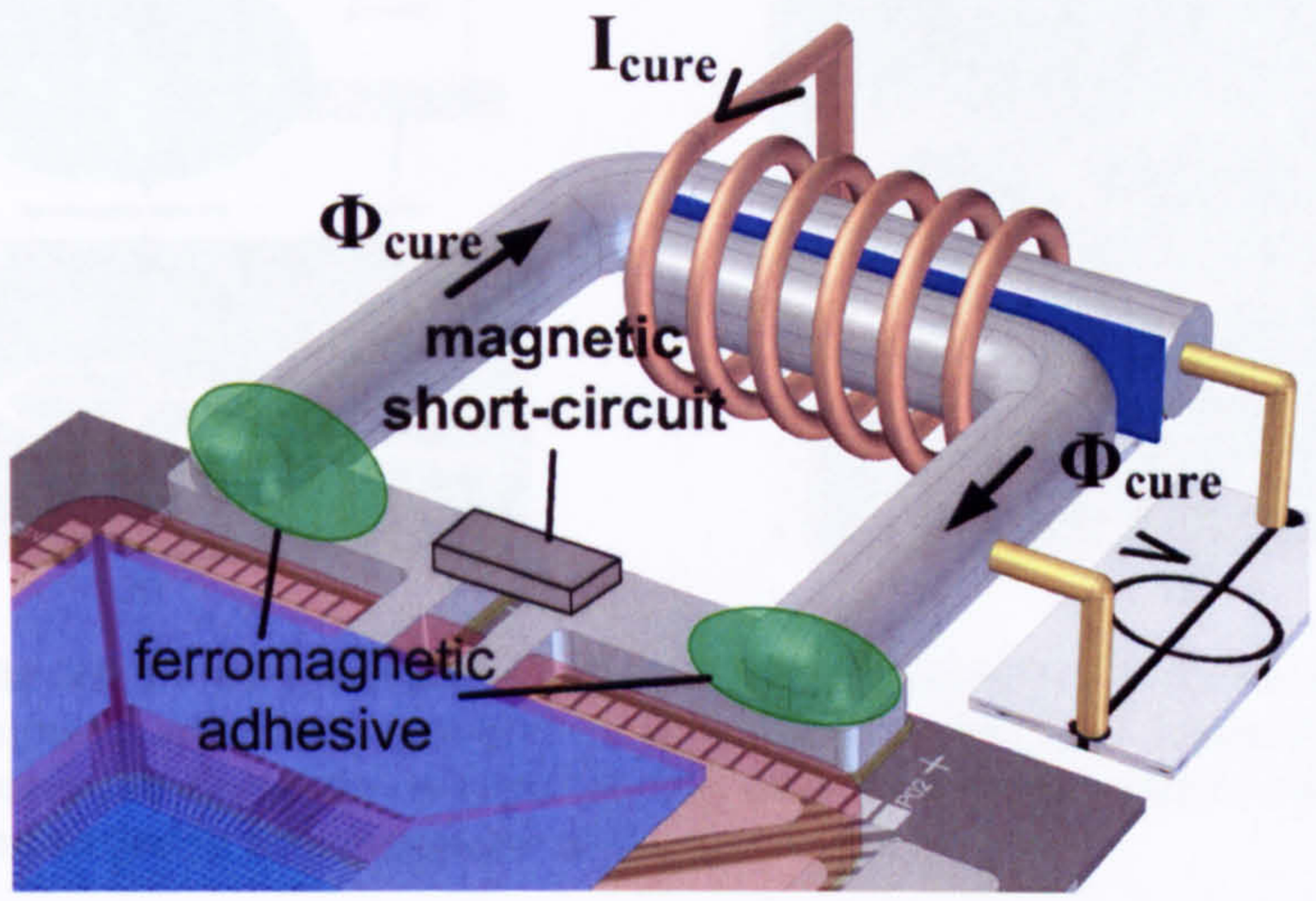

Figure 6-7 Curing of the ferromagnetic adhesive by passing a magnetic flux, Φ_{cure}, through the magnetic path. The magnetic shortcut is placed between the pads to increase the flux for a given current, I_{cure}.

The ferromagnetic adhesive can also be used for the EDD itself and replace the electrical insulator shown in Figure 6-7. This connection however needs to fulfil more requirements. Whereas the only concern of the pads-external driving device interface (P-EDDI) was to maximise the magnetic conductivity, the electrical insulator needs also to have good electrical insulation properties at high voltages. For that purpose, two different assemblies have been designed. In Figure 6-8a, two Fe wires are immersed in the ferromagnetic adhesive. One Fe wire was previously immerged in pure epoxy and cured for 1 hour to get an electrical insulation layer. After 2 hours of curing, the resistance of the two Fe wire ends was measured using a DMM (Fluke® 77III). An "infinite" resistance was observed. In a second measurement, the two Fe wire ends where connected to a high voltage generator and the DMM connected in series as shown in Figure 6-8a. The voltage was then gradually increased from 0V up to 1000V. No current and therefore voltage breakdown was observed; the assembly features has

therefore high voltage insulation. Figure 6-8b shows a second assembly where the two separate Fe wires were directly immerged into the ferromagnetic adhesive with no insulating pre-treatment. After curing of 2h, the electrical resistance was measured to be somewhere between 20MΩ and infinity. The high voltage behaviour was then tested with the same setup as in Figure 6-8a. Up to a voltage of 300V no current flow was observed. Above 300V, electrical breakdown could be observed. After each breakdown the voltage could be increased to a higher value. At 620V the breakdown occurred constantly.

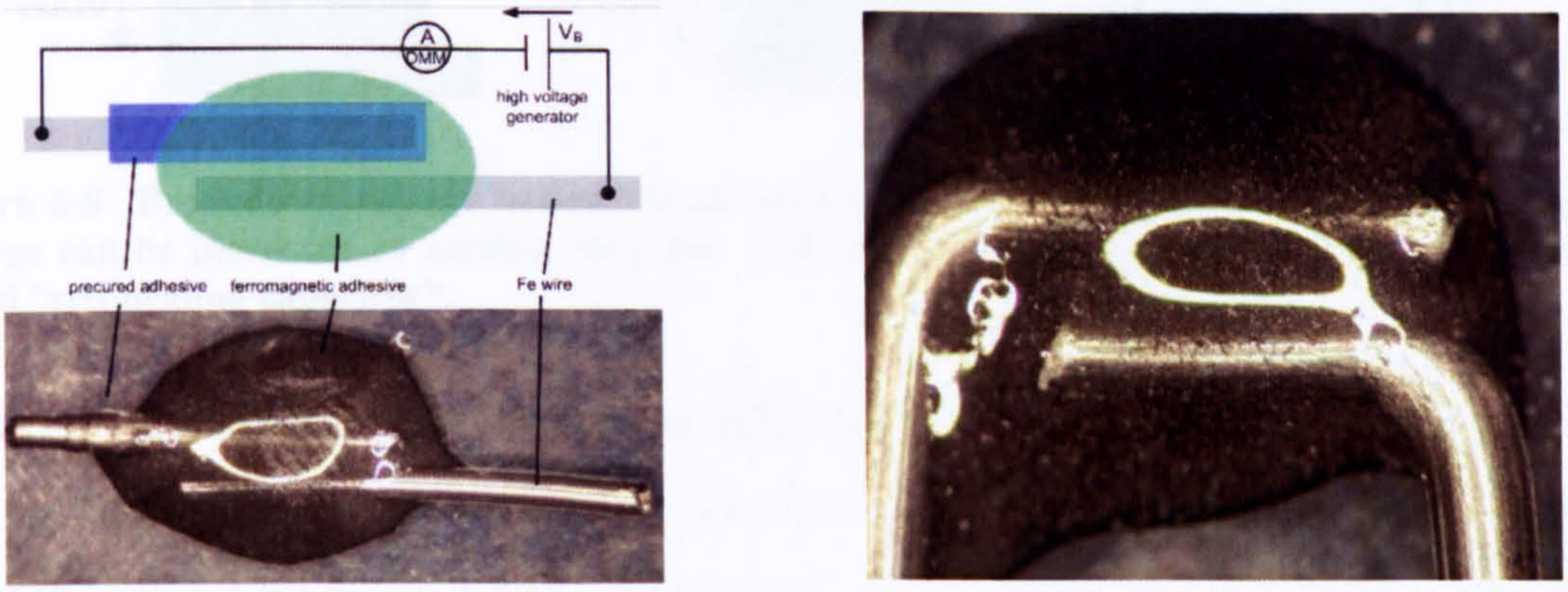

Figure 6-8 a) The left Fe wire features an electrical isolation layer. Both Fe wires are immerged into the ferromagnetic adhesive. A high voltage generator was then connected with a DMM in series that measures the electrical current. b) Close-up of two non insulated Fe wires in L-shape that have been immerged in ferromagnetic adhesive.

The behaviour of the device seen in Figure 6-8b can be described as follows (Figure 6-9). The Fe wires are directly immerged into the ferromagnetic adhesive, therefore have no electrical insulation. The distribution of the Fe particles within the epoxy is never completely homogeneous, even when thoroughly mixed. Therefore, some "paths" within the adhesive are more prone for a breakdown at a certain voltage than others (1). A voltage of 300V is now applied between the two Fe wires. The breakdown occurs at the Fe particle path, which bridges the insulation properties of the epoxy the most closely aligned with Fe particles. This breakdown causes a current, I_B , to flow which burns a part of the aforementioned path away thereby insulating the path for this particular voltage (2, 3). It is more likely that a breakdown appears at a different path. The voltage is now increased to 500V where another breakdown appears in a different path as seen in (4). The voltage is further increased and no breakdown can be seen. From that point it is expected that the electrical connection between the two Fe wires is not prone for breakdowns up to a voltage of 600V. This effect offers interesting processing capabilities for the subsequent external driving device, in

particular the connection of the two ferromagnetic wires. This would be conducted before the external driving device is attached to the μLED.

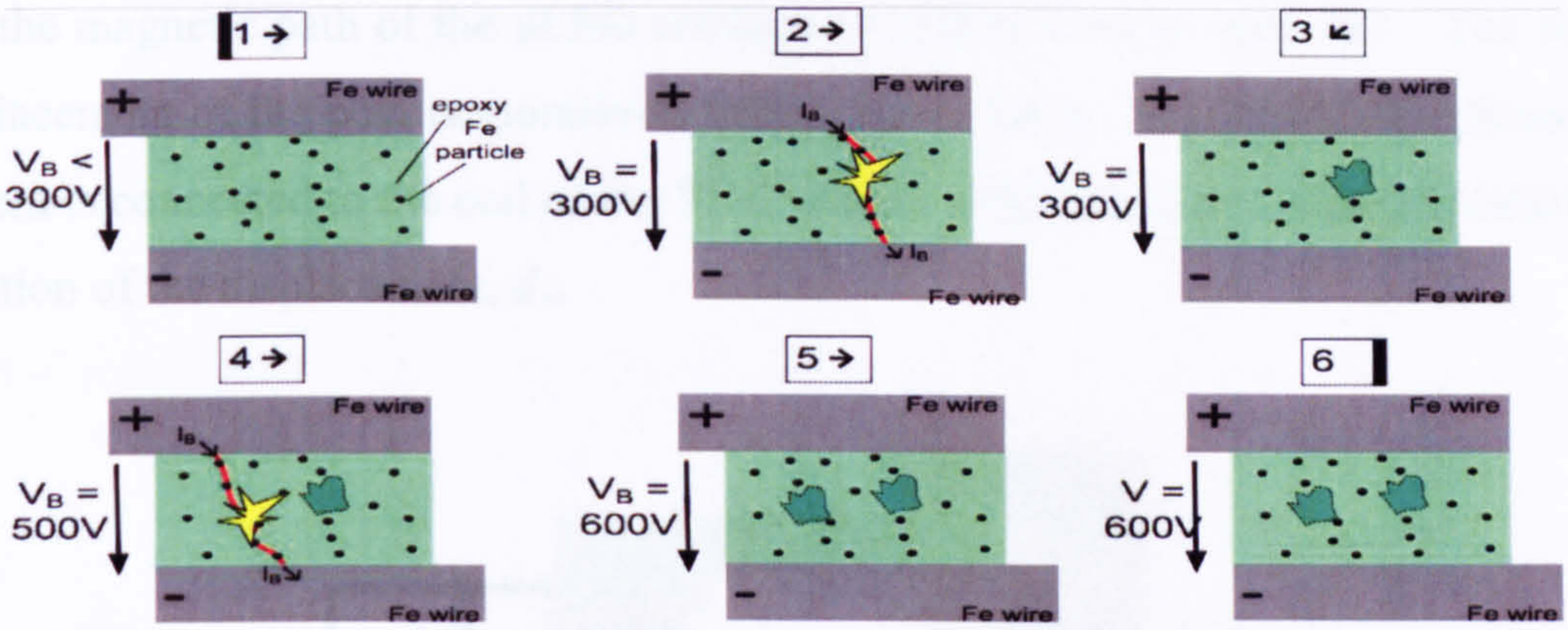

Figure 6-9 Breakdown voltage behaviour of the ferromagnetic adhesive. It is assumed that the voltage can be increased to another step due to properties of the material similar to that of a so called "self healing capacitor".

Figure 6-10 describes how this can be achieved. The blank Fe wires are inserted into the ferromagnetic adhesive (1). A magnetic flux, Φ_{cure} is then passed through the magnetic circuit by using a coil. The other ends of the EDD need to be magnetically short-cut during the curing process to obtain as much flux Φ_{cure}, as possible. This aligns the Fe particles in the best possible way for the magnetic flux (2). It is very likely that the Fe particles align in an unfavourable way, concerning the electrical breakdown voltage, meaning that the effective insulation distance is reduced for this alignment. After curing, a voltage of 620V is applied as long as no breakdown occurs (measured with a DMM as seen in Figure 6-8 (3). From now on the device is unlikely to have any electrical breakdown as long as the voltage is kept below 620V.

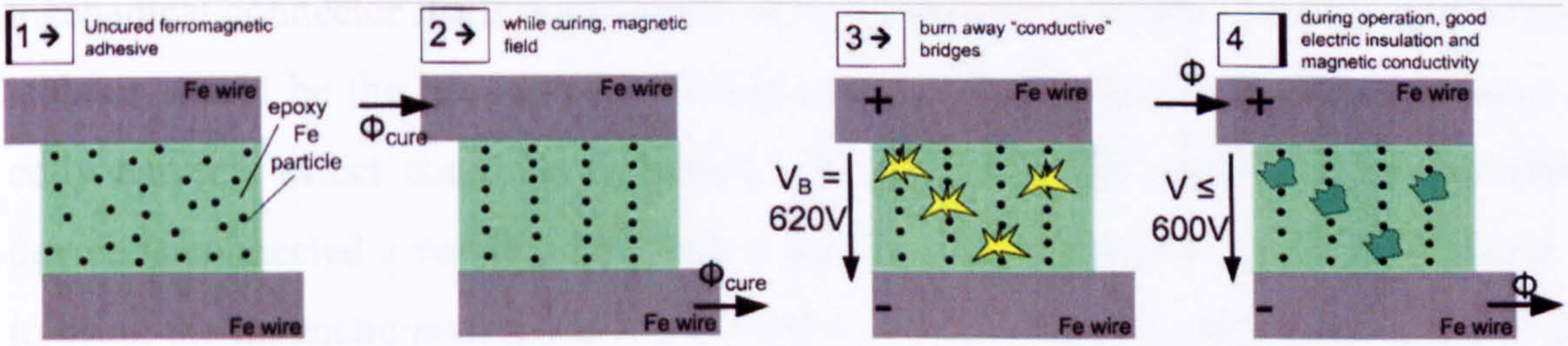

Figure 6-10 After alignment of the ferromagnetic particles during the curing process of the adhesive, a high voltage is applied to burn away possible electrically conductive paths.

6.2.1.3 Measuring the impedance as function of post separation

Modelling of magnetic circuits is not a trivial task. Figure 6-11 shows a possible set up for practical measurements. A detached μLens post is placed into the cavity. The EDD and the magnetic path of the μLED are kept as if they were in operation. The absolute displacement of the post is monitored with a microscope. An impedance measurement system is connected to the coil of the EDD and the impedance, X_L, is then measured as a function of the displacement, d_m.

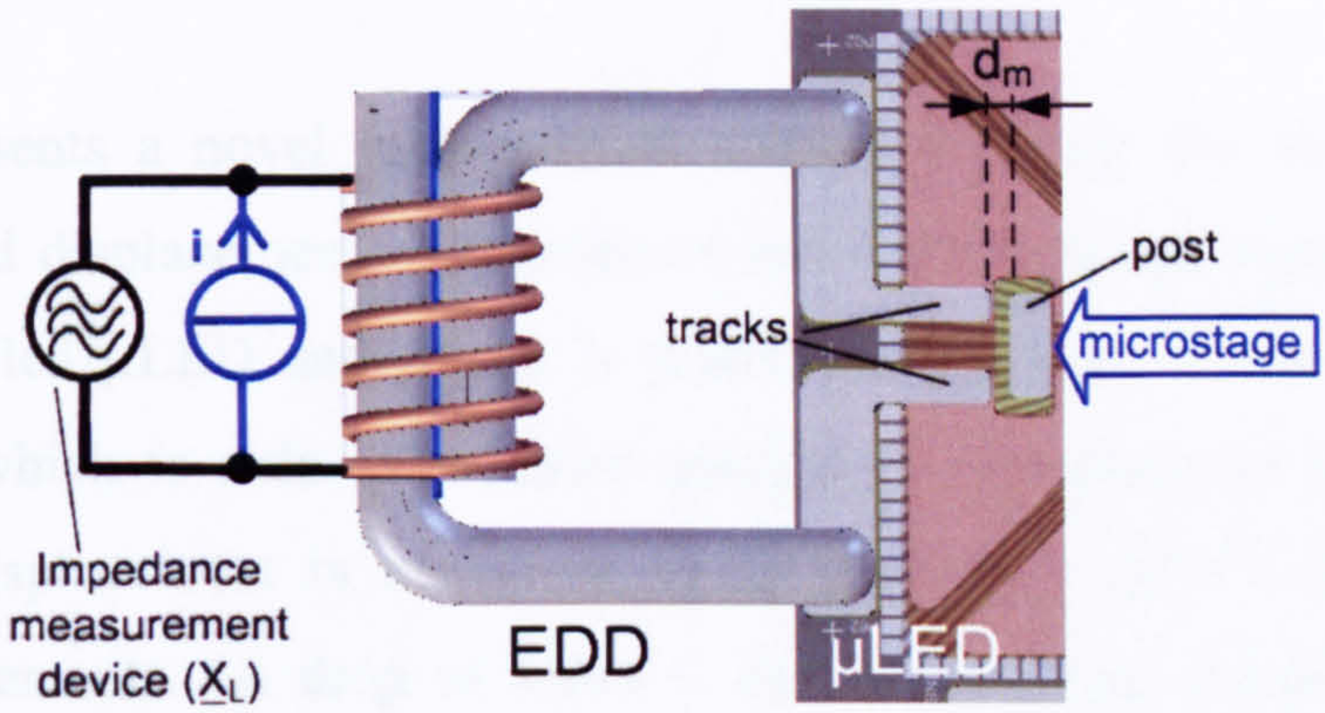

Figure 6-11 Determination of the magnetic impedance as a function of the displacement of the post, d_m.

The smaller d_m, the bigger the value of the inductive impedance. For this measurement, the (imaginary) X_L will be dominant since the coil has a very small (real) resistance R and a small (imaginary) capacitive impedance X_C. The frequency generator of the impedance measurement tool will certainly use a high frequency and a small current and it is not expected that the post would be mechanically influenced by this measurement. The change in displacement would be done with the use of a micro stage indicated in Figure 6-11. This might be practically challenging and care has to be taken that the mechanical connector itself is not made of any magnetic material. Ideally, an electrical isolator would be the best choice, so that even the occurrence of possible influencing eddy currents effect could be discarded. In parallel to the impedance measurement device is connected a variable DC current source. The purpose of the current source is to bring the magnetic material along the entire circuit, into different offset points of the magnetic flux density from where the impedance measurements are taken. Therefore, the magnetic impedance, X_L, is measured as a function of the displacement, d_m, with a magnetic flux offset, Φ_o, taken as parameter which is subsequently caused by the offset current I_o. Knowing the frequency of the impedance measurement system, the inductance L can be found from which the total magnetic resistance of the entire circuit can be derived.

6.2.2 Restoring means

6.2.2.1 Force-displacement measurement by varying the mass on top of the μLens

One problem is the difficulty to measure the force generated electrostatically or magnetically. Analytical and simulated values of the force do exist, but they rely heavily on the current position of the floating electrode with respect to the driving electrodes situated on the μLED. This is very complicated to measure during the movement of the μLens. Therefore, it is difficult to obtain a graph that describes a valid force–displacement relationship of the restoring means.

Figure 6-12 presents a novel measurement method to study the behaviour between applied force and displacement. Quantitative measurements still remain to be carried out. The assembled μLED and μLens is placed onto a high sensitive scale (Mettler Toledo MT5), which is able to measure microgram variations of the mass (Figure 6-13b). The displacement is measured again with the optoNCDT2400, as in the previous measurements. A drop of water is then placed onto the μLens. While the water drop is evaporating, the mass and therefore the force downwards reduce gradually. The reduction of mass is measured by the scale from which the force can be derived. Experiments will show how much the displacement, d_{sc}, of the scale itself will be due to the change in mass. This would then be taken into account with the overall displacement, d. It is however expected, that the displacement, d_{sc}, is negligible. The mass is in that context, a function of the time, t, with the temperature, T, and atmospheric pressure, P, acting as parameter. This function will be nonlinear due to the shape of the water drop, but has no influence over the displacement–force relationship that will be recorded. One of the problems that might be faced is the fact that the evaporation of the water drop might be too fast for the gel bumps to react due to the slopes shown in Figure 5-22c and Figure 5-22d. However, the future use of the non-sticky photo-patternable PDMS structure will very likely alleviated this influence. Another disadvantage of this method is that only the loss of mass can be produced due to the evaporation of water, but not the reverse action. Practical measurements showed that after a certain time, the scale goes into a stand-by mode, where no transmission occurs to the PC anymore. This time constant is much smaller than the evaporation time of a drop. Settings of the scale have been changed but the problem still remained.

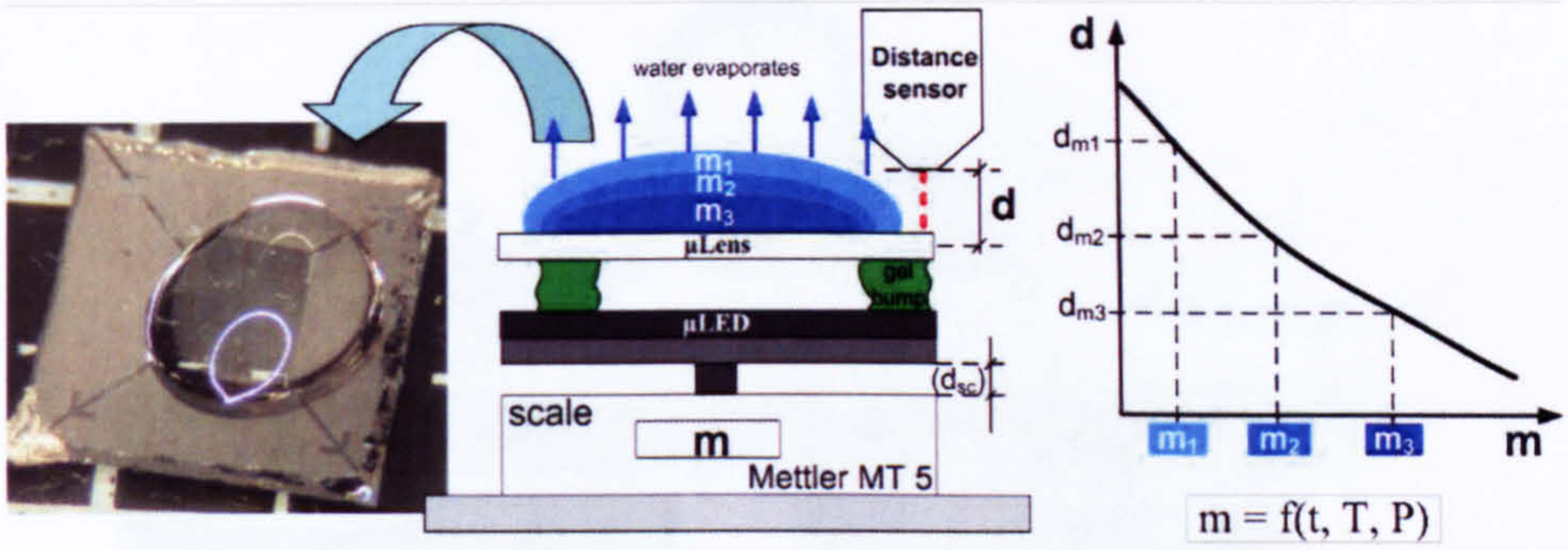

Figure 6-12 The water drop placed on the µLens evaporates over time, therefore reduces the gravitational force that compresses the gel bumps. From this, a force-displacement graph (right) can be established.

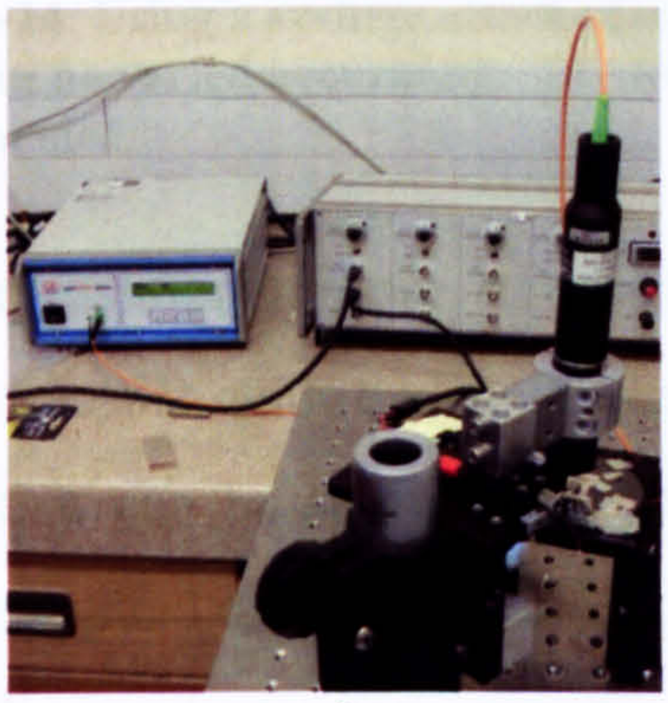

a)

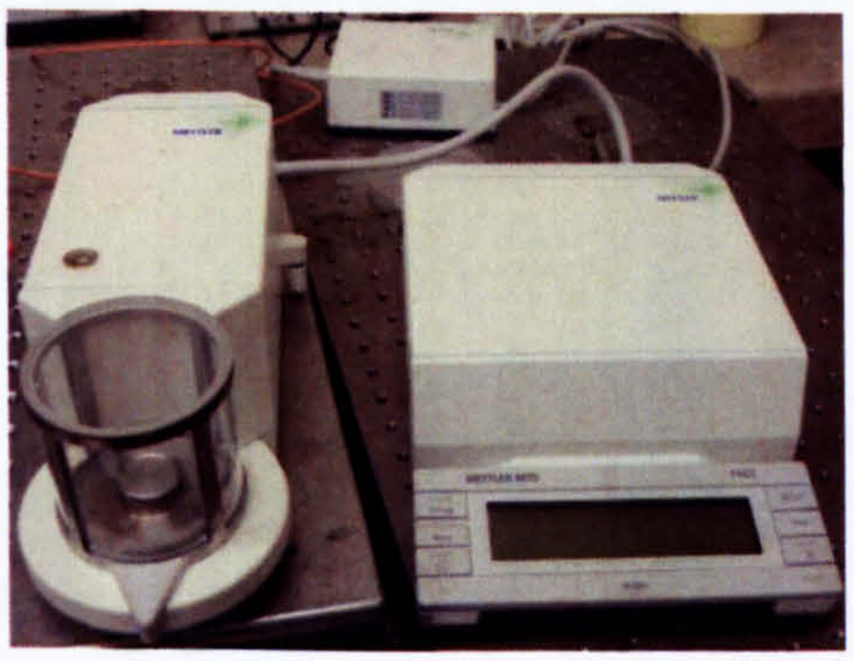

b)

Figure 6-13 a) Confocal chromatic measurement system (micro-epsilon, optoNCDT2400). b) High resolution scale with micro gram resolution (Mettler MT5).

It might however be possible to achieve a mass gain by placing a small tube in the vicinity of the µLens and dispense small amounts of water as shown in Figure 6-14. The vicinity of the exit of the tube is considered to be important, for the purpose that no drops are formed which would only yield mass gain in certain discrete quantities. In addition, the lateral space of the µLens is limited and therefore only small quantities of water should be used. The syringe can be operated in both directions by using the transition stage, meaning that mass could be reduced as well as increased for the investigation of the displacement. A further advantage would be that faster changes in mass could be achieved.

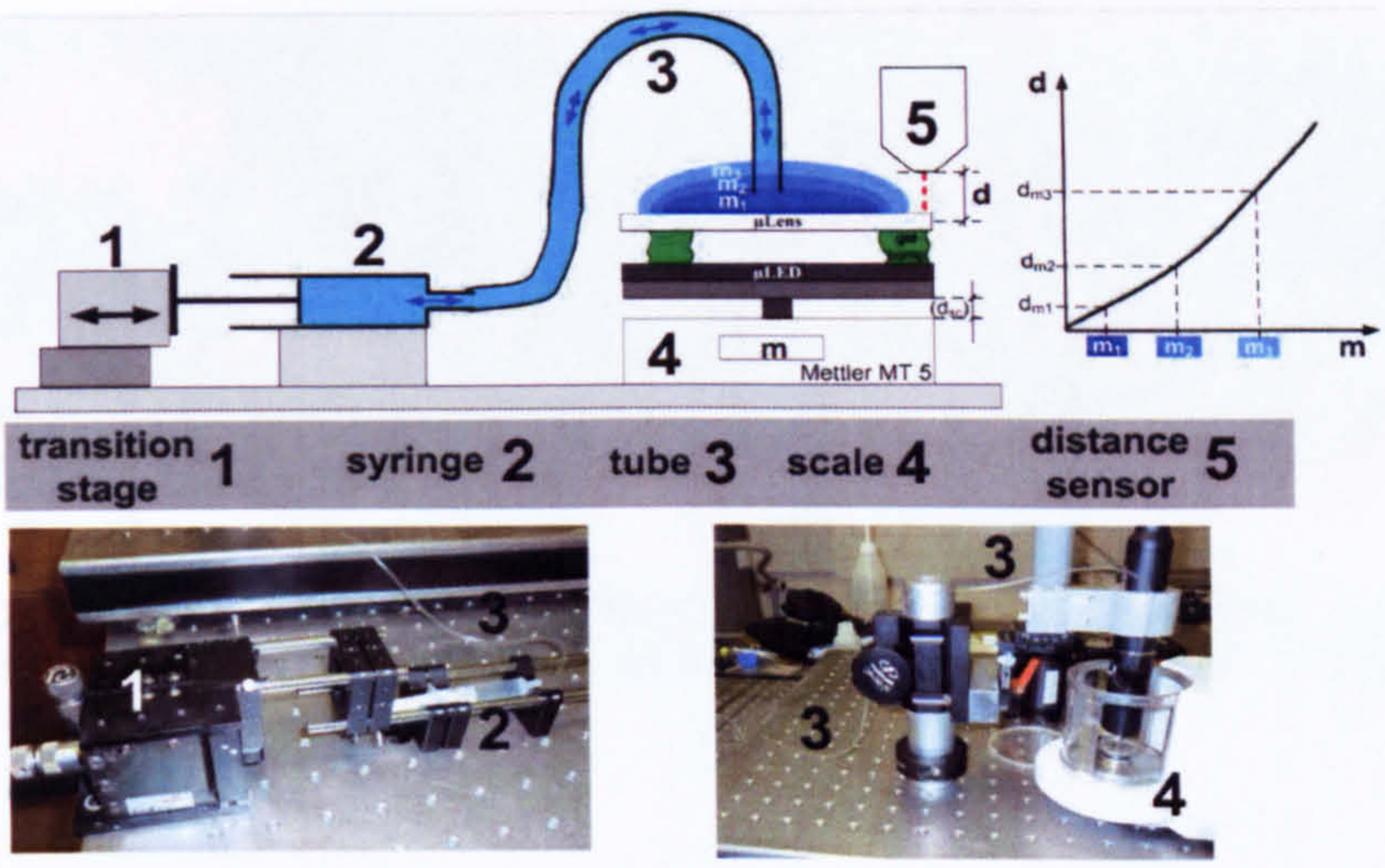

Figure 6-14 Using a syringe attached to a transition stage, the amount of water that is placed on the μLens can be varied accurately. The end of the tube needs to be close to the μLens so that no drops can be formed.

These measurements are of importance, to characterise the restoring means of the device, because with the linear force feedback, one can design models of the restoring means that can be solved by using Laplace transformation. This transformation can only be applied to linear systems and could not be used if the μLens was moved with the nonlinear electrostatic actuator. With this, it is attempted to model the restoring gel bump by using a spring-mass-dashpot system, which is analytically described and set up in SIMULINK® in Chapter 4. If one important part of the moving system can be characterised with different methods, it makes the characterisation of the entire system more plausible and reliable.

6.2.3 Microfabrication of the external driving device

So far, the external driving device has been manufactured by the means of macro fabrication methods. The EDD could be manufactured using microengineering. The author proposes to manufacture the EDD separately and position it afterwards on the prepared μLED. [60] from MISEC at Heriot-Watt has already demonstrated the feasibility of microfabrication of a solenoid and ferromagnetic core of high permeability for the purpose of achieving maximal inductance for electronic applications.

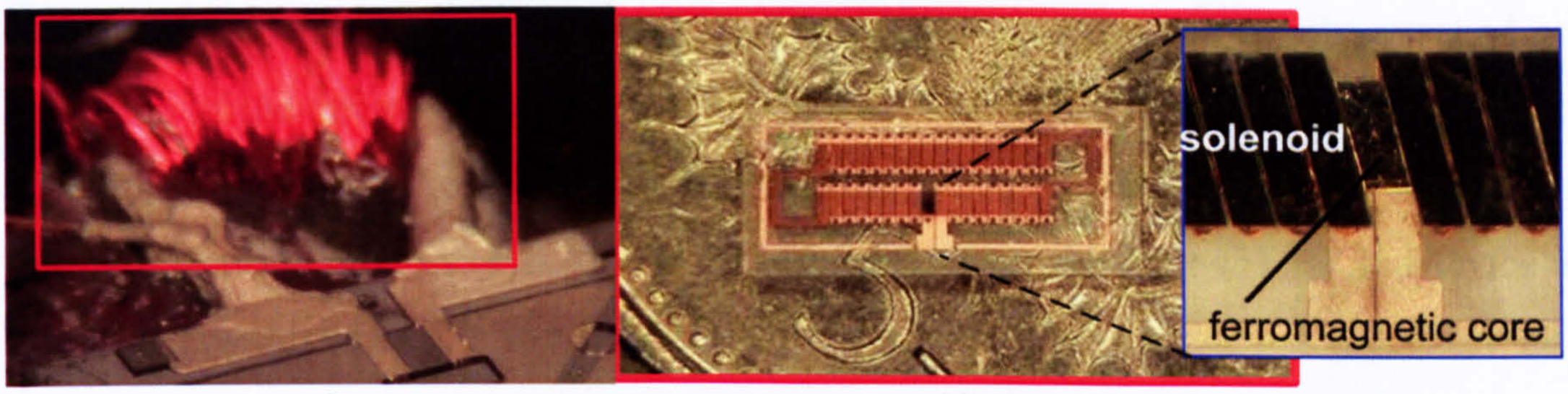

a) b) c)

Figure 6-15 a) Manually crafted EDD. b) Microengineered solenoid of 5mm length. c) Zoomed in image of b) with visible ferromagnetive core of high permeability (b) and c) by courtesy of [60]).

6.2.4 µLED-µLens assembly

This section addresses the possibilities of mass fabrication of a static µLED-µLens assembly via the dynamic actuation plus the determination of the µLens movement and tilt by means of available and/or cost effective equipment.

6.2.4.1 Possible mass fabrication

The External Driving Device (EDD) can provide, if temporary attached to the µLED (Figure 6-16a), interesting possibilities for mass fabrication. A particular advantage is that no expensive alignment machines have to align the µLens on top of the µLED. The only device necessary would be three photo detectors as shown in Figure 6-16b.

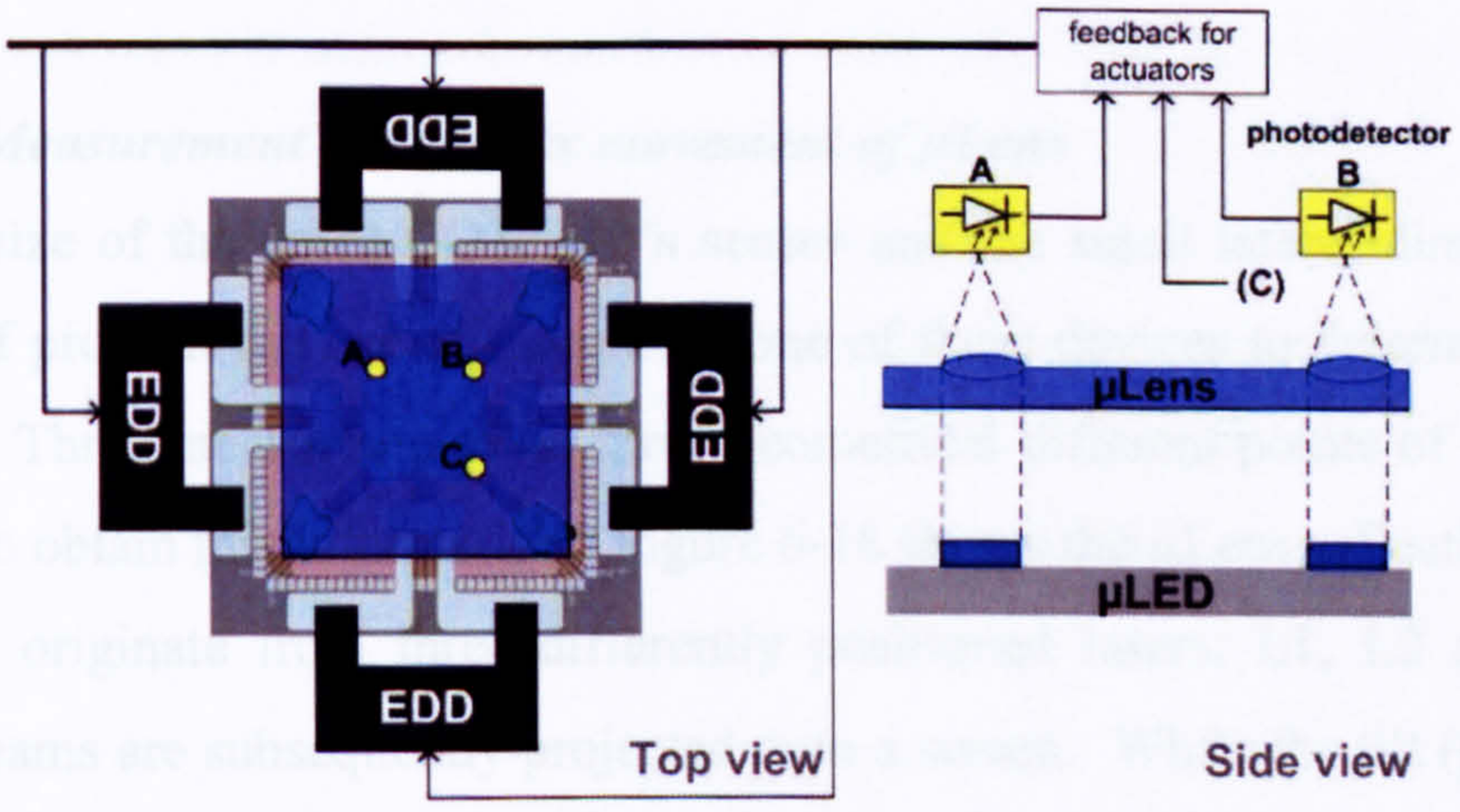

Figure 6-16 a) EDD could be temporarily attached on the µLED just for the alignment. b)Three detectors are at least necessary to detect the position of the µLens. A hill climbing algorithm could be applied in order that the detector gets the maximal intensity when the lenses are aligned.

Gel bumps and UV-curable adhesive are placed into the gel cavities. Gel bumps or restoring means are necessary to counteract capillary forces that are exerted from the UV-adhesive (1). The µLens is then roughly placed onto the µLED so that the posts fit

into the considerably larger cavities (2). The EDDs are then temporarily attached on each side of the device to align the structure (3). The UV-adhesive is then cured with UV-light/UV-laser. The EDDs are still attached to counteract a possible movement during the curing process (4). After curing, the EDDs are removed (5) and the device is sealed afterwards (6).

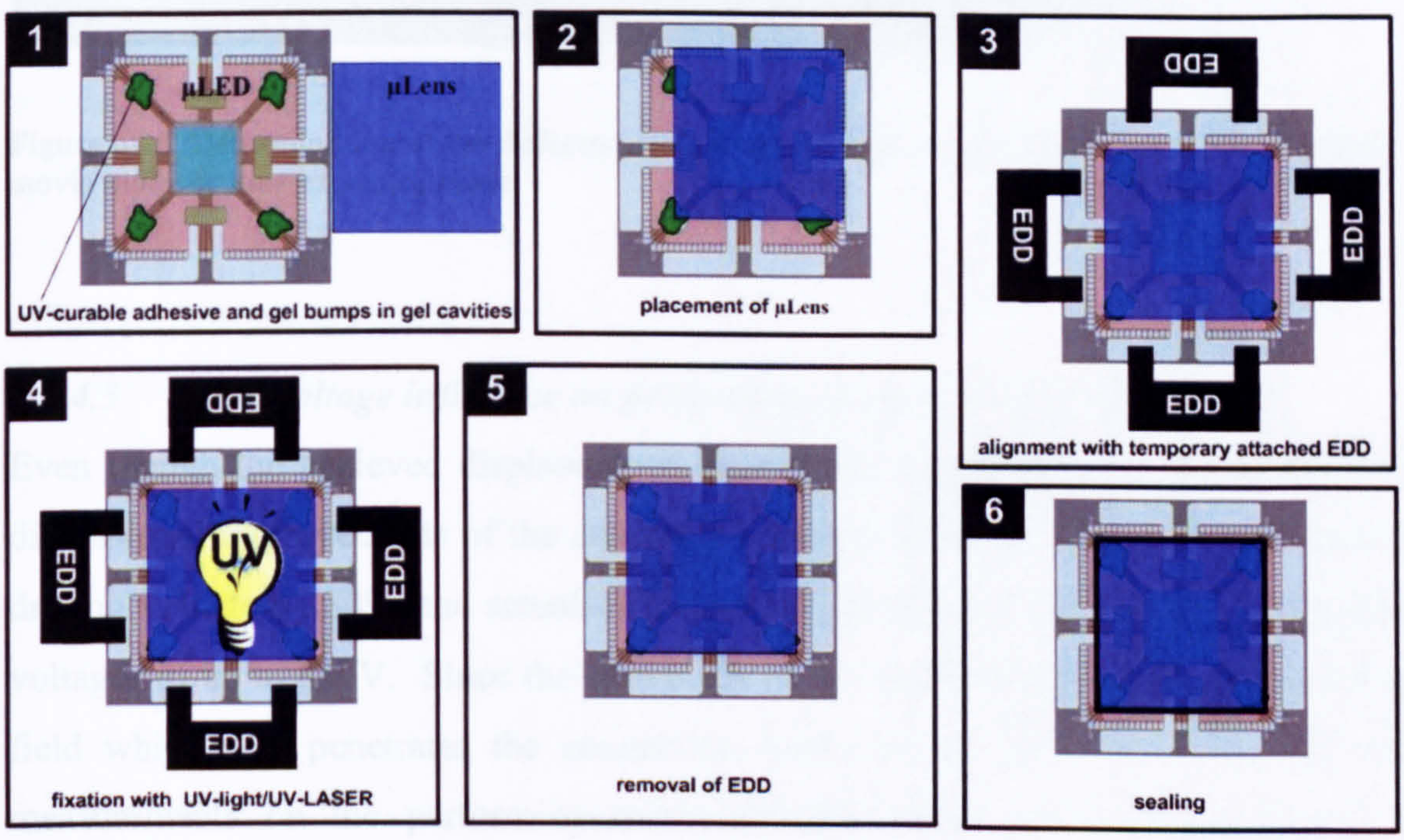

Figure 6-17 Possible mass fabrication process which makes use of temporary attached External Driving Devices (EDDs).

6.2.4.2 Measurement of complex movement of µLens

The sheer size of the optoNCDT2400's sensor and the small lateral dimension of the µLens itself prohibit the use of more than one of these devices to determine the tilt of the µLens. Three measurements on three geometrical different points of the µLens are necessary to obtain this information. Figure 6-18 shows the µLens reflecting three laser beams that originate from three differently positioned lasers, L1, L2 and L3. The reflected beams are subsequently projected onto a screen. While the tilt (pitch and roll) is performed with the electrostatic actuators with predefined voltages as a function of time, the screen is recorded with a digital camera in movie mode or long exposure mode. The behaviour of the pitch and roll can then be investigated since the position of the lasers and the spots on the screen as a function of different voltages and time are known.

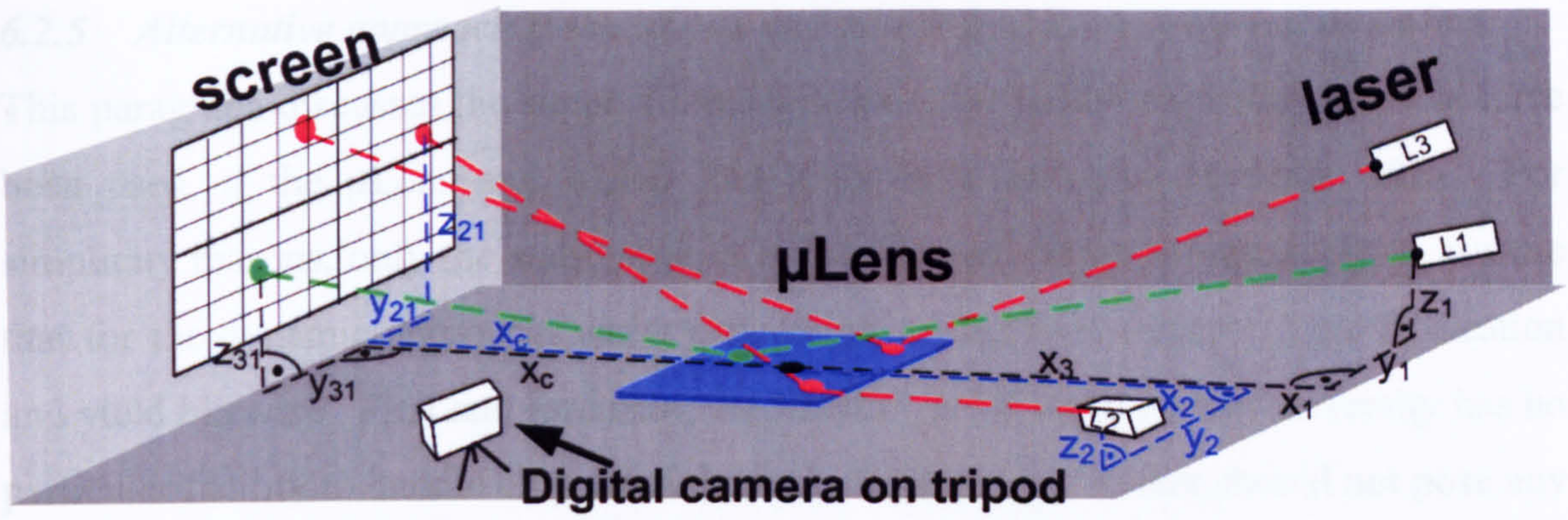

Figure 6-18 Determination of the different tilts by using 3 lasers and a digital camera with either movie mode or long exposure mode.

6.2.4.3 High voltage influence on performing micro-UV-LED array itself

Even though the achieved displacements exceed the requested ones considerably and dimensional improvements of the assembly have the potential to drastically reduce the driving voltage by 80%, the actuation for present devices in vertical direction requires voltages of up to 600V. Since the electrodes on the µLED create a strong electrostatic field which also penetrates the connection tracks to the LED and the LED itself, measurements on the performing micro-UV-LED array are to be conducted. In particular if the electrostatic field is changed over a short period of time, a parasitic electrical influence on the LED-connection tracks cannot be discarded. Few problems are expected for the magnetic actuator, since the magnetic flux is expected to be at a considerable distance towards the connection tracks (by using the entirely electroplated floating electrode device) and well confined within the magnetic path.

6.2.5 Alternative approach if the µLens and µLED had been delivered as wafers

This paragraph discusses the suppositional case of what packaging solution would have been used, if the µLens and µLED had both been delivered in wafer form. For simplicity reasons, only the static approach is addressed but it is reasonable to assume that for the dynamic approach, wafer processing would have improved the fabrication and yield likewise. First and foremost, the MISEC lab at Heriot-Watt University has no particular facility to handle chip sized devices, but handling wafers should not pose any problems. This simplifies the handling already considerably. Another advantage of using wafers is the potential of batch fabrication, at least for the initial steps. This increases the efficiency and yield. The process steps are much easier and more reliable, thereby reducing thermal and chemical influences that originates from the assembly process of single die.

General challenges that were faced are already listed in Table 3-1, Chapter 3. However, in order to propose improvements for the future manufacturing processes, some major problems are alluded in the following. It can be implied from Figure 4-20b in Chapter 4, that single chips glued on a wafer might not be an ideal surface for placing a Cr-glass mask with lateral dimension of about 150mm x 150mm on top. Indeed, despite disturbing capillary and surface tension effects of the photoresist, the non planar and limited surface is a major problem for the exposure and alignment tool (TAMARACK®), since it relies on this property during the alignment process. A further problem was the scratching of the Cr-glass mask, that occurred during the alignment. Figure 6-19a shows an additional problem which is caused by the close vicinity of the already existing alignment marks on the µLED-chip. The alignment marks AC1 and AC2 are only 5.7mm apart. This does not only cause problems with angular misalignment but also makes it impossible to point a separate alignment camera to each of the two alignment marks. Because of that, only one alignment camera could be used during alignment which had to be set on low magnification to capture AC1 and AC2, respectively. Moreover, Figure 6-19a and Figure 6-19b show, that the µLED-chip does not feature any alignment marks at the area between the micro-LED array and the LED-bond-pads, where the µLens is supposed to be placed.

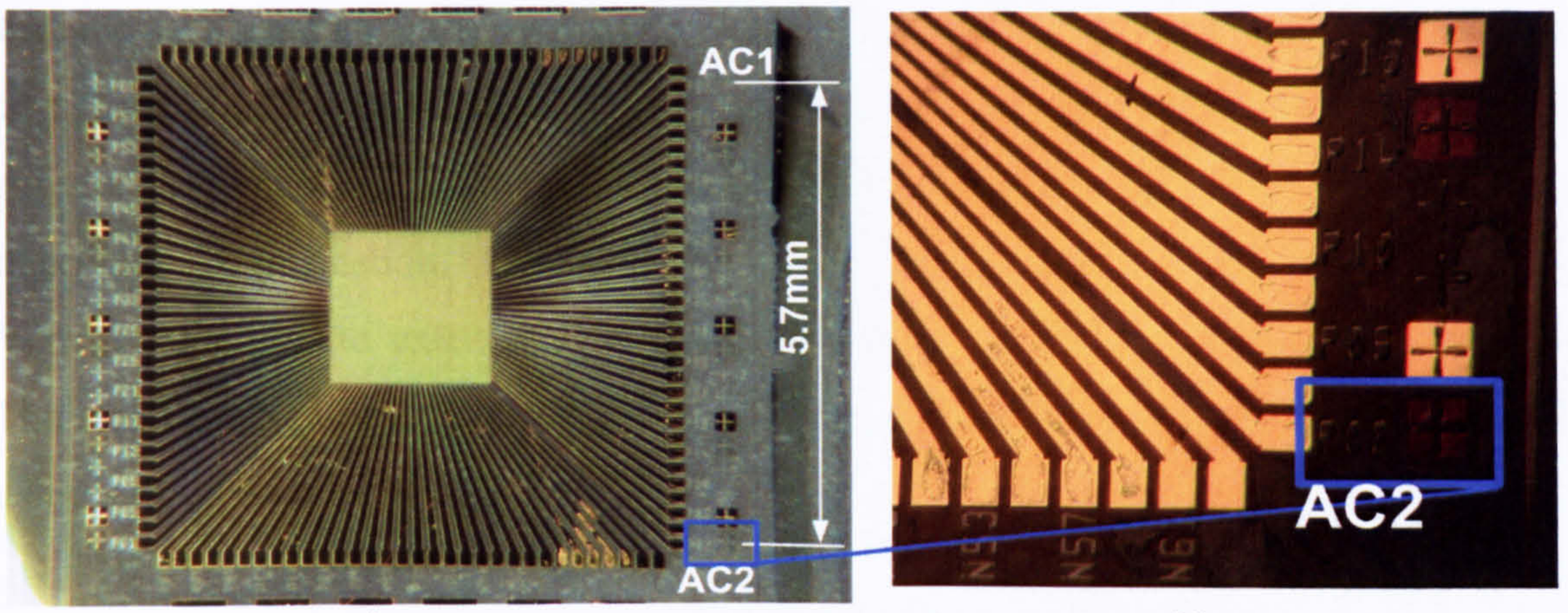

a) b)

Figure 6-19 a) The maximum separation of the alignment marks (AC1, AC2) produced by the chip manufacturer (IoP) was around 5.7 mm. b) Zoomed in picture of a) exhibiting the alignment mark AC2.

The initial given µLens-chips, did not feature any alignment marks with respect to the microlenses as well as alignment marks on the µLED-chip. After intervention of the author, it was agreed that 4 alignment marks were featured on the µLens as shown in Figure 6-20a. The author specified alignment marks, which would have a maximal width of 4µm (ideally 2µm) to comply with the demanded 2µm lateral alignment accuracy (Figure 6-20b). Measurements of the delivered modified microlens array, however, revealed that these important dimensions were by far not achieved. Line width of 10µm were measured and the important cross-section featured a width of around 18µm as shown in Figure 6-20c.

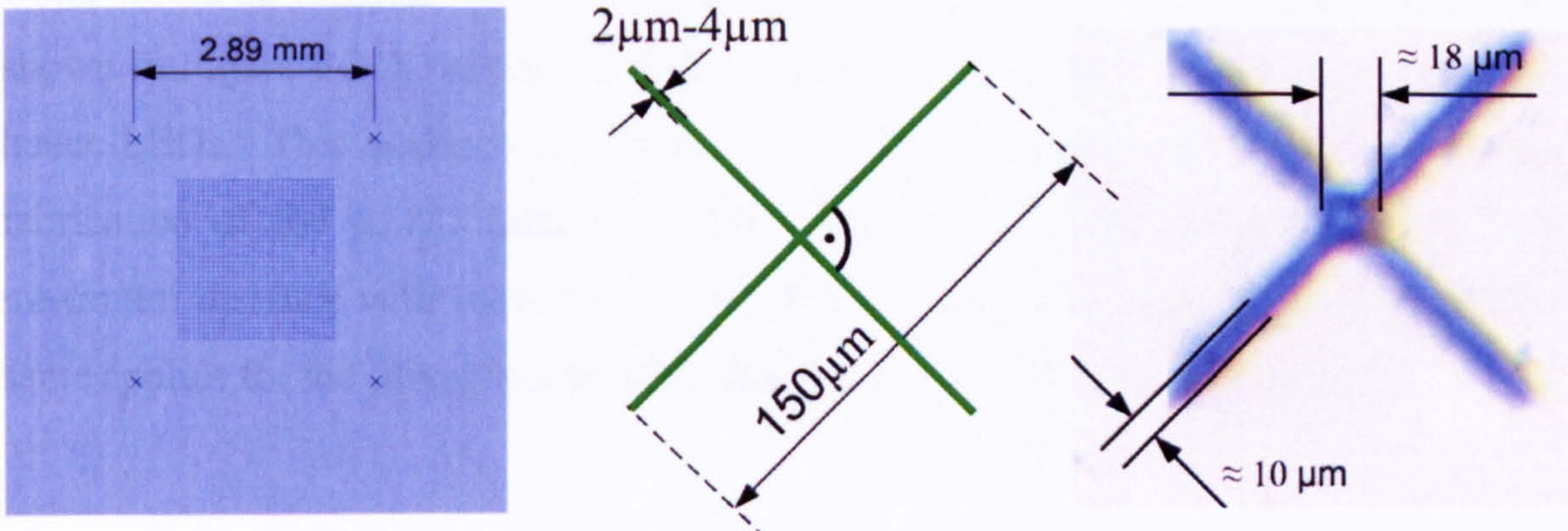

a) b) c)

Figure 6-20 a) 4 alignment marks fabricated by IoP after intervention by the author. b) Demanded alignment mark dimension. c) Obtained alignment mark.

Figure 6-21a shows a partly fabricated dummy-wafer of the first design that features alignment marks on the Cr-glass mask which are relatively far apart from each other, to

achieve best possible wafer alignment. The distance of 70mm of these alignment marks compared with the distance of the μLED alignment marks considerably improves the angular alignment. This allowed to use both cameras of the TAMARACK® with maximum magnification. Figure 6-21b shows a zoomed-in alignment mark, featuring Vernier structures to extend the alignment accuracy beyond the minimal feature size. The smallest alignment features in Figure 6-21b are about 10μm and fabricated in SU8 using a Cr-glass mask.

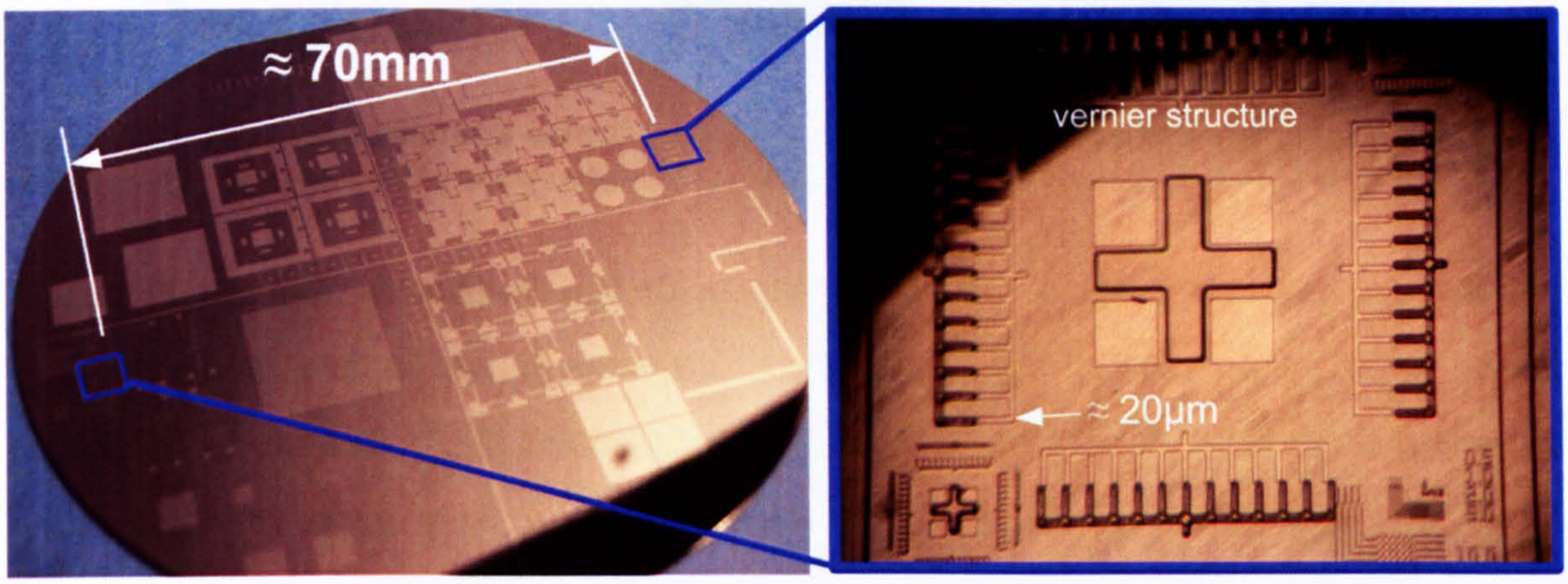

Figure 6-21 a) First design mask where the alignment marks are separated over nearly the entire diameter of the wafer, thereby improving angular alignment accuracy. b) Zoomed-in picture from a) with alignment marks featuring Vernier structures.

Figure 6-22a shows the ideal case in which the μLED structures are delivered as sapphire μLED-wafers featuring embedded μLED-chips. Ideally, the diameter of the wafer would be 76.2mm and feature alignment marks (AW11, AW12) similar to the one shown in Figure 6-21b, which are highly accurate with respect to the μLED-chips and hence LEDs. This assumption is reasonable, if the alignment marks are used for the fabrication of the μLED features. These alignment marks should be spaced with maximum distance with respect to each other for optimising angular alignment. The same applies for the μLens-wafer and its ideal structure shown in Figure 6-22b.

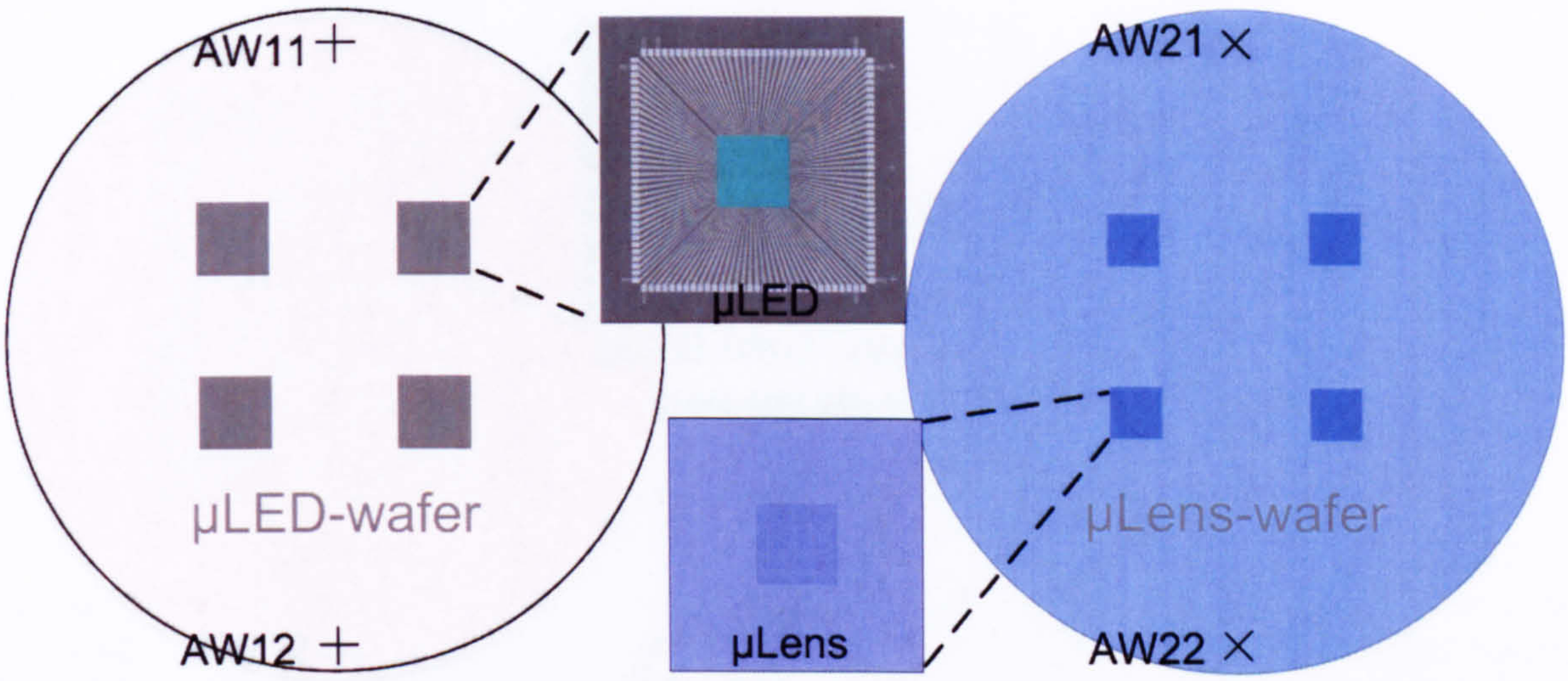

Figure 6-22 a) µLED-wafer with embedded µLED-chip and alignment marks AW11 and AW12, respectively. b) µLens-wafer with embedded µLens-chips and alignment marks (AW21, AW22).

The in Figure 6-22 described alignment marks are used to fabricate structures on the µLED-wafer as well as the µLens-wafer which are highly accurate with respect to the embedded µLens and µLED features (Figure 6-23). Figure 6-23a shows a µLED-wafer with µLED-structures manufactured on each µLED-chip. The material used is either the negative photoresist SU8 or THB. The height of this structure is crucial, since it determines the distance between the µLED and µLens. As already described in Chapter 3.2.3, spinning of a certain photoresist thickness is not accurate enough for this objective. The following Chapter 6.2.5.1 proposes an already partially tested method in which a not yet developed photoresist is lapped to a predetermined thickness. The µLens-structure is fabricated onto the µLens-wafer using the UV-LIGA process.

Theoretically it should be possible to put adhesive on the corners of each of the µLED-structures and place the µLens-wafer on top of the µLED-wafer, thereby facilitating a batch assembly process. The alignment marks AW21 and AW11 as well as AW22 and AW12 need to be accurately aligned. After curing, the assembly would then by diced, yielding 4 assembled µLED-µLens devices which are sealed in a following process step.

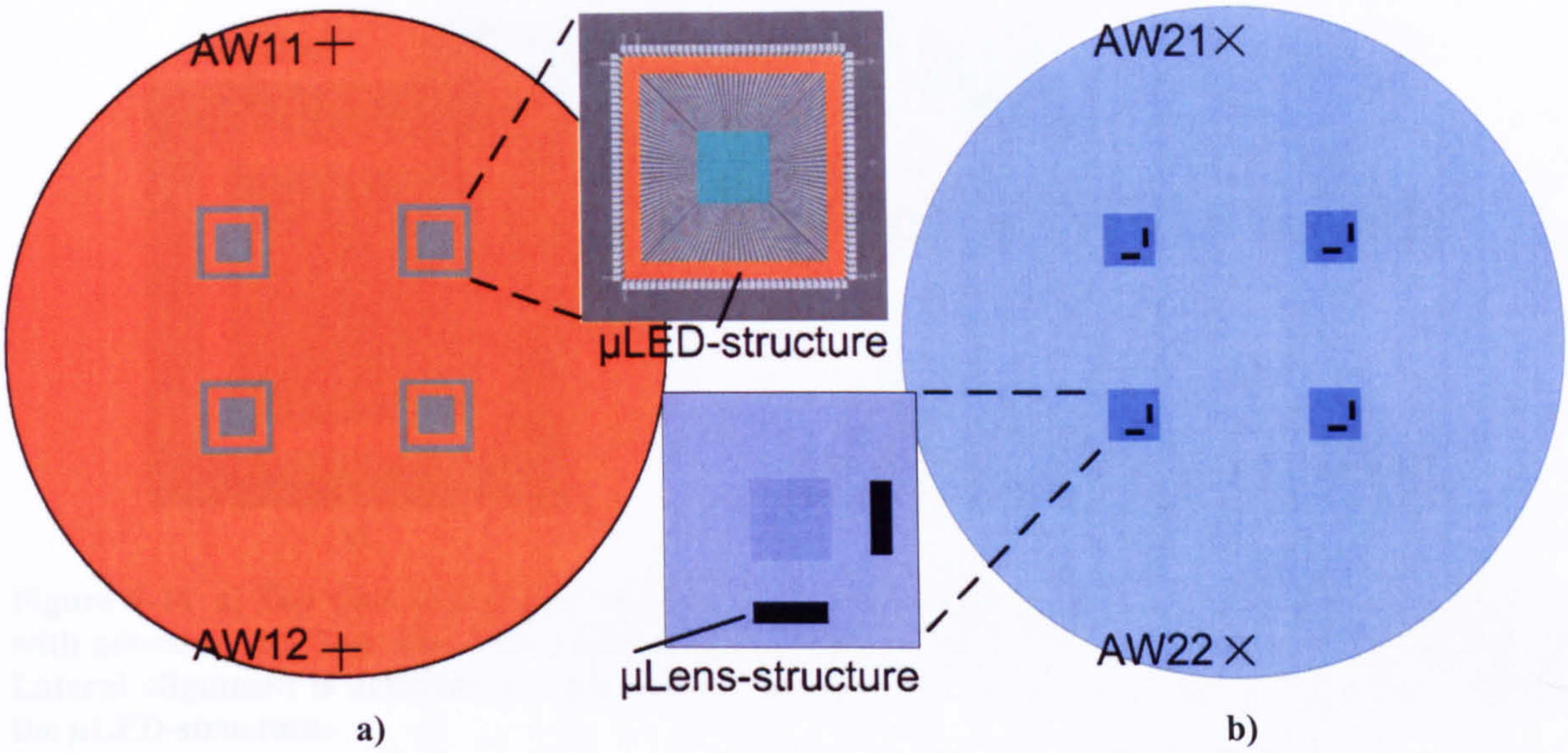

Figure 6-23 a) SU8 or THB structure fabricated on the µLED-wafer by using the alignment marks AW11 and AW12 for accurate alignment. b) Same as a) but for µLens-wafer.

However, this method would only be feasible, if the LED-bond-pads of the µLED do not need to be wire-bonded or if the design of the µLED-chip provided LED-bond-pads on the backside of the device/wafer.

Figure 6-24a and Figure 6-24b(Top) shows the situation just before assembling the µLens and µLED that have been previously diced from the wafers, earlier shown in Figure 6-23. The corners of the µLED-structure feature small drops of adhesive (i.e. UV-curable). The amount of adhesive should be kept at a minimum since the stresses induced by the curing process of the adhesive might compromise the alignment accuracy. The µLens is placed onto the µLED-structure and diagonally shifted so that the µLens-structure touches the edges of the µLED-structure. The µLens-structure aides only the lateral alignment, whereas the µLED-structure serves the purpose of lateral as well as vertical alignment. It is therefore imperative that the µLED-structure is thicker than the µLens-structure as shown in Figure 6-24b (Bottom). After the adhesive is cured, the assembly can be either sealed and then wire-bonded or vice versa. In case the µLens as well as µLED-chips feature proper and accurate alignment marks with respect to each other, only the µLED-structure would be necessary and the µLens could be placed by using a flip-chip bonding machine. The process of achieving accurate thickness of the µLED-structure is described in the following chapter.

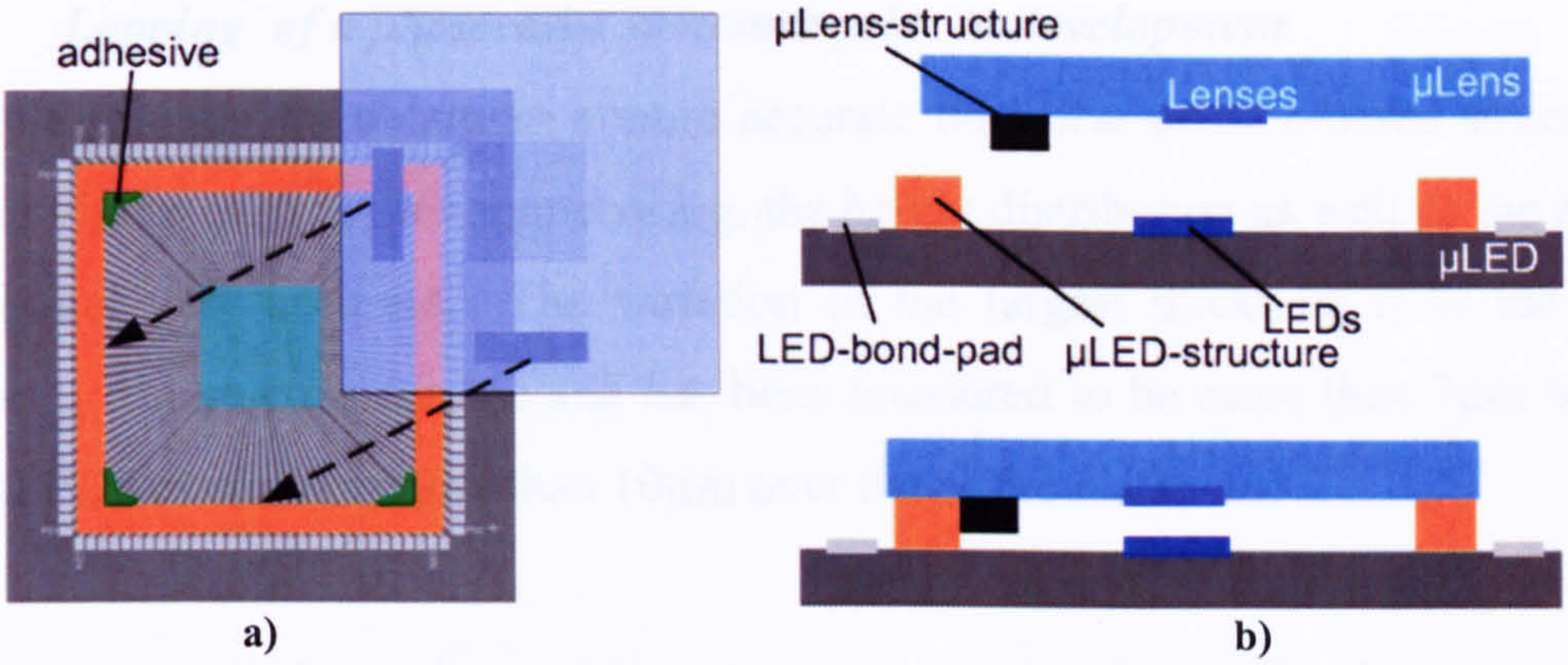

Figure 6-24 a) Top view of a µLens which is placed onto the µLED-structure and fixed afterwards with adhesive. b) Top: side view of the situation on the left hand side. Bottom: assembled device. Lateral alignment is achieved trough the µLED-and µLens-structure, vertical alignment through the µLED-structure.

Figure 6-25 shows a nearly equivalent alignment method as illustrated in Figure 6-24. This approach was inspired through suggestions of Prof Richard Syms during the viva. It differs in the point that the vertical alignment is obtained via a spacer. The spacer can be either micro- or macro-manufactured, thereby offering a variety of processes and hence accuracies. The spacer can be situated either outside (as illustrated) or inside the µLED-structure. To prevent an electrical short-circuit between the connection tracks on the µLED, the spacer material should be an electrically non-conductive material.

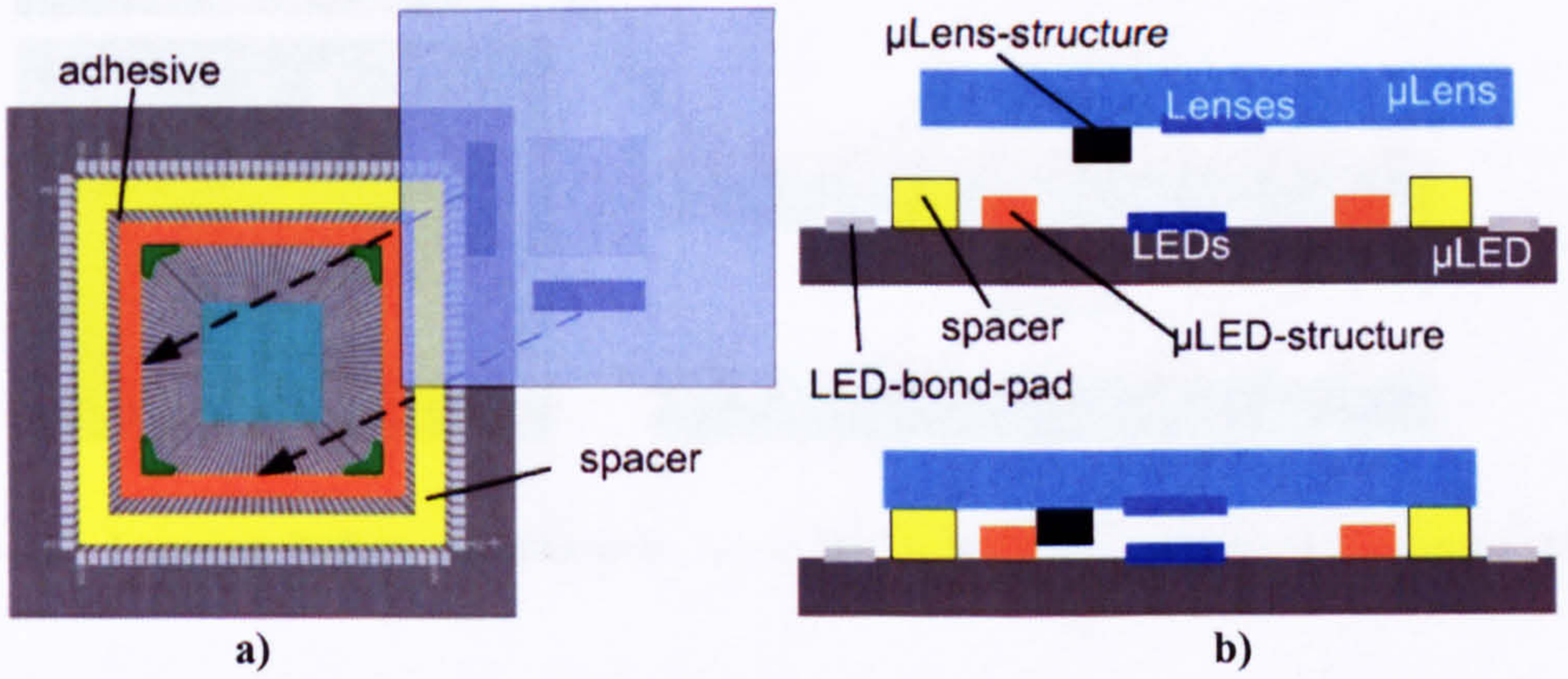

Figure 6-25 a) Top view of µLED with µLED-structure and spacer prior of being assembled. b) Top: side view of the situation shown on the left. Bottom: assembled device. Vertical alignment through spacer, lateral alignment through µLens- and µLED-structure.

6.2.5.1 Lapping of a photoresist structure prior to development

A possible solution for obtaining a more accurate thickness of SU8-based structures is shown in Figure 6-26. After spin-coating, the height distribution as well as the average height is not very accurate. The variation of the largest thickness t_2 to the lowest thickness t_1 can be considerable and has been measured to be more than 7µm within a single µLED structure or more than 10µm over the entire wafer.

The SU8 is spun on the wafer, soft baked, exposed and post baked. Then, the wafer is lapped using a wafer polishing machine. The average height during the lapping process could be observed by a small hole which has already been developed to form a step in order to conduct interferometer measurements. For that reason the sample had to be removed, cleaned and then analysed using the ZYGO® white light interferometer. After the lapping process, the wafer is developed.

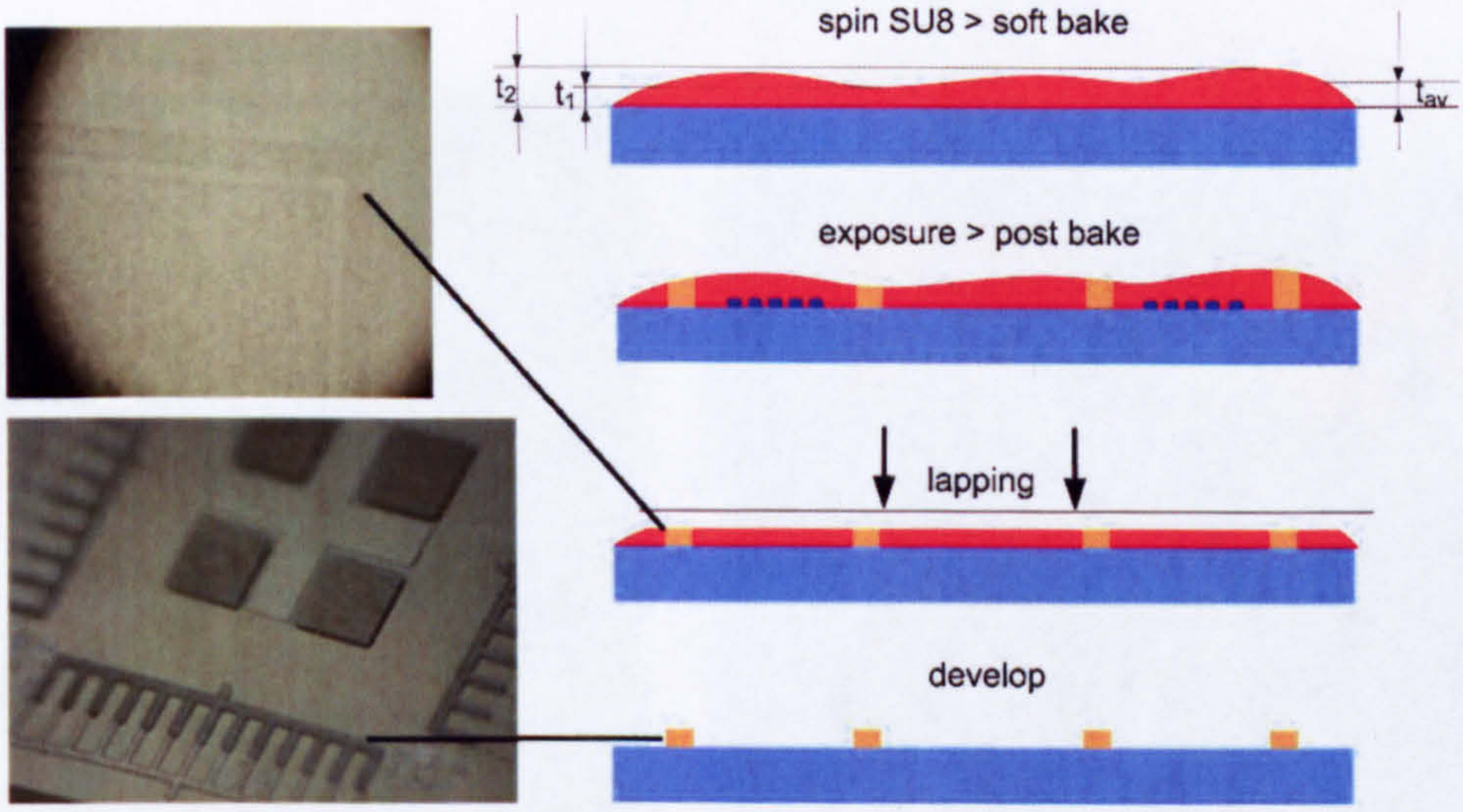

Figure 6-26 Lapping before development in order to protect the fragile structure embedded beneath.

By applying the method proposed above, it is possible to grind fragile structures with a high aspect ratio, as they are embedded within a supporting structure. The same method can also be employed for a single chip. Figure 6-27a shows a micrograph of alignment marks that have been lapped (grinded) before development. Even structures smaller than 20µm withstood the lapping process. In comparison, Figure 6-27b shows the same structure that had been lapped after development. This method resulted in the loss of the small structure.

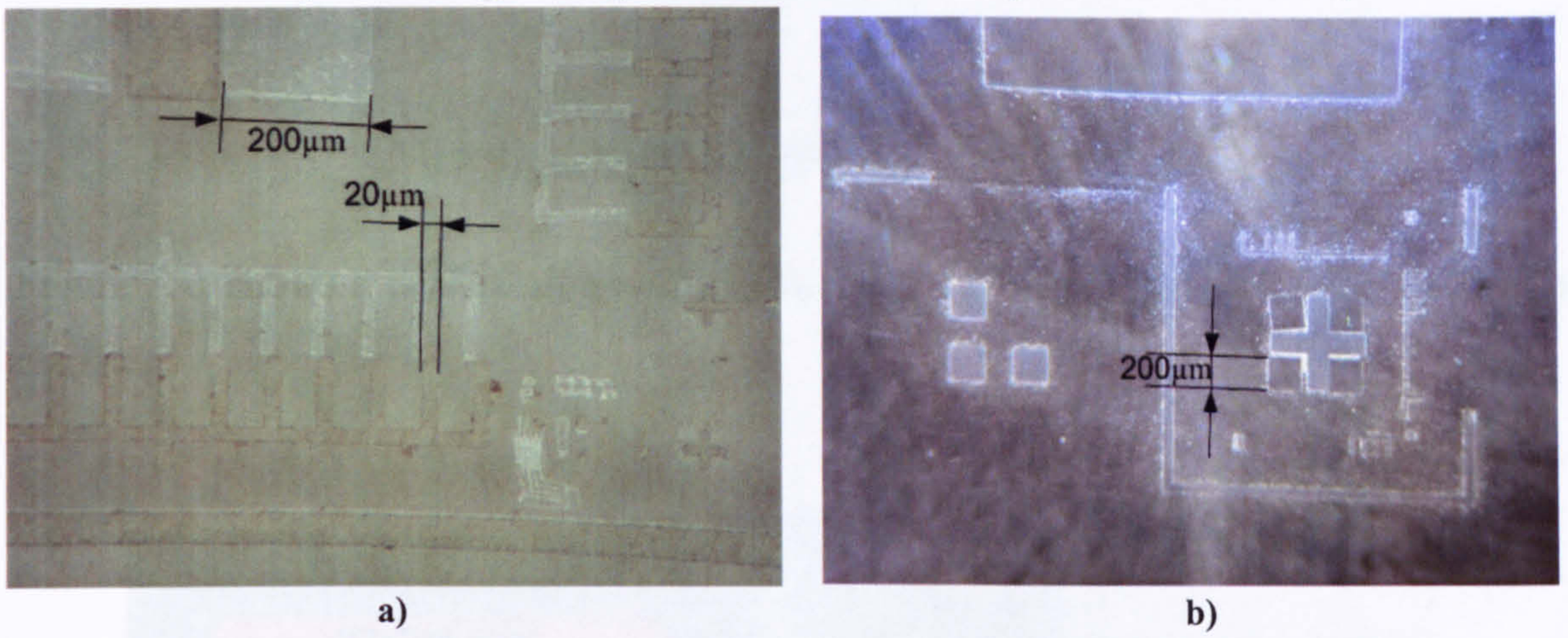

Figure 6-27 a) Wafer developed after grinding (lapping). Small structures are preserved. b) Wafer ground after development. The small structures are partly or entirely destroyed.

As shown in Figure 6-28, the variation in height distribution within the structure was measured with ZYGO® and found to be less than 1.3µm. It is assumed that by further refinement of the process, sub-micron accuracies can be achieved.

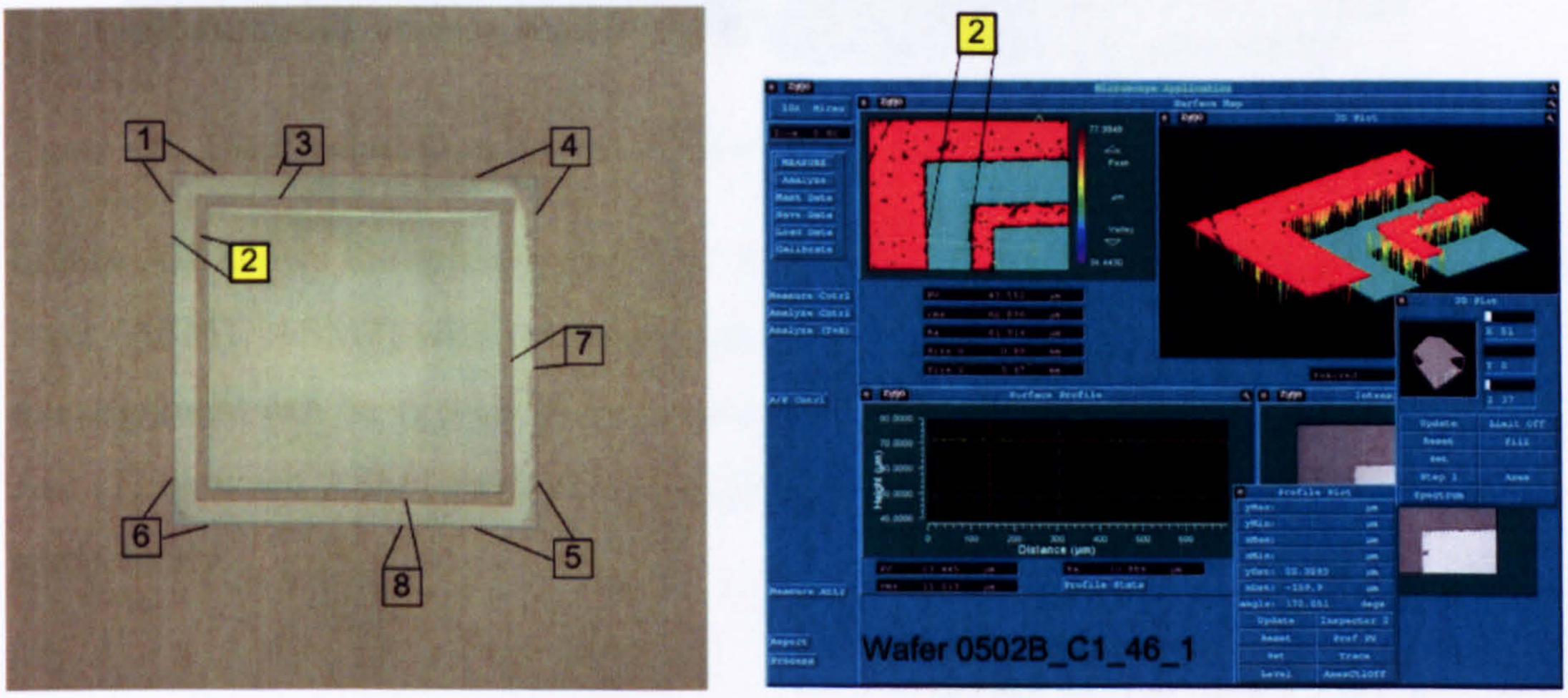

1	22.06µm; 22.2µm	3	22.5µm; 22.2µm	5	23.25µm; 22.5µm	7	23.1µm; 23.3µm
2	22.33µm; 22µm	4	23.1µm; 22.5µm	6	22.7µm; 22.5µm	8	22.6µm; 22.4µm

Figure 6-28 The thickness of a ground structure varies from 22.06µm to 23.3µm. This thickness range of 1.26µm.

A disadvantages of the method is that the lapping occurs for both the exposed and unexposed SU8 parts, which have a different hardness. An alternative method would be to fabricate a protective AZ-layer onto the completely developed and baked SU8 structure. The wafer is then polished within the hard, protecting bulk of the AZ-layer. In the next step the AZ-layer can either be removed by IPA or alternatively the entire wafer is exposed to UV-light and then developed with AZ-developer.

Appendix A

Misalignment Correction Calculation

Figure A-1 shows a perfect alignment of the structure layer with respect to the µLED-chip.

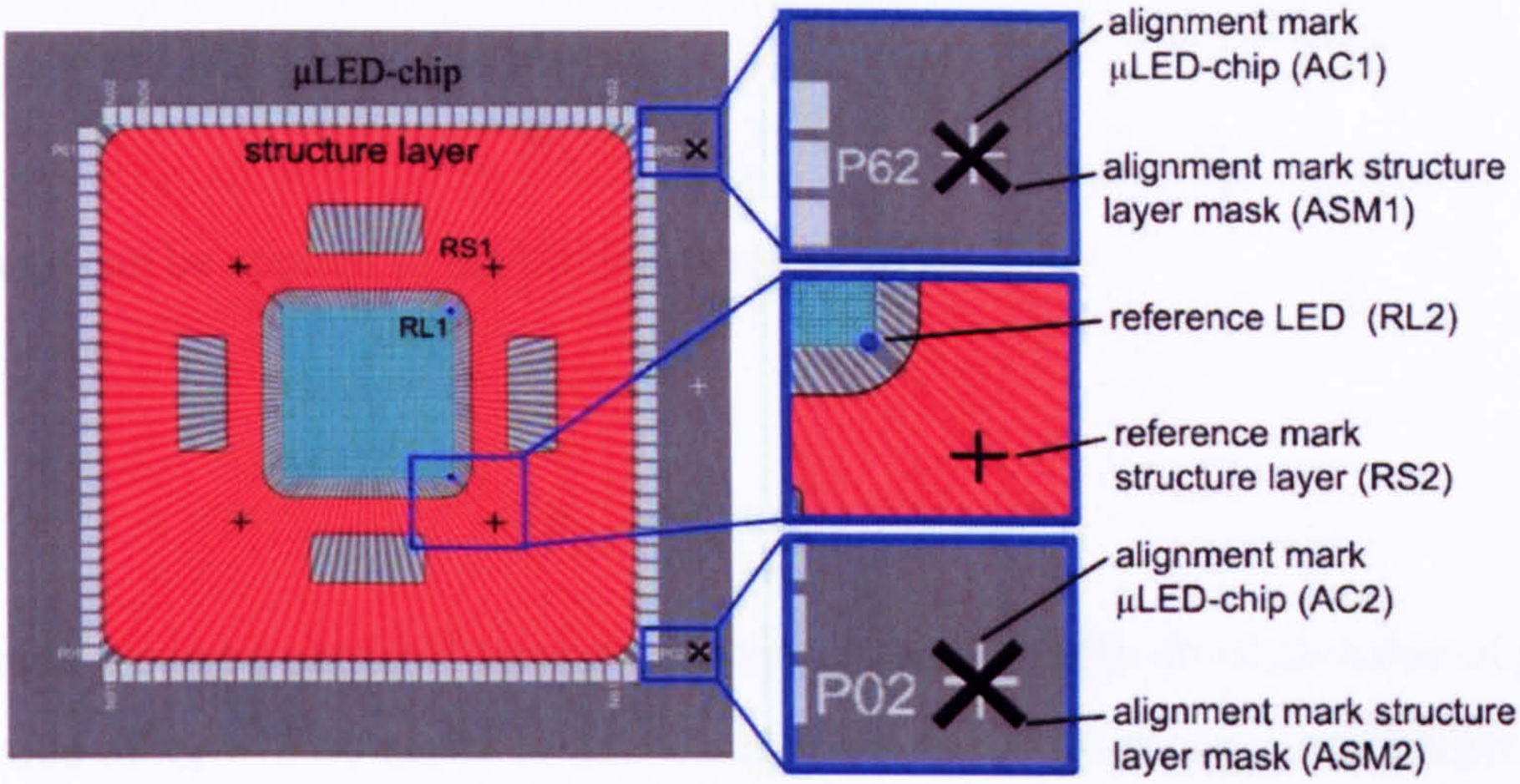

Figure A-1 The structure layer is the only layer on the µLED that needs to be accurately aligned.

Figure A-2 shows the misalignments of the fiducial marks of the mask of the structure layer (ASM1, ASM2) with respect to those of the µLED-chip (AC1, AC2). The lateral misalignment can be expressed in Cartesian vectors. The misalignment seen in Figure A-2 (1) between ASM1 and AC1 is x_1 and y_1 and between ASM2 and AC2 x_2 and y_2 respectively.

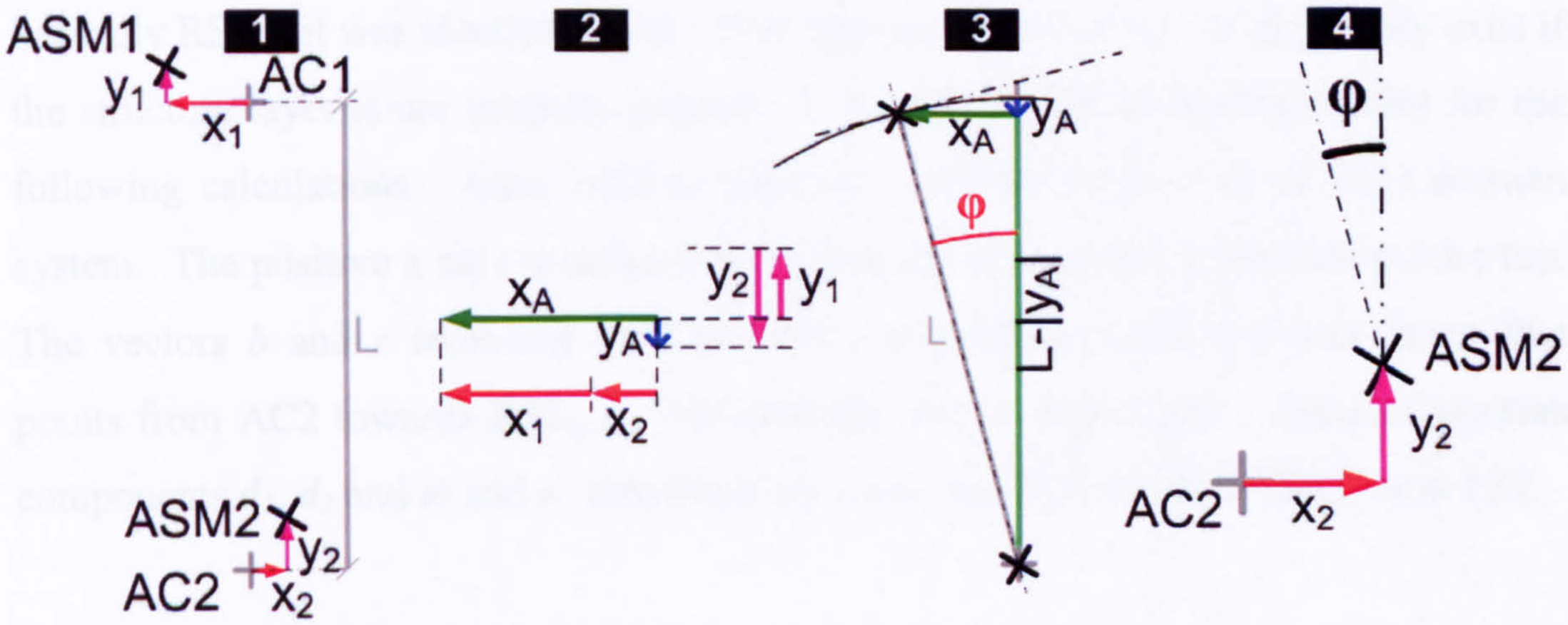

Figure A-2 Analysis of the misalignment between the different fiducial marks and extraction of the important parameters for the correction process.

The misalignment can be expressed with these two pairs of coordinates. However, it is more convenient to characterise the misalignment with a Cartesian component x_2 and y_2 and an angular component φ. In Figure A-2 (2) the alignment marks ASM1 and ASM2 are moved so that ASM2 coincides with AC2. Figure A-2 (3) depicts the vector addition where x_A and y_A are obtained. The positive direction of the vector is defined from left to right and from bottom to top hence:

$$-\mathbf{x}_A = -\mathbf{x}_1 - \mathbf{x}_2 \tag{A-1}$$

The same can be applied to the vertical components

$$-\mathbf{y}_A = \mathbf{y}_1 - \mathbf{y}_2 \tag{A-2}$$

The angle φ can be obtained by trigonometry using either the absolute value of y_A or x_A. The value of x_A will be easier to determine under the microscope, since bigger than y_A, therefore the sine-function is used as described in equation (A-3) and shown in Figure A-2 (3). L is the distance between the alignment marks AC1 and AC2.

$$\varphi = \arcsin\left(\frac{|\mathbf{x}_A|}{L}\right) \tag{A-3}$$

Figure A-3 show the exaggerated misaligned structure layer on top of the μLED-chip. All alignment marks except for $RS2_{ideal}$, are explained in Figure A-1. $RS2_{ideal}$ is basically RS2 if it was ideally aligned. This alignment mark does not physically exist if the structure layer is not properly aligned. It is just used as an auxiliary point for the following calculations. Also, AC2 is taken as point of origin (0,0) of the Cartesian system. The positive x axis is defined to the left and the positive y axis toward the top. The vectors $\boldsymbol{b}$ and $\boldsymbol{c}$ represent the Cartesian components of the position vector that points from AC2 towards $RS2_{ideal}$. Furthermore, the vectors $\boldsymbol{d}$ and $\boldsymbol{e}$ and its Cartesian components d_1, d_2 and e_1 and e_2 constitute the vector that lies between ASM2 and RS2.

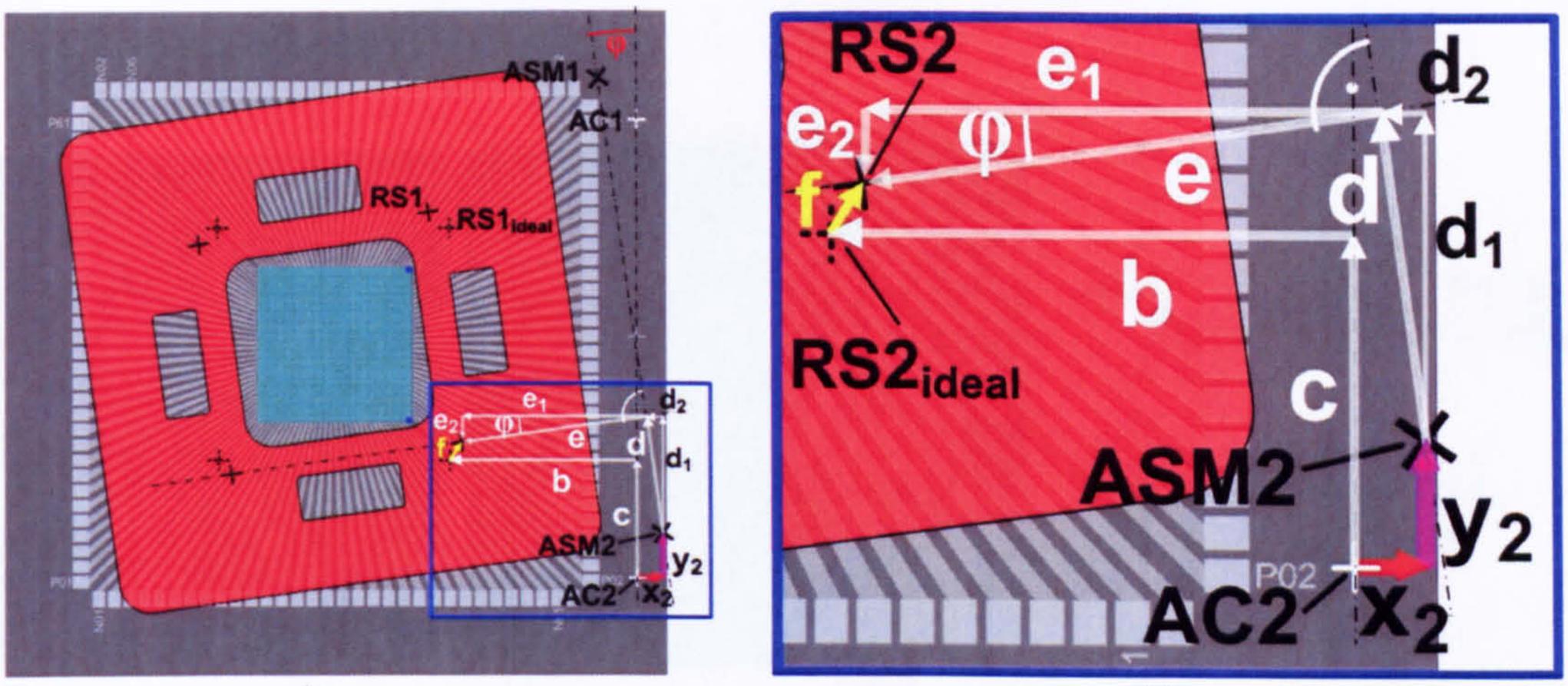

a) b)

Figure A-3 The structure layer is not perfectly aligned towards the μLED.

Using vector geometry the Cartesian displacement vector, ***f***, can be calculated by vector addition

$$\mathbf{f} = \mathbf{x}_2 + \mathbf{y}_2 + \mathbf{d} + \mathbf{e} - \mathbf{b} - \mathbf{c} \tag{A-4}$$

where the above vectors can be seen in Figure A-3. By knowing that the absolute value of ***d*** and ***c*** as well as ***e*** and ***b*** are the same and applying trigonometry using the angle φ as an argument leads subsequently to equation (A-5).

$$\mathbf{f} = \mathbf{y} \cdot \left(y_2 + c \cdot \left(\cos(\varphi) - 1\right) - b \cdot \sin(\varphi)\right) + \mathbf{x} \cdot \left(x_2 + b \cdot \left(1 - \cos(\varphi)\right) - c \cdot \sin(\varphi)\right) \tag{A-5}$$

y and ***x*** stand for the unity direction vectors in y- and x direction. The Cartesian displacement vector, ***f***, and the angular misalignment is obtained which completely describes the (misaligned) position of the structure layer with respect to the μLED-chip. The posts of the μLens can now be deliberately misaligned with regards to the microlens array to completely compensate the initially mentioned misalignment. Figure A-4 shows how the alignment marks for the post mask (AP1) is displaced by the Cartesian vector, ***f***, and the angular misalignment φ with respect to the alignment marks of the lens (AL1). As seen in Figure A-4, the angle φ is established between a parallel of a vertical connection line which stretches between two alignment marks of the μLens (AL1 and AL2) and the straight line between the alignment marks AP1 and AP2. Alternatively the total misalignment could be calculated if, instead of the angle φ, a second Cartesian displacement vector which relates AP2 towards AL1, was used. This might be of better practical use while operating the mask aligner, and can be calculated with vector geometry similar as stated above.

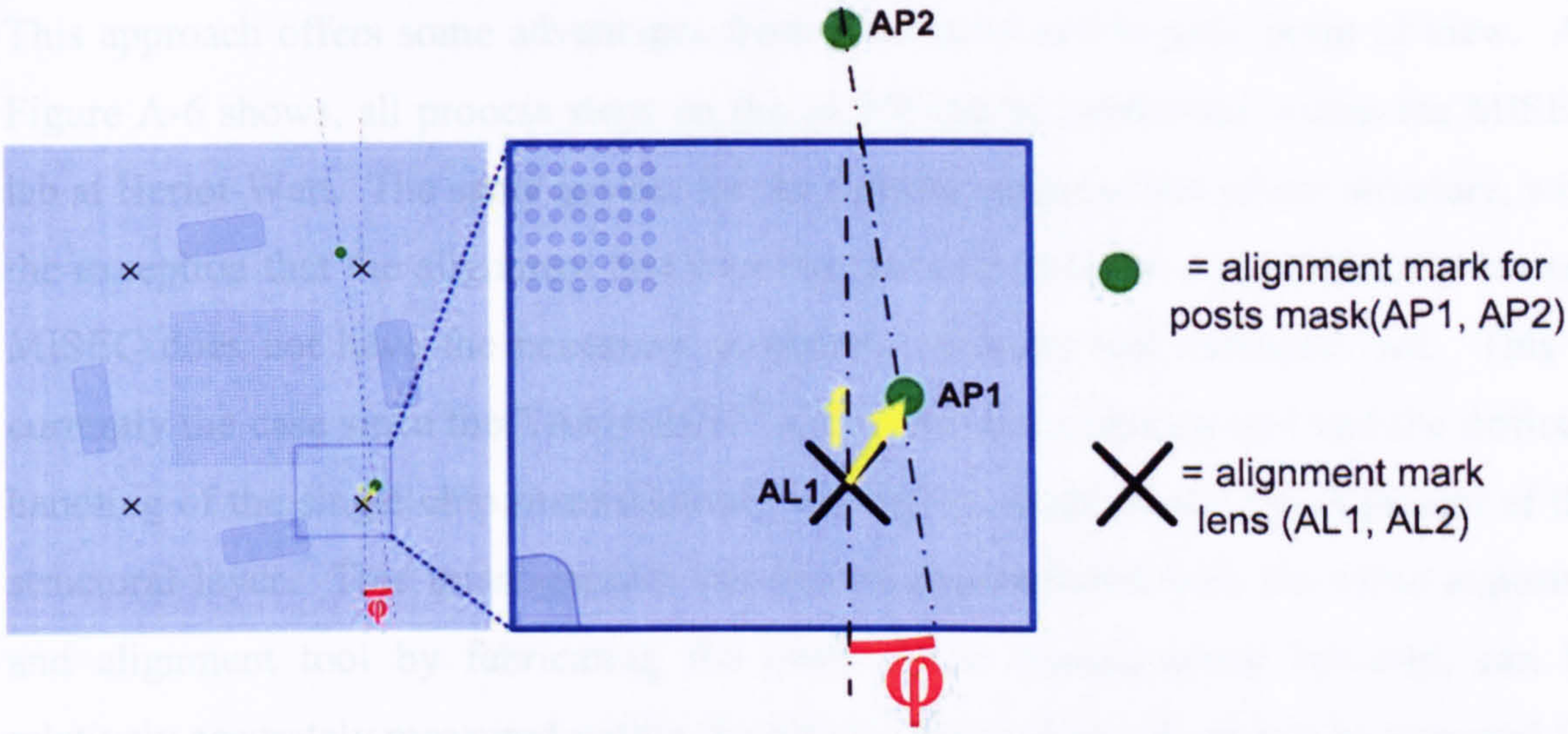

Figure A-4 After knowing *f* and φ, the alignment marks of the post mask (AP1) can be placed exactly *f* apart and an angle *φ* misaligned with respect to the alignment marks of the lens array (AL1).

Figure A-5 shows the assembled μLens on top of the μLED, where the individual microlenses are perfectly aligned towards the micro-LED. The mismatch between μLED and structural layer is compensated with the deliberate misalignment of the post with regards to the μLens. After having placed the posts within the cavities, the diagonal force $\boldsymbol{F}_{actio}$, needs to be applied at the μLens, in order to press the edges of the post C and D to its corresponding wall on the structural layer. This is necessary since the compensational misalignment is performed with respect to these walls.

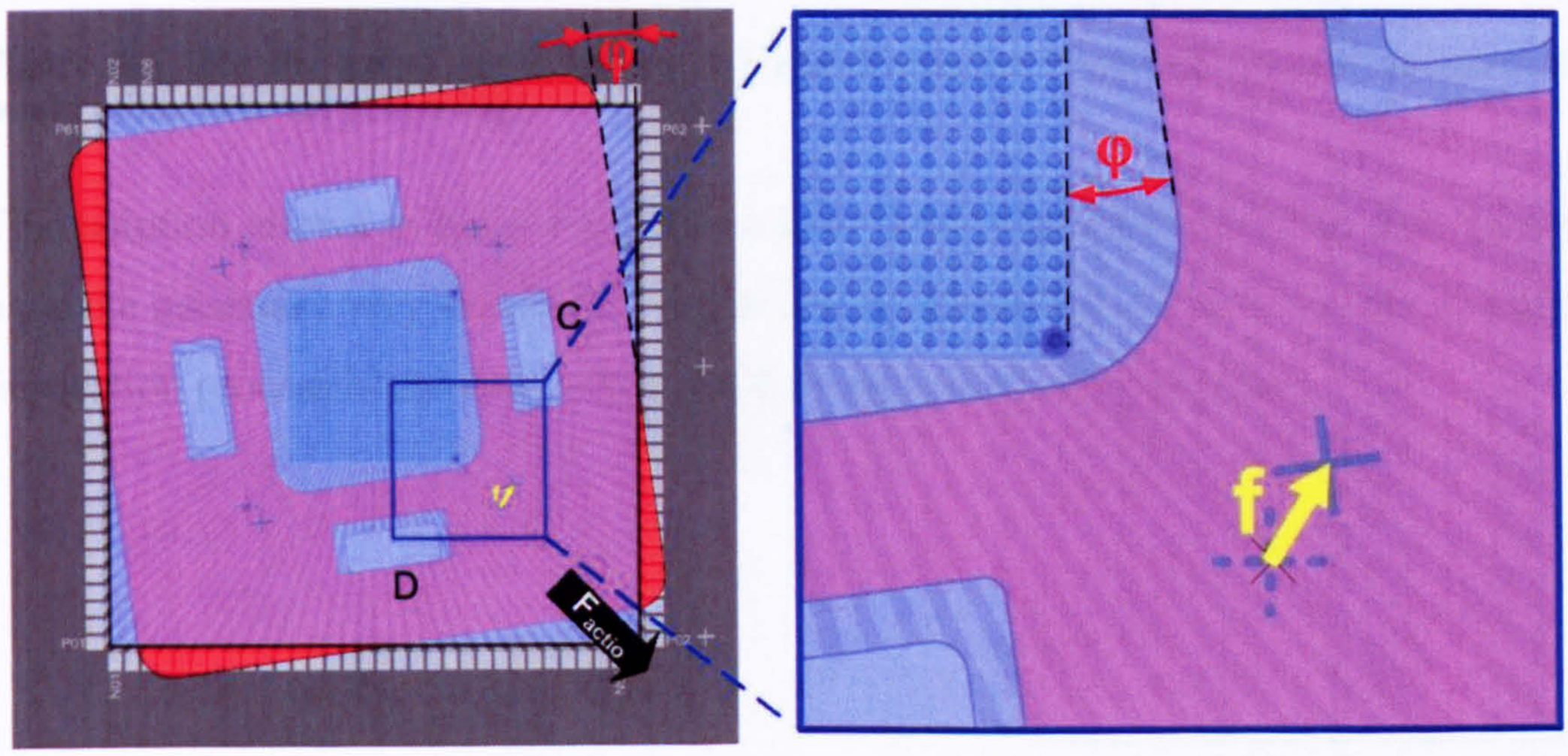

Figure A-5 After placing the μLens with the purposefully "misaligned" posts, the initial misalignment of the structural layer with respect to the micro-LED's is compensated and the individual microlenses correspond with the micro-LED's.

This approach offers some advantages from a financial and logistic point of view. As Figure A-6 shows, all process steps on the μLED can be performed within the MISEC lab at Heriot-Watt. The same applies for the manufacturing of the μLens structure, with the exception that the alignment and exposure process must be done externally in case MISEC does not have the necessary precision alignment and exposure tool. This is currently the case since the TAMARCK® alignment and exposure tool and the difficult handling of the single chip manufacturing inevitably results in the misalignment of the structural layer. This misalignment can not be compensated with the same exposure and alignment tool by fabricating the posts. The misalignment however, can be relatively accurately measured within the MISEC lab and the μLens can be prepared for the external step that needs to be fabricated. After having spun and baked the photoresist, the device can then be sent to an external lab which owns a high accuracy alignment tool, where the exposure can take place. The following steps can then again be done within MISEC.

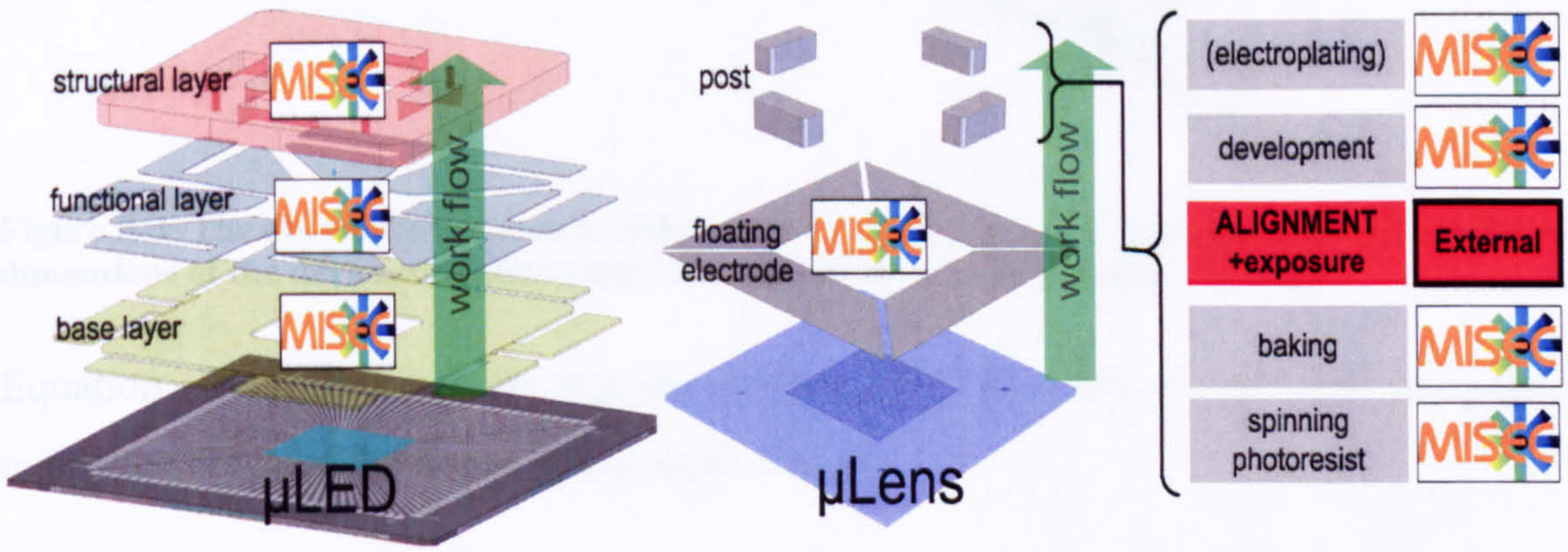

Figure A-6 For the entire device (μLens and μLED) only one fabrication step is necessary that would utilise external processing.

This solution allows to have a highly accurate device produced in a lab that does not have the necessary very expensive equipment, by reasonable costs since only one single fabrication process is involved which needs to be externally conducted.

Appendix B

Electrostatic Force Calculation

Figure B-1 shows a simplified side view of the μLens. h_m is the distance that would be measured if the theorem of intersecting lines are used; t_m stands for the trigonometrically obtained result. The difference in x-direction is a, and in z-direction, b. For the real assembly and dimensions, in particular the relatively small angle φ, this discrepancy can be neglected.

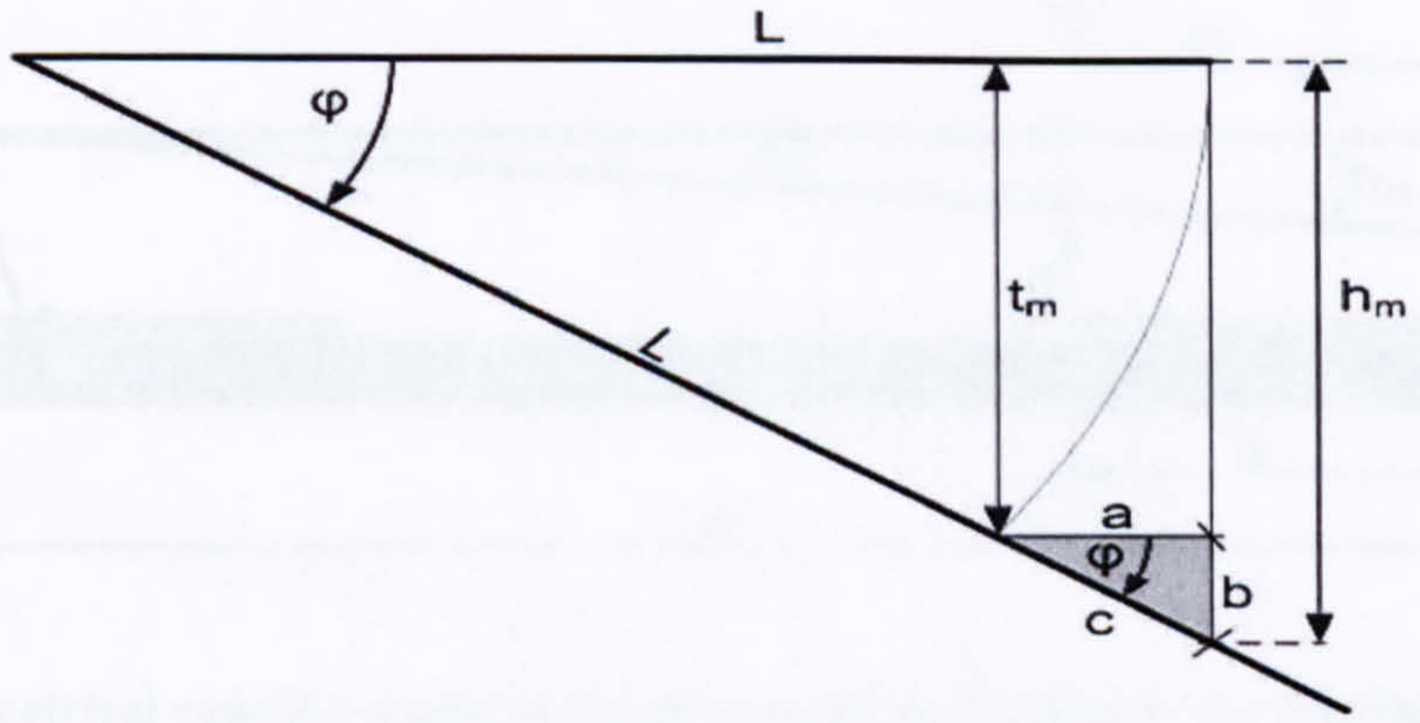

Figure B-1 The difference between t_m and h_m is in x-direction a and in z-direction, b. Given the real dimensions of the device, this difference can be neglected since the angle φ is small.

Equation (B-1) describes the trigonometric relation in order to calculate the vertical mismatch between the above stated approaches

$$a = L \cdot \left(1 - \cos(\varphi)\right) \tag{B-1}$$

with a being the difference between t_m and h_m in x-direction, L being the length between the two gel bumps and φ being the angle between no actuation and actuation of the μLens. By considering a large deflection of 70μm in vertical direction, a would be around 0.5μm. The vertical mismatch is:

$$b = \sin(\varphi) \cdot L \cdot \left(\frac{1}{\cos(\varphi)} - 1\right) \tag{B-2}$$

The numerical value of this vertical difference is in the order of 8,7nm. Both a and b can be neglected for the given task, since the required displacement in the vertical direction has only a magnitude of 10µm. By using the theorem of intersecting lines, the distance, $t_{(x)}$, between the floating and fixed electrodes at a point x, can be determined by knowing the length L, the distance m_2, and the measured height h_m as shown in Figure B-2. h_m can be measured by using the optoNCDT2400. For simplicity reasons, the gel bump situated at the origin of x', y' and z' is regarded as rigid and assumed to act as a perfect hinge.

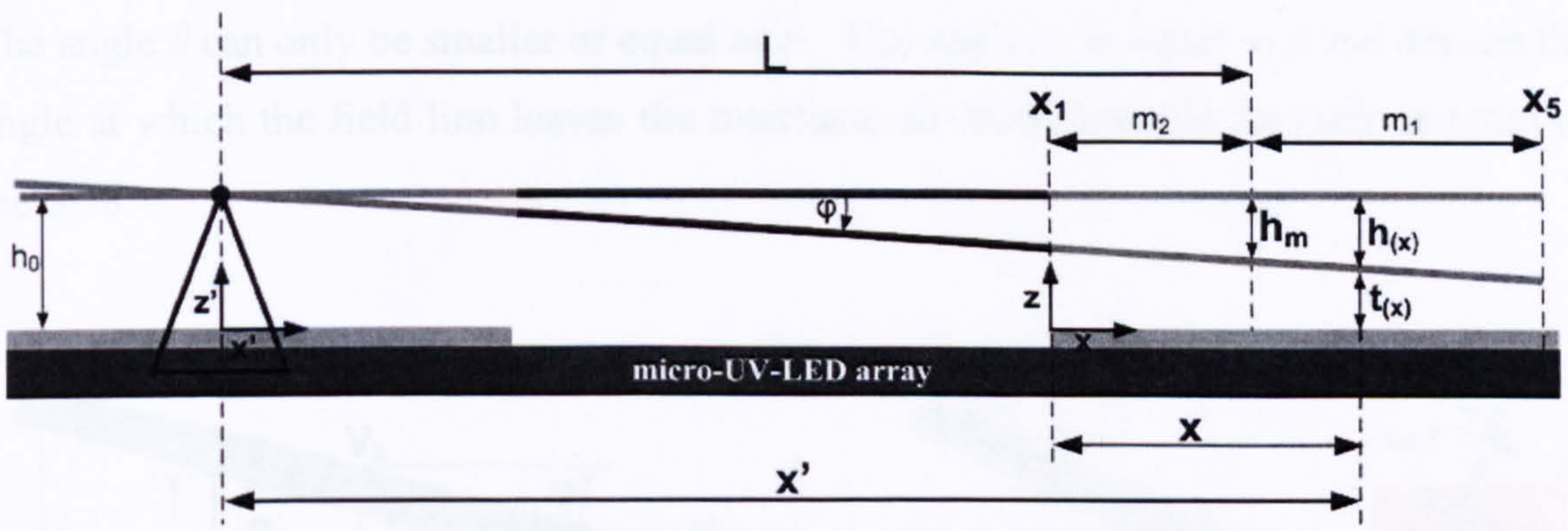

Figure B-2 Geometrical considerations of the movement and tilting of the floating-electrode. h_m is the height measured with the micro-epsilon confocal displacement measurement system. $t_{(x)}$ represents the distance between the electrode and floating electrode at point x.

This leads to:

$$t_{(x)} = h_0 - \frac{h_m \cdot (L - m_2 + x)}{L} = h_0 - h_m + \frac{h_m \cdot m_2}{L} - \frac{h_m \cdot x}{L} \qquad \text{(B-3)}$$

h_0 is the absolute distance between the electrode and floating electrode if no voltage is applied, L the distance between two of the restoring means and m_2 the lateral distance between the start of the electrode and the point of measurement of the vertical deflection.

A simplified picture of the electrostatic field lines going from the floating electrode towards the negative electrode is shown in Figure B-3. For small angles of φ, equation (B-4) becomes:

$$O = \tan(\varphi) \cdot L = S = L \cdot \varphi \,. \tag{B-4}$$

S is the arc length, L the distance between the restoring gel bumps and φ the maximal measured angle of around $16*10^{-3}$rad obtained by measuring the maximal vertical displacement of 70µm with $L = 4442$µm.

The interface of two dielectric materials, such as air and SU8, represents a discontinuity and therefore leads to a certain deflection of an electric field as shown in Figure B-3b. The angle β can only be smaller or equal as φ. The angle α_1 is equal to β and depicts the angle at which the field line leaves the interface, air-SU8, towards the bulk material of the SU8.

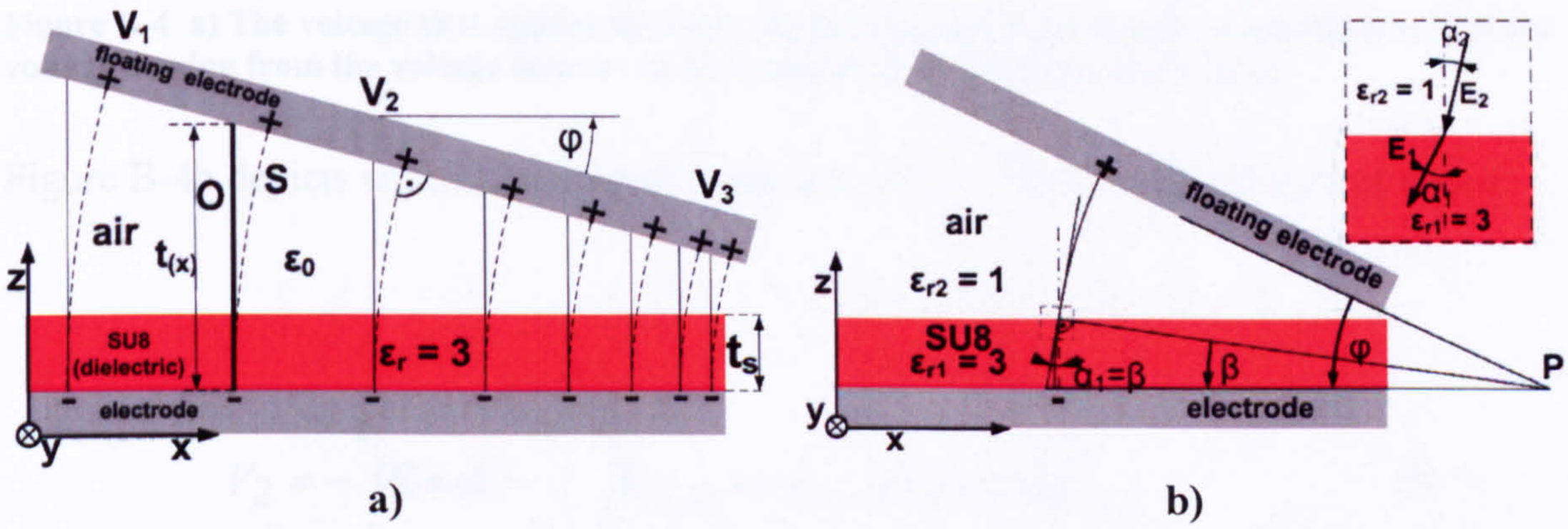

a) b)

Figure B-3 a) *t(x)* is assumed to be the same length as the arc, *S*. Voltage $V_1 = V_2 = V_3$. b) The electrostatic field lines exit the SU8 towards air with an angle of α. This is dependent on β. β is always smaller than φ.

The angle α_2, which describes the angle at which the field line enters the interface, is:

$$\alpha_2 = a\tan\left(\frac{\tan(\alpha_1) \cdot \varepsilon_{r2}}{\varepsilon_{r1}}\right), \tag{B-5}$$

where ε_{r1} is the relative permittivity of air and ε_{r2} the relative permittivity of SU8. Considering the extreme value of α_1=$16*10^{-3}$rad, the resulting angle, α_2, is around $5*10^{-3}$rad. S can be assumed to be equal to $t_{(x)}$, as shown in Figure B-3b.

To calculate the force, which is exerted on the floating electrode, the voltage between the electrodes has to be determined as shown in Figure B-4. The fact that the floating

electrode is tilted towards the fixed electrodes does only cause an inhomogeneous charge density on both types of electrodes. The overall charge on each electrode has still the value of Q. Both capacitances C_1 and C_2 have the same value. Therefore, half of the source voltage is applied on each capacitor.

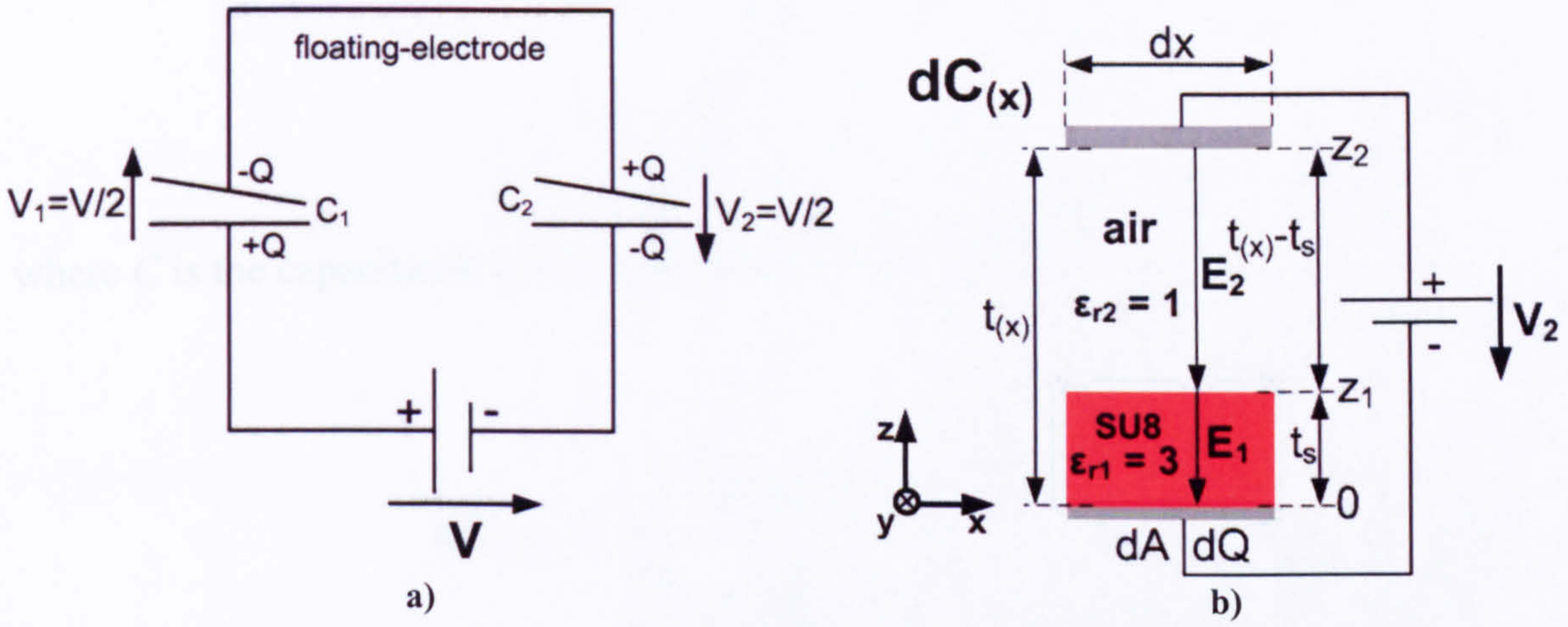

Figure B-4 a) The voltage that applies between the floating electrode and the electrode is half of the voltage coming from the voltage source . b) Determination of the capacitance $dC_{(x)}$.

Figure B-4b depicts an infinitely small capacitor, $dC_{(x)}$. The voltage V_2 is determined:

$$V_2 = -\int_0^{z_2} \mathbf{E} \bullet d\mathbf{l} = -\left(\int_0^{z_1} \mathbf{E}_{1(x)} \bullet d\mathbf{z} + \int_{z_1}^{z_2} \mathbf{E}_{2(x)} \bullet d\mathbf{z} \right), \tag{B-6}$$

where $\boldsymbol{E}_{1(x)}$ is the electric field strength within the air gap, $\boldsymbol{E}_{2(x)}$ the electric field strength within the SU8 and dz the direction segment with its limit 0, z_1 and z_2. The electric field strength depends on the relative permittivity of the dielectric material:

$$\mathbf{E}_{1(x)} = -\mathbf{z} \cdot \frac{dQ}{\varepsilon_0 \cdot \varepsilon_{r1} \cdot dA} \tag{B-7}$$

$$\mathbf{E}_{2(x)} = -\mathbf{z} \cdot \frac{dQ}{\varepsilon_0 \cdot \varepsilon_{r2} \cdot dA} \tag{B-8}$$

where $\boldsymbol{z}$ is the unit vector in z-direction and dQ is the infinite small charge which lingers on the infinite small surface, dA. ε_{r1} is the relative permittivity of SU8 and ε_{r2} the

relative permittivity of air. For the purpose of line integration, it is possible to use the infinitely small charge dQ and area dA since the electrostatic field strength is not dependent on the area. By placing equation (B-7) and equation (B-8) into equation (B-6) and using equation (B-9)

$$C = \frac{Q}{V} \tag{B-9}$$

where C is the capacitance, Q the charge and V the voltage,

$$dC_{(x)} = \frac{\varepsilon_0 \cdot dA}{\frac{t_s}{\varepsilon_{r1}} + t_{(x)} - t_s}, \tag{B-10}$$

where $dC_{(x)}$ is the infinitely small capacitance at point x, $t_{(x)}$ the overall distance between the electrode and floating electrode and t_s the thickness of the SU8. ε_{r2}, the relative permittivity of air, has a value of 1. The energy between two capacitor plates, U, is:

$$U = \frac{1}{2} \cdot C \cdot V_s^2, \tag{B-11}$$

where C is the capacitance and V_s the voltage, which is applied between the two plates of an ordinary capacitance. By applying the del-operator to that scalar energy field, the force F is:

$$\mathbf{F} = \nabla U = \frac{\partial}{\partial z} \frac{1}{2} \cdot C \cdot V_s^2 \tag{B-12}$$

The voltage V_s is replaced by the term $V/2$ to match the chosen nomenclature. Moreover, the infinitely small capacitance, $dC_{(x)}$ as obtained from equation (B-10), is used since the infinitely small force which is exerted via dA is of interest. There the denominator is substituted by the expression, d_{eff}, which stands for the effective

distance, which is a function of $t_{(x)}$ with the parameters t_s and ε_{r1}. d_{eff} is the variable to be differentiated when applying the del-operator such that:

$$d\mathbf{F} = \mathbf{z}\frac{\partial}{\partial d_{eff}}\frac{1}{2}\cdot\frac{\varepsilon_0 \cdot dA \cdot V^2}{d_{eff}\cdot 4} = -\mathbf{z}\frac{\varepsilon_0 \cdot V^2 \cdot dA}{8 \cdot d_{eff}^2} \tag{B-13}$$

This expression is integrated over the entire surface area of the electrode with d_{eff}, replaced by the dimensional variables and parameters of the device.

Now in order to make the following integration simpler and more concise, several variable substitutions are made. d_{eff} becomes

$$d_{eff} = L_1 + t_{(x)} \tag{B-14}$$

with

$$L_1 = \frac{t_s}{\varepsilon_{r1}} - t_s \tag{B-15}$$

Likewise, $t_{(x)}$ becomes

$$t_{(x)} = M_1 - M_0 \cdot x \tag{B-16}$$

with

$$M_1 = h_0 - h_m + \frac{h_m \cdot m_2}{L} \tag{B-17}$$

$$M_0 = \frac{h_m}{L} \tag{B-18}$$

where the different terms are already explained in equation (B-3) and Figure B-4.

As equation (B-13) indicates, the term, d_{eff}, needs to be squared, hence

$$d_{eff}{}^2 = a \cdot x^2 + b \cdot x + c \tag{B-19}$$

with the substitutions:

$$a = M_0{}^2 \tag{B-20}$$

$$b = -2 \cdot L_1 \cdot M_0 - 2 \cdot M_1 \cdot M_0 \tag{B-21}$$

$$c = L_1{}^2 + 2 \cdot L_1 \cdot M_1 + M_1{}^2 \tag{B-22}$$

yields the equation that is the basis for integration where *dydx* is *dA*

$$d\mathbf{F} = -\mathbf{z}\frac{\varepsilon_0 \cdot V^2}{8} \cdot \frac{1}{a \cdot x^2 + b \cdot x + c} dydx \tag{B-23}$$

The force is now calculated by integrating the area parts, R_1, R_2 and R_3 individually. Since R_3 is the area where no electrode is present, the force acting on R_3 needs to be subtracted from the sum of R_1 and R_2. The integration of half of the active area is done by discrete integration of the different geometries and then added together which subsequently yields the total force. Figure B-5 depicts this situation.

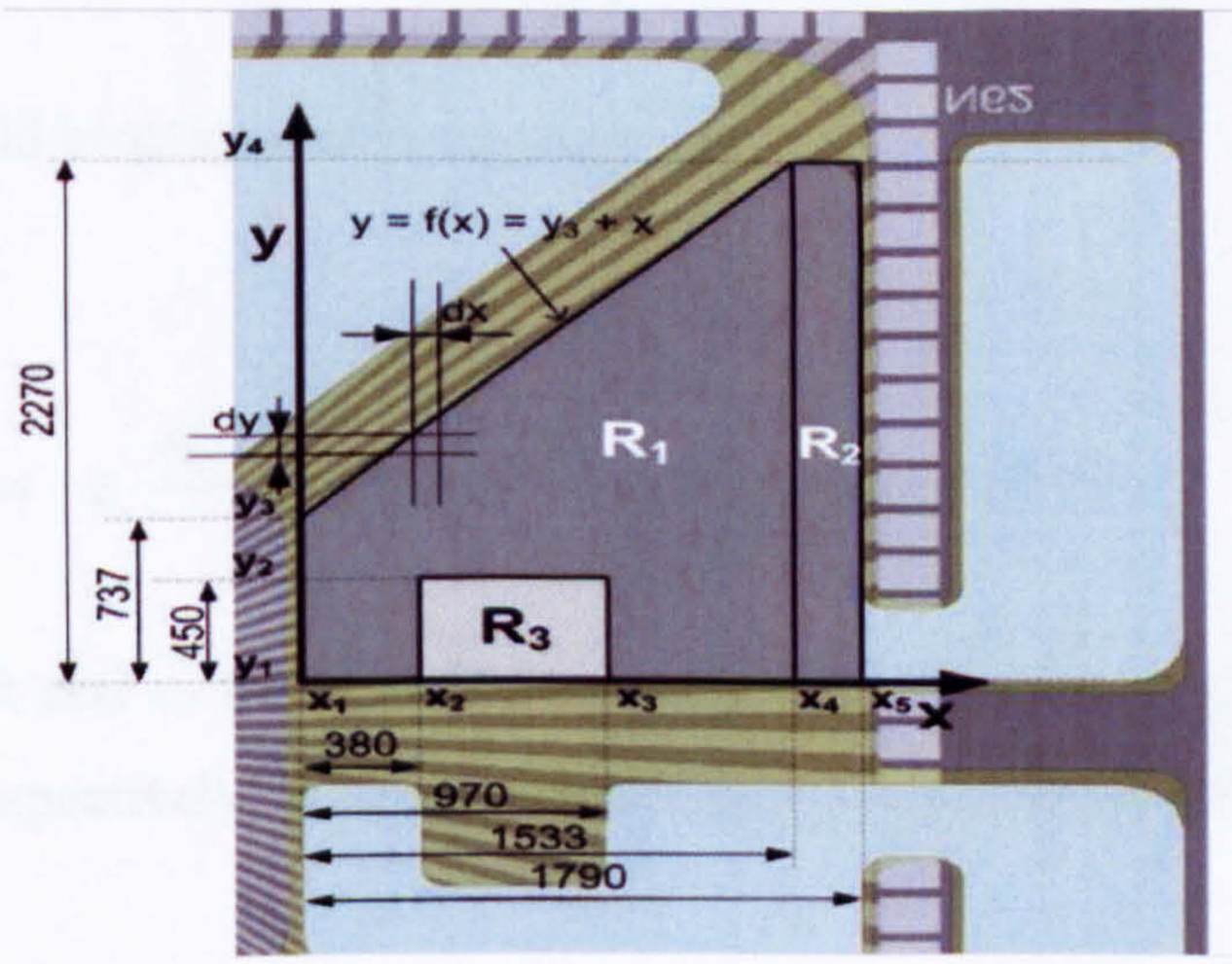

Figure B-5 The integration of half of the active area is done by discrete integration of different geometries and then added together which subsequently yields the total force.

The integral for calculating the force acting on the area of R_1 is:

$$\mathbf{F}_{R_1} = -\mathbf{z} \cdot \frac{\varepsilon_0 \cdot V^2}{8} \int_{x_1=0}^{x_4} \int_{y_1=0}^{y_3+x} \frac{1}{a \cdot x^2 + b \cdot x + c} dydx \tag{B-24}$$

where x_1 is the left, x_4 the right boundary and y_1 and y_2 represents the lower and upper boundary of R_1. All the other terms can be seen from the description of the equations above. After integration:

$$\mathbf{F}_{R_1} = -\mathbf{z} \cdot \frac{\varepsilon_0 \cdot V^2 \cdot y_3}{4} \left(\frac{1}{b} - \frac{1}{2 \cdot a \cdot x_4 + b} \right) -$$
$$\mathbf{z} \cdot \frac{\varepsilon_0 \cdot V^2}{8} \left(\frac{1}{2 \cdot a} \cdot \ln \left| a \cdot x_4{}^2 + b \cdot x_4 + c \right| + \frac{b}{a(2 \cdot a \cdot x_4 + b)} - \frac{1}{2 \cdot a} \cdot \ln |c| - \frac{1}{a} \right) \tag{B-25}$$

The substitution are kept in place to keep the expression as concise as possible. The force that is exerted via the area R_2 is:

$$\mathbf{F}_{R_2} = \mathbf{z} \cdot \frac{\varepsilon_0 \cdot V^2}{8} \int_{x_4}^{x_5} \int_{y_1=0}^{y_4} \frac{1}{a \cdot x^2 + b \cdot x + c} dydx, \tag{B-26}$$

and the resulting integrated function is:

$$\mathbf{F}_{R_2} = -\mathbf{z} \cdot \frac{\varepsilon_0 \cdot V^2 \cdot y_4}{4} \left(\frac{1}{2 \cdot a \cdot x_4 + b} - \frac{1}{2 \cdot a \cdot x_5 + b} \right) \tag{B-27}$$

The force that would be generated by the area R_3 is

$$\mathbf{F}_{R_3} = -\mathbf{z} \cdot \frac{\varepsilon_0 \cdot V^2}{8} \int_{x_2}^{x_3} \int_{y_1=0}^{y_2} \frac{1}{a \cdot x^2 + b \cdot x + c} dydx, \tag{B-28}$$

where x_2 is the left and x_3 the right boundary, and y_1 and y_2 represents the lower and upper boundary, respectively. The integrated form of equation (B-28) is

$$\mathbf{F}_{R_3} = -\mathbf{z} \cdot \frac{\varepsilon_0 \cdot V^2 \cdot y_2}{4} \left(\frac{1}{2 \cdot a \cdot x_2 + b} - \frac{1}{2 \cdot a \cdot x_3 + b} \right). \tag{B-29}$$

For the entire calculation, just one electrode was considered. The resulting force is therefore the sum of F_{R1}, F_{R2} and F_{R3} with F_{R3} being negative, multiplied by a factor of two.

Appendix C

Magnetic Force Calculation

An electrical circuit equivalent representation of the magnetic tracks can be implemented if the permeability of the ferromagnetic is assumed to be linear within the operational range of the device. Figure C-1 illustrates qualitatively how to define the magnetic resistances such as the linear resistance of air and the nonlinear magnetisation curve of an ideal soft magnetic material. The permeability is calculated as the gradient at each point of the curve, which depicts the flux density, B_{Fe}, as a function of the magnetic field intensity H_{Fe} so that:

$$\mu_{Fe} = \lim_{\Delta H_{Fe} \to o} \frac{\Delta B_{Fe}}{\Delta H_{Fe}} \tag{C-1}$$

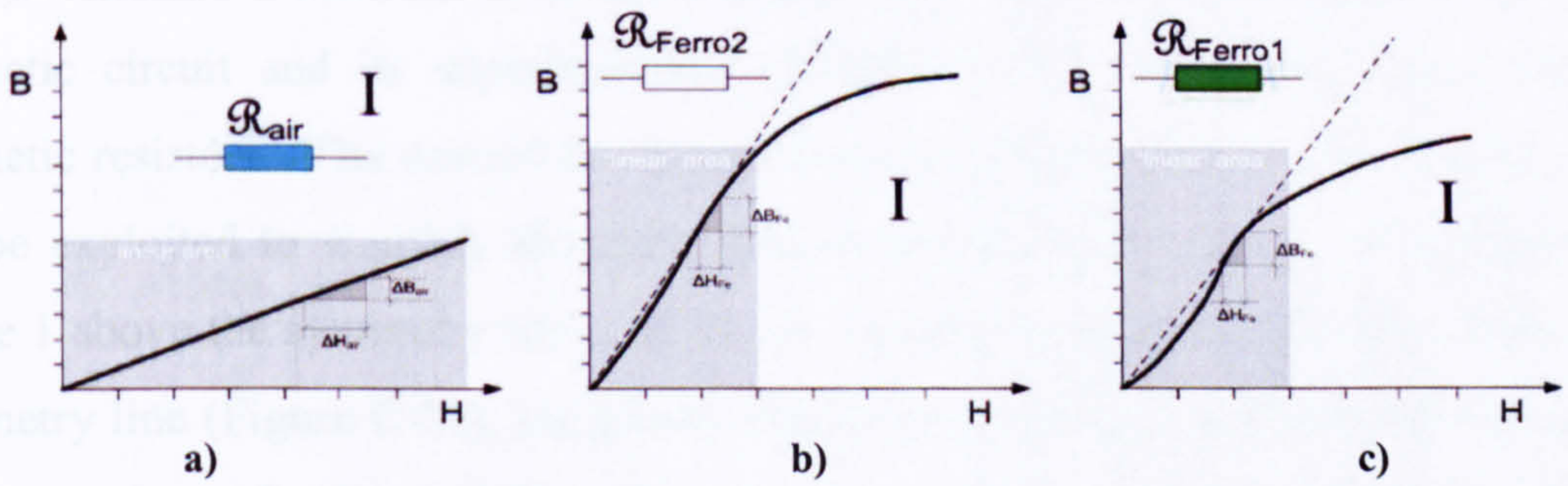

Figure C-1 The simplification made in Figure C-2 is only valid if the magnetic resistance of the ferromagnetic material can be linearised.

The magnetomotive force, Θ, is:

$$\Theta = N \cdot I = \oint_c \mathbf{H} \bullet d\mathbf{l} \tag{C-2}$$

where N is the number of turns of the coil and I is the current flowing through this coil. For a closed loop within the circuit all the magnetic field strengths, which apply over the entire length of each magnetic resistor is the same as Θ. The magnetic flux, Φ, is:

$$\phi = \int_{s} \mathbf{B} \bullet d\mathbf{s} \tag{C-3}$$

where $\boldsymbol{B}$ is the magnetic flux density and ds the infinite small surface where the vector field $\boldsymbol{B}$ passes through. The amount of the magnetic flux density, B, is the magnetic flux Φ divided by the cross-sectional area (S) perpendicular to the flow as shown below.

$$B = \frac{\phi}{S} \tag{C-4}$$

The smaller the cross-section of a magnetic conductor, the higher the magnetic flux density B. The higher the magnetic flux density the more nonlinear the curve gets until it reaches the saturation point. The magnetic resistance, $\mathcal{R}$, is defined as:

$$\Re = \frac{l}{\mu \cdot S} \tag{C-5}$$

Where l is the magnetic path length of the magnetic conductor, μ is the permeability ($\mu_0 \cdot \mu_r$), and S is the cross-sectional area. Figure 3-42 shows the 3D representation of the magnetic circuit and its superimposed schematic of the equivalent circuit with its magnetic resistors. The dashed-dot line shows the symmetry within this circuit, which can be exploited to simplify the equivalent circuit diagram further. The resistors of indice 1 above the symmetry line and the corresponding resistors of indice 2 below the symmetry line (Figure C-2a), are joined together and are then represented without any number at the end. For instance $\mathcal{R}_{aex1}$ and $\mathcal{R}_{aex2}$ are combined to $\mathcal{R}_{aex.}$. The value of $\mathcal{R}_{aex}$ is simply the sum of $\mathcal{R}_{aex1}$ and $\mathcal{R}_{aex2}$. This applies for all other magnetic resistors except for the ones that are crossed by the line of symmetry, which keep their initial value.

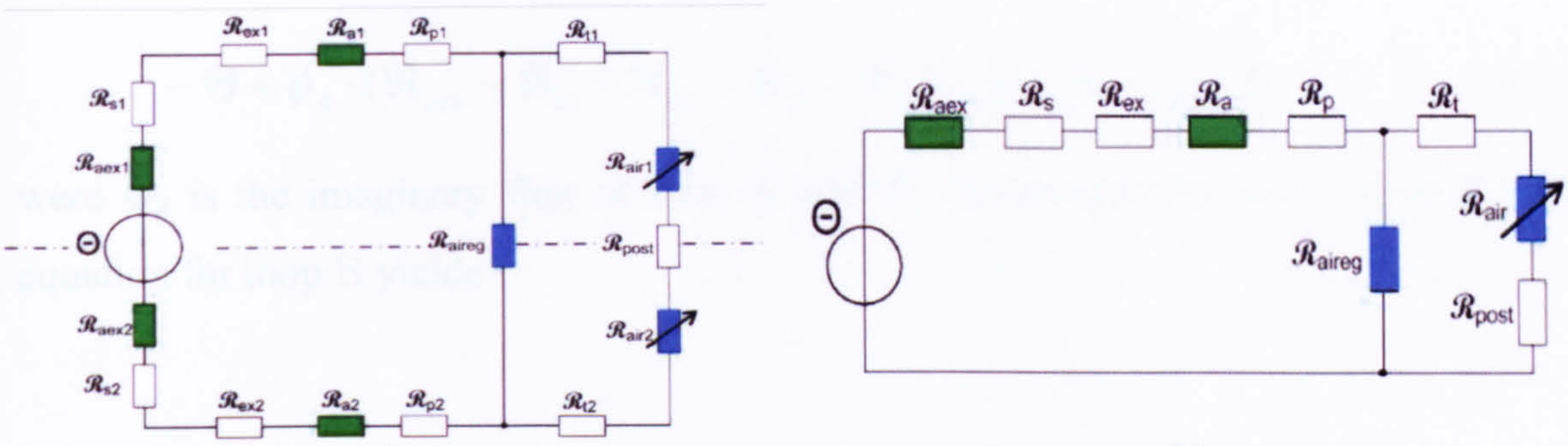

Figure C-2 a) Equivalent electric schematic of the circuit shown in Figure 3-42. The network can only be calculated if the magnetic resistors are assumed to be linear and have NO hysteresis. b) By considering the symmetry network a) can be reduced to the network shown in b).

Figure C-3 shows the same schematic as seen in Figure C-2b, with imaginary magnetic loops and their fluxes, Φ_A and Φ_B. This method yields two linear equations for the two unknown fluxes.

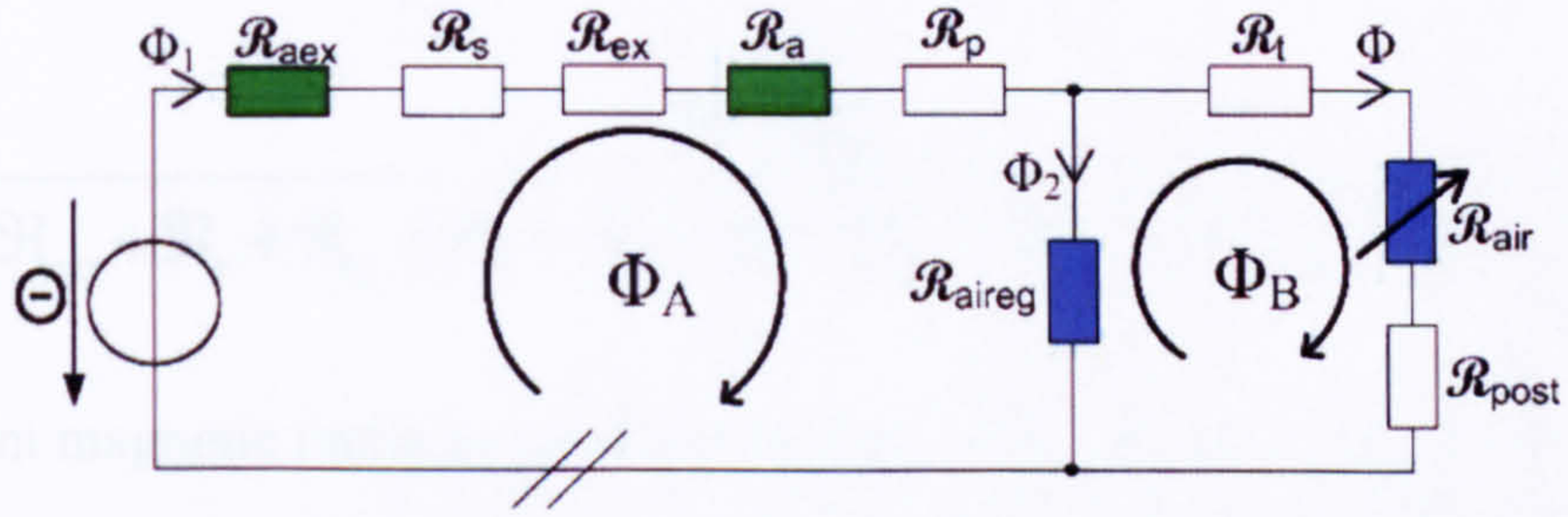

Figure C-3 Two imaginary fluxes, Φ_A and Φ_B are assumed to run in the chosen loops. This methods yields two linear equations for the two unknown variables. This approach ONLY works if the magnetic resistors are assumed to be linear.

For the following equations, Table C-1 gives a list of the nomenclature of the magnetic resistors that are shown in Figure 3-42, Figure C-2 and Figure C-3.

	Magnetic restistance of
$\mathcal{R}_{aex}$	adhesive of the external driving device
$\mathcal{R}_{s}$	material that sandwiches the isolator
$\mathcal{R}_{ex}$	magnetic path of external driving device (EDD)
$\mathcal{R}_{a}$	adhesive connecting EDD with pads

	Magnetic restistance of
$\mathcal{R}_{p}$	magnetic path of pads
$\mathcal{R}_{t}$	magnetic path of the tracks
$\mathcal{R}_{aireg}$	parasitic constant airgap between tracks
$\mathcal{R}_{air}$	variable airgap between tracks and post
$\mathcal{R}_{post}$	magnetic path of the post

Table C-1 Nomenclature of the different magnetic resistors that are used within the following equations.

The equation for loop A yields:

$$-\Theta+\phi_A\cdot(\Re_{aex}+\Re_s+\Re_{ex}+\Re_a+\Re_p)-\phi_B\cdot\Re_{aireg}=0\,, \tag{C-6}$$

were Φ_A is the imaginary flux of loop A and Φ_B the imaginary flux of loop B. The equation for loop B yields:

$$\phi_B\cdot(\Re_t+\Re_{air}+\Re_{post}+\Re_{aireg})-\phi_A\cdot\Re_{aireg}=0\,, \tag{C-7}$$

with Φ_A representing the imaginary flux of loop A and Φ_B the imaginary flux of loop B.

Equation (C-6) is now solved for Φ_A and this term is then inserted into equation (C-7). This equation is then solved for Φ_B which is equal to the wanted flux Φ:

$$\phi=\phi_B=\frac{\Theta\cdot\Re_{aireg}}{(\Re_{aex}+\Re_s+\Re_{ex}+\Re_a+\Re_p)\cdot(\Re_t+\Re_{air}+\Re_{post}+\Re_{aireg})-(\Re_{aireg})^2} \tag{C-8}$$

The different magnetic resistors are calculated by using equation (C-5). The thickness of the ferromagnetic material needs to be determined in order to get all the dimensions necessary for the calculation of the magnetic resistors. The lateral dimensions are already known due to the mask design. The permeability of the material needs to be determined. The magnetic resistors $\mathcal{R}_{air}$, $\mathcal{R}_t$, $\mathcal{R}_p$, $\mathcal{R}_a$, $\mathcal{R}_{ex}$, $\mathcal{R}_s$, and $\mathcal{R}_{aex}$ are constant for the calculations. The only variable dimension is the magnetic path length, d_m, of the magnetic resistor $\mathcal{R}_{air}$ (Figure 3-41), which represents twice the distance of the post to the faces of the tracks. By neglecting fringing fields, the area of the air gap between post and the face of the tracks is:

$$S_{air}=t_m\cdot w_m\,, \tag{C-9}$$

where w_m is the width of the air gap where the magnetic field is situated (Figure 3-41) and t_m is the height/thickness of the magnetic field. Figure 3-41c shows that t_m is not equal to the thickness of the tracks or posts and changes if the post is lifted or depressed due to the vertical movement. For this calculation however, the variable, t_m, is considered to be constant. The magnetic resistance is then calculated:

$$\Re_{air} = \frac{2 \cdot d_m}{\mu \cdot w_m \cdot t_m} \tag{C-10}$$

Knowing the flux, Φ, from equation (C-8), using equation (C-10) and dividing it by S_{air} from equation (C-9), the magnetic flux density of the driving magnetic field is:

$$B_{air} = \frac{\phi}{S_{air}} = \frac{\Theta \cdot \Re_{aireg}}{t_m \cdot w_m \cdot \left[\left(\frac{2 \cdot d_m}{\mu \cdot w_m \cdot t_m} + \Re_l + \Re_{post} + \Re_{aireg} \right) \cdot \left(\Re_{aex} + \Re_s + \Re_{ex} + \Re_a + \Re_p \right) - \left(\Re_{aireg} \right)^2 \right]} \tag{C-11}$$

The magnetic energy, U_m, confined within a volume is:

$$U_{mag} = \frac{1}{2} \int_V \mathbf{B} \bullet \frac{\mathbf{B}}{\mu} dv \tag{C-12}$$

Since the magnetic field to be considered is within air, the permeability is constant. Hence, the dot product can be regarded as a simple multiplication (the vectors ***B*** facing in the same direction). Equation (C-11) is substituted into equation (C-12) and for consistency reasons concerning the chosen coordinate system (x, y, z), the variable d_m is temporarily replaced by x hence:

$$U_{m1} = \frac{1}{2} \int_V \frac{B_{air}^{\ 2}}{\mu} dv = \frac{1}{2} \int_0^{w_m} \int_0^{t_m} \int_0^{d_m} \frac{B_{air}^{\ 2}}{\mu} dy dz dx \tag{C-13}$$

Equation (C-13) only represents the energy stored in one air gap, hence to get the total energy, equation (C-13) is multiplied by 2. Furthermore the integrals for dy and dz yield constants and can be taken out of the integral, hence:

$$U_m = w_m \cdot t_m \cdot \int_0^{d_m} \frac{B_{air}^{\ 2}}{\mu} dx \tag{C-14}$$

and

$$\mathbf{F}_m = -\mathbf{x} \cdot \frac{\partial U_m}{\partial x} = \mathbf{x} \cdot w_m \cdot t_m \cdot \frac{B_{air}{}^2}{\mu} \tag{C-15}$$

where $\boldsymbol{x}$ is the direction vector of unity in x-direction. If B_{air} of equation (C-11) is substituted one obtains:

$$\mathbf{F}_m = \mathbf{x} \cdot \frac{1}{\mu} \cdot \left(\frac{\Theta \cdot \Re_{aireg}}{t_m \cdot w_m \cdot \left[\left(\frac{2 \cdot d_m}{\mu \cdot w_m \cdot t_m} + \Re_t + \Re_{post} + \Re_{aireg} \right) \cdot \left(\Re_{aex} + \Re_s + \Re_{ex} + \Re_a + \Re_p \right) - \left(\Re_{aireg} \right)^2 \right]} \right)^2 \tag{C-16}$$

with d_m being the variable in x-direction representing the air gap.

Appendix D

Processes

D.1 Manufacturing of µLED dummy

Wafer Preparation		
Cleaning	Ultrasonic bath with Decon 90, and pure DI water alone (Acetone and IPA rinse → N2	
Dry	Place µLED on glass wafer and bake for 5min@110°C	

Gluing of µLED on glass wafer		
Spin AZ	Thin layer , 500 // 100 // 20 ; 3000 // 300 // 30	rpm // rpm/s // s
Bake	2 min @ 110°C	
Placement µLED	■ Symmetric placement from the middle of the wafer, edges close to each other (4 or 6) ■ Arrange Si/sapphire-remains around with the same height and the same surface energy in order to reduce surface tension issues. ■ Place small drop of AZ on the edge of remains facing the perimeter of the wafer (that helps additionally to hold the pieces in place)	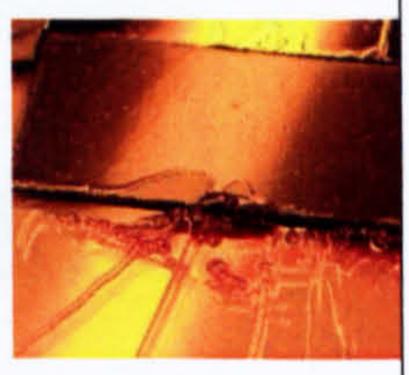
Bake	1min @ 110°C	

1: base layer

SU8-5		
Pouring SU8	■ Place wafer so that the µLED structure is in the middle of the rotation. ■ Pour SU8 over the entire area of the µLED and even slightly over the Si/sapphire remains	
Spin	Height: 6µm 500 // 100 // 20 ; 4000 // 300 // 40 Height: 2.5-2.7µm 500// 100 // 20 ; 4000// 300 // 30 Height: 2.25µm 500// 100 // 20 ; 4000// 300 // 30 (event though the wafer had a asymmetric structure (some silicon remains glued around the 3 x 2 array), it survived easily the centrifugal forces)	rpm // rpm/s // s 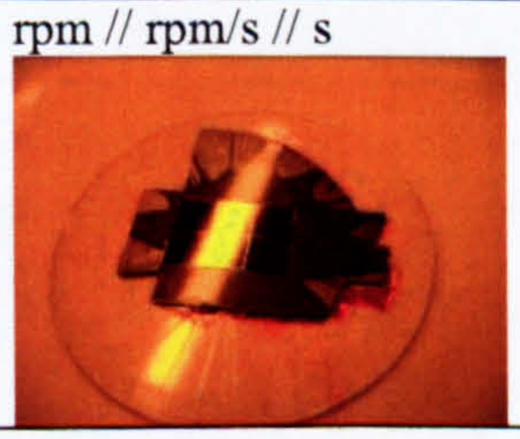
Relax	5 min	
Soft bake	5 min @ 65°C ; 5min @ 95°C	
Exposure	200mJ/cm^2 → approx 9 s with I line filter ; wavelength = 360nm	
Post bake	5min @ 65°C ; 15min @ 95°C	
Development	Around 20 s EC solvent; rinse with EC ;IPA; DI Water; N_2	
Dry	5 min@110°C	

2: functional layer

AZ Preparation for evaporation		
Spin	Height 300 // 100 // 15 ; 1200 (1000) // 30 // 300	rpm // rpm/s // s
Relax	1 min	
Bake	3 min @ 110°C	
Wait	1 h – 1 day	
Exposure	1000mJ/cm^2 (No I-Line filter) approx 17seconds	
Development	7 min in AZ developer / rinse with developer → DI water → N2	
Glueing (or tape at corners (?))	Small drops of 2 component glue on each of the 4 edges, in order to protect the devices from falling down during the evaporation process (unexposed AZ melts)	

Ebeam evaporation		
Ti	1 min 30sec @ 30 mA // 5min@ 50 mA	

AZ removal		
IPA or Acetone	Place wafer (device) into a bath of IPA and wait for 10 minutes with agitation. Alternatively acetone can be used which is more effective but also attacks the SU8 structure more.	
Rinse	(Acetone) →IPA → DI → N2 rinse	

3: structural layer

EITHER

SU8 25 (SU8 showed in many cases delamination especially during electroforming)		
Remove Glue	Remove glue on the 4 edges with a scalpel or needle	
Pouring SU8	■ Place wafer so that the µLED structure is in the middle of the rotation and place Si remains around it to have the same surface energy on the edges; use AZ on the edges (centrifugal force) ■ Pour SU8 over the whole area of the µLED and even slightly over the Si remains	
Spin	Height: 40-55µm 500 // 100 // 30 ; 1500 // 300 // 30	rpm // rpm/s // s
Relax	Relax time 5 min	
Soft bake	3 min @ 65°C ; 6 min @ 95°C	
Exposure	200mJ/cm^2 → approx 20 s with I-line filter wavelength = 360nm	
Wait	1 h	
Post bake	1 min @ 65°C ; 7 min @ 95°C	
Development	Around 3 min min EC solvent; rinse with EC ;IPA; DI Water; N_2	

OR

THB-151N from JSR (THB performs much better concerning adhesion in particular during electroplating)		
Remove Glue	Remove glue on the 4 edges with a scalpel or needle	
Pouring THB	■ Place wafer so that the µLED structure is in the middle of the rotation and place Si/sapphire remains around it to have the same surface energy on the edges; use AZ on the edges (centrifugal force) ■ Pour THB over the entire area of the µLED and even slightly over the Si/sapphire remains	
Spin	Height: 70µm ; 1000 // 300 // 30	rpm // rpm/s // s
Relax	Relax time 5 min	

Bake	5-6 min @ 120 °C	
Wait	1h	
Exposure	1000mJ/cm^2 with I line filter wavelength = 360nm	
Development	Around 15 min with TMA 238; rinse with DI Water; dry with N_2 **(DO NOT USE ACETONE OR IPA!!!)**	

4: electroformed layer

Preparation for electroplating		
Gluing µLED glass wafer	Gluing µLED onto glass wafer with one small drop of epoxy adhesive	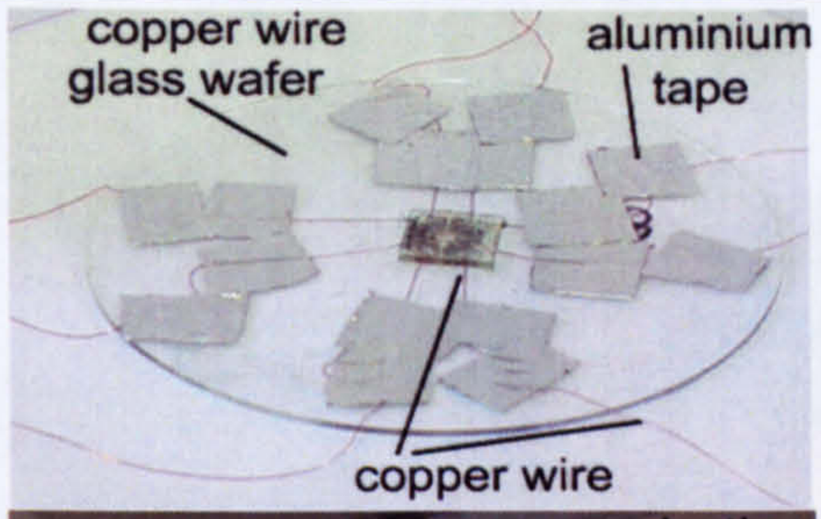
Conductive paint	Using aluminium tape, a thin copper wire is placed onto the glass wafer so that one end is touching the pad of the µLED. This is done with all 8 pads. To establish electrical connection and fixation towards the pads, a small drop of conductive paint is placed onto the wire and pad and left to cure. (Initially conductive adhesive was used, but the electrical connection was inferior compared with conductive paint, and needed a certain time of electroplating to establish connection).	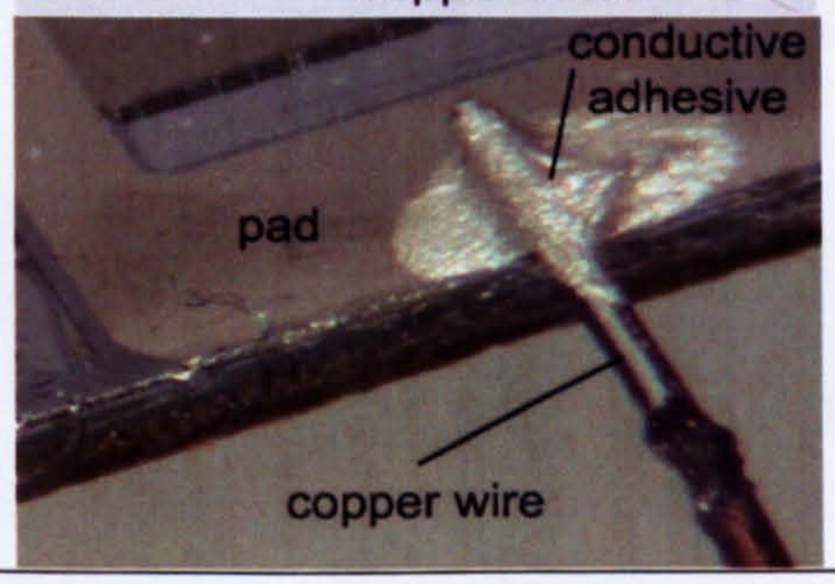
Collective electroplating	All opposite ends of the copper wires are connected together with an auxiliary electrode. The auxiliary electrode helps to control the current density better since the area that is to be electroplated is small and slight changes in the already small current value would influence the current density tremendously. An area of 2.5cm x4cm was used	
Individual electroplating	Each pad and hence electrode of the µLED can be individually addressed for electroplating if only the corresponding wire of the electrode that is to be electroplated is connected to the current source. An auxiliary electrode to control the current density better is also of necessity.	

Electroplating		
Chemical formulation	76 g/l of $Ni(NH_2SO_3)_2$, 30 g/l of boric acid and 1 g/l of fluortensid ($C_{16}H_{20}F_{17}NO_3S$) whereas the pH level of 3.5 to 4 was regulated with amidsulfon acid (40 g/l).	
Parameters	The temperature is kept at 54 °C. A current density of 1.8 A /dm^2 was recommended but 0.3A/dm^2 was used	
Electroplating	At 0.3A/dm^2 a growing rate of approximately 0.3µm/min was observed and confirmed with different measurements. A current of 30mA was used and an auxiliary electrode with an area of 2.5cm times 4cm, which is considerable bigger than the area that is to be electroplated.	

D.2 Manufacturing of the µLens

Wafer Preparation		
Cleaning	Ultrasonic bath with Decon 90, and pure DI water alone	
Additional Cleaning	The AZ layer did not homogenously stick to the sapphire glass (less problems with borosilicate glass). (This is possibly a result of surface tension. Maybe cleaning with more aggressive chemicals (such as HF?) necessary).	

Gluing of µLens on glass wafer		
Spin AZ	Thin layer , 500 // 100 // 20 ; 3000 // 300 // 30	rpm // rpm/s // s
Bake	2 min @ 110°C	
Placement µLED	Symmetric placement from the middle of the wafer, edges close to each other (4 or 6) Arrange Si -remains around with the same height and the same surface energy in order to reduce surface tension issues.	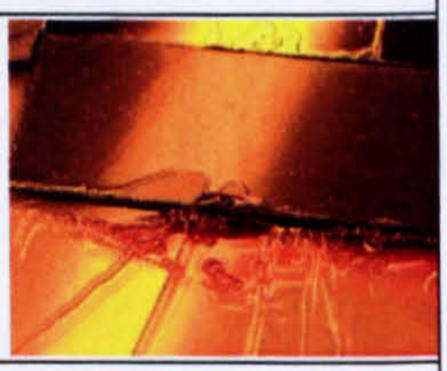
Baking	1min @ 110°C	

1:Floating electrode

AZ Preparation for evaporation			
Spin	Height 15µm Height 20µm	300 // 100 // 15 ; 1200 // 300 // 30 300 // 100 // 15 ; 800 // 300 // 30	rpm // rpm/s // s
Relax	1 min		
Wait	1 h – 1 day		
Bake	3 min @ 110°C		
Exposure	1000mJ/cm^2 (No I-Line filter) Use the mask which covers the microlens array (diagonal lines or no lines)		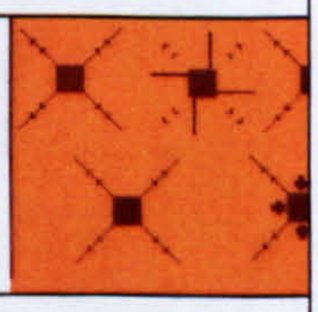
Development	7 min in AZ developer		

Ebeam evaporation or alternatively Silverspray by microstencil		
Ti	1 min30sec@ 30 mA // 2min @ 50 mA	

AZ removal		
IPA or Acetone	Place wafer (device) into a bath of IPA and wait for 10 minutes with agitation. Alternatively acetone can be used which is more effective but also attacks the SU8 structure more.	
Rinse	(Acetone) →IPA → DI → N2 rinse	

2a:SU8 post

SU8-50		
Pouring SU8	Place wafer so that the µLENS structure is in the middle of the rotation.	
Spin	Height: 232-234.7µm 500 // 100 // 20 ; 1000 // 300 // 40 (See **A.3**)	rpm // rpm/s // s
Relax	Relax time 5 min	
Soft bake	6 min @ 65°C ; 1h 25min @ 95°C	
Exposure	40 seconds with I line filter	
Wait	1 h	
Post bake	1-2min @ 65°C ; 20min @ 100°C	
Development	Around 12-14 min EC solvent; rinse with EC ;IPA; DI Water; N_2	

2b:Ni post

AZ Mask for Electroplating (according to datasheet of Microchemicals….Baking and Delays)		
Spin	500 // 100 // 10 ; 1500 // 900 // 30	
Drying	20-30min	
Soft bake	5min @ 60 °C ; 5min @100 °C	
Spin	500 // 100 // 10 ; 1500 // 900 // 30	
Drying	20-30min	
Soft bake	5min @ 60 °C ; 5min @100 °C	

AZ Mask for Electroplating (own trial)		
Spin1	800rpms	
Drying 1	1min	
Soft bake 1	3min @ 110 °C	
Spin2	800rpms	
Drying2	1min	
Soft bake2	6min @ 110 °C	
Cool down on copper block	Start temp 90°C and cool it down for 2hours	
Rehydration	For 70µm thickness approx. 5 to 12 hours (let it rest over night)	

Preparation for electroplating		
Gluing µLens on glass wafer	Gluing µLens on glass wafer with either small drops of epoxy and/or aluminium tape	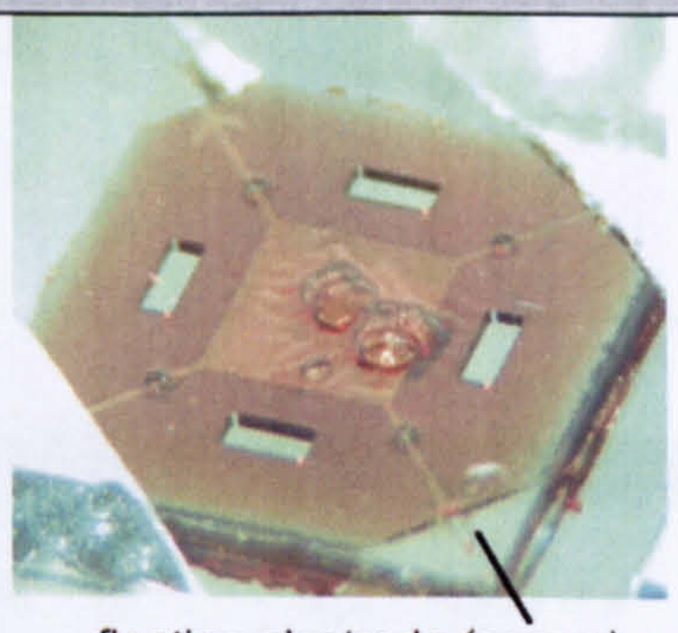
Wire conncetion	Using aluminium tape, a thin copper wire is placed onto the glass wafer so that one end is touching the corners of the floating electrode that have previously been freed from the AZ layer. Electrical connection and fixation towards the floating electrode is established by a small drop of conductive paint.	floating electrode (corner) 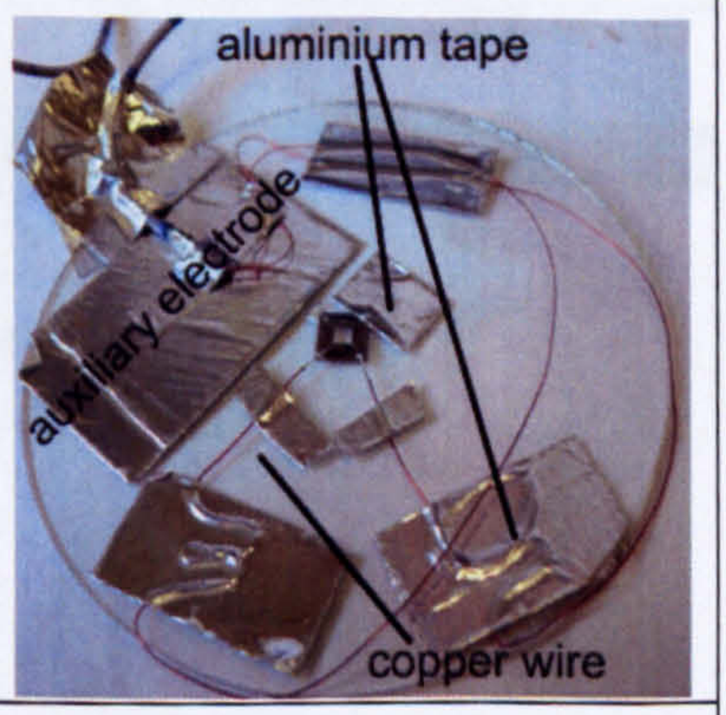
Collective electroplating	All opposite ends of the copper wires are connected together with an auxiliary electrode. The auxiliary electrode helps to control the current density better since the area to be electroplated is small and slight changes in the already small current value would influence the current density tremendously.	
Individual electroplating	Each floating electrode of the µLens can be individually addressed for electroplating if only the corresponding wire is connected to the current source. An auxiliary electrode to control the current density better is also necessary.	

Electroplating		
Chemical formulation	76 g/l of $Ni(NH_2SO_3)_2$, 30 g/l of boric acid and 1 g/l of fluortensid ($C_{16}H_{20}F_{17}NO_3S$) whereas the pH level of 3.5 to 4 was regulated with amidsulfon acid (40 g/l).	
Parameters	The temperature is kept at 54°C. A current density of 1.8 A /dm^2 was recommended but 0.3A/dm^2 was used	
Electroplating	At 0.3A/dm^2 a growing rate of approximately 0.3µm/min was observed and confirmed with different measurements. A current of 30mA was used and an auxiliary electrode with an area of 2.5cm times 4cm, which is considerable bigger than the area that is to be electroplated.	

Removal of structure		
Hotplate	30 sec @ 65 °C ; 10-20 @ 95C°	
While on hotplate	Slide device aside	

D.3 Different spin height for SU8

SU8-5		
Spin	• Height: 6µm 500 // 100 // 20 ; 4000 // 300 // 40 • Height: 2.5-2.7µm 500 // 100 // 20 ; 4000 // 300 // 30 • Height: 2.25µm 500 // 100 // 20 ; 4000 // 300 // 30 • Height: 1-2µm 500 // 100 // 20 ; 5000 // 300 // 45 (added to a already existing structure of 37µm) • Height: 2-3µm 500 // 100 // 15 ; 3000 // 300 // 30 (added to a already existing structure of 37µm)	rpm // rpm/s // s

SU8-25		
Spin	• Height: 37.7-38.3µm 500 // 100 // 15 ; 2000 // 300 // 40 • Height: 35.17-37.5µm 500 // 100 // 15 ; 2000 // 300 // 40	rpm // rpm/s // s

SU8-50		
Spin	• Height: 125-138.5µm 500 // 100 // 15 ; 4000 // 300 // 40 • Height: 166.27-173µm 500 // 100 // 30 ; 2000 // 300 // 35 • Height: 232-234.7 µm 500 // 100 // 20 ; 1000 // 300 // 40	rpm // rpm/s // s

Appendix E

MATLAB® files

E.1 MATLAB® file for displacement measurement using optoNCDT2400 via PC

The following program represents the base programmes that were used for the experimental setup for the electrostatic as well as the magnetic circuit, with all the initialisations and communication to the A/D output card (PCI 6208V, Adlink) and optoNCDT2400. For the closed loop feedback controlled system, PID blocks and the appropriate connections need to be added into the existing SIMULINK® environment (Figure E-1).

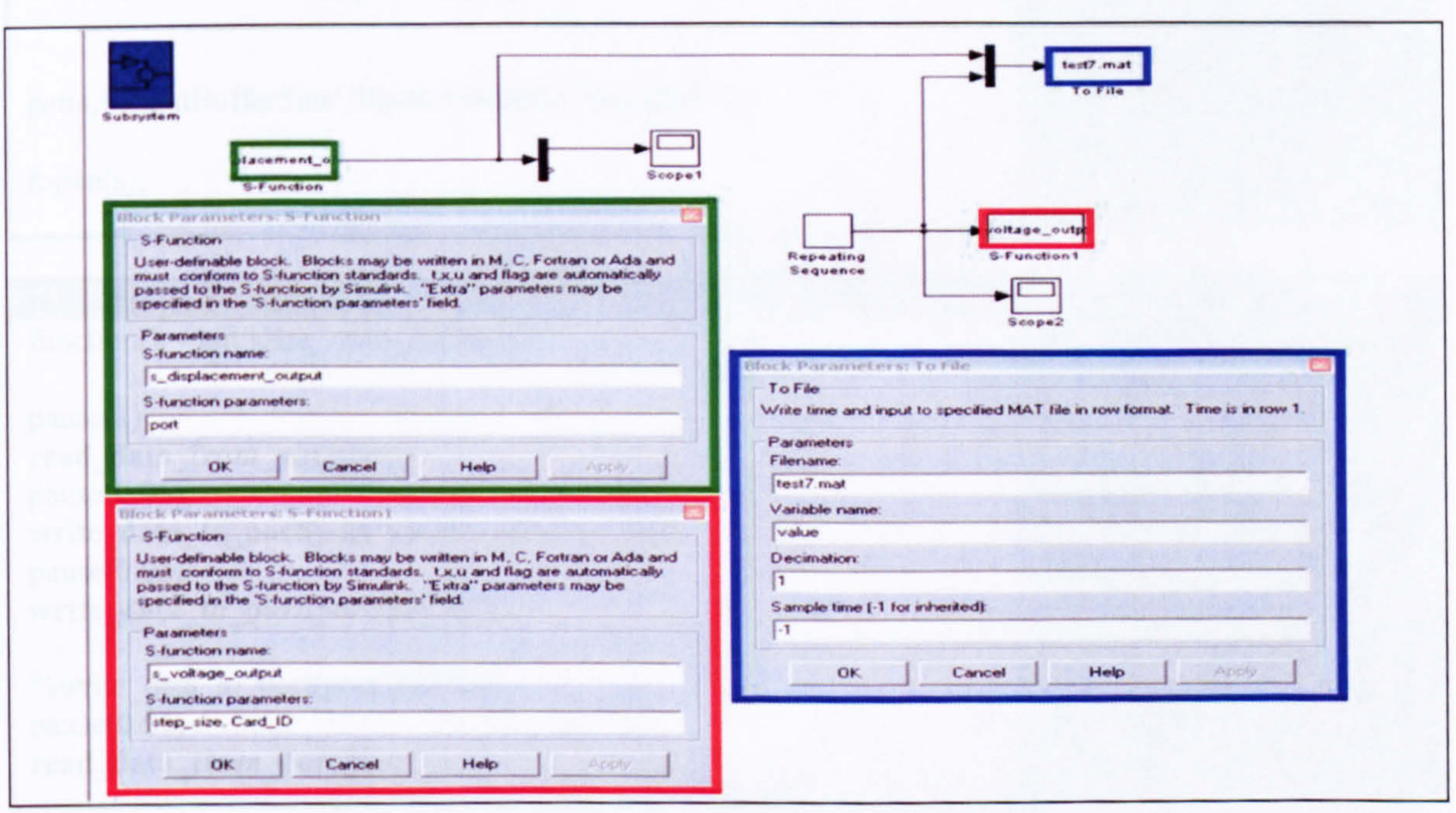

Figure E-1 SIMULINK® environment for basic step response measurements. Scope 1 depicts the displacement data send by the optoNCDT2400; Scope shows the voltage steps that are applied. Both data are stored within the blue ""to File" block. The green and the red box are S-Functions which are explained in detail within the MATLAB® source code shown below.

start_sim.m	Comment

Card_ID=Register_Card(1);
set_voltage(Card_ID,1,0);
port = **initialize_port**;
initialize_opto_2400(port);
global step_size;
global last_output;
last_output = 0;
step_size = 1/15;
	Initialise COM Communication
	Global variable step_size that can be used over the whole project

set_voltage.m

```
function[error_code] = set_voltage(Card_ID,Channel,Voltage)
ao_vwritechannel(Card_ID,Channel,Voltage);
```

Comment
Set voltage output
Function comes with Card

initialize_port.m

```
function[s] = initialize_port()

Bauds_HB      = 115200;        % from the optoNCDT2400 handbook
Databits_HB   = 8;
Parity_HB     = 'None';
Stopbit_HB    = 1;
Flux_control_HB= 'Software';

COM_port = 'COM1';


s = serial(COM_port);
set(s,'BaudRate',Bauds_HB);
set(s,'Databits',Databits_HB);
set(s,'Parity',Parity_HB);
set(s,'StopBits',Stopbit_HB);
set(s,'FlowControl',Flux_control_HB);


get(s,{'InputBufferSize','BytesAvailable','BaudRate'});

fopen(s);
```

Comment

Initialize COM-Port
From the optoNCDT2400 handbook

Device connected to COM1

Creates a serial port object "s"
Sets the Baud rate to 115200

Obtains information from the s variable

Opens file

Initialize_opto_2400.m

```
function[] = initialize_opto_2400(port)

pause(1)
read_data_from_port(port)
pause(0.05)
write_data_to_port(port,'$SOD 1,0,0,0,0,0,0,0')
pause(0.05)
write_data_to_port(port,'$SCA?')

%write_data_to_port(port,'$STS');
pause(0.05)
read_data_from_port(port)
```

Comment
Information taken from Handbook of µ-epsilon

Initialize device by writing data to port and reading data back to check if the port works properly

read_data_from_port.m

```
function[value] = read_data_from_port(port)
Bytes_ready = port.BytesAvailable;
if (Bytes_ready > 0)
   reading = fread(port,Bytes_ready);
   value = char(reading)';
   else
   disp('nothing there');
   value = '0000000';
end
```

Comment
Function to read data from a COM-port

In case bytes are ready then, read data from port

write_data_to_port.m

```
function[] = write_data_to_port(port,String)
fwrite(port,char(String))
```

Comment
Write data to COM-port to be transmitted to device

s_voltage_output.m

```
function [sys,x0,str,ts] = s_voltage_output(t,x,u,flag,step_time,Card_ID)
switch flag,
case 0
    [sys,x0,str,ts]=mdlInitializeSizes(step_time);
case 3
   sys=mdlOutputs(t,x,u,Card_ID);
case { 1, 2, 4, 9 }
   sys=[];
otherwise
   error(['Unhandled flag = ',num2str(flag)]);

end

function [sys,x0,str,ts] = mdlInitializeSizes(step_time)

sizes = simsizes;
sizes.NumContStates  = 0;
sizes.NumDiscStates  = 0;
sizes.NumOutputs     = -1;                % dynamically sized
sizes.NumInputs      = -1;                % dynamically sized
sizes.DirFeedthrough = 1;                 % has direct feedthrough
sizes.NumSampleTimes = 1;
sys = simsizes(sizes);
str = [];
x0  = [];
ts  = [step_time 0];   % inherited sample time

function sys = mdlOutputs(t,x,u,Card_ID)
set_voltage(Card_ID,1,u/100)
%ao_vwritechannel(Card_ID,u(1)/100)
% ao_vwritechannel(Card_ID,1,V_actual_global(2)/100);
% ao_vwritechannel(Card_ID,2,V_actual_global(3)/100);
% ao_vwritechannel(Card_ID,3,V_actual_global(4)/100);
sys = [1];
```

Comment

Simulink s-function that allows to change the output of the voltage output card in the Simulink environment

Gives information about the outputs,inputs,states….of the variable sizes

Set output for 4 output channels separately

s_displacement_output.m

```
function [sys,x0,str,ts] = s_cputime_output(t,x,u,flag,port)
switch flag,
case 0

   [sys,x0,str,ts]=mdlInitializeSizes;
case 3
   sys=mdlOutputs(t,x,u,port);
case { 1, 2, 4, 9 }
   sys=[];
otherwise
   error(['Unhandled flag = ',num2str(flag)]);

end

function [sys,x0,str,ts] = mdlInitializeSizes
global step_size;
sizes = simsizes;
sizes.NumContStates  = 0;
sizes.NumDiscStates  = 0;
sizes.NumOutputs     =2;                  % dynamically sized
sizes.NumInputs      =0;                  % dynamically sized
sizes.DirFeedthrough = 0;                 % has direct feedthrough
sizes.NumSampleTimes = 1;
```

Comment

Simulink s-function that allows to read the current displacement back from the measurement device and use the information in the Simulink environment

```
sys = simsizes(sizes);
str = [];
x0  = [];
ts  = [step_size 0];                    % inherited sample time

function sys = mdlOutputs(t,x,u,port)
global last_output;
% ao_vwritechannel(Card_ID,0,V_actual_global(1)/100);
% ao_vwritechannel(Card_ID,1,V_actual_global(2)/100);
% ao_vwritechannel(Card_ID,2,V_actual_global(3)/100);
% ao_vwritechannel(Card_ID,3,V_actual_global(4)/100);

value = read_current_displacement(port);

if (value == 0)
   sys(1) = last_output;
else
   sys(1) = value;
   last_output = value;
end
sys(2) = cputime;
```

Call function read_current_displacement

s_cputime_output.m

```
function [sys,x0,str,ts] = s_cputime_output(t,x,u,flag)
switch flag,
case 0

   [sys,x0,str,ts]=mdlInitializeSizes;
case 3
   sys=mdlOutputs(t,x,u);
case { 1, 2, 4, 9 }
   sys=[];
otherwise
   error(['Unhandled flag = ',num2str(flag)]);

end

function [sys,x0,str,ts] = mdlInitializeSizes

sizes = simsizes;
sizes.NumContStates  = 0;
sizes.NumDiscStates  = 0;
sizes.NumOutputs     =1;                % dynamically sized
sizes.NumInputs      = 1;               % dynamically sized
sizes.DirFeedthrough = 0;               % has direct feedthrough
sizes.NumSampleTimes = 1;
sys = simsizes(sizes);
str = [];
x0  = [];
ts  = [-1 0];                           % inherited sample time

function sys = mdlOutputs(t,x,u)
% ao_vwritechannel(Card_ID,0,V_actual_global(1)/100);
% ao_vwritechannel(Card_ID,1,V_actual_global(2)/100);
% ao_vwritechannel(Card_ID,2,V_actual_global(3)/100);
% ao_vwritechannel(Card_ID,3,V_actual_global(4)/100);
sys = [cputime];
```

Comment

Simulink s-function that outputs the current cputime (the time since starting MATLAB program enivornment) to provide a unique timestamp for measurements

Read_current_displacement.m

```
function[Displacement] = read_current_displacement(port)


%write_data_to_port(port,'$SRA6')
%pause(0.5)
%write_data_to_port(port,'$SOD 1,0,0,0,0,0,0,0')

%write_data_to_port(port,'$SOD?');
%pause(0.3)
data = read_data_from_port(port);

size_data = size(data);
value=data(size_data(2)-6:size_data(2));
Displacement = str2num(value);
size_Disp = size(Displacement);

Displacement = Displacement / 32767 *1000;

if (size_Disp(1) ~= 1)
   Displacement = 0;
end

if (size_Disp(2) ~= 1)
   Displacement = 0;
end


%data((size_data(2)-18):size_data(2)-14)
```

Comment

Function called by **s_displacement_output.m** to read the current displacement from the displacement measurement device.

Read string of data from device.

Convert raw data to proper data

Convert raw information into displacement
In case no data is available at the port, the output of the function is 0.

define_steps_step.m

Prior to run the simulink file, data of different step sizes and timings need to be entered

```
step        = 50;                          %Voltage step height

min_val     = 0;                           %Minimum voltage
max_val     = 600;                         %Maximum Voltage

time_wait_up  = 300;                       %Time for voltage high
time_wait_down= 1200;                      %Time at zero
initial_wait  = 2000;

signal_length = (max_val-min_val)/step*2+1;
N_steps = (max_val-min_val)/step+1
raw_values = min_val:step:max_val;

values = [];
for i = 1 : N_steps
   values = [values 0 0 raw_values(i) raw_values(i)];
end
values = [values 0];

times = [ 0 initial_wait initial_wait];

for i = 1 : N_steps-1
   times = [times max(times)+time_wait_up max(times)+time_wait_up
max(times)+time_wait_down+time_wait_up
max(times)+time_wait_down+time_wait_up]
end
times = [times max(times)+time_wait_up max(times)+time_wait_up]
times;
```

Comment

This function defines the output-voltage pattern that is used to drive the device. The actual commands are secondary, what is important is that two arrays are created, times and values which define the time and voltage values

The output arrays of this function were used to assess the long-term reliability of the device

values;

disp(sprintf('time for one sequence = %g s (%g
hours)',max(times),max(times)/60/60));
plot(times,values)

Define_steps_sensitivity Prior to run the simulink file, data of different step sizes and timings need to be entered.	Comment

step = 25;
min_val = 0;
max_val = 600;
time_wait = 120;
initial_wait = 300;
 	
signal_length = (max_val-min_val)/step*2+1;
N_steps = (max_val-min_val)/step;
raw_values = min_val:step:max_val;
 	
for i = 1 : length(raw_values)
values(2*i) = raw_values(i);
values(2*i-1) =raw_values(i);
end
times= [0 initial_wait initial_wait];
for i = 1 : N_steps-1;
times = [times max(times)+time_wait max(times)+time_wait];
end
times = [times max(times)+time_wait];
times
values
disp(sprintf('time for one sequence = %g s (%g
hours)',max(times),max(times)/60/60));
%times = [0 2 2 4 4 6 6 8 8 10 10 12];
%values =[1 1 2 2 3 3 4 4 5 5 6];
 	
plot(times,values)
	This function defines the output-voltage pattern that is used to drive the device. The actual commands are secondary, what is important is that two arrays are created, times and values which define the time and voltage values
	
	The output arrays of this function were used to assess the sensitivity of the device

end_sim.m	Comment
close_port(port); instrfind;	

References

[1] M. Tabib-Azar, *Microactuators : electrical, magnetic, thermal, optical, mechanical, chemical & smart structures*. Boston, London: Kluwer Academic, 1998.

[2] J. E. Huber, N. A. Fleck, and M. F. Ashby, "Selection of mechanical actuators based on performance indices," *Proceedings of the Royal Society of London, Series A: Mathematical, Physical and Engineering Sciences*, vol. 453, pp. 2185-2205, 1997.

[3] H. L. Tuller, "Microactuators," Norwell, 1998.

[4] P. B. J. Mohr, M. Stohrmann, U. Wallrabe, "Microactuators fabricated by the LIGA process," *Journal of Micromechanics and Microengineering* vol. 4, pp. 234-241, 1992.

[5] R. Legtenberg, A. W. Groeneveld, and M. Elwenspoek, "Comb-drive actuators for large displacements," *Journal of Micromechanics and Microengineering*, vol. 6, pp. 320-329, 1996.

[6] J. U. Jeon and T. Higuchi, "Electrostatic suspension of dielectrics," *IEEE Transactions on Industrial Electronics*, vol. 45, pp. 938-946, 1998.

[7] J. Jin, T. Higuchi, and M. Kanemoto, "Electrostatic levitator for hard disk media," *IEEE Transactions on Industrial Electronics*, vol. 42, pp. 467-473, 1995.

[8] A. P. Lee, C. F. McConaghy, G. Sommargren, P. Krulevitch, and E. W. Campbell, "Vertical-actuated electrostatic comb drive with in situ capacitive position correction for application in phase shifting diffraction interferometry," *Journal of Microelectromechanical Systems*, vol. 12, pp. 960, 2003.

[9] K. Minami, S. Kawamura, and M. Esashi, "Fabrication of distributed electrostatic micro actuator (DEMA)," *Journal of Microelectromechanical Systems,* , vol. 2, pp. 121-127, 1993.

[10] M. J. Madou, *Fundamentals of microfabrication : the science of miniaturization*, 2nd ed. Boca Raton, FL: CRC Press, 2001.

[11] W. S. N. Trimmer, "Microrobots and Micromechanical Systems," *Sensors and actuators*, vol. 19, pp. 267-287, 1989.

[12] P. Rai-Choudhury, *MEMS and MOEMS technology and applications*. Bellingham, Wash.: SPIE Press, 2000.

[13] B. Wagner, M. Kreutzer, and W. Benecke, "Linear and rotational magnetic micromotors fabricated using silicon technology," Travemuende, D, 1992.

[14] B. Wagner, M. Kruetzer, and W. Beneceke, "Permanent magnet micromotors on silicon substrates," *Journal of Microelectromechanical Systems*, vol. 2, pp. 23-29, 1993.

[15] C. H. Ko, J. J. Yang, J. C. Chiou, S. C. Chen, and T. H. Kao, "Magnetic analysis of a micromachined magnetic actuator using the finite element method," *Proceedings of SPIE - The International Society for Optical Engineering*, vol. 3893, pp. 127-136, 1999.

[16] J. A. Wright, Y.-C. Tai, and S.-C. Chang, "Large-force, fully-integrated MEMS magnetic actuator," presented at International Conference on Solid-State Sensors and Actuators, IEEE, Piscataway, NJ, USA, 1997.

[17] L. K. Lagorce, O. Brand, and M. G. Allen, "Magnetic microactuators based on polymer magnets," *Journal of Microelectromechanical Systems,* , vol. 8, pp. 2-9, 1999.

[18] H. Maekoba, P. Helin, G. Reyne, T. Bourouina, and H. Fujita, "Self-aligned vertical mirror and V-grooves applied to an optical-switch: modeling and optimization of bi-stable operation by electromagnetic actuation," *Sensors and Actuators, A: Physical*, vol. 87, pp. 172-178, 2001.

[19] Q. Zou, U. Sridhar, and R. Lin, "Study on micromachined bimetallic actuation," *Sensors and Actuators, A: Physical*, vol. 78, pp. 212-219, 1999.

[20] W.-H. Chu, M. Mehregany, and R. L. Mullen, "Analysis of tip deflection and force of a bimetallic cantilever microactuator," *Journal of Micromechanics and Microengineering*, vol. 3, pp. 4-7, 1993.

[21] J. T. Butler, V. M. Bright, and W. D. Cowan, "Average power control and positioning of polysilicon thermal actuators," *Sensors and Actuators, A: Physical*, vol. 72, pp. 88-97, 1999.

[22] Y. Wang, Z. Li, D. T. McCormick, and N. C. Tien, "A micromachined RF microrelay with electrothermal actuation," *Sensors and Actuators, A: Physical*, vol. 103, pp. 231-236, 2003.

[23] R. Hickey, D. Sameoto, T. Hubbard, and M. Kujath, "Time and frequency response of two-arm micromachined thermal actuators," *Journal of Micromechanics and Microengineering*, vol. 13, pp. 40-46, 2003.

[24] M. J. Sinclair, "High force low area MEMS thermal actuator," *Thermomechanical Phenomena in Electronic Systems -Proceedings of the Intersociety Conference*, Las Vegas, NV, USA, vol. 1, pp. 127-132, 2000.

[25] G.-B. Lee, R. S. Chen, and C. Kung, "Analysis of the optimal dimension on the electrothermal microactuator," *Journal of Micromechanics and Microengineering*, vol. 12, pp. 291, 2002.

[26] R. A. Conant and R. S. Muller, "Cyclic fatigue testing of surface-micromachined thermal actuators," *Proceedings of the 1998 ASME International Mechanical Engineering Congress,* Anaheim, CA, USA, pp. 273-277, 1998.

[27] H. Veladi, R. R. A. Syms, and H. Zou, "Fiber-pigtailed electrothermal MEMS Iris VOA," *Journal of Lightwave Technology*, vol. 25, pp. 2159-2167, 2007.

[28] W. L. Benard, H. Kahn, A. H. Heuer, and M. A. Huff, "Thin-film shape-memory alloy actuated micropumps," *Journal of Microelectromechanical Systems,* , vol. 7, pp. 245-251, 1998.

[29] Chemat, "Solgel Processing," *www.chemat.com/html/solgel.htm*.

[30] T. Hayashi, T. Inoue, and Y. Akiyama, "Low temperature sintering of PZT powders coated with Pb5Ge3O11 by sol-gel method," *Journal of the European Ceramic Society*, vol. 19, pp. 999, 1999.

[31] J. C. Gunter, S. K. Streiffer, and A. I. Kingon, "Low temperature preparation of sol-gel PZT thin films for pyroelectric and other integrated devices,"*IEEE International Symposium on Applications of Ferroelectrics,*East Brunswick, NJ, USA, pp. 223-226, 1996.

[32] Z. Wei, K. Yamashita, and M. Okuyama, "Low temperature preparation of sol-gel PZT thin film annealed at 160°C by hydrothermal method," *IEEE International Symposium of Application of Ferroelectrics*, Honolulu, HI, USA, pp. 921-924, 2000.

[33] R. W. Whatmore, Q. Zhang, Z. Huang, and R. A. Dorey, "Ferroelectric thin and thick films for microsystems," *Material Science in Semiconductor Processing,* vol. 5, pp. 65-76, 2002.

[34] I. J. Busch-Vishniac, "Case for magnetically driven microactuators," *Sensors and Actuators, A: Physical*, vol. 33, pp. 207-220, 1992.

[35] G. C. Boisset, B. Robertson, W. S. Hsiao, M. R. Taghizadeh, J. Simmons, K. Song, M. Matin, D. A. Thompson, and D. V. Plant, "On-die diffractive alignment structures for packaging of microlens arrays with 2-D optoelectronic device arrays," *IEEE Photonics Technology Letters* , vol. 8, pp. 918-920, 1996.

[36] S. Eitel, S. J. Fancey, H. P. Gauggel, K. H. Gulden, W. Bachtold, and M. R. Taghizadeh, "Highly uniform vertical-cavity surface-emitting lasers integrated with microlens arrays," *IEEE Photonics Technology Letters*, vol. 12, pp. 459-461, 2000.

[37] M. T. Gale, J. Pedersen, H. Schutz, H. Povel, A. Gandorfer, P. Steiner, and P. N. Bernasconi, "Active alignment of replicated microlens arrays on a charge-coupled device imager," *Optical Engineering*, vol. 36, pp. 1510-1517, 1997.

[38] K. W. Oh, C. H. Ahn, and K. P. Roenker, "Flip-chip packaging using micromachined conductive polymer bumps and alignment pedestals for MOEMS," *IEEE Journal on Selected Topics in Quantum Electronics*, vol. 5, pp. 119-126, 1999.

[39] N. R. Basavanhally, M. F. Brady, and D. B. Buchholz, "Optoelectronic packaging of two-dimensional surface active devices," *IEEE Transactions on Components, Packaging, and Manufacturing Technology, Part B: Advanced Packaging,* vol. 19, pp. 107-115, 1996.

[40] A. Tuantranont, V. M. Bright, J. Zhang, W. Zhang, J. A. Neff, and Y. C. Lee, "Optical beam steering using MEMS-controllable microlens array," *Sensors and Actuators, A: Physical*, vol. 91, pp. 363-372, 2001.

[41] K. Hoshino and I. Shimoyama, "An elastic thin-film microlens array with a pneumatic actuator,"*14th IEEE International Conference on Micro Electro Mechanical Systems (MEMS),* Interlaken, CH, pp. 321-324, 2001.

[42] A. Jain and H. Xie, "An electrothermal microlens scanner with low-voltage large-vertical-displacement actuation," *IEEE Photonics Technology Letters*, vol. 17, pp. 1971-1973, 2005.

[43] K. Hedsten, J. Melin, J. Bengtsson, P. Modh, D. Karlen, B. Lofving, R. Nilsson, H. Rodjegard, K. Persson, P. Enoksson, F. Nikolajeff, and G. Andersson, "MEMS-based VCSEL beam steering using replicated polymer diffractive lens," *Sensors and Actuators, A: Physical*, vol. 142, pp. 336-345, 2008.

[44] C.-P.-B. Siu, H. Zeng, and M. Chiao, "Magnetically actuated MEMS microlens scanner for in vivo medical imaging," *Optics Express*, vol. 15, pp. 11154-11166, 2007.

[45] H. W. Choi, E. Gu, "GaN micro-light-emitting diode array with monolithically integrated sapphire microlenses," *Applied Physics Letters*, vol. 84, pp. 2253-2255, 2004.

[46] V. Poher, G. Kennedy, K. Nikolic, H. Zhang, Z. Gong, E. Drakakis, E. Gu, M. Dawson, P. French, P. Degenaar, M. Neil, "Micro-LED arrays: A tool for two-dimensional neuron stimulation," *Journal of Physics D: Applied Physics*, vol. 41, pp. 094014-1 -094014-9, 2008.

[47] C. Griffin, H. W. Choi, C. W. Jeon, J. M. Girkin, M. D. Dawson, G. McConnell, "Beam divergence measurements of InGaN/GaN micro-array light-emitting diodes using confocal microscopy," *Applied Physics Letters*, vol. 86, pp. 041111-1-041111-3, 2005.

[48] S. Sinzinger, J. Jahns, *Microoptics*. Weinheim: Wiley-VCH, 1999.

[49] R. S. D. Daly, M. C. Hutley, "Microlens arrays," *IOP Short Meetings Series No 30*, Teddington, UK, 1991.

[50] T. N. Oder, J. Y. Lin, H. X. Jiang, "Nitride microlens arrays for blue and ultraviolet wavelength applications," *Applied Physics Letters*, vol. 82, pp. 3692-3694, 2003.

[51] E. Hecht, *Optics*, 4 ed. San Francisco: Addison Wesley, 2002.
[52] R. S. Dhariwal, J. M. Torres, and M. P. Y. Desmulliez, "Electric field breakdown at micrometre separations in air and nitrogen at atmospheric pressure," *IEE Proceedings-Science, Measurement and Technology*, vol. 147, pp. 261-265, 2000.
[53] R. M. Christensen, *Theory of viscoelasticity : an introduction*, 2nd ed. ed. New York ; London: Academic, 1982.
[54] Y. M. Haddad, *Viscoelasticity of engineering materials*, London: Chapman & Hall, 1995.
[55] H. Waller, R. Schmidt, *Schwingungslehre fuer Ingenieure*, Springer, Berlin, 1989.
[56] K. G. Hans-Juergen Butt, Michael Kappl, *Physics and Chemistry of Interfaces*, Weinheim, WILEY-VCH, 2003.
[57] P. Molter, Formulation Electroplating Bath, FH Kaiserslautern, Standort Zweibruecken, 2006.
[58] M. Nordstrom, A. Johansson, E. S. Nogueron, B. Clausen, M. Calleja, and A. Boisen, "Investigation of the bond strength between the photo-sensitive polymer SU-8 and gold," *Microelectronic Engineering*, vol. 78-79, pp. 152-157, 2005.
[59] H. Lutz, W. Wendt, *Taschenbuch der Regelungstechnik*: Harry Deutsch, 2002.
[60] D. Flynn, L. Allen, R. Dhariwal, M. P. Y. Desmulliez, "Characterization of Core Materials for Microscale Magnetic Components Operating in the Megahertz Frequency Range," *IEEE Transactions on Magnetics*, vol. 43, pp. 3171-3180, 2007.